Analysis and Extension of Earthquake Rupture Dynamics

A methodological exploration & links to global geodynamic studies

Dissertation zur Erlangung des Doktorgrades
and der Fakultät für Geowissenschaften
der Ludwig-Maximilians-Universität München

Vorgelegt von
Jorge Nicolas Hayek Valencia

München, den 19.09.2024

LMU Munich
Ludwig-Maximilians-Universität München
Faculty of Geosciences

Submitted 19.09.2024;
Date of defense 19.02.2025;
Supervisors
(Erstgutachter) Prof. Dr. Hans-Peter Bunge
(Zweigutachter) Prof. Dr. Alice-Agnes Gabriel

ANALYSIS AND EXTENSION OF EARTHQUAKE RUPTURE DYNAMICS: A METHODOLOGICAL EXPLORATION & LINKS TO GLOBAL GEODYNAMIC STUDIES

Dedicated to Sofie, my family and friends.
We are a mosaic of everyone who has been part of our journey.

Let the unknown inspire, not terrify, after all that's what put us on the shoulders of giants.

- Friendly reminder to the reader

"I learned very early the difference between knowing the name of something and knowing something"

- Richard Feynman

"The purpose of models is not to fit the data but to sharpen the questions"

- Samuel Karlin

Abstract

Geophysics is a broad field that explains phenomenons on earth from an interdisciplinary and data rich perspective. One of its modern ramifications is earthquake rupture dynamics, in which the material properties and the stress field are collapsed onto a compact support in which maximum shear deformation localizes –or the fault plane is defined–, and its contextualization in the framework of friction brings a mechanical understanding of the energy budget throughout the fault, and thus of the dynamic propagation of the rupture. This nonlinear behaviour is reflected in the source characteristics that are identified, interpreted, and validated against observables, such as on-fault asperities, supershear occurrence, backward, bilateral and unilateral propagation, among others. This fundamentally data- and physics-driven approach faces particular challenges in constraining the initial conditions governing fault stresses and strengths, as it is highly sensitive to these parameters.

This dissertation explores the extension of the initial conditions and assumptions used in rupture dynamic models through physics-driven methodologies. We first present a diffuse volumetric fault representation as an alternative to the traditional assumption of an infinitesimally thin fault representation. The study presents a 2D PETSc spectral element adaptation, *se2dr*, which adopts the stress glut method with a steady-state phase-field ansatz to reduce inherent spurious oscillations from the stress discontinuities inherent to the original stress glut method. The model successfully replicates planar interface results, while revealing dynamic complexities such as fault-oblique yielding within the volumetric fault zone. In a next step, we adopt a state-of-art dynamic rupture software *SeisSol* to investigate the dynamics of the 2021 M_w7.4 Maduo earthquake. In this study we inform 3D dynamic rupture simulations, accounting for off-fault plasticity, with geodetically-inferred on-fault stress heterogeneities. The model can explain the event's complex kinematics and observations, in particular the mechanical viability of unilateral supershear propagation across this multi-segment fault system and its associated observational signatures. We further inform 3D dynamic rupture simulations, by coupling its initial conditions to the output of a long-term regional geodynamic model from *pTatin3D*. We develop a workflow to extract a fault geometry from the shear zone emergent from the evolving plastic strain in the long-term model. The study compares the effect of choices of the rheology and its associated stress, consistent with the fault geometry, on the dynamics of earthquake, the energy released, and its impact as an rupture arresting mechanism.

The next part of this dissertation explores potential insights gained from a global geodynamic context, to understand large-scale deformation and the ambient stress field, thereby providing a contextual mechanical framework to regional studies. Following this line of thought, we extract maps of erosional/non-depositional periods, or hiatus, that serve as proxies for vertical surface deflections induce by mantle convection, or dynamic topography. This study highlights the temporal and spatial variation of such hiatus surfaces across continents, offering a test for mantle flow retrodictions and an observational tool to support the identification mantle flow regimes. Finally, we analyze the role of the mantle flow as a driver for the horizontal stress field from an analytical, Couette-Poisseuille flow representation of the asthenosphere. This study provides a process-driven explanation for global stress patterns observed in stress indicators compiled in the World Stress Map. It emphasizes the importance of considering a global domain in geodynamic studies, and carries implications on the expected asthenospheric stress magnitudes.

Acknowledgements

Special thanks to everyone –past, present, and future– who generously share their time, unique personalities, and invaluable life insights. Each one brings a distinct palette of colors to the canvas of life.

I would like to thank to my advisors Alice-Agnes Gabriel and Hans-Peter Bunge. Alice, thank you so much for your continuous support, enthusiastic advice, a lot of patience, and above overall giving me the chance to be part of the rupture dynamics community. Peter, thank you for all the support and encouragement, as well as all the words of advice on how to build opportunities. Especially, thank you for making time to sit by and discuss for hours with me about research.

Thank you Dave May, for taking many times the position of mentorship and huge guide when it came to putting in order thoughts, considering out of the box scenarios as well as challenging an understanding, and of course translating physics into code.

Thanks you, both Alice and Dave, for giving me a glimpse of a thunderstorm from a brainstorming discussion – exploring possibilities in approaching a problem, maintaining a positive stance on outcomes, and wrapping up the most comprehensive delivery on a method.

Thank you Rosa, Elena, Judith and Ira, for helping so much with all the paperwork and in general all the inside knowledge and efforts for keeping me in the country!

My heartfelt gratitude goes to everyone, Casper Pranger, Carsten Uphoff, Duo Li, Ingo Stotz, Mathilde Marchandon, Thomas Ulrich, Sia Ghelichkhan, Beth Kahle, Anthony Jourdon, who also gave me words of advice, took action, and mentored on various lines of research as well as life decisions. I'm scientifically and personally in debt with you all.

To Heiner, for caring about your students' well-being, and your excitement on curiosity-driven research. Also –and according to Lorenzo's thesis– thank you for your donation of electric heaters to the office.

To Jens Oeser, thank you for providing the impeccable computing infrastructure, and being so reliable when any problem popped up, and sorry for causing so many disturbances too. Also thanks for caring and sharing an espresso.

I would also want to thank my colleagues, Berta, Sabrina, Roman, Isabel, Leon, Nico, Zihua, Rachel, Nolwen, Hamish, Gabriel, Dieke, Eugene, Aniko, Taufiq, Artem, and all the others, because "*Geteiltes leid ist halbes leid*", and because a meal tastes better in good company. To everyone who passed by, greeted and shared a coffee, extended an invitation without giving up, or trusted their thoughts freely, thank you, you all often improved my day. I will always cherish sharing a coffee with my peers and engage in respectful, thought-provoking discussions.

The advisors and the research team I have come across during my PhD journey is indeed very hard to find anywhere in the world at a single institution. I'm glad to have met so many brilliant people, and above all, I am glad to have met so much kindness as well as excitement for research.

My special thanks to Sofie, for enduring and supporting me throughout all this journey, breaking my work bubble and ensuring a work-life balance. You kept me sane.

Por último, pero no menos importante, muchas gracias a mi familia, que desde la distancia tuvo paciencia y apoyó mis decisiones en esta vida. Gracias por resistir durante tanto tiempo todos los obstáculos y sucesos de los últimos años; sé que ha sido duro estar alejados por tanto tiempo, intentaré estar más en contacto.

Contents

List of Figures

Chapter 1

Chapter 2

Chapter 3

Chapter 4

Chapter 5

Appendix B

Appendix C

List of Tables

Nomenclature

Acronyms

AMR	Adaptive Mesh Refinement
BHS	Base Hiatus Surfaces
CG	Continuous Galerkin
CMB	Core-Mantle Boundary
DEM	Digital Elevation Model
DG	Discontinuous Galerkin
DSDP	Deep Sea Drilling Project
FD	Finite Differences
FEM	Finite Element Method
FZW	Fault Zone Width
GHM	Geological Hiatus Map
GNSS	Global Navigation Satellite System
GPS	Global Positioning System
InSAR	Interferometric Synthetic Aperture Radar
KMPJF	Kunlun Mountain Pass-Jiangcuo Fault
MCM	Mantle Circulation Model
ODP	Ocean Drilling Project
SCEC	Southern California Earthquake Center
SDF	Signed Distance Function
SEM	Spectral Element Method
SG	Stress Glut
SPOT	Satellite pour l'Observation de la Terre
TSN	Traction-at-Split-Node
WSM	World Stress Map

Part I

INTRODUCTION

Chapter 1

Introduction and Motivation

The need of understanding earthquakes arises from their devastating impact as natural disasters. Earthquakes can cause massive economic losses, claim countless lives, and trigger secondary disasters with unforeseen consequences, such as the nuclear meltdowns caused by the tsunami following the 2011 Tohoku-Oki earthquake in Japan. Most of the world's earthquakes are interplate events that occur at the boundaries of tectonic plates. The strain induced by these movements is accommodated by faults – thin zones of highly localized shear deformation. Faults deform, interact and fail via multiple physical processes (brittle, plastic, viscous) and across large spatial (<1 mm to >100 km) and temporal (<0.001 s to >10.000 yr) scales. In interplate settings, stress builds up as the plates move against one another and is released episodically in earthquakes, accounting for more than 90% of the global seismic energy release (e.g., [50]). However, large earthquakes can also occur away from plate boundaries, and their genesis is not well understood [8,21,57]. These continental intraplate earthquakes, characterized by large recurrence times [65], pose a considerable seismic hazard which is difficult to address in standard operational hazard assessment, often affecting ill-prepared infrastructure. While the general driving mechanisms of intraplate seismicity remain enigmatic, largely due to their low frequency and the challenges associated, they are often associated with stress-inducing interactions between mantle- and lithospheric-scale processes on a wide range of length and time scales. Observational maps on the stress field are traditionally derived from compilations of stress indicators such as the World Stress Map Project [25]. The general understanding is that first-order stress patterns are, to a great extent, the result of compressional forces taking effect at plate boundaries, essentially ridge push and continental collision [71]. This implies that the orientation of intraplate stress is mainly controlled by the geometry of the surrounding plate boundaries [71]. Additionally, continental rifting, isostatic compensation and topography, deglaciation, and lithospheric flexure, are considered the result of second-order processes, producing effects on the large scale stress field [26]. This has motivated the study of Intraplate Earthquakes in the context of lithospheric properties such as lithospheric thickness and heat flow (e.g., Müller et al.[36]). However, in other cases the link of the stress field to lithosphere properties is less obvious, suggesting that significant sublithosphere stress components from large-scale mantle flow may exist [5]. Advances in our understanding of the large scale buoyancy structure of the sublithospheric mantle from mantle circulation models (MCMs) (e.g., Schuberth et al.[51],[52]) can contribute additional key information in the interpretation of the intraplate stress field.

1.1 Dynamic earthquake rupture modeling

Modeling earthquake source processes is a complex, multiphysics, multiscale endeavor of critical societal importance. It links several geoscience-related disciplines –seismology, geodesy, geology, tectonics– with numerical computing, data science, machine learning, applied mathematics, rock mechanics, tribology, and engineering. Dynamic modeling of earthquakes offers a physics-based understanding of the mechanical viability of how earthquakes initiate, propagate and arrest across a fault network by coupling the nonlinear interaction of fault yielding and sliding behaviour to seismic wave propagation. The field is positioned for rapid progress, driven by recent advancements in modeling techniques, development of observational capabilities across multiple disciplines, and laboratory experiments, all aimed at achieving physics-based modeling on scales of interest for hazard and risk assessment. Numerical and hardware advances have enabled the community to explicitly model fully physics-based, non-linear models, that include different degrees of model complexities and physics explicitly (e.g., incorporating high-resolution 3D velocity structure and topography into the models, accounting for fault roughness [58], large multiscale fracture networks [39], modeling coseismic off-fault plasticity using (visco-)plastic non-associative Drucker-Prager rheology [3,66] or nonlinear brittle damage rheologies [38,59,67], and modeling coupled earthquake-driven tsunami generation [1,61]), achieving a high degree of realism for a 3-D earthquake scenario simulations. The research questions that stem from this type of modeling are particularly challenging because each outcome is the result of complex interactions among numerous factors.

While kinematic models of earthquake slip result from solving data-driven inverse problems, dynamic rupture simulations model spontaneous frictional failure across a defined fault system (e.g., Ulrich et al.[61]). Shear failure under compressive stress states is commonly described with the Coulomb criterion (also known as Mohr-Coulomb criterion). In this context, the fracture or frictional resistance is equal to the strength of the rock or fault, for either intact rock failure or rock-on-rock frictional sliding, respectively. Since earthquakes predominantly occur on pre-existing fault interfaces, they are often described as stick-slip frictional instabilities [49]. For frictional sliding, the strength of the fault depends on the friction coefficient, cohesion, and fault normal stress. Widely applied empirical "friction laws" are derived from small-scale laboratory experiments, which describe the co-evolution of slip and traction at an interface, thereby controlling the subsequent rupture evolution and, consequently, the earthquake dynamics. The linear slip-weakening law [31,40] describes how the fault weakens linearly as a function of fault slip over a characteristic slip distance. Laboratory experiments suggest more complex fault rheologies. For instance, the rate-and-state friction law captures the effects of time and slip rate on the friction coefficient [13,47]. This constitutive relation provides a unified model that relates the estimated friction coefficient, the rate of deformation, and a state variable. This state variable describes the physical state of the shearing surface, enabling the capture of the transient evolution of the strength of points of contacts, in accordance to additional characteristics identified from laboratory experiments [14]. Numerically, faults are often implemented as interfaces, or mesh features, on which internal boundary conditions –defined by these friction laws–, are applied. Although interface-based models have yielded very productive research, allowing for the modeling of a wide range of fault network complexities, faults in nature are ultimately not interfaces. Such simplifying assumption may also pose a limitation in the context of meshing an evolving fault system geometry.

Dynamic rupture models face challenges in constraining the conditions governing fault stresses and strengths, as they are highly sensitive to these parameters. The stress state can present a large number of complexities emerging from variations in mechanical properties and force distributions. In combination with the fault rheology, the choice of this stress state governs the rupture propagation style (e.g., pulse vs crack-like dynamics, sub- vs super-shear rupture speeds), transfers (dynamic triggering, branching), and earthquake arrest (e.g., Bai and Ampuero[4], Gabriel et al.[19], Gabriel[20], Kame et al.[33]). Ideally, the initial stress states and fault strength are consistent with the geometry and rheology of the subsurface and fault networks. Due to the lack of direct constraints of on-fault stresses, a common practice is to prescribe an homogeneous initial stress tensor acting on the fault geometry (e.g., Harris et al.[24]). Alternatively, models may inform the stress components by accounting for the overburden lithostatic pressure, as well as a reduction of the deviatoric stress reflecting the expected temperature-dependent brittle-ductile transition variation of the lithosphere (e.g., Scholz[48]). The on-fault pre-stress distribution resulting from an homogeneous regional tectonic loading is only modulated by variations in fault geometry. Smaller pre-stress heterogeneities can emerge from e.g., past earthquakes hosted on the fault, as well as the effective stress transfer from neighboring faults, unmodeled fault geometrical complexities –such as fault roughness, local variations in fault strength, fluid pressure or unknown local variations in tectonic loading– are not taken into account when considering an homogeneous parametrization of the stress tensor orientation. Recent efforts have sought to account for such small-scale heterogeneities by considering the stress drop distribution associated with an earthquake, which can be used to constrain the initial on-fault stress when no other constraints are available (e.g., Jia et al.[32], Tinti et al.[60], Weng and Yang[64]).

1.2 Geodynamic modeling

Mantle convection is a key thermomechanical driver of surface processes. It provides the driving forces necessary to support large-scale horizontal motion in the form of plate tectonics and associated crustal deformation, as well as transient vertical motions, known as dynamic topography[22,23,27,34,41,42]. The growing recognition of the influence of mantle convection in deflecting Earth's surface away from its isostatically compensated state has been explored across different processes through space and time (see Hoggard et al.[27] for a review). Observations analyzed in this context include the stratigraphic development of sedimentary basins, large-scale hiatus signals[16,62,72], regional distortions of glacio-eustatic signals[45], and variations in uplift rates from river profile analyses[46], among others.

Significant progress has been made in understanding the dynamics of 3D-spherical mantle convection over the past years, particularly through scenario simulations that explore the influence of key parameters on mantle flow regimes (see recent review by Zhong and Liu[70]). This progress is continuously leveraged by the rapid advances in modern high-performance computing capabilities.

The maturity of MCMs is evident in their ability to consistently reproduce first-order features and deep Earth structures for the present-day mantle. However, many model features, such as complex rheologies or thermomechanical flow properties, rely on ad-hoc parameterizations and long-range extrapolations, and thus are poorly known. Additionally, mantle convection evolution is a chaotic process. To mitigate this characteristic, geodynamicists assimilate the horizontal surface velocity field into MCMs [11]. These models exploit the constraints on earlier mantle flow states contained in past plate motion models (e.g., Müller et al.[37]), allowing them to guide a mantle convection model started from an arbitrary initial condition onto a trajectory that honors past plate motion constraints. This approach means that MCMs essentially combine two key-information sources on the mantle convection process: geologic observations of Earth's surface motion history and the associated injection of cold, negatively buoyant lithosphere into the mantle, along with a numerical model of the mantle convection process. As the horizontal surface motions are then the model input rather than their output, viable tests of mantle flow retrodictions rely on inferences of vertical lithosphere motion induced by mantle convective systems. These uncertainties and methodological constraints motivate the pursuit of complementary approaches to model and analyze the surface expression of mantle convection, as well as to identify global observables for validation of MCMs.

A key feature in these mantle models is the asthenosphere, a layer characterized by low viscosity and high flow mobility [10]. Research in fluid dynamics, through numerical and analytic modelling techniques (e.g. Bunge and Richards[6], Busse et al.[7]), agrees that high material mobility in the asthenosphere is crucial for promoting the long-wavelength character of mantle flow, necessary to support large-scale horizontal motion in the form of plate tectonics as well as long term dynamic topography [22,23,27,34,41,42]. The pioneering work of W. Jason Morgan and colleagues established the foundational concepts that link plate tectonics and mantle plumes with the flow structure of the mantle. They proposed an asthenosphere actively supplied by hot upwellings [35,44] and introduced a simplified model where the material flux is driven by lateral pressure gradients to explain observations related to ocean bathymetry, heat flow and mantle geochemistry [68,69]. This concept was further extended by Höink *et al.* [28–30] who formulated mantle convection explicitly in the context of pressure- and velocity-driven flow, respectively, Poiseuille and Couette flow. This Poiseuille-Couette representation of the low-viscosity, channelized mantle flow in the lithosphere-asthenosphere region stands as a powerful concept for linking mantle dynamics with geological observations in a testable way.

1.3 Main objectives and outline

The overarching aim of this dissertation revolves around the following research questions: How can we extend and inform rupture dynamic models through physics-driven methodologies? Additionally, how can we harness geodynamic insights to understand the large-scale deformation and the ambient stress field, thereby providing a contextual framework for these mechanical models? The first question is addressed from various perspectives in the first chapters of this dissertation:

Chapter 2 introduces a diffuse volumetric representation of a fault as an alternative to the traditional planar interface description. We have developed *se2dr*, a 2D PETSc spectral element adaptation of stress glut applied to earthquake rupture dynamic simulations, originally from Andrews[2], and combines it with a steady-state phase-field ansatz[56] to reduce the spurious oscillations reported in the original method[12]. We successfully emulate the results from planar interface kinematic and dynamic solutions, while also identifying emerging dynamic complexities from the volumetric representation, such as fault-oblique yielding within the volumetric fault zone. This study demonstrates the flexibility of the method as a numerical alternative for a mesh-independent representation of a fault, potentially allowing for the development of coseismically evolving fault structures under a elegantly simple methodological framework. The model inherently enables exploration of the yielding surface transition into the elastic medium and the identification of dynamic features observed from the analysis of near-fault apparent friction coefficient estimations in laboratory experiments.

In Chapter 3, we investigate the dynamics of the 2021 $M_w 7.4$ Maduo earthquake. For this study, we use *SeisSol*, a high-order numerical method based on the arbitrary high-order derivative discontinuous Galerkin (ADER-DG) scheme (e.g., Dumbser and Käser[15], Pelties et al.[43]), which is considered a state-of-art approach to model rupture dynamics. This study combines 3D dynamic rupture simulations, including off-fault plasticity, with geodetically-inferred on-fault stress heterogeneities to understand the mechanical paradoxes that surround this event, particularly the occurrence of unilateral supershear propagation across a non-planar, multi-segment representation of the fault system. We demonstrate that an integrated analysis of an ensemble of complex dynamic rupture models, high-resolution optical correlation analysis, joint optical-InSAR-slip inversion, and validation by near fault and teleseismic observations can provide a fundamental understanding of the mechanical intricacies that govern the dynamics of this event.

In Chapter 4, we present a loose coupling between long-term regional geodynamic models of strike-slip shear zone evolution and dynamic rupture modeling. The regional long-term visco-plastic model features the evolution of a single non-planar strike-slip fault structure, simulated using *pTatin3D*. We develop methods to extract the fault surface from the shear zones, for use as an internal boundary condition governed by a friction law within *SeisSol*. We demonstrate the impact of different choices of rheologies and associated stress state, consistent with a strike-slip fault geometry, on the dynamics of earthquake rupture and the energy release involved.

The following two chapters are motivated by the need to contextualize the background deformation state in more regional geomechanical models. In these chapters, we examine the insights gained from analyzing the deformation induced by mantle convection, particularly the large-wavelength observational signatures that help identify geodynamic regimes.

Chapter 5 describes the work conducted to map erosional/non-depositional periods, or hiatuses, in the continental geologic record across the Atlantic realm and Australia since the Upper Jurassic, as proxies of vertical surface deflection induced by the mantle, or dynamic topography. This work adopts the Hiatus mapping technique introduced by Friedrich[17], Friedrich et al.[18] and extends its application to other regions, complementing previous studies for Europe[63] and Africa[9]. We identify significant differences in the distribution of hiatuses across and between continents, at the time scale of geologic series –few tens of millions of years–, which is notably shorter than the mantle transit time, which is about 100-200 million years. This compilation may serve as a viable test of mantle flow retrodictions via inferences of evolving dynamic topography.

In Chapter 6 we analyse the role of mantle flow as a stress driver, by generating stress fields from an analytical representation of upper mantle flow. This analytical representation is derived from the superposition of steady-state flow models in the asthenosphere, introduced by Stotz et al.[53],[54],[55]. Our proposed approach offers a process-driven explanation for the global large-scale patterns observed in stress indicators compiled in the World Stress Map database[25]. This representation of asthenospheric flow serves as a tool to test hypotheses related to stress patterns and as a complement to interpret mantle flow states emerging from sophisticated forward models. This study emphasizes the importance of considering the global geometrical distribution of bouyant components in a geodynamic model, and the analysis carries implications on expected asthenospheric stress magnitudes.

Finally, Chapter 7 summarizes the key results of this dissertation, and suggests ideas for future research.

1.4 References

[1] Abrahams, L. S., Krenz, L., Dunham, E. M., Gabriel, A.-A., and Saito, T. (2023). Comparison of methods for coupled earthquake and tsunami modelling. *Geophysical Journal International*, 234(1):404–426. Cited on page/s 4.

[2] Andrews, D. J. (1976). Rupture velocity of plane strain shear cracks. *Journal of Geophysical Research (1896-1977)*, 81(32):5679–5687. Cited on page/s 7.

[3] Andrews, D. J. (2005). Rupture dynamics with energy loss outside the slip zone. *Journal of Geophysical Research: Solid Earth*, 110(B01307). Cited on page/s 4.

[4] Bai, K. and Ampuero, J. (2017). Effect of seismogenic depth and background stress on physical limits of earthquake rupture across fault step overs. *Journal of Geophysical Research: Solid Earth*, 122(12):10–280. Cited on page/s 5.

[5] Bird, P. (1998). Testing hypotheses on plate-driving mechanisms with global lithosphere models including topography, thermal structure, and faults. *Journal of Geophysical Research: Solid Earth*, 103(B5):10115–10129. Cited on page/s 3.

[6] Bunge, H.-P. and Richards, M. A. (1996). The origin of large scale structure in mantle convection: Effects of plate motions and viscosity stratification. *Geophysical Research Letters*, 23(21):2987–2990. Cited on page/s 6.

[7] Busse, F. H., Richards, M. A., and Lenardic, A. (2006). A simple model of high Prandtl and high Rayleigh number convection bounded by thin low-viscosity layers. *Geophysical Journal International*, 164(1):160–167. Cited on page/s 6.

[8] Calais, E., Camelbeeck, T., Stein, S., Liu, M., and Craig, T. (2016). A new paradigm for large earthquakes in stable continental plate interiors. *Geophysical Research Letters*, 43(20):10,621–10,637. Cited on page/s 3.

[9] Carena, S., Bunge, H.-P., and Friedrich, A. M. (2019). Analysis of geological hiatus surfaces across Africa in the Cenozoic and implications for the timescales of convectively-maintained topography. *Canadian Journal of Earth Sciences*, 56(12):1333–1346. Cited on page/s 7.

[10] Cathles, L., Fjeldskar, W., Lenardic, A., Romanowicz, B., Seales, J., and Richards, M. (2023). Influence of the asthenosphere on earth dynamics and evolution. *Scientific Reports*, 13(1):13367. Cited on page/s 6.

[11] Colli, L., Bunge, H.-P., and Schuberth, B. S. A. (2015). On retrodictions of global mantle flow with assimilated surface velocities. *Geophysical Research Letters*, 42(20):8341–8348. Cited on page/s 6.

[12] Dalguer, L. A. and Day, S. M. (2006). Comparison of fault representation methods in finite difference simulations of dynamic rupture. *Bulletin of the Seismological Society of America*, 96(5):1764–1778. Cited on page/s 7.

[13] Dieterich, J. H. (1978). Time-dependent friction and the mechanics of stick-slip. *Pure and Applied Geophysics PAGEOPH*, 116(4-5):790–806. Cited on page/s 4.

[14] Dieterich, J. H. (1979). Modeling of rock friction: 1. experimental results and constitutive equations. *Journal of Geophysical Research: Solid Earth*, 84(B5):2161–2168. Cited on page/s 4.

[15] Dumbser, M. and Käser, M. (2006). An arbitrary high-order discontinuous Galerkin method for elastic waves on unstructured meshes — II. The three-dimensional isotropic case. *Geophysical Journal International*, 167(1):319–336. Cited on page/s 7.

[16] Friedrich, A. M. (2019a). Palaeogeological hiatus surface mapping: a tool to visualize vertical motion of the continents. *Geological Magazine*, 156(2):308–319. Cited on page/s 5.

[17] Friedrich, A. M. (2019b). Palaeogeological hiatus surface mapping: A tool to visualize vertical motion of the continents. *Geological Magazine*, 156(2):308–319. Cited on page/s 7.

[18] Friedrich, A. M., Bunge, H.-P., Rieger, S. M., Colli, L., Ghelichkhan, S., and Nerlich, R. (2018). Stratigraphic framework for the plume mode of mantle convection and the analysis of interregional unconformities on geological maps. *Gondwana Research*, 53:159–188. Cited on page/s 7.

[19] Gabriel, A., Ampuero, J., Dalguer, L., and Mai, P. M. (2013). Source properties of dynamic rupture pulses with off-fault plasticity. *Journal of Geophysical Research: Solid Earth*, 118(8):4117–4126. Cited on page/s 5.

[20] Gabriel, A.-A. (2012). *Physics of dynamic rupture pulses and macroscopic earthquake source properties in elastic and plastic media*. PhD thesis, ETH Zurich. Cited on page/s 5.

[21] Gangopadhyay, A. and Talwani, P. (2003). Symptomatic features of intraplate earthquakes. *Seismological Research Letters*, 74(6):863–883. Cited on page/s 3.

[22] Gurnis, M., Mitrovica, J. X., Ritsema, J., and van Heijst, H.-J. (2000). Constraining mantle density structure using geological evidence of surface uplift rates: The case of the African Superplume. *Geochemistry, Geophysics, Geosystems*, 1(7). Cited on page/s 5, 6.

[23] Hager, B. H. and Richards, M. A. (1989). Long-wavelength variations in Earth's geoid: physical models and dynamical implications. *Philosophical Transactions of the Royal Society of London. Series A, Mathematical and Physical Sciences*, 328(1599):309–327. Cited on page/s 5, 6.

[24] Harris, R. A., Barall, M., Aagaard, B., Ma, S., Roten, D., Olsen, K., Duan, B., Liu, D., Luo, B., Bai, K., Ampuero, J., Kaneko, Y., Gabriel, A., Duru, K., Ulrich, T., Wollherr, S., Shi, Z., Dunham, E., Bydlon, S., Zhang, Z., Chen, X., Somala, S. N., Pelties, C., Tago, J., Cruz-Atienza, V. M., Kozdon, J., Daub, E., Aslam, K., Kase, Y., Withers, K., and Dalguer, L. (2018). A Suite of Exercises for Verifying Dynamic Earthquake Rupture Codes. *Seismological Research Letters*, 89(3):1146–1162. Cited on page/s 5.

[25] Heidbach, O., Rajabi, M., Cui, X., Fuchs, K., Müller, B., Reinecker, J., Reiter, K., Tingay, M., Wenzel, F., and Xie, F. (2018). The World Stress Map database release 2016: Crustal stress pattern across scales. *Tectonophysics*, 744:484–498. Cited on page/s 3, 8.

[26] Heidbach, O., Reinecker, J., Tingay, M., Müller, B., Sperner, B., Fuchs, K., and Wenzel, F. (2007). Plate boundary forces are not enough: second-and third-order stress patterns highlighted in the World Stress Map database. *Tectonics*, 26(6). Cited on page/s 3.

[27] Hoggard, M., Austermann, J., Randel, C., and Stephenson, S. (2021). *Observational Estimates of Dynamic Topography Through Space and Time*, chapter 15, pages 371–411. American Geophysical Union (AGU). Cited on page/s 5, 6.

[28] Höink, T., Jellinek, A. M., and Lenardic, A. (2011). Viscous coupling at the lithosphere-asthenosphere boundary. *Geochemistry, Geophysics, Geosystems*, 12(10). Cited on page/s 6.

[29] Höink, T. and Lenardic, A. (2010). Long wavelength convection, poiseuille–couette flow in the low-viscosity asthenosphere and the strength of plate margins. *Geophysical Journal International*, 180(1):23–33. Cited on page/s 6.

[30] Höink, T., Lenardic, A., and Richards, M. (2012). Depth-dependent viscosity and mantle stress amplification: implications for the role of the asthenosphere in maintaining plate tectonics. *Geophysical Journal International*, 191(1):30–41. Cited on page/s 6.

[31] Ida, Y. (1972). Cohesive force across the tip of a longitudinal-shear crack and Griffith's specific surface energy. *Journal of Geophysical Research*, 77(20):3796–3805. Cited on page/s 4.

[32] Jia, Z., Jin, Z., Marchandon, M., Ulrich, T., Gabriel, A.-A., Fan, W., Shearer, P., Zou, X., Rekoske, J., Bulut, F., Garagon, A., and Fialko, Y. (2023). The complex dynamics of the 2023 Kahramanmaraş, Turkey, Mw 7.8-7.7 earthquake doublet. *Science*, 0:eadi0685. Cited on page/s 5.

[33] Kame, N., Rice, J. R., and Dmowska, R. (2003). Effects of prestress state and rupture velocity on dynamic fault branching. *Journal of Geophysical Research: Solid Earth*, 108(B5). Cited on page/s 5.

[34] McKenzie, D. and Jarvis, G. (1980). The conversion of heat into mechanical work by mantle convection. *Journal of Geophysical Research: Solid Earth*, 85(B11):6093–6096. Cited on page/s 5, 6.

[35] Morgan, J. P. and Smith, W. H. F. (1992). Flattening of the sea-floor depth-age curve as a response to asthenospheric flow. *Nature*, 359(6395):524–527. Cited on page/s 6.

[36] Müller, B., Zoback, M. L., Fuchs, K., Mastin, L., Gregersen, S., Pavoni, N., Stephansson, O., and Ljunggren, C. (1992). Regional patterns of tectonic stress in Europe. *Journal of Geophysical Research: Solid Earth*, 97(B8):11783–11803. Cited on page/s 3.

[37] Müller, R. D., Seton, M., Zahirovic, S., Williams, S. E., Matthews, K. J., Wright, N. M., Shephard, G. E., Maloney, K. T., Barnett-Moore, N., and Hosseinpour, M. (2016). Ocean basin evolution and global-scale plate reorganization events since Pangea breakup. *Annual Review of Earth and Planetary Sciences*, 44:107–138. Cited on page/s 6.

[38] Niu, Z., Gabriel, A.-A., Seelinger, L., and Igel, H. (2024). Modeling and quantifying parameter uncertainty of co-seismic non-classical nonlinearity in rocks. *Journal of Geophysical Research: Solid Earth*, 129(1):e2023JB027149. e2023JB027149 2023JB027149. Cited on page/s 4.

[39] Palgunadi, K. H., Gabriel, A.-A., Garagash, D. I., Ulrich, T., and Mai, P. M. (2024). Rupture dynamics of cascading earthquakes in a multiscale fracture network. *Journal of Geophysical Research: Solid Earth*, 129(3):e2023JB027578. e2023JB027578 2023JB027578. Cited on page/s 4.

[40] Palmer, A. C. and Rice, J. R. (1973). The growth of slip surfaces in the progressive failure of over-consolidated clay. *Proceedings of the Royal Society of London. A. Mathematical and Physical Sciences*, 332(1591):527–548. Cited on page/s 4.

[41] Parsons, B. and Daly, S. (1983). The relationship between surface topography, gravity anomalies, and temperature structure of convection. *Journal of Geophysical Research: Solid Earth*, 88(B2):1129–1144. Cited on page/s 5, 6.

[42] Pekeris, C. L. (1935). Thermal convection in the interior of the earth. *Geophysical Journal International*, 3(8):343–367. Cited on page/s 5, 6.

[43] Pelties, C., de la Puente, J., Ampuero, J.-P., Brietzke, G. B., and Käser, M. (2012). Three-dimensional dynamic rupture simulation with a high-order discontinuous Galerkin method on unstructured tetrahedral meshes. *Journal of Geophysical Research: Solid Earth*, 117(B2). Cited on page/s 7.

[44] Phipps Morgan, J., Morgan, W. J., Zhang, Y.-S., and Smith, W. H. F. (1995). Observational hints for a plume-fed, suboceanic asthenosphere and its role in mantle convection. *Journal of Geophysical Research: Solid Earth*, 100(B7):12753–12767. Cited on page/s 6.

[45] Richards, F. D., Coulson, S. L., Hoggard, M. J., Austermann, J., Dyer, B., and Mitrovica, J. X. (2023). Geodynamically corrected Pliocene shoreline elevations in Australia consistent with midrange projections of Antarctic ice loss. *Science Advances*, 9(46):eadg3035. Cited on page/s 5.

[46] Roberts, G. G. and White, N. (2010). Estimating uplift rate histories from river profiles using African examples. *Journal of Geophysical Research: Solid Earth*, 115(B2):B02406. Cited on page/s 5.

[47] Ruina, A. (1983). Slip instability and state variable friction laws. *Journal of Geophysical Research: Solid Earth*, 88(B12):10359–10370. Cited on page/s 4.

[48] Scholz, C. H. (1988). The brittle-plastic transition and the depth of seismic faulting. *Geologische Rundschau*, 77(1):319–328. Cited on page/s 5.

[49] Scholz, C. H. (1998). Earthquakes and friction laws. *Nature*, 391(6662):37–42. Cited on page/s 4.

[50] Scholz, C. H. (2019). *The mechanics of earthquakes and faulting*. Cambridge university press. Cited on page/s 3.

[51] Schuberth, B., Bunge, H., and Ritsema, J. (2009a). Tomographic filtering of high-resolution mantle circulation models: Can seismic heterogeneity be explained by temperature alone? *Geochemistry, Geophysics, Geosystems*, 10(5). Cited on page/s 3.

[52] Schuberth, B. S. A., Bunge, H.-P., Steinle-Neumann, G., Moder, C., and Oeser, J. (2009b). Thermal versus elastic heterogeneity in high-resolution mantle circulation models with pyrolite composition: High plume excess temperatures in the lowermost mantle. *Geochemistry, Geophysics, Geosystems*, 10(1). Cited on page/s 3.

[53] Stotz, I. L., Iaffaldano, G., and Davies, D. R. (2018). Pressure-driven poiseuille flow: A major component of the torque-balance governing pacific plate motion. *Geophysical Research Letters*, 45(1):117–125. Cited on page/s 8.

[54] Stotz, I. L., Vilacís, B., Hayek, J. N., Bunge, H.-P., and Friedrich, A. M. (2021). Yellowstone Plume Drives Neogene North American Plate Motion Change. *Geophysical Research Letters*, 48(18):e2021GL095079. e2021GL095079 2021GL095079. Cited on page/s 8.

[55] Stotz, I. L., Vilacís, B., Hayek, J. N., Carena, S., and Bunge, H.-P. (2023). Plume driven plate motion changes: New insights from the South Atlantic realm. *Journal of South American Earth Sciences*, 124:104257. Cited on page/s 8.

[56] Sun, Y. and Beckermann, C. (2007). Sharp interface tracking using the phase-field equation. *Journal of Computational Physics*, 220(2):626–653. Cited on page/s 7.

[57] Talwani, P. (2017). On the nature of intraplate earthquakes. *Journal of Seismology*, 21(1):47–68. Cited on page/s 3.

[58] Taufiqurrahman, T., Gabriel, A.-A., Li, D., Ulrich, T., Li, B., Carena, S., Verdecchia, A., and Gallovič, F. (2023). Dynamics, interactions and delays of the 2019 Ridgecrest rupture sequence. *Nature*, 618(7964):308–315. Cited on page/s 4.

[59] Thomas, M. Y. and Bhat, H. S. (2018). Dynamic evolution of off-fault medium during an earthquake: a micromechanics based model. *Geophysical Journal International*, 214(2):1267–1280. Cited on page/s 4.

[60] Tinti, E., Casarotti, E., Ulrich, T., Taufiqurrahman, T., Li, D., and Gabriel, A.-A. (2021). Constraining families of dynamic models using geological, geodetic and strong ground motion data: The Mw 6.5, October 30th, 2016, Norcia earthquake, Italy. *Earth and Planetary Science Letters*, 576:117237. Cited on page/s 5.

[61] Ulrich, T., Vater, S., Madden, E. H., Behrens, J., van Dinther, Y., van Zelst, I., Fielding, E. J., Liang, C., and Gabriel, A.-A. (2019). Coupled, Physics-based Modeling Reveals Earthquake Displacements are Critical to the 2018 Palu, Sulawesi Tsunami. *Pure and Applied Geophysics*, 176(10):4069–4109. Cited on page/s 4.

[62] Vibe, Y., Friedrich, A., Bunge, H.-P., and Clark, S. (2018a). Correlations of oceanic spreading rates and hiatus surface area in the North Atlantic realm. *Lithosphere*, 10(5):677–684. Cited on page/s 5.

[63] Vibe, Y., Friedrich, A. M., Bunge, H.-P., and Clark, S. R. (2018b). Correlations of oceanic spreading rates and hiatus surface area in the North Atlantic realm. *Lithosphere*, 10(5):677–684. Cited on page/s 7.

[64] Weng, H. and Yang, H. (2018). Constraining frictional properties on fault by dynamic rupture simulations and near-field observations. *Journal of Geophysical Research: Solid Earth*, 123(8):6658–6670. Cited on page/s 5.

[65] Williams, R. T., Goodwin, L. B., Sharp, W. D., and Mozley, P. S. (2017). Reading a 400,000-year record of earthquake frequency for an intraplate fault. *Proceedings of the National Academy of Sciences*, 114(19):4893–4898. Cited on page/s 3.

[66] Wollherr, S., Gabriel, A.-A., and Uphoff, C. (2018). Off-fault plasticity in three-dimensional dynamic rupture simulations using a modal Discontinuous Galerkin method on unstructured meshes: Implementation, verification and application. *Geophysical Journal International*, 214(3):1556–1584. Cited on page/s 4.

[67] Xu, S., Ben-Zion, Y., Ampuero, J.-P., and Lyakhovsky, V. (2015). Dynamic Ruptures on a Frictional Interface with Off-Fault Brittle Damage: Feedback Mechanisms and Effects on Slip and Near-Fault Motion. *Pure and Applied Geophysics*, 172(5):1243–1267. Cited on page/s 4.

[68] Yamamoto, M., Morgan, J. P., and Morgan, W. J. (2007a). Global plume-fed asthenosphere flow—I: Motivation and model development. In *Plates, Plumes and Planetary Processes*. Geological Society of America. Cited on page/s 6.

[69] Yamamoto, M., Morgan, J. P., and Morgan, W. J. (2007b). Global plume-fed asthenosphere flow—II: Application to the geochemical segmentation of mid-ocean ridges. In *Plates, Plumes and Planetary Processes*. Geological Society of America. Cited on page/s 6.

[70] Zhong, S. and Liu, X. (2016). The long-wavelength mantle structure and dynamics and their implications for large-scale tectonics and volcanism in the Phanerozoic. *Gondwana Research*, 29(1):83–104. Cited on page/s 5.

[71] Zoback, M. L. (1992). First-and second-order patterns of stress in the lithosphere: The World Stress Map Project. *Journal of Geophysical Research: Solid Earth*, 97(B8):11703–11728. Cited on page/s 3.

[72] Şengör, A. (2009). The large-wavelength deformations of the lithosphere: Materials for a history of the evolution of thought from the earliest times to plate tectonics. In *The Large-Wavelength Deformations of the Lithosphere: Materials for a History of the Evolution of Thought from the Earliest Times to Plate Tectonics*. Geological Society of America. Cited on page/s 5.

Part II

Earthquake Rupture Dynamics

Chapter 2

A diffuse interface method for earthquake rupture dynamics based on a phase-field model

by Hayek, J.N., May, D.A., Pranger, C., & Gabriel, A.-A. (2023). Published in Journal of Geophysical Research: Solid Earth, 128, e2023JB027143. DOI: 10.1029/2023JB027143

Abstract

In traditional modeling approaches, earthquakes are often depicted as displacement discontinuities across zero-thickness surfaces embedded within a linear elastodynamic continuum. This simplification, however, overlooks the intricate nature of natural fault zones and may fail to capture key physical phenomena integral to fault processes. Here, we propose a diffuse interface description for dynamic earthquake rupture modeling to address these limitations and gain deeper insight into fault zones' multifaceted volumetric failure patterns, mechanics, and seismicity. Our model leverages a steady-state phase-field, implying time-independent fault zone geometry, which is defined by the contours of a signed distance function relative to a virtual fault plane. Our approach extends the classical stress glut method, adept at approximating fault-jump conditions through inelastic alterations to stress components. We remove the sharp discontinuities typically introduced by the stress glut approach via our spatially smooth, mesh-independent fault representation while maintaining the method's inherent logical simplicity within the well-established spectral element method framework. We verify our approach using 2D numerical experiments in an open-source spectral element implementation, examining both a kinematically driven Kostrov-like crack and spontaneous dynamic rupture in diffuse fault zones. The capabilities of our methodology are showcased through mesh-independent planar and curved fault zone geometries. Moreover, we highlight that our phase-field-based diffuse rupture dynamics models contain fundamental variations within the fault zone. Dynamic stresses intertwined with a volumetrically applied friction law give rise to oblique plastic shear and fault reactivation, markedly impacting rupture front dynamics and seismic wave radiation. Our results encourage future applications of phase-field-based earthquake modeling.

2.1 Introduction

The mechanics of slip in natural fault networks is a multiscale and multiphysics problem. Observations reveal volumetric fault zone complexities in large ruptures (e.g. Chester and Chester[28], Klinger et al.[75]), small earthquakes (e.g., in the San Jacinto fault zone[27], and even in laboratory events (e.g. high-velocity friction experiments[108]). This complexity is influenced by factors such as inelastic deformation within a larger volume around the principal slip zone (i.e. off-fault damage[22,111]), by geometrically complex fault structures (e.g., Milliner et al.[97],[98], Weldon II and Springer[139]), and by variable rheological properties within the fault zone (e.g., Chester and Logan[29], Faulkner et al.[42]).

Earthquakes can be described as frictional shear fracture of brittle solids along pre-existing weak interfaces (i.e. fault zones). The slip evolution then depends on a friction law, the fault constitutive properties and initial conditions, as well as the fault geometry and the off-fault material. Fault zone complexity promotes the generation of high frequency seismic wave radiation. Such complexity includes stress localization and spatial variation of fault strength[84,85,105,142] and fault system interaction[18,73,89].

In dynamic earthquake rupture simulations, faults are typically idealized as infinitesimally thin interfaces with distinct on- versus off-fault rheologies (e.g., Andrews[7], Ben-Zion and Shi[13], Dunham et al.[39], Gabriel et al.[49], Harris et al.[55],[56], Okubo et al.[105], Templeton and Rice[135]). While progress toward mesh-independent co-seismic faulting representations exists[14,31,50,113,134], geometrical complexities usually have to be explicitly represented in the spatial discretization of the computational domain (e.g., Chaljub et al.[24], Galvez et al.[52]) for example by using unstructured tetrahedral meshes in high order Discontinuous Galerkin methods[36,136,137,143]. However, the geometry and mesh generation process is often laborious (e.g., Chaljub et al.[25], Ramos et al.[115]). Alternatives may include using representations of strong discontinuities at the subelement level using the eXtended Finite Element Method (XFEM)[81,100] or expressing nonplanar faults through curvilinear coordinate transformations (e.g., Duru and Dunham[40], Zhang et al.[148]). A so-called *smeared interface* approach diffuses sharp cracks via smooth transitions between intact and fully damaged material states (e.g.,De Borst et al.[35], Mirzabozorg and Ghaemian[99]). Recently, unified thermodynamically consistent frameworks have been formulated for the smeared modeling of crack and earthquake rupture propagation[50,133] in a Discontinuous Galerkin framework[116], that allow for complex geometries and the use of adaptive mesh refinement, but require non-trivial constitutive parameter selection.

The spectral element method (SEM) has been a method of choice in the computational seismology community for simulating wave propagation in heterogeneous and homogeneous media[76]. It aims to combine the geometrical flexibility of the finite element method with the accuracy of spectral methods interpolating with high-order basis functions (e.g., Igel[65]). The SEM is well suited for highly non-linear problems with non-smooth solutions, including simulations of dynamic rupture[47,74] using a split-node approach[33] and hexahedral spectral elements (e.g., Galvez et al.[52]). SEM allows using non-linear off-fault plasticity[49] and continuum damage[144] but requires, similar to other established dynamic rupture modeling methods, to explicitly discretize fault discontinuities.

An alternative approach for representing a fault as a material discontinuity is the inelastic zone or *stress glut* method. Backus and Mulcahy[8] termed *stress glut* the stress mismatch of a purely elastic medium and the true physical stress. The stress glut method was first established within the context of kinematic earthquake source descriptions, where the region of non-zero stress glut is the internal source[21,26,30,70–72,91–93]. The stress glut[6] and the thick fault zone[86] methods in the context of dynamic rupture modeling have been implemented in the finite difference method[4,6,32,60,86,114]. There, the stress glut approximates the fault-jump conditions through inelastic increments to the stress components in an inelastic zone that is one grid cell wide. While the thick fault method leads to qualitative disagreement, the stress glut method produces qualitatively consistent results with the discontinuous reference solutions. However, it features inherently poor convergence with mesh refinement irrespective of the order of the finite difference approximation that was used[32]. While these inherent challenges have somewhat damped interest in the stress glut method for dynamic rupture earthquake modeling, we demonstrate in this study that a novel stress glut phase-field adaption can yield quantitatively consistent results to discrete fault reference solutions and empirical earthquake frictional behavior.

A classical phase-field approach has not yet been applied to fully dynamic earthquake rupture modeling. Phase-field approaches introduce a scalar phase-field, which varies between 0 and 1, to represent the degree of damage of the material (e.g., Bourdin et al.[19]. One major advantage of "field-based" approaches is that fractures do not need to be explicitly meshed - thus enabling the simulation of spontaneous fracture development (e.g., Bourdin et al.[20]). Critical ingredients of the phase-field formulation are rooted in fracture mechanics, specifically by incorporating a critical fracture energy, which is translated into the regularized continuum sense of gradient damage mechanics[95]. For shear fracture, which is dominating earthquake processes, theoretical methods have been proposed (e.g., Spatschek et al.[128]) and applied for brittle fracture in rock-like materials under constant normal pressure (e.g., Fei and Choo[44],[45], Zhang et al.[147]). Recently, this work has been extended to incorporate a rate- and state-dependent friction law in a promising antiplane quasi-dynamic phase-field model of fault growth and off-fault damage[46].

Here, we modify the concept of stress glut and apply it for the first time in a spectral element method. We combine the method with a spatially smooth and mesh-independent fault representation in a steady-state phase-field approach. We represent the fault geometry as the *zero level set* of a signed distance function (SDF). We demonstrate that in the phase-field framework, dynamic crack propagation can be handled as a standard multi-field problem by using conventional finite element methods. We note that the methodology described in this paper is not strongly tied to a continuous Galerkin or spectral element method but is, in principle, applicable to a discontinuous Galerkin approach for wave propagation[38,141].

Our approach and its numerical implementation are explained in Sections 2.2 and 2.3. We verify our approach in Section 2.4 by performing kinematic and dynamic rupture benchmarks and by comparing our diffuse fault results to those of discrete fault modeling. We explore the flexibility of modeling dynamic rupture mesh independently by generalizing the fault geometry to inclined and curved planes not aligning with the prescribed computational mesh. In Section 2.5, we compare our approach against alternative diffuse crack models, discuss limitations, and anticipate future developments.

2.2 A PHASE-FIELD MODIFIED STRESS GLUT APPROACH

In this section, we formulate an implicit description of a diffuse fault geometry by means of the signed distance function. This description enables us to construct an in-fault reference frame that defines an embedded subdomain. In this sub-region, inelastic deformation can take place as a consequence of frictional yielding, in which the friction coefficient is a function of time or displacement. Using these ingredients, we present an extension of the stress glut method using the phase-field mathematical notion.

2.2.1 A diffuse fault representation using the signed distance function

In this paper, we use the term "diffuse fault" to refer to a fault description of finite thickness. All applications developed in this study model earthquake slip on diffuse faults that are resolved by at least two spectral elements in width. Given a description of a fault as, e.g., a parametric curve $\boldsymbol{x}_f = \boldsymbol{x}_f(a),\ \boldsymbol{x}_f \in \mathbb{R}^2,\ a \in \mathbb{R}$ embedded in the 2D space $\Omega \subseteq \mathbb{R}^2$, we construct an implicit model of the same geometry by defining a field $\varphi(\boldsymbol{x}) \in \mathbb{R},\ \boldsymbol{x} \in \Omega$ that satisfies the following properties:

1. At each point $\boldsymbol{x} \in \Omega$, $|\varphi(\boldsymbol{x})|$ measures the Euclidean distance to the point on the curve $\boldsymbol{x}_f(a)$ that is nearest to it in the same Euclidean sense, i.e.: $|\varphi(\boldsymbol{x})| = \inf_{\Omega} \left\|\boldsymbol{x} - \boldsymbol{x}_f(a)\right\|_2$.

2. The sign of the field $\varphi(\boldsymbol{x})$ (denoted via $\operatorname{sgn}(\varphi)$) is informally given by the side on which the coordinate $\boldsymbol{x}$ is with respect to the curve $\boldsymbol{x}_f$. More formally, given a value for the parameter $a_* = a_*(\boldsymbol{x})$ that minimizes the Euclidean distance between the points $\boldsymbol{x}$ and $\boldsymbol{x}_f(a_*)$, we can define a fault-normal vector $\hat{\boldsymbol{v}} = \boldsymbol{x} - \boldsymbol{x}_f(a_*)$ and a fault-tangent vector $\hat{\boldsymbol{w}} = \boldsymbol{x}'_f(a_*)$, and arbitrarily but consistently assign $\operatorname{sgn}(\varphi(\boldsymbol{x})) = \operatorname{sgn}\left(\hat{w}_1\hat{v}_2 - \hat{w}_2\hat{v}_1\right)$, the sign of the rotation from $\hat{\boldsymbol{v}}$ into $\hat{\boldsymbol{w}}$.

A field that has these properties is called a *signed distance function* (SDF) of the curve $\boldsymbol{x}_f$, and the original curve is partially recovered as the unordered *level set* $\Gamma = \{\boldsymbol{x} : \varphi(\boldsymbol{x}) = 0\}$. In the following discussion, we will assume to only have access to the signed distance function and will forgo reference to the parametric curve $\boldsymbol{x}_f(a)$ and its parameter a. In this regard, the method readily generalizes to a three-dimensional space embedding a fault as a two-dimensional manifold.

We define a right-handed orthonormal fault-local reference frame that is spanned by the normal vector $\boldsymbol{n}(\boldsymbol{x}) = -\nabla\varphi(\boldsymbol{x})$ (which is a unit vector since $|\nabla\varphi(\boldsymbol{x})| = 1$ by definition) and a tangential vector $\boldsymbol{t} = [n_2, -n_1]$. In this case, $\boldsymbol{n}$ points from the negative side of the fault to the positive side of the fault, but this is a rather arbitrary convention, much like the handedness of the fault-local coordinate system.

Here we use the SDF to extend the lower-dimensional fault interface to a finite sub-region $\Sigma \subset \Omega$ that is delineated by the $\pm\delta$ level sets of the SDF, i.e. $\Sigma = \{\boldsymbol{x} \in \Omega : -\delta \leq \varphi(\boldsymbol{x}) \leq +\delta\}$. On account of the smooth nature of the SDF, it can represent a fault in a manner independent of the mesh resolution and orientation as long as the local curvature of the fault plane itself is well resolved.

To implement slip or slip rate dependent friction laws or evaluate results of time-dependent source descriptions, we project material displacement ($\boldsymbol{u}$) and velocity ($\boldsymbol{v}$) vectors onto the $\pm\delta$ level sets. For a given coordinate $\boldsymbol{x} \in \Sigma$, we compute two related coordinates on opposing sides of the fault as follows:

$$\boldsymbol{x}^{+}(\boldsymbol{x}) := \boldsymbol{x} + (\delta - \varphi(\boldsymbol{x}))\boldsymbol{n} \tag{2.1a}$$

$$\boldsymbol{x}^{-}(\boldsymbol{x}) := \boldsymbol{x} - (\delta + \varphi(\boldsymbol{x}))\boldsymbol{n} \tag{2.1b}$$

the effective slip S is then calculated as

$$S(\boldsymbol{x}) = \left[\boldsymbol{u}(\boldsymbol{x}^{+}(\boldsymbol{x})) - \boldsymbol{u}(\boldsymbol{x}^{-}(\boldsymbol{x}))\right] \cdot \boldsymbol{t}(\boldsymbol{x}), \tag{2.2}$$

and the effective slip rate $\dot{S}$ is calculated similarly. This procedure generalizes the mesh-aligned stress glut implementation of Andrews[6]. The magnitudes of shear and normal tractions τ and σ_n on the fault are expressed throughout the diffuse fault subdomain Σ as

$$\tau := \boldsymbol{n} \cdot \overline{\overline{\boldsymbol{\sigma}}} \cdot \boldsymbol{t}, \tag{2.3a}$$

$$\sigma_n := \boldsymbol{n} \cdot \overline{\overline{\boldsymbol{\sigma}}} \cdot \boldsymbol{n}, \tag{2.3b}$$

where $\overline{\overline{\boldsymbol{\sigma}}}$ is the Cauchy stress tensor and the normal stress σ_n is negative under compression. Figure 2.1 illustrates the geometric quantities introduced above, which are associated with the diffuse fault representation.

Note that the slip direction is derived from the evolving displacement field as a consequence of the embedded fault and its conditions. The displacement field evolves relative to the modified stress, where the shear direction and sign in fault local coordinates are inherited from the shear stress component of the stress state outside of the yield envelope. Yielding in our approach is described in the next section.

2.2.2 *Yielding and friction in the diffuse fault stress glut approach*

In this work, we assume a friction coefficient $\mu = \mu(t, \boldsymbol{x}, S, \dot{S}, \ldots)$ that is a function of time t, position, slip, slip rate, and potentially other variables as well. Such a general description of the friction law encompasses the time-dependent Kostrov crack model and the linear slip weakening law that we use in this work to verify our method. We note that other frictional constitutive equations will be supported as well as, e.g., the rate and state friction law[37,124]. A cohesionless frictional yield criterion τ_c is stated as

$$\begin{aligned} |\tau(t, \boldsymbol{x})| &\leq \tau_c(t, \boldsymbol{x}, S, \dot{S}, \ldots) \\ &:= -\mu(t, \boldsymbol{x}, S, \dot{S}, \ldots) \min(0,\ \sigma_n(t, \boldsymbol{x})). \end{aligned} \tag{2.4}$$

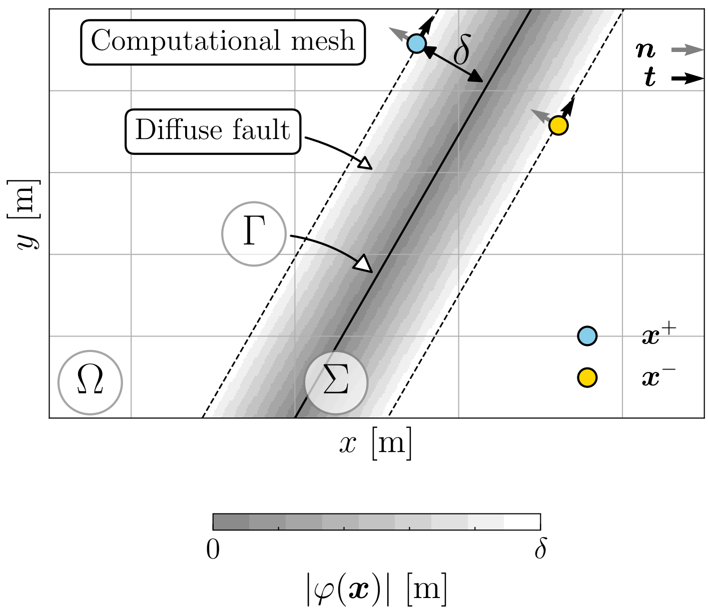

FIGURE 2.1. Schematic of the diffuse fault representation using the signed distance function. The mesh independent fault indicator $\varphi(\boldsymbol{x})$ is defined within an inelastic zone width of 2δ and acts in the subdomain $\Sigma \subset \Omega$. The blue and yellow circles indicate the projected coordinate pairs $\boldsymbol{x}^{+}$ and $\boldsymbol{x}^{-}$ at a distance δ from the zero level set on opposite sides of the fault, as described in the text of Section 2.2.1. Each circle includes the fault local orientation axis $(\boldsymbol{t},\ \boldsymbol{n})$.

The truncation to negative values of normal stress effectively means that free slip (zero shear stress) conditions are applied under tension, in line with the fracture mechanics theory of Palmer and Rice[107]. Note that Day et al.[33] describes an alternative treatment of jump conditions for tensile stresses, which may be explored in future developments of our approach.

A stress state outside of the yield envelope can be relaxed back onto it in the given direction of shear stress by applying a plastic correction, which we write as

$$\overline{\overline{\boldsymbol{\sigma}}}_f = \overline{\overline{\boldsymbol{\sigma}}}_e - [\tau - \tau_c \operatorname{sgn} \tau] \, [\boldsymbol{n} \otimes \boldsymbol{t} + \boldsymbol{t} \otimes \boldsymbol{n}] \,, \tag{2.5}$$

where the subscript f on the modified stress tensor denotes fault or friction, and the subscript e denotes *elastic*. The map $\overline{\overline{\boldsymbol{\sigma}}}_e \rightarrow \overline{\overline{\boldsymbol{\sigma}}}_f$ for stress states that are outside of the yield envelope is achieved in plasticity models in a more subtle way by introducing a plastic strain increment of unknown magnitude and solving for said magnitude such that stress equals strength. This subtlety is not needed in the stress glut approach, as will be further clarified in the following. Under shear failure, the introduction of the stress limiter develops a transversely isotropic constitutive behavior with a plane of isotropy perpendicular to the direction $\boldsymbol{n}$. See Sharples et al.[126] for an extensive examination of the formulation and behavior of transversely isotropic materials in failure. In addition, we introduce an additional term in the yielding criterion in Eq. (2.4). This change aims to include the implicit assumptions in traditional planar interface models. Its effects are further described in Section 2.4 and analyzed in Section 2.5.1.

We consider a modified yielding criterion that omits the contribution from the term $G\,(\nabla(\boldsymbol{u} \cdot \boldsymbol{n})) \cdot \boldsymbol{t}$. This simplification is motivated by 2D shear-driven deformation in planar Couette flow solutions[140]. Importantly, this alteration is only applied when evaluating the yielding criterion, not during the elasticity update (see algorithm 1). This formulation aims to emulate fault normal continuity at interfacial node pairs that exists in traditional dynamic rupture implementations for comparability of our diffuse fault representation to established models for mode II dynamic rupture. Then, such criterion becomes

$$|\tau - G\,(\nabla(\boldsymbol{u} \cdot \boldsymbol{n})) \cdot \boldsymbol{t}| \leq \tau_c, \tag{2.6}$$

where G is the shear modulus. This interface yielding criterion may be interpreted as a modified Hooke's law that includes rotations in addition to strains within an infinitesimal continuum volume or as an alternative constitutive regularization of stresses within the inelastic zone, which limits a part of the shear stress components.

In the following, we refer to the yielding criterion introduced in Eq. (2.4) as *"volumetric yielding"*, while we refer to the inequality criterion in Eq. (2.6) as *"interface yielding"*. The simplifying assumption of negligible change in fault normal displacements of the interface yielding may introduce numerical artifacts within a wide diffuse fault zone, which we further discuss in A.3. We will find that the volumetric yielding criterion is preferred for continuous fault zone representations throughout Section 2.4.

A major challenge associated with the classical stress glut method is the inherently sharp transition between on-fault and off-fault rheologies, which can lead to poor convergence properties and spurious oscillations, especially if the boundaries of the fault zone Σ intersect with grid cells[32,86].

This situation frequently occurs when modeling the fault independent of the mesh through level sets of the signed distance function, as described in this work. To address this difficulty, we define a time-invariant and smooth parameter $\phi \in [0,1]$ based on the signed distance function, i.e. $\phi = \phi(\varphi)$, with $\phi(0) \approx 1$ and $\lim_{\varphi \gg \delta} \phi(\varphi) = 0$. We suggest here to take a function $\phi(\varphi)$ of the form:

$$\phi(\varphi, A, \varphi_c) = \tfrac{1}{2}(1 - \tanh(A[|\varphi| - \varphi_c])), \tag{2.7}$$

where $A,\ \varphi_c$ are positive, nonzero parameters that influence the nature of the smooth transition from within the inelastic continuous fault zone to the elastic matrix of the host rock. In the following, we refer to the parameters $A,\ \varphi_c$ as *'blending parameters'*. Eq. (2.7) is motivated by the steady-state equilibrium profile obtained in thermodynamically derived phase-field models [12], where it describes the phase-field parameter variation normal to a given interface [129].

A stress tensor that is *smoothly* distributed over the domain Σ but *approximately* satisfying the yield limit (2.4) everywhere can be redefined as

$$\begin{aligned} \overline{\overline{\boldsymbol{\sigma}}}_f(t, \boldsymbol{x}) = &\ \overline{\overline{\boldsymbol{\sigma}}}_e(t, \boldsymbol{x}) \\ &- \phi(\varphi(\boldsymbol{x}))\,[\tau - \tau_c \operatorname{sgn} \tau]\,(t, \boldsymbol{x})\,[\boldsymbol{n} \otimes \boldsymbol{t} + \boldsymbol{t} \otimes \boldsymbol{n}]\,(\boldsymbol{x}). \end{aligned} \tag{2.8}$$

The continuity conditions for both the traction components of stress and the fault normal displacement are implicitly enforced as they are integral parts of the continuum problem formulation. The shear stress correction is continuous by the phase-field approach.

2.2.3 *Elastodynamics of dynamic rupture*

The elastic stress tensor is given by the constitutive relation

$$\overline{\overline{\boldsymbol{\sigma}}} = 2G\overline{\overline{\boldsymbol{\varepsilon}}} + \lambda\,\mathrm{tr}(\overline{\overline{\boldsymbol{\varepsilon}}})\mathbb{I} = \overline{\overline{\mathbf{C}}} : \overline{\overline{\boldsymbol{\varepsilon}}}, \tag{2.9}$$

where $\overline{\overline{\mathbf{C}}}$ is the fourth order constitutive tensor, composed of the Lamé parameters λ, G; $\mathbb{I}$ is the second order unit tensor, and $\overline{\overline{\boldsymbol{\varepsilon}}}$ is the strain tensor defined as the symmetric gradient of the displacement $\boldsymbol{u}$:

$$\overline{\overline{\boldsymbol{\varepsilon}}} = \frac{1}{2}\left[\nabla \boldsymbol{u} + (\nabla \boldsymbol{u})^T\right]. \tag{2.10}$$

The dynamic momentum balance governs the wave-mediated evolution of friction on the fault and is expressed as

$$\rho \frac{\partial^2 \boldsymbol{u}}{\partial t^2} = \nabla \cdot \overline{\overline{\boldsymbol{\sigma}}}, \tag{2.11}$$

where ρ is the density. The problem is closed and applying boundary conditions on the fault, further explained in Section 2.3 and model-specific initial conditions that are given in Section 2.4.

In all models presented, we impose a free-surface boundary condition along the entire boundary of Ω, that is we enforce $\overline{\overline{\boldsymbol{\sigma}}}\boldsymbol{n} = \boldsymbol{0}$ on $\partial\Omega$.

2.3 NUMERICAL IMPLEMENTATION

2.3.1 *Spectral elements for a phase-field method*

We use *se2dr*, a rupture dynamics extension of the stress glut method of Andrews[6], implemented in the 2D wave propagation spectral element method *se2wave* using the high-level library *PETSc*[1,9–11], as our linear algebra backend.

Our implementation uses a structured quadrilateral mesh to discretize the domain Ω. The SEM nodal basis is given by a Lagrange polynomial, which in combination with a Gauss-Legendre-Lobatto quadrature rule, the discretization results in a diagonal mass matrix $\boldsymbol{M}$. By construction, the SEM discretization allows for the flexibility of having locally (element-wise) defined material coefficient (ρ, λ, G) over the domain and also localized stresses element-wise. *se2wave* wave propagation functionality has been previously applied in Yuan et al.[146].

We use an explicit Newmark method as the time integration scheme, a conventional choice for wave propagation problems in SEM[76,77,112], which allows the direct solution of a system of second-order differential equations. Within the Newmark family, we adopt the explicit central differences rule scheme[62]. The computation of the internal forces and the application of the dynamic fault constraints in the procedure are further described below.

For the calculation of the internal forces step, we compute the stress tensor at each quadrature point by using the discrete version of

$$\boldsymbol{y} = \nabla \cdot \overline{\overline{\boldsymbol{\sigma}}}, \tag{2.12}$$

where $\boldsymbol{y}$ is an arbitrary vector. Using Voigt notation, the divergence of stress shown in Eq. (2.12) is given by

$$\boldsymbol{y} = \boldsymbol{B}^T\boldsymbol{\sigma} = \begin{pmatrix} \frac{\partial}{\partial x} & 0 & \frac{\partial}{\partial y} \\ 0 & \frac{\partial}{\partial y} & \frac{\partial}{\partial x} \end{pmatrix} \begin{pmatrix} \sigma_{xx} \\ \sigma_{yy} \\ \sigma_{xy} \end{pmatrix}, \tag{2.13}$$

where $\boldsymbol{\sigma} = (\sigma_{xx}, \sigma_{yy}, \sigma_{xy})^T$ is the Voigt representation of the stress tensor $\overline{\overline{\boldsymbol{\sigma}}}$. Similarly, the strain is described as $\boldsymbol{\varepsilon} = (\varepsilon_{xx}, \varepsilon_{yy}, 2\varepsilon_{xy})^T$, which we calculate from a displacement field as $\boldsymbol{\varepsilon} = \boldsymbol{B}\boldsymbol{u}$. We then relate both stress and strain vectors under the linear, isotropic relation in the same notation as

$$\boldsymbol{\sigma} = \boldsymbol{C}\boldsymbol{\varepsilon} = \begin{pmatrix} 2G+\lambda & \lambda & 0 \\ \lambda & 2G+\lambda & 0 \\ 0 & 0 & G \end{pmatrix} \begin{pmatrix} \varepsilon_{xx} \\ \varepsilon_{yy} \\ 2\varepsilon_{xy} \end{pmatrix}. \tag{2.14}$$

We damp spurious oscillations generated along fault by using viscous Kelvin-Voigt damping. For this, we add a term $\eta\dot{\varepsilon}$ to the calculation of the elastic stress field following Day and Ely[34], and thus apply viscous behavior to both volumetric and deviatoric deformations. There, the viscous relaxation time $\eta = 0.3\ \Delta t$, and Δt is the simulation time step, inspired after the Kelvin-Voigt damping parameters in Galvez et al.[52]. Without Kelvin-Voigt damping, spurious oscillations arise in the velocity field, as shown in Figure A.13. It will be useful to develop a deeper understanding of the stability of our method in future work, e.g., on the basis of a semi-discrete energy balance (e.g., Kozdon et al.[79]).

To implement our stress glut extension, we modify the Voigt stress vector within Σ according to a friction law under a yield criterion. In our case, we use the stress components in a fault-local orientation σ_n and τ to evaluate the yield criterion.

The stress modification is summarized in algorithm 1. The slip and slip rate are updated in accordance with the displacement and velocity fields derived from the modified stress field. Our approach does not require a nonlinear or iterative solve in each time step. Alternative friction laws may require additional steps to update their dependent variables (such as the state variable following Kaneko et al.[74]).

2.3.2 *Numerical discretization*

Numerical modeling for seismic wave propagation typically acts as a low-pass filter, accurately propagating low frequencies through the mesh, whilst high frequencies undergo undesired alteration due to numerical dispersion and dissipation[87,125]. The upper limit of the resolved frequency, conventionally called f_{max}[54], can be quantified in terms of a number of grid points or elements per shortest wavelength. In the context of SEM, the number of nodes per minimum wavelength follows

$$N_G = \frac{p\,\zeta_{min}}{h}, \tag{2.15}$$

where p is the polynomial degree to represent the basis functions within a Q_p element of size h. We use these parameters to define the spatial resolution of our SEM simulations. The minimum wavelength is defined as

$$\zeta_{min} = \min(V_s)/f_{max}. \tag{2.16}$$

For all simulations shown here (unless otherwise stated), we use Q_3 elements. Each element contains 4×4 Gauss-Legendre-Lobatto integration points with an average spacing of $\Delta x = h/3$.

2.4 KINEMATIC AND DYNAMIC RUPTURE EARTHQUAKE MODELING

We have introduced our steady-state phase-field stress glut method as a diffuse interface approach. Here, we apply this approach to earthquake modeling. We explore two well-defined problems: Kostrov's kinematically driven self-similar crack[78] and the spontaneous dynamic rupture SCEC

Algorithm 1 Pseudocode for the stress modification scheme with the diffuse fault representation.

Input: $\boldsymbol{\varepsilon}, \varphi, \delta, \boldsymbol{n}, \boldsymbol{t}$ and material parameters at quadrature point. For the Kelvin-Voigt damping, we use $\dot{\boldsymbol{\varepsilon}}$, and η, the viscous relaxation time.

Output Updated Voigt stress vector $\boldsymbol{\sigma}_f$ at quadrature point

$\boldsymbol{\sigma} \leftarrow C(\boldsymbol{\varepsilon} + \eta\dot{\boldsymbol{\varepsilon}})$
if $|\varphi| > \delta$ **then** ▷ Pure elastic matrix
  $\boldsymbol{\sigma}_f \leftarrow \boldsymbol{\sigma}$
else ▷ Embedded crack subdomain
  $\boldsymbol{\sigma} \leftarrow \boldsymbol{\sigma} + \boldsymbol{\sigma}_{bg}$ ▷ Add background stress
  Calculate the fault local normal and tangential stress components
  $\sigma_n = \boldsymbol{n} \cdot \boldsymbol{\sigma}\boldsymbol{n}$
  $\tau = \boldsymbol{t} \cdot \boldsymbol{\sigma}\boldsymbol{n}$
  Evaluate the friction coefficient μ following the corresponding friction law to calculate the yielding stress
  $\tau_c \leftarrow -\mu \min(\sigma_n, 0)$ ▷ Free-slip for tensile normal stress

  Check the selected yielding criterion
  if YieldCriterionType = Volumetric **then**
    $F_{yc} = |\tau| - \tau_c$
  else if YieldCriterionType = Interface **then**
    $F_{yc} = |\tau - G(\nabla(\boldsymbol{u} \cdot \boldsymbol{n})) \cdot \boldsymbol{t}| - \tau_c$
  end if

  if $F_{yc} \geq 0$ **then** ▷ Failure criterion reached
    $\boldsymbol{\sigma}_f \leftarrow \boldsymbol{\sigma} + \phi(\varphi)[\tau_c \operatorname{sgn}(\tau) - \tau](\boldsymbol{n} \otimes \boldsymbol{t} + \boldsymbol{t} \otimes \boldsymbol{n})$
  else ▷ Failure criterion not met
    $\boldsymbol{\sigma}_f \leftarrow \boldsymbol{\sigma}$
  end if
  $\boldsymbol{\sigma}_f \leftarrow \boldsymbol{\sigma}_f - \boldsymbol{\sigma}_{bg}$ ▷ Remove background stress
end if

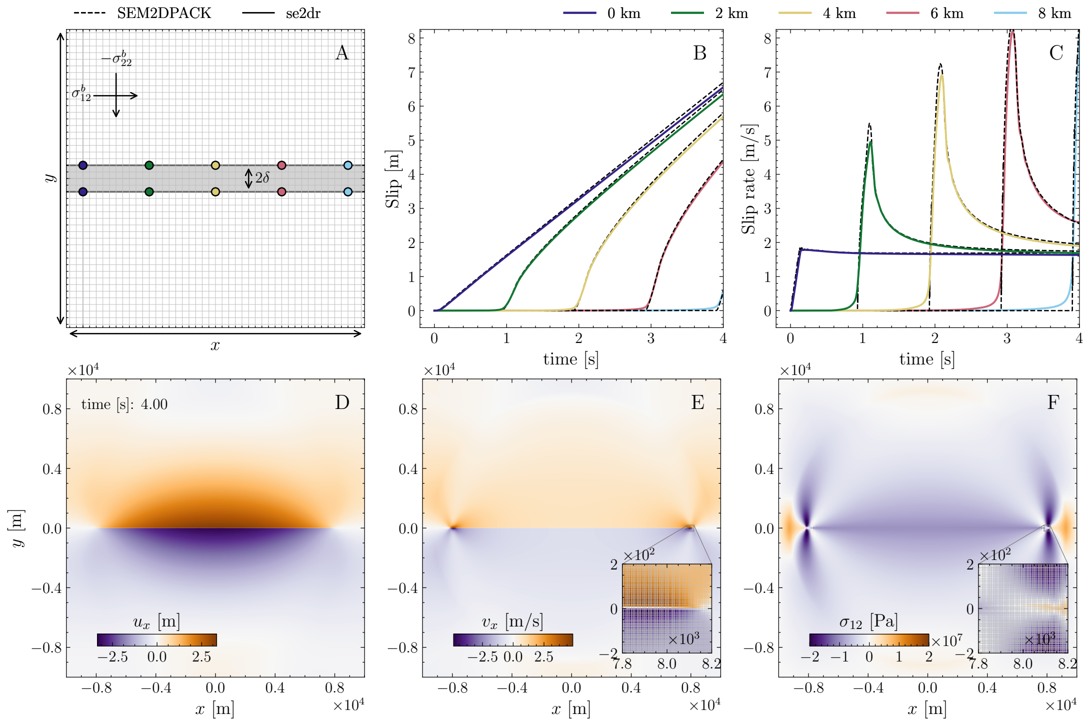

FIGURE 2.2. Phase-field stress glut model results for a kinematic Kostrov crack with the mesh-aligned configuration using our diffuse fault zone approach. The model portrays an in-plane right-lateral shear fracture under compression using the volumetric yielding criterion. The structured mesh is composed of square Q_3 elements with a width of $h = 25\,\text{m}$. The fault zone half thickness equals one element width, $\delta = h$. The model evolves for $4\,\text{s}$ of simulation time. (A) Illustrates the embedded fault in the mesh and the distribution of the receiver pairs at increasing along-strike distance from the hypocenter indicated by color, where the slip and slip rates are extracted. The next subfigures include our adopted metric of (B) slip and (C) slip rate profiles in continuous lines, compared against an SEM split node discrete fault reference solution as dashed lines. We also show the corresponding x-component snapshots at $t = 4\,\text{s}$ for the (D) displacement, (E) velocity, and (F) shear stress.

benchmark TPV3 [57]. Both these problems consider in-plane, mode II rupture propagation. We use *SEM2DPACK* [3] to provide discrete fault reference solutions and compare results by evaluating time series of slip and slip rate at specific points along the fault for *SEM2DPACK* and our *se2dr* implementation. We set the reference solutions with elements of polynomial order 6 and a cell refinement $h = 100\,\text{m}$ for both kinematic and dynamic models. The phase-field smoothing parameters are set to $A = 12/\delta,\ \varphi_c = 0.65\,\delta$ based on manual calibration.

2.4.1 *Kinematic self-similar Kostrov crack*

In the following, we vary fault geometry by first considering a straight, mesh-aligned but diffuse fault. Then, we rotate this diffuse fault to not align with the computational mesh, expecting comparable

Parameter	Value
Density (ρ)	$2500\,\mathrm{kg\,m^{-3}}$
P-wave velocity (V_p)	$4000\,\mathrm{m\,s^{-1}}$
S-wave velocity (V_s)	$2309\,\mathrm{m\,s^{-1}}$
Rupture speed (V_r)	$2000\,\mathrm{m\,s^{-1}}$
Normal stress (σ_{22}^b)	$-40\,\mathrm{MPa}$
Shear stress (σ_{12}^b)	$20\,\mathrm{MPa}$
Characteristic distance (L)	$250\,\mathrm{m}$
μ_s	0.5
μ_d	0.25

TABLE 2.1. Parameters describing our Kostrov-like self-similarly propagating kinematic shear crack model.

results in important aspects. Finally, we perturb the straight diffuse fault geometry to achieve a curved, sigmoidal geometry. This last model configuration deviates from the reference benchmarks and solutions but provides important information on the geometrical flexibility of our approach. Kostrov's non-singular self-similar shear crack is driven by a time-weakening friction law

$$\mu(x_\Gamma, t) = \max\{\mu_d, \mu_s - (\mu_s - \mu_d)(V_r t - |x_\Gamma|)/L\}, \tag{2.17}$$

where rupture evolves under a prescribed constant rupture propagation velocity V_r and L is the model characteristic distance. The friction coefficient decreases from a static friction coefficient μ_s to a dynamic friction coefficient μ_d. This model assumes that the rupture starts from the origin and propagates self-similarly along the fault defined as the arc length integral $x_\Gamma = \int_\Gamma \sqrt{1 + (dx_f(a)/da)^2}\, da$ as a measure of the accumulated length along the prescribed zero level set geometry x_f, parameterized by the variable a. Our model assumes a homogeneous isotropic elastic medium and a predefined fault interface loaded by background normal and shear tractions as defined by Madariaga et al.[86]. The setup allows for analysis of the phase-field relations between fault slip, slip rate, and shear stress under imposed reactions, which avoids the full complexity of spontaneous rupture dynamics. The model parameters are summarized in table Table 2.1. We solve our problem in a domain that spans a 20 km×20 km area, with a fault length spanning throughout the domain.

In this first model, we demonstrate that a phase-field simulation can resemble a discrete fault solution in difference to previous findings analyzing thick fault or stress glut fault approaches[32,114]. Figure 2.2 summarizes the setup and results of a horizontal Kostrov-like kinematic crack simulation performed with squared Q_3 and cell size $h = 25$ m, using the volumetric yielding criterion (see Section 2.2.1), and fault zone half-width $\delta = h$ (see Figure 2.2 A), plotted alongside the discrete SEM split-node reference solution. The phase-field solutions are computed in the diffuse interface model using Eq. (2.2)).

We observe close agreement between the diffuse interface and reference models in the time series of slip and slip rate, shown for 5 receiver-pairs located along the fault zone. Phase-field fault slip appears slightly smeared out at its onset and asymptotically very slightly underestimates the classical Kostrov crack solution (Figure 2.2 B). In the diffuse model, the slip rate peak is also slightly delayed and lower in amplitude with respect to the discrete fault reference. Analogous to the reference, slip rates asymptotically fall off after the rupture front has passed (Figure 2.2 C). The snapshot of particle displacement at 4 seconds simulation time (Figure 2.2 D) illustrates the smooth, well-resolved solution everywhere in our domain. The corresponding velocity and shear stress fields are equally well resolved (Figure 2.2 E,F). The zoom-in to the fault zone reveals no out-of-plane rotation of the rupture tip. In general, the phase-field model does not introduce dynamic differences on the scale of the diffuse fault, in difference to what was reported in alternative diffuse interface simulations of the same benchmark (cf. Fig. 2 in Gabriel et al.[50]).

Changing the yielding criterion (Eq. (2.4) or (2.6)) will lead to only minor differences. The results using the volumetric yielding are smoother in comparison to the diffuse interface yielding criterion as shown in A.3, Figure A.2(A)).

In our next example, we first demonstrate the mesh independence of our method. Second, we show that the increased demands on the accuracy of mesh-independent simulations can be addressed by using more elements to resolve the fault zone. We rotate the phase-field and stress tensors that constitute the fault geometry and initial conditions by 20° counter-clockwise from the first Kostrov-crack example. Although the computational mesh is not aligned with the fault, the stress background conditions and model assumptions continue to be the same as in the horizontal configuration. For our tilted configuration, we use the volumetric yielding criterion and a fault zone consisting of a total of 5 elements, $\delta = 2.5h$. Again, we use Q_3-elements, and an element size $h = 25$ m.

Figure 2.3 shows slip (A) and slip rate (B) time series recorded along the fault and the x-components of the displacement (C) and velocity fields (D) in the domain. We illustrate that the stress glut phase-field model captures the kinematics, i.e. the fault slip (A) and slip rate (B), of the now mesh-independently evolving self-similar Kostrov crack. The slip and slip rate amplitudes are slightly reduced compared to the split-node reference solution, The slip rate time series shows secondary complexities developing within the fault zone after the main rupture front has passed (also visible in D) that do not appear in the reference solution. The emanated seismic waves in terms of displacement (C) and velocity fields (D) are very smooth and agree with those generated in the previous mesh-aligned model.

In our first example, the diffuse fault was perfectly aligned with the element edges. Our smooth phase-field function defined in (2.7) was orthogonal to the element edges and reproduced the split-node reference solution using only two high-order elements, $\delta = h$. The tilted model using this minimal fault zone half-with $\delta = h$ (low opacity lines in Figure 2.3(A, B)), however, produces significantly reduced slip rate amplitude. The slip rate profiles do not show the correct asymptotic behavior after the peak slip rate compared to the reference model and as was observed in the mesh-aligned configuration for the same fault zone resolution. We show in Figure 2.3(A, B) that the additional challenges of resolving crack propagation now not orthogonal to the element edges require higher accuracy, which can be achieved by using more elements to resolve our stress glut phase-field fault zone. Earlier smeared crack models (e.g., Rots and Blaauwendraad[120]) have also considered resolving the crack thicknesses with more than 1-2 elements in their models. However, the stress glut approach has been restricted to using $\delta = h$ in earlier work.

Increasing δ/h for a given polynomial order and thus increasing the number of elements that describe the fault zone inelastic rupture kinematics in the case of the tilted Kostrov Model leads to the expected asymptotic behavior. Figure A.7 shows h-refinement while keeping δ/h fixed to 2.5. Choosing a larger δ/h leads to better convergence of the numerical solution. In the case of dynamic rupture in the TPV3 model, finding an appropriate δ/h for a given polynomial degree is more complex. In our TPV3 simulations, the width of the nucleation patch is fixed to equal the thickness of the fault zone, which challenges convergence analysis due to the sensitivity of nucleation of spontaneous dynamic rupture to the size (and shape) of the nucleation patch (e.g., Gabriel et al.[48], Galis et al.[51]). An accurate representation of deformation within the fault zone is governed by the interplay of the δ/h ratio, the polynomial order of the elements, and their alignment with the grid. Furthermore, the ratio between δ and the cohesive zone size characterizes the accurate representation of the deformation at the rupture tip stress transition (see A.5). These factors are useful to characterize resolution requirements that lead to accurate fault zone modeling. Additionally, the nucleation zone size should be carefully chosen due to the rupture sensitivity to it.

In Supplementary Figure A.2(B), we show the results of the same model using the interface yielding criterion. In comparison to using a volumetric yielding criterion, we see small-scale deviations from the reference slip-rate time series. As we will discuss in the following dynamic rupture examples, these may result from physical fault zone effects. We conclude that for non-mesh-aligned phase-field models, more elements resolving the diffuse fault zone and using the volumetric yielding criterion are beneficial for quantitatively resembling discrete kinematic rupture propagation.

To further evaluate the geometrical flexibility of the method, we distort the planar Kostrov crack into a sigmoidal curve. The zero level set is parameterized as

$$\Gamma = \left\{ \left(a,\ A_s \frac{(1-k)a}{(1-2|a|)k+1} \right)\ \forall\ a \in \mathbb{R} \right\} \tag{2.18}$$

with parameters $k \in (-1, 0)$ and $A_s \in \mathbb{R}$, which control the curvature and the scale of the function, respectively. We make the particular choice to set $k = -2 \times 10^{-4}$ and $A_s = 2$, which results in the sigmoidal fault configuration shown in Figure 2.4. In our model, such a curve is prescribed as a discrete set of 4×10^5 points. By performing a nearest neighbor search, we identify the closest point on the curve to the quadrature points and use it to initialize the phase-field throughout the domain. In future developments, this can be replaced by, e.g., a fast marching method approach to enable a re-initialization at every time step. Such flexibility is advantageous in the context of studies involving time-dependent evolution of fault geometries, where it would be necessary to recalculate the signed distance function at every time step.

Figure 2.4 shows the result for the sigmoid configuration using the volumetric yielding criterion, with blending parameters held equal to the tilted configuration and a fault thickness of $\delta = 2.5h$. Its results lead to slip and slip rate profiles well comparable to the discrete fault reference solution, slightly reduced in amplitude, similar to the tilted configuration. Again, our slip rate shows small oscillations behind the rupture front. Note that here, the kinematic model defines the background stress components in fault local coordinates, which implies a spatially heterogeneous background stress for a curved geometry. For this reason, metrics based on the sampling of the near field of a

Parameter	In nucleation zone	Outside nucleation z.
Density ρ	$2670\,\mathrm{kg\,m^{-3}}$	$2670\,\mathrm{kg\,m^{-3}}$
P wave speed V_p	$6000\,\mathrm{m\,s^{-1}}$	$6000\,\mathrm{m\,s^{-1}}$
S wave speed V_s	$3464\,\mathrm{m\,s^{-1}}$	$3464\,\mathrm{m\,s^{-1}}$
Normal stress σ_{22}^b	$-120\,\mathrm{MPa}$	$-120\,\mathrm{MPa}$
Shear stress σ_{12}^b	$81.6\,\mathrm{MPa}$	$70\,\mathrm{MPa}$
Critical slip dist. D_c	$0.40\,\mathrm{m}$	$0.40\,\mathrm{m}$
Static friction μ_s	0.677	0.677
Dynamic friction μ_d	0.525	0.525

TABLE 2.2. Parameters describing the community benchmark TPV3 for a spontaneous dynamic rupture crack[55]. Fault normal stress is negative under compression.

kinematic model are comparable to the metrics obtained from a planar simulation in Figure 2.3. Further away from the fault, the shear stress wavefield mapped on fault local coordinates shows larger regions of lowered differential stress located at the convex side of the curved fault.

2.4.2 *Spontaneous dynamic rupture*

We model dynamic earthquake rupture in the 2D version of the SCEC/USGS community benchmark problem TPV3 for elastic spontaneous rupture propagation[55]. Our TPV3 configuration extends the kinematic Kostrov models to spontaneous dynamic rupture propagation. This model uses a linear slip weakening friction law[63] given by

$$\mu(x,t) = \max\{\mu_d, \mu_s - (\mu_s - \mu_d)|S(x,t)|/D_c\}, \tag{2.19}$$

where D_c is the critical slip distance, and S is the slip, which we extract from the displacement field, as in Eq. (2.2). The model contains a sharp overstressed nucleation patch that initiates self-sustained dynamic rupture. The patch is defined by a length of 3 km, and it is located within a fault of 30 km length as defined in Harris et al.[57], within a 60 km×60 km domain, and the conditions depicted in Table 2.2.

We compare this model first in the mesh-aligned configuration in Figure 2.5. We find that the results are quantitatively comparable with the discrete fault reference solution of the TPV3 benchmark calculated with *SEM2DPACK*. In this example, we use the interface-yielding criterion. At around $t = 0.6\,\mathrm{s}$, the rupture front leaves the overstressed nucleation region, propagating spontaneously along the planar fault. We observe in our results a slight delay in rupture speed compared to the reference solution by comparing the arrival times of the peak slip rate at the receivers along the fault. Comparable to the reference, the fault slip rate approaches an asymptotic fall-off behavior after the rupture front has passed. The arrival of the stopping phases when the propagating rupture front reaches the fault edges is observed as an abrupt reduction of the slip rate magnitude after 6 s of simulation time near the end of the profiles. Note that the fault-limiting edges are located well within the simulation domain, far from the limiting boundaries. The model domain is chosen large enough to avoid wave reflections from the domain boundaries.

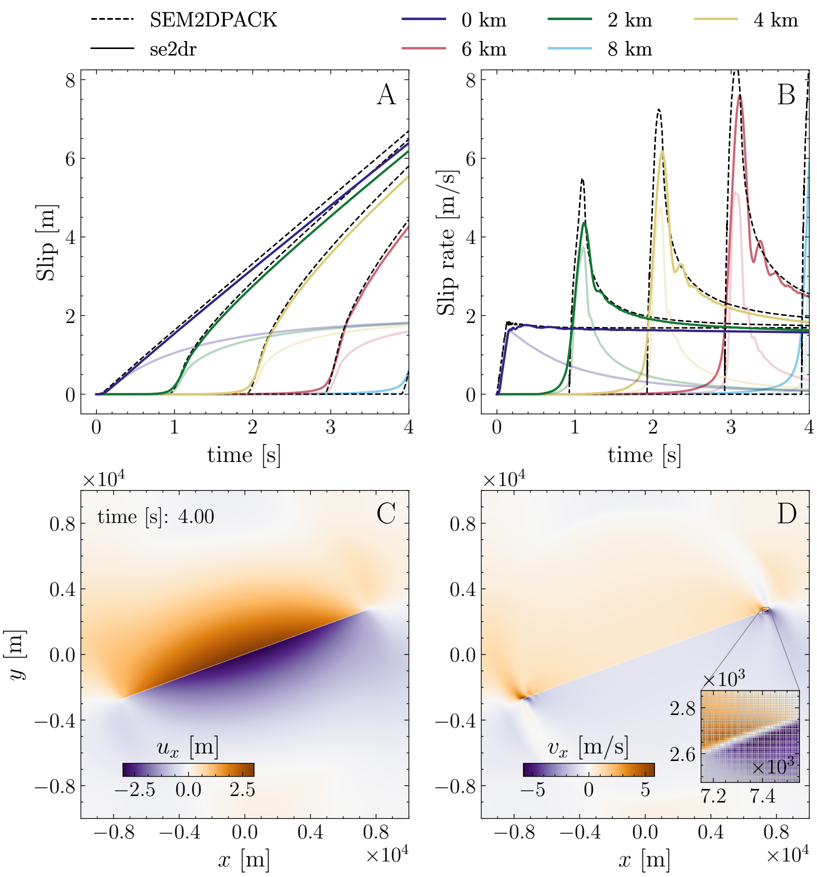

FIGURE 2.3. Phase-field stress glut model: Kostrov-like crack model under a tilted, mesh independent geometry. The model uses the same mesh and model parameters as in Figure 2.2, with a 20° counterclockwise tilting, relative to the mesh axis, and a wider fault zone ($\delta = 2.5h$). The model uses the volumetric yielding criterion. The figure depicts (A) the slip profile and (B) the slip rate profile compared against an SEM split node discrete fault reference solution at receiver pairs with increasing along-strike distance from the hypocenter indicated by color. Additionally, the figure contains the x−component of the (C) displacement and the (D) velocity field with an inlet focused on the propagating front. In (A) and (B), we highlight the effect of choosing fewer elements to resolve the fault zone width δ by plotting the slip and slip rate results of the same tilted model using $\delta = h$ in lower opacity.

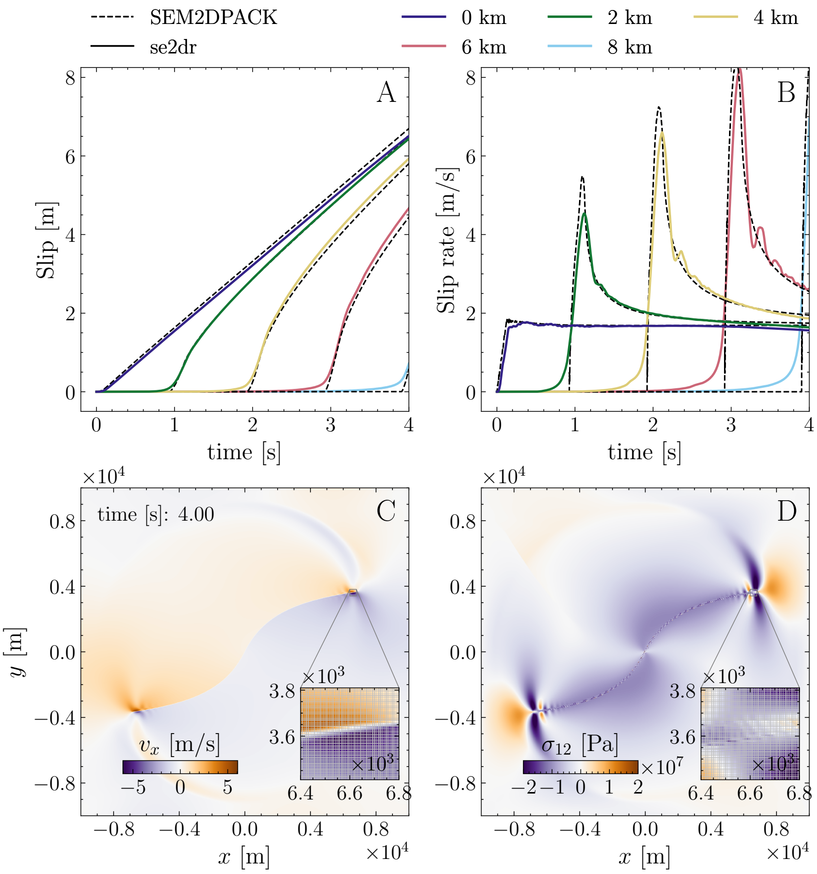

FIGURE 2.4. Phase-field stress glut model: Kostrov-like crack with a sigmoid shape. The model uses the same mesh parameters and thickness of the diffuse zone ($\delta = 2.5h$) as in Figure 2.3. This configuration depicts a sigmoid shape with a zero-level set following Eq. (2.18), using the volumetric yielding criterion. The figure contains (A) the slip profile and (B) the slip rate profile compared against an SEM split node discrete fault reference solution, with receiver pairs at increasing along-strike distance from the hypocenter indicated by color, and (C) the $x-$component of the velocity field and (D) the shear component of the stress in fault local coordinates.

The mesh-aligned dynamic rupture solution using the volumetric yielding criterion shows a small secondary pulse in the slip rate profiles that originates at the transitional interface between the nucleation patch and the remainder of the fault zone. We find that the fault zone shear stress distribution at the sharp edge of the nucleation patch defined in the benchmark causes fault-oblique yielding across the full fault zone width. The resulting stress shadowing temporarily counteracts local yielding in the phase-field model, while a non-disturbed single spontaneous rupture front develops in the discrete fault reference. Later, with the continuous development of the stress field through time, this location also eventually reaches the yield surface, generating delayed reactivation at the hypocenter, causing a secondary slip rate pulse.

Delayed, co-seismic fault reactivation has been reported in real earthquakes, such as during the 2019 northern Peru intraslab earthquake [138], the 2011 Tohoku earthquake [80] and the 1984 Morgan Hill earthquake [15]. Fault reactivation in discrete fault dynamic rupture simulations can be caused by several model complexities, including pulse-like rupture growing stresses after the passage of its healing front [48,101] and the presence of a fault damage zone, approximated as a low rigidity layer surrounding a discrete fault [61,64].

Figure 2.6(A) shows slip rates using the volumetric yielding criterion. In comparison, introducing the interface yielding produces a solution closer to the discontinuous reference, free of secondary slip pulses, as seen in Figure 2.6(B). Our analyzed metrics of interest, the slip and slip rate, are extracted from the difference between the displacement field components along the fault parallel direction at $\pm\delta$. As a result, asymmetries in the rupture front may introduce a brief fluctuation in the slip rate metric before the main slip rate peak arrival. We note that this fluctuation can result in negative values of slip rate when we use the 'interface yielding criterion' (e.g., in Figure 2.5(C) and Figure 2.6(B)). A comparison of these results against solutions using both yielding criteria is given in A.3.

As before, for the Kostrov-like crack, we rotate the dynamic rupture model into a configuration that is out of alignment with the computational mesh (Figure 2.7). Our experiments show that our choice of fault thickness affects the rupture initiation process in our adaptation of the TPV3 benchmark with a fixed overstress as a direct consequence of setting the nucleation zone width equal to the variable width of the fault zone (i.e. 2δ) within our fault representation. Figure 2.7 shows a numerical example that uses a fault half-thickness parameter $\delta = 1.43h$, which leads to the qualitatively expected behavior of the rupture. This half-thickness is chosen based on the diagonal length of a square element to ensure that a whole element falls within half of the inelastic zone. When $\delta = 4.0h$, we observe the development of small-amplitude slip pulses in the form of reverberating fault zone waves within the nucleation patch. Later, after the rupture has successfully initiated, the velocity wavefield follows the expected overall behavior in line with the mesh-aligned configuration. At small values of $\delta = 1.0h$, the nucleation size is smaller, and we observe complete dissipation of the rupture front over time, leading to dying (unsustained) rupture. For higher values of δ, the fault zone half-thickness relative to the element width (e.g., $\delta = 4.0h$), trapped waves develop within the fault zone. As detailed in A.1, our approach results in an effective modification of the stiffness tensor, leading to a transversely isotropic material within the fault zone. This leads to a locally modified shear modulus relative to the rest of the domain. Constructively interfering fault zone

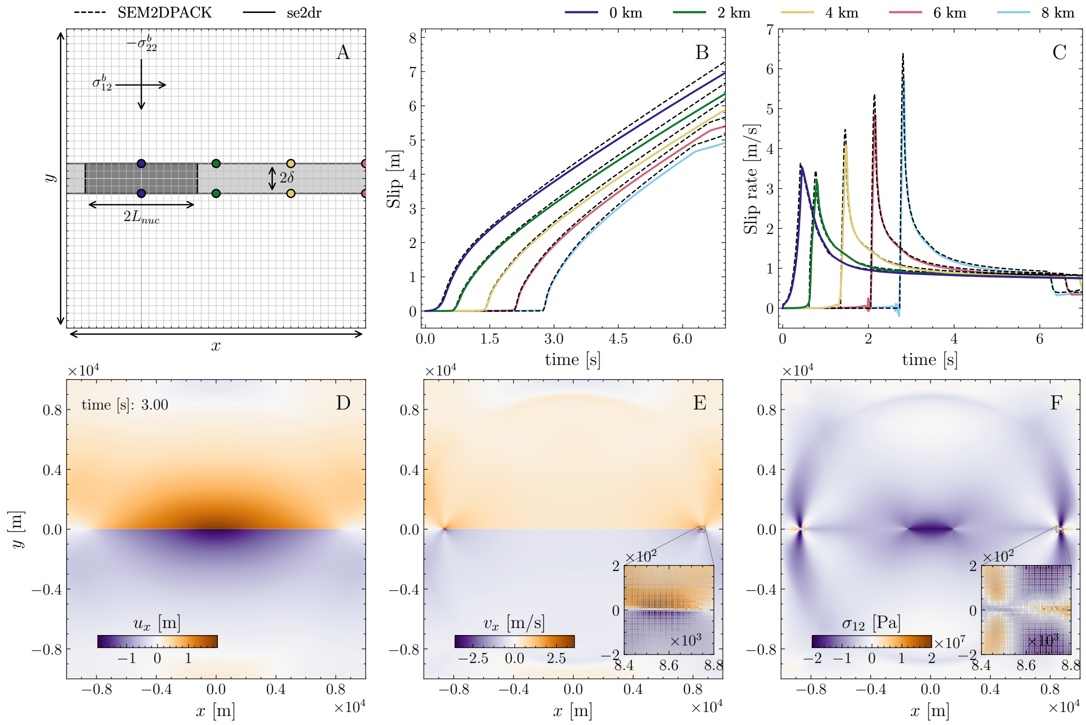

FIGURE 2.5. Phase-field stress glut model: Mesh-aligned TPV3. The mesh is composed of squared Q_3 elements and element width $h = 25\,\mathrm{m}$. This model uses the interface-yielding criterion. The fault zone parameter $\delta = h$, and the system evolves for $7\,\mathrm{s}$ of simulation time. (A) Illustrates the model configuration, including the location of the nucleation within the fault zone and the receiver pairs at increasing along-strike distance from the hypocenter indicated by color. Next to it, the figure includes the (B) slip and (C) slip rate profiles compared against the reference solution profiles. The figure also includes the result's corresponding $x-$component snapshot at t=3 s for the displacement (D), velocity (E), and shear stress (F).

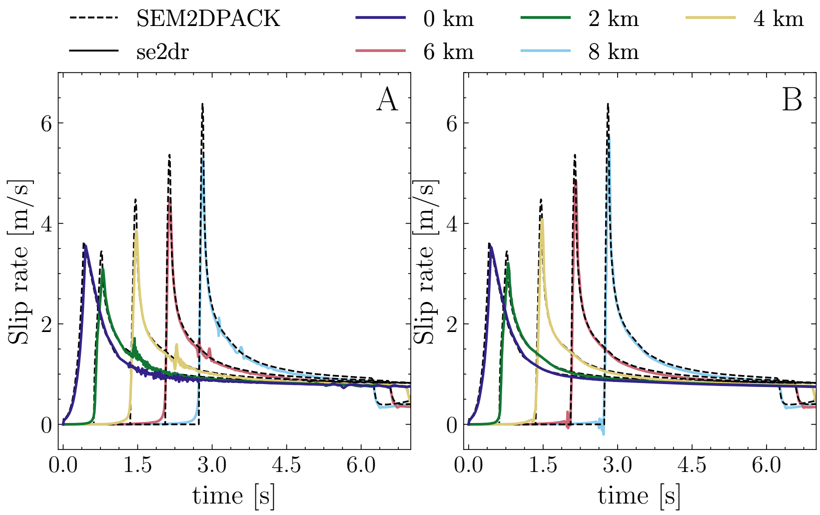

FIGURE 2.6. Comparison of the 2D TPV3 dynamic rupture solution yielding criteria, with square Q_3 elements of width $h = 25\,\mathrm{m}$, and blending parameters as in Figure 2.5. (A) shows the simulation results at receiver pairs with increasing along-strike distance from the hypocenter indicated by color, using the volumetric yielding criterion, while (B) depicts the results using the interface yielding criterion.

waves later form a coherent rupture front, producing a complex wavefield in the interior of the fault zone and exciting high-frequency seismic radiation visible in the velocity field in the vicinity of the nucleation patch in the fault normal direction (Figure 2.7, panels with $\delta = 4\,h$). Since we do not allow material failure outside the prescribed finite thickness fault zone, which is stationary in time, newly yielding localization of secondary faults, continuously growing away from the inelastic subdomain of the main fault, are not expected as a contributing source to high frequency in the model.

The effects of different choices of δ in our non-mesh-aligned numerical tests agree with previous findings (e.g., Gabriel et al.[48], Galis et al.[51], Huang et al.[61]): slight variations of the nucleation size, for a fixed prescribed overstress, can lead to unsuccessful initiation of the rupture process on the lower end of the parameter space allowing for self-sustained rupture, implying that the initiation is not sufficiently strong for supporting rupture to spontaneously propagate and develop into a self-sustained propagating rupture. In the overcritical limit, larger patches introduce changes in rupture dynamics, including changes in rupture style and speed, such as super-shear transitions and higher slip-rate amplitudes.

2.4.3 Spectral properties of the modeled seismic wavefield

For the element choice in our mesh, the shear wave velocity assumed for the TPV3 model, and assuming several integration points per minimum frequency as $\zeta_{min} = 30$ due to the relatively low polynomial order used, we can assess the upper cut-off frequency as approximately 13 Hz. We chose

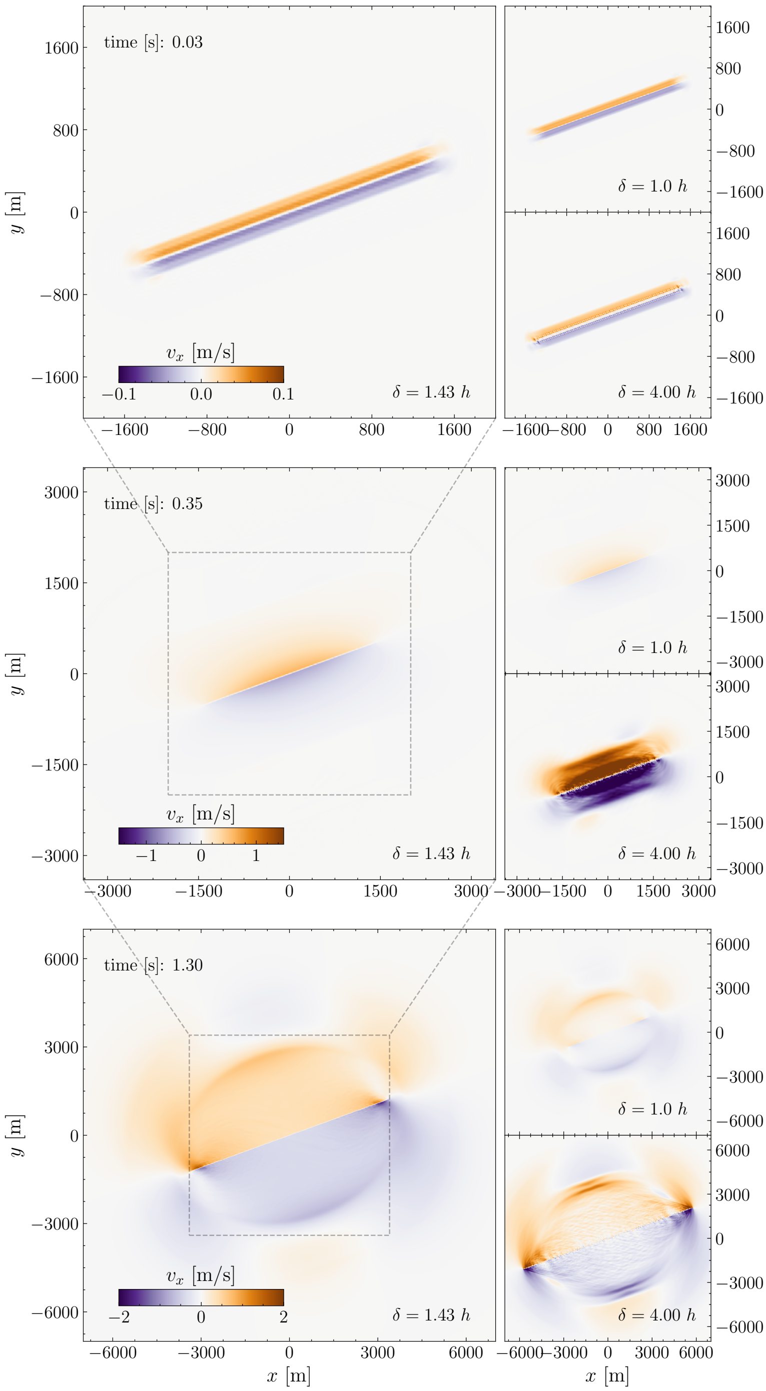

FIGURE 2.7. Phase-field stress glut model: Variation of the δ parameter for tilted TPV3 simulations. The mesh is composed of square Q_3 elements of width $h = 25\,\mathrm{m}$. The figure includes three sets of frames per time step. Each frame set contains the x-component of the velocity field and showcases three values of the half inelastic zone parameter δ; h, $1.43h$, and $4h$. The models here use the volumetric yielding criterion. Each figure subset depicts on the left column the expected qualitative behavior for the intermediate half inelastic zone thickness. On the right column, the subset illustrates two end-members of the δ parameter variation: on the top, the dissipation of the rupture front, and below, the formation of small amplitude resonance in the velocity field within the nucleation zone. In our numerical simulations, we link the size of the nucleation zone to the corresponding thickness of the fault zone. As a consequence, the behavior of the numerical simulation is sensitive to the chosen fault width 2δ.

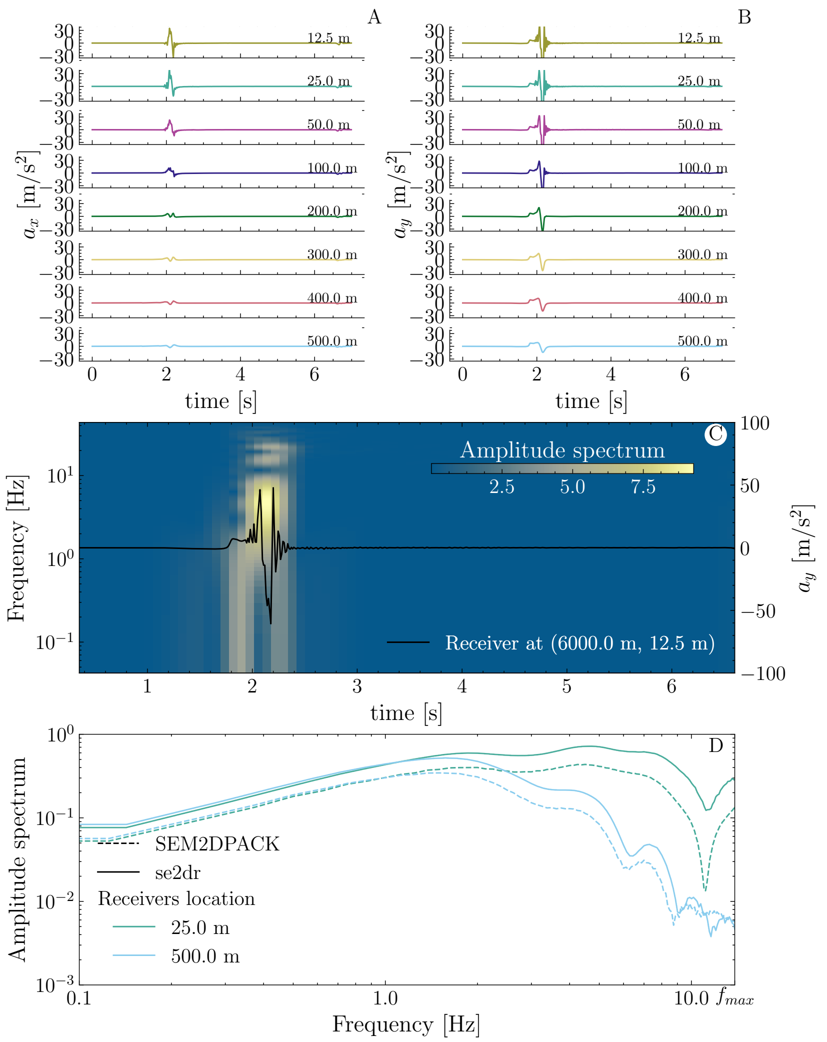

FIGURE 2.8. Phase-field stress glut model, TPV3 mesh-aligned model: Variation of the (A) $x-$ and (B) $y-$components of synthetic accelerograms, at stations located at $6\,\mathrm{km}$ along the fault, and varying distances normal to the fault for the simulation in Figure 2.5. (C) Spectrogram extracted from the $y-$component of the acceleration from a receiver at the coordinates ($6\,\mathrm{km}$, $25\,\mathrm{m}$). (D) Amplitude spectra of the fault-normal accelerograms at two receivers at $6\,\mathrm{km}$ along the fault and, $25\,\mathrm{m}$ and $500\,\mathrm{m}$ normal to the fault, simulated with se2dr (continuous and dotted lines for each yielding criterion used) and the split-node discrete fault approach in *SEM2DPACK* (dashed lines). All spectra are shown to the numerically resolved f_{max}=$13\,\mathrm{Hz}$.

this value for ζ_{min} from the suggested range of $10-30$ for low (<4) element order after Seriani and Priolo[125]. For the mesh settings of the reference solution and an assumed $\zeta_{min}=10$, the reference solution has an upper cut-off frequency of 20 Hz. With this information, we limit the upper band of the frequency spectra in Figure 2.8(D) to the cut-off frequency.

Rupture acceleration and deceleration generate high-frequency seismic wave radiation[84]. For this reason, we expect a roughly flat signal in the spectra of the acceleration records for the kinematic model, where the rupture velocity is constant. The amplitude spectrum from receivers in the Kostrov kinematic model solution is shown in A.2. For the dynamic model, we extract the along-fault (A) and fault-normal (B) accelerograms in Figure 2.8 from receivers at different distances normal to the fault. The accelerogram spectral amplitudes of the dynamic model in Figure 2.8(D) at two receiver locations; both 6 km along the fault from the fault center, and respectively at a distance of 25 m and 500 m normal to the fault, are increasing until just above 1 Hz, with amplitudes systematically higher than the reference solution.

Discrete coseismic off-fault damage has been considered to enhance high-frequency radiation in acoustic recordings during stick-slip events[23,54]. Okubo et al.[105] finds significant high-frequency radiation caused by secondary discrete fractures in simulations compared to the no-off-fault damage case. In our diffuse simulation using an interface-yielding criterion, we overall observe a similar trend as in the reference solution, with no significant shift towards the high frequencies. Analogous to the reference solution, the frequency content decays rapidly with the fault-normal distance, roughly reduced by one order of magnitude near the upper cut-off frequency. However, the fault-reactivation slip pulse (observed in Figure 2.5, using the volumetric yielding criterion) contributes to the higher frequency content, shifting the amplitude spectra upwards towards the upper cut-off frequency in comparison to the reference solution. This high-frequency contribution can be seen in Figure A.4.

2.4.4 Resolution refinement analysis

A formal convergence analysis requires an analytical solution that is not available for our steady-state phase-field diffuse fault approach. Instead, we present refinement analysis by means of comparison to a high-resolution reference solution[110,143] and illustrate convergence toward the reference solution under h- and $p-$refinement and variation of blending parameters.

We here choose a steady-state phase-field description of the diffuse transition from the yielded, inelastic region into the pure elastic media, which offers a flexible numerical approach for the mesh-independent representation of a discontinuity. The selection of the blending parameters influences the accuracy of our metrics of interest, the slip and slip rate, against the high-resolution reference solution. Steeper transitions lead to spurious oscillations behind the rupture front, a product of Gibbs phenomena, with strong signal amplitudes, while smoother transitions lead to reduced signal amplitude. Our choice, although not optimized, is intended to balance the trade-offs of end-member choices in the blending parameter space. Future work may explore physic-based considerations to inform these choices.

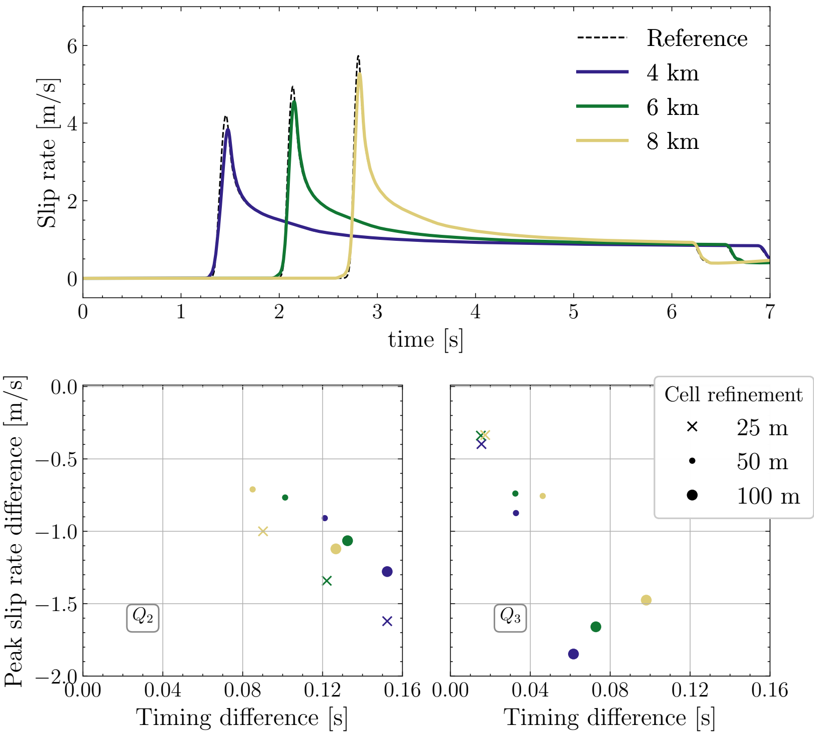

FIGURE 2.9. Filtered (Butterworth with $f_c = 10\,\mathrm{Hz}$) slip rate profiles. The top row shows the simulation slip rate results to the TPV3 mesh-aligned model with alternative blending parameters $A = 18/\delta$, $\varphi_c = 0.65\delta$. These results use Q_3 elements with $h = 25\,\mathrm{m}$ and $\delta = h$ and an interface-yielding criterion color-coded by station location along the fault. The second row depicts the difference between the peak slip rate and timing between the reference and our simulation results from filtered slip rate profiles from three receivers at 4, 6 and 8 km along the fault. The scatter plots include such differences for the blended Q_2 and Q_3 elements in the simulations and various element sizes. The marker symbol depicts the cell refinement used in each simulation. Results here are filtered to extract and compare the peak slip rate values and timings in (B) and (C) across different refinement levels.

The blending variables may be interpreted as additionally introduced degrees of freedom to fit against a reference solution; alternatively, they can be further constrained under phase-field theory and be considered a proxy for material damage. Variation of the blending parameters influences the accuracy against a reference solution. Figure 2.9 (top row) shows the solution to the TPV3 benchmark problem by using a set of blending parameters $A = 18/\delta$, $\varphi_c = 0.65\delta$, i.e. a steeper blending than in the result from Figure 2.5, also using the interface yielding criterion.

The results approach the reference solution, reflected in reduced differences in peak slip rate amplitude and timing. For this choice of blending parameters, we perform mesh refinement analysis and a variation of the simulation polynomial degree for the dynamic rupture TPV3 benchmark, which we compare against the well-defined high-resolution reference solution to the benchmark problem. We use a Butterworth filter with a cut-off frequency of 10 Hz for solutions with different mesh size and order of polynomial refinements ($h-$ and $p-$refinements respectively) and compare how the peak slip rate of our results differ from the reference in terms of amplitude and timing, as seen in Figure 2.9 (bottom row). We evaluate the differences for the receivers located at 4, 6, and 8 km along the fault.

Our results show systematically lower amplitudes for our Q_3-element solutions. However, we also report on results when further increasing the resolution in the simulations. $p-$refinement leads to faster growth of the peak slip rate amplitude towards the reference and reduced timing differences for the different receivers along the fault. The systematic delay in timing gets reduced by cell refinement, which also affects the inelastic fault zone width. The amplitude of the peak slip rate depends on the discretization within the fault zone and the blending parameters used, as it describes the offset from the elastic stress response and its transition into the elastic media at the quadrature points within the subdomain. Also, using Q_2-element fails to reproduce the asymptotic fall-off behind the peak slip rate arrival (Figure A.12), denoting a requirement for higher spatial resolution.

Our method reproduces the reference solution at a relatively low polynomial refinement for a given phase-field distribution choice. Its accuracy is affected by the resolution of the yielding elements, implying that adaptive mesh refinement can be applied to the method for future optimization purposes. Higher polynomial orders can be tested after optimizing our implementation to establish that the method maintains the same numerical accuracy (convergence order) as the classical SEM.

2.5 Discussion

Dalguer and Day[32] assessed the accuracy of the Traction at Split Node (TSN) method, the thick fault proposed by Madariaga et al.[86], and the stress glut from Andrews[4] in a staggered grid finite difference discretization. The explicit incorporation of discontinuous velocity nodes in the TSN method allows for a natural partition of the equations of motion at each side of the fault surface on which the split nodes are located. In this context, the stress glut and the thick fault methods require a fixed fault thickness with respect to the computational grid resolution. The stress glut method's fault zone width is two halves of contiguous elements, i.e., an inelastic zone of one grid step, with the fault center defined as the common border defining a plane of shear-stress grid points. The thick fault places the fault halfway between two shear-stress planes, and the fault zone thickness is two grid steps. Under these assumptions, the stress glut method reproduces well the qualitative features of the discrete fault reference solution but with quantitative deficiencies. It was reported that the rupture velocity remained systematically low. The thick fault reported a misfit in rupture time of 30% and higher, which then failed to match the rupture behavior of the reference solution qualitatively. One of the main conclusions of Dalguer and Day[32] was that the formulation of the jump condition mainly controls the solution accuracy in finite-difference spontaneous rupture simulations.

In this work, we have modified the stress glut approach and have improved the solution accuracy by using a steady-state phase-field model, enabling a smooth transition between the yield stress and the elastic shear stress. Our stress glut extension to the framework of SEM in the mesh-aligned configuration shows overall qualitative and quantitative agreement with 2D benchmarks of kinematic and dynamic rupture problems when verified against a split-node SEM reference from Ampuero[3]. In general, the solutions show an expected systematic delay of the rupture front arrival (that is, slower rupture speed), depending on the prescribed half-thickness of the fault zone δ, relative to the element dimensions. Introducing the diffuse interface description reduces fault zone spurious oscillations introduced by Gibbs phenomena due to the stress discontinuity from the imposed limiter on the stress. Similar to the typical employed visco-elastic Kelvin-Voigt damping in split-node SEM dynamic rupture modeling, and equivalent to introducing off-fault plasticity or damage[7,33,49,144], our diffuse fault zone introduces reduction of amplitude in both slip and slip rate metrics as well as in rupture speed. A higher $p-$refinement level combined with $h-$refinement and our proposed blending function (e.g. Figure 2.5) approach the reference solution in the mesh-aligned case, with reduced spurious oscillations behind the rupture front.

2.5.1 Physical interpretation of the stress field of a diffuse fault

Andrews[6] pointed out that embedding a crack through the stress glut formulation affects the neighboring stress in an irregular way that can be compared to the Eshelby inclusion problem[41]. The complexity of the stress field incurred by such inelastic 'inclusions' increases when it interacts with the evolving stress field around the dynamically propagating rupture and may prevent locations within the fault zone from reaching the yielding surface at a specific time.

This increased complexity in the stress field directly affects our dynamic rupture results, as before the onset of yielding and development of the fully spontaneous rupture front, distributed shear stress locally shadows the fault zone regions at the vicinity of the transition between the nucleation patch and the rest of the fault zone. The incipient rupture develops asymmetrical dynamic normal stress evolution, which leads to fault-oblique yielding within the fault zone. Note that this oblique geometry characterizes shear-driven deformation between two surfaces undergoing relative motion at each side of the embedded fault zone. The fault geometries used in this study are prescribed and do not evolve in time, hence, by construction, our models do not permit the development of spontaneous Riedel-type shear structures. However, the observed emergence of oblique yielding within the fault surface may be interpreted as an evolving fault-zone internal shear band. This phenomenon at the vicinity of the boundary between the prescribed nucleation patch and the remainder of the prescribed fault zone alters the timing of the onset of rupture at locations neighboring the nucleation patch when using a volumetric yielding criterion in mesh-aligned numerical simulations. These temporally 'dynamically locked' patches are later reactivated by evolving stresses in their vicinity, producing a measurable, small amplitude propagating secondary slip-pulse. We note that the TPV3 model setup includes a challenging characteristic, as it contains a sharp transition between the nucleation asperity and the rest of the fault [51]; however, we also observe dynamically impacted fault zone yielding in alternative descriptions of the nucleation patch (see in A.3, Figure A.3).

We designed the interface yielding criterion as defined in Eq. (2.6) to suppress the observed tendency for fault-oblique yielding at asperities within the fault zone. As further discussed in A.3, this alternative yielding criterion implies the yielding of all regions behind a fully spontaneous fault zone rupture front. It is a justifiable assumption applied to our diffuse fault when our goal is merely to emulate the results from planar, discrete fault representations. However, for thicker fault zones, the interface yielding assumption introduces perturbations on the stress field within the fault zone, especially at the vicinity of the rupture front, which in turn introduce spurious oscillations of the shear stress component propagating in fault-strike direction (as we show in kinematic and dynamic rupture simulations). This simplification can also be perceived as a variation of Hooke's law that integrates rotations along with strains in evaluating the yield criterion without affecting the elasticity update.

Distinct features are evident throughout the fault-parallel internal deformation within the inelastic zone, as shown in Figure 2.10. These features include slip-strengthening behavior, double slip-weakening, and nonlinear weakening behavior with long tails. Such behaviors have been assumed to reflect true frictional behavior [94,103,104,106,121]. However, Xu et al.[145] argued that they might instead capture rupture behavior in off-fault locations. Hence, the latter perspective supports the development of indirect approaches to estimate rupture properties.

2.5.2 Mesh independence

Our steady-state phase-field approach does not require the mesh to be designed to align with a pre-existing fault. We show that kinematic and dynamic rupture can evolve independently of the spectral element boundaries. Results obtained with the mesh-aligned relative to the dynamic rupture problem lead to a close match with the reference solution. Non-aligned mesh configurations using Q_3 elements show a general amplitude reduction in the slip and slip rate metrics and grow closer to the reference solution –as the mesh-aligned case– when increasing the fault zone width. Alternatively, the non-aligned mesh solutions require an increased spatial resolution of the diffuse fault zone to reach the same level of agreement with the fault-interface reference solution as in the

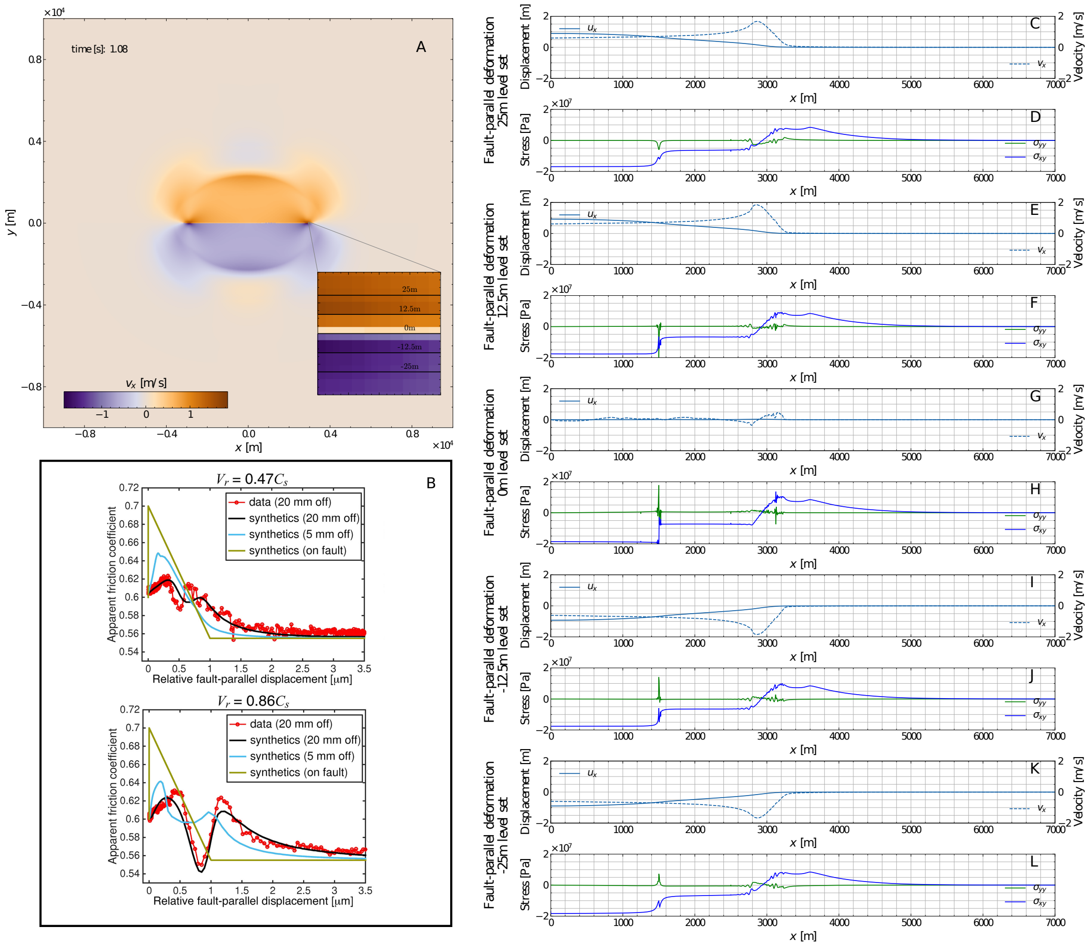

Figure 2.10. Internal deformation of the horizontal TPV3 model using Q_4 square elements of width 25m, $\delta = 12.5$m, and the volumetric yielding criterion, embedded in a 20×20 km domain size. (A) Depicts the snapshot of the x-component of the velocity field, with a zoom-in on the rupture tip and an indication of the extracted transects. (B) Contains an extract from Xu et al.[145] indicating the apparent friction coefficient constructed from experimental data and from numerical synthetics computed by shear-to-normal stress ratio, using different vertical offsets from the fault for different rupture velocities. Fault-parallel transects extracted at the (C, D) 25 m, (E, F) 12.5 m, (G, H) 0 m, (I, J) -12.5 m, and (K, L) -25 m level sets after 1.08 s of simulation time. The transects are equidistantly sampled, amounting to 10,000 points from the center of the domain to 10 km at the end of the domain. Each row axis pair contains first a plot of the x-component of the displacement (solid lines) and velocity (dashed lines), respectively, and second, the shear and normal stress component (color-coded) sampled as a function of distance along the fault per level set of interest. The profiles are only shown from 0 to 7 km distance from the epicenter along the fault

mesh-aligned case. This effect becomes especially apparent for the spontaneous dynamic rupture models, where a low integration point density of the elements constituting the nucleation patch may prevent self-sustained spontaneously propagating rupture due to the sensitivity of dynamic rupture to nucleation size, shape and procedure (e.g., Bizzarri[17], Festa and Vilotte[47], Gabriel et al.[48],[49], Galis et al.[51], Lu et al.[82], Shi et al.[127]). Alternative nucleation strategies that are smooth in space and/or time can reduce numerical artifacts in spontaneous dynamic rupture problems, such as stress localization in the surroundings of a sharply defined nucleation patch. Such smooth approaches also minimize the influence of a potentially ill-constrained nucleation procedure on the subsequent stages of realistic earthquake scenario simulations (e.g., Biemiller et al.[16], Harris et al.[58]). We observe comparable numerical artifacts, apparent especially in the stress fields, at quadrature points of element cells located only partially within the diffuse fault zone, e.g., in the mesh-independent fault configurations using low polynomial order (see Figure 2.4, Figure 2.7, Figure A.4). Increasing fault zone width can mitigate this issue. However, at the same time, too high nucleation overstresses should be avoided.

2.5.3 *Alternative smeared crack models*

Smeared crack models have been applied within the framework of finite element methods to model the fracture mechanics of mode I, II, and mixed-mode cracks in concrete. Thereby, the so-called *"stress locking"*[119,120] phenomenon refers to spurious stress build-up around the cracking elements, which may pollute the numerical results and lead to an overestimated energy dissipation and non-zero residual strength of a cracked structure. The cause of this spurious stress transfer has been related to a poor kinematic representation of the discontinuous displacement field in the vicinity of the macroscopic crack[66,67]. Unless the direction of the macroscopic crack (represented by a band of cracking elements) is parallel to the edges of finite elements, the directions of maximum principal strain determined from the finite element interpolation at individual integration points of the element deviate from the normal to the crack band. The principal lateral stress has a non-zero projection on the crack-band normal, generating spurious cohesive forces. However, higher-order elements offer better kinematic flexibility, such that they can partially relax the spurious stresses by adjusting the interpolated displacement field. Jirásek and Zimmermann[68],[69] deals with stress locking and instability via a varying scalar damage parameter as a function of the crack deformation of a mixed-mode embedded crack.

The diffuse thick fault approach presented here keeps the crack width fixed throughout the simulation, which may perturb the stress component at elements crossing the fault interface. This argues in favor of considering non-local approaches in the future or extending our approach into a non-steady-state phase-field method. Non-local gradient models enrich the local constitutive relations with first-order or higher-order gradients of a state variable or according to associated thermodynamic forces (e.g., Marotti de Sciarra[88]). Non-local integral models involve weighted averages of a state variable around that point (e.g., Lyakhovsky et al.[83]). Such models may rely on an invariant-based formulation, as it is also used in inelastic yielding models (e.g., Templeton and

Rice[135]), to evaluate and update an energy function to condition the evolution of a damage parameter. Peerlings et al.[109] describe the responses obtained from non-local and gradient damage approaches as qualitatively similar. Gradient-dependent formulations include all non-local model features essential for describing localization phenomena, with non-negligible quantitative differences arising from the absence of high-order derivatives in the gradient formulation. We may also want to choose a functional based on a non-local plasticity formulation describing the transition from the inelastic to the pure elastic domain within our fault-local compact support as an alternative to our blending approach to reinforce the diffuse character of the method and avoid localization. This treatment may be approached by defining the yielding condition and metrics in an average sense, which offers an alternative treatment to the stress localization described in Section 2.5.1. Future work may explore the physical constraints to inform the blending parameters that mathematically define our diffuse fault model.

Recently, Fei and Choo[43],[44],[45] have described phase-field models of geological motivated rock fracture that incorporate pressure dependence and frictional contacts for mode I, II, and mixed crack modes. Their approach is formulated as a set of governing equations for different contact conditions in the finite element method framework where frictional energy dissipation emerges in the crack driving force during slip. Their method is proposed to allow arbitrary interface geometry representation without an explicit function or enriched basis, an advantage of phase-field methods. It can also accommodate contact constraints without a dedicated algorithm. Their approach ensures that the nonslip direction's stress tensor component is compatible between the interface and bulk regions. This results in modifying the separation between the volumetric-deviatoric stress decomposition approach proposed by Amor et al.[2]. Our formulation of the modified stress tensor in Eq. (2.5) resembles theirs for a prescribed shape of stationary crack interface for the phase evolution equation. Our blending function and signed distance function variables play an equivalent role to the degradation function on their phase-field variable. After modifying the stress in their approach, they use Newton's method to solve the discretized momentum balance equation, and the nodal increment in displacement requires explicitly solving for an updated stiffness tensor to calculate the element-wise Jacobian at the end of each time step. In this context, the crack driving force is calculated from the change of the plastic strain and used to calculate the updated phase-field variable.

A diffuse description motivated by steady-state phase-field profiles allows us to explore the yielding surface's transition into elastic media as a distribution across the fault representation while keeping its logical simplicity in the formulation. This allows the method to be ported into alternative numerical frameworks. Development of our representation into the framework of phase-field requires critical ingredients of the phase-field formulation (based on the theory of fractures of Griffith and Taylor[53]), such as introducing a phase-field evolution equation and the incorporation of a critical fracture energy which translates into the regularized continuum gradient damage mechanics[96]. This increases the complexity in its formulation and introduces parameters to solve for. However, the evolution of the phase-field, and thus the fault-normal growth at different distances along the embedded inclusion of the yielding surface, is pertinent to natural observations. Fault lateral growth is observed in nature as changes in the structural fault complexity along the propagation direction of the parent fault [111]. Such variation may avoid accumulating localized stress components throughout time at the inter-element boundary within the numerical grid. In addition, such a hypothetical spectral-element-based phase-field method would avoid explicitly calculating an updated stiffness tensor at the end of each time step.

In contrast to our diffuse fault representation with constant blending and respective parameters, alternative diffuse fault models incorporating increased thermomechanical complexities have been developed. A contemporaneous diffuse crack representation incorporating finite strain nonlinear material behavior and multi-physics coupling into dynamic earthquake rupture modeling is described by Gabriel et al.[50] using the GPR model [117,118]. The model uses a first-order hyperbolic model of inelasticity coupled to finite strain elasto-visco-plasticity of continuum mechanics [132] and is extended for dynamic rupture using a high-order Discontinuous Galerkin scheme and the ExaHype PDE engine [116]. Their model also permits the representation of arbitrarily complex geometries via a diffuse interface approach. In neither of their two scalar fields, the local material damage describing the fault geometry and secondary cracks and the solid volume fraction function need to be mesh-aligned, allowing faults and cracks with complex topology and using adaptive Cartesian meshes (AMR). However, the problem of parameter selection for their unified model of continuum mechanics is a non-trivial task due to the large amounts of parameters and may require numerical optimization algorithms applied to data obtained from observations and laboratory experiments. Our method also requires locally high resolution to describe the diffuse fault zone and would benefit from the future implementation of fault zone AMR, building upon previous implementations of SEM with AMR (e.g., Rudi et al.[122],[123], Tanarro et al.[130]).

2.5.4 Outlook

Here, we explore simple 2D benchmarks for kinematic and spontaneous dynamic earthquake rupture, including geometrical complexities on a structured mesh. The next step can involve exploring the method's potential for modeling branching and crossing faults. In future work, fault junctions and geometrical complexities such as sharp bends may be implemented using hierarchy levels of fault entities with their respectively defined independent fault zone characteristics and updating the stress field in an iterative manner. In that way, for example, handling different thicknesses of fault zones per hierarchy level would be possible. However, stress concentrations associated with sharp bends or junctions may require careful analysis [5,137]. Fault intersections and dynamic fault interactions alter the spatial distribution of stress concentrations (e.g., Taufiqurrahman et al.[131]) as well as influence the earthquake energy budget (e.g., Okubo et al.[105]), thus, directly affect earthquake rupture dynamics. Future extension of our approach to 3D is essential for direct observational constraints and verification studying real earthquakes. 3D unit elements are well established in spectral element methods applied to seismic wave propagation (e.g., Komatitsch and Tromp[76]) and rupture dynamics [52] and Andrews[6] demonstrates the feasibility of strategies to evaluate the slip and slip rate from the shear traction components in 3D calculations. Thus, we expect that modifying our approach via a diffuse description of the stress glut should readily be extendable to 3D.

Applications of our method may help to further our understanding of fault zone evolution and the effects of internal rheology distribution at coseismic time scales. SEM is a volumetric method that allows for variable material parameters and mesh independence. In principle, this will allow our method to model time-evolving fault geometries, e.g., to capture the coupling between different physical mechanisms on-fault and within the bulk and evaluate their relative importance for rupture dynamics.

Thorough additional analysis will be required to extend our approach to rate-and-state friction. While such implementation and analysis are outside the scope of the paper, we envision that the main changes required to incorporate rate-and-state friction within our method are:

- Define a state variable at points living along the zero-level set contour (not defined within the volume).
- Change the method to evaluate the friction (between lines 7 and 8 in Algorithm 1).
- Modify the time integrator to use adaptive time-stepping.
- Add the evolution of the ODE for each state variable within the exiting time loop used to advance the displacement solution.

2.6 Conclusion

In this work, we present a novel steady-state phase-field model for rupture dynamics that extends the stress glut approach[6]. Using the high-order accurate and geometrically flexible framework of spectral elements, our diffuse fault zone formulation results in comparable kinematic and dynamic rupture propagation to the conventional planar traction at split node spectral element method for dynamic rupture simulations. Our approach supports a general description of the evolution of the effective friction coefficient, which dictates fault yielding and sliding as a function of time, location, slip, slip rate, and potential additional variables. To verify our approach, we first compare mesh-aligned kinematic and dynamic rupture model solutions. Our stress glut spectral element implementation aligns well with the discrete fault split-node spectral element reference solutions. Moving beyond the conventional planar interface, we introduce a diffuse fault zone description. This novel representation condenses fault volumetric complexities into a distribution within a compact support. This diffuse fault description follows a prescribed blending function that characterizes the transition from the inelastic state of the embedded crack to the pure elastic state of the surrounding rock matrix. Our model demonstrates its versatility using mesh-independent planar and curved fault geometries, simplifying the often tedious task of mesh generation. Importantly, our steady-state phase-field formulation is not restricted to spectral element methods: Our diffuse description of the fault zone is independent of the type of spatial discretization, conserving the original logical simplicity of the stress glut approach. This offers potential extensions to existing seismic wave propagation codes, facilitating more realistic dynamic rupture simulations. Distinct differences emerge in the stress and velocity fields generated by our fault representation compared to planar interface reference solutions. The resulting dynamic stress complexity interacts with the volumetric friction law, leading to dynamic fault reactivation and co-seismic, fault-oblique yielding patterns within the fault zone, depending on the chosen yielding criteria. These differences alter rupture front dynamics and seismic wave radiation, unveiling additional earthquake source complexities potentially overlooked in classical approaches. We conclude that a diffuse fault representation may offer a closer approximation to the complex physics of earthquakes while providing greater modeling flexibility. Our study opens new possibilities for phase-field-based modeling in earthquake physics.

Acknowledgments

This work was supported by the European Research Council (ERC) under the European Union's Horizon 2020 research and innovation programme (TEAR, Grant agreement No. 852992).

The authors acknowledge additional support from ChEESE (ERC Grant No. 823844), the National Science Foundation (NSF Grant No. EAR-2121666), and the Southern California Earthquake Center (SCEC Grant No. 21112). Computing resources were provided by the Institute of Geophysics of LMU Munich [102]. We thank the two reviewers, Eric M. Dunham, and one anonymous reviewer, the editor Satoshi Ide, and the associate editor, for their thoughtful and constructive comments. We also thank Jean-Paul Ampuero for openly providing *SEM2DPACK* and Duo Li for helpful discussions.

Open research

The code *se2dr* [59] is openly available online as a branch of *se2wave* [90] at the repository https://bitbucket.org/dmay/se2wave. Instructions to run and reproduce our tests can be found under the following Zenodo repository 10.5281/zenodo.8402020.

2.7 References

[1] Abhyankar, S., Brown, J., Constantinescu, E. M., Ghosh, D., Smith, B. F., and Zhang, H. (2018). PETSc/TS: A Modern Scalable ODE/DAE Solver Library. *arXiv preprint arXiv:1806.01437*. Cited on page/s 23.

[2] Amor, H., Marigo, J.-J., and Maurini, C. (2009). Regularized formulation of the variational brittle fracture with unilateral contact: Numerical experiments. *Journal of the Mechanics and Physics of Solids*, 57(8):1209–1229. Cited on page/s 45.

[3] Ampuero, J.-P. (2012). *SEM2DPACK:A Spectral Element Method tool for 2D wave propagation and earthquake source dynamics User's Guide*. Cited on page/s 26, 41.

[4] Andrews, D. J. (1976). Rupture propagation with finite stress in antiplane strain. *Journal of Geophysical Research (1896-1977)*, 81(20):3575–3582. Cited on page/s 17, 40.

[5] Andrews, D. J. (1989). Mechanics of fault junctions. *Journal of Geophysical Research: Solid Earth*, 94(B7):9389–9397. Cited on page/s 46.

[6] Andrews, D. J. (1999). Test of two methods for faulting on finite-difference calculations. *Bulletin of the Seismological Society of America*, 89(4):931–937. Cited on page/s 17, 19, 23, 41, 46, 47.

[7] Andrews, D. J. (2005). Rupture dynamics with energy loss outside the slip zone. *Journal of Geophysical Research: Solid Earth*, 110(B01307). Cited on page/s 16, 41.

[8] Backus, G. and Mulcahy, M. (1976). Moment tensors and other phenomenological descriptions of seismic sources—I. Continuous displacements. *Geophysical Journal International*, 46(2):341–361. Cited on page/s 17.

[9] Balay, S., Abhyankar, S., Adams, M. F., Brown, J., Brune, P., Buschelman, K., Dalcin, L., Dener, A., Eijkhout, V., Gropp, W. D., Karpeyev, D., Kaushik, D., Knepley, M. G., May, D. A., McInnes, L. C., Mills, R. T., Munson, T., Rupp, K., Sanan, P., Smith, B. F., Zampini, S., Zhang, H., and Zhang, H. (2019). PETSc Web page. https://www.mcs.anl.gov/petsc. Cited on page/s 23.

[10] Balay, S., Abhyankar, S., Adams, M. F., Brown, J., Brune, P., Buschelman, K., Dalcin, L., Dener, A., Eijkhout, V., Gropp, W. D., Karpeyev, D., Kaushik, D., Knepley, M. G., May, D. A., McInnes, L. C., Mills, R. T., Munson, T., Rupp, K., Sanan, P., Smith, B. F., Zampini, S., Zhang, H., and Zhang, H. (2020). PETSc users manual. Technical Report ANL-95/11 - Revision 3.14, Argonne National Laboratory. Cited on page/s 23.

[11] Balay, S., Gropp, W. D., McInnes, L. C., and Smith, B. F. (1997). Efficient management of parallelism in object oriented numerical software libraries. In Arge, E., Bruaset, A. M., and Langtangen, H. P., editors, *Modern Software Tools in Scientific Computing*, pages 163–202. Birkhäuser Press. Cited on page/s 23.

[12] Beckermann, C., Diepers, H.-J., Steinbach, I., Karma, A., and Tong, X. (1999). Modeling melt convection in phase-field simulations of solidification. *Journal of Computational Physics*, 154(2):468–496. Cited on page/s 22.

[13] Ben-Zion, Y. and Shi, Z. (2005). Dynamic rupture on a material interface with spontaneous generation of plastic strain in the bulk. *Earth and Planetary Science Letters*, 236(1):486–496. Cited on page/s 16.

[14] Benjemaa, M., Glinsky-Olivier, N., Cruz-Atienza, V. M., Virieux, J., and Piperno, S. (2007). Dynamic non-planar crack rupture by a finite volume method. *Geophysical Journal International*, 171(1):271–285. Cited on page/s 16.

[15] Beroza, G. C. and Spudich, P. (1988). Linearized inversion for fault rupture behavior: Application to the 1984 Morgan Hill, California, earthquake. *Journal of Geophysical Research: Solid Earth*, 93(B6):6275–6296. Cited on page/s 33.

[16] Biemiller, J., Gabriel, A.-A., and Ulrich, T. (2022). The dynamics of unlikely slip: 3d modeling of low-angle normal fault rupture at the mai'iu fault, papua new guinea. *Geochemistry, Geophysics, Geosystems*, 23(5):e2021GC010298. Cited on page/s 44.

[17] Bizzarri, A. (2010). How to Promote Earthquake Ruptures: Different Nucleation Strategies in a Dynamic Model with Slip-Weakening Friction. *Bulletin of the Seismological Society of America*, 100(3):923–940. Cited on page/s 44.

[18] Boore, D. M. and Joyner, W. B. (1978). The influence of rupture incoherence on seismic directivity. *Bulletin of the Seismological Society of America*, 68(2):283–300. Cited on page/s 16.

[19] Bourdin, B., Francfort, G., and Marigo, J.-J. (2000). Numerical experiments in revisited brittle fracture. *Journal of the Mechanics and Physics of Solids*, 48(4):797–826. Cited on page/s 17.

[20] Bourdin, B., Francfort, G. A., and Marigo, J.-J. (2008). The variational approach to fracture. *Journal of Elasticity*, 91(1):5–148. Cited on page/s 17.

[21] Bukchin, B. (1995). Determination of stress glut moments of total degree 2 from teleseismic surface wave amplitude spectra. *Tectonophysics*, 248(3):185–191. Focal Mechanism and Seismotectonics. Cited on page/s 17.

[22] Cappa, F., Perrin, C., Manighetti, I., and Delor, E. (2014). Off-fault long-term damage: A condition to account for generic, triangular earthquake slip profiles. *Geochemistry, Geophysics, Geosystems*, 15(4):1476–1493. Cited on page/s 16.

[23] Castro, R. R. and Ben-Zion, Y. (2013). Potential Signatures of Damage-Related Radiation from Aftershocks of the 4 April 2010 (Mw 7.2) El Mayor–Cucapah Earthquake, Baja California, México. *Bulletin of the Seismological Society of America*, 103(2A):1130–1140. Cited on page/s 38.

[24] Chaljub, E., Maufroy, E., Moczo, P., Kristek, J., Hollender, F., Bard, P.-Y., Priolo, E., Klin, P., de Martin, F., Zhang, Z., Zhang, W., and Chen, X. (2015). 3-D numerical simulations of earthquake ground motion in sedimentary basins: testing accuracy through stringent models. *Geophysical Journal International*, 201(1):90–111. Cited on page/s 16.

[25] Chaljub, E., Moczo, P., Tsuno, S., Bard, P.-Y., Kristek, J., Käser, M., Stupazzini, M., and Kristekova, M. (2010). Quantitative Comparison of Four Numerical Predictions of 3D Ground Motion in the Grenoble Valley, France. *Bulletin of the Seismological Society of America*, 100(4):1427–1455. Cited on page/s 16.

[26] Chen, P., Jordan, T. H., and Zhao, L. (2005). Finite-Moment Tensor of the 3 September 2002 Yorba Linda Earthquake. *Bulletin of the Seismological Society of America*, 95(3):1170–1180. Cited on page/s 17.

[27] Cheng, Y., Ross, Z. E., and Ben-Zion, Y. (2018). Diverse Volumetric Faulting Patterns in the San Jacinto Fault Zone. *Journal of Geophysical Research: Solid Earth*, 123(6):5068–5081. Cited on page/s 16.

[28] Chester, F. M. and Chester, J. S. (1998). Ultracataclasite structure and friction processes of the Punchbowl fault, San Andreas system, California. *Tectonophysics*, 295(1):199–221. Cited on page/s 16.

[29] Chester, F. M. and Logan, J. M. (1986). Implications for mechanical properties of brittle faults from observations of the Punchbowl fault zone, California. *pure and applied geophysics*, 124(1):79–106. Cited on page/s 16.

[30] Clévédé, E., Bouin, M.-P., Bukchin, B., Mostinskiy, A., and Patau, G. (2004). New constraints on the rupture process of the 1999 August 17 Izmit earthquake deduced from estimates of stress glut rate moments. *Geophysical Journal International*, 159(3):931–942. Cited on page/s 17.

[31] Cruz-Atienza, V. M. and Virieux, J. (2004). Dynamic rupture simulation of non-planar faults with a finite-difference approach. *Geophysical Journal International*, 158(3):939–954. Cited on page/s 16.

[32] Dalguer, L. A. and Day, S. M. (2006). Comparison of fault representation methods in finite difference simulations of dynamic rupture. *Bulletin of the Seismological Society of America*, 96(5):1764–1778. Cited on page/s 17, 21, 27, 40, 41.

[33] Day, S. M., Dalguer, L. A., Lapusta, N., and Liu, Y. (2005). Comparison of finite difference and boundary integral solutions to three-dimensional spontaneous rupture. *Journal of Geophysical Research: Solid Earth*, 110(B12). Cited on page/s 16, 21, 41.

[34] Day, S. M. and Ely, G. P. (2002). Effect of a Shallow Weak Zone on Fault Rupture: Numerical Simulation of Scale-Model Experiments. *Bulletin of the Seismological Society of America*, 92(8):3022–3041. Cited on page/s 24.

[35] De Borst, R., Remmers, J. J. C., Needleman, A., and Abellan, M.-A. (2004). Discrete vs smeared crack models for concrete fracture: bridging the gap. *International Journal for Numerical and Analytical Methods in Geomechanics*, 28(7-8):583–607. Cited on page/s 16.

[36] de la Puente, J., Ampuero, J.-P., and Käser, M. (2009). Dynamic rupture modeling on unstructured meshes using a discontinuous Galerkin method. *Journal of Geophysical Research: Solid Earth*, 114(B10302):1–17. Cited on page/s 16.

[37] Dieterich, J. H. (1981). Constitutive properties of faults with simulated gouge. In Carter, N. L., Friedman, M., Logan, J. M., and Stearns, D. W., editors, *Monograph 24: Mechanical Behavior of Crustal Rocks*, pages 103–120. American Geophysical Union (AGU). Cited on page/s 19.

[38] Dumbser, M. and Käser, M. (2006). An arbitrary high-order discontinuous Galerkin method for elastic waves on unstructured meshes — II. The three-dimensional isotropic case. *Geophysical Journal International*, 167(1):319–336. Cited on page/s 17.

[39] Dunham, E. M., Belanger, D., Cong, L., and Kozdon, J. E. (2011). Earthquake Ruptures with Strongly Rate-Weakening Friction and Off-Fault Plasticity, Part 1: Planar Faults. *Bulletin of the Seismological Society of America*, 101(5):2296–2307. Cited on page/s 16.

[40] Duru, K. and Dunham, E. M. (2016). Dynamic earthquake rupture simulations on nonplanar faults embedded in 3d geometrically complex, heterogeneous elastic solids. *Journal of Computational Physics*, 305:185–207. Cited on page/s 16.

[41] Eshelby, J. D. and Peierls, R. E. (1957). The determination of the elastic field of an ellipsoidal inclusion, and related problems. *Proceedings of the Royal Society of London. Series A. Mathematical and Physical Sciences*, 241(1226):376–396. Cited on page/s 41.

[42] Faulkner, D., Lewis, A., and Rutter, E. (2003). On the internal structure and mechanics of large strike-slip fault zones: field observations of the Carboneras fault in southeastern Spain. *Tectonophysics*, 367(3):235–251. Cited on page/s 16.

[43] Fei, F. and Choo, J. (2019). A phase-field method for modeling cracks with frictional contact. *International Journal for Numerical Methods in Engineering*, 121(4):740–762. Cited on page/s 45.

[44] Fei, F. and Choo, J. (2020). A phase-field model of frictional shear fracture in geologic materials. *Computer Methods in Applied Mechanics and Engineering*, 369:113265. Cited on page/s 17, 45.

[45] Fei, F. and Choo, J. (2021). Double-phase-field formulation for mixed-mode fracture in rocks. *Computer Methods in Applied Mechanics and Engineering*, 376:113655. Cited on page/s 17, 45.

[46] Fei, F., Mia, M. S., Elbanna, A. E., and Choo, J. (2023). A phase-field model for quasi-dynamic nucleation, growth, and propagation of rate-and-state faults. *International Journal for Numerical and Analytical Methods in Geomechanics*, 47(2):187–211. Cited on page/s 17.

[47] Festa, G. and Vilotte, J.-P. (2006). Influence of the rupture initiation on the intersonic transition: Crack-like versus pulse-like modes. *Geophysical Research Letters*, 33(15). Cited on page/s 16, 44.

[48] Gabriel, A.-A., Ampuero, J.-P., Dalguer, L. A., and Mai, P. M. (2012). The transition of dynamic rupture

styles in elastic media under velocity-weakening friction. *Journal of Geophysical Research: Solid Earth*, 117(B9). Cited on page/s 29, 33, 35, 44.

[49] Gabriel, A.-A., Ampuero, J.-P., Dalguer, L. A., and Mai, P. M. (2013). Source properties of dynamic rupture pulses with off-fault plasticity. *Journal of Geophysical Research: Solid Earth*, 118(8):4117–4126. Cited on page/s 16, 41, 44.

[50] Gabriel, A.-A., Li, D., Chiocchetti, S., Tavelli, M., Peshkov, I., Romenski, E., and Dumbser, M. (2021). A unified first-order hyperbolic model for nonlinear dynamic rupture processes in diffuse fracture zones. *Philosophical Transactions of the Royal Society A: Mathematical, Physical and Engineering Sciences*, 379(2196):20200130. Cited on page/s 16, 28, 46.

[51] Galis, M., Pelties, C., Kristek, J., Moczo, P., Ampuero, J.-P., and Mai, P. M. (2015). On the initiation of sustained slip-weakening ruptures by localized stresses. *Geophysical Journal International*, 200(2):890–909. Cited on page/s 29, 35, 42, 44.

[52] Galvez, P., Ampuero, J.-P., Dalguer, L. A., Somala, S. N., and Nissen-Meyer, T. (2014). Dynamic earthquake rupture modelled with an unstructured 3-D spectral element method applied to the 2011 M9 Tohoku earthquake. *Geophysical Journal International*, 198(2):1222–1240. Cited on page/s 16, 24, 46.

[53] Griffith, A. A. and Taylor, G. I. (1921). VI. The phenomena of rupture and flow in solids. *Philosophical Transactions of the Royal Society of London. Series A, Containing Papers of a Mathematical or Physical Character*, 221(582-593):163–198. Cited on page/s 45.

[54] Hanks, T. C. (1982). f_{max}. *Bulletin of the Seismological Society of America*, 72(6A):1867–1879. Cited on page/s 24, 38.

[55] Harris, R. A., Barall, M., Aagaard, B., Ma, S., Roten, D., Olsen, K., Duan, B., Liu, D., Luo, B., Bai, K., Ampuero, J.-P., Kaneko, Y., Gabriel, A.-A., Duru, K., Ulrich, T., Wollherr, S., Shi, Z., Dunham, E., Bydlon, S., Zhang, Z., Chen, X., Somala, S. N., Pelties, C., Tago, J., Cruz-Atienza, V. M., Kozdon, J., Daub, E., Aslam, K., Kase, Y., Withers, K., and Dalguer, L. (2018). A Suite of Exercises for Verifying Dynamic Earthquake Rupture Codes. *Seismological Research Letters*, 89(3):1146–1162. Cited on page/s 16, 30.

[56] Harris, R. A., Barall, M., Andrews, D. J., Duan, B., Ma, S., Dunham, E. M., Gabriel, A.-A., Kaneko, Y., Kase, Y., Aagaard, B. T., Oglesby, D. D., Ampuero, J.-P., Hanks, T. C., and Abrahamson, N. (2011). Verifying a Computational Method for Predicting Extreme Ground Motion. *Seismological Research Letters*, 82(5):638–644. Cited on page/s 16.

[57] Harris, R. A., Barall, M., Archuleta, R., Dunham, E., Aagaard, B., Ampuero, J.-P., Bhat, H., Cruz-Atienza, V., Dalguer, L., Dawson, P., Day, S., Duan, B., Ely, G., Kaneko, Y., Kase, Y., Lapusta, N., Liu, Y., Ma, S., Oglesby, D., Olsen, K., Pitarka, A., Song, S., and Templeton, E. (2009). The SCEC/USGS dynamic earthquake rupture code verification exercise. *Seismological Research Letters*, 80(1):119–126. Cited on page/s 26, 30.

[58] Harris, R. A., Barall, M., Lockner, D. A., Moore, D. E., Ponce, D. A., Graymer, R. W., Funning, G., Morrow, C. A., Kyriakopoulos, C., and Eberhart-Phillips, D. (2021). A geology and geodesy based model of dynamic earthquake rupture on the rodgers creek-hayward-calaveras fault system, california. *Journal of Geophysical Research: Solid Earth*, 126(3):e2020JB020577. Cited on page/s 44.

[59] Hayek, J. N., May, D. A., Pranger, C., and Gabriel, A.-A. (2023). se2dr. Software. Cited on page/s 48.

[60] Herrendörfer, R., Gerya, T., and van Dinther, Y. (2018). An Invariant Rate- and State-Dependent Friction Formulation for Viscoeastoplastic Earthquake Cycle Simulations. *Journal of Geophysical Research: Solid Earth*, 123(6):5018–5051. Cited on page/s 17.

[61] Huang, Y., Ampuero, J.-P., and Helmberger, D. V. (2014). Earthquake ruptures modulated by waves in damaged fault zones. *Journal of Geophysical Research: Solid Earth*, 119(4):3133–3154. Cited on page/s 33, 35.

[62] Hughes, T. J. R. (2000). Chapter 9 - Algorithms for Hyperbolic and Hyperbolic-Parabolic Problems. In *The Finite Element Method: Linear Static and Dynamic Finite Element Analysis*, pages 490 – 567. Dover Publications. Cited on page/s 23.

[63] Ida, Y. (1972). Cohesive force across the tip of a longitudinal-shear crack and Griffith's specific surface energy. *Journal of Geophysical Research*, 77(20):3796–3805. Cited on page/s 30.

[64] Idini, B. and Ampuero, J.-P. (2020). Fault-Zone Damage Promotes Pulse-Like Rupture and Back-Propagating Fronts via Quasi-Static Effects. *Geophysical Research Letters*, 47(23):e2020GL090736. e2020GL090736 10.1029/2020GL090736. Cited on page/s 33.

[65] Igel, H. (2017). *Computational Seismology: A practical introduction*. Oxford University Press, USA. Cited on page/s 16.

[66] Jirásek, M. and Zimmermann, T. (1998a). Analysis of rotating crack model. *Journal of Engineering Mechanics*, 124(8):842–851. Cited on page/s 44.

[67] Jirásek, M. and Zimmermann, T. (1998b). Rotating crack model with transition to scalar damage. *Journal of Engineering Mechanics*, 124(3):277–284. Cited on page/s 44.

[68] Jirásek, M. and Zimmermann, T. (2001a). Embedded crack model: I. Basic formulation. *International Journal for Numerical Methods in Engineering*, 50(6):1269–1290. Cited on page/s 44.

[69] Jirásek, M. and Zimmermann, T. (2001b). Embedded crack model. Part II: combination with smeared cracks. *International Journal for Numerical Methods in Engineering*, 50(6):1291–1305. Cited on page/s 44.

[70] Jordan, T. H. and Juarez, A. (2019). Representation of complex seismic sources by orthogonal moment-tensor fields. *Geophysical Journal International*, 216(3):1867–1889. Cited on page/s 17.

[71] Jordan, T. H. and Juarez, A. (2020). Erratum: 'Representation of complex seismic sources by orthogonal moment–tensor fields'. *Geophysical Journal International*, 222(2):1333–1338. Cited on page/s 17.

[72] Jordan, T. H. and Juarez, A. (2021). Stress–strain characterization of seismic source fields using moment measures of mechanism complexity. *Geophysical Journal International*, 227(1):591–616. Cited on page/s 17.

[73] Kame, N. and Uchida, K. (2008). Seismic radiation from dynamic coalescence, and the reconstruction of dynamic source parameters on a planar fault. *Geophysical Journal International*, 174(2):696–706. Cited on page/s 16.

[74] Kaneko, Y., Lapusta, N., and Ampuero, J.-P. (2008). Spectral element modeling of spontaneous earthquake rupture on rate and state faults: Effect of velocity-strengthening friction at shallow depths. *Journal of Geophysical Research: Solid Earth*, 113(B9). Cited on page/s 16, 24.

[75] Klinger, Y., Okubo, K., Vallage, A., Champenois, J., Delorme, A., Rougier, E., Lei, Z., Knight, E. E., Munjiza, A., Satriano, C., Baize, S., Langridge, R., and Bhat, H. S. (2018). Earthquake damage patterns resolve complex rupture processes. *Geophysical Research Letters*, 45(19):10,279–10,287. Cited on page/s 16.

[76] Komatitsch, D. and Tromp, J. (1999). Introduction to the spectral element method for three-dimensional seismic wave propagation. *Geophysical Journal International*, 139(3):806–822. Cited on page/s 16, 23, 46.

[77] Komatitsch, D. and Tromp, J. (2002). Spectral-element simulations of global seismic wave propagation—I. Validation. *Geophysical Journal International*, 149(2):390–412. Cited on page/s 23.

[78] Kostrov, B. V. (1964). Selfsimilar problems of propagation of shear cracks. *Journal of Applied Mathematics and Mechanics*, 28(5):889–898. Cited on page/s 24.

[79] Kozdon, J. E., Dunham, E. M., and Nordström, J. (2013). Simulation of dynamic earthquake ruptures in complex geometries using high-order finite difference methods. *Journal of Scientific Computing*, 55:92–124. Cited on page/s 24.

[80] Lee, S.-J., Huang, B.-S., Ando, M., Chiu, H.-C., and Wang, J.-H. (2011). Evidence of large scale repeating slip during the 2011 Tohoku-Oki earthquake. *Geophysical Research Letters*, 38(19). Cited on page/s 33.

[81] Liu, F. and Borja, R. I. (2013). Extended finite element framework for fault rupture dynamics including bulk plasticity. *International Journal for Numerical and Analytical Methods in Geomechanics*, 37(18):3087–3111. Cited on page/s 16.

[82] Lu, X., Lapusta, N., and Rosakis, A. J. (2009). Analysis of supershear transition regimes in rupture experiments: The effect of nucleation conditions and friction parameters. *Geophysical Journal International*, 177(2):717–732. Cited on page/s 44.

[83] Lyakhovsky, V., Hamiel, Y., and Ben-Zion, Y. (2011). A non-local visco-elastic damage model and dynamic fracturing. *Journal of the Mechanics and Physics of Solids*, 59(9):1752–1776. Cited on page/s 44.

[84] Madariaga, R. (1977). High-frequency radiation from crack (stress drop) models of earthquake faulting. *Geophysical Journal International*, 51(3):625–651. Cited on page/s 16, 38.

[85] Madariaga, R. (1983). High frequency radiation from dynamic earthquake. *Ann. Geophys*, 1:17. Cited on page/s 16.

[86] Madariaga, R., Olsen, K., and Archuleta, R. (1998). Modeling dynamic rupture in a 3D earthquake fault model. *Bulletin of the Seismological Society of America*, 88(5):1182–1197. Cited on page/s 17, 21, 27, 40.

[87] Marfurt, K. J. (1984). Accuracy of finite-difference and finite-element modeling of the scalar and elastic wave equations. *Geophysics*, 49(5):533–549. Cited on page/s 24.

[88] Marotti de Sciarra, F. (2009). A nonlocal model with strain-based damage. *International Journal of Solids and Structures*, 46(22):4107–4122. Cited on page/s 44.

[89] Marty, S., Passelègue, F. X., Aubry, J., Bhat, H. S., Schubnel, A., and Madariaga, R. (2019). Origin of high-frequency radiation during laboratory earthquakes. *Geophysical Research Letters*, 46(7):3755–3763. Cited on page/s 16.

[90] May, D. A. (2020). se2wave. Software. Cited on page/s 48.

[91] McGuire, J. J. (2017). A MATLAB Toolbox for Estimating the Second Moments of Earthquake Ruptures. *Seismological Research Letters*, 88(2A):371–378. Cited on page/s 17.

[92] McGuire, J. J., Zhao, L., and Jordan, T. H. (2001). Teleseismic inversion for the second degree moments of earthquake space-time distributions. *Geophysical Journal International*, 145(3):661–678. Cited on page/s 17.

[93] McGuire, J. J., Zhao, L., and Jordan, T. H. (2002). Predominance of Unilateral Rupture for a Global Catalog of Large Earthquakes. *Bulletin of the Seismological Society of America*, 92(8):3309–3317. Cited on page/s 17.

[94] McLaskey, G. C., Kilgore, B. D., and Beeler, N. M. (2015). Slip-pulse rupture behavior on a 2 m granite fault. *Geophysical Research Letters*, 42(17):7039–7045. Cited on page/s 42.

[95] Miehe, C. and Schänzel, L.-M. (2014). Phase field modeling of fracture in rubbery polymers. Part I: Finite elasticity coupled with brittle failure. *Journal of the Mechanics and Physics of Solids*, 65:93–113. Cited on page/s 17.

[96] Miehe, C., Schänzel, L.-M., and Ulmer, H. (2015). Phase field modeling of fracture in multi-physics problems. part i. balance of crack surface and failure criteria for brittle crack propagation in thermo-elastic solids. *Computer Methods in Applied Mechanics and Engineering*, 294:449–485. Cited on page/s 45.

[97] Milliner, C., Donnellan, A., Aati, S., Avouac, J.-P., Zinke, R., Dolan, J. F., Wang, K., and Bürgmann, R. (2021). Bookshelf Kinematics and the Effect of Dilatation on Fault Zone Inelastic Deformation: Examples From Optical Image Correlation Measurements of the 2019 Ridgecrest Earthquake Sequence. *Journal of Geophysical Research: Solid Earth*, 126(3):e2020JB020551. e2020JB020551 2020JB020551. Cited on page/s 16.

[98] Milliner, C. W. D., Dolan, J. F., Hollingsworth, J., Leprince, S., Ayoub, F., and Sammis, C. G. (2015). Quantifying near-field and off-fault deformation patterns of the 1992 Mw 7.3 Landers earthquake. *Geochemistry, Geophysics, Geosystems*, 16(5):1577–1598. Cited on page/s 16.

[99] Mirzabozorg, H. and Ghaemian, M. (2005). Non-linear behavior of mass concrete in three-dimensional problems using a smeared crack approach. *Earthquake Engineering & Structural Dynamics*, 34(3):247–269. Cited on page/s 16.

[100] Moës, N., Dolbow, J., and Belytschko, T. (1999). A finite element method for crack growth without remeshing. *International Journal for Numerical Methods in Engineering*, 46(1):131–150. Cited on page/s 16.

[101] Nielsen, S. and Madariaga, R. (2003). On the Self-Healing Fracture Mode. *Bulletin of the Seismological Society of America*, 93(6):2375–2388. Cited on page/s 33.

[102] Oeser, J., Bunge, H.-P., and Mohr, M. (2006). Cluster design in the earth sciences tethys. In Gerndt, M. and Kranzlmüller, D., editors, *High Performance Computing and Communications*, pages 31–40, Berlin, Heidelberg. Springer Berlin Heidelberg. Cited on page/s 48.

[103] Ohnaka, M. and Kuwahara, Y. (1990). Characteristic features of local breakdown near a crack-tip in the transition zone from nucleation to unstable rupture during stick-slip shear failure. *Tectonophysics*, 175(1):197–220. Earthquake Source Processes. Cited on page/s 42.

[104] Ohnaka, M. and Yamashita, T. (1989). A cohesive zone model for dynamic shear faulting based on experimentally inferred constitutive relation and strong motion source parameters. *Journal of Geophysical Research: Solid Earth*, 94(B4):4089–4104. Cited on page/s 42.

[105] Okubo, K., Bhat, H. S., Rougier, E., Marty, S., Schubnel, A., Lei, Z., Knight, E. E., and Klinger, Y. (2019). Dynamics, radiation, and overall energy budget of earthquake rupture with coseismic off-fault damage. *Journal of Geophysical Research: Solid Earth*, 124(11):11771–11801. Cited on page/s 16, 38, 46.

[106] Okubo, P. G. and Dieterich, J. H. (1981). Fracture energy of stick-slip events in a large scale biaxial experiment. *Geophysical Research Letters*, 8(8):887–890. Cited on page/s 42.

[107] Palmer, A. C. and Rice, J. R. (1973). The growth of slip surfaces in the progressive failure of over-consolidated clay. *Proceedings of the Royal Society of London. A. Mathematical and Physical Sciences*, 332(1591):527–548. Cited on page/s 21.

[108] Passelègue, F. X., Spagnuolo, E., Violay, M., Nielsen, S., Di Toro, G., and Schubnel, A. (2016). Frictional evolution, acoustic emissions activity, and off-fault damage in simulated faults sheared at seismic slip rates. *Journal of Geophysical Research: Solid Earth*, 121(10):7490–7513. Cited on page/s 16.

[109] Peerlings, R., Borst, de, R., Brekelmans, W., and Vree, de, J. (1996). Gradient enhanced damage for quasi-brittle materials. *International Journal for Numerical Methods in Engineering*, 39(19):3391–3403. Cited on page/s 45.

[110] Pelties, C., de la Puente, J., Ampuero, J.-P., Brietzke, G. B., and Käser, M. (2012). Three-dimensional dynamic rupture simulation with a high-order discontinuous galerkin method on unstructured tetrahedral meshes. *Journal of*

Geophysical Research: Solid Earth, 117(B2). Cited on page/s 38.

[111] Perrin, C., Manighetti, I., and Gaudemer, Y. (2016). Off-fault tip splay networks: A genetic and generic property of faults indicative of their long-term propagation. *Comptes Rendus Geoscience*, 348(1):52–60. From past to current tectonics. Cited on page/s 16, 46.

[112] Peter, D., Komatitsch, D., Luo, Y., Martin, R., Le Goff, N., Casarotti, E., Le Loher, P., Magnoni, F., Liu, Q., Blitz, C., Nissen-Meyer, T., Basini, P., and Tromp, J. (2011). Forward and adjoint simulations of seismic wave propagation on fully unstructured hexahedral meshes. *Geophysical Journal International*, 186(2):721–739. Cited on page/s 23.

[113] Pranger, C., Sanan, P., May, D. A., Le Pourhiet, L., and Gabriel, A.-A. (2022). Rate and state friction as a spatially regularized transient viscous flow law. *Journal of Geophysical Research: Solid Earth*, 127(6):e2021JB023511. e2021JB023511 2021JB023511. Cited on page/s 16.

[114] Preuss, S., Herrendörfer, R., Gerya, T., Ampuero, J.-P., and van Dinther, Y. (2019). Seismic and aseismic fault growth lead to different fault orientations. *Journal of Geophysical Research: Solid Earth*, 124(8):8867–8889. Cited on page/s 17, 27.

[115] Ramos, M. D., Thakur, P., Huang, Y., Harris, R. A., and Ryan, K. J. (2022). Working with Dynamic Earthquake Rupture Models: A Practical Guide. *Seismological Research Letters*, 93(4):2096–2110. Cited on page/s 16.

[116] Reinarz, A., Charrier, D. E., Bader, M., Bovard, L., Dumbser, M., Duru, K., Fambri, F., Gabriel, A.-A., Gallard, J.-M., Köppel, S., et al. (2020). Exahype: an engine for parallel dynamically adaptive simulations of wave problems. *Computer Physics Communications*, 254:107251. Cited on page/s 16, 46.

[117] Resnyansky, A. D., Romensky, E. I., and Bourne, N. K. (2003). Constitutive modeling of fracture waves. *Journal of Applied Physics*, 93(3):1537–1545. Cited on page/s 46.

[118] Romenskii, E. I. (2007). Deformation model for brittle materials and the structure of failure waves. *Journal of applied mechanics and technical physics*, 48(3):437–444. Cited on page/s 46.

[119] Rots, J. G. (1988). *Computational modeling of concrete fracture*. PhD thesis, Delft University of Technology. Cited on page/s 44.

[120] Rots, J. G. and Blaauwendraad, J. (1989). Crack models for concrete: discrete or smeared? fixed, multi-directional or rotating? *HERON, 34 (1), 1989*. Cited on page/s 28, 44.

[121] Rubino, V., Rosakis, A. J., and Lapusta, N. (2017). Understanding dynamic friction through spontaneously evolving laboratory earthquakes. *Nature Communications*, 8(1):15991. Cited on page/s 42.

[122] Rudi, J., Malossi, A. C. I., Isaac, T., Stadler, G., Gurnis, M., Staar, P. W. J., Ineichen, Y., Bekas, C., Curioni, A., and Ghattas, O. (2015). An extreme-scale implicit solver for complex pdes: Highly heterogeneous flow in earth's mantle. In *Proceedings of the International Conference for High Performance Computing, Networking, Storage and Analysis*, SC '15, New York, NY, USA. Association for Computing Machinery. Cited on page/s 46.

[123] Rudi, J., Stadler, G., and Ghattas, O. (2017). Weighted BFBT Preconditioner for Stokes Flow Problems with Highly Heterogeneous Viscosity. *SIAM Journal on Scientific Computing*, 39(5):S272–S297. Cited on page/s 46.

[124] Ruina, A. (1983). Slip instability and state variable friction laws. *Journal of Geophysical Research: Solid Earth*, 88(B12):10359–10370. Cited on page/s 19.

[125] Seriani, G. and Priolo, E. (1994). Spectral element method for acoustic wave simulation in heterogeneous media. *Finite elements in analysis and design*, 16(3):337–348. Cited on page/s 24, 38.

[126] Sharples, W., Moresi, L., Velic, M., Jadamec, M., and May, D. (2016). Simulating faults and plate boundaries with a transversely isotropic plasticity model. *Physics of the Earth and Planetary Interiors*, 252:77–90. Cited on page/s 21.

[127] Shi, Z., Ben-Zion, Y., and Needleman, A. (2008). Properties of dynamic rupture and energy partition in a solid with a frictional interface. *Journal of the Mechanics and Physics of Solids*, 56(1):5–24. Cited on page/s 44.

[128] Spatschek, R., Brener, E., and Karma, A. (2011). Phase field modeling of crack propagation. *Philosophical Magazine*, 91(1):75–95. Cited on page/s 17.

[129] Sun, Y. and Beckermann, C. (2007). Sharp interface tracking using the phase-field equation. *Journal of Computational Physics*, 220(2):626–653. Cited on page/s 22.

[130] Tanarro, Á., Mallor, F., Offermans, N., Peplinski, A., Vinuesa, R., and Schlatter, P. (2020). Enabling adaptive mesh refinement for spectral-element simulations of turbulence around wing sections. *Flow, Turbulence and Combustion*, 105(2):415–436. Cited on page/s 46.

[131] Taufiqurrahman, T., Gabriel, A.-A., Li, D., Ulrich, T., Li, B., Carena, S., Verdecchia, A., and Gallovič, F. (2023). Dynamics, interactions and delays of the 2019 ridgecrest rupture sequence. *Nature*, 618(7964):308–315. Cited on page/s 46.

[132] Tavelli, M., Chiocchetti, S., Romenski, E., Gabriel, A.-A., and Dumbser, M. (2020). Space-time adaptive ADER discontinuous Galerkin schemes for nonlinear hyperelasticity with material failure. *Journal of Computational Physics*, 422:109758. Cited on page/s 46.

[133] Tavelli, M., Dumbser, M., Charrier, D. E., Rannabauer, L., Weinzierl, T., and Bader, M. (2019a). A simple diffuse interface approach on adaptive Cartesian grids for the linear elastic wave equations with complex topography. *Journal of Computational Physics*, 386:158–189. Cited on page/s 16.

[134] Tavelli, M., Dumbser, M., Charrier, D. E., Rannabauer, L., Weinzierl, T., and Bader, M. (2019b). A simple diffuse interface approach on adaptive cartesian grids for the linear elastic wave equations with complex topography. *Journal of Computational Physics*, 386:158–189. Cited on page/s 16.

[135] Templeton, E. L. and Rice, J. R. (2008). Off-fault plasticity and earthquake rupture dynamics: 1. Dry materials or neglect of fluid pressure changes. *Journal of Geophysical Research: Solid Earth*, 113(B09306). Cited on page/s 16, 45.

[136] Ulrich, T., Gabriel, A.-A., Ampuero, J.-P., and Xu, W. (2019). Dynamic viability of the 2016 Mw 7.8 Kaikōura earthquake cascade on weak crustal faults. *Nature Communications*, 10(1):1213. Cited on page/s 16.

[137] Uphoff, C., May, D. A., and Gabriel, A.-A. (2022). A discontinuous Galerkin method for sequences of earthquakes and aseismic slip on multiple faults using unstructured curvilinear grids. *Geophysical Journal International*, 233(1):586–626. Cited on page/s 16, 46.

[138] Vallée, M., Xie, Y., Grandin, R., Villegas-Lanza, J. C., Nocquet, J.-M., Vaca, S., Meng, L., Ampuero, J. P., Mothes, P., Jarrin, P., Sierra Farfán, C., and Rolandone, F. (2023). Self-reactivated rupture during the 2019 M_*w*=8 northern Peru intraslab earthquake. *Earth and Planetary Science Letters*, 601:117886. Cited on page/s 33.

[139] Weldon II, R. J. and Springer, J. E. (1988). Active faulting near the Cajon Pass well, southern California; Implications for the stress orientation near the San Andreas Fault. *Geophysical Research Letters*, 15(9):993–996. Cited on page/s 16.

[140] White, F. (2006). *Viscous Fluid Flow*. McGraw-Hill international edition. McGraw-Hill Higher Education. Cited on page/s 21.

[141] Wilcox, L. C., Stadler, G., Burstedde, C., and Ghattas, O. (2010). A high-order discontinuous galerkin method for wave propagation through coupled elastic–acoustic media. *Journal of Computational Physics*, 229(24):9373–9396. Cited on page/s 17.

[142] Withers, K. B., Olsen, K. B., Day, S. M., and Shi, Z. (2018). Ground Motion and Intraevent Variability from 3D Deterministic Broadband (0–7.5 Hz) Simulations along a Nonplanar Strike-Slip Fault. *Bulletin of the Seismological Society of America*, 109(1):229–250. Cited on page/s 16.

[143] Wollherr, S., Gabriel, A.-A., and Uphoff, C. (2018). Off-fault plasticity in three-dimensional dynamic rupture simulations using a modal Discontinuous Galerkin method on unstructured meshes: Implementation, verification and application. *Geophysical Journal International*, 214(3):1556–1584. Cited on page/s 16, 38.

[144] Xu, S., Ben-Zion, Y., Ampuero, J.-P., and Lyakhovsky, V. (2015). Dynamic ruptures on a frictional interface with off-fault brittle damage: Feedback mechanisms and effects on slip and near-fault motion. *Pure and Applied Geophysics*, 172(5):1243–1267. Cited on page/s 16, 41.

[145] Xu, S., Fukuyama, E., and Yamashita, F. (2019). Robust estimation of rupture properties at propagating front of laboratory earthquakes. *Journal of Geophysical Research: Solid Earth*, 124(1):766–787. Cited on page/s 42, 43.

[146] Yuan, S., Gessele, K., Gabriel, A.-A., May, D. A., Wassermann, J., and Igel, H. (2021). Seismic source tracking with six degree-of-freedom ground motion observations. *Journal of Geophysical Research: Solid Earth*, 126(3):e2020JB021112. Cited on page/s 23.

[147] Zhang, X., Sloan, S. W., Vignes, C., and Sheng, D. (2017). A modification of the phase-field model for mixed mode crack propagation in rock-like materials. *Computer Methods in Applied Mechanics and Engineering*, 322:123–136. Cited on page/s 17.

[148] Zhang, Z., Zhang, W., and Chen, X. (2014). Three-dimensional curved grid finite-difference modelling for non-planar rupture dynamics. *Geophysical Journal International*, 199(2):860–879. Cited on page/s 16.

Chapter 3

Non-typical supershear rupture: fault heterogeneity and segmentation govern unilateral supershear and cascading multi-fault rupture in the 2021 Mw7.4 Maduo Earthquake

by Hayek J.N. , Marchandon M., Li D. , Pousse Beltran L., Hollingsworth J., Li T., Gabriel A.-A. (2024).
Published in Geophysical Research Letters, 51, e2024GL110128. DOI:10.1029/2024GL110128.

Abstract

Previous geodetic and teleseismic observations of the 2021 M_w7.4 Maduo earthquake imply surprising but difficult-to-constrain complexity, including rupture across multiple fault segments and supershear rupture. Here, we present an integrated analysis of multi-fault 3D dynamic rupture models, high-resolution optical correlation analysis, and joint optical-InSAR slip inversion. Our preferred model, validated by the teleseismic multi-peak moment rate release, includes unilateral eastward double-onset supershear speeds and cascading rupture dynamically triggering two adjacent fault branches.

We propose that pronounced along-strike variation in fracture energy, complex fault geometries, and multi-scale variable prestress drives this event's complex rupture dynamics. We illustrate how supershear transition has signatures in modeled and observed off-fault deformation. Our study opens new avenues to combine observations and models to better understand complex earthquake dynamics, including local and potentially repeating supershear episodes across immature faults or under heterogeneous stress and strength conditions, which are potentially not unusual.

3.1 Introduction

On May 22, 2021, the Maduo earthquake, a M_w7.4 strike-slip event, struck the northeastern Tibetan Plateau (Figure 3.1A), affecting the local population[76] and infrastructure (e.g., Zhu et al.[96]. The earthquake ruptured the eastern segment of the Kunlun Mountain Pass–Jiangcuo Fault (KMPJF), a NW-trending left-lateral strike-slip branch fault south of the East Kunlun fault bounding the Bayan Har Block[29]. The 2021 Maduo event is the largest earthquake in China since the 2008 M_w7.9 Wenchuan earthquake (Figure 3.1A) and resulted in complex surface rupture[58,91].

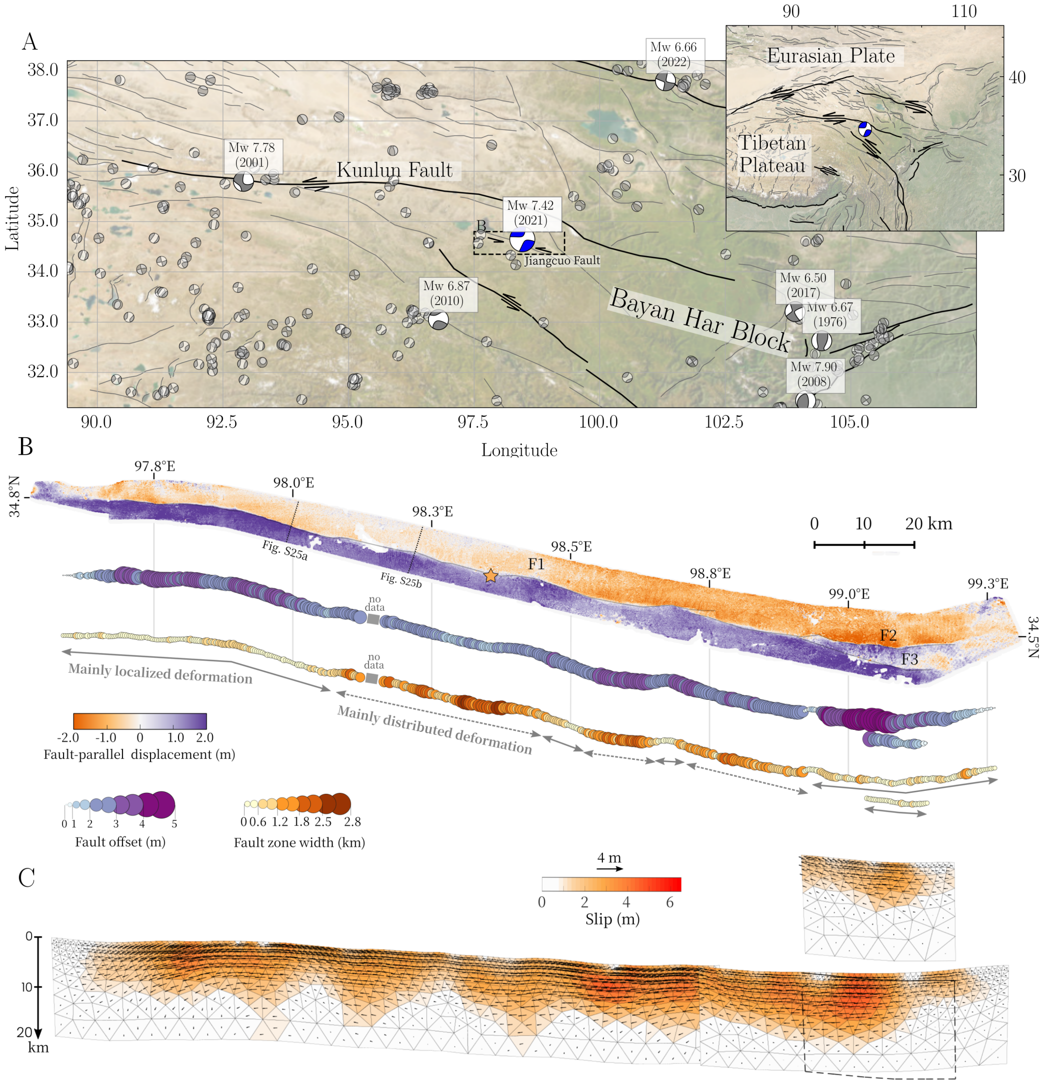

FIGURE 3.1. (A) Tectonic setting of the study area showing the regional active faults of the Tibet Plateau (black lines,[70]) and the moment tensor mechanisms of past earthquakes (gray beachballs, extracted from the global Central Moment Tensor database[21,22]). $M_w \geq 6.5$ focal mechanisms are labeled and highlighted using larger beachball diagrams. Superimposed is the 2021 M_w7.4 Maduo earthquake USGS moment tensor mechanism (blue). The top-right inset shows a zoom-out view of the study area. (B) Top: Surface fault-parallel displacement field of the M_w7.4 Maduo event inferred from the correlation of SPOT-6 optical satellite imagery (Supplementary Information Text B.1). The gray lines indicate the surface fault traces extracted from the fault-parallel displacement field and the dotted black lines locate the profiles shown in Figure S5. Middle and bottom: Fault offsets and fault zone width along the fault strike measured from the fault-parallel surface displacement field. (C) Slip amplitude and rake for the Maduo earthquake estimated from a joint inversion of InSAR and optical data. The assumed fault geometry comprises one main fault and two branching segments in the east, consistent with the dynamic rupture simulation.

The major strike-slip faults surrounding the Bayan Har block all hosted large earthquakes with magnitudes >6.5 in China since 1997 [38,93,97]. In contrast, no major earthquake occurred on the KMPJF, which does not have a clear geomorphological expression and was only partly mapped before the Maduo earthquake [91].

Previous studies focused on analyzing the static, kinematic, and dynamic source properties of the Maduo earthquake using geodetic, teleseismic, and field data [28,29,34,42,58,62,82,90,92]. Most joint inversions, combining geodetic and teleseismic observation, agree on the earthquake propagating across multiple fault segments with varying rupture speeds (e.g., He et al.[33], Jin and Fialko[42], Wang et al.[80], Yue et al.[92]). The rupture speed inferred for the eastward-propagating front falls in the range of 3–5 km/s [49,92,94] whereas the westward propagation is inferred as 2.5–2.8 km/s [13,83]. However, the mechanical relationship between potential supershear rupture episodes and regional tectonics remains highly debated, partially due to the non-uniqueness of the results from various data-driven and physics-based models [13,24,83,92,94].

Geometrically complex fault systems, such as the KMPJF, may be expected to host smaller and slower earthquakes compared to more mature faults [12,39,54,60,67], rendering the magnitude and inferred kinematic complexity of the Maduo earthquake surprising. However, several sizeable strike-slip earthquakes have occurred across geometrically complex faults including the 1992 Landers, the 2016 Kaikoura, the 2019 Ridgecrest, and the 2023 Kahramanmaraş earthquakes [26,30,32,64]. The complexity of the KMPJF is evident in the coseismic surface damage distribution, as constrained by geodetic observations [47,48] and field measurements [91]. The details of the surface rupture expression may correlate with subsurface rupture dynamics, multi-fault interaction, fault orientation with respect to the regional stress field and near-fault plasticity [40,50,63,72,84,85].

Together with a new analysis of high-resolution optical SPOT-6/7 data, the 2021 Maduo earthquake provides a unique opportunity to understand the underlying physics of multi-segment bilateral rupture across a complex fault system and related observables. We demonstrate that combining high-resolution optical and InSAR data analysis with 3D multi-fault dynamic rupture simulations can constrain dynamically viable pre- and co-seismic fault system mechanics and help reduce the non-uniqueness in earthquake source observations.

Our study combines 3D dynamic rupture simulations with joint optical and InSAR geodetic source inversion and surface damage measurements. The simulations incorporate optically-derived multi-segment non-planar fault geometry, data-constrained heterogeneous initial stress, off-fault Drucker-Prager plasticity, strong velocity-weakening rate-and-state friction, topography, and 3D subsurface velocity structure. Our preferred model reproduces the observed characteristics of the Maduo earthquake, such as multi-peak moment rate release, heterogeneous fault slip distribution, and multi-fault rupture. We compare the modeled co-seismic distribution of off-fault deformation with fault damage from surface geodetic measurements and identify geodetic off-fault signatures of supershear rupture onset. We illustrate the importance of key model ingredients by contrasting them with less optimal rupture scenarios. We propose that along-strike variations in fracture energy and fault geometry and 3D variable multi-scale prestress govern the complex multi-segment rupture dynamics and favor unilateral double-onset supershear propagation.

3.2 METHODS

3.2.1 *Geodetic analysis*

We perform joint InSAR (Sentinel-1 imagery) and optical geodetic analysis of the Maduo earthquake. We measure the horizontal surface displacement field from the correlation of high-resolution SPOT-6/7 satellite imagery (Figure 3.1B, Supplementary Information Text B.1). This allows us to map the surface rupture traces and analyze the pattern of near-fault deformation. We infer a main segment (F1 in Figure 3.1B) connected to a shorter segment (F2) via a restraining step-over and a third smaller segment (F3), branching south-eastward from the main segment. We measure the amount and variability of surface fault slip and fault zone width from stacked perpendicular profiles of the SPOT-6/7 surface displacement field, regularly spaced along the fault strike (Supplementary Information Text B.1). Assuming a homogeneous elastic half-space, we combine Sentinel-2 optical data at a resolution of 40 m with InSAR data to infer the static slip distribution at depth from a constrained least-square inversion (Supplementary Information Text B.1, Figures S1-S4). Here, all faults are assumed 83°N dipping for simplicity (Figure S2). Note that this constant-dip-angle assumption does not impact significantly the inferred slip distribution (Supplementary Information Text B.2, Figures S6-7).

3.2.2 *3D dynamic rupture simulations*

We simulate 3D dynamic rupture across multiple fault segments and the associated seismic wave propagation using the open-source software *SeisSol*[35,46,59,77] (Supplementary Information Text B.3). Dynamic rupture models require initial conditions, including fault geometry, prestress, frictional fault strength, and subsurface elastic and plastic material properties[26,31,61].

We construct the fault geometry by extruding the geodetically inferred surface fault traces at depth, assuming variable dip angles constrained from a systematic geodetic sensitivity analysis (Supplementary Information Text B.2, Figure S6) and relocated aftershock distributions[81]. In our preferred dynamic rupture model, we assume a northward-dipping angle of 83° for the main fault segment, and 85° south for the segments F2 and F3. Segment F2 is shallowly connected to the main segment, while F3 is disconnected. Our constructed fault geometries for segments F1 and F3 agree with most previous studies. The assumed sub-vertical south-dipping dip-angle of segment F2 is consistent with aftershock distributions[23,33,43,81,83] but inconsistent with estimates based on geodetic data[13,42,82,95] and Supplementary Information Text B.2, Figure S6. However, an alternative dynamic rupture scenario in which all segments are 83°N dipping fails to rupture segments F2 and F3 (Figure S18).

Our assumed prestress is depth-dependent and multi-scale; we combine a laterally uniform ambient tectonic loading resembling the regional stress state with geodetically constrained small-scale on-fault stress heterogeneities and depth-dependent normal stress. The resulting combined on-fault and off-fault initial shear and normal stress distribution are heterogeneous on the scale of the non-planar fault geometry.

We set a uniform non-Andersonian homogeneous background stress orientation (Figure S8A,B,C, S9) guided by regional moment tensor inversion [88]. This prestress resembles sinistral strike-slip faulting with the maximum compressive stress direction $\hat{S}_{\text{Hmax}}$ =N78°E and the stress shape ratio $\nu = 0.5$. We assume depth-dependent effective normal stresses following a hydrostatic gradient characterized by a pore fluid-pressure ratio of $\gamma = \rho_{water}/\rho_{rock} = 0.37$ (Supplementary Information Text B.3, Figure S10A). While all fault segments vertically extend to 20 km depth, we mimic the brittle-ductile transition at $\sim$ 10 km by smoothly reducing deviatoric stresses to zero (Figure S10B, Ulrich et al.[75]).

In addition to the regional ambient prestress, which is modulated by the non-planar fault geometry (e.g., Biemiller et al.[8]), we add small-scale prestress variability inferred from our geodetic slip model (Supplementary Information Text B.3, Jia et al.[41], Tinti et al.[74]). The geodetically inferred prestress variability enhances the shear stresses in optimally oriented portions of the fault by a maximum of ∼3 MPa within the seismogenic zone (Figure S9A). It also reduces the shear stress at strong geometrical bends by ∼1 MPa, while generally increasing the normal stresses up to 2.9 MPa on F3 (Figure S9B). On-fault pre-stress heterogeneities modulate but do not drive rupture dynamics or the final slip distribution as illustrated in an alternative dynamic rupture scenario without prestress heterogeneities (Supplementary Information Text B.5, Figures S12, S13).

A fast velocity-weakening rate-and-state friction law governs the strength of all faults [20,27]. All friction parameters are listed in Table S1. We include a 1 km shallow velocity-strengthening layer (Figure S8E). This is a simplifying assumption, as the observed early afterslip occurs within the top 2-3 km of the upper crust and varies along-strike [24,43]. However, a dynamic rupture model with a 3 km deep velocity-strengthening layer fails to activate F3 (Supplementary Information Text B.6 and Figure S14).

The seismic S parameter [3,4,18] characterizes the relative fault strength governing dynamic rupture propagation and arrest by balancing fracture energy and strain energy release [15]. It is defined as the ratio between the peak and residual strengths, τ_p and τ_r relative to the background level of initial loading τ_0, so that $S = (\tau_p - \tau_0)/(\tau_0 - \tau_r)$. In our framework, complex initial stress and fault geometries modulate the closeness to failure before the onset of rupture and the relative fault strength.

We allow for the characteristic slip distance D_{RS} to vary along-strike as a proxy for heterogeneous fracture energy, enabling us to vary it independently of the S parameter. Fracture energy fundamentally affects dynamic rupture nucleation, propagation and arrest, and is potentially inferrable from seismological observations [2].

We account for regional 3D velocity structure [87], with a resolution of 0.5 degrees laterally and 5 km resolution with depth (Figure S8D). We include off-fault plasticity described by non-associative Drucker-Prager visco-plastic rheology [6,86]. We use a bulk friction coefficient of 0.5 and a bulk plastic cohesion C_{off} proportional to the 3D variable shear modulus μ as $C_{off} = 2 \times 10^{-4}\mu$ (Table B.1) throughout the entire domain [66,72]. The volumetric bulk initial stresses governing off-fault plasticity are the same as the depth-dependent, laterally uniform ambient tectonic prestress.

3.3 RESULTS

3.3.1 *Heterogeneous near-surface deformation and homogeneous fault slip at depth from joint geodetic analysis*

The 6 m resolution SPOT 6/7 fault-parallel displacement field shown in Figure 3.1B reveals a highly heterogeneous deformation pattern along the rupture trace. Deformation ranges from very localized (<0.6 km), i.e., sharp discontinuities in the surface displacement field in the vicinity of the fault, to broader shear zones (>1.8 km), i.e., more gradual displacement changes across a wider fault zone (Figure S5). This is reflected in strong variations of our measured fault zone width along strike (Figure 3.1B).

Westward of the epicenter, surface deformation can be divided into two distinct regions: (i) a 30 km long segment where deformation is broadly distributed, characterized by an average fault zone width of 1538 m; (ii) a 40 km segment at the western end of the rupture, where deformation is highly localized, and the mean fault zone width is 425 m. Eastward of the epicenter, surface deformation is more heterogeneous. We identify three areas of localized deformation with a mean fault zone width of 747 m, 587 m, and 568 m, from west to east, respectively. These are separated by two areas of distributed deformation with a mean fault zone width of 1660 m and 1213 m, respectively.

We infer considerable surface fault offsets (Figure 3.1B) of 2.44 m on average. The fault offsets tend to be larger where deformation is localized. However, there are exceptions, e.g., near latitude 98.65°E. We identify three distinct regions of high surface slip located at the western and eastern ends of the rupture surface expression, respectively, and near longitude 98.65°E.

Our joint InSAR Sentinel-1 and optical Sentinel-2 geodetic slip model is shown in Figure 3.1C and features overall smooth, shallow (<10 km depth) and high-amplitude fault slip, in agreement with previous geodetic and teleseismic slip models (e.g., Jin and Fialko[42], Li et al.[49]). We resolve three areas of large slip reaching 6 m and a significant dip-slip component at the western end of fault segment F1. Slip across segment F3 is, on average, lower and shallower than for the two main fault segments, F1 and F2.

We use our joint geodetic analysis to inform and verify a suite of dynamic rupture simulations. Subsequently, we discuss signatures of rupture complexity in the on- and off-fault geodetic data.

3.3.2 *Multi-fault 3D dynamic rupture scenarios*

To find a preferred rupture scenario, we explore an ensemble of more than 100 dynamic rupture scenarios varying fault fracture energy, off-fault material strength, prestress, and fault segmentation. We initiate all rupture scenarios at the USGS hypocentre (Supplementary Information Text B.3). Our preferred model features cascading dynamic rupture across multiple segments and double-onset, unilateral supershear along the eastern faults (Figure 3.2). It matches key observed characteristics

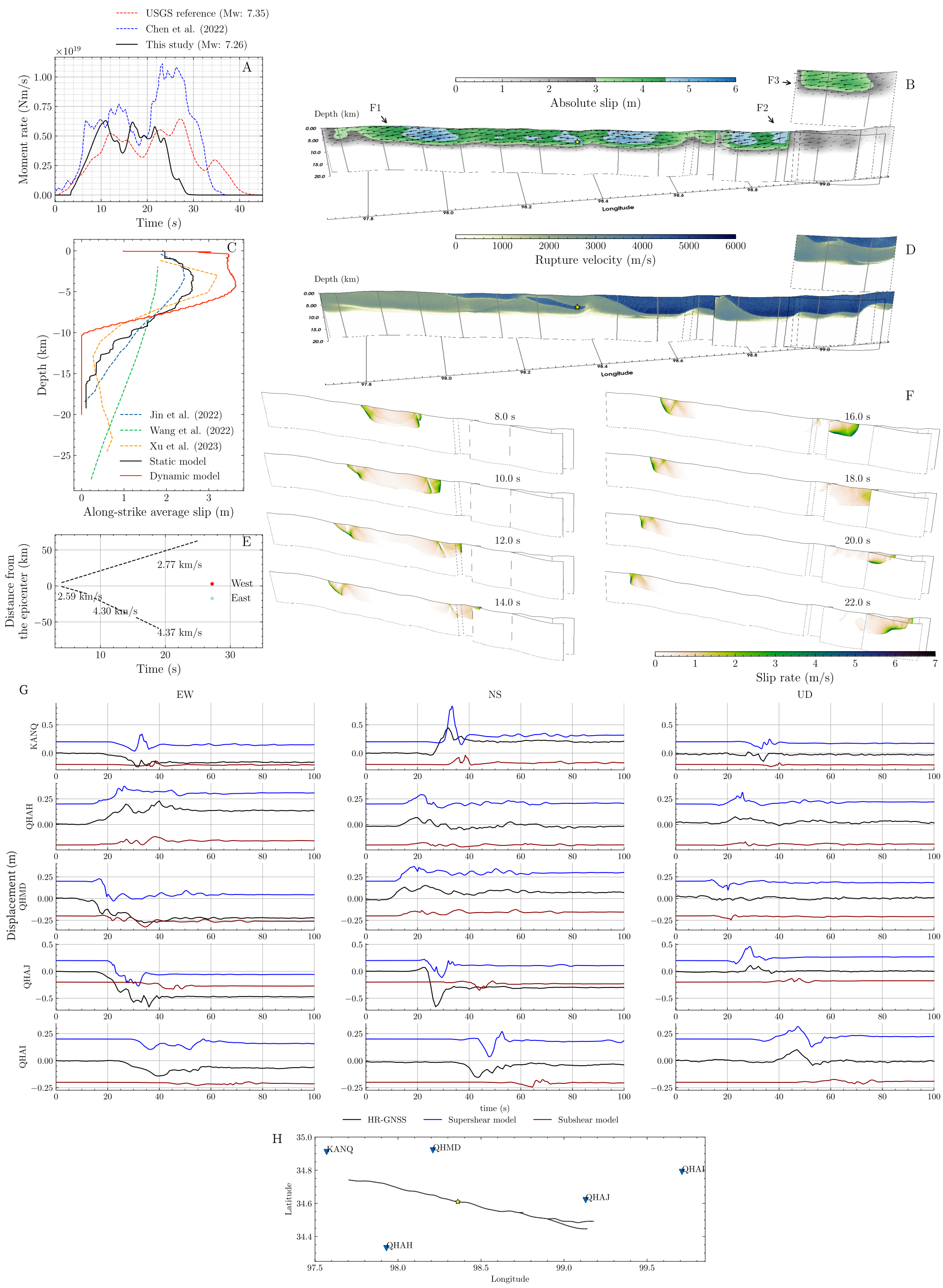

FIGURE 3.2. (A) Modeled moment rate function of the preferred dynamic rupture scenario for the 2021 M_w7.4 Maduo earthquake (black). The finite fault moment rate functions from USGS[78] and Chen et al.[13] are shown as red and blue dashed lines, respectively. (B) Modeled fault slip amplitude on the fault segments (F1, F2, and F3) in a three-dimensional perspective view. Fault slip along segment F3, which is located close to F2, is shown in the top inset. The vertical axis indicates the depth below the Plateau surface from 0 to 20 km. Black vectors indicate the slip direction of the rupture front (rake). Contour lines every 10 km from the epicenter are indicated as gray solid lines on the fault. (C) Comparison of the distribution of average slip with depth for our dynamic and static models as well as other published slip models. (D) Distribution of the rupture velocity on the fault. (E) Rupture velocities of westward and eastward propagating fronts with distance from the epicenter, along a transect at 3.5 km depth. The rupture velocities estimated along different fault portions are indicated as dashed lines. (F) Snapshots of fault slip rate shown every two seconds between t=8.0 s to t=22.0 s of simulation time. (G) Comparison of observed displacement components from high-rate GNSS receivers near the fault[17] with synthetic data for two dynamic rupture scenarios: unilateral supershear and bilateral subshear propagation (see Supplementary Information Text B.10 for an extended comparison using additional GNSS stations).

of the event, including the multi-peak moment rate release and the overall on-fault slip distribution (Figure 3.2A,B).

Figure 3.2A compares the dynamic rupture moment rate release with teleseismic inferences by the USGS and Chen et al.[13]. Our preferred model has a total seismic moment of 0.98×10^{20} N m, equivalent to an on-fault moment magnitude of M_w7.26. Our modeled on-fault moment rate release resembles the two major peaks of the USGS source time function at 13 and 20 s, within the expected uncertainties. Overall, the teleseismic inferences have a slightly longer duration, which may be attributed to differences between our on-fault model results and teleseismic inferences, assumed fault geometries and velocity structure, source time functions, and resolution differences.

Our dynamic model results in an average slip $\sim$ 1.5 m larger than the static model (Figure 3.1C, Figure 3.2B, and C). We observe three sub-regions of high slip accumulation (Figure 3.1C, Figure 3.2B), two on the main branch with a maximum slip of 5.2 m and 4.8 m, 37 km west and 11 km east of the hypocenter respectively, while the third high slip patch is located on F2 with a max slip of 4.8 m, 40 km east of the hypocenter.

Figure 3.2D, and E show rupture velocity on the fault and at 3.5 km depth. Spontaneous rupture propagates bilaterally to the northwest and southeast (Figure 3.2F and Movie S1). While there is limited along-strike variability in seismic wave speeds given by the velocity model, rupture speed varies significantly. The westward rupture front travels at an average speed of 2.77 km s^{-1} for 24 s before arresting the edge of the main fault F1 (Figure 3.2D,E,F and Movie S1). We observe early, transient supershear to the west, which is not self-sustained but leads to higher shallower rupture velocities from 12 km to 30 km west to the hypocenter at shallow depths ($<$ 1.9 km, Figure 3.2D). The eastward propagating rupture front transitions to supershear speeds twice along the main fault and after "jumping" to fault segment F2 (Figure 3.2D). At rupture onset, the eastward rupture speed is slightly slower than the westward one with 2.59 km s^{-1}, being delayed due to a non-optimally oriented fault bend at the Eastern segment (Figure S8). After $\sim$ 10 s, the rupture accelerates to 4.30 km s^{-1} which is close to the local P-wave speed (4.48 km s^{-1}, Figure 3.2E). The first transition from subshear to sustained supershear rupture occurs when the rupture front breaks through the free surface 8 km east of the hypocenter (Figure 3.2D,F). The surface rupture initiates a supershear transition by P-wave diffraction at the free surface (e.g., Hu et al.[36], Kaneko and Lapusta[45], Tang et al.[71], Xu et al.[89]). The supershear rupture front then dynamically triggers coseismic slip on F2 and F3 at about 14 s and 18.5 s, respectively (Figure 3.2F). The second eastward supershear transition occurs soon after the onset of rupture on F2 at about 45 km along strike from the epicenter (Figure 3.2D). Eastward rupture then arrests when reaching the eastern end of the third branch at 28 s (Figure 3.2F). It remains difficult to determine whether supershear rupture during the Maduo earthquake was initiated due to free surface effects or other mechanisms, such as Burridge-Andrews supershear daughter crack nucleation[5,11] or rupture jumping[37]. An alternative dynamic rupture model, which dampens the free surface effect by using a 3 km deep velocity strengthening layer (Supplementary Information Text B.6, Figure S14), preserves supershear rupture across the east part of the fault system, but the rupture does not propagate to F3.

We find that a decrease in characteristic slip distance D_{RS} for 20 km along-strike the eastern main fault away from the hypocenter (Figure S8F) is required to facilitate dynamic triggering of the southernmost fault branches F2 and F3. In our preferred model, the relatively high prestress around the nucleation area promotes initial supershear fronts in both directions, while only the propagating front along the eastern fault sustains. There, locally lower D_{RS} decreases fracture energy [15], favors supershear rupture speeds, and increases dynamically accumulating fault slip. In Figures S24 and S26, we show alternative models with homogeneously small and large D_{RS} leading to either bilateral sub- or bilateral supershear rupture, respectively (Supplementary Information Text B.9). Both models fail to rupture all fault segments and cannot reproduce neither the characteristic moment rate release peaks nor their duration. Furthermore, both models generate large off-fault plasticity in the western section of the fault system, which does not compare well to observations (section 3.3.3, Figure 3.3, S25, S27).

We illustrate the significance of incorporating off-fault plasticity to match the geodetically observed distribution of off-fault damage in Figures S29 and S31 (Supplementary Information Text B.9). These alternative scenarios have lower and higher bulk plastic cohesion, respectively, affecting the width of the off-fault plastic strain pattern and the rupture energy budget. We illustrate the importance of fault geometries in two exemplary alternative models with varying segmentation and dipping angles in Figures S16 and S18. When F1 and F2 are modeled as a continuous segment, the rupture succeeds in dynamically activating F3. However the off-fault plastic strain pattern changes towards the easternmost branches (Supplementary Information Text B.7). In contrast, segments F2 and F3 are not rupturing in an alternative model where these segments are not continuous but dip 83° northward (Figure S18).

The initial conditions of our preferred dynamic rupture model yield highly heterogeneous relative fault strength, as illustrated by the on-fault variability of the S parameter (Figure S8I). Regions of low $S < 1.2$ characterize the southeastern faults, facilitating dynamic triggering of the adjacent segments F2 and F3 and favoring local supershear rupture velocities. Several locally stronger fault portions act as barriers, as indicated by higher S values in the eastern part of the fault system. Figures S20 and S22 show alternative models with different choices for the ambient stress orientation (Supplementary Information Text B.8). A smaller $\hat{S}_{\mathrm{Hmax}}$ angle ($\hat{S}_{\mathrm{Hmax}} \approx$ N68°E) yields larger slip along the F1 and F2 segments (Fig. S20), larger simulated offsets, and larger off-fault deformation at the eastern segments of the fault system (Fig. S21) compared to the preferred model. Larger $\hat{S}_{\mathrm{Hmax}}$ orientation ($\hat{S}_{\mathrm{Hmax}} \approx$ N88°E) results in longer rupture duration and uniformly subshear rupture speeds, reduced on-fault slip, off-fault plastic strain, and simulated offsets, and the inability to dynamically trigger F3 (Fig. S22).

3.3.3 *Modeled off-fault deformation*

Our dynamically modeled surface deformation matches the GPS observations [79], although the horizontal components are slightly underestimated (Figure S32A-B). We observe the largest misfit in orientation and amplitude at station QHAJ, potentially due to unmodelled local fault zone structures. Our preferred forward simulation also reproduces the surface deformation inferred from both the ascending and descending interferograms, with minor divergence near the fault trace

(Figure S32C-H).

Figure 3.2G compares the observed displacement time series from 5 near-fault high-rate GNSS stations [17] with our preferred unilateral supershear model and an alternative subshear model (Figure S22). The arrival time, duration, shape, and amplitude of the displacement time-series are well reproduced by our preferred model. In contrast, the synthetics of the subshear model are systematically lower in amplitude and delayed in timing. This discrepancy is particularly visible for the eastward stations (e.g., QHAJ and QHAI), where the first arrivals in the subshear model are delayed by 15 seconds compared to the observations, while the preferred supershear model's timing better aligns with the observations with misfits less than 5 seconds. The better performance of the supershear model is also demonstrated for other medium-distant stations (Figure S33).

Figure 3.3A shows a map view and 3D cross-sections of the plastic strain accumulated during the dynamic rupture simulation. The surface distribution of off-fault plastic deformation varies along strike, with a wider distribution observed further away from the epicenter and significant local variations. Analyzing the modeled plastic strain along fault-perpendicular transects (Figure 3.3B and Supplementary Information Text B.4) reveals two zones of reduced deformation width located at 97.85°E-98.15°E and 98.25°E-98.45°E (inset b in Figure 3.3A and Figure 3.3B). These zones are separated by local peaks in off-fault plastic deformation corresponding to fault geometrical complexities such as fault kinks and intersections (insets a, c, and e in Figure 3.3A). In addition, we observe that the plastic strain distribution is strongly asymmetric across the fault. A higher level of plastic strain is observed on the northern part of segment F1, although 3D cross-sections c and d show a subtle southward asymmetry (Figure 3.3A). In contrast, the modeled off-fault deformation localizes toward the south across segment F2.

3.4 DISCUSSION

3.4.1 *Unilateral supershear and cascading dynamic rupture*

The observational evidence for supershear rupture during the Maduo event remains debated. Several studies report asymmetric rupture with supershear velocity to the east from kinematic finite fault inversion and back-projection analysis [49,51,92,94]. However, bilateral transient supershear episodes have also been inferred using similar methodologies and datasets [14,88]. Wei et al.[83] argue for sustained subshear speed of the entire rupture from back-projection and multiple point source inversion, which is in line with the joint geodetic and teleseismic inversion of Chen et al.[13]. Our geodetically constrained dynamic rupture simulations indicate energetic nucleation and eastward unilateral, cascading supershear rupture speeds with a double transition from sub- to supershear speeds that would complicate observational inferences. The model's average eastward supershear and westward subshear speeds of $\sim$3.4 km s^{-1} and $\sim$2.18 km s^{-1}, respectively, fall within the range of observational values (2.82 km s^{-1} to 5 km s^{-1} and 2 km s^{-1} to 3 km s^{-1}, respectively [49,51,92,94]).

Cascading spontaneous rupture dynamically triggering both southeastern fault branches is a key constraint in identifying the dynamic parameters of our preferred simulation. Our models suggest

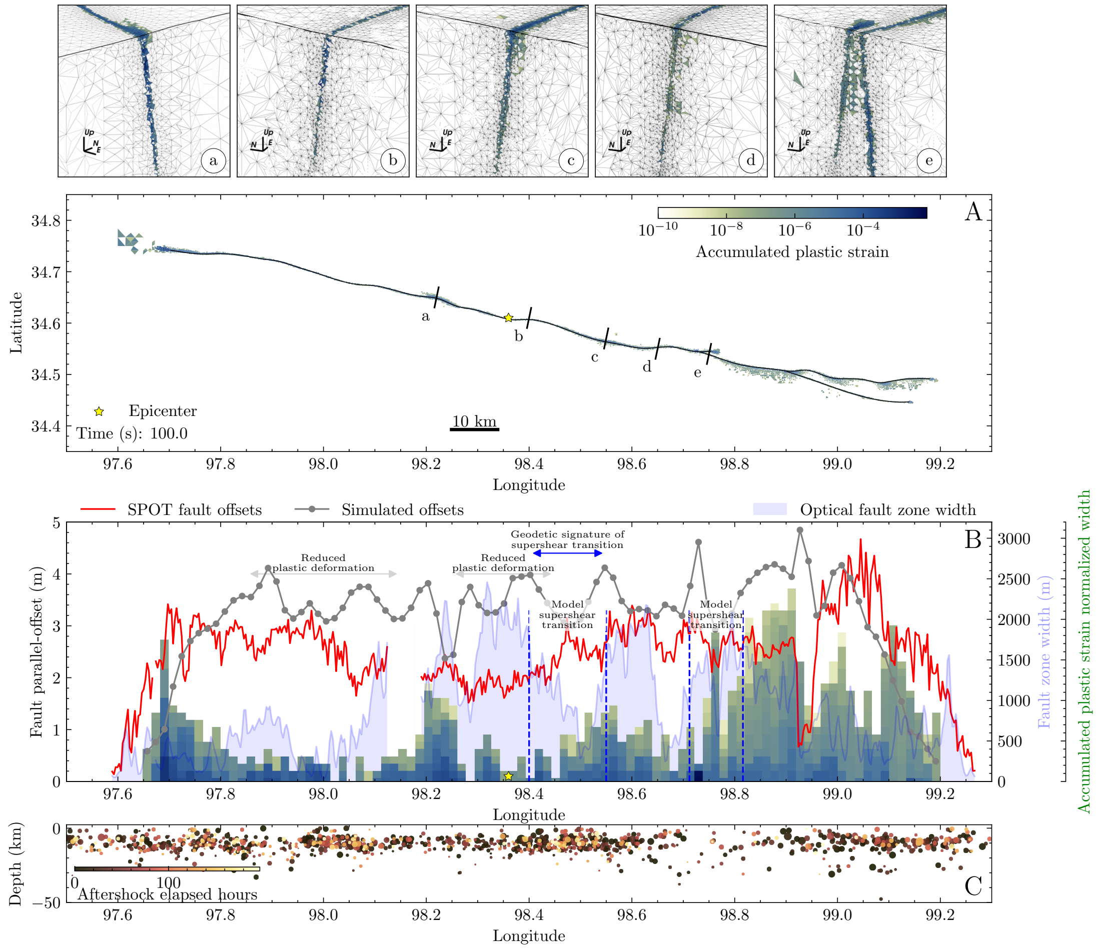

Figure 3.3. (A) Map view of the accumulated plastic strain at the surface at the end of the dynamic rupture simulation. The USGS epicenter is marked with a star. The top-panel insets (a-e) show a three-dimensional perspective view of the plastic strain accumulation at five chosen locations indicated by black lines in (A). (B) Comparison of the optically-inferred fault-parallel offsets (red) and fault zone width (shadowed light blue area) with the simulated fault offsets (gray) and off-fault plasticity (histogram). The histogram depicts the along-strike variation of surface accumulated plastic strain derived from 94 transects along-strike composed of 100 sampling points over a width of 8.88 km. Vertical blue dashed lines mark the two supershear transitions in our preferred model while the horizontal blue line locates the signature of supershear transition in the optical data. (C) Depth versus longitude distribution of aftershocks from the catalog of Wang et al.[81].

that the dynamic triggering of the eastern branches may not have happened without an eastward supershear rupture front. We demonstrate that along-fault variations in fracture energy can be a key driver of diverse ranges of rupture speeds during the same earthquake. The second onset of eastward supershear rupture is also located at the free surface but aided by dynamic rupture jumping across highly stressed step-over faults of variable dip [37,71]. Wen et al.[84] analyzed dynamic rupture models with realistic fault geometry and variable regional stresses to demonstrate the impact of compressive stress orientation on fault slip, dynamic triggering, and supershear propagation. Our simulations additionally integrate regional geodetic constraints [47,48] and explore the importance of frictional variability, small-scale heterogeneity in local fault stress and complex off-fault rheology on coseismic rupture dynamics.

3.4.2 Geodetic off-fault signatures of rupture complexity

Quantifying the degree of localization of the near-fault deformation from fault zone width (FZW) measurements can help unravel the mechanical behavior of the shallow crust. However, interpretation of such data is difficult due to several mechanisms superimposing and producing similar off-fault deformation patterns [57]. For example, a wide optically inferred fault zone width can be interpreted either as the elastic bulk response of a localized decrease of slip in the shallow part of the fault (i.e., the shallow slip deficit [25]) or as distributed inelastic deformation [7,25,56,68]. While both mechanisms may occur simultaneously within the crust [7,25,44,52,53,57,65,69], their respective contributions to the observed surface deformation remain difficult to untangle. In addition, a wide fault zone width may also result from the shallow soil response to coseismic rupture.

Here, we compare our geodetic observations of distributed deformation through the estimated FZW with the plastic strain distribution of our preferred dynamic rupture model. In this model, off-fault plastic deformation is generally more widespread in the eastern sections of the fault system due to the higher dynamic stresses induced by the supershear rupture front [20,40]. In addition, the plastic strain is mainly located on the compressive side of the fault due to the shallow angle of the maximum compressive stress to the fault (~20°) [73]; and is modulated by the geometric fault strike variations [19,85]. The simulated distribution of plastic strain remains similar for different plasticity parameterizations (Supplementary Information Text B.9), while the amplitude of off-fault plastic strain changes (Figure S29,S31).

Our comparison suggests that the optically inferred distributed deformation can be at least partially attributed to off-fault plastic deformation. The measured optical FZW and the modeled plastic deformation width show strikingly similar along-strike variability at several locations (Figure 3.3): (i) a narrow peak of enlarged fault zone width between 98.20° and 98.25°; (ii) a 10 km long zone of large optical FZW centered on longitude 98.60° coinciding with a peak in the plastic deformation width; and (iii) three peaks in the amount of modeled off-fault plasticity on segment F2 correlating with three (less pronounced) peaks in the optical data.

The optical FZW and modeled plastic deformation width also show various disagreements. Near the epicenter, between 98.3° and 98.45°, the optical fault zone width is large, 1800 m on average, whereas our preferred model does not show widespread off-fault plastic deformation. At this particular location, the large optical FZW may partly be attributed to the local geomorphology, which is characterized by Quaternary sand-dunes and swampy terrain where deformation cannot easily localize[91]. Moreover, this part of the fault experienced the largest shallow afterslip[24], suggesting that the large FZW inferred from our observations may be due to a deficit of shallow slip.

We interpret an observed drastic local reduction of optically inferred fault zone width as a possible geodetic signature of the first supershear transitions of the eastward propagating front. Simpler 2D numerical models have shown that the location of supershear transition can be associated with a sharp local reduction of the damage zone width[40,73] due to the spatial contraction of the stress field around the rupture tip. In nature, this effect has been observed using high-resolution optical data, albeit once only, for the 2001 M_s 7.8 Kunlun earthquake[40]. The drastic and localized reduction of the optically-inferred fault zone width at 98.5° (Figure 3.1 and Figure 3.3B) occurs at a straight portion of the fault and does not appear to correlate with variations in the sub-surface material, but does correlate with the first onset of eastward supershear rupture propagation in our preferred dynamic rupture model. The reduction of the modeled off-fault plastic strain width is more gradual in our 3D model than in previous studies, which is likely due to the more gradual onset of supershear rupture at different fault depths (Figure 3.2D), as well as mixed mode-II-III rupture (Figure 3.1C, Figure 3.2B), depth-dependent initial stress (Fig. S8A-C), heterogeneous fault friction and non-planar, segmented fault geometry (Figure 3.1C, Figure 3.2B).

Our results imply that a high level of fault maturity, as well as homogeneous stress-strength conditions and geometric simplicity, may not necessarily be required preconditions for supershear rupture. Local and potentially repeating supershear episodes across immature faults or under heterogeneous stress and strength conditions have been inferred for the 2023 Turkey earthquake doublet[1,16,41] and may be more common than previously thought.

A remarkable, well-resolved gap in aftershock seismicity[81] between 98.65° – 98.9° (Figure 3.3C), which has been proposed to indicate locally high stress release[83], may provide additional evidence for eastward supershear propagation. Postseismic quiescence on supershear segments has been previously observed and may reflect comparably homogeneous strength-stress conditions on geometrically simple and mature faults[9,10]. In sharp contrast, the Maduo earthquake's gap of aftershocks encompasses a major step-over and several fault bends. While the second supershear transition also aligns with a gap in aftershocks, its signature is less clear in both optical data and our model, possibly due to the spatial proximity to geometric fault complexities.

The relative fault strength of our preferred scenario is highly heterogeneous (S ratio, Figure S8I), with localized weak asperities and strong strength barriers. Moreover, the Jiangcuo fault that ruptured during the Maduo earthquake does not have a pronounced geomorphological expression and was only partly mapped before the occurrence of the event. Its cumulative long-term displacement has been measured at only two locations and is low (<5 km[48]). The fault's low geodetic slip rates (1.2±0.8 mm/an[97]) also suggest that this fault is likely immature.

While we discuss alternative models (Figs. S12-S31), we cannot rule out that different geometry, friction, or off-fault parameterizations may reproduce the available observations of rupture characteristics equally well as our preferred model (e.g., Tinti et al.[74]. Denser and joint seismic, geodetic and optical time-dependent near-fault observations may help to shed light on dynamic trade-offs, for example, by enabling more direct constraints of D_{RS} (e.g., Mikumo et al.[55]), and better constraining the timing of rupture (e.g., Gabriel et al.[26], Wang et al.[80]).

3.5 Conclusion

We demonstrate that an integrated analysis of an ensemble of multi-fault 3D dynamic rupture models, high-resolution optical correlation analysis, joint optical-InSAR-slip inversion, and validation by teleseismic observations can help to develop a fundamental understanding of the mechanical conditions that may have governed the complex dynamics of the 2021 M_w7.4 Maduo earthquake. We extract high-resolution surface rupture traces from optical correlation and invert for a static slip model using InSAR and optical data, providing information on small-scale fault heterogeneous stress. Our preferred dynamic rupture model accounts for multi-segment fault geometry, varying dip angles along the fault, multi-scale stress heterogeneities, and variation in fault fracture energy. It can explain the event's complex kinematics, such as a multi-peak moment rate release, unilateral supershear rupture, and dynamic triggering of secondary branches. In the west, despite the modeled smoother fault morphology, dynamic rupture does not transition to supershear in our preferred model. This may be attributed to insufficient stress accumulation and local variations in fault friction properties, which might not favor supershear despite the smoother fault surface. In contrast, the unexpected transition to supershear in the east, sustained despite rupture jumping across the complex, more segmented fault system geometry, highlights the potential importance of fault heterogeneities and complex stress fields efficiently promoting supershear propagation under seemingly unfavorable conditions. Our understanding of the actual fault geometrical structure at depth is limited, being inferred from surface measurements. We explore the sensitivity of rupture dynamics to fault segmentation, tectonic prestress, off-fault plasticity, and frictional fault parameters. By comparing geodetic and dynamic rupture off-fault plastic damage measures, we identify observational signatures of supershear rupture. Our results imply that a high level of fault maturity, as well as homogeneous stress-strength conditions and geometric simplicity, may not necessarily be required preconditions for supershear rupture. This study opens new avenues to observe and better understand such - potentially not unusual - complex earthquake dynamics and their underlying driving factors.

Acknowledgments

This work was supported by the European Union's Horizon 2020 research and innovation programme (TEAR ERC Starting; grant no. 852992) and Horizon Europe (ChEESE-2P, grant no. 101093038; DT-GEO, grant no. 101058129; and Geo-INQUIRE, grant no. 101058518), the National Science Foundation (grant nos. EAR-2225286, EAR-2121568, OAC-2139536, OAC-2311208), the National Aeronautics and Space Administration (grant no. 80NSSC20K0495). JH acknowledges financial support from the Agence Nationale de la Recherche (ANR) under grant ANR-22-CE01-0028-01. We thank Solène Antoine, Chenglong Li, and Thomas Ulrich for valuable discussions. We acknowledge the Editor Germán Prieto, Ruth Harris, and one anonymous reviewer for their thoughtful and constructive comments.

Open Research

All data required to reproduce the dynamic rupture scenario, as well as the geodetic displacement fields (Sentinel-1, Sentinel-2, and SPOT6/7), the geodetic slip model, the SPOT 6/7 fault offsets, and the fault zone width estimates, are available at https://syncandshare.lrz.de/getlink/fiSV331jEB8RP59JgQFCf5/. The data will be fully archived at Zenodo at acceptance.

We use the SeisSol software package available on GitHub (https://github.com/SeisSol/SeisSol) to simulate all dynamic models. We use SeisSol, version 202103_Sumatra-686-gf8e01a54 (master branch on commit 9e8fa8a24dbc421a4b8395616bcab6a58e4cd4cd, v1.1.3, 2024)

The procedure to download and run the code is described in the SeisSol documentation (seissol.readthedocs.io/en/latest/). Downloading and compiling instructions are at https://seissol.readthedocs.io/en/latest/compiling-seissol.html. Instructions for setting up and running simulations are at https://seissol.readthedocs.io/en/latest/configuration.html. Quickstart containerized installations and introductory materials are provided in the docker container and Jupyter Notebooks at https://github.com/SeisSol/Training. Example problems and model configuration files are provided at https://github.com/SeisSol/Examples, many of which reproduce the SCEC 3D Dynamic Rupture benchmark problems described at https://strike.scec.org/cvws/benchmark_descriptions.html. The pseudo-dynamic simulation using a kinematic slip model on the fault to calculate fault stress heterogeneity is stated in the document (https://seissol.readthedocs.io/en/latest/slip-rate-on-DR.html)

We use the following projection for the dynamic simulation: EPSG:3415. The Global Positioning System (GPS) three-component coseismic offsets used to compare with our dynamic rupture model synthetics are from Wang et al.[79]. The Sentinel-2 optical images are freely available and were downloaded from the European Space Agency website (https://dataspace.copernicus.eu/) SAR Copernicus Sentinel-1 data captured by ESA are freely available and were downloaded from PEPS archive operated by CNES (https://peps.cnes.fr/rocket/#/home).

InSAR data were pre-processed using the online service GDM-SAR supported by Formater (https://www.poleterresolide.fr), ISDeform (https://www.isdeform.fr/) and CNES (https://cnes.fr/fr)

Additional information

Competing interests The authors declare no competing interests.

3.6 REFERENCES

[1] Abdelmeguid, M., Zhao, C., Yalcinkaya, E., Gazetas, G., Elbanna, A., and Rosakis, A. (2023). Dynamics of episodic supershear in the 2023 M7.8 Kahramanmaraş/Pazarcik earthquake, revealed by near-field records and computational modeling. *Communications Earth & Environment*, 4(1):456. Cited on page/s 69.

[2] Abercrombie, R. E. (2021). Resolution and uncertainties in estimates of earthquake stress drop and energy release. *Philosophical Transactions of the Royal Society A: Mathematical, Physical and Engineering Sciences*, 379(2196):20200131. Cited on page/s 61.

[3] Aki, K. and Richards, P. G. (2002). *Quantitative seismology*. University Science Books. Cited on page/s 61.

[4] Andrews, D. J. (1976). Rupture propagation with finite stress in antiplane strain. *Journal of Geophysical Research (1896-1977)*, 81(20):3575–3582. Cited on page/s 61.

[5] Andrews, D. J. (1985). Dynamic plane-strain shear rupture with a slip-weakening friction law calculated by a boundary integral method. *Bulletin of the Seismological Society of America*, 75(1):1–21. Cited on page/s 64.

[6] Andrews, D. J. (2005). Rupture dynamics with energy loss outside the slip zone. *Journal of Geophysical Research: Solid Earth*, 110(B01307). Cited on page/s 61.

[7] Antoine, S. L., Klinger, Y., Delorme, A., Wang, K., Bürgmann, R., and Gold, R. D. (2021). Diffuse deformation and surface faulting distribution from submetric image correlation along the 2019 Ridgecrest, California, ruptures. *Bulletin of the Seismological Society of America*, 111(5):2275–2302. Cited on page/s 68.

[8] Biemiller, J., Gabriel, A.-A., and Ulrich, T. (2022). The Dynamics of Unlikely Slip: 3D Modeling of Low-Angle Normal Fault Rupture at the Mai'iu Fault, Papua New Guinea. *Geochemistry, Geophysics, Geosystems*, 23(5):e2021GC010298. e2021GC010298 2021GC010298. Cited on page/s 61.

[9] Bouchon, M. and Karabulut, H. (2008). The aftershock signature of supershear earthquakes. *Science*, 320(5881):1323–1325. Cited on page/s 69.

[10] Bouchon, M., Karabulut, H., Bouin, M.-P., Schmittbuhl, J., Vallée, M., Archuleta, R., Das, S., Renard, F., and Marsan, D. (2010). Faulting characteristics of supershear earthquakes. *Tectonophysics*, 493(3-4):244–253. Cited on page/s 69.

[11] Burridge, R. (1973). Admissible Speeds for Plane-Strain Self-Similar Shear Cracks with Friction but Lacking Cohesion. *Geophysical Journal International*, 35(4):439–455. Cited on page/s 64.

[12] Cappa, F., Perrin, C., Manighetti, I., and Delor, E. (2014). Off-fault long-term damage: A condition to account for generic, triangular earthquake slip profiles. *Geochemistry, Geophysics, Geosystems*, 15(4):1476–1493. Cited on page/s 59.

[13] Chen, K., Avouac, J.-P., Geng, J., Liang, C., Zhang, Z., Li, Z., and Zhang, S. (2022). The 2021 Mw 7.4 Madoi earthquake: An archetype bilateral slip-pulse rupture arrested at a splay fault. *Geophysical Research Letters*, 49(2):e2021GL095243. Cited on page/s 59, 60, 63, 64, 66.

[14] Cheng, C., Wang, D., Yao, Q., Fang, L., Xu, S., Huang, Z., Liu, T., Wang, Z., and Huang, X. (2023). The 2021 Mw 7.3 Madoi, China Earthquake: Transient Supershear Ruptures On a Presumed Immature Strike-slip Fault. *Journal of Geophysical Research: Solid Earth*, page e2022JB024641. e2022JB024641 2022JB024641. Cited on page/s 66.

[15] Cocco, M., Aretusini, S., Cornelio, C., Nielsen, S. B., Spagnuolo, E., Tinti, E., and Di Toro, G. (2023). Fracture energy and breakdown work during earthquakes. *Annual Review of Earth and Planetary Sciences*, 51(1):217–252. Cited on page/s 61, 65.

[16] Delouis, B., van den Ende, M., and Ampuero, J.-P. (2023). Kinematic rupture model of the February 6th 2023 Mw7. 8 Turkey earthquake from a large set of near-source strong motion records combined by GNSS offsets reveals intermittent supershear rupture. *Authorea Preprints*. Cited on page/s 69.

[17] Ding, K., Wang, Q., Li, Z., He, P., Zhang, P., Chen, J., You, X., and Zhao, L. (2022). Rapid Source Determination of the 2021 Mw 7.4 Maduo Earthquake by a Dense High-Rate GNSS Network in the Tibetan Plateau. *Seismological Research Letters*, 93(6):3234–3245. Cited on page/s 63, 66.

[18] Dunham, E. M. (2007). Conditions governing the occurrence of supershear ruptures under slip-weakening friction. *Journal of Geophysical Research: Solid Earth*, 112(B7). Cited on page/s 61.

[19] Dunham, E. M., Belanger, D., Cong, L., and Kozdon, J. E. (2011a). Earthquake ruptures with strongly rate-weakening friction and off-fault plasticity, part 2: Nonplanar faults. *Bulletin of the Seismological Society of America*, 101(5):2308–2322. Cited on page/s 68.

[20] Dunham, E. M., Belanger, D., Cong, L., and Kozdon, J. E. (2011b). Earthquake Ruptures with Strongly Rate-Weakening Friction and Off-Fault Plasticity, Part 1: Planar Faults. *Bulletin of the Seismological Society of America*, 101(5):2296–2307. Cited on page/s 61, 68.

[21] Dziewonski, A. M., Chou, T.-A., and Woodhouse, J. H. (1981). Determination of earthquake source parameters from waveform data for studies of global and regional seismicity. *Journal of Geophysical Research: Solid Earth*, 86(B4):2825–2852. Cited on page/s 58.

[22] Ekström, G., Nettles, M., and Dziewoński, A. (2012). The global CMT project 2004–2010: Centroid-moment tensors for 13,017 earthquakes. *Physics of the Earth and Planetary Interiors*, 200-201:1–9. Cited on page/s 58.

[23] Fan, X., Zhang, G., Zhao, D., Xie, C., Huang, C., and Shan, X. (2022). Fault geometry and kinematics of the 2021 Mw 7.3 Maduo earthquake from aftershocks and InSAR observations. *Frontiers in Earth Science*, 10. Cited on page/s 60.

[24] Fang, J., Ou, Q., Wright, T. J., Okuwaki, R., Amey, R. M., Craig, T. J., Elliott, J. R., Hooper, A., Lazeckỳ, M., and Maghsoudi, Y. (2022). Earthquake cycle deformation associated with the 2021 Mw 7.4 Maduo (Eastern Tibet) earthquake: An intrablock rupture event on a slow-slipping fault from Sentinel-1 InSAR and teleseismic data. *Journal of Geophysical Research: Solid Earth*, 127(11):e2022JB024268. Cited on page/s 59, 61, 69.

[25] Fialko, Y., Sandwell, D., Simons, M., and Rosen, P. (2005). Three-dimensional deformation caused by the Bam, Iran, earthquake and the origin of shallow slip deficit. *Nature*, 435(7040):295–299. Cited on page/s 68.

[26] Gabriel, A., Ulrich, T., Marchandon, M., Biemiller, J., and Rekoske, J. (2023). 3D Dynamic Rupture Modeling of the 6 February 2023, Kahramanmaraş, Turkey Mw 7.8 and 7.7 Earthquake Doublet Using Early Observations. *The Seismic Record*, 3(4):342–356. Cited on page/s 59, 60, 70.

[27] Gabriel, A.-A., Ampuero, J.-P., Dalguer, L. A., and Mai, P. M. (2012). The transition of dynamic rupture styles in elastic media under velocity-weakening friction. *Journal of Geophysical Research: Solid Earth*, 117(B9). Cited on page/s 61.

[28] Gao, Z., Li, Y., Shan, X., and Zhu, C. (2021). Earthquake Magnitude Estimation from High-Rate GNSS Data: A Case Study of the 2021 Mw 7.3 Maduo Earthquake. *Remote Sensing*, 13(21). Cited on page/s 59.

[29] Guo, R., Yang, H., Li, Y., Zheng, Y., and Zhang, L. (2021). Complex Slip Distribution of the 2021 Mw 7.4 Maduo, China, Earthquake: An Event Occurring on the Slowly Slipping Fault. *Seismological Research Letters*, 93(2A):653–665. Cited on page/s 57, 59.

[30] Hamling, I. J., Hreinsdóttir, S., Clark, K., Elliott, J., Liang, C., Fielding, E., Litchfield, N., Villamor, P., Wallace, L., Wright, T. J., et al. (2017). Complex multifault rupture during the 2016 m w 7.8 kaikōura earthquake, new zealand. *Science*, 356(6334):eaam7194. Cited on page/s 59.

[31] Harris, R. A., Barall, M., Aagaard, B., Ma, S., Roten, D., Olsen, K., Duan, B., Liu, D., Luo, B., Bai, K., Ampuero, J., Kaneko, Y., Gabriel, A., Duru, K., Ulrich, T., Wollherr, S., Shi, Z., Dunham, E., Bydlon, S., Zhang, Z., Chen, X., Somala, S. N., Pelties, C., Tago, J., Cruz-Atienza, V. M., Kozdon, J., Daub, E., Aslam, K., Kase, Y., Withers, K., and Dalguer, L. (2018). A Suite of Exercises for Verifying Dynamic Earthquake Rupture Codes. *Seismological Research Letters*, 89(3):1146–1162. Cited on page/s 60.

[32] Hauksson, E., Jones, L. M., Hutton, K., and Eberhart-Phillips, D. (1993). The 1992 landers earthquake sequence: Seismological observations. *Journal of Geophysical Research: Solid Earth*, 98(B11):19835–19858. Cited on page/s 59.

[33] He, K., Wen, Y., Xu, C., and Zhao, Y. (2021a). Fault Geometry and Slip Distribution of the 2021 Mw 7.4 Maduo, China, Earthquake Inferred from InSAR Measurements and Relocated Aftershocks. *Seismological Research Letters*, 93(1):8–20. Cited on page/s 59, 60.

[34] He, L., Feng, G., Wu, X., Lu, H., Xu, W., Wang, Y., Liu, J., Hu, J., and Li, Z. (2021b). Coseismic and Early Postseismic Slip Models of the 2021 Mw 7.4 Maduo Earthquake (Western China) Estimated by Space-Based Geodetic Data. *Geophysical Research Letters*, 48(24):e2021GL095860. e2021GL095860 2021GL095860. Cited on page/s 59.

[35] Heinecke, A., Breuer, A., Rettenberger, S., Bader, M., Gabriel, A.-A., Pelties, C., Bode, A., Barth, W., Liao, X.-K., Vaidyanathan, K., Smelyanskiy, M., and Dubey, P. (2014). Petascale high order dynamic rupture earthquake simulations on heterogeneous supercomputers. In *SC '14: Proceedings of the International Conference for High Performance Computing, Networking, Storage and Analysis*, pages 3–14. Cited on page/s 60.

[36] Hu, F., Oglesby, D. D., and Chen, X. (2021). The effect of depth-dependent stress in controlling free-surface-induced supershear rupture on strike-slip faults. *Journal of Geophysical Research: Solid Earth*, 126(5):e2020JB021459. e2020JB021459 2020JB021459. Cited on page/s 64.

[37] Hu, F., Xu, J., Zhang, Z., and Chen, X. (2016). Supershear transition mechanism induced by step over geometry. *Journal of Geophysical Research: Solid Earth*, 121(12):8738–8749. Cited on page/s 64, 68.

[38] Huang, L., Zhang, B., and Shi, Y. (2021). Stress Transfer at the Northeastern End of the Bayan Har Block and Its Implications for Seismic Hazards: Insights From Numerical Simulations. *Earth and Space Science*, 8(12):e2021EA001947. e2021EA001947 2021EA001947. Cited on page/s 59.

[39] Huang, Y., Ampuero, J.-P., and Helmberger, D. V. (2014). Earthquake ruptures modulated by waves in damaged fault zones. *Journal of Geophysical Research: Solid Earth*, 119(4):3133–3154. Cited on page/s 59.

[40] Jara, J., Bruhat, L., Thomas, M. Y., Antoine, S. L., Okubo, K., Rougier, E., Rosakis, A. J., Sammis, C. G., Klinger, Y., Jolivet, R., and Bhat, H. S. (2021). Signature of transition to supershear rupture speed in the coseismic off-fault damage zone. *Proc Math Phys Eng Sci*, 477(2255):20210364. Cited on page/s 59, 68, 69.

[41] Jia, Z., Jin, Z., Marchandon, M., Ulrich, T., Gabriel, A.-A., Fan, W., Shearer, P., Zou, X., Rekoske, J., Bulut, F., Garagon, A., and Fialko, Y. (2023). The complex dynamics of the 2023 Kahramanmaraş, Turkey, Mw 7.8-7.7 earthquake doublet. *Science*, 0:eadi0685. Cited on page/s 61, 69.

[42] Jin, Z. and Fialko, Y. (2021). Coseismic and early postseismic deformation due to the 2021 M7.4 Maduo (China) earthquake. *Geophysical Research Letters*, 48(21):e2021GL095213. e2021GL095213 2021GL095213. Cited on page/s 59, 60, 62.

[43] Jin, Z., Fialko, Y., Yang, H., and Li, Y. (2023). Transient deformation excited by the 2021 M7.4 Maduo (China) earthquake: Evidence of a deep shear zone. *Journal of Geophysical Research: Solid Earth*, 128(8):e2023JB026643. e2023JB026643 2023JB026643. Cited on page/s 60, 61.

[44] Kaneko, Y. and Fialko, Y. (2011). Shallow slip deficit due to large strike-slip earthquakes in dynamic rupture simulations with elasto-plastic off-fault response. *Geophysical Journal International*, 186(3):1389–1403. Cited on page/s 68.

[45] Kaneko, Y. and Lapusta, N. (2010). Supershear transition due to a free surface in 3-D simulations of spontaneous dynamic rupture on vertical strike-slip faults. *Tectonophysics*, 493(3):272–284. Earthquake supershear rupture speeds. Cited on page/s 64.

[46] Käser, M. and Dumbser, M. (2006). An arbitrary high-order discontinuous Galerkin method for elastic waves on unstructured meshes — I. The two-dimensional isotropic case with external source terms. *Geophysical Journal International*, 166(2):855–877. Cited on page/s 60.

[47] Li, C., Li, T., Hollingsworth, J., Zhang, Y., Qian, L., and Shan, X. (2023a). Strain threshold for the formation of coseismic surface rupture. *Geophysical Research Letters*, 50(16):e2023GL103666. Cited on page/s 59, 68.

[48] Li, C., Li, T., Shan, X., and Zhang, G. (2023b). Extremely Large Off-Fault Deformation during the 2021 M w 7.4 Maduo, Tibetan Plateau, Earthquake. *Seismological Society of America*, 94(1):39–51. Cited on page/s 59, 68, 69.

[49] Li, Q., Wan, Y., Li, C., Tang, H., Tan, K., and Wang, D. (2022). Source Process Featuring Asymmetric Rupture Velocities of the 2021 Mw 7.4 Maduo, China, Earthquake from Teleseismic and Geodetic Data. *Seismological Research Letters*, 93(3):1429–1439. Cited on page/s 59, 62, 66.

[50] Liu-Zeng, J., Liu, Z., Liu, X., Milliner, C., Rodriguez Padilla, A. M., Xu, S., Avouac, J.-P., Yao, W., Klinger, Y., Han, L., Shao, Y., Yan, X., Aati, S., and Shao, Z. (2024). Fault orientation trumps fault maturity in controlling coseismic rupture characteristics of the 2021 maduo earthquake. *AGU Advances*, 5(2):e2023AV001134. Cited on page/s 59.

[51] Lyu, M., Chen, K., Xue, C., Zang, N., Zhang, W., and Wei, G. (2022). Overall subshear but locally supershear rupture of the 2021 Mw 7.4 Maduo earthquake from high-rate GNSS waveforms and three-dimensional InSAR deformation. *Tectonophysics*, 839:229542. Cited on page/s 66.

[52] Ma, H., Feng, J., Wang, Q., Zhao, J., Zou, Z., Yuan, Z., and Li, M. (2022). Stress and Strain Characteristics before the Mw 7.3 Maduo Earthquake and Its Implications for Future Earthquakes on the Maqin–Maqu Fault. *Bulletin of the Seismological Society of America*, 112(5):2454–2467. Cited on page/s 68.

[53] Ma, S. (2008). A physical model for widespread near-surface and fault zone damage induced by earthquakes. *Geochemistry, Geophysics, Geosystems*, 9(11). Cited on page/s 68.

[54] Manighetti, I., Caulet, C., Barros, L. D., Perrin, C., Cappa, F., and Gaudemer, Y. (2015). Generic along-strike segmentation of Afar normal faults, East Africa: Implications on fault growth and stress heterogeneity on seismogenic fault planes. *Geochemistry, Geophysics, Geosystems*, 16:443–467. Cited on page/s 59.

[55] Mikumo, T., Olsen, K. B., Fukuyama, E., and Yagi, Y. (2003). Stress-Breakdown Time and Slip-Weakening Distance

Inferred from Slip-Velocity Functions on Earthquake Faults. *Bulletin of the Seismological Society of America*, 93(1):264–282. Cited on page/s 70.

[56] Milliner, C. W. D., Dolan, J. F., Hollingsworth, J., Leprince, S., Ayoub, F., and Sammis, C. G. (2015). Quantifying near-field and off-fault deformation patterns of the 1992 Mw 7.3 Landers earthquake. *Geochemistry, Geophysics, Geosystems*, 16(5):1577–1598. Cited on page/s 68.

[57] Nevitt, J. M., Brooks, B. A., Catchings, R. D., Goldman, M. R., Ericksen, T. L., and Glennie, C. L. (2020). Mechanics of near-field deformation during co-and post-seismic shallow fault slip. *Scientific Reports*, 10(1):5031. Cited on page/s 68.

[58] Pan, J., Li, H., Chevalier, M.-L., Tapponnier, P., Bai, M., Li, C., Liu, F., Liu, D., Wu, K., Wang, P., Li, C., Lu, H., and Chen, P. (2022). Co-seismic rupture of the 2021, Mw7.4 Maduo earthquake (northern Tibet): Short-cutting of the Kunlun fault big bend. *Earth and Planetary Science Letters*, 594:117703. Cited on page/s 57, 59.

[59] Pelties, C., Gabriel, A.-A., and Ampuero, J.-P. (2014). Verification of an ADER-DG method for complex dynamic rupture problems. *Geoscientific Model Development*, 7(3):847–866. Cited on page/s 60.

[60] Perrin, C., Manighetti, I., and Gaudemer, Y. (2016). Off-fault tip splay networks: A genetic and generic property of faults indicative of their long-term propagation. *Comptes Rendus Geoscience*, 348(1):52–60. Cited on page/s 59.

[61] Ramos, M. D., Thakur, P., Huang, Y., Harris, R. A., and Ryan, K. J. (2022). Working with Dynamic Earthquake Rupture Models: A Practical Guide. *Seismological Research Letters*, 93(4):2096–2110. Cited on page/s 60.

[62] Ren, J., Zhang, Z., Gai, H., and Kang, W. (2021). Typical Riedel shear structures of the coseismic surface rupture zone produced by the 2021 Mw 7.3 Maduo earthquake, Qinghai, China, and the implications for seismic hazards in the block interior. *Natural Hazards Research*, 1(4):145–152. Cited on page/s 59.

[63] Rodriguez Padilla, A. M. and Oskin, M. E. (2023). Displacement Hazard from Distributed Ruptures in Strike-Slip Earthquakes. *Bulletin of the Seismological Society of America*, 113(6):2730–2745. Cited on page/s 59.

[64] Ross, Z. E., Idini, B., Jia, Z., Stephenson, O. L., Zhong, M., Wang, X., Zhan, Z., Simons, M., Fielding, E. J., Yun, S.-H., Hauksson, E., Moore, A. W., Liu, Z., and Jung, J. (2019). Hierarchical interlocked orthogonal faulting in the 2019 ridgecrest earthquake sequence. *Science*, 366(6463):346–351. Cited on page/s 59.

[65] Roten, D., Olsen, K. B., and Day, S. M. (2017). Off-fault deformations and shallow slip deficit from dynamic rupture simulations with fault zone plasticity. *Geophysical Research Letters*, 44(15):7733–7742. Cited on page/s 68.

[66] Roten, D., Olsen, K. B., Day, S. M., Cui, Y., and Fäh, D. (2014). Expected seismic shaking in Los Angeles reduced by San Andreas fault zone plasticity. *Geophysical Research Letters*, 41(8):2769–2777. Cited on page/s 61.

[67] Schwartz, D. P. and Coppersmith, K. J. (1984). Fault behavior and characteristic earthquakes: Examples from the wasatch and san andreas fault zones. *Journal of Geophysical Research: Solid Earth*, 89(B7):5681–5698. Cited on page/s 59.

[68] Scott, C. P., Arrowsmith, J. R., Nissen, E., Lajoie, L., Maruyama, T., and Chiba, T. (2018). The M7 2016 Kumamoto, Japan, earthquake: 3-D deformation along the fault and within the damage zone constrained from differential lidar topography. *Journal of Geophysical Research: Solid Earth*, 123(7):6138–6155. Cited on page/s 68.

[69] Simons, M., Fialko, Y., and Rivera, L. (2002). Coseismic deformation from the 1999 M w 7.1 Hector Mine, California, earthquake as inferred from InSAR and GPS observations. *Bulletin of the Seismological Society of America*, 92(4):1390–1402. Cited on page/s 68.

[70] Styron, R., Taylor, M., and Okoronkwo, K. (2010). Database of Active Structures From the Indo-Asian Collision. *Eos, Transactions American Geophysical Union*, 91(20):181–182. Cited on page/s 58.

[71] Tang, R., Yuan, J., and Gan, L. (2021). Free-surface-induced supershear transition in 3-d simulations of spontaneous dynamic rupture on oblique faults. *Geophysical Research Letters*, 48(3):e2020GL091621. e2020GL091621 2020GL091621. Cited on page/s 64, 68.

[72] Taufiqurrahman, T., Gabriel, A.-A., Li, D., Ulrich, T., Li, B., Carena, S., Verdecchia, A., and Gallovič, F. (2023). Dynamics, interactions and delays of the 2019 Ridgecrest rupture sequence. *Nature*, 618(7964):308–315. Cited on page/s 59, 61.

[73] Templeton, E. L. and Rice, J. R. (2008). Off-fault plasticity and earthquake rupture dynamics: 1. Dry materials or neglect of fluid pressure changes. *Journal of Geophysical Research: Solid Earth*, 113(B09306). Cited on page/s 68, 69.

[74] Tinti, E., Casarotti, E., Ulrich, T., Taufiqurrahman, T., Li, D., and Gabriel, A.-A. (2021). Constraining families of dynamic models using geological, geodetic and strong ground motion data: The Mw 6.5, October 30th, 2016, Norcia earthquake, Italy. *Earth and Planetary Science Letters*, 576:117237. Cited on page/s 61, 69.

[75] Ulrich, T., Gabriel, A.-A., Ampuero, J.-P., and Xu, W. (2019). Dynamic viability of the 2016 Mw 7.8 Kaikōura earthquake cascade on weak crustal faults. *Nature communications*, 10(1):1213. Cited on page/s 61.

[76] UNICEF China (2021). UNICEF Sends Supplies to Children Affected by an Earthquake in Qinghai Province. Cited on page/s 57.

[77] Uphoff, C., Rettenberger, S., Bader, M., Madden, E. H., Ulrich, T., Wollherr, S., and Gabriel, A.-A. (2017). Extreme scale multi-physics simulations of the tsunamigenic 2004 sumatra megathrust earthquake. In *Proceedings of the International Conference for High Performance Computing, Networking, Storage and Analysis*, SC '17, New York, NY, USA. Association for Computing Machinery. Cited on page/s 60.

[78] USGS (2021). Overview: M7.3 - Southern Qinghai, China. Cited on page/s 63.

[79] Wang, M., Wang, F., Jiang, X., Tian, J., Li, Y., Sun, J., and Shen, Z.-K. (2021a). GPS determined coseismic slip of the 2021 Mw 7.4 Maduo, China, earthquake and its tectonic implication. *Geophysical Journal International*, 228(3):2048–2055. Cited on page/s 65, 71.

[80] Wang, S., Song, C., Li, S., and Li, X. (2022). Resolving co-and early post-seismic slip variations of the 2021 Mw 7.4 Madoi earthquake in east Bayan Har block with a block-wide distributed deformation mode from satellite synthetic aperture radar data. *Earth Planet. Phys*, 6(1):108–122. Cited on page/s 59, 70.

[81] Wang, W., Fang, L., Wu, J., Tu, H., Chen, L., Lai, G., and Zhang, L. (2021b). Aftershock sequence relocation of the 2021 Ms 7.4 Maduo earthquake, Qinghai, China. *Science China Earth Sciences*, 64:1371–1380. Cited on page/s 60, 67, 69.

[82] Wei, G., Chen, K., Lyu, M., Gong, W., Dal Zilio, L., Ye, L., and Tu, H. (2023). Complex strike-slip faulting during the 2021 Mw7.4 Maduo earthquake. *Communications Earth & Environment*, 4(1):319. Cited on page/s 59, 60.

[83] Wei, S., Zeng, H., Shi, Q., Liu, J., Luo, H., Hu, W., Li, Y., Wang, W., Ma, Z., Liu-Zeng, J., and Wang, T. (2022). Simultaneous rupture propagation through fault bifurcation of the 2021 Mw 7.4 Maduo earthquake. *Geophysical Research Letters*, 49(21):e2022GL100283. e2022GL100283 2022GL100283. Cited on page/s 59, 60, 66, 69.

[84] Wen, Y., Cai, J., He, K., and Xu, C. (2024). Dynamic Rupture of the 2021 MW 7.4 Maduo Earthquake: An Intra-Block Event Controlled by Fault Geometry. *J. Geophys. Res.*, 129(1):e2023JB027247. Cited on page/s 59, 68.

[85] Wollherr, S., Gabriel, A.-A., and Mai, P. M. (2019). Landers 1992 "reloaded": Integrative dynamic earthquake rupture modeling. *Journal of Geophysical Research: Solid Earth*, 124(7):6666–6702. Cited on page/s 59, 68.

[86] Wollherr, S., Gabriel, A.-A., and Uphoff, C. (2018). Off-fault plasticity in three-dimensional dynamic rupture simulations using a modal Discontinuous Galerkin method on unstructured meshes: Implementation, verification and application. *Geophysical Journal International*, 214(3):1556–1584. Cited on page/s 61.

[87] Xin, H., Zhang, H., Kang, M., He, R., Gao, L., and Gao, J. (2018). High-Resolution Lithospheric Velocity Structure of Continental China by Double-Difference Seismic Travel-Time Tomography. *Seismological Research Letters*, 90(1):229–241. Cited on page/s 61.

[88] Xu, B. and Zhang, Y. (2023). Joint inversion of centroid moment tensor for large earthquakes by combining teleseismic P-wave and W-phase records. *Geophysical Journal International*, 234(2):1143–1156. Cited on page/s 61, 66.

[89] Xu, J., Zhang, H., and Chen, X. (2015). Rupture phase diagrams for a planar fault in 3-D full-space and half-space. *Geophysical Journal International*, 202(3):2194–2206. Cited on page/s 64.

[90] Yuan, J. and Li, Y. (2023). Complex fault geometry controls dynamic rupture of the 2021 Mw7.4 Maduo earthquake, NE Tibetan Plateau. *Tectonophysics*, 868:230105. Cited on page/s 59.

[91] Yuan, Z., Li, T., Su, P., Sun, H., Ha, G., Guo, P., Chen, G., and Thompson Jobe, J. (2022). Large Surface-Rupture Gaps and Low Surface Fault Slip of the 2021 Mw 7.4 Maduo Earthquake Along a Low-Activity Strike-Slip Fault, Tibetan Plateau. *Geophysical Research Letters*, 49(6):e2021GL096874. e2021GL096874 2021GL096874. Cited on page/s 57, 59, 69.

[92] Yue, H., Shen, Z.-K., Zhao, Z., Wang, T., Cao, B., Li, Z., Bao, X., Zhao, L., Song, X., Ge, Z., Ren, C., Lu, W., Zhang, Y., Liu-Zeng, J., Wang, M., Huang, Q., Zhou, S., and Xue, L. (2022). Rupture process of the 2021 M7.4 Maduo earthquake and implication for deformation mode of the Songpan-Ganzi terrane in Tibetan Plateau. *Proceedings of the National Academy of Sciences*, 119(23):e2116445119. Cited on page/s 59, 66.

[93] Zhang, P., Deng, Q., Zhang, G., Ma, J., Gan, W., Min, W., Mao, F., and Wang, Q. (2003). Active tectonic blocks and strong earthquakes in the continent of China. *Science in China Series D: Earth Sciences*, 46(2):13–24. Cited on page/s 59.

[94] Zhang, X., Feng, W., Du, H., Samsonov, S., and Yi, L. (2022). Supershear rupture during the 2021 Mw 7.4

Maduo, China, earthquake. *Geophysical Research Letters*, 49(6):e2022GL097984. e2022GL097984 2022GL097984. Cited on page/s 59, 66.

[95] Zhao, D., Qu, C., Chen, H., Shan, X., Song, X., and Gong, W. (2021). Tectonic and Geometric Control on Fault Kinematics of the 2021 Mw7.3 Maduo (China) Earthquake Inferred From Interseismic, Coseismic, and Postseismic InSAR Observations. *Geophysical Research Letters*, 48(18):e2021GL095417. e2021GL095417 2021GL095417. Cited on page/s 60.

[96] Zhu, M., Chen, F., Fu, B., Chen, W., Qiao, Y., Shi, P., Zhou, W., Lin, H., Liao, Y., and Gao, S. (2023). Earthquake-induced risk assessment of cultural heritage based on InSAR and seismic intensity: A case study of Zhalang temple affected by the 2021 Mw 7.4 Maduo (China) earthquake. *International Journal of Disaster Risk Reduction*, 84:103482. Cited on page/s 57.

[97] Zhu, Y., Diao, F., Fu, Y., Liu, C., and Xiong, X. (2021). Slip rate of the seismogenic fault of the 2021 Maduo earthquake in western China inferred from GPS observations. *Science China Earth Sciences*, 64(8):1363–1370. Cited on page/s 59, 69.

Chapter 4

Coupling 3D geodynamics and dynamic earthquake rupture: fault geometry, rheology and stresses across timescales

by Jourdon A., Hayek J.N., May D.A., Gabriel A.-A. (In rev). Submitted to JGR: Solid Earth. DOI:10.48550/arXiv.2407.20609

Abstract

Tectonic deformation crucially shapes the Earth's surface, with strain localization resulting in the formation of shear zones and faults that accommodate significant tectonic displacement. Earthquake dynamic rupture models, which provide valuable insights into earthquake mechanics and seismic ground motions, rely on initial conditions such as pre-stress states and fault geometry. However, these are often inadequately constrained due to observational limitations. To address these challenges, we develop a new method that loosely couples 3D geodynamic models to 3D dynamic rupture simulations, providing a mechanically consistent framework for earthquake analysis. Our approach does not prescribe fault geometry but derives it from the underlying lithospheric rheology and tectonic velocities using the medial axis transform. We perform three long-term geodynamics models of a strike-slip geodynamic system, each involving different continental crust rheology. We link these with nine dynamic rupture models, in which we investigate the role of varying fracture energy and plastic strain energy dissipation in the dynamic rupture behavior. These simulations suggest that for our fault, long-term rheology, and geodynamic system, a plausible critical linear slip weakening distance falls within $D_c \in [0.6, 1.5]$. Our results indicate that the long-term 3D stress field favors slip on fault segments better aligned with the regional plate motion and that minor variations in the long-term 3D stress field can strongly affect rupture dynamics, providing a physical mechanism for arresting earthquake propagation. Our geodynamically informed earthquake models highlight the need for detailed 3D fault modeling across time scales for a comprehensive understanding of earthquake mechanics.

4.1 Introduction

Tectonic deformation plays a crucial role in shaping Earth's surface. Strain localization leads to the formation of shear zones at depth and faults at the surface, accommodating a significant portion of plate displacement within plate boundaries. Over millions of years, deformation can be considered as a spatially and temporally continuous process of visco-plastic strain localization (e.g., Gerya[40], Kirby and Kronenberg[65], Ranalli[96], Ranalli and Murphy[97]). At shorter timescales, strain localization involves the alternation of continuous visco-elastic deformation (e.g., Perfettini and Avouac[91], Wahr and Wyss[120]) and discontinuous, almost instantaneous elasto-plastic deformation events rapidly releasing strain energy: earthquakes (e.g., Cocco et al.[26], Gabriel et al.[34]). In active geodynamic systems, long-term tectonic forces and lithospheric responses pose the initial conditions governing earthquake nucleation, propagation, and arrest. However, long-term plate boundary formation and short-term earthquake mechanics are typically studied separately, and understanding their relationships across timescales and spatial scales remains a challenge [69].

The long-term visco-plastic mechanical behavior of the lithosphere heavily depends on rock rheology, which is influenced by chemical composition and the temperature field (e.g., Bürgmann and Dresen[23], Burov[24]), which are in turn impacted by the lithospheric geodynamic history (e.g., Beaumont et al.[11], Jourdon et al.[57],[60], Manatschal et al.[79]). The effect of continental crust rheology on strain localization has been extensively studied. It has been revealed that a lower continental crust deforming exclusively viscously (i.e., a weak crust) promotes diffuse deformation, low reliefs, and relatively low stress states. Conversely, continental crust with alternating layers of brittle/plastic and viscous/ductile behavior favors strain localization, supports high reliefs, and generates higher stresses [20,22,24]. However, how the long-term rheology of continental crust influences earthquake mechanics remains unresolved.

Understanding earthquake dynamics is crucial for comprehending fault system interactions, assessing earthquake risks, and mitigating their impact. In tectonically active areas, the increasingly dense recording of seismic ground motion and geodetic deformation during and in between earthquakes contribute to establishing physical models to study earthquake dynamics (e.g., Barbot et al.[10], Jia et al.[53]). Among available approaches, dynamic rupture modeling provides forward models simulating earthquake evolution on fault surfaces non-linearly coupled to seismic wave propagation (e.g., Harris et al.[43], Ramos et al.[95]). However, this approach must rely on initial conditions, such as a mechanically self-consistent pre-stress state loading a fault before an earthquake and accurate 3D fault geometry. Constraining these initial conditions is a significant challenge (e.g., Hayek et al.[45], Tarnowski et al.[107]). Nonetheless, the pre-stress state and the fault geometry significantly impact how earthquakes propagate (e.g., crack- vs. pulse-like dynamics and subshear vs. supershear rupture speeds) and arrest (e.g., Bai and Ampuero[9], Kame et al.[61]) and the associated radiation of seismic waves and ground shaking (e.g., Harris et al.[44], Taufiqurrahman et al.[108]).

Recent studies have used long-term geodynamic models to constrain fault geometry and pre-stress states linked to earthquake dynamic rupture simulations [78,102,118,119,124]. This approach, based on 2D visco-elasto-plastic long-term subduction simulations, embeds a long seismic cycle counting several thousands of years between two events, along with slip-rate dependent friction laws to generate stick-slip behavior on faults [48,116,117]. Despite recent advances in modeling rupture dynamics in finite, deforming fault zones [13,32,35,46,93,109], linking long-term geodynamic models to 3D dynamic rupture models typically requires constructing infinitesimally thin 2D fault surfaces from geodynamic volumetric shear zones. Moreover, the rupture dynamics models revealed a strong dependency on lithological variations resolved by the long-term model, which are capable of slowing, stopping, or accelerating the rupture when passed and thus significantly altering co-seismic deformation. However, limitations exist and include the extension from 2D to 3D to also resolve lateral, along-strike stress variations due to geometric and rheological variations [124].

In this study, we first employ pTatin3D [81,82], a 3D long-term visco-plastic thermo-mechanical open-source finite element software, to simulate the geodynamic evolution of strike-slip deformation over geological timescales. Using a new approach based on the medial axis transform, we extract 3D fault geometry, stress state, topography, and density as initial conditions for 3D dynamic rupture models performed with SeisSol, a short-term dynamic rupture and seismic wave propagation open-source discontinuous Galerkin software using unstructured tetrahedral meshes. This approach allows us to automatically extract 3D volumetric shear zones and map them into complex 2D fault interfaces. We loosely couple (i.e., one-way link) volumetric fields such as stress and density from the long-term models and the dynamic rupture models and address the challenge of obtaining complex fault surfaces from a volumetric shear zone.

We investigate the relationships between long-term continental crust rheology and rupture dynamics by generating three long-term models with different crustal rheologies. In nine geodynamically constrained 3D dynamic rupture models, we compare purely elastic media with varying fracture energy and models that additionally introduce off-fault deformation through plasticity. We show that for our system, a dynamically plausible critical slip weakening distance falls within $D_c \in [0.6, 1.5]$. We establish a link between crustal rheology and rupture dynamics by comparing the rupture generated in a quartz-anorthite crust, a full quartz crust, and a full anorthite crust. Produced earthquakes exhibit a shorter surface rupture length, a smaller rupture surface area, and less accumulated slip in a quartz-dominated crust than in an anorthite-dominated crust. We also demonstrate how the long-term 3D stress field favors slip on fault segments better aligned with the regional plate motion and how minor variations in the long-term 3D stress field can strongly affect the rupture dynamics, providing a physical mechanism for arresting earthquake propagation.

4.2 Long-term geodynamic modelling

4.2.1 *Governing equations*

To simulate the long-term evolution of the deformation of the lithosphere, we utilize pTatin3D [81,82], a massively parallel visco-plastic finite element software. This software solves for the conservation of momentum (Eq. (4.1)) and mass (Eq. (4.2)) for an incompressible material:

$$\nabla \cdot (2\eta(\mathbf{u}, p, T)\underline{\underline{\dot{\boldsymbol{\varepsilon}}}}(\mathbf{u})) - \nabla p + \rho(p, T)\mathbf{g} = \mathbf{0}, \tag{4.1}$$

$$\nabla \cdot \mathbf{u} = 0. \tag{4.2}$$

Here, $\eta(\mathbf{u}, p, T)$ is the non-linear viscosity, while $\underline{\underline{\dot{\boldsymbol{\varepsilon}}}}(\mathbf{u})$ is the strain rate tensor defined as:

$$\underline{\underline{\dot{\boldsymbol{\varepsilon}}}}(\mathbf{u}) := \frac{1}{2}\left(\nabla \mathbf{u} + \nabla \mathbf{u}^T\right) \tag{4.3}$$

with p the pressure, ρ the density, g the gravity acceleration vector and $\mathbf{u}$ the velocity. The viscosity is highly dependent on temperature; thus, we solve the conservation of the thermal energy for an incompressible medium

$$\rho_0 C_p \left(\frac{\partial T}{\partial t} + \mathbf{u} \cdot \nabla T \right) = \nabla \cdot (k \nabla T) + H_0 + H_s, \tag{4.4}$$

with T the temperature, C_p the thermal heat capacity, k the thermal conductivity and ρ_0 the reference density. Heat sources considered here include an initial heat production H_0 depending on the lithology and simulating the radiogenic heat source of continental rocks and the heat dissipation due to the mechanical work

$$H_s = \frac{2\eta}{\rho_0 C_p} \underline{\underline{\dot{\varepsilon}}}(\mathbf{u}) : \underline{\underline{\dot{\varepsilon}}}(\mathbf{u}). \tag{4.5}$$

In addition, to account for density variations due to temperature and pressure, we use the Boussinesq approximation and vary ρ according to

$$\rho(p, T) := \rho_0 (1 - \alpha(T - T_0) + \beta(p - p_0)), \tag{4.6}$$

with ρ_0 the density of the material at $p = p_0$ and $T = T_0$, α the thermal expansion and β the compressibility.

4.2.2 Rheological model

The long-term rheology of the lithosphere is simulated using non-linear flow laws. The ductile behavior is modelled using Arrhenius' type flow laws

$$\eta_v(\mathbf{u}, p, T) := A^{-\frac{1}{n}} \left(\dot{\varepsilon}^{II}(\mathbf{u}) \right)^{\frac{1}{n} - 1} \exp\left(\frac{Q + pV}{nRT} \right), \tag{4.7}$$

where A the pre-exponential factor, n the exponent and Q the molar activation energy are material-specific parameters obtained from laboratory experiments, R is the molar gas constant, V the activation volume and

$$\dot{\varepsilon}^{II}(\mathbf{u}) := \sqrt{\frac{1}{2} \underline{\underline{\dot{\varepsilon}}}(\mathbf{u}) : \underline{\underline{\dot{\varepsilon}}}(\mathbf{u})}, \tag{4.8}$$

the norm of the strain-rate tensor defined by Eq. (4.3).

Moreover, the brittle behavior of the lithosphere is simulated using a Drucker-Prager yield criterion:

$$\sigma_y(p) := C \cos\phi + p \sin\phi\,, \tag{4.9}$$

adapted to continuum mechanics by expressing it in terms of viscosity:

$$\eta_p(\mathbf{u}, p) := \frac{\sigma_y(p)}{\dot{\varepsilon}^{II}(\mathbf{u})}, \tag{4.10}$$

with C the cohesion of the material and ϕ its friction angle. In addition, we model the plastic softening with a linear decrease of the friction angle with the accumulation of plastic strain following

$$\phi = \phi_0 - \frac{\epsilon_p - \epsilon_{min}}{\epsilon_{max} - \epsilon_{min}}(\phi_0 - \phi_\infty), \tag{4.11}$$

with ϕ_0 the friction angle of undamaged rocks, ϕ_∞ the friction angle of the fully softened rocks, ϵ_{min} and ϵ_{max} the amount of plastic strain between which the friction angle decreases and ϵ_p the cumulative plastic strain computed as

$$\epsilon_p = \int \dot{\varepsilon}^{II}(\mathbf{u})\, dt, \tag{4.12}$$

when the material behaves plastically.

Finally, the viscosity of the lithosphere is evaluated with

$$\eta(\mathbf{u}, p, T) = \min\left(\eta_v(\mathbf{u}, p, T), \eta_p(\mathbf{u}, p)\right). \tag{4.13}$$

4.2.3 Initial conditions

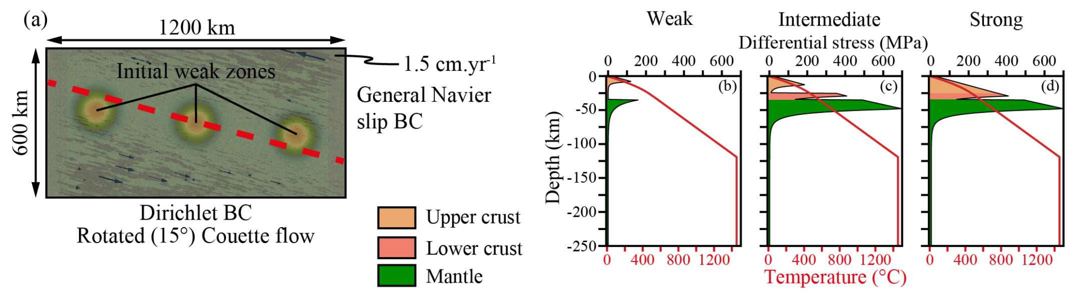

FIGURE 4.1. Initial and boundary conditions of the long-term geodynamic model. (a) Map view of the domain. The colours show the initial weak zones imposed with a Gaussian repartitioning of random initial plastic strain that reduces the friction angle according to Eq. (4.11). The black arrows show the initial velocity field. (b),(c),(d) Yield stress envelopes of the lithosphere computed for a strain-rate norm of 10^{-15} s^{-1} for the weak (b), intermediate (c) and strong models (d).

The modelled domain Ω is represented in Cartesian coordinates, with x and z defining the horizontal plane, y representing the vertical direction and $\mathbf{e_x}$, $\mathbf{e_y}$, $\mathbf{e_z}$ the three unit vectors defining the coordinate system. The origin of the domain is located at point $\mathbf{O} = [0, -200, 0]^T$, and its overall size is $1200 \times 200 \times 600$ km^3 (Figure 4.1a). The model is divided into four initially flat layers, each representing specific geological materials and simulated using rheological properties reported in Table 4.1. The upper continental crust ranges from 0 to −25 km, the lower continental crust from −25 to −35 km, the lithospheric mantle from −35 to −120 km, and the asthenosphere from −120 km.

	Units	Upper crust			Lower crust			Mantle
		M1	M2	M3	M1	M2	M3	
A	$\text{MPa}^{-n}.\text{s}^{-1}$	6.7×10^{-6}	6.7×10^{-6}	13.4637	6.7×10^{-6}	13.4637	13.4637	2.5×10^{4}
n	-	2.4	2.4	3	2.4	3	3	3.5
Q	kJ.mol^{-1}	156	156	345	156	345	345	532
V	$\text{m}^3.\text{mol}^{-1}$	0	0	3.8×10^{-5}	0	3.8×10^{-5}	3.8×10^{-5}	8×10^{-6}
C_0	MPa	20	20	20	20	20	20	20
C_∞	MPa	5	5	5	5	5	5	5
ϵ_i	-	0	0	0	0	0	0	0
ϵ_e	-	0.5	0.5	0.5	0.5	0.5	0.5	0.5
β	Pa^{-1}	10^{-11}	10^{-11}	10^{-11}	10^{-11}	10^{-11}	10^{-11}	10^{-11}
α	K^{-1}	3×10^{-5}	3×10^{-5}	3×10^{-5}	3×10^{-5}	3×10^{-5}	3×10^{-5}	3×10^{-5}
k	$\text{W.m}^{-1}.\text{K}^{-1}$	2.7	2.7	2.7	2.85	2.85	2.85	3.3
H_0	$\mu\text{W.m}^{-3}$	1.5	1.5	1.5	1.5	0.3	0.3	0
ρ_0	kg.m^{-3}	2700	2700	2700	2850	2850	2850	3300

TABLE 4.1. Rheological and thermal parameters for the long-term geodynamic models. A, n, Q, and V are the pre-exponential factor, the exponent, the activation energy, and the activation volume of the Arrhenius law, respectively (Eq. 4.7). C_0 and C_∞ are the initial cohesion and the cohesion after softening. ϵ_i and ϵ_e are the plastic strains at which softening starts and stops (Eq. 4.11). β is the compressibility of the material and α is the thermal expansion coefficient for the Boussinesq approximation (Eq. 4.6), k the thermal conductivity, H_0 the initial radiogenic heat source and ρ_0 the initial density.

The distinct rheological properties of each layer allow for the consideration of different behaviors and mechanical responses within the lithosphere and asthenosphere. By incorporating these rheological variations, the model aims to accurately capture the geodynamic processes occurring within the Earth's lithosphere. In addition, to assess the importance of the lithosphere's long-term mechanical behavior on earthquake dynamics, three distinct lithosphere rheologies are considered. The first model considers a weak continental crust (Figure 4.1b) entirely made of quartz[97]. The decoupling level between the crust and mantle is located around −20 km, and the whole lower crust exhibits a ductile behavior. The second model considers a continental crust composed of two layers (Figure 4.1c), an upper crust made of quartz[97] and a lower crust made of anorthite[100]. The anorthite in the lower crust introduces a stronger layer between the mantle and the upper crust, constraining the main decoupling level between the upper crust and the lower crust. The third model considers a single-layer continental crust (Figure 4.1d) made of anorthite[100]. This model exhibits an almost fully plastic behavior from the surface to the mantle, removing any decoupling within the crust and between the crust and the mantle. In all models, the mantle is simulated with a dry olivine flow law[49].

The initial temperature field is the solution of the steady-state heat equation:

$$\nabla \cdot (k \nabla T) + H_0 = 0\,,$$

with the boundary conditions $T = 0°\text{C}\ \forall y = 0$ and $T = 1450°\text{C}\ \forall y = -200$ km. In addition, to simulate an adiabatic thermal gradient maintained by mantle convection, we set the asthenospheric mantle conductivity to 70 $\text{W.m}^{-1}.\text{K}^{-1}$ only for this initial steady-state solve. Other parameters are reported in Table 4.1.

4.2.4 Boundary conditions

In this study, we produce strike-slip deformation models by imposing far-field plate motion on the domain's vertical sides. To avoid imposing a velocity discontinuity on the faces on which the velocity field changes polarity, we employ a newly developed method presented in Jourdon *et al.* [59]. This method requires providing a direction in which the velocity must be constrained, and the stress tensor must be applied along faces. In addition, this method can only be applied for velocity directions that are not orthogonal to the boundaries of the domain, explaining why we apply rotations of $\theta = 15^\circ$ in our boundary conditions.

Thus, to use this method, we divide the boundary of the domain into three sets: Γ_D the set of boundaries using Dirichlet conditions, Γ_N the set of boundaries using Neumann conditions, and Γ_S the set of boundaries using Navier-slip conditions. On faces of normal $\mathbf{e_z}$, we impose Dirichlet boundary conditions defined by a rotated horizontal Couette flow:

$$\bar{u}_x = \|\bar{\mathbf{u}}\| \left(\frac{2}{L_z} z - 1 \right) ,$$
$$\bar{u}_z = 0 ,$$

with L_z the length of the domain in the z direction and $\|\bar{\mathbf{u}}\|$ the relative velocity of plates.

On faces of normal $\mathbf{e_x}$ we impose the generalized Navier-slip boundary conditions defined by:

$$\mathbf{u} \cdot \mathbf{n} = 0 ,$$

where $\mathbf{n}$ is defined as the unit vector orthogonal to the velocity field imposed on the Dirichlet boundaries:

$$\mathbf{n} = \begin{bmatrix} -\bar{u}_z \\ 0 \\ \bar{u}_x \end{bmatrix} \|\bar{\mathbf{u}}\|^{-1} .$$

In addition, we impose stress constraints in a coordinate system in which $\mathbf{n}$ is one of the basis vectors. To do so, let us denote

$$\underline{\underline{\mathbf{\Lambda}}} = \begin{bmatrix} \mathbf{n} & \mathbf{t}_1 & \mathbf{t}_2 \end{bmatrix} ,$$

the matrix of the three orthogonal basis vectors forming a new coordinate system. The imposed stress is thus defined as $\left(\underline{\underline{\mathbf{\Lambda} \boldsymbol{G} \mathbf{\Lambda}^T}} \right) \mathbf{n}$ where

$$\underline{\underline{\boldsymbol{G}}} := \underline{\underline{\boldsymbol{\mathcal{H}}}} \odot \left(\underline{\underline{\mathbf{\Lambda}}}^T \underline{\underline{\boldsymbol{\tau}}}_S \underline{\underline{\mathbf{\Lambda}}} \right) ,$$

with

$$\underline{\underline{\boldsymbol{\tau}}}_S := 2\eta \underline{\underline{\dot{\boldsymbol{\varepsilon}}}}(\bar{\mathbf{u}}),$$

and $\underline{\underline{\mathcal{H}}}$ a Boolean tensor designed to collect terms for which we apply a constraint ($\mathcal{H}_{ij} = 1$) and the terms that are treated as unknown ($\mathcal{H}_{ij} = 0$) which in our case is:

$$\underline{\underline{\mathcal{H}}} = \begin{bmatrix} 0 & 1 & 1 \\ 1 & 1 & 1 \\ 1 & 1 & 0 \end{bmatrix}.$$

More details about the method to apply such boundary conditions can be found in Jourdon *et al.*[59].

In addition, we apply a Neumann free surface condition, $\underline{\underline{\sigma}}\mathbf{n} = \mathbf{0}$ to the top face and a constant value for $\mathbf{u}\cdot\mathbf{n}$ over the base of the domain (Γ_{base}) to ensure the compatibility constraint $\int_{\partial\Omega} \mathbf{u}\cdot\mathbf{n}\, dS = 0$ is satisfied. The constant for the normal component of the velocity is referred to as a compensation velocity (u_c) and is computed as

$$\begin{aligned} \int_{\partial\Omega} \mathbf{u}\cdot\mathbf{n}\, dS &= \int_{\Gamma_{\text{base}}} \mathbf{u}\cdot\mathbf{n}\, dS + \int_{\partial\Omega\setminus\Gamma_{\text{base}}} \mathbf{u}\cdot\mathbf{n}\, dS \\ &= u_c \int_{\Gamma_{\text{base}}} 1\, dS + \int_{\partial\Omega\setminus\Gamma_{\text{base}}} \mathbf{u}\cdot\mathbf{n}\, dS \\ &= 0. \end{aligned}$$

4.3 TRANSFORMING VOLUMETRIC SHEAR ZONES INTO FAULT SURFACES

The transformation of a volumetric shear zone into a fault surface poses a significant challenge to the Earth sciences community (e.g., Duclaux et al.[28], Neuharth et al.[86], Pan et al.[88]) as well as industry (e.g., An et al.[2], Gersztenkorn and Marfurt[39], Gibson et al.[41], Hale[42], Marfurt et al.[80]) for the generation of subsurface models. Here, this poses a critical step in linking long-term geodynamic models with short-term earthquake dynamic rupture models. Fundamentally, the question at hand is how to accurately capture the geometry of a complex 3D volume and represent it as a 2D surface.

Varying approaches to surface reconstruction from cloud points have been proposed[14], with 3D problems being more challenging than 2D ones, especially with respect to scalability[92,106]. Conventionally, fault surface reconstruction is performed via manual fault interpretation. Automatic approaches involve the identification of discontinuities of seismic horizons through seismic attributes[18,80,103,115] or statistical approaches[122]. However, there are no established rules or definitive recipes for the required transformation process. Thus, we develop a method that involves condensing a relatively large volume, spanning a few kilometers, into a smaller set of points, typically within the range of a few tens or hundreds of meters. This condensed point set allows for the identification of a surface that can be further meshed using Delaunay triangulation.

To accomplish this transformation, we employ a geometric construct called the medial axis, which provides a framework for capturing the essential geometric features of the volumetric shear zone while reducing its representation to a simplified 2D surface. The medial axis transform is sometimes referred to as "skeletonization". By using the medial axis, which characterizes the central core or skeleton of the shear zone, we can effectively extract a subset of points that retain the essential characteristics of the original volume.

In the subsequent steps, we employed a combination of Paraview [1,8], PyVista [105], and custom C code (for efficiency) to extract 2D fault surfaces from 3D shear zones.

4.3.1 Shear zone identification

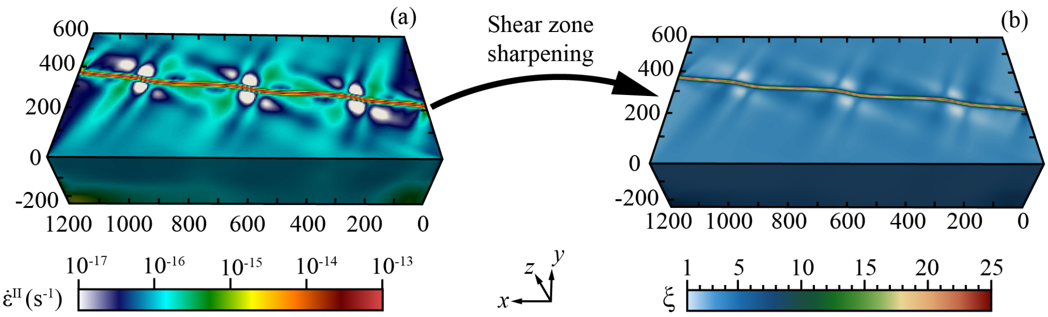

Figure 4.2. 3D long-term thermo-mechanical model. (a) Norm of the strain-rate tensor. The red area shows the most localized active deformation, i.e., a shear zone. (b) Result of applying the filter described in Eq (4.14).

The initial step in extracting faults from shear zones involves determining the criteria for identifying what constitutes a shear zone. At its core, a shear zone can be defined as an area of localized strain, where the spatial derivative of displacement (for finite strain) or velocity (for active strain) is the most important. In this study, our focus is on active deformation, specifically on the strain rate. Since velocity is a three-component vector, its spatial derivative corresponds to a nine-component tensor defined by Eq. (4.3). To assess the intensity of the strain rate tensor and identify regions of localized deformation, we employ the norm of the tensor described by Eq. (4.8). This quantity represents the degree of localization of the deformation: higher values indicate more localized deformation. However, since the absolute value of this quantity is dependent on the velocities and distances within the domain, it is challenging to establish a universal threshold above which deformation can be considered localized. As a result, the strain-rate norm is used as a relative measure specific to each model, and its threshold may vary for different models. Experimental observations suggest that a localized shear zone can be established when there is a difference of approximately three to four orders of magnitude compared to areas with the lowest strain rates (e.g., Brune[21], Jourdon et al.[56], Le Pourhiet et al.[71], Liao and Gerya[73], Neuharth et al.[85], Sternai et al.[104]). Nonetheless, we observe that our models with similar initial and boundary conditions tend to exhibit similar strain rate values.

To simplify the dimension reduction process, we apply an additional filter to the strain-rate norm, resulting in a new scalar field:

$$\xi = \exp\left(\log_{10}\left(\dot{\varepsilon}^{II}\right) - \min\left(\log_{10}\left(\dot{\varepsilon}^{II}\right)\right)\right). \qquad (4.14)$$

The purpose of this fault indicator function is to enhance the visualization of shear zones and provide an initial treatment for the volume-to-surface transformation (Figure 4.2). By using the scalar field ξ, we construct surfaces of isovalues of ξ that encapsulate the shear zones. For the model presented in Figure 4.3a, a value of $\xi = 20$ was utilized. However, for the same reasons that there is no universal value of $\dot{\varepsilon}^{II}$ to define a localized shear zone, there is no universal value of ξ, and a case-specific value must be chosen. Additionally, we compute the outward-pointing normal vectors to these surfaces, which correspond to the shear zone boundaries (Figure 4.3a).

By applying these techniques, we can effectively identify complex shear zones within the volumetric data and prepare them for further analysis and transformation into surface faults.

4.3.2 *Medial axis and surface meshing*

To reduce the dimensionality of the shear zones, we employ the shrinking-ball algorithm described in Ma *et al.*[76] to approximate the medial axis. However, shear zones extracted from numerical models are often characterized by surface roughness, which can introduce noise in the medial axis representation. Additionally, in regions such as the brittle-ductile transition within the lower continental crust or along the Moho, shear zones can flatten and spread over large distances, losing their relevance for earthquake dynamic rupture modeling and fault characterization as brittle objects.

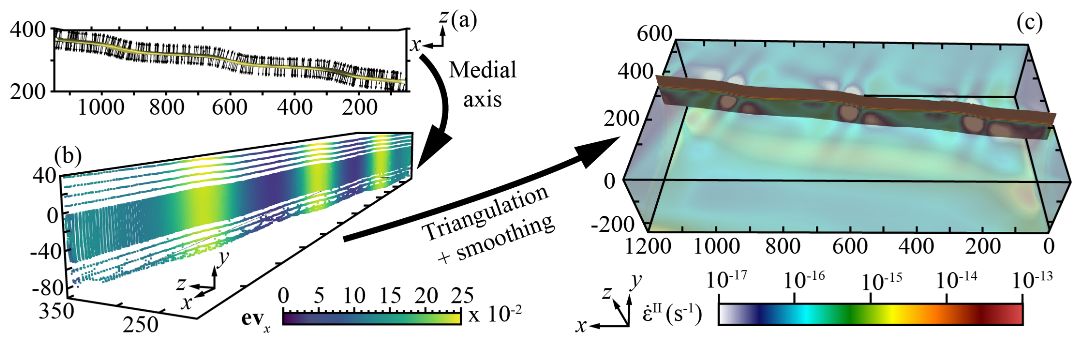

FIGURE 4.3. (a) Contour of isovalue of $\xi = 20$ and normal vectors of this envelope at each point. (b) Medial axis of the envelope shown in (a). Colours show the x component of one of the eigenvectors of the covariance matrix computed with Eq. (4.15) illustrating the changes in orientation of the medial axis. (c) Fault surface reconstructed from the medial axis using Delaunay triangulation and smoothing.

To address these issues and mitigate noise and effects associated with purely ductile deformation, we compute the geometric characteristics of the shear zone's medial axis. At each point with coordinates $\mathbf{x} = (x_1, x_2, x_3)^T$, we calculate the covariance matrix $\underline{\underline{C}}$ of the spatial distribution of the set of points $\mathbf{X} = \{\mathbf{x}_1, \mathbf{x}_2, ..., \mathbf{x}_n\}$ within a sphere $\mathcal{S}$ of radius r_s where

$$C_{ij} = \frac{1}{n} \sum_{k=1}^{n} (x_{ki} - \bar{x}_i)(x_{kj} - \bar{x}_j) \quad \forall \mathbf{x} \in \mathcal{S}(r_s), \tag{4.15}$$

and $\bar{\mathbf{x}}$ is the arithmetic mean

$$\bar{\mathbf{x}} = \frac{1}{n}\sum_{k=1}^{n} \mathbf{x}_k. \tag{4.16}$$

The choice of r_s is crucial as it determines the distance within which points are considered to contribute to the covariance matrix. However, to capture first-order orientation variations, the distance r_s needs to be adjusted to represent a characteristic distance within which the orientation of the shear zone is representative of its surroundings. After obtaining the covariance matrix for each point, we compute the eigenvectors associated with these matrices. The orientation of these eigenvectors provides information about the general orientation of the medial axis (Figure 4.3b), allowing us to remove points that deviate significantly from this orientation.

The remaining set of points is then utilized to create a surface using Delaunay triangulation. However, because the Delaunay triangulation attempts to connect all points with a given distance, this meshing process can result in a rough surface. Therefore, to obtain a smooth 2D surface, we apply a Laplacian smoothing (Figure 4.3c).

4.3.3 *Geometrically complex examples*

To demonstrate the applicability of the fault extraction method to different geodynamic scenarios and resulting fault types, here we consider a scenario involving a strike-slip shear zone splitting into two branches and an ocean-continent subduction producing two distinct shear-zones, a megathrust, and a conjugate thrust fault.

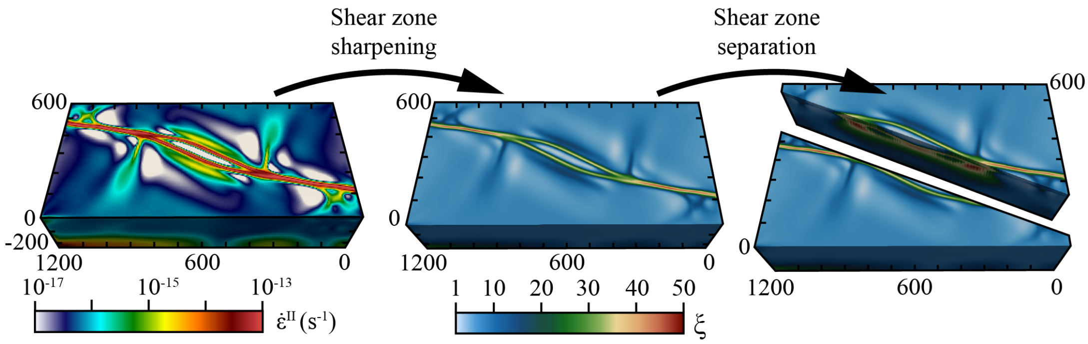

Figure 4.4. (a) Strain-rate norm (Eq. 4.8) showing the shear zone splitting. (b) Shear zone sharpening using the ξ filter (Eq. 4.14). (c) Volume splitting to isolate the two branches of the shear zone.

In the case of a shear zone splitting into two branches (Figure 4.4a), we first apply the ξ filter to sharpen the shear zone (Figure 4.4b) and split the volume into two pieces to isolate the two branches of the shear zone (Figure 4.4c). For each volume, we extract the contour of the shear zone using $\xi = 20$ (Figure 4.5a) before computing the medial axis (Figure 4.5b) and applying Delaunay triangulation and Laplacian smoothing (Figure 4.5c).

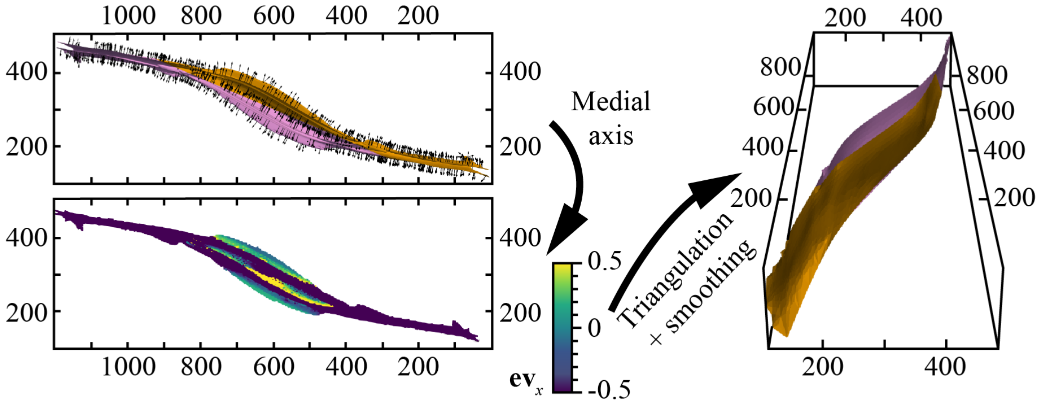

FIGURE 4.5. (a) Contour of the shear zone for $\xi = 20$. The two colours indicate the contour from the two volumes represented in Figure 4.4c. The black arrows show the normal vectors to the surface of the contour $\xi = 20$. (b) Medial axis of the two contours shown in panel (a). The colours indicate the value of the x component of one of the eigenvectors of the covariance matrix computed with Eq. (4.15) illustrating the changes in orientation of the medial axis. (c) Fault surfaces of the two branches after Delaunay triangulation and Laplacian smoothing.

In the case of the subduction model (Figure 4.6a) we also apply the ξ filter (Figure 4.6b) to ease the extraction of the shear zone contour (Figure 4.6c).

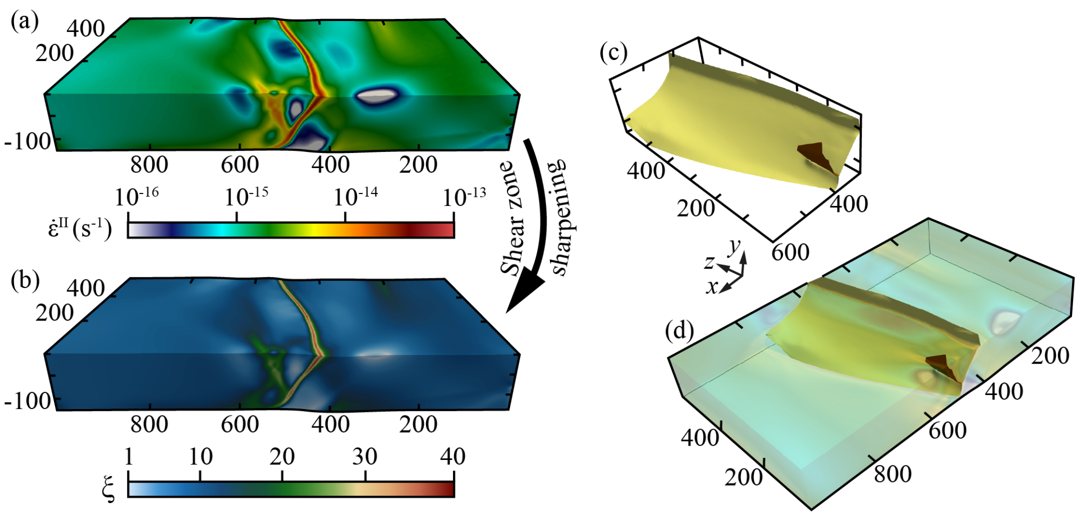

FIGURE 4.6. Extraction of fault surface from a 3D subduction (collision) experiment including a megathrust and a conjugate thrust fault. (a) Strain-rate norm (Eq. 4.8). (b) ξ value (Eq. 4.14). (c) 3D view of the two extracted faults (red and yellow surfaces) (d) 3D view of the two extracted faults within the domain.

4.4 DYNAMIC RUPTURE MODELING USING 3D LONG-TERM GEODYNAMIC MODEL DATA

4.4.1 *Governing equations*

To model 3D dynamic rupture and seismic wave propagation with high-order accuracy in space and time, we utilize SeisSol (https://github.com/SeisSol/SeisSol)[47,68,89,114], which employs fully non-uniform, unstructured tetrahedral meshes that statically adapt to geometrically complex 3D geological structures, such as non-planar mutually intersecting faults and topography. The code has been applied to model complex and/or poorly instrumented real earthquakes and earthquake scenarios in various tectonic contexts (e.g., Biemiller et al.[15], Gabriel et al.[36], Ramos et al.[94], Taufiqurrahman et al.[108], Tinti et al.[111], Ulrich et al.[112], Wang et al.[121]). SeisSol solves for the dynamic conservation of momentum

$$\rho \frac{\partial \mathbf{u}}{\partial t} - \nabla \cdot \underline{\underline{\boldsymbol{\sigma}}} = \mathbf{0} \tag{4.17}$$

following the constitutive relationship

$$\underline{\underline{\dot{\boldsymbol{\sigma}}}} - \lambda \nabla \cdot \mathbf{u} \underline{\underline{\boldsymbol{I}}} - G \underline{\underline{\dot{\boldsymbol{\varepsilon}}}}(\mathbf{u}) = \underline{\underline{0}}, \tag{4.18}$$

with λ and G the Lamé parameters and ρ the density of the material. Eq. (4.17) is discretized using the discontinuous Galerkin method with arbitrary high-order derivative (ADER) time-stepping[29]. SeisSol uses an end-to-end optimization for high-performance computing infrastructure[19,47,67,114] and is verified in a wide range of community benchmarks[90] by the SCEC/USGS Dynamic Rupture Code Verification project[43]. The description of non-trivial initial conditions for SeisSol is provided by ASAGI (a pArallel Server for Adaptive GeoInformation, Rettenberger *et al.*[98]), an open-source library with a simple interface to access material and geographic datasets. ASAGI represents geoinformation on Cartesian meshes which are defined and populated with field files via a self-describing NetCDF file. ASAGI organizes Cartesian data sets for dynamically adaptive simulations by automatically migrating the corresponding data tiles across compute nodes as required for efficient access.

4.4.2 *Deviatoric stress and pressure*

In addition to utilizing the long-term geodynamic model to obtain the fault geometry, we extract the 3D stress state to reconstruct self-consistent initial conditions for the dynamic rupture model. The long-term geodynamic model solves for an incompressible visco-plastic Stokes flow, therefore the deviatoric stress tensor can be directly obtained from

$$\underline{\underline{\boldsymbol{\tau}}}(\mathbf{u}, p) := 2\eta(\mathbf{u}, p)\underline{\underline{\dot{\boldsymbol{\varepsilon}}}}(\mathbf{u}), \tag{4.19}$$

and already accounts for the long-term rheology (including the 3D temperature field), the geometry of the fault, the topography, and the volume forces.

Parameters	Units	
λ	Pa	PREM
G	Pa	PREM
μ_s	-	0.6
μ_d	-	0.1
D_c	m	$\{0.1, 0.6, 1, 1.5, 1.7\}$
C_d	MPa.km^{-1}	1
C_∞	MPa	1
y_r	km	5
ϕ_v	°	30
C_v	MPa	$100 \rightarrow 5$

TABLE 4.2. 3D dynamic rupture model parameters. λ and G are the two Lamé parameters extracted from PREM[31]. μ_s and μ_d are the static and dynamic friction coefficients, respectively. D_c is the critical slip distance. C_d is the on-fault cohesion slope, C_∞ is the on-fault maximum cohesion, y_r is the depth at which the maximum cohesion is reached (Eq. 4.23). ϕ_v is the volume friction angle for the models involving off-fault plasticity and C_v the volume cohesion varying with the long-term plastic strain according to Eq. (4.11).

In addition, although we obtain the pressure from the solution of Eqs. (4.1) & (4.2), this pressure satisfies the incompressibility constraint and thus can result in negative values. To avoid using negative values to represent the confining pressure and construct the full stress tensor, we utilize a different approach. Based on Jourdon *et al.* (2022)[58] we compute the confining pressure p_c related to the density structure in 3D described by

$$\nabla \cdot (\nabla p_c) = \nabla \cdot (\rho \mathbf{g}), \tag{4.20}$$

with the boundary conditions $p_c = 0$ at the surface and $\nabla p_c \cdot \mathbf{n} = \rho \mathbf{g} \cdot \mathbf{n}$ along the other boundaries, with $\mathbf{n}$ the outward pointing normal vector to the face. Then, we compute the full stress tensor as

$$\underline{\underline{\boldsymbol{\sigma}}}(\mathbf{u}, p, p_c) := \underline{\underline{\boldsymbol{\tau}}}(\mathbf{u}, p) - p_c \underline{\underline{\boldsymbol{I}}}. \tag{4.21}$$

To transfer the information from the long-term geodynamic model to the dynamic rupture model, we perform interpolation with iso-parametric Q_1 elements from the mesh of pTatin3D to a structured grid. This structured grid is used to interpolate values at the nodes of the unstructured tetrahedral mesh of the dynamic rupture model using ASAGI.

4.4.3 *Material parameters*

In dynamic earthquake rupture simulations, faults are typically idealized as infinitesimally thin interfaces separating distinct on- from off-fault rheologies (e.g.,Andrews[6], Ben-Zion and Shi[12], Dunham et al.[30], Gabriel et al.[33], Hayek et al.[46], Okubo et al.[87], Templeton and Rice[110]).

On-fault parameters

The static strength of crustal rocks can be high[25]. However, during co-seismic rupture, fault friction drops due to dynamic weakening processes (e.g., Di Toro et al.[27], Kammer et al.[62], Kostrov and

Riznichenko[66]). We employ a linear slip-weakening friction law[4] describing the friction coefficient evolution with respect to the amount of slip along the fault

$$\mu(S, D_c) := \mu_s - \frac{\mu_s - \mu_d}{D_c} \min(S, D_c), \tag{4.22}$$

with μ_s the static friction coefficient, μ_d the dynamic friction coefficient, D_c the critical slip distance and S the slip defined as

$$S = \int_0^t \|\mathbf{u}(s)\| ds,$$

where s is the fault surface. We assume static and dynamic friction values from laboratory experiments[25,27,84,101] in all our models. Most of our models consider a uniform D_c. However, we also show two simulations with heterogeneous D_c along the fault described by fractal hierarchical patches[52].

Moreover, to avoid a zero yield stress due to $p_c = 0$ at the surface we introduce an on-fault frictional cohesion $C(y)$[43] defined as

$$C(y) := C_d(\max(y, y_r) - y_r) + C_\infty, \tag{4.23}$$

with $C_d = 1$ MPa.km^{-1} the slope, $y_r = 5$ km the depth at which the cohesion does not change anymore, $C_\infty = 1$ MPa the cohesion when $y < y_r$. Note that $y_r < 0$ and y decreases with depth.

Combining Eqs. (4.22) & (4.23) gives the fault's yield strength

$$\tau_f = -C(y) - \min(0, \sigma_n)\mu(S, D_c), \tag{4.24}$$

allowing to evaluate if failure may occur.

In addition, to ensure consistency of the pressure and temperature-dependent stress tensor, we utilize the density extracted from the long-term geodynamic model. Finally, utilizing the stress state extracted from the long-term geodynamic model and the dynamic rupture friction coefficients, the fault's relative strength R can be evaluated from the ratio of the potential maximum stress drop to frictional strength drop[7] as

$$R = \frac{|\tau_s| - \mu_d|\sigma_n|}{(\mu_s - \mu_d)|\sigma_n|}, \tag{4.25}$$

where

$$\sigma_n = \mathbf{n} \cdot \underline{\underline{\sigma}}\mathbf{n},$$

and

$$\tau_s = \mathbf{t} \cdot \underline{\underline{\sigma}}\mathbf{n},$$

with $\mathbf{n}$ being the normal vector to the fault at a given point and $\mathbf{t}$ being the tangent vector in the direction of the slip.

Figure 4.7 shows the initial R value on the fault for each considered long-term rheology. The faults and stress states extracted from the long-term geodynamic models with an upper crust composed of quartz (models 1 and 2) display an area of negative R values corresponding to the

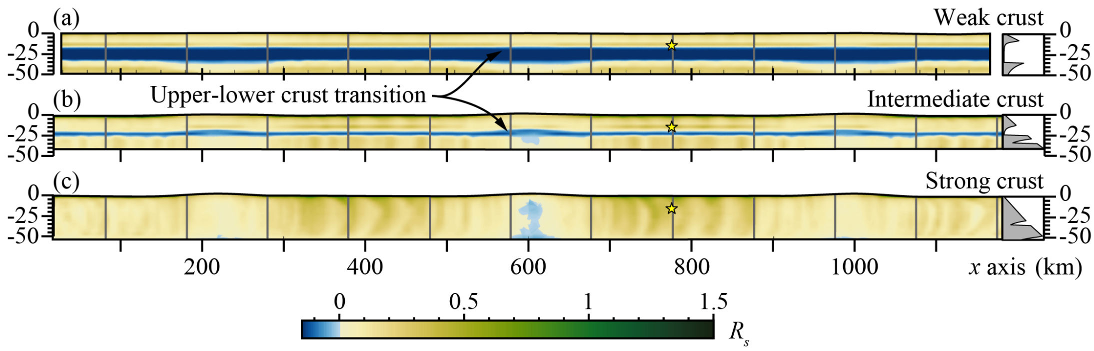

FIGURE 4.7. The initial R ratio illustrating dynamic rupture relative fault strength computed with Eq. (4.25) for the long-term crustal rheology of a (a) full quartz crust, (b) quartz upper crust and anorthite lower crust, (c) full anorthite crust. The blue colours represent negative values of R and indicate that $|\tau_s| < \mu_d|\sigma_n|$.

location of the ductile decoupling layer arising directly from the long-term mechanical behavior of the crust. The shallower part of the faults (i.e., above the surface of $R < 0$) can be interpreted as the seismogenic crust. Conversely, the fault and stress state extracted from the model composed with a fully anorthite crust does not show $R < 0$, indicating that the initial shear stress is everywhere above the dynamic strength of the fault, theoretically allowing rupture propagation on the entire fault surface.

Off-fault parameters

The dynamic rupture models that will be presented in sections 4.5.2, 4.5.3, and 4.5.3 include co-seismic off-fault plasticity[6,125], allowing to capture volumetric plastic deformation around the fault. As for the long-term geodynamic models, we also use a Drucker-Prager plasticity criterion described by Eq. (4.9) to define the yield stress. However, for the dynamic rupture models, the friction angle in the volume is set to $\phi_v = 30°$. To ensure consistency between the long-term rheology, stress state, finite deformation, and the dynamic rupture models parameters, the plastic cohesion for the off-fault plasticity is set using Eq. (4.11) in which we replaced ϕ by the volume cohesion C_v varying between 100 MPa and 5 MPa. The high value of 100 MPa ensures that the plastic yielding will not be reached far from the fault where no long-term deformation occurred.

4.4.4 *Nucleation*

In dynamic rupture models, rupture nucleation requires only a small portion of the fault, a critical nucleation size[99], to reach failure for rupture to initiate, even though other parts of the fault may remain below critical stress levels[62]. Multiple techniques exist for nucleating dynamic earthquake ruptures, such as locally elevating shear stress, reducing the effective static frictional strength, or applying time-weakening forced nucleation strategies[5,16,44,50]. A spatially and temporally smooth nucleation patch avoids numerical artifacts[37,43].

Here we adopt a smooth time-weakening kinematic nucleation strategy by enforcing the time at which the friction coefficient reaches the dynamic value within a circular nucleation patch centered at the hypocenter. We choose the hypocenter to be located in the middle of one of the segments between the bends of our faults. We parameterize the forced rupture time within the nucleation patch of radius r_c as

$$t_{forced} = \left(1 - \exp\left(\frac{r^2}{r^2 - r_c^2}\right)\right) t_a + t_b,$$

where $r = ||\mathbf{x} - \mathbf{x}_c||$. There, $r_c = 5$ km is the radius across which the friction coefficient smoothly decreases, x_i the coordinates at the fault's surface and x_{c_i} the coordinates of the hypocenter defined at $\mathbf{x}_c = [777, 275, -15.5]^T$ km, including scaling and offset from the start for the forced nucleation timing $t_a = 500$ and $t_b = 0.2$. Once the nucleation is sufficiently large, it is overtaken by spontaneous dynamic propagation of the rupture governed by the choice of friction law.

4.5 Results

To show how the long-term rheology, 3D stress-state, and fault geometry can influence the dynamics of the rupture during an earthquake, we first perform 3 geodynamic models with pTatin3d[81,82] over 6 to 8 million years each with a different continental crust rheology and 14 dynamic rupture models with SeisSol[47,68,89,114] varying rupture energy parameters with and without off-fault plasticity. We briefly present six models in section 4.5.2 and, in more detail, three additional models with off-fault plasticity in sections 4.5.2, 4.5.3 and 4.5.3.

4.5.1 *Long-term geodynamic model*

After 6 to 8 million years (Myr), the three long-term 3D geodynamic models develop a localized strike-slip shear zone (Figure 4.8a,e,i) with slight compression around the initial weak zone locations. The long-term rheological properties of the crust significantly influence the topographic response to deformation (Figure 4.8b,f,j). For instance, the model featuring a crust composed solely of quartz (the weaker model) exhibits topographic variations ranging from -0.5 km to 0.5 km, whereas the model with a crust composed entirely of anorthite (the stronger model) shows amplitudes ranging from -2 km to 2 km. Furthermore, segments of the shear zone undergoing transpression/compression yield positive topography (mountain ranges), while segments experiencing transtension/extension result in negative topography (basins).

In the three models, the geodynamically modelled plastic strain (Figure 4.8c,g,k) illustrates the finite deformation, highlighting the advection and offset of the initial weak zones caused by the shear zone motion, as well as the accumulated strain, which delineates the highly localized shear zone at the center, alongside diffuse deformation oriented perpendicular to the main shear zone of the three models. Those perpendicular diffuse deformation zones are inherited from the early phase of the model during which the strain starts to localize at the initial weak zones. Moreover, although

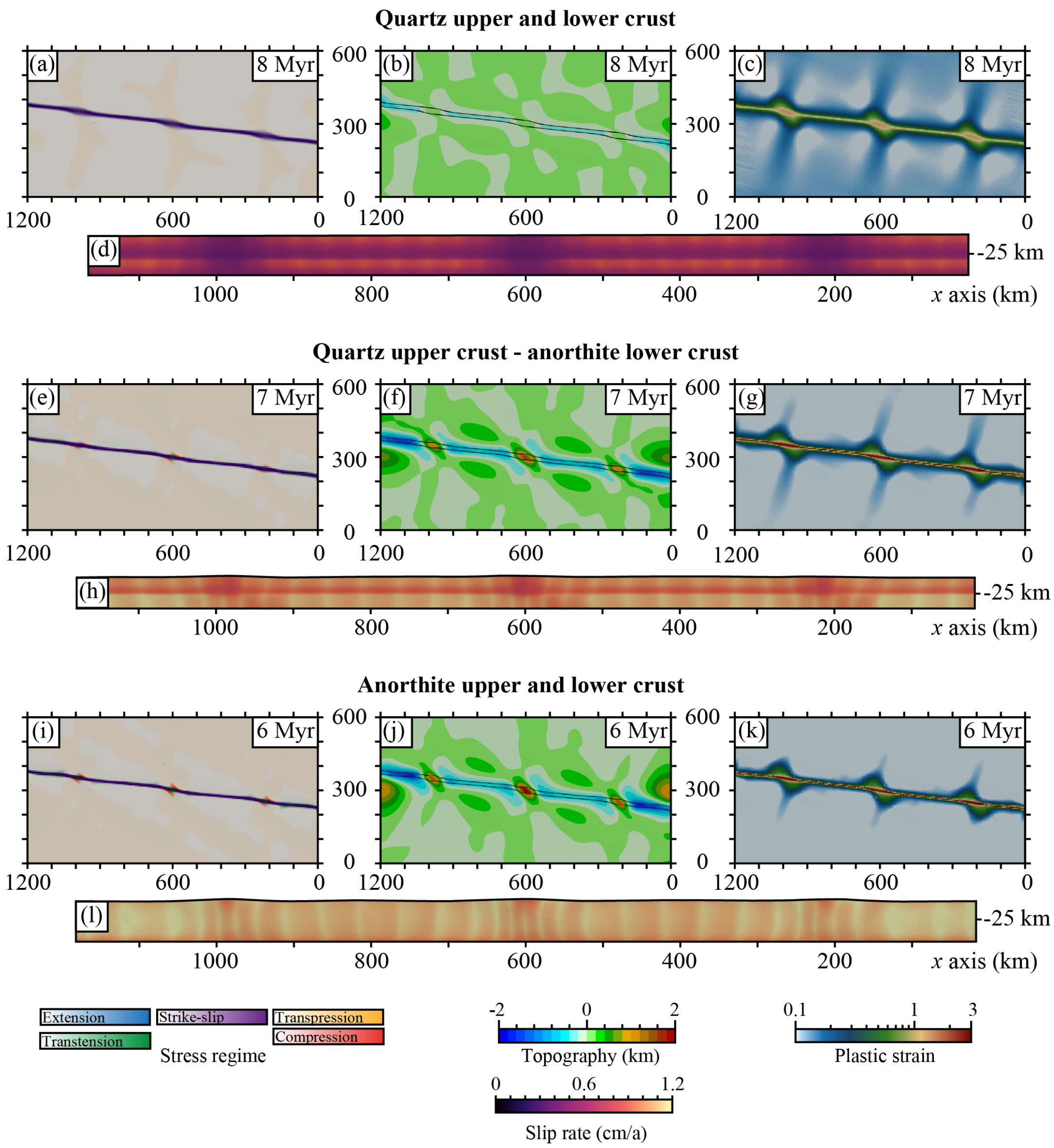

FIGURE 4.8. Long-term 3D geodynamic models. (a-d) Single-layer model: quartz upper and lower crust. (e-h) Two-layer model: quartz upper crust and anorthite lower crust. (i-l) Single-layer model: anorthite upper and lower crust. (a,e,i) Map view of the stress regime in active deformation zones. (b,f,j) Map view of the topography. (c,g,k) Map view of the plastic strain. (d,h,l) Long-term slip rate computed on the fault's surface.

the geometry of the main shear zone remains relatively simple for all models, slight variations in orientation occur as it approaches the initial weak zone locations, leading to the formation of higher topography and a variation from strike-slip stress regime to transtension at the center of the shear zone and compression around. These minor geometric variations contribute to form a non-planar shear zone and, thus, a non-planar reconstructed fault surface.

Once the corresponding fault surfaces are reconstructed, it becomes possible to evaluate the long-term slip rate across the faults (Figure 4.8d,h,l). Once again, the crustal rheology significantly influences how much of the plate velocity imposed through boundary conditions is accommodated by the faults. For instance, in the weakest model (quartz upper and lower crust), slip rates range from 0.4 $cm.a^{-1}$ to 0.7 $cm.a^{-1}$. In contrast, the model with intermediate rheology (quartz upper crust and anorthite lower crust) accommodates slip rates from 0.7 $cm.a^{-1}$ to 1.2 $cm.a^{-1}$, while the strongest model (anorthite upper and lower crust) exhibits slip rates ranging between 0.8 $cm.a^{-1}$ and 1.2 $cm.a^{-1}$. Additionally, in all three models, the long-term slip rate is influenced by geometric variations occurring at $x \approx 200, 400, 600$ km, and where applicable, by the brittle-ductile transition between depths of -20 km and -25 km, characterized by lower slip rates.

4.5.2 3D dynamic rupture: two-layered-crust models

Coseismic fracture energy variation

During dynamic rupture, accumulating fault slip reduces the effective friction coefficient from its static to its dynamic value according to the linear slip-weakening friction law in Eq. (4.22). The critical slip-weakening distance (D_c) denotes the slip value over which friction decreases and correlates with the coseismic fracture energy dissipated during slip (Sec. 4.4.3). Frictional parameters for dynamic rupture simulations are typically adopted from laboratory experiments. However, it is uncertain how valid it is to extrapolate results from the laboratory scale to the field scale (e.g., Cocco et al.[26], Kammer et al.[62]). Thus, we conducted six purely elastic models under a range of D_c values.

Figure 4.10 illustrates the dynamic rupture fault slip that accumulated at the end of the simulation for each two-layer-crust model. All models show that dynamic rupture never penetrates the lower crust, which is consistent with the locally low on-fault strength parameter R at depth (Figure 4.7a).

For model M1 with $D_c = 0.6$ m (Figure 4.10a), along-strike rupture extends 200 km left and 400 km right of the hypocenter. A secondary 150 km long rupture segment, located 600 km left of the nucleation location, is dynamically triggered 200 seconds after the initiation of the rupture as shown in the moment rate release (Figure 4.9b). Most of the slip accumulation occurs within a 200 km radius around the hypocenter, representing the segment between fault bends at $x \approx 600$ km and $x \approx 1000$ km. Figure 4.11 displays the rupture velocity on the fault, showing a correlation between decreased accumulated slip and reduced rupture velocity at 100-150 km from the hypocenter, corresponding to locations where the fault orientation slightly changes and the long-term stress regime varies (Figure 4.8). The M1 simulation results in an earthquake of magnitude $M_w = 8.34$ (Table 4.3).

For model M2 with $D_c = 1$ m (Figure 4.10b), dynamic rupture remains contained within the fault segment between fault bends at $x \approx 600$ km and $x \approx 1000$ km. The first 150 km around the hypocenter accumulate fault slip similar to the M1 ($D_c = 0.6$) m simulation. The rupture velocity (Figure 4.11b) slows near the fault's bends. The resulting earthquake magnitude is $M_w = 8.16$ (Table 4.3).

Further increasing D_c progressively reduces the rupture extent (Figure 4.10c,d), while the accumulated slip near the nucleation area remains relatively constant (approximately 15 to 20 m) and moment rates show peak values that are very close to each other (Figure 4.9b). The moment magnitude of the modelled earthquakes decreases slightly ($M_w = 8.07$ for $D_c = 1.5$m and $M_w = 8.04$ for $D_c = 1.7$ m, see Table 4.3). We observe delayed rupture initiation and slower propagation at the earthquake's onset (Figure 4.11c,d).

Simulations varying D_c as fractal hierarchical patches [51] illustrate how non-uniform multi-scale critical slip-weakening distances may affect rupture dynamics. Figure 4.10e shows the accumulated slip for model M5 with D_c varying from 0.6 m to 1.6 m, exhibiting characteristics of both $D_c = 1$ m (M2) and $D_c = 0.6$ m (M1) simulations and resulting in a magnitude $M_w = 8.21$ (Table 4.3). However, varying D_c introduces rheological variations on the fault's surface, observable at rupture area edges. Variations in critical slip-weakening distance influence the rupture velocity (Figure 4.11e), adding smaller scale perturbations during the propagation of the rupture compared to a uniform D_c.

Finally, the simulation M6 with D_c varying from 1.1 m to 2 m (Figure 4.10f) shows slip patterns similar to the M3 simulation ($D_c = 1.5$ m) but with a delayed rupture initiation by 90 seconds. In this scenario, the earthquake magnitude is $M_w = 8.09$ (Table 4.3).

These simulations suggest that for our fault, long-term rheology, and geodynamic system, a dynamically plausible critical slip weakening distance falls within $D_c \in [0.6, 1.5]$. Lower values may yield unrealistically large earthquakes, while higher values delay the rupture initiation, indicating insufficient stress from the long-term geodynamic evolution to initiate rupture. Moreover, variations in uniform D_c between 0.6 m and 2 m do not affect the first-order behavior of dynamic rupture and are thus omitted from the next experiments.

Off-fault plasticity

We next introduce off-fault plasticity into our dynamic rupture models. This requires loosely coupling stresses everywhere in the 3D domain, not restricted to the fault surfaces. Based on calibration performed on the critical slip-weakening distance, we conducted a simulation with $D_c = 0.6$ m, with an upper crust composed of quartz and a lower crust composed of anorthite. Figure 4.12 illustrates the evolution of the rupture on the fault through accumulated slip and in the volume through off-fault plastic deformation. After 30 seconds of simulation, the rupture spans a radius of 40 km around the hypocenter, with plastic deformation accumulating on the surface within a roughly 1 km thick zone and around the fault plane at depth within a thinner, approximately 500 m thick zone. The rupture propagates symmetrically on both sides of the hypocenter, and plastic deformation localizes in a broader area around the fault. It exhibits a positive flower-like structure with a thin (approximately 500 m) plastic deformation zone at depth and a thicker (around 2 to 3 km) deformation zone at the surface.

After 70 seconds, the rupture reaches the fault's bends located around the initial long-term weak zones ($x \approx$ 600, 1000 km), breaking the symmetry of the propagation. Consequently, the rupture accumulates less slip and plastic strain, gradually fading and ultimately stopping after 130 seconds. The moment rate decreases drastically at $\sim$ 80 seconds, showing that the mechanical work required to pass through the fault's bend increases and consumes energy (Figure 4.9b). The slip pattern compares well to the elastic simulation with D_c = 1 m. The resulting magnitude is $M_w = 8.19$ for a surface rupture length of 550 km and a rupture area of 9120 km^2 (Table 4.3).

Compared with the model M1 (Figure 4.10a) using the same D_c parameter but without off-fault plasticity, this model shows that all the characteristics of the rupture have been reduced (Table 4.3, M7). This behaviour is due to the plastic strain dissipating some of the earthquake energy, thus reducing the energy left for the rupture itself.

4.5.3 *Dynamic rupture: single-layer crust models*

To study the relationships between the long-term rheology and the dynamics of the rupture, we performed dynamic rupture experiments with and without off-fault plasticity. However, in the following section, we only discuss the simulation with off-fault plasticity for the quartz upper and lower crust model, which is assimilated as a weak crust in terms of long-term rheology, and for the anorthite upper and lower crust model, which is assimilated as a strong crust.

Quartz upper and lower crust (weak rheology)

In this model, we choose a critical slip-weakening distance of D_c = 0.6 m, consistent with the value used for the quartz upper crust and anorthite lower crust model (Section 4.5.2). The spontaneous rupture initiation occurs slightly before 80 seconds (Figure 4.13 and Figure 4.9a), propagating symmetrically away from the hypocenter. The propagation of the rupture along the brittle-ductile boundary is ahead of the propagation near the surface until approximately 120 seconds when the rupture at depth reaches the fault's geometrical variations located at $x \approx$ 600, 1000 km at 250 km from the hypocenter in both directions (Figure 4.13).

The off-fault deformation width around the fault (Figure 4.13) is narrower compared to the quartz-anorthite model (Figure 4.12), covering only a few hundred meters both at the surface and ar depth. The rupture ceases after 170 seconds of simulation time, corresponding to a 90-second long earthquake of magnitude $M_w = 8.02$, with a surface rupture length of 434 km and a rupture surface area of 7336 km^2. Compared to the rupture generated in the quartz-anorthite model, the full quartz model produces a shorter surface rupture length, a smaller rupture surface area, and less accumulated slip, with an average slip of 6.6 m compared to 9.4 m for the quartz-anorthite model (Table 4.3). The accumulated slip pattern also shows higher accumulation within the nearest 100 km radius around the hypocenter before progressively decreasing towards the fault's geometrical variations.

Overall, this model generates an earthquake that is qualitatively similar to the earthquake generated in the quartz-anorthite model but with a smaller magnitude.

Anorthite upper and lower crust (strong rheology)

This model employs an anorthite long-term rheology for both the upper and lower crust, resulting in significantly higher crustal strength compared to models using a quartz rheology for the upper crust. Consequently, there is an absence of the brittle-ductile transition and higher stresses (Figure 4.7) on the fault. As a result, the rupture propagates across the entire fault's surface from the surface to a depth of 50 km (Figure 4.14).

Upon initiation, dynamic rupture first propagates at depth before extending across the whole fault. Initially symmetric, the propagation becomes asymmetric upon reaching the fault's surface geometrical variations located at $x \approx 600, 1000$. The rupture propagates first in the 0 to -25 km depth before progressing in the second half of the fault (-25 to -50 km). During passage through the fault's bends, the amplitude of accumulated slip reduces from $\sim$ 100 to $\sim$ 40 m. In addition, while rupture passes through the bends, the moment rate shows a significant decrease from 1.8×10^{21} $Nm.s^{-1}$ to 0.3×10^{21} $Nm.s^{-1}$ (Figure 4.9c).

In contrast to previous models where rupture is stopped by the fault's geometrical heterogeneity, here, the rupture passes through the pronounced fault bends and continues. Passing the fault's bend at $x \approx 600$ km, the amplitude of accumulated slip increases to a magnitude similar to that near the hypocenter (~ 100 m), and the moment rate increases again to a value of 1.6×10^{21} $Nm.s^{-1}$ (Figure 4.9c). This result indicates that the long-term 3D stress field favors slip on fault segments better aligned with the regional plate motion (i.e., long-term boundary conditions). At 200 seconds (100 seconds after the rupture initiation), the rupture reaches another fault bend at $x \approx 200$ km, where the magnitude of accumulated slip decreases to approximately 40 m within this region. By the simulation's end, the entire fault ruptures, with two high-magnitude slip patches corresponding to fault segments better aligned with the plate velocity field.

During rupture, off-fault plastic deformation propagates near the fault within a region reaching up to 10 km in width, illustrated in panels (1) of Figure 4.14. Similar to the quartz-anorthite model, the off-fault strain exhibits a positive flower-like structure, with a width ranging from a few meters at depth to several kilometers at the surface (Table 4.3).

The simulated earthquake has a magnitude of $M_w = 9.34$, generating a surface rupture length of 1165 km, a rupture area of 62,465 km^2, and an average slip of 48 m. These quantities are exceedingly high compared to natural expectations (Figure 4.9c, d), attributable to the very strong long-term rheology employed. However, this simulation provides valuable insights into rupture behavior when crossing a fault bend and the interplay between stress state, fault geometry, and their influence on rupture dynamics.

The coseismic off-fault plastic strain is influenced by the stress state of the long-term model, which depends on the imposed crustal rheology. Consequently, in a strong crust model, the stress state more readily reaches plastic yielding during a coseismic rupture in a dynamic model that accounts for off-fault plasticity compared to a weak crust model. This results in a wide zone off-fault of high plastic strain values in the strong crust model, unlike for the weak crustal rheology.

Model	OFP	Crust composition	D_c (m)	Average slip (m)	Rupture area (km^2)	Surface rupture length (km)	M_w
M1	No	Q-A	0.6	9.3	15,087	773	8.33
M2	No	Q-A	1	10.1	7,572	540	8.16
M3	No	Q-A	1.5	10.2	5,619	461	8.07
M4	No	Q-A	1.7	10.4	5,012	386	8.04
M5	No	Q-A	0.6-1.6	9.5	9,771	600	8.21
M6	No	Q-A	1.1-2	10	5,970	493	8.09
M7	Yes	Q-A	0.6	9.3	9,120	550	8.19
M8	Yes	Q	0.6	6.6	7,336	434	8.02
M9	Yes	A	1	48.2	62,465	1,166	9.34
M10	Yes	Q	0.1	8.2	21,310	1,051	8.39
M11	No	Q	0.6	6.6	7,142	417	8.01
M12	No	A	0.6	51.8	62,944	1,165	9.37
M13	No	A	1	48.2	62,465	1,165	9.35
M14	Yes	Q-A	1	10.4	5,611	339	8.08

Table 4.3. Principal characteristics of the rupture for each models. OFP: Off-fault plasticity, Q: quartz, A: anorthite.

4.6 Discussion

4.6.1 Relationships between long-term geodynamics and earthquakes dynamics

Effect of 3D fault geometry on dynamic rupture propagation

The reconstructed fault geometry remains simple yet non-planar. While the first order orientation of the fault strike is approximately N 100°E (west-northwest - east-southeast) over 1000 km, introducing initial weak zones at a 7° angle with respect to the velocity field introduces a slight obliquity accommodated in long-term deformation by local variations in fault orientation (approximately N 95°E). These local variations occur every 400 km and span roughly 100 km. Despite their small scale, such variations significantly influence the geodynamic characteristics of the system, which in turn impacts the rupture dynamics.

The three long-term geodynamic models, although defined with different rheologies, exhibit a stress regime variation from purely strike-slip to compressional (Figure 4.8e,i) and a topographic high (Figure 4.8b,f,j) when transitioning from 400 km long segments to 100 km long geometrical heterogeneity. Long-term slip rates also decrease slightly across fault bends (Figure 4.8d,h,l). As our results indicate, this combination affects the 3D stress state of the fault and, consequently, the rupture dynamics during an earthquake.

The dynamic ruptures depicted in Figure 4.12, Figure 4.13, and Figure 4.14 all demonstrate that the rupture velocity and accumulated slip decrease near fault bends [64,74,77]. In weaker crusts, where stresses are lower, rupture halts upon reaching fault geometrical heterogeneity (Figure 4.12 and Figure 4.13). However, in sufficiently strong crusts, the rupture passes through, behaving similarly on the other side of the heterogeneity.

This behavior highlights how minor variations in the long-term 3D stress field can strongly affect the rupture dynamics, providing a physical mechanism for halting earthquake propagation.

Relationship between long-term rheology and rupture propagation

Dynamic rupture models highlight the sensitivity of the rupture propagation to the long-term rheology of the crust. The flow laws used to model the continental crust influence both the depth of the brittle-ductile transition and the stress field. For instance, the anorthite rheology, gathering feldspar-rich rocks like granulites, gabbros, or diorites that constitute the lower continental crust at first order, undergoes plastic deformation until temperatures of approximately 700°C (Figure 4.1). This behavior extends the depth of the brittle-ductile transition and thus increases the crustal stress. While stresses required for viscous deformation of rocks decrease exponentially with temperature (and thus depth, Eq. 4.7), the plastic yield stress criterion increases with depth (Eq. 4.10). Consequently, the long-term stress field contains this information and significantly influences the thickness of the seismogenic zone and, thus, rupture dynamics.

Models featuring an upper crust composed of quartz, related to granitic-like rocks, exhibit a brittle-ductile transition ranging from 15 km to 20 km depth (Figure 4.7a,b). This viscous layer acts as a decoupling layer for long-term crustal mechanical behavior and as a barrier to rupture propagation at earthquake timescales.

Conversely, models with a full anorthite crust composition show no brittle-ductile transition (Figure 4.7c) due to the much greater strength of feldspar-rich rocks compared to quartz-rich rocks. The absence of a ductile layer permits the rupture propagation throughout the entire fault thickness. Additionally, because feldspar-rich rocks do not readily flow at crustal temperatures, the total stress accumulated along the fault is higher, enabling rupture propagation through geometric variations where fault orientation changes.

Thus, linking long-term geodynamic models with dynamic rupture models establishes mechanical relationships between timescales and assesses the first-order importance of crust composition and long-term rheology in earthquake mechanics. This approach allows us to incorporate physics-informed stress states of a lithosphere with a multilayered strength structure into dynamic rupture models. Without this method, we would need to explicitly define a stress variation function to represent transitions between brittle and ductile regimes based on compositions that may not always be known at depth. This is significant for dynamic rupture models because no single strength profile can represent all types of continental lithosphere[24].

Interpretation of the long-term stress and implication on earthquake dynamics

The stress field derived from long-term geodynamic models incorporates shear zone geometry, lithosphere rheology, temperature field, volume forces, and topography, resulting directly from momentum and thermal energy conservation given material parameters. However, these models compute stresses based on the visco-plastic behavior of the lithosphere over extended periods of time, with typical time steps covering thousands of years. Thus, the stresses, re-evaluated at each time step, can be interpreted as the result of loading over this period.

Since our long-term geodynamic models do not account for small time-scale elastic energy dissipation, such as the seismic cycle, the obtained stress values represent the stress state of a system that has not dissipated elastic energy over thousands of years. However, in nature, despite the observation of the seismic cycle, large-magnitude earthquakes still occur. This suggests that not all accumulated energy dissipates through small-magnitude earthquakes and that long-term visco-plastic lithospheric behaviour and large-scale tectonic plate boundary forces are the first-order drivers responsible for large-magnitude earthquakes. As illustrated in Figure 4.9d, geodynamically informed earthquakes produce high magnitudes, yet for realistic long-term rheologies, they adhere to scaling relationships between M_w and surface rupture length established from natural observations.

In addition, our experiments involve a single fault surface with slight geometrical variations. Given how these variations strongly impact the stress state and the dynamics of the rupture, accounting for more complicated fault geometries and possible interactions between tectonic structures within a fault network may contribute to dissipating elastic energy more efficiently during the rupture propagation, which would reduce the magnitude of the modelled earthquakes. Moreover, in the presented models, we imposed the nucleation location due to an absence of a stress state favorable to spontaneous nucleation. In addition, the shallow frictional cohesion included with Eq. (4.23) prevents the simulation from developing near-surface spontaneous nucleation. However, as van Zelst *et al.*[119] proposed that long-term geodynamic model pre-stress could predict spontaneous nucleation for dynamic rupture, it is possible that introducing more complexity in the fault network and geometry distributes 3D stresses more consistently to natural cases favoring spontaneous nucleation.

This implies that utilizing long-term geodynamic models to provide information about 3D fault geometry and stress state is valid but should be limited to large-magnitude earthquakes. Alternatively, one could use the long-term stress state and fault geometry in a seismic cycle simulation, which performs intermediate-scale elastic energy dissipation, and then transfer the resulting stresses to dynamic rupture simulations.

4.6.2 *Limitations*

The method proposed in this study is effective for identifying and characterizing first-order localized shear zones. However, in 3D long-term geodynamic models, it is not uncommon for major shear zones to be accompanied by diffuse deformation. Unfortunately, due to their low strain rate values, highly diffuse deformation or non-localized shear zones cannot be accurately extracted. This is because the creation of ξ isovalues surfaces for such cases results in very large volumes, leading to a noisy approximation of the medial axis.

The method's limitations primarily stem from its inability to handle extremely diffuse deformation, as the strain rate values associated with such zones do not allow for the extraction of well-defined and localized shear zones. As a result, further developments or alternative approaches may be required to address the characterization of highly diffuse deformation in long-term geodynamic models.

It is important to acknowledge these limitations and consider their implications when applying the proposed method in scenarios where diffuse deformation is significant.

In this study, we link 3D geodynamic models with 3D dynamic rupture simulations that require prescribed nucleation. Coseismically, the slip-dependent fault weakening behavior governed by aging law rate-and-state friction is similar to that governed by linear slip-weakening friction (e.g., Bizzarri and Cocco[17], Garagash[38], Kaneko et al.[63]). Alternative choices for frictional constitutive laws in dynamic rupture simulations, such as rate-and-state friction, may favour less ad-hoc dynamic nucleation. 3D earthquake cycle simulations use rate-and-state friction to seamlessly integrate spontaneous aseismic nucleation with dynamic rupture[55,70,72,75,83]. However, these simulations pose significant methodological and computational challenges, especially when addressing complex interactions of geometry, friction, and structural properties[54,113].

4.7 Conclusions

This study provides loose coupling between long-term 3D geodynamic models of strike-slip fault evolution — featuring a single non-planar strike-slip fault — and dynamic rupture modelling. We introduce a new method to extract and reconstruct complex fault surfaces from 3D volumetric shear zones. Our key findings are:

- Utilizing our method for fault surface reconstruction from volumetric shear zones allows for the evaluation of the long-term slip rate across the faults.
- The dynamic rupture models show that for the geodynamic system considered, the geometry of the fault, the rheology of the crust, and the long-term stress-state, a suitable critical slip weakening distance falls within $D_c \in [0.6, 1.5]$.
- The long-term rheology significantly influences the stress state and long-term slip rate on the fault, thereby impacting rupture dynamics and plastic strain localization. Crusts with a thicker ductile layer promote a lower stress state that will produce smaller magnitude earthquakes with shorter surface rupture length, smaller rupture surface area, and less accumulated slip.
- The long-term geometry of the fault plays a crucial role in determining the stress regime at locations of geometrical variations, thereby influencing rupture dynamics by favoring slip on fault segments better aligned with the regional plate motion (i.e., long-term boundary conditions). This behavior highlights how minor variations in the long-term 3D stress field can strongly affect the rupture dynamics, providing a physical mechanism for halting earthquake propagation.
- Because feldspar-rich rocks do not readily flow at crustal temperatures, the total stress accumulated along the fault is higher, enabling rupture propagation through geometric variations where fault orientation changes.
- Geodynamically informed earthquakes exhibit high magnitudes ($M_w \geq 8$), which we interpret as resulting from a medium where elastic energy is not released by smaller events during the seismic cycle.

These findings highlight the interactions between long-term geodynamic processes and short-term earthquake dynamics, shedding light on the importance of considering the long-term mechanics to simulate and understand the dynamic rupture behavior.

Open Research

The long-term geodynamic models have been performed using pTatin3d, an open-source software publicly available at https://bitbucket.org/dmay/ptatin-total-dev. The git branch used to produce the results is anthony_jourdon/oblique-nitsche-poissonP. Options file to reproduce the models can be found at https://zenodo.org/records/12646159 in ptatin-options_file.tar.gz with the DOI 10.5281/zenodo.12646158.

The fault surface reconstruction from volumetric shear zone has been performed using an open-source software that we developed and that is publicly available at https://bitbucket.org/jourdon_anthony/ptatin3d-extract-faults-tools.

Dynamic rupture models were performed using SeisSol, an open-source software publicly available at https://github.com/SeisSol/SeisSol. The input files and meshes necessary to reproduce the results can be found at https://zenodo.org/records/12646159 in ptatin3d_OWL_Seissol-SimpleFault.tar.xz with the DOI 10.5281/zenodo.12646158.

Acknowledgments

This work has been supported by the European Union's Horizon 2020 research and innovation programme (TEAR ERC Starting grant no. 852992). AJ acknowledges additional support by the French government, through the UCAJEDI Investments in the Future project managed by the National Research Agency (ANR) under reference number ANR-15-IDEX-01. DAM and AAG acknowledge additional support from the National Science Foundation (grant nos. EAR-2121568, OAC-2311208). AAG acknowledges additional support from Horizon Europe (ChEESE-2P, grant no. 101093038; DT-GEO, grant no. 101058129; and Geo-INQUIRE, grant no. 101058518), from the National Science Foundation (grant nos. EAR-2225286, OAC-2139536), and the National Aeronautics and Space Administration (grant no. 80NSSC20K0495).

The authors gratefully acknowledge the Gauss Centre for Supercomputing e.V. (https://www.gauss-centre.eu) for providing computing time on the GCS Supercomputer SuperMUC-NG at the Leibniz Supercomputing Centre (https://www.lrz.de) through project pn49ha. The authors are grateful to the Université Côte d'Azur's Center for High-Performance Computing (OPAL infrastructure) for providing resources and support through project CT3D. Dave A. May and Alice-Agnes Gabriel acknowledge financial support from the National Science Foundation (NSF Grant EAR-2121568).

4.8 REFERENCES

[1] Ahrens, J., Geveci, B., and Law, C. (2005). 36 - ParaView: An End-User Tool for Large-Data Visualization. In Hansen, C. D. and Johnson, C. R., editors, *Visualization Handbook*, pages 717–731. Butterworth-Heinemann, Burlington. Cited on page/s 87.

[2] An, Y., Guo, J., Ye, Q., Childs, C., Walsh, J., and Dong, R. (2021). Deep convolutional neural network for automatic fault recognition from 3D seismic datasets. *Computers and Geosciences*, 153. Cited on page/s 86.

[3] Anderson, J. G., Biasi, G. P., and Wesnousky, S. G. (2017). Fault-scaling relationships depend on the average fault-slip rate. *Bulletin of the Seismological Society of America*, 107(6):2561–2577. Cited on page/s 113.

[4] Andrews, D. J. (1976). Rupture propagation with finite stress in antiplane strain. *Journal of Geophysical Research*, 81(20):3575–3582. Cited on page/s 93.

[5] Andrews, D. J. (2004). Rupture Models with Dynamically Determined Breakdown Displacement. *Bulletin of the Seismological Society of America*, 94(3):769–775. Cited on page/s 94.

[6] Andrews, D. J. (2005). Rupture dynamics with energy loss outside the slip zone. *Journal of Geophysical Research: Solid Earth*, 110(B01307). Cited on page/s 92, 94.

[7] Aochi, H. and Madariaga, R. (2003). The 1999 Izmit, Turkey, earthquake: Nonplanar fault structure, dynamic rupture process, and strong ground motion. *Bull. Seismol. Soc. Am.*, 93(3):1249–1266. Cited on page/s 93.

[8] Ayachit, U. (2015). *The ParaView Guide: A Parallel Visualization Application*. Kitware, Inc., Clifton Park, NY, USA. Cited on page/s 87.

[9] Bai, K. and Ampuero, J.-P. (2017). Effect of seismogenic depth and background stress on physical limits of earthquake rupture across fault step overs. *Journal of Geophysical Research: Solid Earth*, 122:10,280–10,298. Cited on page/s 80.

[10] Barbot, S., Lapusta, N., and Avouac, J.-P. (2012). Under the hood of the earthquake machine: Toward predictive modeling of the seismic cycle. *Science*, 336:707–710. Cited on page/s 80.

[11] Beaumont, C., Jamieson, R., Butler, J., and Warren, C. (2009). Crustal structure : A key constraint on the mechanism of ultra-high-pressure rock exhumation. *Earth and Planetary Science Letters*, 287:116–129. Cited on page/s 80.

[12] Ben-Zion, Y. and Shi, Z. (2005). Dynamic rupture on a material interface with spontaneous generation of plastic strain in the bulk. *Earth and Planetary Science Letters*, 236(1):486–496. Cited on page/s 92.

[13] Benjemaa, M., Glinsky-Olivier, N., Cruz-Atienza, V. M., Virieux, J., and Piperno, S. (2007). Dynamic non-planar crack rupture by a finite volume method. *Geophysical Journal International*, 171(1):271–285. Cited on page/s 80.

[14] Berger, M., Tagliasacchi, A., Seversky, L. M., Alliez, P., Levine, J. A., Sharf, A., and Silva, C. T. (2014). State of the Art in Surface Reconstruction from Point Clouds. In Lefebvre, S. and Spagnuolo, M., editors, *Eurographics 2014 - State of the Art Reports*. The Eurographics Association. Cited on page/s 86.

[15] Biemiller, J., Gabriel, A.-A., and Ulrich, T. (2023). Dueling dynamics of low-angle normal fault rupture with splay faulting and off-fault damage. *Nature Communications*. Cited on page/s 91.

[16] Bizzarri, A. (2010). How to Promote Earthquake Ruptures: Different Nucleation Strategies in a Dynamic Model with Slip-Weakening Friction. *Bulletin of the Seismological Society of America*, 100(3):923–940. Cited on page/s 94.

[17] Bizzarri, A. and Cocco, M. (2003). Slip-weakening behavior during the propagation of dynamic ruptures obeying rate- and state-dependent friction laws. *Journal of Geophysical Research*, 108(B8). Cited on page/s 104.

[18] Boe, T. H. and Daber, R. (2010). Seismic Features And the Human Eye: RGB Blending of Azimuthal Curvatures For Enhancement of Fault And Fracture Interpretation. In *SEG Technical Program Expanded Abstracts 2010*, pages SEG–2010–1535. Society of Exploration Geophysicists. Cited on page/s 86.

[19] Breuer, A., Heinecke, A., Rettenberger, S., Bader, M., Gabriel, A.-A., and Pelties, C. (2014). Sustained Petascale Performance of Seismic Simulations with SeisSol on SuperMUC. In *Supercomputing. ISC 2014. Lecture Notes in Computer Science, vol 8488*, pages 1–18. Springer. Cited on page/s 91.

[20] Brun, J.-P., Buck, R., McClay, K., Kusznir, N., Louden, K. E., and McKenzie, D. (1999). Narrow rifts versus wide rifts: Inferences for the mechanics of rifting from laboratory experiments [and discussion]. *Philosophical Transactions: Mathematical, Physical and Engineering Sciences*, 357(1753):695–712. Cited on page/s 80.

[21] Brune, S. (2014). Evolution of stress and fault patterns in oblique rift systems: 3-d numerical lithospheric-scale experiments from rift to breakup. *Geochemistry, Geophysics, Geosystems*, 15:3392–3415. Cited on page/s 87.

[22] Buck, W. R. (1991). Modes of continental lithospheric extension. *Journal of Geophysical Research*, 96(B12):20161–20178. Cited on page/s 80.

[23] Bürgmann, R. and Dresen, G. (2008). Rheology of the Lower Crust and Upper Mantle : Evidence from Rock Mechanics , Geodesy , and Field Observations. *Annual Review of Earth and Planetary Sciences*, 36:531–567. Cited on page/s 80.

[24] Burov, E. (2011). Rheology and strength of the lithosphere. *Marine and Petroleum Geology*, 28(8):1402–1443. Cited on page/s 80, 102.

[25] Byerlee, J. (1978). Friction of rocks. *Pure and Applied Geophysics*, 116(4-5):615–626. Cited on page/s 92, 93.

[26] Cocco, M., Aretusini, S., Cornelio, C., Nielsen, S. B., Spagnuolo, E., Tinti, E., and Di Toro, G. (2023). Fracture energy and breakdown work during earthquakes. *Annual Review of Earth and Planetary Sciences*, 51(1):217–252. Cited on page/s 80, 97.

[27] Di Toro, G., Han, R., Hirose, T., De Paola, N., Nielsen, S., Mizoguchi, K., Ferri, F., Cocco, M., and Shimamoto, T. (2011). Fault lubrication during earthquakes. *Nature*, 471(7339):494–498. Cited on page/s 92, 93.

[28] Duclaux, G., Huismans, R. S., and May, D. A. (2020). Rotation, narrowing, and preferential reactivation of brittle structures during oblique rifting. *Earth and Planetary Science Letters*, 531. Cited on page/s 86.

[29] Dumbser, M. and Käser, M. (2006). An arbitrary high-order discontinuous Galerkin method for elastic waves on unstructured meshes—II. The three-dimensional isotropic case. *Geophysical Journal International*, 167(1):319–336. Cited on page/s 91.

[30] Dunham, E. M., Belanger, D., Cong, L., and Kozdon, J. E. (2011). Earthquake Ruptures with Strongly Rate-Weakening Friction and Off-Fault Plasticity, Part 1: Planar Faults. *Bulletin of the Seismological Society of America*, 101(5):2296–2307. Cited on page/s 92.

[31] Dziewonski, A. M. and Anderson, D. L. (1981). Preliminary reference earth model. *Physics of the Earth and Planetary Interiors*, 25:297–356. Cited on page/s 92.

[32] Fei, F., Mia, M. S., Elbanna, A. E., and Choo, J. (2023). A phase-field model for quasi-dynamic nucleation, growth, and propagation of rate-and-state faults. *International Journal for Numerical and Analytical Methods in Geomechanics*, 47(2):187–211. Cited on page/s 80.

[33] Gabriel, A.-A., Ampuero, J.-P., Dalguer, L. A., and Mai, P. M. (2013). Source properties of dynamic rupture pulses with off-fault plasticity. *Journal of Geophysical Research: Solid Earth*, 118(8):4117–4126. Cited on page/s 92.

[34] Gabriel, A.-A., Garagash, D. I., Palgunadi, K. H., and Mai, P. M. (2024). Fault size–dependent fracture energy explains multiscale seismicity and cascading earthquakes. *Science*, 385(6707):eadj9587. Cited on page/s 80.

[35] Gabriel, A.-A., Li, D., Chiocchetti, S., Tavelli, M., Peshkov, I., Romenski, E., and Dumbser, M. (2021). A unified first-order hyperbolic model for nonlinear dynamic rupture processes in diffuse fracture zones. *Philosophical Transactions of the Royal Society A: Mathematical, Physical and Engineering Sciences*, 379(2196):20200130. Cited on page/s 80.

[36] Gabriel, A.-A., Ulrich, T., Marchandon, M., Biemiller, J., and Rekoske, J. (2023). 3D Dynamic Rupture Modeling of the 6 February 2023, Kahramanmaraş, Turkey Mw 7.8 and 7.7 Earthquake Doublet Using Early Observations. *Seismic Record*, 3:342–356. Cited on page/s 91.

[37] Galis, M., Pelties, C., Kristek, J., Moczo, P., Ampuero, J.-P., and Mai, P. M. (2015). On the initiation of sustained slip-weakening ruptures by localized stresses. *Geophysical Journal International*, 200(2):890–909. Cited on page/s 95.

[38] Garagash, D. I. (2021). racture mechanics of rate-and-state faults and fluid injection induced slip. *Philosophical Transactions of the Royal Society A*, 379(2196). Cited on page/s 104.

[39] Gersztenkorn, A. and Marfurt, K. J. (1999). Eigenstructure-based coherence computations as an aid to 3-D structural and stratigraphic mapping. *GEOPHYSICS*, 64:1468–1479. Cited on page/s 86.

[40] Gerya, T. V. (2019). *Introduction to numerical geodynamic modelling*. Cambridge University Press, Cambridge, second edition edition. Cited on page/s 80.

[41] Gibson, D., Spann, M., Turner, J., and Wright, T. (2005). Fault surface detection in 3-d seismic data. *IEEE Transactions on Geoscience and Remote Sensing*, 43:2094–2101. Cited on page/s 86.

[42] Hale, D. (2012). Fault Surfaces and Fault Throws From 3D Seismic Images. In *SEG International Exposition and Annual Meeting*, pages SEG–2012–0734. SEG. Cited on page/s 86.

[43] Harris, R. A., Barall, M., Aagaard, B., Ma, S., Roten, D., Olsen, K., Duan, B., Liu, D., Luo, B., Bai, K., Ampuero, J., Kaneko, Y., Gabriel, A., Duru, K., Ulrich, T., Wollherr, S., Shi, Z., Dunham, E., Bydlon, S., Zhang, Z., Chen, X., Somala,

S. N., Pelties, C., Tago, J., Cruz-Atienza, V. M., Kozdon, J., Daub, E., Aslam, K., Kase, Y., Withers, K., and Dalguer, L. (2018). A Suite of Exercises for Verifying Dynamic Earthquake Rupture Codes. *Seismological Research Letters*, 89(3):1146–1162. Cited on page/s 80, 91, 93, 95.

[44] Harris, R. A., Barall, M., Lockner, D. A., Moore, D. E., Ponce, D. A., Graymer, R. W., Funning, G., Morrow, C. A., Kyriakopoulos, C., and Eberhart-Phillips, D. (2021). A geology and geodesy based model of dynamic earthquake rupture on the rodgers creek-hayward-calaveras fault system, california. *Journal of Geophysical Research: Solid Earth*, 126(3):e2020JB020577. e2020JB020577 2020JB020577. Cited on page/s 80, 94.

[45] Hayek, J. N., Li, D., Marchandon, M., Gabriel, A.-A., L., P.-B., and J., H. (2024). Non-typical supershear rupture: fault heterogeneity and segmentation govern unilateral supershear and cascading multi-fault rupture in the 2021 Mw 7.4 Maduo Earthquake . EarthArxiv. Cited on page/s 80.

[46] Hayek, J. N., May, D. A., Pranger, C., and Gabriel, A.-A. (2023). A diffuse interface method for earthquake rupture dynamics based on a phase-field model. *Journal of Geophysical Research: Solid Earth*, 128(12):e2023JB027143. e2023JB027143 2023JB027143. Cited on page/s 80, 92.

[47] Heinecke, A., Breuer, A., Rettenberger, S., Bader, M., Gabriel, A. A., Pelties, C., Bode, A., Barth, W., Liao, X. K., Vaidyanathan, K., Smelyanskiy, M., and Dubey, P. (2014). Petascale high order dynamic rupture earthquake simulations on heterogeneous supercomputers. In *SC'14: International Conference for High-Performance Computing, Networking, Storage and Analysis*. Cited on page/s 91, 95.

[48] Herrendörfer, R., Gerya, T., and van Dinther, Y. (2018). An invariant rate- and state-dependent friction formulation for viscoeastoplastic earthquake cycle simulations. *Journal of Geophysical Research: Solid Earth*, 123:5018–5051. Cited on page/s 80.

[49] Hirth, G. and Kohlstedt, D. L. (2003). Rheology of the Upper Mantle and the Mantle Wedge: A View from the Experimentalists. *Geophysical Monograph*, 138:83–105. Cited on page/s 84.

[50] Hu, F., Huang, H., and Chen, X. (2017). Effect of the time-weakening friction law during the nucleation process. *Earthquake Science*, 30(2):91–96. Cited on page/s 94.

[51] Ide, S. and Aochi, H. (2005). Earthquakes as multiscale dynamic ruptures with heterogeneous fracture surface energy. *Journal of Geophysical Research: Solid Earth*, 110(B11). Cited on page/s 98.

[52] Ide, S. and Aochi, H. (2014). Modeling earthquakes using fractal circular patch models with lessons from the 2011 Tohoku-Oki earthquake. *Journal of Disaster Research*, 9(3):264–271. Cited on page/s 93.

[53] Jia, Z., Jin, Z., Marchandon, M., Ulrich, T., Gabriel, A.-A., Fan, W., Shearer, P., Zou, X., Rekoske, J., Bulut, F., Garagon, A., and Fialko, Y. (2023). The complex dynamics of the 2023 Kahramanmaraş, Turkey, Mw 7.8-7.7 earthquake doublet. *Science*, 0:eadi0685. Cited on page/s 80.

[54] Jiang, J., Erickson, B. A., Lambert, V. R., Ampuero, J.-P., Ando, R., Barbot, S. D., Cattania, C., Zilio, L. D., Duan, B., Dunham, E. M., Gabriel, A.-A., Lapusta, N., Li, D., Li, M., Liu, D., Liu, Y., Ozawa, S., Pranger, C., and van Dinther, Y. (2022). Community-driven code comparisons for three-dimensional dynamic modeling of sequences of earthquakes and aseismic slip. *Journal of Geophysical Research: Solid Earth*, 127(3):e2021JB023519. e2021JB023519 2021JB023519. Cited on page/s 104.

[55] Jiang, J. and Lapusta, N. (2016). Deeper penetration of large earthquakes on seismically quiescent faults. *Science*, 352(6291):1293–1297. Cited on page/s 104.

[56] Jourdon, A., Kergaravat, C., Duclaux, G., and Huguen, C. (2021). Looking beyond kinematics: 3D thermo-mechanical modelling reveals the dynamics of transform margins. *Solid Earth*, 12:1211–1232. Cited on page/s 87.

[57] Jourdon, A., Le Pourhiet, L., Mouthereau, F., and Masini, E. (2019). Role of rift maturity on the architecture and shortening distribution in mountain belts. *Earth and Planetary Science Letters*, 512:89–99. Cited on page/s 80.

[58] Jourdon, A. and May, D. A. (2022). An efficient partial-differential-equation-based method to compute pressure boundary conditions in regional geodynamic models. *Solid Earth*, 13(6):1107–1125. Cited on page/s 92.

[59] Jourdon, A., May, D. A., and Gabriel, A.-A. (2024). Generalisation of the Navier-slip boundary condition to arbitrary directions: Application to 3D oblique geodynamic simulations. Cited on page/s 85, 86.

[60] Jourdon, A., Mouthereau, F., Le Pourhiet, L., and Callot, J.-P. (2020). Topographic and tectonic evolution of mountain belts controlled by salt thickness and rift architecture. *Tectonics*, 39:1–14. Cited on page/s 80.

[61] Kame, N., Rice, J. R., and Dmowska, R. (2003). Effects of prestress state and rupture velocity on dynamic fault

branching. *Journal of Geophysical Research: Solid Earth*, 108. Cited on page/s 80.

[62] Kammer, D. S., McLaskey, G. C., Abercrombie, R. E., Ampuero, J.-P., Cattania, C., Cocco, M., Dal Zilio, L., Dresen, G., Gabriel, A.-A., Ke, C.-Y., Marone, C., Selvadurai, P. A., and Tinti, E. (2024). Energy dissipation in earthquakes. arXiv. Cited on page/s 92, 94, 97.

[63] Kaneko, Y., Lapusta, N., and Ampuero, J. (2008). Spectral element modeling of spontaneous earthquake rupture on rate and state faults: Effect of velocity-strengthening friction at shallow depths. *Journal of Geophysical Research*, 113(B9). Cited on page/s 104.

[64] Kase, Y. and Day, S. M. (2006). Spontaneous rupture processes on a bending fault. *Geophysical Research Letters*, 33(10). Cited on page/s 101.

[65] Kirby, S. H. and Kronenberg, A. K. (1987). Rheology of the lithosphere: Selected topics. *Reviews of Geophysics*, 25(6):1219–1244. Cited on page/s 80.

[66] Kostrov, V. and Riznichenko, V. (1976). Seismic moment and energy of earthquakes, and seismic flow of rock. *International Journal of Rock Mechanics and Mining Sciences & Geomechanics Abstracts*, 13(1):A4. Cited on page/s 93.

[67] Krenz, L., Uphoff, C., Ulrich, T., Gabriel, A.-A., Abrahams, L., Dunham, E., and Bader, M. (2021). 3D acoustic-elastic coupling with gravity: the dynamics of the 2018 Palu, Sulawesi earthquake and tsunami. In *Proceedings of the International Conference for High-Performance Computing, Networking, Storage and Analysis*, SC '21, New York, NY, USA. ACM. Cited on page/s 91.

[68] Käser, M. and Dumbser, M. (2006). An arbitrary high-order discontinuous Galerkin method for elastic waves on unstructured meshes — I. The two-dimensional isotropic case with external source terms. *Geophysical Journal International*, 166(2):855–877. Cited on page/s 91, 95.

[69] Lapusta, N. (2019). Modeling earthquake source processes: from tectonics to dynamic rupture. In *AGU Fall Meeting 2019*. AGU. Cited on page/s 80.

[70] Lapusta, N. and Liu, Y. (2009). Three-dimensional boundary integral modeling of spontaneous earthquake sequences and aseismic slip. *Journal of Geophysical Research: Solid Earth*, 114(B9). Cited on page/s 104.

[71] Le Pourhiet, L., May, D. A., Huille, L., Watremez, L., and Leroy, S. (2017). A genetic link between transform and hyper-extended margins. *Earth and Planetary Science Letters*, 465:184–192. Cited on page/s 87.

[72] Li, D. and Gabriel, A.-A. (2024). Linking 3D long-term slow-slip cycle models with rupture dynamics: The nucleation of the 2014 Mw 7.3 Guerrero, Mexico earthquake. *AGU Advances*, 5(e2023AV000979). Cited on page/s 104.

[73] Liao, J. and Gerya, T. (2015). From continental rifting to sea floor spreading : Insight from 3D thermo-mechanical modeling. *Gondwana Research*, 28:1329–1343. Cited on page/s 87.

[74] Lozos, J. C., Oglesby, D. D., Duan, B., and Wesnousky, S. G. (2011). The Effects of Double Fault Bends on Rupture Propagation: A Geometrical Parameter Study. *Bulletin of the Seismological Society of America*, 101(1):385–398. Cited on page/s 101.

[75] Luo, B., Duan, B., and Liu, D. (2020). 3D Finite-Element Modeling of Dynamic Rupture and Aseismic Slip over Earthquake Cycles on Geometrically Complex Faults. *Bulletin of the Seismological Society of America*, 110(6):2619–2637. Cited on page/s 104.

[76] Ma, J., Bae, S. W., and Choi, S. (2012). 3D medial axis point approximation using nearest neighbors and the normal field. *Visual Computer*, 28(1):7–19. Cited on page/s 88.

[77] Ma, S. (2022). Dynamic off-fault failure and tsunamigenesis at strike-slip restraining bends: Fully-coupled models of dynamic rupture, ocean acoustic waves, and tsunami in a shallow bay. *Tectonophysics*, 838:229496. Cited on page/s 101.

[78] Madden, E. H., Bader, M., Behrens, J., van Dinther, Y., Gabriel, A.-A., Rannabauer, L., Ulrich, T., Uphoff, C., Vater, S., and van Zelst, I. (2020). Linked 3-D modelling of megathrust earthquake-tsunami events: from subduction to tsunami run up. *Geophysical Journal International*, 224(1):487–516. Cited on page/s 80.

[79] Manatschal, G., Lavier, L., and Chenin, P. (2015). The role of inheritance in forming and deforming hyper-extended rift systems and creating collisional orogens. *Gondwana Research*, 27:140–164. Cited on page/s 80.

[80] Marfurt, K. J., Kirlin, R. L., Farmer, S. L., and Bahorich, M. S. (1998). 3-D seismic attributes using a semblance-based coherency algorithm. *Geophysics*, 63:1150–1165. Cited on page/s 86.

[81] May, D. A., Brown, J., and Le Pourhiet, L. (2014). pTatin3D : High-Performance Methods for Long-Term Lithospheric Dynamics. In *Proceeding SC'14 Proceedings of the International Conference for High Performance Computing, Networking,*

Storage and Analysis:, pages 274–284, New Orleans. Cited on page/s 81, 95.

[82] May, D. A., Brown, J., and Le Pourhiet, L. (2015). A scalable , matrix-free multigrid preconditioner for finite element discretizations of heterogeneous Stokes flow. *Computer Methods in Applied Mechanics and Engineering*, 290:496–523. Cited on page/s 81, 95.

[83] Meng, Q. and Duan, B. (2022). Dynamic Modeling of Interactions between Shallow Slow-Slip Events and Subduction Earthquakes. *Seismological Research Letters*, 94(1):206–216. Cited on page/s 104.

[84] Moore, D. E. and Lockner, D. A. (2007). Comparative Deformation Behavior of Minerals in Serpentinized Ultramafic Rock: Application to the Slab-Mantle Interface in Subduction Zones. *International Geology Review*, 49(5):401–415. Cited on page/s 93.

[85] Neuharth, D., Brune, S., Glerum, A., Heine, C., and Welford, J. K. (2021). Formation of continental microplates through rift linkage: Numerical modelling and its application to the flemish cap and sao paulo plateau. *Geochemistry, Geophysics, Geosystems*, 22:e2020GC009615. Cited on page/s 87.

[86] Neuharth, D., Brune, S., Wrona, T., Glerum, A., Braun, J., and Yuan, X. (2022). Evolution of rift systems and their fault networks in response to surface processes. *Tectonics*, 41. Cited on page/s 86.

[87] Okubo, K., Bhat, H. S., Rougier, E., Marty, S., Schubnel, A., Lei, Z., Knight, E. E., and Klinger, Y. (2019). Dynamics, radiation, and overall energy budget of earthquake rupture with coseismic off-fault damage. *Journal of Geophysical Research: Solid Earth*, 124(11):11771–11801. Cited on page/s 92.

[88] Pan, S., Naliboff, J., Bell, R., and Jackson, C. (2022). Bridging Spatiotemporal Scales of Normal Fault Growth During Continental Extension Using High-Resolution 3D Numerical Models. *Geochemistry, Geophysics, Geosystems*, 23. Cited on page/s 86.

[89] Pelties, C., de la Puente, J., Ampuero, J.-P., Brietzke, G. B., and Käser, M. (2012). Three-dimensional dynamic rupture simulation with a high-order discontinuous Galerkin method on unstructured tetrahedral meshes. *Journal of Geophysical Research: Solid Earth*, 117(2):1–15. Cited on page/s 91, 95.

[90] Pelties, C., Gabriel, A. A., and Ampuero, J. P. (2014). Verification of an ADER-DG method for complex dynamic rupture problems. *Geoscientific Model Development*, 7(3):847–866. Cited on page/s 91.

[91] Perfettini, H. and Avouac, J. P. (2004). Stress transfer and strain rate variations during the seismic cycle. *Journal of Geophysical Research: Solid Earth*, 109. Cited on page/s 80.

[92] Peters, R. (2018). *"Geographical point cloud modelling with the 3D medial axis transform"*. Dissertation (tu delft), Delft University of Technology. Cited on page/s 86.

[93] Pranger, C., Sanan, P., May, D. A., Le Pourhiet, L., and Gabriel, A.-A. (2022). Rate and state friction as a spatially regularized transient viscous flow law. *Journal of Geophysical Research: Solid Earth*, 127(6):e2021JB023511. e2021JB023511 2021JB023511. Cited on page/s 80.

[94] Ramos, M. D., Huang, Y., Ulrich, T., Li, D., Gabriel, A.-A., and Thomas, A. M. (2021). Assessing Margin-Wide Rupture Behaviors Along the Cascadia Megathrust With 3-D Dynamic Rupture Simulations. *Journal of Geophysical Research: Solid Earth*, 126(7):e2021JB022005. _eprint: https://onlinelibrary.wiley.com/doi/pdf/10.1029/2021JB022005. Cited on page/s 91.

[95] Ramos, M. D., Thakur, P., Huang, Y., Harris, R. A., and Ryan, K. J. (2022). Working with Dynamic Earthquake Rupture Models: A Practical Guide. *Seismological Research Letters*, 93(4):2096–2110. Cited on page/s 80.

[96] Ranalli, G. (1997). Rheology of the lithosphere in space and time. *Geological Society, London, Special Publications*, 121(1):19–37. Cited on page/s 80.

[97] Ranalli, G. and Murphy, D. C. (1987). Rheological stratification of the lithosphere. *Tectonophysics*, 132:281–295. Cited on page/s 80, 84.

[98] Rettenberger, S., Meister, O., Bader, M., and Gabriel, A.-A. (2016). ASAGI: A Parallel Server for Adaptive Geoinformation. In *Proceedings of the Exascale applications and Software Conference 2016*, EASC '16, pages 2:1–2:9, New York, NY, USA. ACM. Cited on page/s 91.

[99] Rubin, A. M. and Ampuero, J.-P. (2005). Earthquake nucleation on (aging) rate and state faults. *Journal of Geophysical Research: Solid Earth*, 110(B11). Cited on page/s 94.

[100] Rybacki, E. and Dresen, G. (2000). Dislocation and diffusion creep of synthetic anorthite aggregates. *Journal of Geophysical Research: Solid Earth*, 105(B11):26017–26036. Cited on page/s 84.

[101] Scholz, C. H. (2019). *The mechanics of earthquakes and faulting*. Cambridge university press. Cited on page/s 93.

[102] Sobolev, S. V. and Muldashev, I. A. (2017). Modeling seismic cycles of great megathrust earthquakes across the scales with focus at postseismic phase. *Geochemistry, Geophysics, Geosystems*, 18:4387–4408. Cited on page/s 80.

[103] Song, J., Mu, X., Li, Z., Wang, C., and Sun, Y. (2012). *A faults identification method using dip guided facet model edge detector*, pages 1–5. Society of Exploration Geophysicists. Cited on page/s 86.

[104] Sternai, P., Avouac, J.-p., Jolivet, L., Faccenna, C., Gerya, T., Wolfgang, T., and Menant, A. (2016). On the influence of the asthenospheric flow on the tectonics and topography at a collision-subduction transition zones : Comparison with the eastern tibetan margin. *Journal of Geodynamics*, 100:184–197. Cited on page/s 87.

[105] Sullivan, C. B. and Kaszynski, A. (2019). PyVista: 3D plotting and mesh analysis through a streamlined interface for the Visualization Toolkit (VTK). *Journal of Open Source Software*, 4(37):1450. Cited on page/s 87.

[106] Tagliasacchi, A., Delame, T., Spagnuolo, M., Amenta, N., and Telea, A. (2016). 3D Skeletons: A State-of-the-Art Report. *Computer Graphics Forum*, 35(2):573–597. Cited on page/s 86.

[107] Tarnowski, J. M., Kyriakopoulos, C., Oglesby, D. D., Cooke, M. L., and Stern, A. (2022). The effects of pre-stress assumptions on dynamic rupture with complex fault geometry in the san gorgonio pass, california, region. *Geosphere*, 18(6):1710–1725. Cited on page/s 80.

[108] Taufiqurrahman, T., Gabriel, A.-A., Li, D., Ulrich, T., Li, B., Carena, S., Verdecchia, A., and Gallovič, F. (2023). Dynamics, interactions and delays of the 2019 Ridgecrest rupture sequence. *Nature*, 618(7964):308–315. Cited on page/s 80, 91.

[109] Tavelli, M., Chiocchetti, S., Romenski, E., Gabriel, A.-A., and Dumbser, M. (2020). Space-time adaptive ADER discontinuous Galerkin schemes for nonlinear hyperelasticity with material failure. *Journal of Computational Physics*, 422:109758. Cited on page/s 80.

[110] Templeton, E. L. and Rice, J. R. (2008). Off-fault plasticity and earthquake rupture dynamics: 1. Dry materials or neglect of fluid pressure changes. *Journal of Geophysical Research: Solid Earth*, 113(B09306). Cited on page/s 92.

[111] Tinti, E., Casarotti, E., Ulrich, T., Taufiqurrahman, T., Li, D., and Gabriel, A.-A. (2021). Constraining families of dynamic models using geological, geodetic and strong ground motion data: the Mw 6.5, October 30th, 2016, Norcia earthquake, Italy. *Earth Planet Sci. Lett.*, 576:117237. Cited on page/s 91.

[112] Ulrich, T., Gabriel, A.-A., Ampuero, J.-P., and Xu, W. (2019). Dynamic viability of the 2016 Mw 7.8 Kaikōura earthquake cascade on weak crustal faults. *Nature Communications*, 10(1):1213. Cited on page/s 91.

[113] Uphoff, C., May, D. A., and Gabriel, A.-A. (2023). A discontinuous Galerkin method for sequences of earthquakes and aseismic slip on multiple faults using unstructured curvilinear grids. *Geophysical Journal International*, 233(1):586–626. Cited on page/s 104.

[114] Uphoff, C., Rettenberger, S., Bader, M., Madden, E., Ulrich, T., Wollherr, S., and Gabriel, A.-A. (2017). Extreme scale multi-physics simulations of the tsunamigenic 2004 Sumatra megathrust earthquake. In *Proceedings of the International Conference for High Performance Computing, networking, Storage and Analysis, SC 2017*. Cited on page/s 91, 95.

[115] Van Bemmel, P. P. and Pepper, R. E. (2000). Seismic signal processing method and apparatus for generating a cube of variance values. US Patent 6,151,555. Cited on page/s 86.

[116] Van Dinther, Y., Gerya, T. V., Dalguer, L. A., Mai, P. M., Morra, G., and Giardini, D. (2013). The seismic cycle at subduction thrusts: Insights from seismo-thermo- mechanical models. *Journal of Geophysical Research: Solid Earth*, 118(12):6183–6202. Cited on page/s 80.

[117] Van Dinther, Y., Mai, P. M., Dalguer, L. A., and Gerya, T. V. (2014). Modeling the seismic cycle in subduction zones: The role and spatiotemporal occurrence of off-megathrust earthquakes. *Geophysical Research Letters*, 41(4):1194–1201. Cited on page/s 80.

[118] van Zelst, I., Rannabauer, L., Gabriel, A. A., and van Dinther, Y. (2022). Earthquake rupture on multiple splay faults and its effect on tsunamis. *Journal of Geophysical Research: Solid Earth*, 127. Cited on page/s 80.

[119] van Zelst, I., Wollherr, S., Gabriel, A. A., Madden, E. H., and van Dinther, Y. (2019). Modeling Megathrust Earthquakes Across Scales: One-way Coupling From Geodynamics and Seismic Cycles to Dynamic Rupture. *Journal of Geophysical Research: Solid Earth*, 124(11):11414–11446. Cited on page/s 80, 103.

[120] Wahr, J. and Wyss, M. (1980). Interpretation of postseismic deformation with a viscoelastic relaxation model. *Journal of Geophysical Research*, 85(B11):6471–6477. Cited on page/s 80.

[121] Wang, T. A., Dunham, E. M., Krenz, L., Abrahams, L. S., Segall, P., and Yoder, M. R. (2024). Dynamic rupture simulations of caldera collapse earthquakes: Effects of wave radiation, magma viscosity, and evidence of complex nucleation at kilauea 2018. *Journal of Geophysical Research: Solid Earth*, 129(4):e2023JB028280. Cited on page/s 91.

[122] Wang, Y., Ouillon, G., Woessner, J., Sornette, D., and Husen, S. (2013). Automatic reconstruction of fault networks from seismicity catalogs including location uncertainty. *Journal of Geophysical Research: Solid Earth*, 118(11):5956–5975. Cited on page/s 86.

[123] Wells, D. L. and Coppersmith, K. J. (1994). New empical relationship between magnitude, rupture length, rupture width, rupture area, and surface displacement. *Bulletin of the Seismological Society of America*, 84(4):974–1002. Cited on page/s 113.

[124] Wirp, A. S., Gabriel, A.-A., Schmeller, M., Madden, E. H., van Zelst, I., Krenz, L., van Dinther, Y., and Rannabauer, L. (2021). 3D Linked Subduction, Dynamic Rupture, Tsunami, and Inundation Modeling: Dynamic Effects of Supershear and Tsunami Earthquakes, Hypocenter Location, and Shallow Fault Slip. *Frontiers in Earth Science*, 9(June). Cited on page/s 80, 81.

[125] Wollherr, S., Gabriel, A.-A., and Uphoff, C. (2018). Off-fault plasticity in three-dimensional dynamic rupture simulations using a modal Discontinuous Galerkin method on unstructured meshes: Implementation, verification and application. *Geophysical Journal International*, 214(3):1556–1584. Cited on page/s 94.

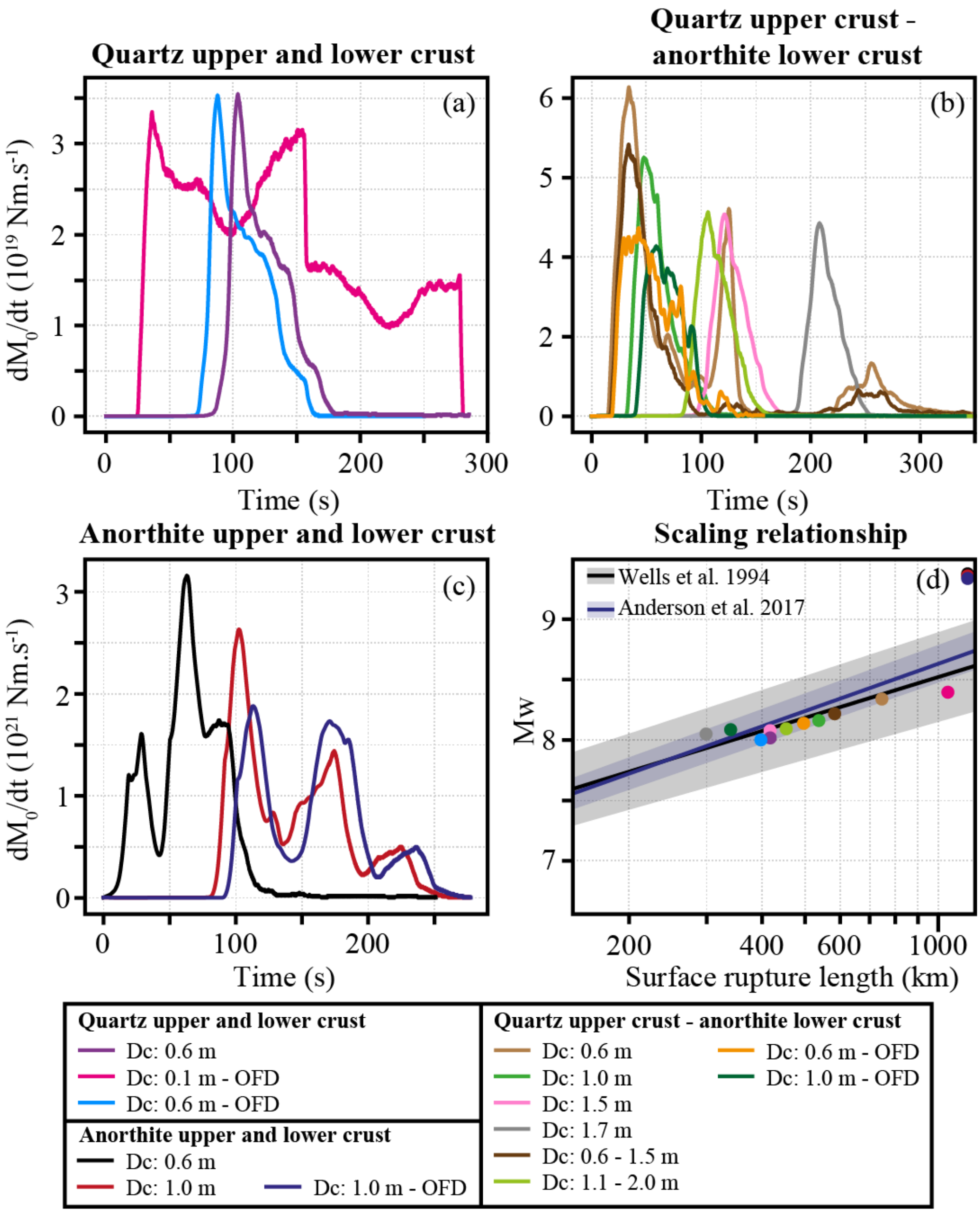

FIGURE 4.9. (a,b,c) Moment release rate dM_0/dt of the earthquake dynamic rupture simulations for (a) the single-layer quartz upper and lower crust models, (b) the two-layer quartz upper crust and anorthite lower crust models, (c) the single-layer anorthite upper and lower crust models. (d) Scaling relationship between the surface rupture length and the magnitude M_w. The colored dots show our experiments and the black and blue lines show the empirical scaling relationships for strike-slip faults from Wells *et al.* [123] and Anderson *et al.* [3], respectively.

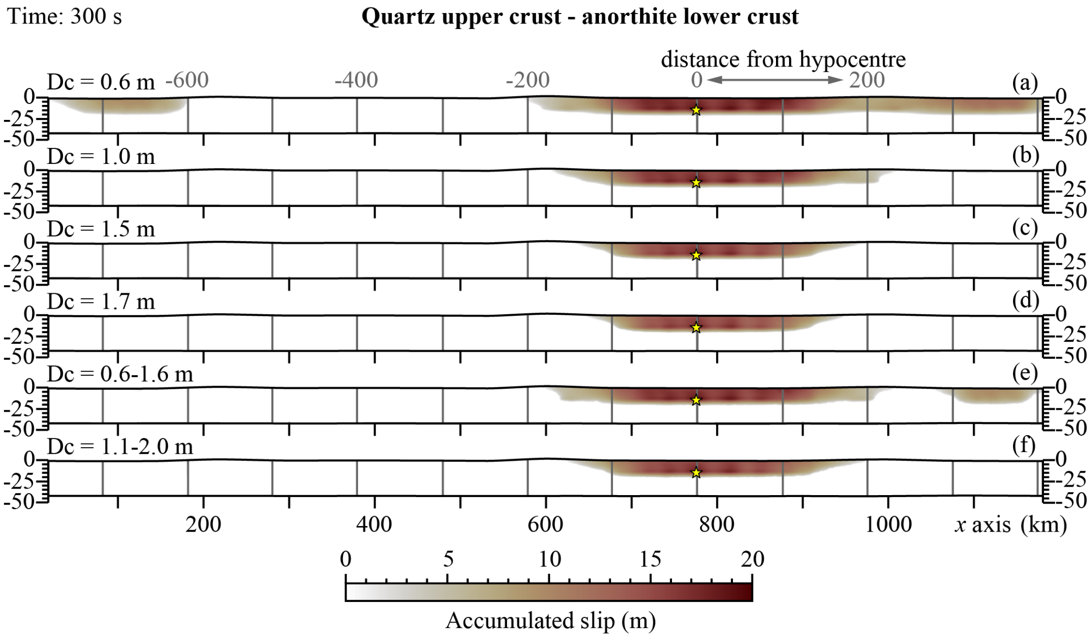

FIGURE 4.10. Fault slip for the simulated earthquakes with D_c variations on the fault extracted from the two-layers-crust model with a quartz upper crust and anorthite lower crust. Elastic 3D dynamic rupture simulations without off-fault plasticity. (a) M1: $D_c = 0.6$ m. (b) M2: $D_c = 1$ m. (c) M3: $D_c = 1.5$ m. (d) M4: $D_c = 1.7$ m. (e) M5: $D_c \in [0.6, 1.6]$ m with fractal hierarchical patches. (f) M6: $D_c \in [1.1, 2]$ m with fractal hierarchical patches.

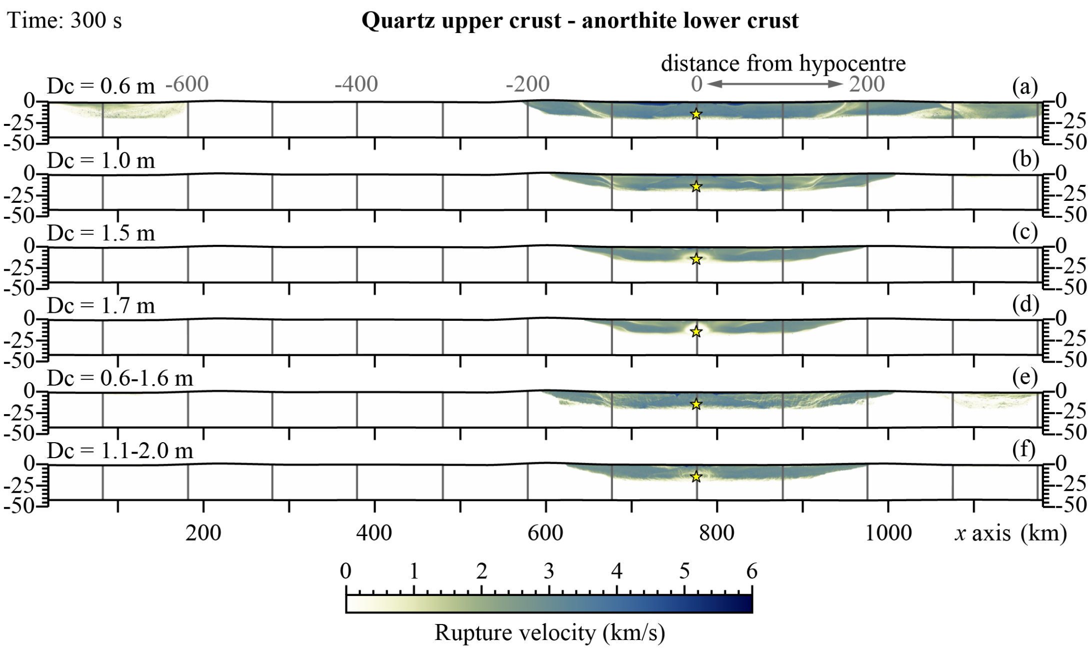

FIGURE 4.11. Rupture velocity for the simulated earthquakes with D_c variations on the fault extracted from the two-layers-crust model with a quartz upper crust and anorthite lower crust. Elastic 3D dynamic rupture simulations without off-fault plasticity. (a) M1: $D_c = 0.6$ m. (b) M2: $D_c = 1$ m. (c) M3: $D_c = 1.5$ m. (d) M4: $D_c = 1.7$ m. (e) M5: $D_c \in [0.6, 1.6]$ m in fractal hierarchical patches. (f) M6: $D_c \in [1.1, 2]$ m in fractal hierarchical patches.

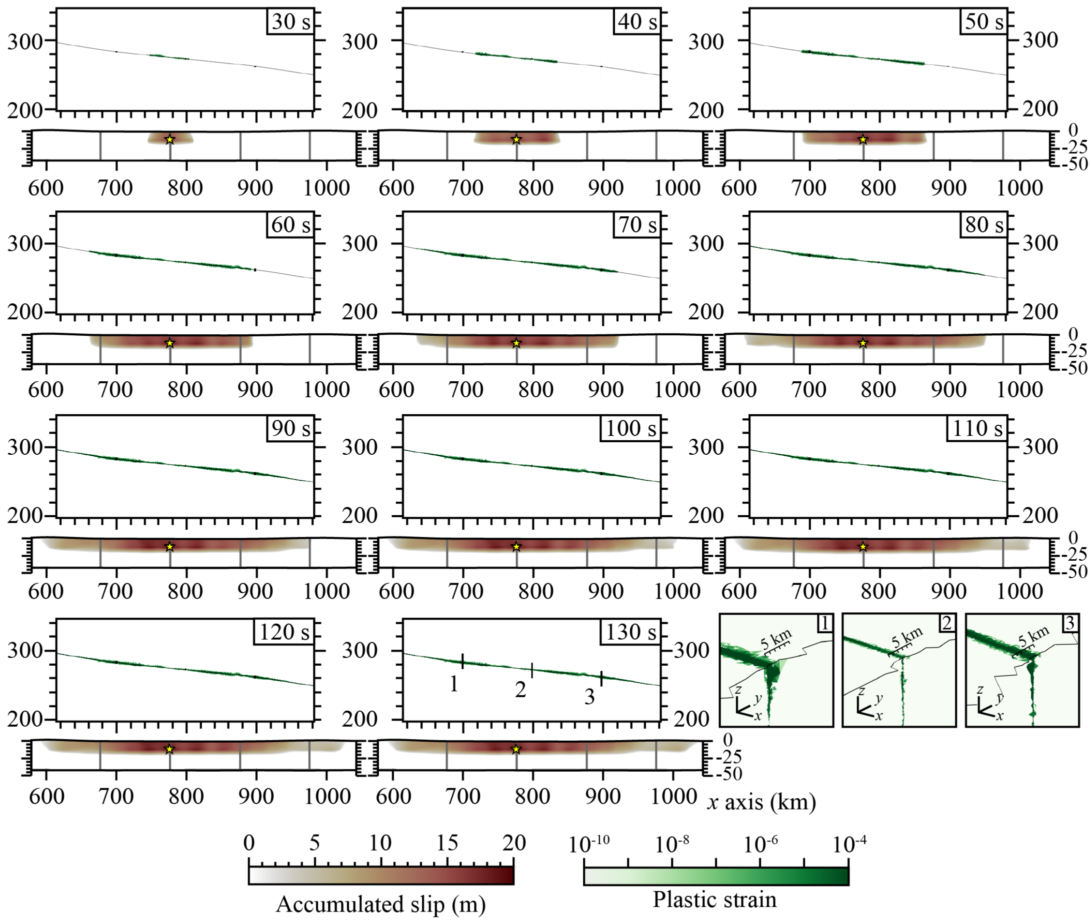

FIGURE 4.12. Evolution of the on-fault accumulated slip and off-fault plastic strain for $D_c = 0.6$ m in the model with a quartz upper crust and an anorthite lower crust. The trace of the fault (thin black line) is represented in map view with the accumulated plastic strain. The three zoomed cross-sections (1, 2, 3) are indicated on the map. Below the map view, a zoom of the fault's surface between $x \approx 600$ km and $x \approx 1000$ km shows the accumulated slip at the given time. The vertical grey lines are spaced every 100 km starting from the hypocenter. The length scale between the map and the fault's surface are the same.

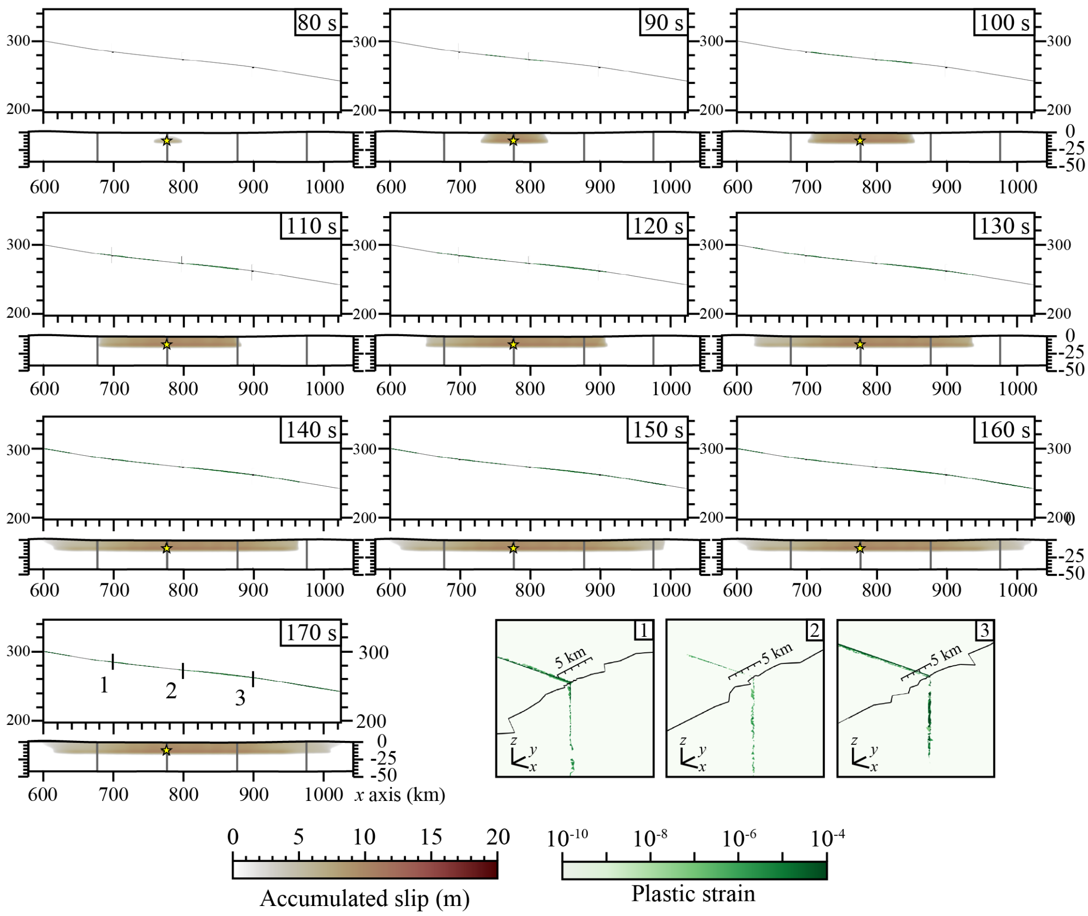

FIGURE 4.13. Evolution of the on-fault accumulated slip and off-fault plastic strain for $D_c = 0.6$ m in the model with a quartz upper crust and lower crust. The trace of the fault (thin black line) is represented in map view with the accumulated plastic strain. The three zoomed cross-sections (1, 2, 3) are indicated on the map. Below the map view, a zoom of the fault's surface between $x \approx 600$ km and $x \approx 1000$ km shows the accumulated slip at the given time. The vertical grey lines are spaced every 100 km starting from the hypocenter. The length scale between the map and the fault's surface are the same.

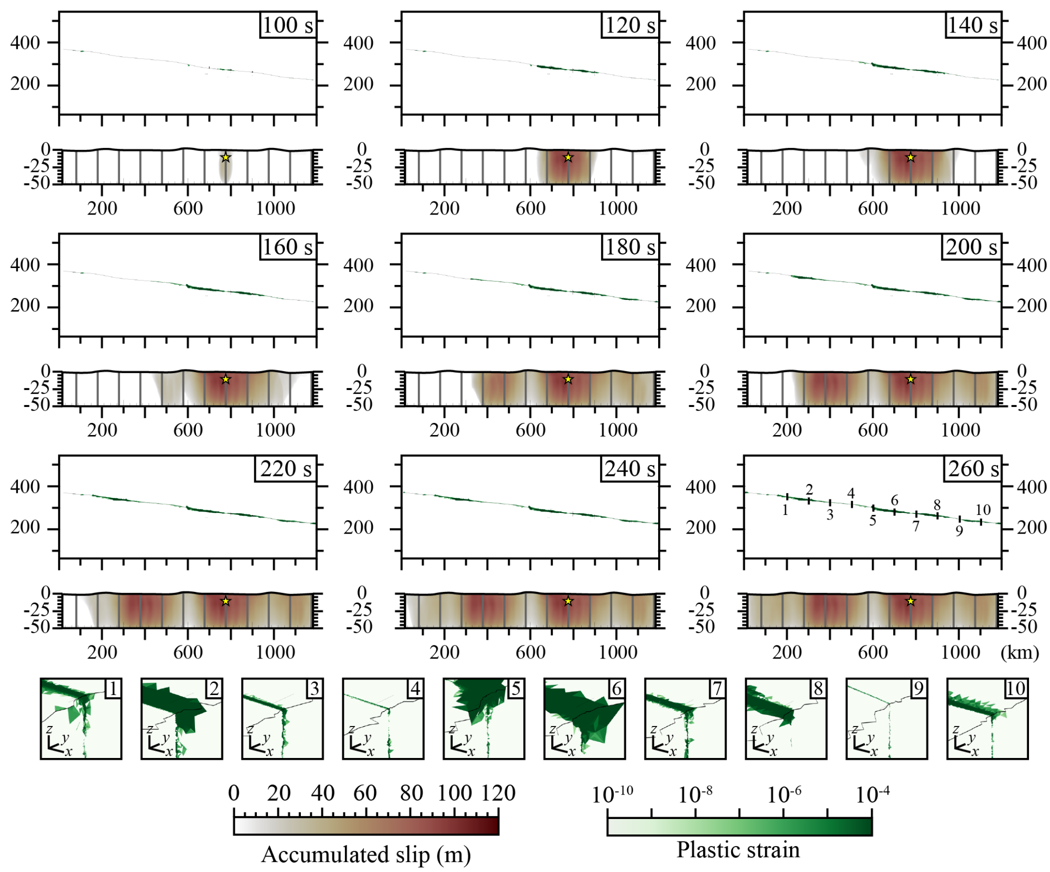

FIGURE 4.14. Evolution of the on-fault accumulated slip and off-fault plastic strain for $D_c = 1$ m in the model with an anorthite upper crust and lower crust. The trace of the fault (thin black line) is represented in map view with the accumulated plastic strain. The ten zoomed cross-sections (1-10) are indicated on the map. Below the map view, a zoom of the fault's surface between $x \approx 600$ km and $x \approx 1000$ km shows the accumulated slip at the given time. The vertical grey lines are spaced every 100 km starting from the hypocenter. The length scales of the map and the fault's surface are the same, but the fault's surface is vertically exaggerated by a factor of 3.3.

Part III

Observational Global Geodynamics

Chapter 5

Continent-scale Hiatus Maps for the Atlantic Realm and Australia since the Upper Jurassic and links to mantle flow induced dynamic topography

by Hayek J.N., Vilacís B., Bunge H.-P., Friedrich A.M., Carena S. and Vibe Y. (2020). Published in Proceedings of the Royal Society A. 4762020039020200390. DOI: 10.1098/rspa.2020.0390. This chapter also includes the paper correction (2021), published in Proc. R. Soc. A. 4772021043720210437. DOI: 10.1098/rspa.2021.0437

Abstract

Interregional geological maps hold important information for geodynamic models. Here we use such maps to visualize major conformable and unconformable contacts at interregional scales and at the level of geologic series from the Upper Jurassic onward across North and South America, Europe, Africa and Australia. We extract hiatus information from these paleogeological maps, which we plot in a paleogeographical reference frame to link the maps to the plate and plume modes of mantle convection. We assume that interregional patterns of hiatus surfaces are proxy records of continent-scale mantle-induced vertical motion of the lithosphere. We find significant differences in the distribution of hiatus across and between continents at the timescale of geologic series, that is ten to a few tens of millions of years (Myrs). This is smaller than the mantle transit time, which, as the timescale of convection, is about 100-200 Myrs. Our results imply that different timescales for convection and topography in convective support must be an integral component of time-dependent geodynamic Earth models, consistent with the presence of a weaker upper mantle relative to the lower mantle. Additional geological constraints together with interregional geological maps at the resolution of stages (1-2 Myrs), are needed to assist in future geodynamic interpretations of interregional geologic hiatus.

5.1 Introduction

An early success in geodynamics was the quantitative description of mantle convection by a boundary-layer model of high Rayleigh number and low Reynolds number flow [142]. The model came into its own when mantle convection was explored explicitly in terms of the plate and plume mode (e.g., Davies[40],[41], Davies and Richards[42]). The former is associated with the cold upper thermal boundary layer, which is the lithosphere, and the latter with the hot lower thermal boundary layer, which sources plumes.

The plate mode has since then been mapped by kinematic models of lithosphere motion for the Cenozoic[56] and Mesozoic (e.g., Müller et al.[102]). Its temporal evolution has been linked to the generation of large-scale mantle heterogeneity through the history of subduction[85,114] and assimilated into global mantle convection simulations[9,15,93] to construct mantle circulation models, which from here on we will call MCM. Recently, the plume mode has been imaged by seismic tomography as localised upwellings that rise from the core-mantle boundary (CMB) to the base of the lithosphere[49,103,116], and the boundary-layer nature of mantle convection is now widely recognized.

Geodynamicists also understood early on that mantle convection deflects the Earth's surface away from its isostatically compensated state[107]. Termed "dynamic topography" by Hager et al.[63] the deflections are receiving renewed attention (e.g., Braun[10]), particularly as an agent in passive margin environments[12], where the proximity to a base-level allows one to gauge topographic changes better than at other places.

The boundary-layer interpretation of mantle flow makes it convenient to interpret the sedimentary expression of dynamic topography explicitly in terms of the plate and plume modes. For the plate mode, the approach was pioneered using the sedimentary record from the *Cretaceous Interior Seaway* and the cratonic interior of North America (e.g., Burgess et al.[16], Mitrovica et al.[96]) because surface depressions induced by mantle downwellings in these regions left accommodation space to preserve a sedimentary archive. Other regions, such as the Cretaceous Eromanga Sea in Australia[61,64] and a regional unconformity of Cretaceous-Eocene age in southeast Asia[23] also record plate-mode-related vertical motion. Recently, MCMs have modelled the evolution of plate-mode-related dynamic topography since the Cretaceous[100].

It is more difficult to map the stratigraphic expression of the plume mode because the positive surface deflections create erosional/non-depositional environments, which leave time gaps in the sedimentary record. Field observations of the surface expression of the plume mode document changes in drainage patterns (e.g., Cox[34]) and a dome-shaped uplift of 1-2 km (e.g., Şengör[36], Rainbird and Ernst[109], Saunders et al.[123]) over a radius of 1000-2000 km. The resulting discontinuity surfaces in the sedimentary record are known as unconformities (e.g., Miall[95]), although their wavelengths are so large and their amplitudes so little that at large distances an unconformity may locally be recorded as a disconformity. They preserve time missing (hiatus) from the geological record[51]. To this end, an approach of hiatus-area mapping was introduced[50,51] to highlight the long wavelength nature of sedimentation records as explored by Sloss[130,131]. It visualizes interregional-scale unconformities because, at continental scales, what is normally perceived as a lack of data (material eroded or not deposited) becomes part of the dynamic topography signal. The method has been applied to map the temporal and spatial patterns of conformable and unconformable geological contacts across Europe[145] and Africa[21].

Continent-scale geological maps, such as the 1:5 Million International Geological Map of Europe and Adjacent Areas (IGME 5000)[1], are crucial databases to reveal hiatus area of geodynamic origin, that is falcogeny in the sense of Şengör[37]. They provide internally consistent compilations of geological observations, including chronostratigraphic age, lithology, and geolocalization of the strata, at the scale of thousands of kilometres. This links them naturally to continent-scale elevation changes induced by mantle flow. Here we explore interregional-scale geological maps. We identify temporal and spatial patterns of geological hiatus contacts across North and South America, Europe, Africa and Australia, under the assumption that interregional-scale conformable and unconformable contacts are proxy records of paleotopography and vertical motion. We organize our paper as follows: first, we explain our hiatus mapping method. Then we present results starting from hiatus maps for the Upper Jurassic. We find significant differences in the spatial extent of hiatus area across and between continents at the timescale of geologic series, ten to a few tens of millions of years (Myrs), which is considerably smaller than the mantle transit time [70]. We note that this negates the concepts of Stille [136,137] and Sloss [130], who argued for global synchronicity cycles. Finally, we discuss our results, place them into a geodynamic context, explore their implications for dynamic Earth models, and draw conclusions.

5.2 Data Compilation, Preparation, and Uncertainties

We mapped conformable and unconformable contacts at the resolution of geological series because this is the most frequently adopted temporal resolution among interregional geologic maps [50]. We also opted to map hiatus from the Upper Jurassic onward, to remain within a timescale comparable to the mantle transit time, which is about 100-200 Myrs [70]. To this end, we took the digital vector maps of Europe, Australia, and North America, which describe the chronostratigraphic units within specific temporal and spatial resolutions. For South America, we compiled individual country-scale information, since only this was available at the temporal resolution of series.
Diverse Open-Access Databases [1,22,35,53,62,71,76,86,89,111,127,128] provide digital information from geological maps as vector files. Some maps include information from the continental shelf and other seafloor features. We did not use this information because it also includes magnetic isochron data, which is not related to the sedimentation paleoenvironment. However, oceanic pointwise information in the form of localized stratigraphic columns from the ocean drilling program (ODP) can record oceanic hiatus events. For this reason, we imported offshore data from ODP [104] Legs 100-190 and DSDP [43] Legs 1-95. Additionally, we used [21] for the Cenozoic series of Africa augmented by further information for the Upper and Lower Cretaceous. Table 5.1 summarizes our compilation of geological information. The geological maps published at continent and country-scale vary both in spatial and temporal resolution. Some maps are resolved at the series level. Others provide finer or coarser geological time intervals, such as combinations of series, stages, or systems, as defined in the chronostratigraphic chart [26,105]. For instance, the map may state *Paleogene* for the units shown. Thus time resolution falls within three categories: series, series/stages/systems mix, and systems. The maps moreover use distinct naming conventions for age descriptions, including different abbreviations, languages, and aggregations of time units. To handle the diversity, we adopted a standardization procedure and harmonized the time resolution among the maps. We saturated all subseries information to the series level and brought the geological unit conventions to a standard

reference. This translates languages, abbreviations, and combinations or ranges of geological units to the numerical value of geological time. For instance, a polygon defined as *Oligocene-Miocene* or *Chattian-Langhian* time has the same time range after the standardization and spans two series (~30 Myrs). For polygons with systems resolution we assigned the hiatus information to the base of the polygon's age range. For South America our procedure brought the country-specific maps to a unified continent-scale format. An exception had to be made for Argentina, where the temporal resolution was available only at the systems level.

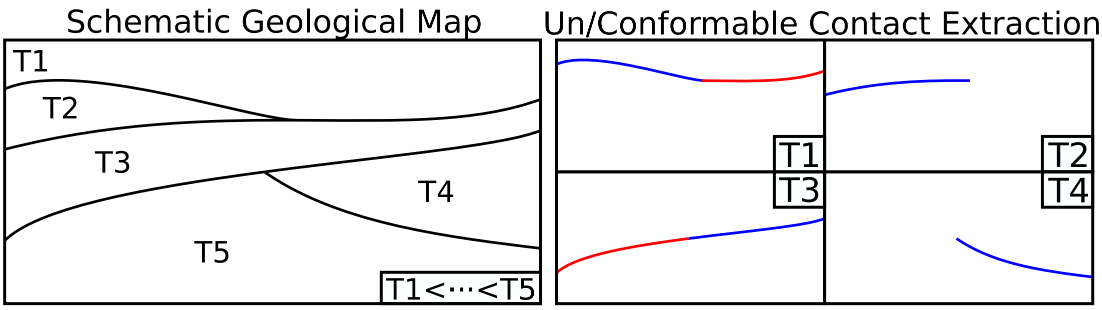

FIGURE 5.2. **(Left)**: Schematic geological map for five consecutive chronostratigraphic units (T1 to T5) with T1 youngest and T5 oldest. **(Right)**: Schematic showing the extraction of un/conformable contacts for a target unit. Conformable lines for the target unit are the contours of the preceding unit. Unconformable contacts contour the contact of the unit with units older than the immediately preceding one.

Following Carena et al.[21] we define *conformity* if a target series sits atop the one immediately preceding it in the chronostratigraphic chart, regardless of whether either series has missing stages. We define *unconformity* as the complementary state to *conformity*. This holds for any place where one or more series immediately preceding the target series are missing. The definitions apply regardless of the physical contact type between both **rock** units. Figure 5.1 and Figure 5.2 provide a schematic illustration of hiatus and the extraction process for un/conformable contacts[50]. To delimit hiatus for a given series we also include in the maps any occurrence of the immediately preceding series and categorize the signal as conformable.

Since the temporal resolution is restricted to the series level, the un/conformity represents a time span that varies for different series. For instance, unconformity at the base of the Miocene datum is at least 11 Myrs, because this is the duration of the Oligocene series. Unconformity at the base of the Paleocene datum lasts a minimum of 34 Myrs, which is the duration of the Upper Cretaceous series. We note, however, that the hiatus duration could be longer for either case. In the former, rocks of Lower and Middle Miocene and/or Upper and Middle Eocene could be missing. In the latter, rocks of Lower and Middle Paleocene and/or Lower Cretaceous could be absent. The uncertainty of a hiatus transforms into a spatial uncertainty when plate motions are taken into account. If we take the current global root mean square (RMS) plate velocity of 5 cm/yr[44] as a representative value, temporal uncertainty for a hiatus at the series level (10-30 Myrs) translates into a minimum spatial uncertainty of 500-1500 km. Moreover, by saturating temporal resolution to the series level, we underestimate the total amount of hiatus because unconformities and hiatus at

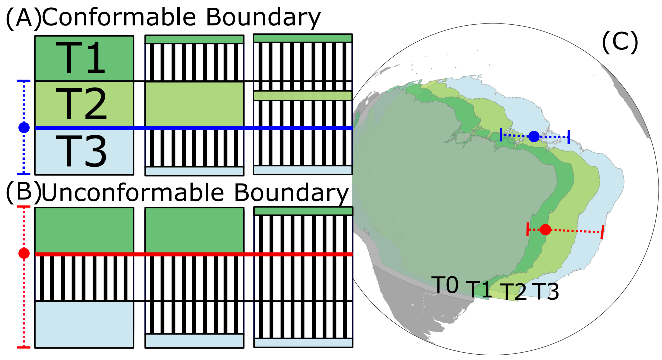

FIGURE 5.3. Schematic illustration of the temporal and spatial uncertainty of hiatus mapping[21,50,51,145]. **(A)** and **(B)** show conformable and unconformable contacts, respectively. **(C)** displays how temporal uncertainty translates into spatial uncertainty for the paleogeographical reconstruction representing hiatus.

the resolution of stages may be masked at the stratigraphic resolution of series. Figure 5.3 illustrates these uncertainties.

Region		Temporal resolution	Spatial resolution	Reference
Australia		Series and Stages	1:1 Million	Geoscience Australia[111]
Europe		Series	1:5 Million	BGR[1]
North America		Series and Stages	1:5 Million	USGS[53]
South America	Argentina	Systems	1:2.5 Million	SEGEMAR[127]
	Bolivia	Series	1:1 Million	SERGEOTECMIN[22]
	Brazil	Series	1: 250 000	CPRM[35]
	Chile	Stages	1:1 Million	SERNAGEOMIN[128]
	Colombia	Stages	1:1 Million	SGC[76]
	Ecuador	Series	1:100 000	MAGAP[89]
	Peru	Stages	1:100 000	INGEMMNET[71]
	Uruguay	Series	1:500 000	MIEM[86]
	Venezuela	Series	1:500 000	USGS[62]
Africa		Series and Systems	1 : 5 Million *	[21]
Ocean Drilling Projects		Series	-	[43,104]

TABLE 5.1. Geological maps used in this work with their respective spatial and temporal resolution. Compilations performed at the country level for South America (see text). * Africa hiatus information taken from[21] with hiatus information added for Upper and Lower Cretaceous. Offshore data imported from ODP[104] Legs 100-190 and DSDP[43] Legs 1-95 as pointwise signal.

5.3 RESULTS

5.3.1 *Geological Hiatus Maps*

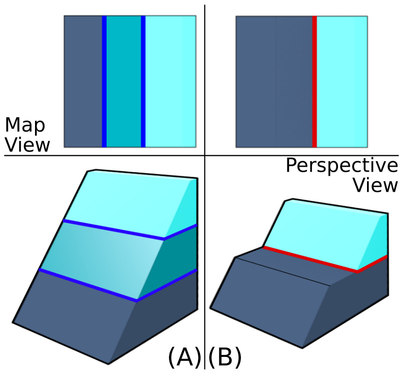

Figure 5.1. **(Left)**: Schematic map (top) and perspective view (bottom) of geological units in conformable contact (blue lines). **(Right)**: Same scheme showing an unconformable contact (red line), where the middle unit is missing, representing a gap (hiatus) in the geologic record.

Figure 5.4 shows hiatus mapped with our method for North and South America, Europe, Africa, and Australia for eight geologic series. This yields a set of eight **Geological Hiatus Maps (GHMs)**, beginning with the Lower Cretaceous (i.e., hiatus here meaning that the Upper Jurassic is missing). We use *pyGPlates*[99] to reconstruct each hiatus to its past tectonic setting with a global Mesozoic-Cenozoic plate motion model[102] tied to a reference frame of Indo-Atlantic hotspots[18,106] and present the extracted signal in a plate tectonic configuration corresponding to the base of each series. Red and blue colours depict un/conformable contacts, respectively. Blank regions indicate the absence of the considered series and its immediately preceding unit.

In the following, we describe the results for each GHM. **Base of Pleistocene** datum, Figure 5.4(A), presents North and South America, Greenland, and Australia with predominantly unconformable contacts. Conformable contacts exist in the High Plains of North America, parts of South America, and the Australian *Nullarbor Plain*. Europe is dominated by conformable contacts. Africa shows a mix of un/conformable contacts, with conformable contacts located in the northwest and in the Kalahari and Congo Basins. Unconformable contacts extend through the East African Highlands and the Sahara desert. **Base of Pliocene** datum, Figure 5.4(B), exposes conformable contacts in North and South America, around the Gulf of Mexico, the *Basin and Range*, the *Rocky Mountains* front, the Brazilian Highlands and the western Amazon Basin. Australia shows sparse conformable contacts throughout the continent and isolated unconformable contacts in the north and in the southeast. Conformable contacts cover eastern Europe and the Iberian Peninsula, while unconformable contacts prevail in western/central Europe and in tectonically active regions in the Mediterranean. Africa exhibits unconformable contacts in the Congo Basin and the Canary-Atlas region, while conformable contacts occur in the Kalahari Basin, the Afar region, and the northern edges of the continent. **Base of Miocene** datum, Figure 5.4(C), is dominated by unconformable contacts across the continents. Unconformable contacts abound in the western part of North America, Brazil, and much of Europe, whereas isolated hiatuses exist in Australia and Africa. Conformable contacts are exposed in Greenland, western and easternmost Europe and the Kalahari Basin. **Base of Oligocene** datum, Figure 5.4(D), exposes conformable contacts in many regions, with a striking absence of signal across South America. Unconformable contacts are mapped in the western parts of North America, the Afar region and in Europe. **Base of Eocene** datum, Figure 5.4(E), features a mix of signals. Unconformable contacts exist in eastern Africa, Europe, and the western parts of North America adjacent to conformable contacts in the plains of Canada. South America lacks information except for conformable contacts in the eastern Amazon. Africa reveals conformable contacts in its northern parts and the Kalahari Basin, but signal is absent in the central and southern parts of

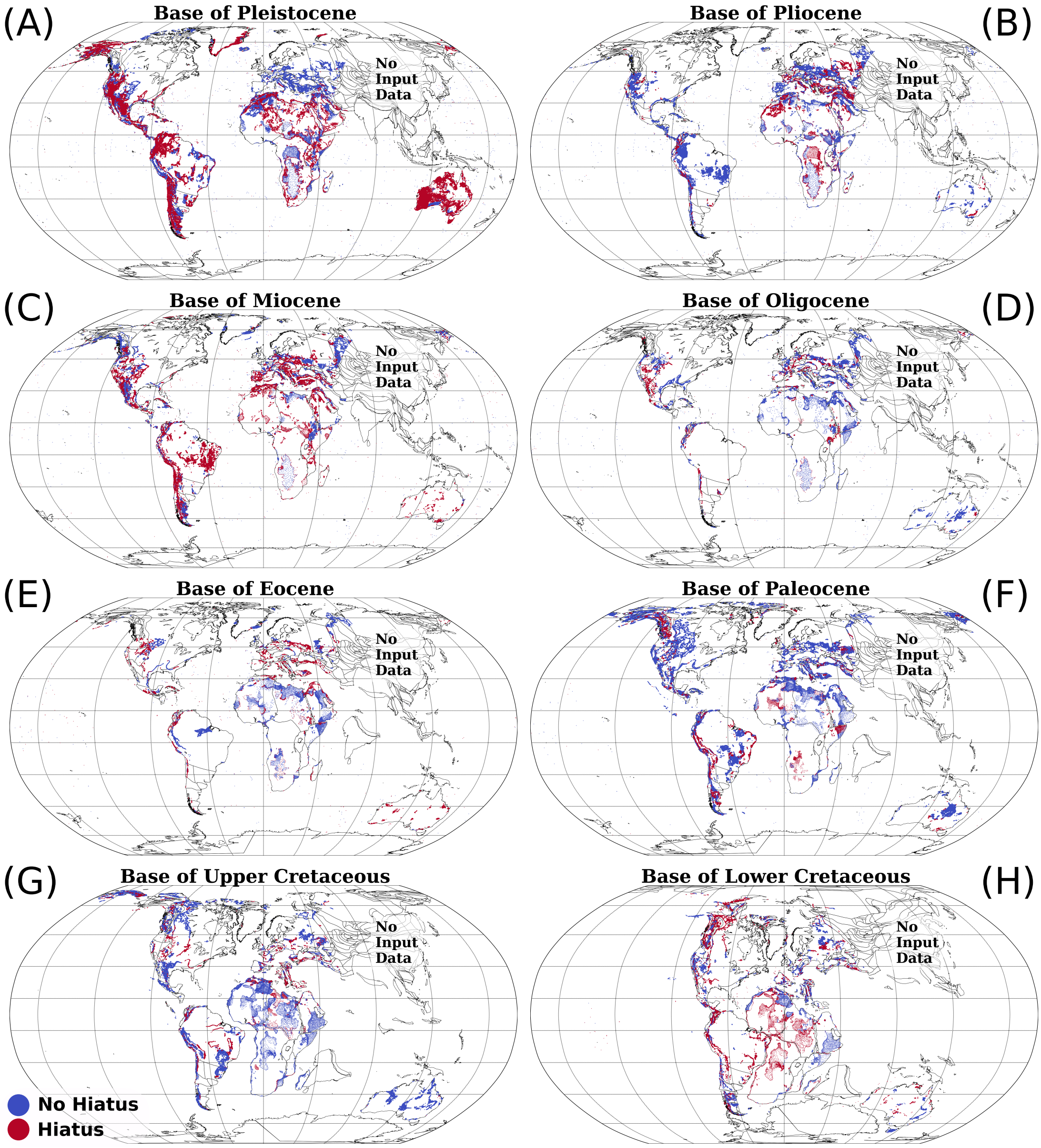

Figure 5.4. Geological Hiatus Maps (GHMs) at chronostratigraphic division of series [26] from the Base of Pleistocene datum to the Base of Lower Cretaceous datum **(A)-(H)** reconstructed paleogeographically with a global Mesozoic-Cenozoic plate motion model [102] tied to a reference frame of Indo-Atlantic hotspots [106] and shown in a plate tectonic configuration corresponding to the base of each series. Red/blue points represent un/conformable contacts, respectively. Blank regions indicate absence of considered series and its immediately preceding unit. See text for further information.

the continent. Scattered unconformable contacts are mapped across Australia. **Base of Paleocene** datum, Figure 5.4(F), reveals abundant conformable contacts across North and South America, Europe, North Africa, and Australia. Unconformable contacts are located in the northwestern part of North America and Greenland. South America exposes unconformable contacts along the Andes and the east coast of Brazil. Africa shows clusters of unconformable contacts in the Kalahari Basin, the northern Djoue Basin, and the Afar region. Unconformable contacts are mapped in southern Australia near Tasmania. **Base of Upper Cretaceous** datum, Figure 5.4(G), is characterized by unconformable contacts, which prevail across Europe, and the western parts of North America. Conformable contacts are mapped in Canada, Mexico, Africa, the Parana region of South America, and Australia. Finally, **Base of Lower Cretaceous** datum, Figure 5.4(H), exhibits a mix of un/conformable contacts. Most notable are unconformable contacts in Alaska and Africa as well as a lack of signal throughout much of South America. We point out that the absence of Mesozoic/Cenozoic strata across much of Scandinavia and the cratonic part of North America precludes hiatus mapping for the Mesozoic/Cenozoic series in these regions.

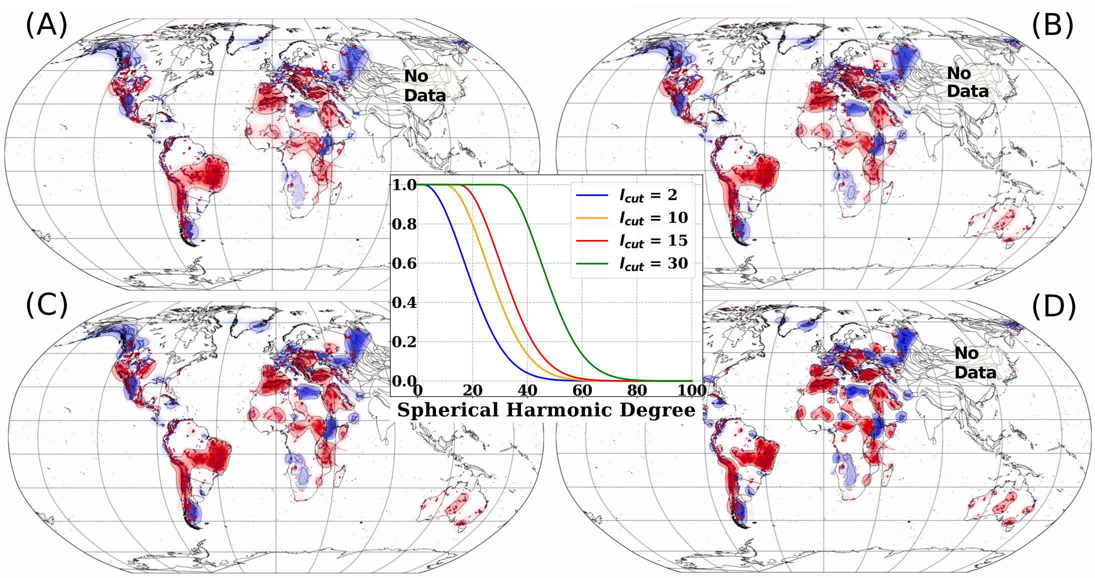

FIGURE 5.5. Base of Miocene Hiatus Surface (BHS) obtained by expanding the Miocene Geological Hiatus Map (GHM) (Figure 5.4 C) in fully normalized[134] spherical harmonics (SH) and convolving with a Gaussian taper at four different cut off values for degree 2 **(A)**, 10 **(B)**, 15 **(C)**, and 30 **(D)**, respectively. Red/blue areas represent un/conformable surfaces. Black dotted lines contour the SH signal at the ± 0.1 amplitude. Hiatus data from the input GHM shown as blue/red dots. Center plot: four Gaussian tapers applied in the SH expansion, see text.

5.3.2 *Base Hiatus Surfaces*

The GHMs allow us to perform a spherical harmonics expansion of the hiatus signal to create **Base Hiatus Surface (BHS)**. We adopted *pyshtools*[148] with fully normalized spherical harmonic coefficients[134], using a global equidistant grid of 720/1440 points in latitude/longitude for a resolution of ≈ 30 km between grid nodes. Numerical values of 1/-1 were assigned to un/conformable signal, respectively. Each grid node was then initialized with the nearest hiatus value that falls within a radius of 1/2 of the grid node distance. Otherwise, the grid node value was set to zero.

We performed the expansion up to spherical harmonic degree 100. However, our assumption of a geodynamic origin for interregional-scale hiatus implies the choice of a spectral window that one should consider in the **BHS** representations. Longstanding arguments based on dynamic models of the Geoid suggest a dominant contribution to dynamic topography of spherical harmonic degree 2[115]. The dominance of the longest wavelength components for convectively maintained topography was challenged recently by an observational database of >2000 spot measurements of residual bathymetry in the oceanic realm[66]. The latter suggests that contributions up to and including degree 30 are required to represent topography in convective support. Figure 5.5 illustrates the difference and reports **BHS** for the Base of Miocene datum for four cut off degrees (2, 10, 15, and 30) and a tapered Gaussian smoothing to the spectral coefficients. The taper width of 40 degrees allows the contribution of spectral components beyond the cut off. For the long-wavelength cut off at degree 2 there remains a 30% contribution of the original signal at degree 27, while the degree 30 cut off maintains 30% of the original signal up to degree 55. We report **BHS** starting with the Lower Cretaceous and assuming an intermediate cut off at degree 15 in Figure 5.6.

The **BHS** provides information on the temporal evolution in the ratio of the area of conformal surface relative to the total area of conformal and unconformal surface. The latter can be plotted both aggregated over all continents and separate for each. The aggregated curve (Figure 5.7) achieves a maximum in the ratio of conformable surface relative to the total area of conformable and unconformable surface at the Base of Paleocene and the Base of Upper Cretaceous (corresponding to topography of the Upper and Lower Cretaceous). There are also two prominent maxima in the ratio of the area of unconformable surface relative to the total area of conformable and unconformable surface at the Base of Miocene and the Base of Pleistocene, respectively. The curves for individual continents (Figure 5.8) are more variable. They reveal considerable differences between continents and series.

5.4 DISCUSSION

Geodynamicists have long recognised the essential role of dynamic topography in studies of the Geoid because the mass anomalies associated with surface deflections yield gravity anomalies of comparable amplitude to the flow-inducing mantle density variations. Geoid models therefore account for dynamic topography as well as mantle density heterogeneity (e.g., Forte and Peltier[48], Ricard et al.[113], Richards and Hager[115]). However, it is difficult to separate dynamic topography from

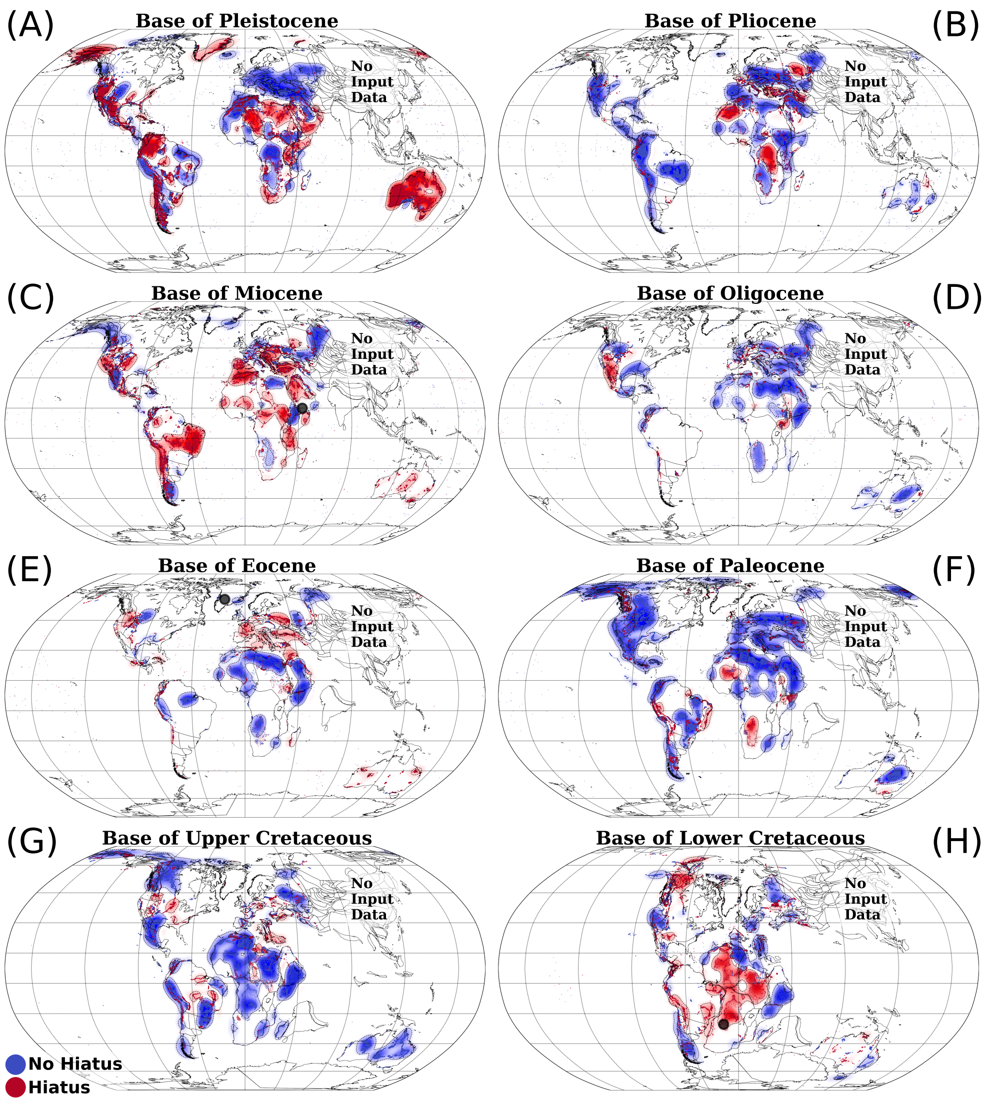

Figure 5.6. Base Hiatus Surface (BHS) obtained by expanding the Geological Hiatus Maps (GHMs) (Figure 5.4) in fully normalized[134] spherical harmonics (SH) and convolving with a Gaussian taper starting at degree 15 (compare Figure 5.5). BHS shown at chronostratigraphic division of series[26] from the Base of Pleistocene to the Base of Lower Cretaceous **(A)-(H)** reconstructed paleogeographically with a global Mesozoic-Cenozoic plate motion model[102] tied to a reference frame of Indo-Atlantic hotspots[106] and placed into a plate tectonic configuration corresponding to the base of each series. Blue/red colours represent no-/hiatus surfaces, indicative of low/high topography in the preceding series, respectively. Black dotted lines contour the SH signal at the ± 0.1 amplitude. Hiatus data from the input GHMs shown as blue/red dots. Black circles at Base of Miocene **(C)**, Base of Eocene **(E)** and Base of Lower Cretaceous **(G)** maps correspond to location of flood basalts associated with Afar, Iceland and Tristan hotspots[33]. Blank regions indicate absence of series and its immediately preceding unit, suggesting long hiatus duration. See text for further information.

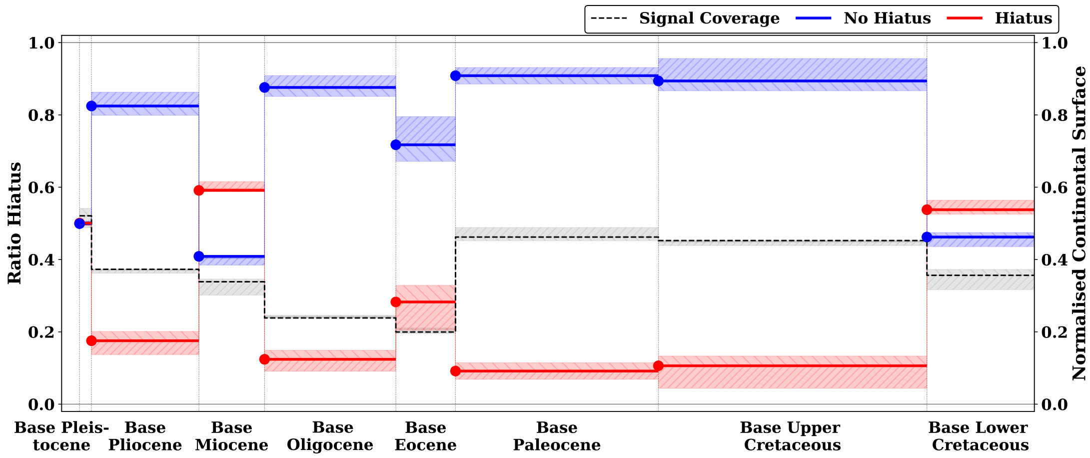

FIGURE 5.7. Ratio of the area of un/conformal (solid red/blue lines) surface relative to the total area of conformal and unconformal surface aggregated over North/South America, Europe, Africa and Australia from the Base of Lower Cretaceous to the Base of Pleistocene, indicative of mean relative elevation (blue=low, red=high) across the continents in the preceding series (see text). The spherical harmonics (SH) area of conformal and unconformable surface is taken within the amplitude range (≥ 0.1) for a tapered cut off at degree 15 (see Figure 5.6). The // and \\ shaded envelopes represent the ratio variations that correspond to tapered cut offs in the SH surface at degree 2 and 30, respectively (compare Figure 5.5). A maximum in the ratio of conformable surface at the Base of Paleocene and Base of Upper Cretaceous (corresponding to mean topography in the Upper and Lower Cretaceous) relative to the total area of conformal and unconformal surface agrees with global sea-level curves (e.g., Müller et al.[101], Rowley[119]). Two maxima in the ratio of unconformable surface relative to the total area of conformal and unconformal surface at the Base of Miocene and the Base of Pleistocene coincide with the onset of glaciation in Antarctica[108] and the Northern Hemisphere[90], respectively (see text). The total area (within the amplitude range (≥ 0.1) for a tapered cut off at degree 15) of conformal and unconformal surface relative to the total area of the considered continents is shown by the grey curve. The grey hatched // and \\ shaded envelopes represent the ratio variations that correspond to tapered cut offs in the SH area at degree 2 and 30, respectively.

topography in isostatic support[47,75,110] outside the oceanic realm[66]. This has led some to doubt the existence of dynamic topography[97].

The transient nature of dynamic topography suggests to overcome this difficulty by turning to geologic archives. Ahead of his time, Bond[7,8] analysed continent-scale sediment distributions to argue for substantial uplift of continental platforms. He concluded that Africa, for instance, experienced late Tertiary uplift relative to other continents[6], in agreement with Burke and Whiteman[19]. Our interregional hiatus maps also turn to sedimentary archives, in the form of interregional unconformities. But we note that the existence of such unconformities has long been known (e.g., Belousov and Maxwell[4], Blackwelder[5], Şengör[37],[38], Levorsen[84], Sloss[131],[132], Stille[137], Suess[140], Vail et al.[143], Wheeler[147]) and that some have pointed out the need of physical models for their interpretation (e.g., Burgess et al.[16], Şengör[38]).

Our **GHMs** locate sedimentary rocks of any origin, including volcanic effusive and pyroclastic products that, for the purpose of mapping depositional sequences, behave like sediments. Thus, to first order, the time slices in Figure 5.4 show, where sediments were or were not deposited

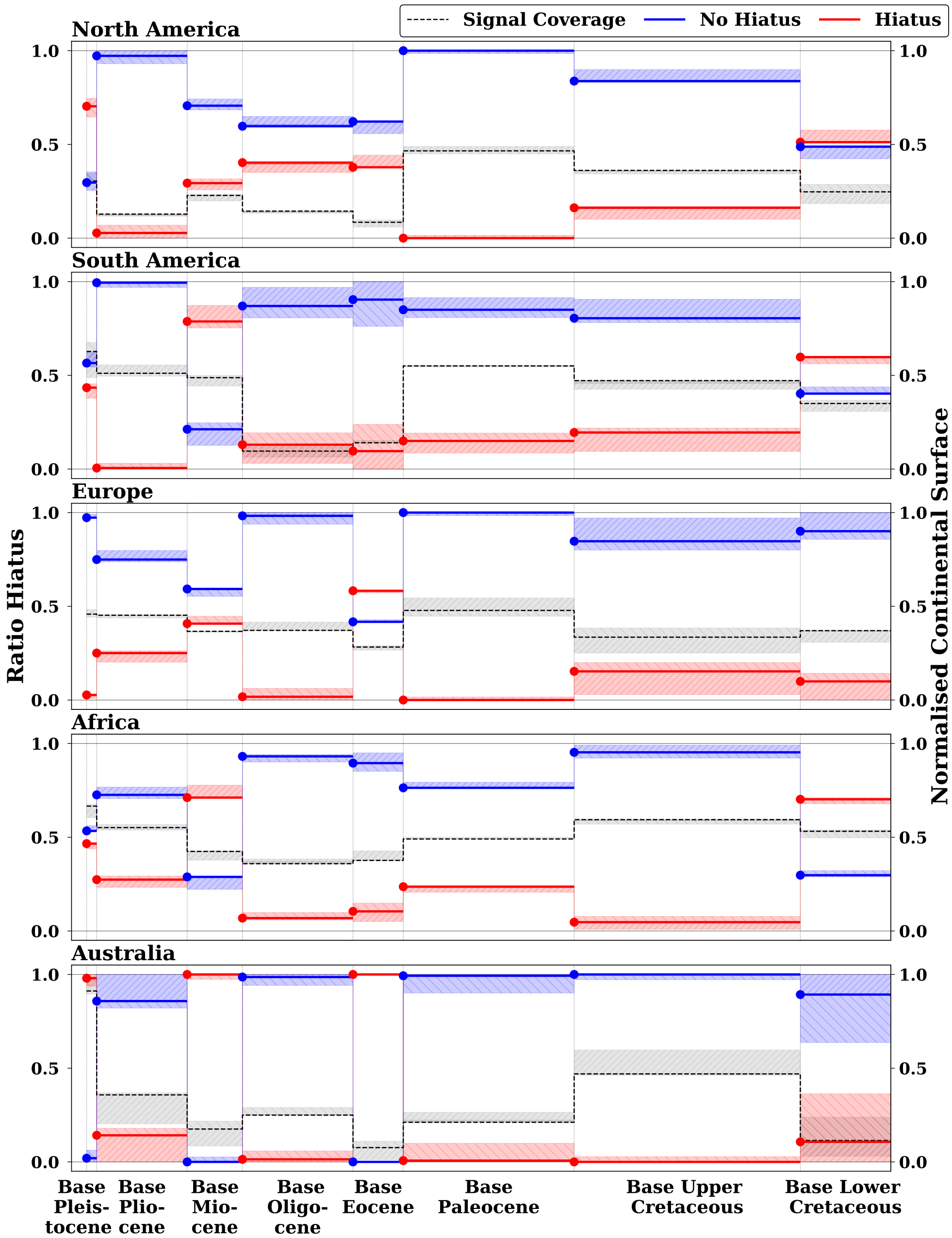

FIGURE 5.8. Same as Figure 5.7, but for individual continents. The curves are more variable and reveal considerable differences between continents and series. See text for interpretation.

(or deposited and then eroded before the deposition of the next series) in the series immediately preceding the target series. Surfaces of unconformable contact (marked in red) in the **BHS** (Figure 5.6) define regions in the series immediately preceding the target series that undergo erosion and/or non-deposition, whereas areas of conformable contact (marked in blue) identify depositional regions. At the interregional scales invoked, this serves as a proxy for either exhumation and surface uplift, or burial and subsidence. Lack of signal in the **BHS** indicates the absence of sediments in the target series and its immediately preceding series. This describes regions that may have undergone intense and/or long-lasting erosion or non-deposition and suggests intense and/or persistent exhumation and surface uplift [21,50,51,145]. Examples for un/conformable surfaces and for lack of signal can be identified in the **BHS**.

South America reveals a continent-scale lack of signal at the Base of Eocene and the Base of Oligocene (Figure 5.6(D)/(E)), indicating early Tertiary uplift in the region. This coincides temporally with the onset of rapid South Atlantic spreading rates [32] and an Eocene subaerial exposure of the Rio Grande Rise at Drill Site 516 [3]. There are also reports from thermochronological data and landscape analysis for post-rift Eocene reactivation in Brazil [25,74,82] and Argentina [80], and there is a Paleogene hiatus documented in Andean Foreland Basins [68].

Expansion of the total unconformable area from one time slice to the next indicates the onset of relative subsidence; it means that sediments now deposit in areas that previously underwent erosion/non-deposition. A significant expansion of unconformable area in central and northern Africa occurs at the Base of the Lower Cretaceous when compared to the Base of Upper Cretaceous (Figure 5.6(G)/(H)) and suggests that the Lower Cretaceous was a period of subsidence in Africa. An exception is the South African Plateau (SAP). It reveals a lack of signal suggestive of net high elevation. While this agrees with reports by some authors [2,52,141] calling for a Cretaceous age of the SAP topography, others suggest more recent Oligo-Miocene or younger uplift phases [17,21]. Another major expansion of unconformable area across Africa occurs at the Base of Miocene when compared with the Base of Oligocene (Figure 5.6(C)/(D)). It implies relative subsidence in the Miocene and suggests that the Oligocene was a period of uplift in most of the continent, as noted by several authors [6,21,36] and reviewed very effectively by Burke and Gunnell [17]. A recent geologic/geodynamic analysis suggests that Africa may cover different dynamic topography domains owing to its large area. Carena et al. [21] took the presence of Upper Cretaceous to Eocene exposed marine sediments in the interior of northern Africa together with the absence of exposed Oligocene to Pleistocene marine sediments there as evidence that this region uplifted significantly after the end of the Eocene, remaining high since. Oligocene to recent sediments in northern Africa are exclusively of continental origin. Far less marine sedimentation exists in the southern half of Africa for the Cenozoic series, where it is limited to coastal regions. While none of the exposed Cenozoic sediments in the interior of southern Africa are marine, there is a complete absence of coastal marine sediments in the Oligocene and Pleistocene. From this, and from the observation that some Miocene and Pliocene marine sediments along the southern coast are now at elevations significantly above 200 m, Carena et al. [21] inferred that southernmost Africa reached a high elevation in the Oligocene, subsided in the Miocene-Pliocene, and has been high again since the Pleistocene.

Europe features a strong expansion of unconformable area at the Base of Eocene when compared to the Base of Paleocene (Figure 5.6(E)/(F)), indicative of relative subsidence in the Eocene. We note

that the above examples of expanding unconformable area follow each in the wake of major plume events (i.e., Tristan, Lower Cretaceous; Afar, Oligocene; and Iceland, Paleocene, see Figure 5.6). Conformable area expansion from one time slice to the next indicates continued subsidence [21,50,145]. Prominent examples include Australia at the Base of Upper Cretaceous when compared to the Base of Lower Cretaceous (Figure 5.6(G)/(H)), and western North America at the Base of Paleocene when compared to the Base of Upper Cretaceous (Figure 5.6(F)/(G)). Continent-scale subsidence implied by growing conformable area in these regions has been linked to subduction at the eastern margin of Gondwana [65,91] and to the descent of the Farallon Plate beneath western North America [16,96,133].
Figure 5.7 and Figure 5.8 show the temporal evolution in the ratio of the area of un/conformal surface relative to the total area of conformal and unconformal surface, both aggregated over all continents and separate for each. The aggregated curve (Figure 5.7) reveals a sea-level signal. It is indicated by a maximum in the ratio of the area of conformable surface at the Base of Paleocene and the Base of Upper Cretaceous (corresponding to the Upper and Lower Cretaceous, respectively) relative to the total area of conformal and unconformal surface. The maximum agrees with global sea-level curves even when the amplitude of the latter is not well constrained (e.g., Müller et al.[101], Rowley[119]). There are also two prominent maxima in the ratio of the area of unconformable surface relative to the total area of conformal and unconformal surface at the Base of Miocene and the Base of Pleistocene. These coincide with the onset of glaciation in Antarctica [108] and the Northern Hemisphere [90], respectively.
The curves for individual continents (Figure 5.8) provide additional information: a sharp decline for North America in the ratio of conformable surface relative to the total area of conformal and unconformal surface at the Base of Eocene marks the disappearance of the *Interior Seaway* in the western part of the continent. South America displays a gradual growth with time in the ratio of conformable surface relative to the total area of conformal and unconformal surface. The lack of signal at the Base of Eocene and the Base of Oligocene, which we noticed before in the **BHS** (Figure 5.6(D)/(E)), is evinced in Figure 5.8 by the drop in the grey curve reporting the ratio of the total conformal and unconformal surface relative to the total area of South America. Europe's ratio of conformable surface relative to the total area of conformal and unconformal surface sinks dramatically at the Base Eocene, in agreement with the continent-scale growth of unconformable surface and the implied Eocene subsidence that followed the arrival of the Iceland Plume. Africa incurs two increases in the ratio of unconformable surface relative to the total conformal and unconformal surface at the Base of Lower Cretaceous and the Base of Miocene, presumably reflecting Lower Cretaceous and Miocene subsidence as discussed before. Notable for Australia is the increase in the ratio of conformable surface to the total un/conformable surface at the Base of Upper Cretaceous, attributed to Australia's eastward passage over subducted oceanic lithosphere. These results are in broad agreement with the analyses of Bond[7],[8] and support the notion that there are no stable continental platforms [98].
In our discussion we must point to the severe limitations of our method. First: GHMs strongly depend on the spatio-temporal resolution and accuracy of data compiled on geological maps. This means that the duration over which a particular hiatus area is defined depends on the temporal resolution of the input geological map, as noted before (see Figure 5.3). Our analysis is limited to

the series level. But true hiatus is likely longer than indicated by the missing series, because at any one location sedimentary successions represent only a small portion of a series. This implies large temporal uncertainties in our analysis, even when only one series is absent or when the adjacent series is not fully represented in the field. While our saturation of the time intervals to the series level is dictated by the data (i.e., the geological convention), it inevitably hides shorter duration lacunae and thereby avoids artifacts related to the Sadler effect [120]. This is critical, because if shorter duration lacunae are hidden, shorter duration events from lithospheric processes may be conflated with longer duration mantle-driven signals. Essentially our method favors large time intervals and hides shorter time intervals. Krob et al. [81] deduced an uplift duration signal of 50 Myrs for the Parana-Etendeka plume. So even at the temporal resolution of series it may be difficult to detect plume related uplift events. A similar difficulty arises when continents move laterally over different dynamic topography domains in relatively short geological time frames [11]. Future stratigraphic work should therefore respond to the geodynamic need for more precise dating of hiatus. Interregional geological maps at the resolution of stages (1-2 Myrs) are needed to reduce the uncertainties and to assist in geodynamic interpretations of hiatus.

Second: GHMs on their own do not identify the lithospheric or sublithospheric causes for continental vertical motion. Models predicting continental rise under increased horizontal stress (e.g., Ziegler et al.[149]), lithospheric folding [24] or delamination (e.g., Levander et al.[83], Schott and Schmeling[125]), which act as tectonic mechanisms within the lithosphere, must be distinguished from deeper, mantle related effects, such as the influence of rising plumes or pressure-driven asthenosphere flow. Detailed biostratigraphy and geomorphological methods of slope investigation or planation surfaces [60] are needed in the identification of broad scale (falcogenic) structures in the sense of Şengör [37]. It is clear that viable dynamic models of lithosphere motion must provide for a coupling of tectonic and mantle related forces (e.g., Stotz et al.[139]) to represent the behavior of the lithosphere as the combination of lithospheric and sublithospheric effects.

Third: GHMs are well constrained in lateral extend but not in amplitude. The latter requires independent calibration, for example, by using thermochronological data [46]. A variety of inferences provide constraints on surface uplift of the lithosphere. They include studies of river profiles (e.g., Roberts and White[118]), sediment compaction [73] and provenance [36,94], landform analysis [60] based on planation surfaces [78], paleoaltimetry [79], or the analysis of sediment budgets at the scale of continental margins [59,121,122]. Passive margins have been advocated as suitable locations for such studies [12]. MacGregor [88] summarizes episodes of margin uplift for South America and Africa, and similar inferences have been made for the Arctic [45] and the European passive margin of the North Atlantic, summarized in the Stratagem project ([138] and references therein). Inferences for an active post-rift evolution of passive margins have been collected into propositions for geodynamic models [57]. Geological hiatus maps suggest to extend the studies to broader spatial scales beyond passive margins.

Geodynamic implications

Geodynamicists explore mantle convection in terms of the plate and plume modes. Hiatus maps reveal the plate mode as broad conformable surfaces at the Base of Upper Cretaceous in Australia (Figure 5.6(G)) and the Base of Paleocene in western North America (Figure 5.6(F)), as noted before. Unconformable surfaces and areas of lack of signal located away from active plate margins are instead expressions of the plume mode. Seismic evidence suggests a strong plume mode [49,103,116], imaged for the upper [29,124,144] and the lower mantle as prominent regions of seismically slow velocities (e.g., Hosseini et al.[69], Kennett et al.[77], Ritsema et al.[117], Simmons et al.[129]). The geodynamic analysis of these anomalies remains under debate and permits interpretations of the lower mantle anomalies primarily by elevated temperature [39,126,129] or combinations of thermal and compositional effects [87,92]. The repeated appearance of continent-scale hiatus surfaces in our maps provides additional constraints. It implies significant positive mantle buoyancies presumably related to elevated temperature.

The distribution of un/conformable surface varies at the timescale of geologic series, (i.e., ten to a few tens of Myrs). This is considerably faster than the mantle transit time which, as the timescale for convection, is about 100-200 Myrs [20,70]. The difference in the convective timescale and the timescale for topography in convective support is illustrated by geodynamic kernels. They reflect the properties of dynamic Earth models and depend strongly upon the assumed rheology (see Colli et al.[30] for a review). For internal loads (e.g., hot rising plumes or cold sinking slabs) passing through a uniform-viscosity mantle, the kernels predict a continuous evolution of the induced surface deflections. In other words, a comparable timescale for convection and convectively-maintained topography is implied and borne out in laboratory models of isoviscous mantle flow [58]. The presence of a weaker upper mantle relative to the lower mantle, which is consistent with inferences from geodynamics [115] and mineral physics modelling [112], amplifies surface deflections for loads passing through the upper mantle. This property of dynamic Earth models makes rapid changes of convectively-maintained topography geodynamically plausible.

Geological hiatus maps have implications for time-dependent geodynamic Earth models: progress has been made in understanding how to retrodict past mantle states. Early backward advection schemes (e.g., Bunge and Richards[14], Steinberger and O'Connell[135]) have given way to a formal inverse problem based on adjoint equations that provide sensitivity information in a geodynamic model relative to earlier system states. Adjoint equations have been derived for incompressible [13,67,72], compressible [54] and thermo-chemical [55] mantle flow, and the uniqueness property of the inverse problem has been related to the tangential component of the surface velocity field of the convection model [28]. Knowledge of the latter is essential to ensure convergence [27,146]. While plate motions are a primary surface expression of mantle convection (e.g., Davies and Richards[42]), one needs to assimilate the tangential component of the surface velocity field (i.e., a past plate motion model) to solve the inverse problem. This makes past plate motions the input of retrodictions rather than their output, and suggests linking viable tests of retrodictions to inferences of past dynamic topography so that uncertain model parameters and state estimates can be assessed [31]. Put differently: the horizontal motion of the lithosphere cannot be predicted from mantle flow restorations, because reconstructions of past plate motion act as an input to the inverse problem, implying that it is not viable to construct self-consistent models of plate tectonics that are testable against the geologic record. However, mantle convection also induces vertical motion in the form of dynamic topography, as noted before. These can be inferred from a mantle flow retrodiction, because they are an output of the inverse problem. Geologic constraints on the history of convectively induced vertical motion of the lithosphere (that is the evolution of past dynamic topography) therefore are crucial observations to test the validity of the geodynamic modeling parameters assumed in mantle flow retrodictions. Our results imply that changes in convectively-maintained topography at the timescale of geologic series and over spatial scales of a few thousand kilometres must be an integral component of time-dependent geodynamic Earth models.

5.5 Conclusion

The analysis of continent-scale geological maps yields powerful information for constraining large-scale geodynamic processes and models. By providing consistent compilations of geologic observations at the scale of thousands of kilometres, continent-scale geologic maps link naturally to large-scale mantle flow induced elevation changes known as "dynamic topography" [10,63]. While the latter is difficult to separate by geophysical or geodetic means from the current isostatic topography of our planet outside the oceanic realm [66], its transient nature leaves signals in sedimentary archives as conformable and unconformable (hiatus) time boundaries traceable over hundreds to thousands of kilometres. We have applied a hiatus mapping method, introduced by Friedrich[50], Friedrich et al.[51], as a first-order technique that uses a single manipulation of existing geological maps to construct hiatus surfaces at the temporal resolution of series across North and South America, Europe, Africa and Australia starting from the Upper Jurassic. We find significant differences in the spatial extent of hiatus surface across and between continents at the timescale of geologic series, ten to a few tens of millions of years (Myrs). This is considerably smaller than the mantle transit time [70] and may reflect the effects of rapid lateral motion of continents over different dynamic topography domains in relatively short geological time-frames [11] as well as vigorous upper mantle flow in the asthenosphere facilitated by a viscosity reduction from the lower to the upper mantle as implied by response functions for dynamic Earth models (e.g., Richards and Hager[115]). The recurrent appearance of continent-scale hiatus surfaces is consistent with the existence of significant positive mantle buoyancies, presumably induced by thermal effects and elevated temperature. This supports the notion of a strong plume mode in the mantle convection system. In the future it is necessary to compile interregional geological maps at the temporal resolution of stages, most of which span 1-2 Myrs in duration, to reduce uncertainty and to assist in improved geodynamic interpretations of hiatus through time-dependent geodynamic Earth models capable of retrodicting past mantle flow states.

Acknowledgments

The authors thank the two reviewers, A. M. C. Şengör and S. Zahirovic, the editor J. Braun, as well as G. Meinhold, L. Colli, and S. Ghelichkhan for their constructive comments on the manuscript. This research has been supported by the European Union's Horizon 2020 Research and Innovation Programme under the ERC-2019-STG project TEAR, grant no. 852992.

Open Research

As supplementary material the fully normalised spherical harmonics coefficients [134] are provided for the base of each geological time series for the Cenozoic and Cretaceous.

Additional information

Author Contributions. Y. wrote the original hiatus extraction script for Europe. Vilacís, B. and Hayek, J.N. extended it, analysed and compiled the different data sources, processed the resulting Geological Hiatus Maps, participated in the study design, and drafted the manuscript. Carena, S. provided the Africa data and hiatus signal. Bunge, H.-P. and Friedrich, A. designed and coordinated the the study and critically revised the manuscript. All authors gave final approval for publication and agree to be held accountable for the work performed therein.
Competing interests The authors declare no competing interests.

5.6 References

[1] Asch, K. (2004). IGME 5000. 1:5 million international geological map of Europe and adjacent areas. *BGR (Hannover)*. Cited on page/s 122, 123, 125.

[2] Baby, G., Guillocheau, F., Boulogne, C., Robin, C., and Dall'Asta, M. (2018). Uplift history of a transform continental margin revealed by the stratigraphic record: The case of the Agulhas transform margin along the Southern African Plateau. *Tectonophysics*, 731:104–130. Cited on page/s 133.

[3] Barker, P. F. (1983). Tectonic evolution and subsidence history of the Rio-Grande Rise. *Initial Reports of the Deep Sea Drilling Project*, 72(DEC):953–976. Cited on page/s 133.

[4] Belousov, V. V. and Maxwell, J. C. (1962). *Basic problems in geotectonics*. McGraw-Hill, New York, USA. Cited on page/s 131.

[5] Blackwelder, E. (1909). The valuation of unconformities. *The Journal of Geology*, 17(3):289–299. Cited on page/s 131.

[6] Bond, G. C. (1978a). Evidence for late Tertiary uplift of Africa relative to North America, South America, Australia and Europe. *The Journal of Geology*, 86(1):47–65. Cited on page/s 131, 133.

[7] Bond, G. C. (1978b). Speculations on real sea-level changes and vertical motions of continents at selected times in the Cretaceous and Tertiary Periods. *Geology*, 6(4):247–250. Cited on page/s 131, 134.

[8] Bond, G. C. (1979). Evidence for some uplifts of large magnitude in continental platforms. *Tectonophysics*, 61(1-3):285–305. Cited on page/s 131, 134.

[9] Bower, D. J., Gurnis, M., and Seton, M. (2013). Lower mantle structure from paleogeographically constrained dynamic Earth models. *Geochemistry, Geophysics, Geosystems*, 14(1):44–63. Cited on page/s 122.

[10] Braun, J. (2010). The many surface expressions of mantle dynamics. *Nature Geoscience*, 3:825–833. Cited on page/s 122, 137.

[11] Braun, J., Guillocheau, F., Robin, C., Baby, G., and Jelsma, H. (2014). Rapid erosion of the southern african plateau as it climbs over a mantle superswell. *Journal of Geophysical Research: Solid Earth*, 119(7):6093–6112. Cited on page/s 135, 137.

[12] Bunge, H.-P. and Glasmacher, U. A. (2018). Models and observations of vertical motion (MoveOn) associated with rifting to passive margins: Preface. *Gondwana Research*, 53:1–8. Cited on page/s 122, 135.

[13] Bunge, H.-P., Hagelberg, C. R., and Travis, B. J. (2003). Mantle circulation models with variational data assimilation: Inferring past mantle flow and structure from plate motion histories and seismic tomography. *Geophysical Journal International*, 152(2):280–301. Cited on page/s 136.

[14] Bunge, H.-P. and Richards, M. A. (1992). The backward-problem of plate tectonics and mantle convection, (abstract). *Eos Transactions AGU*, 73(14):281. Spring Meeting suppl. Cited on page/s 136.

[15] Bunge, H.-P., Richards, M. A., Lithgow-Bertelloni, C., Baumgardner, J. R., Grand, S. P., and Romanowicz, B. A. (1998). Time scales and heterogeneous structure in geodynamic earth models. *Science*, 280(5360):91–95. Cited on page/s 122.

[16] Burgess, P. M., Gurnis, M., and Moresi, L. (1997). Formation of sequences in the cratonic interior of North America by interaction between mantle, eustatic, and stratigraphic processes. *Geological Society of America Bulletin*, 109(12):1515–1535. Cited on page/s 122, 131, 134.

[17] Burke, K. and Gunnell, Y. (2008). *The African erosion surface: A continental-scale synthesis of geomorphology, tectonics, and environmental change over the past 180 million years*, volume 201. Geological Society of America, Boulder, Colorado, USA. Cited on page/s 133.

[18] Burke, K. and Torsvik, T. H. (2004). Derivation of Large Igneous Provinces of the past 200 million years from long-term heterogeneities in the deep mantle. *Earth and Planetary Science Letters*, 227(3):531–538. Cited on page/s 126.

[19] Burke, K. and Whiteman, A. J. (1973). Uplift, rifting and break-up of Africa. In Tarling, D. H. and Runcorn, S. K., editors, *Implications of Continental Drift to the Earth Sciences,*. Academic Press, London & New York. Cited on page/s 131.

[20] Butterworth, N. P., Talsma, A. S., Müller, R. D., Seton, M., Bunge, H.-P., Schuberth, B. S. A., Shephard, G. E., and Heine, C. (2014). Geological, tomographic, kinematic and geodynamic constraints on the dynamics of sinking slabs. *Journal of Geodynamics*, 73:1–13. Cited on page/s 136.

[21] Carena, S., Bunge, H.-P., and Friedrich, A. M. (2019). Analysis of geological hiatus surfaces across Africa in the Cenozoic and implications for the timescales of convectively-maintained topography. *Canadian Journal of Earth Sciences*, 56(12):1333–1346. Cited on page/s 122, 123, 124, 125, 133, 134.

[22] Claure Zapata, M., Lema Patiño, R., Riera Kilibarda, C., and Suarez Soruco, R. (2012). Mapa geológico de Bolivia, 2000. SERGEOMIN, Servicio Geológico Minero. La Paz, Bolivia. Cited on page/s 123, 125.

[23] Clements, B., Burgess, P. M., Hall, R., and Cottam, M. A. (2011). Subsidence and uplift by slab-related mantle dynamics: a driving mechanism for the Late Cretaceous and Cenozoic evolution of continental SE Asia? *Geological Society, London, Special Publications*, 355(1):37–51. Cited on page/s 122.

[24] Cloetingh, S., Burov, E., Beekman, F., Andeweg, B., Andriessen, P., Garcia-Castellanos, D., de Vicente, G., and Vegas, R. (2002). Lithospheric folding in Iberia. *Tectonics*, 21(5):5–1–5–26. Cited on page/s 135.

[25] Cogné, N., Gallagher, K., Cobbold, P. R., Riccomini, C., and Gautheron, C. (2012). Post-breakup tectonics in southeast Brazil from thermochronological data and combined inverse-forward thermal history modeling. *Journal of Geophysical Research: Solid Earth*, 117(B11):B11413. Cited on page/s 133.

[26] Cohen, K. M., Harper, D., and Gibbard, P. L. (2018/08). Ics international chronostratigraphic chart. www.stratigraphy.org. Cited on page/s 123, 127, 130.

[27] Colli, L., Bunge, H.-P., and Oeser, J. (2020). Impact of model inconsistencies on reconstructions of past mantle flow obtained using the adjoint method. *Geophysical Journal International*, 221(1):617–639. Cited on page/s 136.

[28] Colli, L., Bunge, H.-P., and Schuberth, B. S. A. (2015). On retrodictions of global mantle flow with assimilated surface velocities. *Geophysical Research Letters*, 42(20):8341–8348. Cited on page/s 136.

[29] Colli, L., Fichtner, A., and Bunge, H.-P. (2013). Full waveform tomography of the upper mantle in the South Atlantic region: Imaging a westward fluxing shallow asthenosphere? *Tectonophysics*, 604:26–40. Cited on page/s 136.

[30] Colli, L., Ghelichkhan, S., and Bunge, H.-P. (2016). On the ratio of dynamic topography and gravity anomalies in a

dynamic Earth. *Geophysical Research Letters*, 43(6):2510–2516. Cited on page/s 136.

[31] Colli, L., Ghelichkhan, S., Bunge, H.-P., and Oeser, J. (2018). Retrodictions of mid paleogene mantle flow and dynamic topography in the atlantic region from compressible high resolution adjoint mantle convection models: Sensitivity to deep mantle viscosity and tomographic input model. *Gondwana Research*, 53:252–272. Cited on page/s 136.

[32] Colli, L., Stotz, I., Bunge, H.-P., Smethurst, M., Clark, S. R., Iaffaldano, G., Tassara, A., Guillocheau, F., and Bianchi, M. C. (2014). Rapid South Atlantic spreading changes and coeval vertical motion in surrounding continents: Evidence for temporal changes of pressure-driven upper mantle flow. *Tectonics*, 33(7):1304–1321. Cited on page/s 133.

[33] Courtillot, V., Davaille, A., Besse, J., and Stock, J. (2003). Three distinct types of hotspots in the Earth's mantle. *Earth and Planetary Science Letters*, 205(3-4):295–308. Cited on page/s 130.

[34] Cox, K. G. (1989). The role of mantle plumes in the development of continental drainage patterns. *Nature*, 342(6252):873–877. Cited on page/s 122.

[35] CPRM and Serviço Geológico do Brasil (2010). Carta geológica do Brasil ao milionésimo. Brasília, Brazil. Cited on page/s 123, 125.

[36] Şengör, A. M. C. (2001). Elevation as indicator of mantle-plume activity. *Mantle plumes: Their identification through time*, 352:183–245. Cited on page/s 122, 133, 135.

[37] Şengör, A. M. C. (2003). *The large wavelength deformations of the Lithosphere: Materials for a history of the evolution of thought from the earliest times to plate tectonics*. Geological Society of America, Memoir no. 196. Cited on page/s 122, 131, 135.

[38] Şengör, A. M. C. (2016). What is the use of the history of geology to a practicing geologist? The propaedeutical case of stratigraphy. *The Journal of Geology*, 124(6):643–698. Cited on page/s 131.

[39] Davies, D. R., Goes, S., Davies, J. H., Schuberth, B. S. A., Bunge, H.-P., and Ritsema, J. (2012). Reconciling dynamic and seismic models of Earth's lower mantle: The dominant role of thermal heterogeneity. *Earth and Planetary Science Letters*, 353:253–269. Cited on page/s 136.

[40] Davies, G. F. (1988). Ocean bathymetry and mantle convection: 1. Large-scale flow and hotspots. *Journal of Geophysical Research*, 93(B9):10467–10480. Cited on page/s 122.

[41] Davies, G. F. (1999). *Dynamic Earth: Plates, plumes and mantle convection*. Cambridge University Press, Cambridge, United Kingdom. Cited on page/s 122.

[42] Davies, G. F. and Richards, M. A. (1992). Mantle convection. *The Journal of Geology*, 100(2):151–206. Cited on page/s 122, 136.

[43] Deep Sea Drilling Project (1968–1983). Deep Sea Drilling Project (DSDP). Legs 1–96, Sites 1–624. Cited on page/s 123, 125.

[44] DeMets, C., Gordon, R. G., and Argus, D. F. (2010). Geologically current plate motions. *Geophysical Journal International*, 181(1):1–80. Cited on page/s 124.

[45] Dörr, N., Lisker, F., Clift, P. D., Carter, A., Gee, D. G., Tebenkov, A. M., and Spiegel, C. (2012). Late Mesozoic–Cenozoic exhumation history of northern Svalbard and its regional significance: Constraints from apatite fission track analysis. *Tectonophysics*, 514:81–92. Cited on page/s 135.

[46] Ehlers, T. A. and Farley, K. A. (2003). Apatite (U–Th)/He thermochronometry: Methods and applications to problems in tectonic and surface processes. *Earth and Planetary Science Letters*, 206(1-2):1–14. Cited on page/s 135.

[47] Fishwick, S. and Bastow, I. D. (2011). Towards a better understanding of African topography: A review of passive-source seismic studies of the African crust and upper mantle. *Geological Society, London, Special Publications*, 357(1):343–371. Cited on page/s 131.

[48] Forte, A. M. and Peltier, R. (1991). Viscous flow models of global geophysical observables: 1. forward problems. *Journal of Geophysical Research: Solid Earth*, 96(B12):20131–20159. Cited on page/s 129.

[49] French, S. W. and Romanowicz, B. A. (2015). Broad plumes rooted at the base of the Earth's mantle beneath major hotspots. *Nature*, 525(7567):95–99. Cited on page/s 122, 136.

[50] Friedrich, A. M. (2019). Palaeogeological hiatus surface mapping: A tool to visualize vertical motion of the continents. *Geological Magazine*, 156(2):308–319. Cited on page/s 122, 123, 124, 125, 133, 134, 137.

[51] Friedrich, A. M., Bunge, H.-P., Rieger, S. M., Colli, L., Ghelichkhan, S., and Nerlich, R. (2018). Stratigraphic framework for the plume mode of mantle convection and the analysis of interregional unconformities on geological

maps. *Gondwana Research*, 53:159–188. Cited on page/s 122, 125, 133, 137.

[52] Gallagher, K. and Brown, R. (1999). Denudation and uplift at passive margins: The record on the Atlantic Margin of southern Africa. *Philosophical Transactions of the Royal Society of London. Series A: Mathematical, Physical and Engineering Sciences*, 357(1753):835–859. Cited on page/s 133.

[53] Garrity, C. P. and Soller, D. R. (2009). Database of the Geologic Map of North America: Adapted from the map by J.C. Reed, Jr. and others (2005). Technical report, United States Geological Survey (USGS). Cited on page/s 123, 125.

[54] Ghelichkhan, S. and Bunge, H.-P. (2016). The compressible adjoint equations in geodynamics: Derivation and numerical assessment. *GEM-International Journal on Geomathematics*, 7(1):1–30. Cited on page/s 136.

[55] Ghelichkhan, S. and Bunge, H.-P. (2018). The adjoint equations for thermochemical compressible mantle convection: Derivation and verification by twin experiments. *Proceedings of the Royal Society A*, 474(2220):20180329. Cited on page/s 136.

[56] Gordon, R. G. and Jurdy, D. M. (1986). Cenozoic global plate motions. *Journal of Geophysical Research: Solid Earth*, 91(B12):12389–12406. Cited on page/s 122.

[57] Green, P. F., Japsen, P., Chalmers, J. A., Bonow, J. M., and Duddy, I. R. (2018). Post-breakup burial and exhumation of passive continental margins: Seven propositions to inform geodynamic models. *Gondwana Research*, 53:58–81. Cited on page/s 135.

[58] Griffiths, R. W., Gurnis, M., and Eitelberg, G. (1989). Holographic measurements of surface topography in laboratory models of mantle hotspots. *Geophysical Journal International*, 96(3):477–495. Cited on page/s 136.

[59] Guillocheau, F., Rouby, D., Robin, C., Helm, C., Rolland, N., Le Carlier de Veslud, C., and Braun, J. (2012). Quantification and causes of the terrigeneous sediment budget at the scale of a continental margin: A new method applied to the Namibia-South Africa margin. *Basin Research*, 24(1):3–30. Cited on page/s 135.

[60] Guillocheau, F., Simon, B., Baby, G., Bessin, P., Robin, C., and Dauteuil, O. (2018). Planation surfaces as a record of mantle dynamics: The case example of Africa. *Gondwana Research*, 53:82–98. Cited on page/s 135.

[61] Gurnis, M., Müller, R. D., and Moresi, L. (1998). Cretaceous vertical motion of australia and the australian-antarctic discordance. *Science*, 279(5356):1499–1504. Cited on page/s 122.

[62] Hackley, P., Urbani, F., Karlsen, A. W., and Garrity, C. P. (2004). Geological shaded relief map of Venezuela. *USGS Open File Report*, 2005:1–2. Cited on page/s 123, 125.

[63] Hager, B. H., Clayton, R. W., Richards, M. A., Comer, R. P., and Dziewonski, A. M. (1985). Lower mantle heterogeneity, dynamic topography and the geoid. *Nature*, 313:541–545. Cited on page/s 122, 137.

[64] Harrington, L., Zahirovic, S., Salles, T., Braz, C., and Müller, R. D. (2019). Tectonic, geodynamic and surface process driving forces of australia's paleogeography since the jurassic. In Keep, M. and Moss, S., editors, *The Sedimentary Basins of Western Australia V: Proceedings of the Petroleum Exploration Society of Australia Symposium, Perth, WA*, page 29. Cited on page/s 122.

[65] Heine, C., Müller, R. D., Steinberger, B., and DiCaprio, L. (2010). Integrating deep Earth dynamics in paleogeographic reconstructions of Australia. *Tectonophysics*, 483(1-2):135–150. Cited on page/s 134.

[66] Hoggard, M. J., Winterbourne, J., Czarnota, K., and White, N. (2017). Oceanic residual depth measurements, the plate cooling model, and global dynamic topography. *Journal of Geophysical Research: Solid Earth*, 122(3):2328–2372. Cited on page/s 129, 131, 137.

[67] Horbach, A., Bunge, H.-P., and Oeser, J. (2014). The adjoint method in geodynamics: Derivation from a general operator formulation and application to the initial condition problem in a high resolution mantle circulation model. *GEM-International Journal on Geomathematics*, 5(2):163–194. Cited on page/s 136.

[68] Horton, B. K. (2018). Sedimentary record of Andean mountain building. *Earth-Science Reviews*, 178:279–309. Cited on page/s 133.

[69] Hosseini, K., Sigloch, K., Tsekhmistrenko, M., Zaheri, A., Nissen-Meyer, T., and Igel, H. (2020). Global mantle structure from multifrequency tomography using P, PP and P-diffracted waves. *Geophysical Journal International*, 220(1):96–141. Cited on page/s 136.

[70] Iaffaldano, G. and Bunge, H.-P. (2015). Rapid plate motion variations through geological time: Observations serving geodynamic interpretation. *Annual Review of Earth and Planetary Sciences*, 43:571–592. Cited on page/s 123, 136, 137.

[71] INGEMMET and Instituto Geológico, Minero y Metalúrgico (2016). GEOCATMIN: Geología nacional millón

1:1.000.000, Perú, 2016. Lima, Peru. Cited on page/s 123, 125.

[72] Ismail-Zadeh, A., Schubert, G., Tsepelev, I., and Korotkii, A. (2004). Inverse problem of thermal convection: Numerical approach and application to mantle plume restoration. *Physics of the Earth and Planetary Interiors*, 145(1-4):99–114. Cited on page/s 136.

[73] Japsen, P. (2018). Sonic velocity of chalk, sandstone and marine shale controlled by effective stress: Velocity-depth anomalies as a proxy for vertical movements. *Gondwana Research*, 53:145–158. Cited on page/s 135.

[74] Japsen, P., Bonow, J. M., Green, P. F., Cobbold, P. R., Chiossi, D., Lilletveit, R., Magnavita, L. P., and Pedreira, A. (2012). Episodic burial and exhumation in NE Brazil after opening of the South Atlantic. *Bulletin*, 124(5-6):800–816. Cited on page/s 133.

[75] Jones, A. G., Afonso, J. C., and Fullea, J. (2017). Geochemical and geophysical constrains on the dynamic topography of the Southern African Plateau. *Geochemistry, Geophysics, Geosystems*, 18(10):3556–3575. Cited on page/s 131.

[76] Jorge, G., Montes Ramírez, N., Almanza Meléndez, M., Alcárcel Gutiérrez, F., Madrid Montoya, C., and Diederix, H. (2015). Geological map of colombia 2015. *Journal of International Geosciences*, 40(3):201–212. Cited on page/s 123, 125.

[77] Kennett, B. L. N., Widiyantoro, S., and van der Hilst, R. D. (1998). Joint seismic tomography for bulk sound and shear wave speed in the earth's mantle. *Journal of Geophysical Research: Solid Earth*, 103(B6):12469–12493. Cited on page/s 136.

[78] King, L. C. (1955). Pediplanation and isostasy: An example from South Africa. *Quarterly Journal of the Geological Society*, 111(1-4):353–359. Cited on page/s 135.

[79] Kohn, M. J., editor (2018). *Paleoaltimetry: Geochemical and thermodynamic approaches*, volume 66 of *Reviews in Mineralogy and Geochemistry*. De Gruyter. Cited on page/s 135.

[80] Kollenz, S., Glasmacher, U. A., Rossello, E. A., Stockli, D. F., Schad, S., and Pereyra, R. E. (2017). Thermochronological constraints on the Cambrian to recent geological evolution of the Argentina passive continental margin. *Tectonophysics*, 716:182–203. Cited on page/s 133.

[81] Krob, F. C., Glasmacher, U. A., Bunge, H.-P., Friedrich, A. M., and Hackspacher, P. C. (2020). Application of stratigraphic frameworks and thermochronological data on the mesozoic sw gondwana intraplate environment to retrieve the paraná-etendeka plume movement. *Gondwana Research*, 84:81 – 110. Cited on page/s 135.

[82] Krob, F. C., Glasmacher, U. A., Karl, M., Perner, M., Hackspacher, P. C., and Stockli, D. F. (2019). Multi-chronometer thermochronological modelling of the Late Neoproterozoic to recent t-T-evolution of the SE coastal region of Brazil. *Journal of South American Earth Sciences*, 92:77–94. Cited on page/s 133.

[83] Levander, A., Schmandt, B., Miller, M. S., Liu, K., Karlstrom, K. E., Crow, R. S., Lee, C. T. A., and Humphreys, E. D. (2011). Continuing Colorado plateau uplift by delamination-style convective lithospheric downwelling. *Nature*, 472(7344):461–U540. Cited on page/s 135.

[84] Levorsen, A. I. (1933). Studies in paleogeology. *AAPG Bulletin*, 17(9):1107–1132. Cited on page/s 131.

[85] Lithgow-Bertelloni, C. and Richards, M. A. (1998). The dynamics of Cenozoic and Mesozoic plate motions. *Reviews of Geophysics*, 36(1):27–78. Cited on page/s 122.

[86] Loureiro, J., Pérez Cerdán, F., Spoturno, J., Faraone, M., Guerrero, S., and Sánchez Bettucci, L. (2016). Versión digital y actualización del mapa geológico del Uruguay de DINAMIGE a escala 1:500.000. In *VIII Congreso Uruguayo de Geología 2016*. MIEM, Ministerio de Industria, Energia y Minería. Montevideo, Uruguay. Cited on page/s 123, 125.

[87] Lu, C., Forte, A. M., Simmons, N. A., Grand, S. P., Kajan, M., Lai, H., and Garnero, E. (2020). The sensitivity of joint inversions of seismic and geodynamic data to mantle viscosity. *Geochemistry, Geophysics, Geosystems*, 21(4):e2019GC008648. Cited on page/s 136.

[88] MacGregor, D. S. (2013). Late Cretaceous–Cenozoic sediment and turbidite reservoir supply to South Atlantic margins. *Geological Society, London, Special Publications*, 369(1):109–128. Cited on page/s 135.

[89] MAGAP and Ministerio de Agricultura y Ganaderia (2005). Mapa hidrogeológico de Ecuador. Quito, Ecuador. Cited on page/s 123, 125.

[90] Maslin, M. A., Haug, G. H., Sarnthein, M., and Tiedemann, R. (1996). The progressive intensification of northern hemisphere glaciation as seen from the North Pacific. *Geologische Rundschau*, 85(3):452–465. Cited on page/s 131, 134.

[91] Matthews, K. J., Hale, A. J., Gurnis, M., Müller, R. D., and DiCaprio, L. (2011). Dynamic subsidence of Eastern Australia during the Cretaceous. *Gondwana Research*, 19(2):372–383. Cited on page/s 134.

[92] McNamara, A. K. (2019). A review of large low shear velocity provinces and ultra low velocity zones. *Tectonophysics*, 760:199–220. Cited on page/s 136.

[93] McNamara, A. K. and Zhong, S. (2005). Degree-one mantle convection: Dependence on internal heating and temperature-dependent rheology. *Geophysical Research Letters*, 32(1):L01301. Cited on page/s 122.

[94] Meinhold, G. (2010). Rutile and its applications in earth sciences. *Earth–Science Reviews*, 102(1):1–28. Cited on page/s 135.

[95] Miall, A. D. (2016). The valuation of unconformities. *Earth-Science Reviews*, 163:22–71. Cited on page/s 122.

[96] Mitrovica, J. X., Beaumont, C., and Jarvis, G. T. (1989). Tilting of continental interiors by the dynamical effects of subduction. *Tectonics*, 8(5):1079–1094. Cited on page/s 122, 134.

[97] Molnar, P., England, P. C., and Jones, C. H. (2015). Mantle dynamics, isostasy, and the support of high terrain. *Journal of Geophysical Research: Solid Earth*, 120(3):1932–1957. Cited on page/s 131.

[98] Moucha, R., Forte, A. M., Mitrovica, J. X., Rowley, D. B., Quéré, S., Simmons, N. A., and Grand, S. P. (2008). Dynamic topography and long-term sea-level variations: There is no such thing as a stable continental platform. *Earth and Planetary Science Letters*, 271(1):101–108. Cited on page/s 134.

[99] Müller, R. D., Cannon, J., Qin, X., Watson, R. J., Gurnis, M., Williams, S., Pfaffelmoser, T., Seton, M., Russell, S. H. J., and Zahirovic, S. (2018). Gplates: Building a virtual earth through deep time. *Geochemistry, Geophysics, Geosystems*, 19(7):2243–2261. Cited on page/s 126.

[100] Müller, R. D., Hassan, R., Gurnis, M., Flament, N., and Williams, S. E. (2018). Dynamic topography of passive continental margins and their hinterlands since the Cretaceous. *Gondwana Research*, 53:225–251. Cited on page/s 122.

[101] Müller, R. D., Sdrolias, M., Gaina, C., Steinberger, B., and Heine, C. (2008). Long-term sea-level fluctuations driven by ocean basin dynamics. *Science*, 319(5868):1357–1362. Cited on page/s 131, 134.

[102] Müller, R. D., Seton, M., Zahirovic, S., Williams, S. E., Matthews, K. J., Wright, N. M., Shephard, G. E., Maloney, K. T., Barnett-Moore, N., Hosseinpour, M., Bower, D. J., and Cannon, J. (2016). Ocean basin evolution and global-scale plate reorganization events since Pangea breakup. *Annual Review of Earth and Planetary Sciences*, 44(1):107–138. Cited on page/s 122, 126, 127, 130.

[103] Nelson, P. L. and Grand, S. P. (2018). Lower-mantle plume beneath the Yellowstone hotspot revealed by core waves. *Nature Geoscience*, 11(4):280–284. Cited on page/s 122, 136.

[104] Ocean Drilling Program (1985–2004). Ocean Drilling Program (ODP). Legs 100–210, Sites 625–1277. Cited on page/s 123, 125.

[105] Ogg, J. G., Ogg, G. M., and Gradstein, F. M. (2016). 1 - introduction. In Ogg, J. G., Ogg, G. M., and Gradstein, F. M., editors, *A Concise Geologic Time Scale*, pages 1 – 8. Elsevier. Cited on page/s 123.

[106] O'Neill, C., Müller, R. D., and Steinberger, B. (2005). On the uncertainties in hot spot reconstructions and the significance of moving hot spot reference frames. *Geochemistry, Geophysics, Geosystems*, 6(4):Q04003. Cited on page/s 126, 127, 130.

[107] Pekeris, C. L. (1935). Thermal convection in the interior of the earth. *Geophysical Journal International*, 3:343–367. Cited on page/s 122.

[108] Petersen, S. V. and Schrag, D. P. (2015). Antarctic ice growth before and after the Eocene-Oligocene transition: New estimates from clumped isotope paleothermometry. *Paleoceanography*, 30(10):1305–1317. Cited on page/s 131, 134.

[109] Rainbird, R. H. and Ernst, R. E. (2001). The sedimentary record of mantle-plume uplift. *Special Papers-Geological Society of America*, 352:227–246. Cited on page/s 122.

[110] Ravenna, M., Lebedev, S., Fullea, J., and Adam, J. M.-C. (2018). Shear-wave velocity structure of southern Africa's lithosphere: Variations in the thickness and composition of cratons and their effect on topography. *Geochemistry, Geophysics, Geosystems*, 19(5):1499–1518. Cited on page/s 131.

[111] Raymond, O. L., Gallagher, R., Shaw, R., Yeates, A. N., Doutch, H. F., Palfreyman, W. D., Blake, D. H., and Highet, L. (2012). Surface geology of Australia 1:2.5 million scale dataset 2012 edition. Commonwealth of Australia (Geoscience Australia). Cited on page/s 123, 125.

[112] Reali, R., Van Orman, J. A., Pigott, J. S., Jackson, J. M., Boioli, F., Carrez, P., and Cordier, P. (2019). The role of diffusion-driven pure climb creep on the rheology of bridgmanite under lower mantle conditions. *Scientific Reports*, 9(1):2053. Cited on page/s 136.

[113] Ricard, Y., Fleitout, L., and Froidevaux, C. (1984). Geoid heights and lithospheric stresses for a dynamic Earth. *Annales Geophysicae*, 2(3):267–286. Cited on page/s 129.

[114] Richards, M. A. and Engebretson, D. C. (1992). Large-scale mantle convection and the history of subduction. *Nature*, 355(6359):437–440. Cited on page/s 122.

[115] Richards, M. A. and Hager, B. H. (1984). Geoid anomalies in a dynamic Earth. *Journal of Geophysical Research: Solid Earth*, 89(B7):5987–6002. Cited on page/s 129, 136, 137.

[116] Rickers, F., Fichtner, A., and Trampert, J. (2013). The Iceland-Jan Mayen plume system and its impact on mantle dynamics in the North Atlantic region: Evidence from full-waveform inversion. *Earth and Planetary Science Letters*, 367:39–51. Cited on page/s 122, 136.

[117] Ritsema, J., Deuss, A., van Heijst, H. J., and Woodhouse, J. H. (2011). S40RTS: A degree-40 shear-velocity model for the mantle from new Rayleigh wave dispersion, teleseismic traveltime and normal-mode splitting function measurements. *Geophysical Journal International*, 184(3):1223–1236. Cited on page/s 136.

[118] Roberts, G. G. and White, N. (2010). Estimating uplift rate histories from river profiles using African examples. *Journal of Geophysical Research: Solid Earth*, 115(B2):B02406. Cited on page/s 135.

[119] Rowley, D. B. (2017). Earth's constant mean elevation: Implication for long-term sea level controlled by oceanic lithosphere dynamics in a Pitman world. *The Journal of Geology*, 125(2):141–153. Cited on page/s 131, 134.

[120] Sadler, P. M. (1981). Sediment accumulation rates and the completeness of stratigraphic sections. *The Journal of Geology*, 89(5):569–584. Cited on page/s 135.

[121] Said, A., Moder, C., Clark, S., and Abdelmalak, M. M. (2015a). Sedimentary budgets of the tanzania coastal basin and implications for uplift history of the east african rift system. *Journal of African Earth Sciences*, 111:288 – 295. Cited on page/s 135.

[122] Said, A., Moder, C., Clark, S., and Ghorbal, B. (2015b). Cretaceous-cenozoic sedimentary budgets of the southern mozambique basin: Implications for uplift history of the south african plateau. *Journal of African Earth Sciences*, 109:1 – 10. Cited on page/s 135.

[123] Saunders, A. D., Jones, S. M., Morgan, L. A., Pierce, K. L., Widdowson, M., and Xu, Y. G. (2007). Regional uplift associated with continental large igneous provinces: The roles of mantle plumes and the lithosphere. *Chemical Geology*, 241(3-4):282–318. Cited on page/s 122.

[124] Schaeffer, A. J. and Lebedev, S. (2013). Global shear speed structure of the upper mantle and transition zone. *Geophysical Journal International*, 194(1):417–449. Cited on page/s 136.

[125] Schott, B. and Schmeling, H. (1998). Delamination and detachment of a lithospheric root. *Tectonophysics*, 296(3-4):225–247. Cited on page/s 135.

[126] Schuberth, B. S. A., Bunge, H.-P., and Ritsema, J. (2009). Tomographic filtering of high-resolution mantle circulation models: Can seismic heterogeneity be explained by temperature alone? *Geochemistry, Geophysics, Geosystems*, 10(5):Q05W03. Cited on page/s 136.

[127] SEGEMAR and Servicio Geológico Minero Argentino (2017). Mapa geológico de Argentina. San Martín, Argentina. Cited on page/s 123, 125.

[128] SERNAGEOMIN and Servicio Nacional de Geología y Minería (2003). Mapa geológico de Chile: Versión digital. Santiago, Chile. Cited on page/s 123, 125.

[129] Simmons, N. A., Forte, A. M., and Grand, S. P. (2009). Joint seismic, geodynamic and mineral physical constraints on three-dimensional mantle heterogeneity: Implications for the relative importance of thermal versus compositional heterogeneity. *Geophysical Journal International*, 177(3):1284–1304. Cited on page/s 136.

[130] Sloss, L. (1972). Synchrony of phanerozoic sedimentary-tectonic events of the north american craton and the russian platform. In *24th International Geological Congress, Montreal*, volume 6, pages 24–32. Cited on page/s 122, 123.

[131] Sloss, L. L. (1963). Sequences in the cratonic interior of North America. *Geological Society of America Bulletin*, 74(2):93–114. Cited on page/s 122, 131.

[132] Sloss, L. L. (1992). Tectonic episodes of cratons: Conflicting North American concepts. *Terra Nova*, 4(3):320–328. Cited on page/s 131.

[133] Spasojevic, S., Liu, L., and Gurnis, M. (2009). Adjoint models of mantle convection with seismic, plate motion, and stratigraphic constraints: North America since the Late Cretaceous. *Geochemistry, Geophysics, Geosystems*,

10(5):Q05W02. Cited on page/s 134.

[134] Stacey, F. D. and Davis, P. M. (2008). *Physics of the Earth*. Cambridge University Press, New York, USA. Cited on page/s 128, 129, 130, 138.

[135] Steinberger, B. and O'Connell, R. J. (1997). Changes of the Earth's rotation axis owing to advection of mantle density heterogeneities. *Nature*, 387(6629):169–173. Cited on page/s 136.

[136] Stille, H. (1919). Die Begriffe Orogenese und Epirogenese. *Zeitschrift der Deutschen Geologischen Gesellschaft*, 71:164–208. Cited on page/s 123.

[137] Stille, H. (1924). Grundfragen der Vergleichenden Tektonik. *Gebrüder Borntraeger*, 71:1–443. Cited on page/s 123, 131.

[138] Stoker, M. S. and Shannon, P. M. (2005). Neogene evolution of the NW European Atlantic margin: Results from the STRATAGEM project. *Marine and Petroleum Geology*, 22(9–10):965–968. Cited on page/s 135.

[139] Stotz, I. L., Iaffaldano, G., and Davies, D. R. (2017). Late miocene pacific plate kinematic change explained with coupled global models of mantle and lithosphere dynamics. *Geophysical Research Letters*, 44(14):7177–7186. Cited on page/s 135.

[140] Suess, E. (1883). *Das Antlitz der Erde: Erster Band*. F. Tempsky, Prag und Wien, and G. Freytag, Leipzig. Cited on page/s 131.

[141] Tinker, J., de Wit, M., and Brown, R. (2008). Mesozoic exhumation of the southern Cape, South Africa, quantified using apatite fission track thermochronology. *Tectonophysics*, 455(1-4):77–93. Cited on page/s 133.

[142] Turcotte, D. L. and Oxburgh, E. R. (1967). Finite amplitude convective cells and continental drift. *Journal of Fluid Mechanics*, 28(1):29–42. Cited on page/s 121.

[143] Vail, P. R., Mitchum Jr, R. M., and Thompson III, S. (1977). Seismic stratigraphy and global changes of sea level: Part 4. Global cycles of relative changes of sea level: Section 2. Application of seismic reflection configuration to stratigraphic interpretation. In *Seismic Stratigraphy: Applications to Hydrocarbon Exploration*, pages 83–97. American Association of Petroleum Geologists, Memoir no. 26. Cited on page/s 131.

[144] van Herwaarden, D. P., Boehm, C., Afanasiev, M., Thrastarson, S., Krischer, L., Trampert, J., and Fichtner, A. (2020). Accelerated full-waveform inversion using dynamic mini-batches. *Geophysical Journal International*, 221(2):1427–1438. Cited on page/s 136.

[145] Vibe, Y., Friedrich, A. M., Bunge, H.-P., and Clark, S. R. (2018). Correlations of oceanic spreading rates and hiatus surface area in the North Atlantic realm. *Lithosphere*, 10(5):677–684. Cited on page/s 122, 125, 133, 134.

[146] Vynnytska, L. and Bunge, H.-P. (2015). Restoring past mantle convection structure through fluid dynamic inverse theory: Regularisation through surface velocity boundary conditions. *GEM-International Journal on Geomathematics*, 6(1):83–100. Cited on page/s 136.

[147] Wheeler, H. E. (1958). Time-stratigraphy. *AAPG Bulletin*, 42(5):1047–1063. Cited on page/s 131.

[148] Wieczorek, M. A. and Meschede, M. (2018). Shtools: Tools for working with spherical harmonics. *Geochemistry, Geophysics, Geosystems*, 19(8):2574–2592. Cited on page/s 129.

[149] Ziegler, P. A., Cloetingh, S., and van Wees, J.-D. (1995). Dynamics of intra-plate compressional deformation: The alpine foreland and other examples. *Tectonophysics*, 252(1):7 – 59. Cited on page/s 135.

Chapter 6

First-order global stress patterns inferred from upper mantle flow models

by Hayek J.N., Stotz I.L, Bunge H.-P., and Carena S. (2025). Published in Proceedings of the Royal Society A. DOI: 10.1098/rspa.2024.0969.

Abstract

Knowledge of the lithosphere stress field is critical to the evaluation of reservoir response related to energy resources and waste storage, as well as for hazard and risk assessment. We show with statistical comparisons of modelled and observed stress fields that a simple analytic flow model, where asthenosphere flux is driven by lateral pressure gradients and motion of overlying tectonic plates, explains first-order global stress patterns from the World Stress Map. The model separates the flow into components related to plumes, slabs and plate motion, and suggests the potential to identify geodynamically plausible stress provinces, i.e. regions affected predominantly by specific flow components. It also reveals three distinct basal shear traction regimes, depending on whether asthenosphere locally moves faster, slower or at the same speed as the plate above, so that some regions are subject to driving or resisting tractions while others are nearly traction-free. Predicted deviatoric stresses within the asthenosphere are less than a few MPa. The model compares favorably to results from Mantle Circulation Models and implies that realistic upper mantle flow geometries, i.e. the specific spatial distribution of plumes, slabs, plate-induced flow and their superposition, are essential for interpreting stress field patterns at global and regional scales.

6.1 Introduction

The stress field exerts a first-order control on the mechanical response of inherited tectonic structures[22,106]. Knowledge of the stress state at different spatial and temporal scales is vital for assessing reservoir response for CO_2 (e.g.,[63,83]), H_2 (e.g.,[54]), nuclear waste storage (e.g.,[23]), or monitoring groundwater and energy related subsurface resources, e.g., geothermal energy[25]. Insight into the undisturbed prestress state is also fundamental for evaluating earthquake dynamics, seismic cycles (e.g.,[7,48,50,95]), and the related hazard and risk (e.g.,[65,79]). Understanding the first-order stress drivers is particularly critical for drawing inferences about regions with limited data coverage, enabling reliance on more than just the local stress indicators within intraplate settings. This is crucial for understanding intraplate seismic events (see [94] for an overview), which are characterized by their rarity and low contribution towards the global average seismic moment release [49], yet feature considerable stress drop records [1,51,81]. These events are difficult to account for in standard seismic hazard assessments, with potentially significant consequences for the infrastructure.

The World Stress Map [31,32] is a well-known compilation of stress indicators. It is a continuously growing and openly available database that has been used to describe the present-day first-order state of the stress field [107,108], as well as to inform the initial conditions in geomechanical models (e.g., [104,105]). Early efforts to compile stresses include the reports of stress magnitude data in Scandinavia [30]. Later, Sykes and Sbar published the first regional and global stress compilations [80,93]. The availability of data from a multitude of techniques further motivated efforts to develop the global database of indicators of stress tensor orientations. Due to the variability of data sources, a quality categorization scheme was adopted to bridge the collected stress orientations on a global scale [34,84,107,108]. The records in the current state of the dataset contain the maximum horizontal stress orientations estimated from proxies like earthquake focal mechanism inversions, borehole breakouts, hydraulic fractures, overcoring, drilling induced tensile fractures, active fault kinematic indicators and volcanic vent alignments [33,107]. Most of these proxies are concentrated at plate boundaries. In intraplate settings, the reduced coverage reflects both the lower frequency of major tectonic or orogenic events and the related large recurrence time of earthquakes, resulting in a limited understanding of the stress state within these regions (Figure 6.1A).

Previous studies have identified regional scale patterns of stress indicators (e.g. [107]). Coblentz and Richardson [14] estimated well-determined bin-wise $\hat{S}_{\mathrm{Hmax}}$ orientations by performing a Rayleigh metric on the available dataset at the time. The Rayleigh metric is a statistical examination of departure from uniform distributions. It takes the form of a von Mises distribution, a symmetrical, unimodal distribution, the circular equivalent of the normal distribution [61]. In addition, studies include a double-angle technique [18] to account for the characteristic range of $\hat{S}_{\mathrm{Hmax}}$ data (0° to 180°), to avoid overestimating the dispersion when performing the Rayleigh metric (i.e., 0° and 180° being the same orientation but resulting in high dispersion) [14,34]. With this consideration, the Rayleigh metric is calculated as

$$\bar{R} = \sqrt{\bar{C}^2 + \bar{S}^2}, \quad \text{where} \quad \bar{C} = \frac{1}{n}\sum_{i=1}^{n} \cos\, 2\theta_i, \quad \text{and} \quad \bar{S} = \frac{1}{n}\sum_{i=1}^{n} \sin\, 2\theta_i, \tag{6.1}$$

for n being the number of bin-wise observations, and θ_i the azimuth orientation of $\hat{S}_{\mathrm{Hmax}}$. There, $\bar{R}$ measures the dispersion of a given set of $\hat{S}_{\mathrm{Hmax}}$ orientations within a bin, which is compared against a cut-off value. $\bar{R}$ can vary from 0 to 1; low $\bar{R}$ values are indicative of high dispersion and if it exceeds a certain critical value, the null hypothesis that the data come from a random distribution can be rejected at a specific confidence level. The approach can be adopted and applied to the current release of stress indicators from the WSM database [32]. This results in the bin-averaged $\hat{S}_{\mathrm{Hmax}}$ distribution depicted in Figure 6.1B, which reveals clear patterns across different continental areas. In this subfigure, the binned dispersion among the averaged indicators is represented by a Rayleigh metric using the same cut-off criteria as Coblentz and Richardson [14], with red color for binned centroids where $\bar{R} > 0.7$, and blue otherwise.

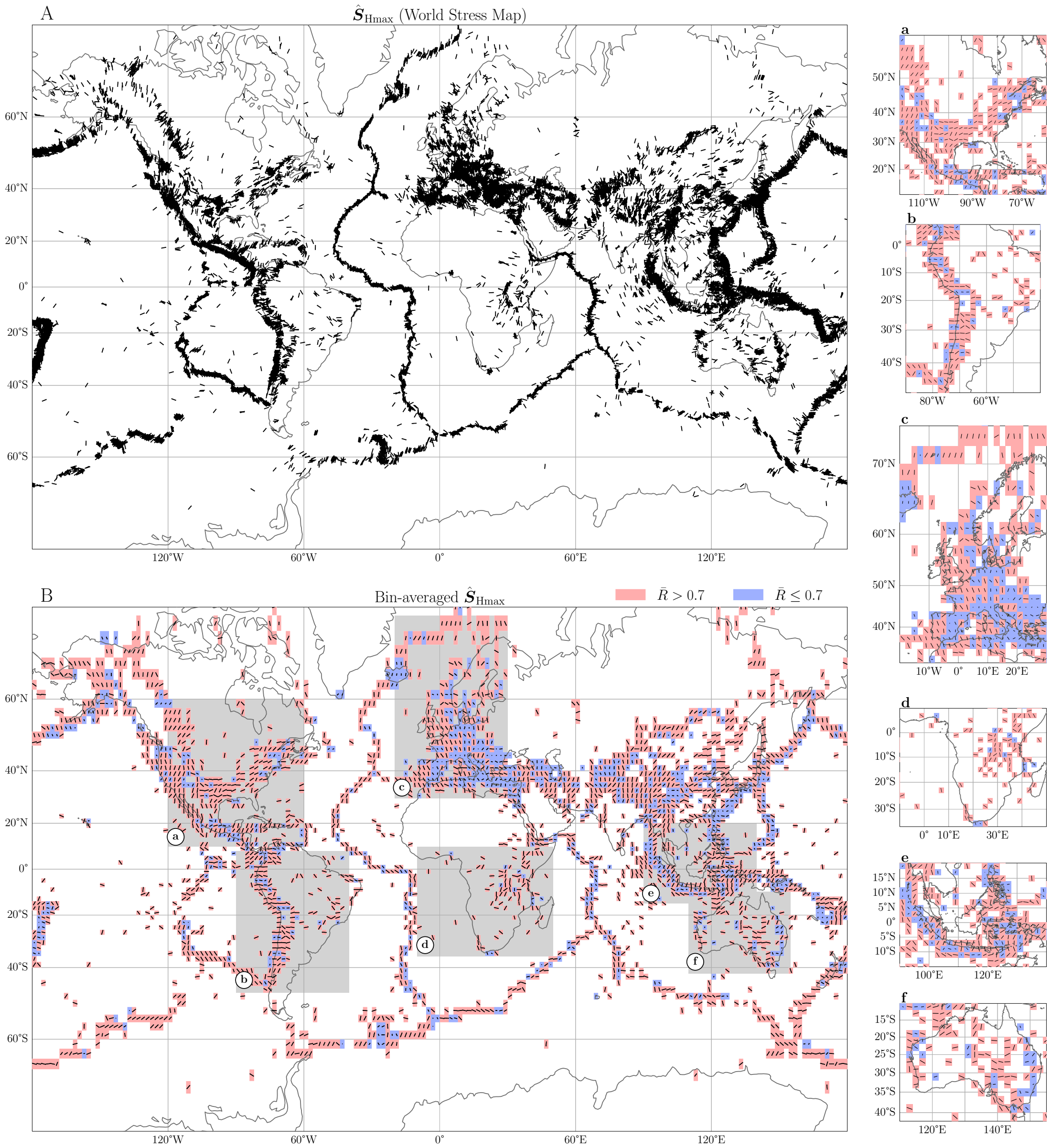

FIGURE 6.1. Stress Indicators and derived dispersion metrics. (A) Azimuth of maximum horizontal stress indicators of quality A-C from the World Stress Map database[32]. (B) Bin-averaged azimuth of the stress indicators within $2° \times 2°$ cells, using the same cut-off criteria as[14] and employing a smaller binning size and updated dataset. Binned dispersion among the averaged indicators is represented by a Rayleigh metric, with red color for binned centroids where $\bar{R} > 0.7$, and blue otherwise (see text). Gray areas (**a-f**) show regions of geodynamic interest, zoomed-in on the right column.

North America (Figure 6.1B.**a**) exhibits a large wavelength trend towards the northeast, along with shorter wavelength bin indicators of lower accuracy clustered along the west coast. The South American-Nazca plate boundary (Figure 6.1B.**b**) shows an eastern trending bin azimuth, in the overall direction of the subducting Nazca plate motion. On the southern boundary of the Nazca plate $\hat{S}_{\mathrm{Hmax}}$ consistently trends towards the north west, while the western boundary comprises lower accuracy trends towards the north east. The bin-averaged $\hat{S}_{\mathrm{Hmax}}$ indicators throughout Europe (Figure 6.1B.**c**) are oriented towards the east to south-east in Scandinavia, while the rest of the mainland transitions from a south-east azimuthal orientation to an east orientation with lower bin accuracy surrounding the Mediterranean sea [67]. Southern Africa is regarded as an extensional setting. At long wavelengths, the binned maximum compressional stress indicators (Figure 6.1B.**d**) are oriented north to northeast, as expected for east-west extension. The Indonesian region, along the northern boundary of the Australian and Eurasian plate, displays a compressive stress azimuth orientation perpendicular to the subduction geometry (Figure 6.1B.**e**), following the Java and Timor trenches. This direction changes rapidly to an orientation that parallels the plate boundary within the Indo-Australian plate, perpendicular to the plate motion. The plate-scale stress in this region is described as variable and not sub-parallel to the absolute plate motions [96]. Australia (Figure 6.1B.**f**) has a mostly East-West maximum compressive stress orientation axis, and a northeastern orientation on the northern part of the continent. This overall stress orientation has been the object of research due to its misalignment relative to the plate motion [73]. Alternative smooth representations for the $\hat{S}_{\mathrm{Hmax}}$ dataset exist that use a quality- and distance-weighted algorithm [31]. An expert-driven interpretation of the global stress field may also highlight the large-scale patterns of $\hat{S}_{\mathrm{Hmax}}$ and the dominant tectonic stress regimes (strike-slip, extensional or compressional) as seen in Appendix C.1.

The recognition of a significant large-scale component in the stress field with horizontal stress directions aligned over entire continents prompted work to analyse stress field patterns with tectonic and geodynamic models. Early on, tectonic simulations at global [76–78] and regional [13,15,16,40,74] scales often relied on elastic membrane models to account for boundary and drag forces, following a view by Forsyth and Uyeda [20] on plate driving and resistive torques. Geodynamicists subsequently focused on mantle convection related driving forces. By employing global mantle flow models [26,57,68,71,85] they showed that the mantle exerts first-order controls on the stress field. Similar conclusions were drawn from tectonic models, which explicitly included active mantle flow effects [3,5,10,99,100]. It is, of course, reasonable to expect a strong mantle flow effect on the large-scale stress field. But global mantle flow models are complex and key input parameters, such as rheology and thermo-chemical flow properties, remain poorly known. This motivates us to adopt a simpler approach, where we analyse the stress field with elementary fluid dynamic models, aimed at advancing our conceptual understanding of how mantle flow impacts the global stress field. To this end, it is known that the asthenosphere, a low-viscosity channel that underlies Earth's lithosphere (see [12,75] for reviews), strongly affects global mantle flow by inducing long wavelength horizontal flow in the uppermost mantle [8]. This is evident from Figure 6.2 A-D, where we visualize the velocity field of a mantle circulation model (MCM) (e.g., [9]) with a streamflow representation. The streamlines reveal the existence of only a few major up- and downwellings in the deeper mantle (Figure 6.2E). These join

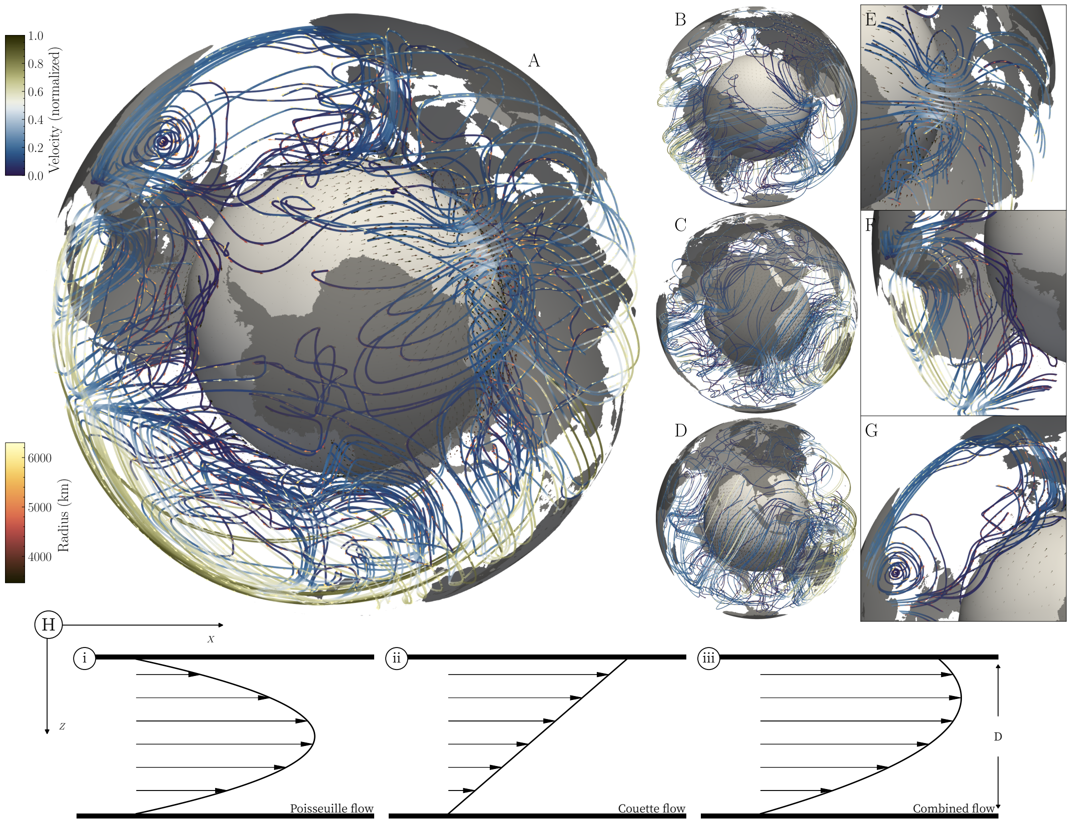

FIGURE 6.2. Streamline representation for present-day velocity field of a mantle circulation model [56]. Two sets of source seeds enter forward streamline integration: 53 seeds placed at 3500 km radius beneath estimated surface locations of mantle upwellings [36], and 83 seeds placed at 5500 km radius sampled from surface locations of convergent plate boundaries. Streamline colour scale (blue=min, brown=max) indicates normalized flow velocity. Two sets of 3D vector fields are superimposed: one sampled along streamlines using a constant vector length, the other sampled at core-mantle boundary (CMB), with vector length scaled with velocity at each spatial location. Colour scale of vectors indicates respective radial location. Grey sphere at centre represents CMB, and continental geometries with a slight opacity are placed on the surface for spatial reference. Insets show view angles of the model focused (A) on Antarctica, (B) South America, the South Atlantic, (C) South Africa, and (D) the Indian Ocean and South Asia, as well as upwellings (E), further highlighted by including the vector field set at CMB, and downwellings (F,G). Note the high velocity and long distance flow in the asthenosphere connecting a limited number of mantle up- and downwellings. (H) Schematic of (i) Poiseuille flow, described by a parabolic profile, driven by a lateral pressure gradient, and seen as a proxy for active asthenosphere flow capable of driving overlying plate, (ii) Couette flow, described a linear profile of shear driven fluid motion between two surfaces where one moves tangentially relative to the other, and seen as proxy for passive asthenosphere flow driven by motion of the overlying plate, (iii) superposition of both. Visualization generated with PyVista [90].

via shallow horizontal asthenosphere flow over thousands of km into large-scale convection cells (Figure 6.2F-G) of the mantle circulation system. Additional complexities may modify the behaviour of the asthenosphere (e.g., interruptions to the continuity of the asthenosphere at subduction slabs) which motivate further studies.

In a fluid dynamic context, mantle material flowing in a low-viscosity asthenosphere channel can be described in terms of Couette and Poiseuille flow (Figure 6.2H). The former is driven by movements of overlying tectonic plates, while the latter is driven by lateral pressure gradients, with the relative importance of Couette to Poiseuille flow depending upon the degree to which plates locally inhibit or drive underlying asthenosphere flow. Early work linked the Poiseuille flow to rising mantle plumes, proposing that hot plume upwellings induce lateral pressure variations to drive asthenosphere flux (e.g.,[72]). Subsequently, a series of geodynamic studies drew attention to the fact that lateral pressure variations in the asthenosphere also arise from cold downwellings, associated with subduction of tectonic plates (e.g.,[41–43]). In other words, lateral pressure variations are an intrinsic feature of asthenosphere flow driven by mantle up- and downwellings.

In the following, we adopt a Poiseuille-Couette representation of low-viscosity channelized asthenosphere flow, and analyze the associated first-order stresses that emerge from an assumed present-day flow state of the asthenosphere. We find that the principal stress predictions within the asthenosphere compare well with the bin-averaged observations as represented by the WSM. Our analytic formulation allows us to perform a stress analysis in terms of the contributing Couette and Poiseuille flow components, i.e. plate driven flow and flow induced by rising plumes and sinking slabs. It also helps us to isolate the stress patterns associated with basic flow geometries, i.e. the specific spatial distribution of plumes, subduction zones, plate motion and their superposition, which reveals important geometrical flow effects in the stress pattern. We organise our manuscript as follows. Chapter 6.2 lays out the basic theory together with our adopted flow parameters. Chapter 6.3 reports results, including detailed statistical comparisons of our model predictions with observations from the WSM. We also compute plate driving and resisting sublithosphere tractions. This is followed in chapter 6.4 by a discussion, where we suggest the potential to identify distinct stress and traction regimes for different tectonic plates and subregions based on flow geometry effects. We also place our results into the context of earlier work, evaluate the predicted amplitudes of stress and traction fields, and compare to stress field predictions made from MCMs. Finally, we draw conclusions in chapter 6.5.

6.2 Stress prediction from analytical velocity model

We use a simple analytical global velocity flow model[86,88,89] to estimate the mid-asthenosphere flow velocity field. The model is based on the assumptions of velocity-driven Couette flow, pressure-driven Poiseuille flow, and their superposition. To compute the present-day Couette flow induced by the rigid rotations of plates in the underlying asthenosphere, we use the plate velocity model at present-day from Müller *et al.*[66]. We assume that the Couette flow is half the surface velocity at mid-asthenosphere depth. For simplicity, the lower boundary of the channelized flow is assumed as a non-moving rigid sphere. We separate the contributions of the pressure-driven Poiseuille flow originating from upwelling plumes (sources) and downwelling slabs (sinks). Mantle upwelling-derived Poiseuille flow is estimated at a point as the total effect of the active plume sources under consideration as

$$\boldsymbol{u}_{plume} = \sum_{i=1}^{N} \frac{D^2}{8\mu} \frac{\Delta p_{pl_i}}{\Delta x_i} \hat{\boldsymbol{e}}_{\phi_i}, \tag{6.2}$$

where N is the total number of plume sources, D, Δp_{pl_i}, and Δx_i are the respective parameters for the i^{th} plume source, and $\hat{\boldsymbol{e}}_{\phi_i}$ is the unit vector in the azimuthal direction from the corresponding source towards each grid node. D is the thickness of the asthenospheric channel, for which we assume a value of 1.1×10^5 m, and μ its viscosity, taken as 5×10^{19} Pa s. We estimate the excess pressure for a plume source as $\Delta p_{pl_i} = \rho g h_0 \tilde{\Phi}_i$, with the density $\rho = 3300\,\mathrm{kg\,m^{-3}}$, $g = 9.8\,\mathrm{m\,s^{-2}}$, and a reference topographic height $h_0 = 1400$ m, weighted by $\tilde{\Phi}_i$ which is the mass flux entry Φ_i normalized relative to the maximum listed value in Table C.1. This choice agrees with observational estimates of dynamic topography (e.g.,[37]). Δx_i is the geodetic distance between the source and the grid node. The method has been proven practical in analysing the effect of plumes as driving forces of plate motion changes[86,88,89]. An in-depth review, as well as an acknowledgment of limitations, is described in Stotz *et al.*[86]. For our study we select 25 plume locations from the combined list of the 15 strongest buoyancy flux plume estimations from King and Adam[52] and the 15 strongest buoyancy flux plume estimations from Hoggard *et al.*[36], after removing duplicates. The list is given in Table C.1. Our simplest model assumes that each plume has the same buoyancy flux. Additionally, we consider the plume flux estimates from King and Adam[52] and from Hoggard *et al.*[36], also included in Table C.1, where the influx varies between plumes. To estimate the velocity field from mantle downwellings, we focus on the slabs-induced Poiseuille flow at sampled locations given by

$$\boldsymbol{u}_{slab} = \sum_{j=1}^{M} -\frac{D^2}{8\mu} \frac{\Delta p_{sl_j}}{\Delta x_j} \hat{\boldsymbol{e}}_{\varphi_j}, \tag{6.3}$$

similar to the plume calculation. In this case M is the total number of sinks that compose the collection of slabs. Δp_{sl_j} are the respective parameters for the j^{th} slab nodal sink and $\hat{\boldsymbol{e}}_{\varphi_j}$ the respective azimuthal direction from the nodal sink to the grid point. We estimate the slab-induced pressure change as $\Delta p_{sl_j} = \rho g h_1$, where in this case $h_1 = 200$ m. This representation of a slab-induced flow is explained in detail by Wang *et al.*[98], where it is used to estimate paleo-mantle-flow patterns.

We sample the domain using a Fibonacci lattice sphere, an effective way to obtain an evenly distributed set of points for discretizing the spherical surface, composed of 2400 points. At each node we calculate the effect of the imposed sources, sinks, and the state of the instantaneous velocity field at present day emerging from the Couette component of the velocity field. We use a convex hull algorithm[2] to determine the connectivity relation among the sampled points across the spherical surface to generate a shell mesh and calculate the velocity vector gradients numerically. With the discrete velocity field defined, we next adopt a steady-state, incompressible, isotropic and

Newtonian rheology as the constitutive relation to estimate the stresses. This translates into a linear viscous approximation, so that the deviatoric stress $\overline{\overline{\boldsymbol{\sigma}}}$ is related to the deviatoric strain rate $\overline{\overline{\boldsymbol{\varepsilon}}}$ (with constant volume) as

$$\overline{\overline{\boldsymbol{\sigma}}} = 2\mu\,\overline{\overline{\boldsymbol{\varepsilon}}}, \tag{6.4}$$

where we choose $\mu = 5 \times 10^{19}$ Pa s, as noted before, within the range of estimates for asthenosphere viscosity [12,45,70,75]. The strain rate tensor $\overline{\overline{\boldsymbol{\varepsilon}}}$ is related to the velocity vector gradient as

$$\overline{\overline{\boldsymbol{\varepsilon}}} = \mathrm{sym}(\nabla \boldsymbol{u}) = \frac{1}{2}\left[\nabla \boldsymbol{u} + (\nabla \boldsymbol{u})^T\right]. \tag{6.5}$$

We project the calculated stresses from a Cartesian coordinate system to a shell-local reference frame. We define the orthonormal local coordinate system with the set $[\hat{\boldsymbol{n}}_r\ \hat{\boldsymbol{t}}_E\ \hat{\boldsymbol{t}}_N]$, corresponding to the radial (normal to the spherical surface), eastward, and northward directions at each sampling point. We calculate the stress in the local coordinate system as

$$\overline{\overline{\boldsymbol{\sigma}}}' = \begin{bmatrix} \overline{\overline{\boldsymbol{\sigma}}} : (\hat{\boldsymbol{n}}_r \otimes \hat{\boldsymbol{n}}_r) & \overline{\overline{\boldsymbol{\sigma}}} : (\hat{\boldsymbol{t}}_E \otimes \hat{\boldsymbol{n}}_r) & \overline{\overline{\boldsymbol{\sigma}}} : (\hat{\boldsymbol{t}}_N \otimes \hat{\boldsymbol{n}}_r) \\ \overline{\overline{\boldsymbol{\sigma}}} : (\hat{\boldsymbol{n}}_r \otimes \hat{\boldsymbol{t}}_E) & \overline{\overline{\boldsymbol{\sigma}}} : (\hat{\boldsymbol{t}}_E \otimes \hat{\boldsymbol{t}}_E) & \overline{\overline{\boldsymbol{\sigma}}} : (\hat{\boldsymbol{t}}_N \otimes \hat{\boldsymbol{t}}_E) \\ \overline{\overline{\boldsymbol{\sigma}}} : (\hat{\boldsymbol{n}}_r \otimes \hat{\boldsymbol{t}}_N) & \overline{\overline{\boldsymbol{\sigma}}} : (\hat{\boldsymbol{t}}_E \otimes \hat{\boldsymbol{t}}_N) & \overline{\overline{\boldsymbol{\sigma}}} : (\hat{\boldsymbol{t}}_N \otimes \hat{\boldsymbol{t}}_N) \end{bmatrix}. \tag{6.6}$$

We take the stress components within the tangential plane of the spherical surface generated by $[\hat{\boldsymbol{t}}_E\ \hat{\boldsymbol{t}}_N]$. We solve for the respective eigenvectors and sort them according to their eigenvalues, which correspond to $\hat{S}_{\mathrm{Hmax}}$ and $\hat{S}_{\mathrm{hmin}}$ respectively (with S_{Hmax} and S_{hmin} as the quantities including its respective magnitudes). We refer to negative eigenvalues from the deviatoric stress tensor as tensile, while positive eigenvalues are here referred to as compressive. Note as well that such negative eigenvalues would potentially be positive if the confining stress was considered. One may interpret this as applying an operator on the model results to represent the output of the model into synthetic observables to be evaluated against the available data.

6.3 RESULTS

Figure 6.3 shows the Couette, the plume Poiseuille and the slab Poiseuille components in each row, and in each column their respective velocity and horizontal stress axes. Figure 6.3A shows the Couette component velocity field. It inherently captures information from diverging and converging plate boundaries within S_{hmin} and S_{Hmax} respectively. Locations of large tensile S_{hmin} (Figure 6.3B) are mainly concentrated around mid-ocean ridges, large compressive S_{Hmax} locations (Figure 6.3C) are mainly found at subduction margins, both oriented perpendicular to the plate boundary geometry. The Poiseuille-driven components introduce gradients that modify the velocity field within interregional scales. The slab flow introduces velocity variations that decay away from the vicinity to the subduction zones (Figure 6.3D-F). Plumes introduce subregional divergent flow that modifies the velocity field radially from each point source. The superposition of all plumes,

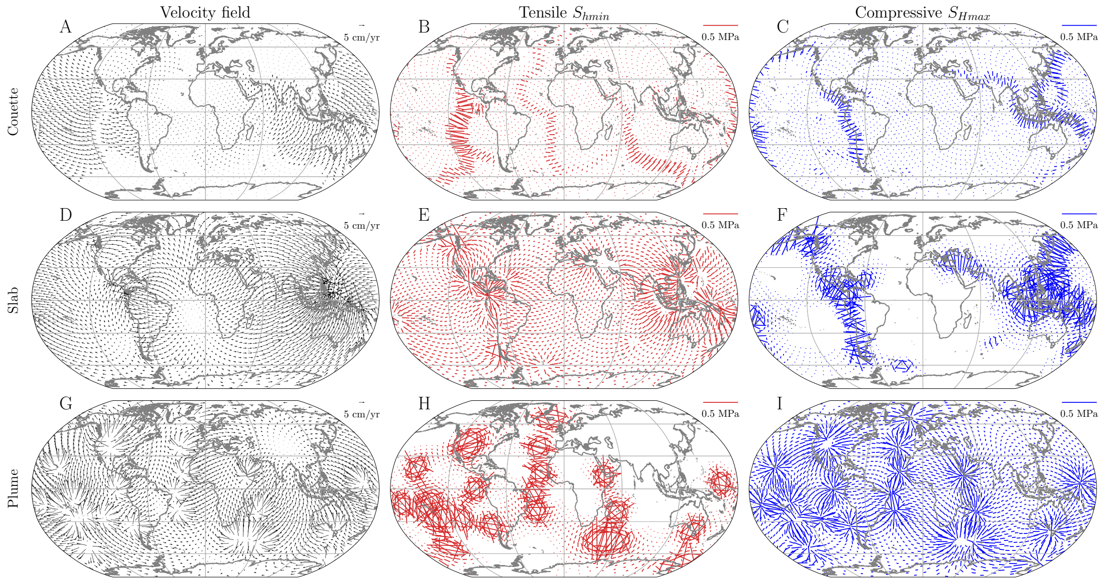

FIGURE 6.3. Flow components of an analytical model for asthenosphere flow and stress. Each row depicts the Couette, Slab, and Plume components, respectively. Couette component derived from the rigid body rotation of global plate motion model [66]. The slab component is modelled as a global velocity field sink term at sampled converging plate boundary locations. The plume component contains 25 global velocity field source locations from the union of the highest buoyancy influx plume locations listed in [52] and [36], where we take the same constant inflow buoyancy contribution (Φ_C) for all source locations, for simplicity. Columns depict the velocity field due to the effects of each flow component separately, and the derived S_{hmin} and S_{Hmax} fields. Velocity vectors correspond to velocities at the back end of the arrow.

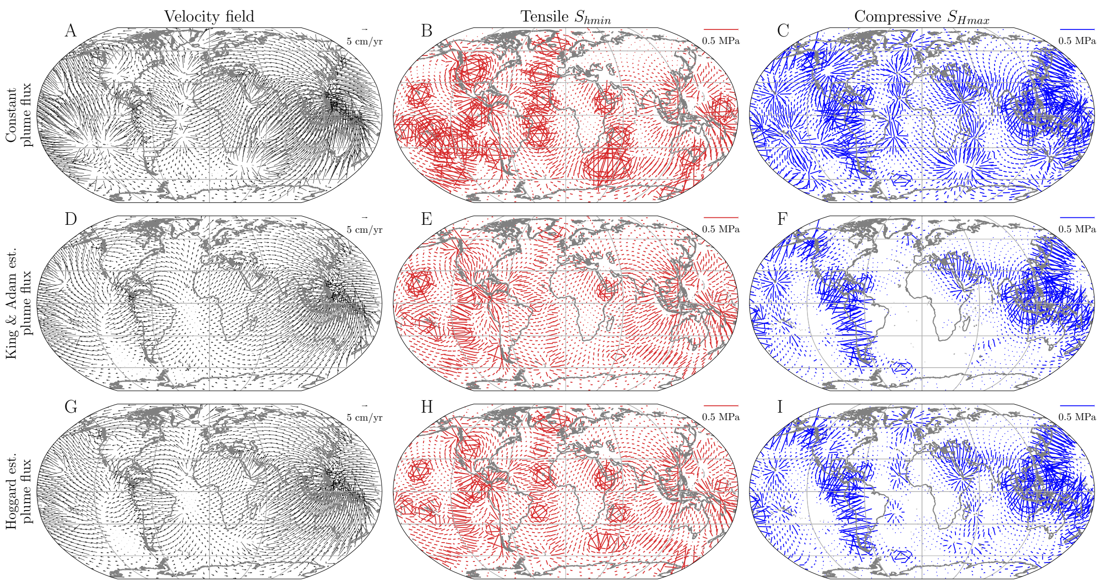

Figure 6.4. Total flow of an analytical model for asthenosphere flow and stress, for different plume buoyancy inflow estimates. First, second and third row depict, respectively, superpositions (Couette, Slabs, Plumes) of the velocity field components from Figure 6.3, using constant plume buoyancy inflow Φ_C, a plume buoyancy inflow Φ_{KA} after King and Adam [52], and a plume buoyancy inflow Φ_H from Hoggard *et al.* [36]. Columns show total velocity field and its associated S_{hmin} and S_{Hmax} fields. Velocity vector arrows correspond to the velocities at the back end of the arrow.

and their effect on the resulting horizontal stress field, depends on their geometrical arrangement and their assigned plume buoyancy flux. Figure 6.3G-I shows the velocity and horizontal stress axes for the simplest plume flow model, where we assume a constant buoyancy flux for each plume.

Figure 6.4 shows the total asthenosphere velocity field, and associated horizontal stresses, resulting from adding together all flow components. We compute three models that differ by their choice of plume influx strength: a constant strength for all plumes, or a plume influx based on estimates from King and Adam [52] or from Hoggard *et al.* [36]. We refer to these models respectively as Φ_C, Φ_{KA}, and Φ_H. For each velocity field, we extract the vector gradients and estimate the associated horizontal stress axes. The total flow model using Φ_C (Figure 6.4A-C) overestimates the strength of weaker plumes. As a result it largely overprints the gradients induced by the Couette component at the locations of mid-ocean ridges. The model featuring Φ_{KA} (Figure 6.4D-F) assigns large strengths to plumes in the Pacific hemisphere, in particular the Hawaii hotspot, with lower relative contributions from other plumes as outlined in Table C.1. Model Φ_H (Figure 6.4G-I) shows a more evenly distributed plume contribution globally.

In Figure 6.5 we compare the alignment of our estimated $\hat{S}_{\mathrm{Hmax}}$ against the bin-averaged observations for model Φ_H. We adopt a 45° threshold in our comparisons to set the boundary between noncorrelation and correlation, following the choice done by Bird [3]. He used a 45° threshold to analyze the correlation of the mean alignment between a global model and the observed directions

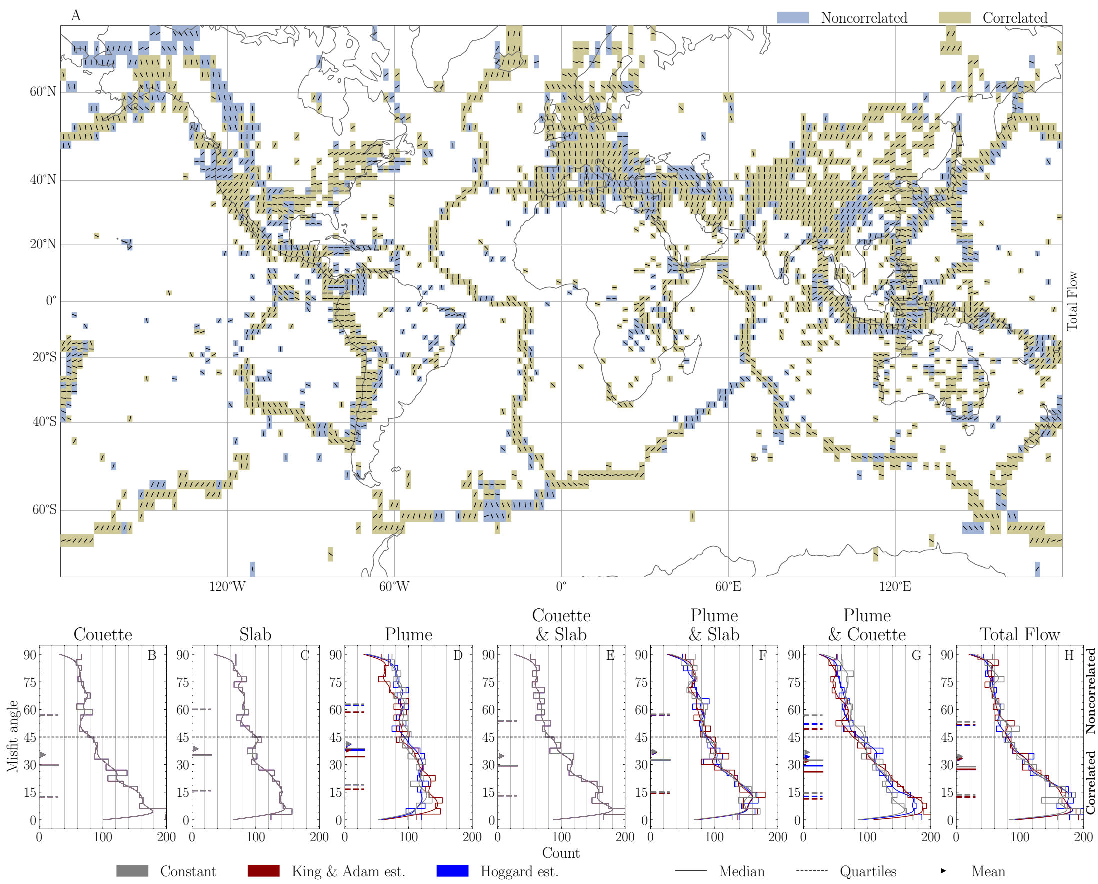

FIGURE 6.5. Azimuth map of $\hat{S}_{\mathrm{Hmax}}$ derived from total flow model, featuring Φ_H plume influx component, and alignment histograms for each flow model component and combinations. (A) illustrates spatial distribution of modelled $\hat{S}_{\mathrm{Hmax}}$ orientations, either correlated (green) or noncorrelated (blue) relative to bin-averaged observed azimuthal data for Φ_H plume influx. We also present alignment bin histograms for the (B) Couette, and the Poiseuille-driven (C) slab, and (D) plume components, as well as (E-G) combinations. The (H) total flow, including all three components, is also provided. Subfigures B-H contain histograms, and their corresponding kernel density estimations. We also provide the 25th and 75th percentile quartiles denoted by horizontal dashed lines, the median marked by a continuous horizontal line, and the mean error in stress direction is indicated by a triangular marker, all on the left of each subplot. Each set of statistical parameters is color-coded according to the plume buoyancy influx used in each considered flow model.

from the WSM. He argued that this threshold was sufficient to evaluate the correlation between the model and observation, due to the large internal inconsistencies associated with the stress observations dataset[4]. Bird also pointed out that, given the observational uncertainty, it was doubtful that any model will match the observations better than the mean error of 25°[3].

While some misaligned bin-averaged centroids (blue boxes in Figure 6.1B) coincide with regions of high dispersion according to the bin-wise Rayleigh metric, there are still low-dispersion bins that are poorly predicted by our model. Upon removing the high-dispersion bins in our azimuthal comparison, the histogram pattern does not show a significant improvement (See Appendix C.6; Figure C.9). This indicates that the model misfit is not solely due to high dispersion in the observed stress direction, and that azimuthal misfit between our model and observation can still occur even in low-dispersion bins. Figure 6.5B-H show histograms of alignment between the model and the bin-averaged observations. The spatial distribution of bin-averaged comparisons for partial flow components is included in Appendix C.4. The histograms from partial and total flow contributions have a mean alignment that is well-correlated. The best performing model, in terms of a misfit angle of the mean $\hat{S}_{\text{Hmax}}$ distribution, is the Couette flow component in combination with the plume model using Φ_{KA}. The stress alignment is good at convergent and divergent plate boundaries, where most of the bins are located. This, by construction, results in a histogram distribution that is skewed towards correlation. The slab component describes convergent boundaries and nearby plate interiors well. Globally the $\hat{S}_{\text{Hmax}}$ patterns emerging from the plume component alone do not fit as well (see histogram in Figure 6.5D and Figure C.6 and Figure C.7 in Appendix C.4 for the spatial variation of stress azimuth comparisons for the plume component) as the other single flow components. But subregionally they provide a good fit. As a result, there is a set of bins with good correlation, in addition to poorly correlated bins, so that the shape of the distribution is slightly skewed towards correlation. The overall fit is improved when combining the contributions from flow components. In particular, all combinations including a Couette component perform well, as they include a fit in both active and passive plate boundaries, as well as Poiseuille-driven gradients that dominate the stresses at plate interiors.

Regional stress azimuth maps and flow regimes

Figure 6.6 compares the model performance relative to $\hat{S}_{\text{Hmax}}$ in regions chosen in Figure 6.1(**a**-**f**). Figure 6.6A shows North America, where most of the misalignment of the modeled stress with the bin-averaged $\hat{S}_{\text{Hmax}}$ is located along the Rocky mountains. The model performance slightly improves in the southern portion of North America when considering a Φ_{KA} (Figure C.2) plume contribution. Figure 6.6B shows Europe, with misalignment around the northern margin of the Mediterranean, and a pattern of good correlation elsewehere that describes a radial azimuth orientation centered on Iceland and extending across the Scandinavian peninsula, central European mainland, and the Iberian peninsula. It is interesting that in Southeast Asia (Figure 6.6C) the model reproduces the 90° change in $\hat{S}_{\text{Hmax}}$ orientation from the Java trench to the interior of the Indo-Australian plate. In other words, the model reproduces the observed stress rotation in the Indo-Australian plate away

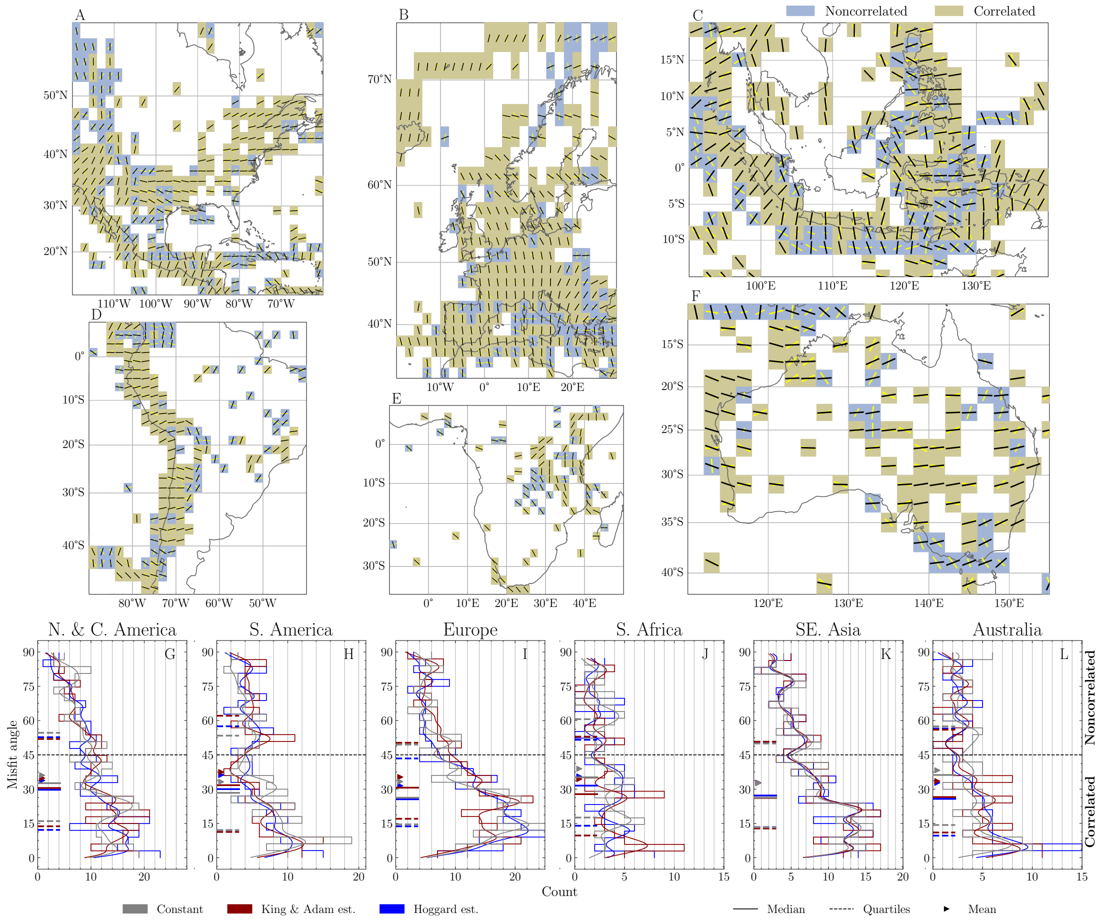

FIGURE 6.6. Regional extent $\hat{S}_{\mathrm{Hmax}}$ azimuth maps and their bin-averaged alignment histograms, for total flow featuring the Φ_H plume influx component. Zoom in of the $\hat{S}_{\mathrm{Hmax}}$ alignment map in Figure 6.5A, focusing on (A) North America, (B) Europe, (C) Indonesia, (D) South America, (E) South Africa, and (F) Australia. The alignment between our model and the bin-averaged azimuth observation are compiled in each histogram, including the same statistical parameters as in Figure 6.5 (G-L). Each set of statistical parameters is color-coded according to the plume buoyancy influx component.

from the subduction zone. Within the latter, $\hat{S}_{\mathrm{Hmax}}$ is perpendicular to plate motion. Figure 6.6D covers South America. Here the model reproduces most of the azimuth directions along the Andes. The major misalignments are located along the southern Altiplano in the Andes cordillera, central east Colombia, and scattered bins in Brazil above 20°S. Figure 6.6E focuses on the southeastern Nubian and western Somali plates, with correlated bins located around the East African Rift system, and in the southernmost part of the continent. The noncorrelated bins are sparsely distributed, with a significant concentration centered around Congo and Zambia, southwest of the East African Rift. Figure 6.6F shows Australia, where the model reproduces the well-known east-west $\hat{S}_{\mathrm{Hmax}}$ orientation that is orientated perpendicular to plate motion. Misalignments are located in the southeast of the mainland and in a north-south azimuth around the McDonnell Range.

Histograms in Figure 6.6G-L evaluate the regional performance of $\hat{S}_{\mathrm{Hmax}}$ emerging from the total flow. The histograms include all three options of plume inflow strength. Overall, the histograms show a good correlation across the regions, with a slight variation due to the choice of plume influx estimate (Φ_C, Φ_{KA} and Φ_H). North and Central America (Figure 6.6G) is characterized by a distribution where the majority of the bins is correlated. The histogram for the region of South America (Figure 6.6H) shows a bimodal distribution. A peak of good correlation owes to a well-correlated majority of bins along the Andes, while a second and wider peak reflects a distribution of noncorrelated bins that is sparsely located across the mainland. The histogram for Europe (Figure 6.6I) shows good correlation with the data. Models using Φ_C and Φ_H yield a slightly better fit than the King and Adam plume flux model Φ_{KA}. The histogram for the southern part of Africa (Figure 6.6J) features a wide statistical distribution. The mean alignment of about 40° falls within the correlated classification, although we note the limited number of bins in this region. The histogram for southeast Asia (Figure 6.6K) is largely skewed towards correlation. The variation due to the plume flux choice is near negligible. The histogram for Australia (Figure 6.6L) features a bimodal behaviour dominated by the overall correlated alignment of the total flow, and the more localized noncorrelated bins. Weighted plume flux choices (Φ_{KA}, Φ_H) result in models better aligned to the observations than a constant plume flux (Φ_C). The misalignment in the distribution is due to the clustered bins from the Java Trench in the north, bins scattered across the center of the Australian continent, and bins located at the northernmost and southernmost margins of the east coast.

Our analytic model allows us to perform a component analysis in order to evaluate statistically the impact of each flow type, and their combinations, on the selected regions. We do so in Figure 6.7. Regions best represented by a single flow type are highlighted with a gray background, whereas combinations of flow components that best reflect each area are marked with a star. Figure 6.7A_2 shows that South America best portrays the stress azimuth generated by a Couette component. Australia instead (Figure 6.7A_6) exhibits no correlation with the stress predicted from a Couette component alone. Its bin-averaged $\hat{S}_{\mathrm{Hmax}}$ is best explained by a slab poiseuille flow, as expected by its proximity to subducting plates (Figure 6.7B_6). Europe is the best representative of the plume component, influenced by Atlantic plumes. The fit is slightly affected by the choice in plume weights (Figure 6.7C_3), with best results achieved for Φ_{KA}. South Africa is also well characterized by the plume component, using Φ_H (Figure 6.7C_4), which captures the bin-averaged $\hat{S}_{\mathrm{Hmax}}$ direction around the East African Rift. Southeast Asia most closely resembles a combination of Couette and slab flow

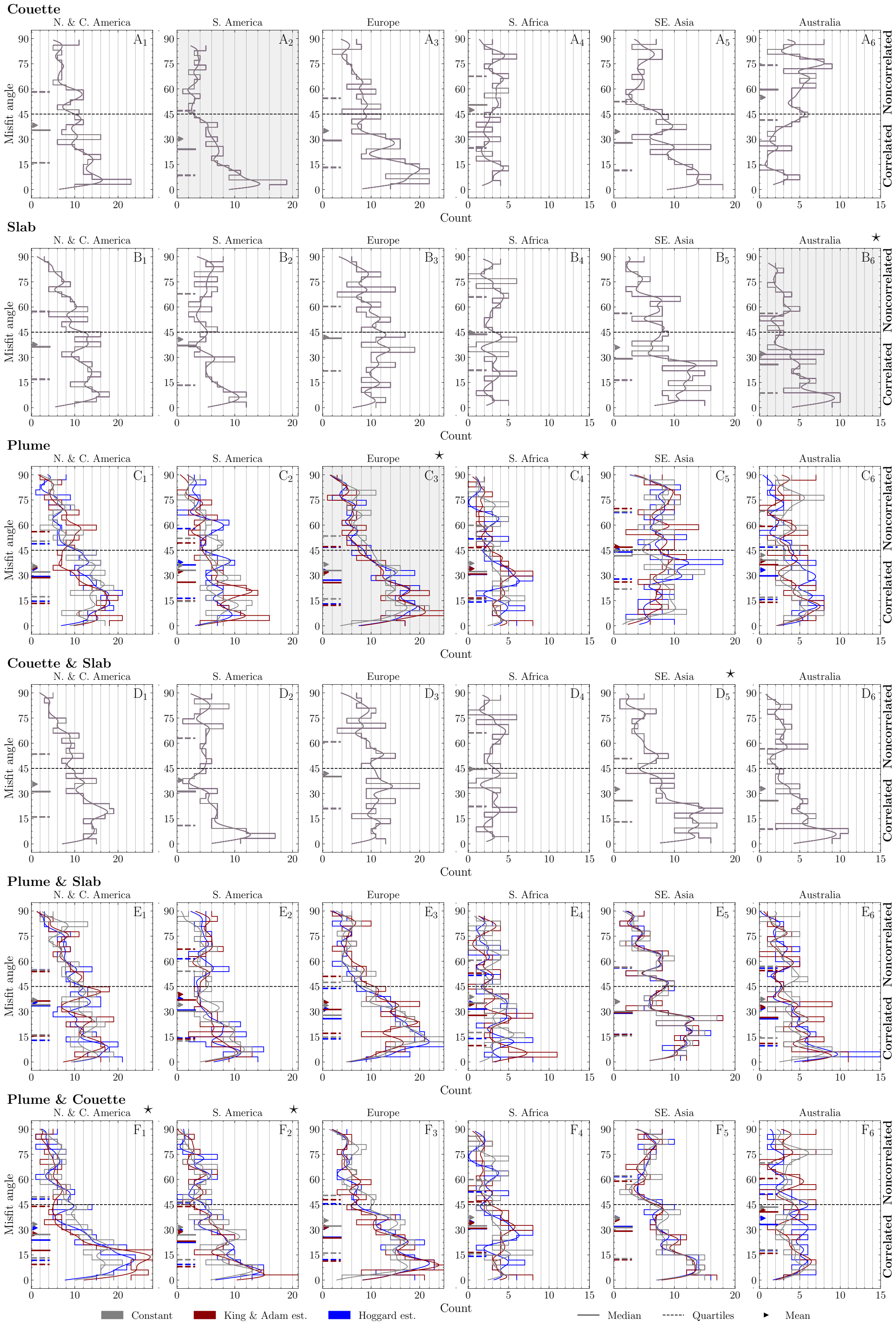

FIGURE 6.7. Histograms of azimuth alignment against bin-averaged stress indicators for each regional extent and modeled flow components. Gray background denotes the best representative regions for a single flow component (row-wise). A star marks the partial combination of flow components that best describes a chosen region (column-wise). This comparison excludes the total combination of flow components.

(Figure 6.7E_5). It well describes the $\hat{S}_{\mathrm{Hmax}}$ alignment perpendicular to the plate motion within the Australian plate, the $\hat{S}_{\mathrm{Hmax}}$ perpendicular to the subduction margin on the southwest, and the North-South stress azimuth within the Sunda plate. The regions of North and Central America, and South America, are best described by a plume and Couette flow component combination (Figure 6.7F_1,F_2). Specifically for North and Central America, the superposition of flow components provides an better fit than individual components on their own (Figure 6.7A_1,C_1). This may reflect a complex flow setting at a plate boundary and in the presence of the Yellowstone plume. Although the stress alignment for South America is well-captured by a Couette flow (Figure 6.7A_2), as noted before, the fit improves upon accounting for the effects of the plume component arising from Atlantic plumes.

Asthenosphere stress pattern analysis from simplified geometries

Our regional analysis of the flow components reveals distinct flow patterns near plumes, subduction zones, and Couette regimes. We bring out this geometrical control more clearly in Figure 6.8, which isolates the stress patterns associated with basic flow geometries. The velocity field induced by a single linear slab (i.e., a simplified representation of subduction in South America) is shown in Figure 6.8A. The magnitude of the velocity vectors increases towards the line of sinks, as expected from Poiseuille flow. In other words, the velocity field (excluding nodes in the immediate vicinity of the parameterized geometry) experiences extension in a slab-perpendicular direction as indicated by $\hat{S}_{\mathrm{hmin}}$. The orientation of $\hat{S}_{\mathrm{Hmax}}$ is perpendicular to the flow direction (Figure 6.8C) and thus an intrinsic characteristic of the geometrical arrangement. In the immediate vicinity of the slab geometry, the spatial gradients capture the convergent character of the flow and induce a spatial change in the $\hat{S}_{\mathrm{Hmax}}$ orientation (more evident in a streamflow representation, as shown in Figure 6.8D). Figure 6.8E-H depicts the velocity and stress patterns for a semicircular slab (i.e., a simplified representation of the slab distribution in the northwestern Pacific, or the Java trench). The same effects as noted before are seen on the convex (outside) side of the semicircle. $\hat{S}_{\mathrm{hmin}}$ and $\hat{S}_{\mathrm{Hmax}}$ are orientated parallel and perpendicular to the flow direction, respectively. But there is a stress amplification on the convex side, while stresses are reduced on the concave side. The stress amplification/reduction on either side of the curved slab is as a function of the slab curvature as seen from Figure C.8. The stress component patterns associated with a Couette flow derived from rigid rotations depend on the relative location of the Euler pole. Figure 6.8I-L show that for an Euler pole far from the plate (i.e., a simplified representation of the Nazca plate), significant stresses accumulate at the plate boundaries –tensile at locations of spreading and compressional at convergent boundaries– while the small internal deformation reflects the plate' rigid character. Figure 6.8M-P show the case of a rigid motion with an Euler vector within the plate (i.e., a simplified representation of the North American plate). There, the coherent stress direction varies significantly in amplitude and direction relative to the Euler vector along the plate perimeter, reflecting the proximity to the Euler pole. Finally, Figure 6.8Q-T show the velocity and axial stress fields from a combination of the Couette flow (with an Euler pole far away from the plate as in Figure 6.8I), and a slab component away from the convergent plate boundary (e.g., flat slab geometry as described for

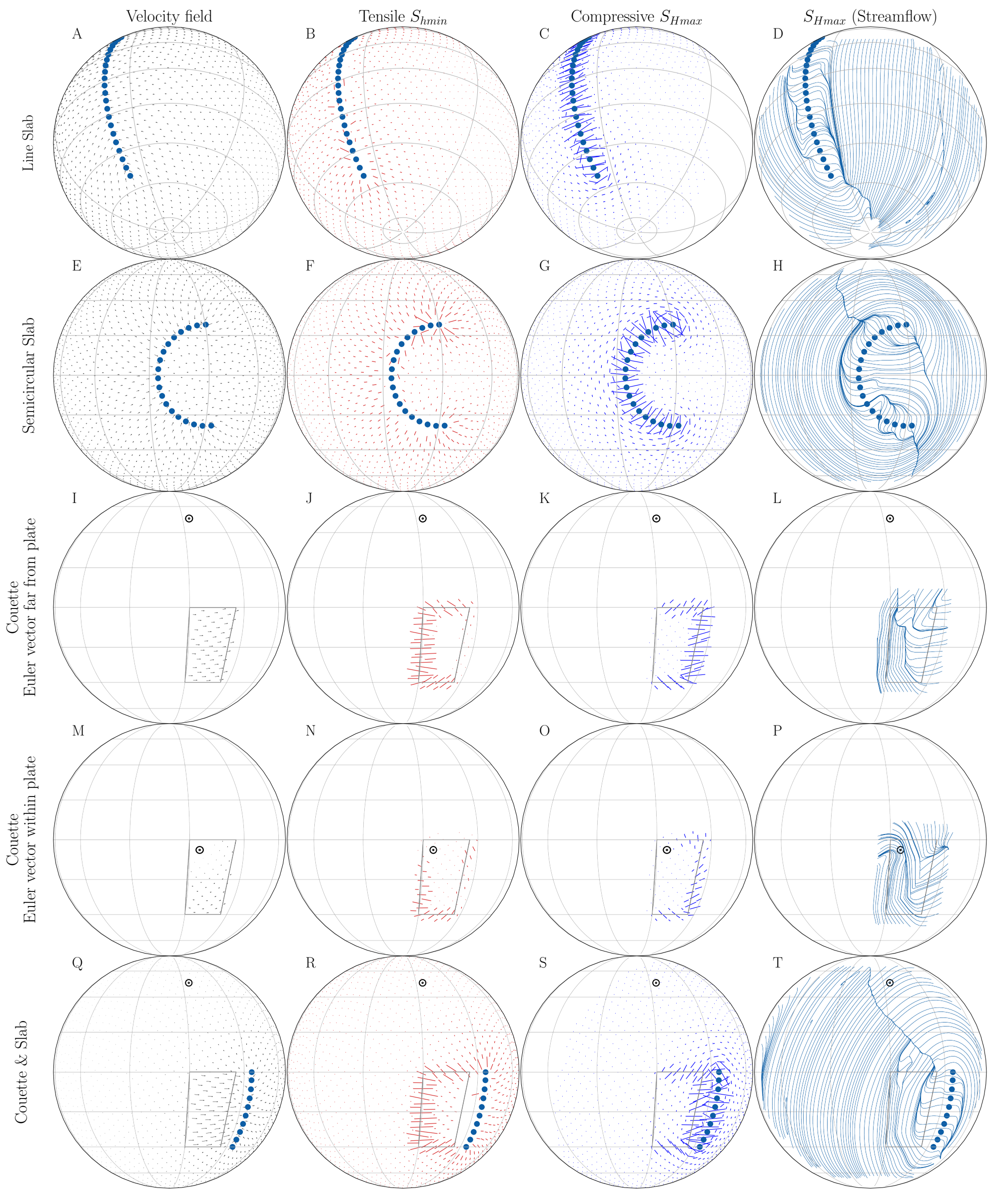

FIGURE 6.8. Stress analysis emerging from basic geometrical setups. Each row shows different simplified convergent boundary geometries: They include lineal (A-D), and semicircular (E-H) slab shapes. Rows (I-L) and (M-P) include the Couette flow emerging from rigid body rotation for a block relative to, first, an Euler pole far from the plate (I-L), and second within the plate (M-P), depicted by the "⊙" symbol. The last row shows the superposition between the Couette flow emerging from the rigid rotation of a block with an Euler pole far away from the plate, and a line slab not aligned with the block boundary (Q-T). Each column indicates the effect of such geometry in the (left to right) velocity field derived from an analytical model, and correspondingly, S_{hmin} and S_{Hmax} fields, as well as the surface integrated streamflow from the $\hat{S}_{\mathrm{Hmax}}$ azimuth field.

various subduction regions in the Americas [59]). Figure 6.8Q shows that the velocity field within the rigid block is increased by the presence of the nearby slab (compare to Figure 6.8I). Elsewhere, the velocity field behaves according to the presence of a small linear slab. Figure 6.8R shows the $\hat{S}_{\text{hmin}}$ field. It behaves like the combination of a Couette and a slab Poiseuille. The compressive $\hat{S}_{\text{Hmax}}$ in Figure 6.8S is concentrated between the convergent boundary of the rigid block and the slab, orientated perpendicular to both. Compared to a slab alone, it shows an asymmetric region of $\hat{S}_{\text{Hmax}}$ extended towards the plate boundary. In this region, the tensile $\hat{S}_{\text{hmin}}$ field is reduced, implying that the horizontal deviatoric stress axes are all compressive. This extended region of $\hat{S}_{\text{Hmax}}$ perpendicular to the slab at subduction boundaries within continental regions, may characterize the west coast of North and South America, as well as the flat slab in Asia, though further assumptions are required for the location of the slab parametrization.

On the tractions relative to rigid rotations

In addition to the horizontal stress axes field pattern as it emerges from the flow geometry, we look at the plate driving and resisting tractions. The tractions reflect how our modelled asthenospheric flow behaves relative to the rigid rotation of the plate above. We compute the tractions at every grid nodal position as

$$\boldsymbol{\tau} = -\mu \frac{\Delta \boldsymbol{u}}{0.5\, D}, \text{ with } \Delta \boldsymbol{u} = \boldsymbol{u}_P - \boldsymbol{u}, \tag{6.7}$$

where $\boldsymbol{u}$ is our estimate for the channelized asthenospheric velocity field, and $\boldsymbol{u}_P$ is the velocity field at the top of the channel, which we assume as the plate velocity. μ and D are respectively the viscosity and the thickness of the asthenospheric channel, as noted before. Figure 6.9 shows the traction vector field corresponding to the asthenosphere total flow velocity and assuming the plume influx estimate from Hoggard [36], Φ_H. Results from assuming the plume influx estimate from King and Adams [52], Φ_{KA} are shown in Appendix C.3; Figure C.3. The traction estimates are on the order of few MPa. Additionally the figure contains the tractions due to the individual flow components and combinations. We also include in each map the scalar field resulting from the projected traction vectors into the plate velocity directions as $\boldsymbol{\tau} \cdot \hat{\boldsymbol{u}}_P$, indicated by color. In line with Eq. 6.7, positive projected traction values indicate regions in which the channelized flow velocity projection in the direction of the plate velocity field is larger than the plate velocity itself (or $\boldsymbol{u} \cdot \hat{\boldsymbol{u}}_P > u_P$). Negative values indicate that the projected flow component is either antiparallel or less than the plate velocity. A threshold of ±0.5 MPa indicates the active or resistive role of the projected tractions, shown in continuous or dashed contour lines, respectively. The areas outside of the contour lines are regions where the projected velocities are comparable to plate velocities, and thus result in low values of projected tractions.

Figure 6.9A shows that large regions of the Earth are subject to active plate driving tractions, as illustrated by continuous contour lines. They include the Indo-Australian, Pacific and South American plates, the east and north of the North American plate, as well as a major part of northern Africa. Smaller regions are subject to resistive tractions, as illustrated by dashed contour lines. They

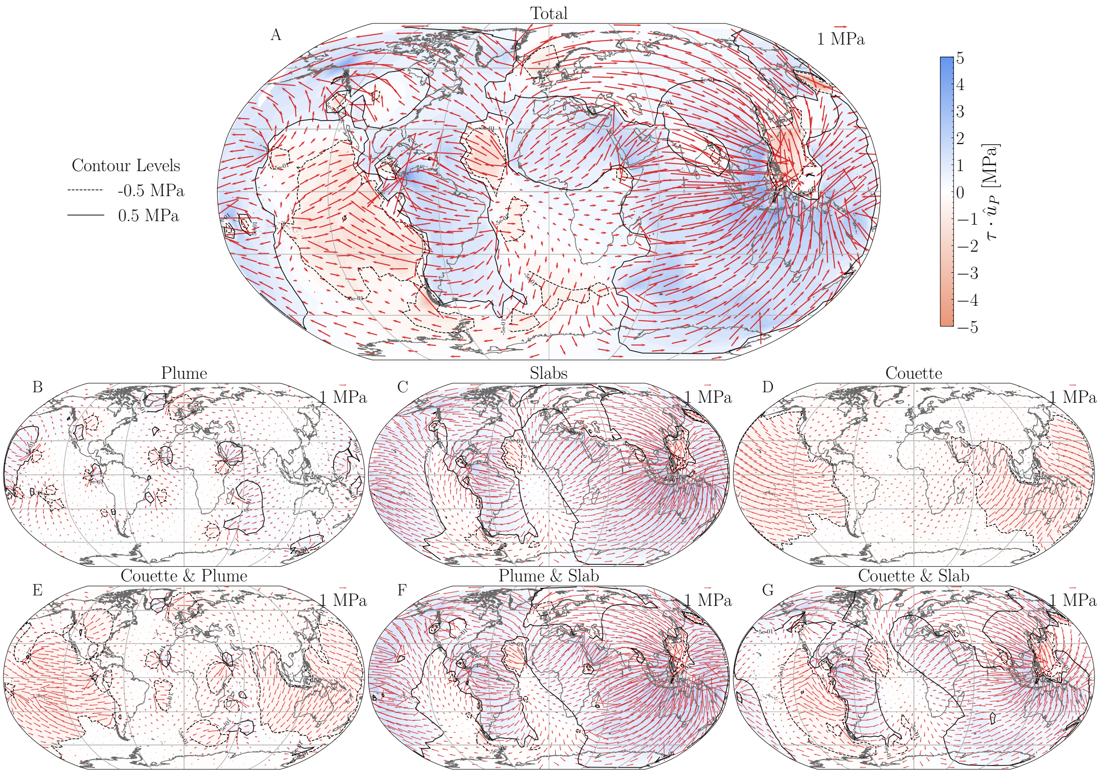

FIGURE 6.9. Tractions for total flow (A) and flow derived from single or combined flow components (B-G) relative to the plate velocities. The plume component features an inflow Φ_H. The tractions of Poiseuille-only flow components are computed relative to zero magnitude plate velocities. The colormap indicates the magnitude resulting from the traction vector projected into the surface velocity direction ($\boldsymbol{\tau} \cdot \hat{\boldsymbol{u}}_P$), with blue/red colors indicating forward/resistive tractions. The solid and dashed black contour line highlights, respectively, the $\pm 0.5\,\mathrm{MPa}$ level sets from the projected traction magnitude field.

include the East Pacific rise, Central and Southern Mid-Atlantic ridges, the Sandwich plate, the Drake Passage, the Phillipine Sea, and the Norwegian Sea. The remaining areas (e.g., southern Africa and the south Atlantic, as well as northern Eurasia and the center of the North American plate) are subject to small projected tractions. In other words, plate velocities in these regions are comparable to the asthenosphere flow velocity in the direction of plate motion, so that tractions are minimal. Note that different traction regimes can occur within a single plate. Figure 6.9B shows the tractions from the plume flow component. The plume induced tractions computed relative to a static surface are characterized by radial traction vectors relative to each plume location. When these traction vectors are projected against the directions of rigid plate velocities, they decompose into resistive and driving regions around the hotspot. The regions around Hawaii, Yellowstone, Afar, and the western region of the Indo-Australian plates, experience the effective superposed tractions due to multiple plume sources in the vicinity. This superposition leads to an asymmetry between the resistive and driving regions when the tractions are projected onto the present-day rigid plate velocity directions. Figure 6.9C shows the tractions from the slab flow component, computed relative to a static plate. This component provides driving tractions for most of North America, South America, Africa and the central and western Europe region, as well as the Indo-Australian plates and Asia mainland. Regions of resistive tractions are more confined and primarily appear in west of the Drake passage in South America, the central Atlantic, and the Philippine plate. It provides driving tractions for the northwestern margin of North America, South America, North of Africa and Mediterranean region, and the northeastern subduction margin of the Indo-Australian plate. Note that the projected driving tractions decay away from the active margins. This reflects the spatial extent of the negative Poiseuille component, as it decreases away from the sink (e.g., Figure 6.8A). The slow moving Antartic plate, on the east, shows projected driving tractions as a response to the far field effects of the west Pacific subduction margins. We point out that the strength of the Cascadia and the Hellenic subduction zones, and hence their associated tractions, are likely overpredicted in our formulation, due to our simplified assumption of constant slab buoyancy per unit length. Figure 6.9D shows the tractions from the Couette component. By construction, this flow can only be a fraction of the plate velocity, and therefore emerges as a purely negative contribution in the projected tractions. The distribution and magnitude of these tractions depend on the Eulerian reference frame of the plate velocity model[66]. Figure 6.9E shows the combined effect of Couette and plume flow. There, the projected driving tractions induced by the plume component at the source locations are enhanced, when compared to the plume component alone. The apparent resistive tractions from the Couette component alone in Figure 6.9D now includes more short wavelength variations from the Plume component superposition. Figure 6.9F depicts the combined plume and slab Poiseuille components. Also in this case, the combination of the flow components results in stronger driving tractions compared to plume or slab component alone with embedded resistive locations. Finally, in Figure 6.9G we show the combined effect of the Couette and the slab flow.

6.4 Discussion

Mantle convection is the dominant driver for large scale tectonic processes on Earth. Prime examples of its surface expressions include dynamic topography[35] and plate motions[58]. It is thus entirely reasonable to expect that mantle flow significantly affects the global stress field. Following this reasoning, numerous geodynamic studies investigated mantle flow effects on stress patterns either by using global mantle flow models on their own (e.g., [85]) or in combination with models that represent the lithosphere[26,57,68,71]. They confirm that the mantle exerts first-order effects on the stress field. Similar conclusions were drawn from regional scale tectonic models coupled to mantle flow (e.g., [10,99]). They also found that an active driving component from mantle flow beneath plates is essential to explain the stress field. These earlier findings are important. But the profound understanding in geodynamics that has emerged over the past two decades about the central role played in mantle dynamics by a low viscosity and highly mobile asthenosphere (see [12,75] for recent reviews) allows us to go a step further. Specifically the Poiseuille-Couette nature of the flow expressed in this low viscosity channel[41–43] allows us to adopt a simple global analytical description of channelized flow, based on the superposition of Poiseuille and Couette flow components in the asthenosphere[86,88,89]. From this approach we analyzed for the first time the asthenospheric stress field and separated it in terms of the contributing upper mantle flow components. In other words, from the analytic flow field we derived its associated stresses, extracted their horizontal field components, represented them in terms of the contributing flow components, and compared them to stress indicators compiled in the WSM that provide a reduced description of the stress tensor.

Geometrical effects in stress field patterns of asthenosphere flow

The close correspondence, both globally and regionally, between modeled and observed stress field as represented by $\hat{S}_{\mathrm{Hmax}}$ is a significant finding. The agreement includes areas of intuitive $\hat{S}_{\mathrm{Hmax}}$ orientation, where the azimuth orientation is aligned with plate velocities. For instance, the $\hat{S}_{\mathrm{Hmax}}$ alignment globally with plate velocities at ridges is a consequence of the Couette component emerging from rigid rotations at plate boundaries. This flow style leads to divergence with an axis parallel to the spreading direction, and thus a maximum compressional axis parallel to the ridge geometry. South America is reasonably well fit by a Couette flow regime, and so is to a lesser degree Europe (Figure 6.7A_2,A_3, Figure C.4). Some regions also reveal a strong plume Poiseuille flow regime. This is particularly evident for Europe, where the fit to $\hat{S}_{\mathrm{Hmax}}$ improves considerably when one accounts for the plume Poiseuille component associated with Atlantic hotspots to the west of Europe (Figure 6.7C_3). Eastern and southern Africa are also subject to the plume Poiseuille regime sourced from the Afar hotspot (Figure 6.7C_4). North and Central America are best explained by a combination of Couette and plume flow components (Figure 6.7F_1), and so is South America (Figure 6.7F_2). Importantly, our analytic model correctly predicts regions where stress patterns have traditionally been considered as unintuitive due to their misalignment with plate velocities, such as in South-east Asia (Figure 6.7D_5). The region displays a prominent stress rotation. In the vicinity of the subduction zone $\hat{S}_{\mathrm{Hmax}}$ is perpendicular to the trench, as expected. But it turns trench-parallel further into the Indo-Australian plate [96]. In Australia (Figure 6.7B_6) $\hat{S}_{\mathrm{Hmax}}$ is also perpendicular to the velocity field [73]. Our analysis shows that this misalignment is caused by the slab Poiseuille component and precisely reflects the dominance of negative buoyancies, or sinks, over the Couette component in these regions. The slab flow regime induces a $\hat{S}_{\mathrm{hmin}}$ orientation towards the trench, which by definition implies a perpendicular $\hat{S}_{\mathrm{Hmax}}$ orientation as shown in Figure 6.8A-H. Our results have a number of implications. First, they illustrate that realistic upper mantle flow geometries, i.e. the specific spatial distribution of plumes, slabs, plate induced Couette flow and their superposition, are essential in the interpretation of stress field patterns at global and regional scales. The use of global scale models is therefore advised. Second, they suggest the potential to identify geodynamically plausible stress provinces, i.e. regions that are affected predominantly by a specific mantle flow component. Our analytic formulation provides a computationally effective method to do so. Third, our results indicate that long-term strength of the continental lithosphere is likely contained within the seismogenic layer, as has been argued for from earthquake focal depths [60], see [47] for a recent review.

Stress field patterns inferred from lithosphere models

Stress field predictions from lithosphere models have a long tradition. The work has often been performed with elastic membrane models that account for boundary and drag forces, both at global [76–78] and regional [13,15,16,40,74] scales. In other words, driving forces at spreading centers and convergent plate boundaries computed from the assumption of so-called ridge push and slab pull forces [20] are balanced against resistive basal drag forces beneath plates, computed from the assumption of a mantle at rest. Richardson [76] reports that ridge push forces are good predictors of $\hat{S}_{\mathrm{Hmax}}$ for stable North America, western Europe and South America, while intraplate stress directions in the Indo-Australian plate are not consistent with dominant roles for ridge push, slab pull or basal drag related to absolute plate motion. Our results help us to understand these earlier findings. A balance of edge forces at spreading centers and convergent plate boundaries against resistive basal drag forces necessarily predicts stress fields that pertain to a Couette regime. The predictions will be successful in regions where Couette flow is important, such as North and South America and Europe. They will be less successful in slab Poiseuille flow dominated regions, such as Australia, as noted before. Regional stress field predictions have also been performed with thin viscous sheet models, motivated by the insight that orogenic topography at plate convergence zones should act as an important contributor to regional stress patterns (e.g., [38]). The models balance horizontal gradients of the deviatoric stress required to deform the sheet against gradients in its gravitational potential energy. They also incorporate an indentation, i.e. an advancing plate. This allows them to account for external geometrical information of the plate convergence zone. Thin viscous sheet models have been successful, for instance, in the Tibetan region [39]. Our model also fits the stress field in Tibet, without the explicit inclusion of topography. The region is located at a convergent margin and dominated by the Couette component (Figure C.4), which enters our models as an external information through surface plate velocities. In other words, external plate kinematic information is seemingly important in the prediction of stress field patterns at orogenic plate convergence zones, in our and in thin viscous sheet models. The stress field orientation away from Tibet, on the scale of the east Asian mainland, is well described by the slab component of the flow (Figure C.5). The simultaneous fitting of both Tibet and the eastern Asia mainland in our models thus emerges from the combined Poiseuille and Couette flow in this region. This implies that a large part of the stress field orientation in east Asia could be linked to mantle flow, as noted before[99,100]. A well known lithosphere model is the SHELLS model by Kong and Bird[53]. It is a technically sophisticated quasi-static lithosphere model that includes an accurate description of topography, plate boundaries, laterally varying heat flow, brittle weakness via tectonic faults, and laterally varying crust and mantle lithosphere layer thicknesses. Bird[3] used this model and assumed a resistive role for the mantle to test the hypothesis of Forsyth and Uyeda[20]) on plate driving forces. He pointed out that while the resulting models were kinematically correct, their stress field predictions anticorrelated with the data. His models made better predictions of stress direction upon incorporating a simple representation of Earth's present mantle convection to account for active plate driving tractions. In doing so, Bird was a pioneer to incorporate the characteristics of Poiseuille-driven asthenosphere flow into lithosphere models.

Amplitudes of S_{Hmax} and basal shear tractions beneath plates

Our models predict S_{Hmax} amplitudes from internal flow deformation in the asthenosphere of < 1 MPa. This is expected in light of the smooth flow field, with horizontal velocity gradients of cms/yr over thousands of km, i.e. strain rates of 10^{-8} per year. However, our analytic formulation provides insight into the scaling of S_{Hmax} relative to key parameters. For instance, we could choose a higher asthenosphere viscosity, which is constrained by inferences of glacial rebound[12] and plate motion changes[45]. This would raise the Couette flow related stresses locally at plate boundaries. But interregional stresses from Poiseuille flow would remain unchanged, since flow velocities scale inversely with the viscosity. We could also increase the pressure gradient assigned to plumes, which comes from estimates of dynamic topography[35]. But it is unlikely that our assumed value (1400 m) could be raised by more than a factor of two. Our slab flow component assures a slab-induced downwelling volumetric flux from a 100 km thick sinking slab, along with 100 km entrained material on either side, assuming a sinking speed of 5 cm/yr (see[97] for details). This yields an overturn of mantle material within one mantle transit time (e.g.,[44]) and is probably an upper bound. We also modeled plumes in our formulation as point sources, for the sake of simplicity. If we convolved the point representation with a Gaussian distribution, this would yield larger flow velocities, while leaving pressure gradient and viscosity unchanged. But independent constraints for asthenosphere velocities in the vicinity of plumes (e.g.,[29]) would limit the computed flow velocities to within a factor of ten. In summary we expect S_{Hmax} amplitudes from internal asthenosphere flow deformation to remain < 1 MPa for reasonable parameter choices. If one assumes that intraplate stresses away from orogenic topography are linked primarily to internal asthenosphere flow deformation, as suggested by the close correspondence between modeled and observed stress field, one also would expect intraplate stresses as represented by $\hat{S}_{\mathrm{Hmax}}$ to remain < 1 MPa. Although this inference is speculative, it fits with arguments from wedge taper geometry [91], fluid overpressure [92] and results from SHELLS lithosphere modelling [5,11] that advocate low (0.1) effective fault friction values. It is, of course, challenging to compare the amplitude of modelled stress values against observations, because it is difficult to measure the deviatoric component magnitude of the stress tensor. Direct inferences are limited to S_{hmin} estimates from loading techniques [64], which correspond to a component of the total stress tensor. Values derived from such studies indicate small deviatoric stress levels when corrected for the gradients due to confining stress. The latter are ≈ 27 MPa/km, such that borehole estimates of stress would reach up to 10^2 MPa. We point to ongoing efforts to derive stress magnitudes in addition to their orientation [19,62,104].

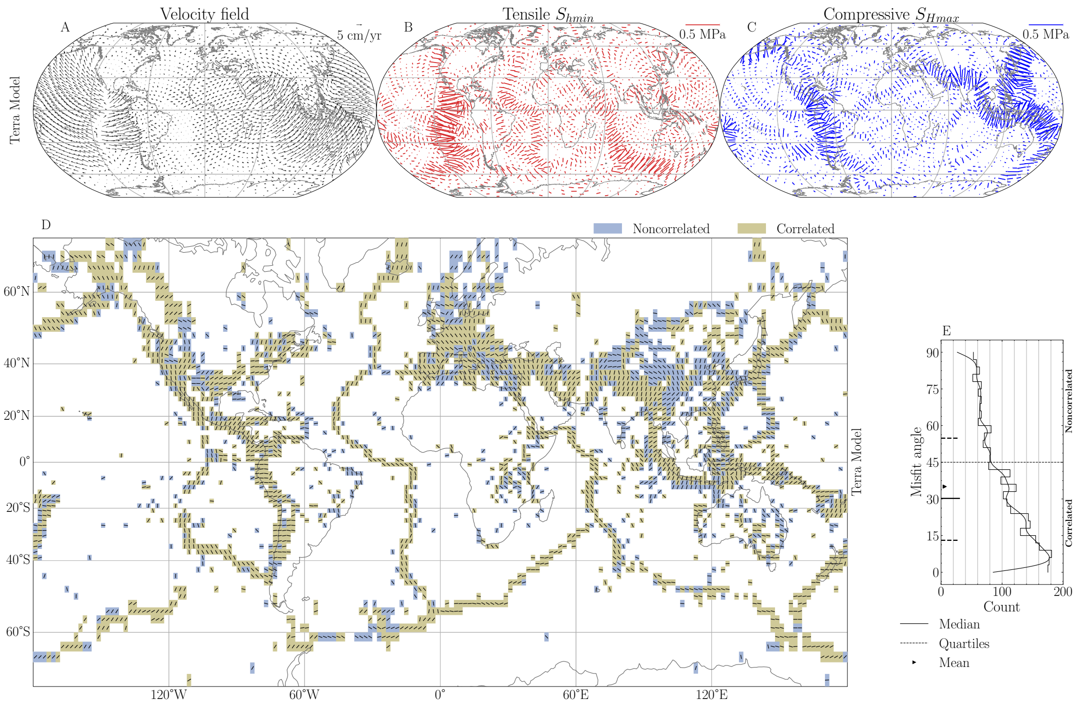

FIGURE 6.10. Asthenospheric velocity and stress fields derived from Mantle Circulation Model (MCM). (A) velocity field sampled at 169 km depth. (B,C) derived S_{hmin} and S_{Hmax} . (D) S_{Hmax} azimuth comparison against bin-averaged observations. (E) histograms of azimuth alignment. The parameter choice for this MCM can be found in Appendix C.7.

Our models predict amplitudes of basal shear tractions beneath tectonic plates of < 10 MPa. The value is expected in light of the vertical velocity gradients of cms/yr over 100 km between the asthenosphere and overlying plates. Similar arguments as before hold on how the traction magnitude would scale relative to key model parameters. Bird and other authors [5,26,69,85] found mean basal shear tractions of no more than 1 MPa for the largest non-subducting plates, consistent with our predictions. Bird also reports that the minimum misfit in his models occurs with low trench resistance magnitudes of 2×10^{12} N m^{-1}. The latter is comparable to the plate driving forces one would obtain from line integrations of basal shear tractions ($\propto$ 1 MPa) over distances of $\propto 10^3$ km in his and our models. In other words, trench resistance and plate driving forces seemingly achieve similar magnitudes. Observational evidence for low trench resistance values has emerged from investigations that model gravitational potential energy [55], constrain fault strength from heat flow measurements [24], analyse locked and creeping subduction zone faults [27], or study earthquake stress rotations [28]. Indicators for low shear strength in megathrust settings are reviewed by Brodsky et al.[7].

We close our discussion on basal shear tractions with an intriguing albeit expected result: the interaction of channelized flow with rigid rotations of tectonic plates above naturally yields three distinct traction regimes, depending on whether asthenosphere flow locally moves faster, slower or comparable to the plate motion above. In our models most of the Australian and North American plates experience active forward driving tractions, while the Nazca plate and parts of the African plate in the central Atlantic are subject to resistive (Couette) traction. Other regions, such as southern Africa, northern Eurasia, and the central portion of North America (Midwest and Central Plains) are nearly traction free, since plate motion locally matches the asthenosphere flow velocities beneath. This geometrical effect would be absent from lithosphere stress models driven by edge torques over an immobile mantle, because the latter would only experience resistive tractions from Couette regimes [16]. To summarize: one should account for active mantle flow and realistic upper mantle flow geometries, i.e. the spatial distribution of plumes, slabs, plate induced Couette flow and their superposition, to identify plausible lithosphere traction regimes. The use of global scale models is therefore advised.

Limitations and comparison to Mantle Circulation Models

Our approach requires informed choices for the relative variation in slab and plume flux strength. We could include alternative plume flux catalogs, or vary the strength of subduction systems regionally, guided by e.g. slab age or sinking velocity. Our models also omit many important physical effects. For instance, we assumed a Newtonian flow rheology: if relaxed into a non-Newtonian flow, for which there is strong evidence [46], the asthenosphere would adopt a plug flow profile [82] with modified vertical velocity gradients. We also excluded the influence of cratonic keels, which have been shown to perturb asthenospheric flow (e.g., [17,21,68]). Other factors, such as the isostatic and flexural response of plates [101], density and strength variations within the lithosphere [6] and topography were also ignored. It is now possible to account for some of these complexities by combining global mantle flow models with global lithosphere models [71,87]. A complete prediction of the lithosphere stress field would require considering lithosphere components such as topography, embedded fault weakness, and a choice in lithosphere rheology (for instance, coupling the tractions with SHELLS). The approach allows one to maintain the geometrical effects of plate/mantle interactions, i.e. the interaction of mantle up- and downwellings, plate driven Couette flow and their superposition.

This is essential for understanding the global stress field, as noted before, and would be lost in models that adopt simplified geometries. But global computational simulations are expensive and lack the ability to separate flow components analytically.

To this end it is instructive to compute stress fields numerically from mantle circulation models (MCMs) in Figure 6.10. MCMs are geodynamic earth models. They solve conservation equations for global mantle flow and assimilate plate motion histories at the surface to overcome poorly known initial condition effects (e.g.[9]). This means that buoyancies (up- and downwellings) arise spontaneously in the flow, while the assimilated plate motions induce Couette flow. Simply put, MCMs are dynamic earth models that naturally yield Poiseuille/Couette flow to account for the geometrical effects of plate/mantle interactions. By now they reach grid point resolutions of 10 km throughout the mantle, allowing them to represent global mantle flow at Earth-like convective vigor. Importantly, they resolve a low viscosity asthenosphere with $\mu = 5 \times 10^{19}$ Pa s, the value adopted in our analytic models. This makes it possible to compare their stress field predictions directly to our analytic results. Figure 6.10A shows the horizontal velocity field extracted from a high resolution MCM at mid-asthenosphere depth, together with the principle horizontal stress components (Figure 6.10 B,C), as done for our analytical model. Of course, we cannot separate the MCM derived velocity and stress fields into the contributing flow components, unlike we did for our analytical model (see Figure 6.5). But velocity and stress field amplitudes are similar to the analytic results, supporting the plume and slab flux choices we made in our analytic approach. We also compare the MCM results against the bin-averaged observation of stress indicators, in map view and as histogram (Figure 6.10 D,E), as we did for the analytic results in Figure 6.5 A,H. The histogram distribution and the stress azimuth fit of $\approx 35°$ for MCM and analytic model are comparable. In other words, both approaches yield a good fit to the global stress field. This is expected, because both include the Poiseuille component (either parameterized or flow derived) and account for Couette flow from surface plate motion. The latter is crucial in fitting the global stress field (see Figure 6.5B). To sum up: global stress field predictions from MCMs and analytic asthenosphere flow models yield comparable results, because both account for the essential Poiseuille/Couette flow nature in the asthenosphere. While MCMs allow one to include complex physical effects, albeit at high computational cost, the computational efficiency of analytic models enables hypothesis testing and yields insight from the ability to perform component analysis.

An asthenospheric flow state Ansatz for hypothesis testing

Poiseuille-Couette flow is a powerful concept to explain the stress field in the asthenosphere. It isolates the essential geometrical and physical flow effects of the asthenosphere and their interaction with the lithosphere. It thus creates first-order expectations and interpretations of the stress patterns that would arise from complex MCMs. The approach, and the level of understanding it permits, is akin to an *Ansatz* for the asthenosphere flow state, i.e., an educated guess for hypotheses testing that yields informed expectations for a variety of flow regimes. For instance, a plume-fed asthenosphere has been advocated for the upper mantle flow regime[72,102,103]. In this regime spreading ridges would act as sinks, where asthenosphere material is transferred into the lithosphere above. Our approach lets us treat this assumption straightforwardly as an additional flow component (Figure 6.11). The resulting total velocity field (Figure 6.11A) and the derived S_{hmin} and S_{Hmax} components (Figure 6.11B,C respectively) illustrate how the plume-fed asthenosphere would overprint the effect of flow divergence along ridges, by adding a compressional flow component of material moving towards the sinks at ridge locations. In this case the global comparison against observables deteriorates (Figure 6.11D), due to noncorrelated $\hat{S}_{\mathrm{Hmax}}$ at ridges. This is plain in the histograms, where the correlation at ridge locations is unfavorable relative to observations (Figure 6.11E). The effect propagates into the histograms for multiple flow components (Figure 6.11F-L), so that the overall correlation is diminished. This result sets an expectation that could to be tested further with complex numerical simulations of the plume-fed asthenosphere hypothesis.

6.5 Conclusion

We find that a simple, versatile and computationally inexpensive asthenospheric flow state Ansatz based on Poiseuille/Couette flow is effective to explore the influence of mantle flow on global stress field patterns as represented by the World Stress Map. The analytic approach:

1. shows that the first-order stress field can be linked to Poiseuille/Couette flow in the asthenosphere, with flow components related to rising plumes, sinking slabs and movement of overlying plates. Further exploring of this influence in the lithosphere requires explicit coupling with a lithosphere model.

2. advances the process-based understanding of lithospheric stress field patterns and is easily reparameterized to allow for wide-ranging hypothesis testing.

3. suggests the potential to identify geodynamically plausible stress provinces in the asthenosphere, i.e. regions affected predominantly by specific flow components.

4. illustrates that seemingly unintuitive regional stress patterns, where $\hat{S}_{\mathrm{Hmax}}$ is oriented perpendicular to plate motion, for instance in Australia and South East Asia, emerge in the vicinity of subduction zones from slab-induced Poiseuille flow, whereas plumes drive radial stress patterns at subregional scale, for instance, in Europe and the East African Rift. The transfer of these asthenospheric stress patterns into the lithosphere require explicit lithosphere model coupling.

5. reveals that tractions at the base of the lithosphere vary spatially with distinct plate driving, resistive, or neutral (traction-free) regions, such that three specific basal shear traction regimes can be identified, depending on whether asthenosphere locally moves faster, slower or comparable to plate motion above.

6. implies that realistic upper mantle flow geometries, i.e. the specific spatial distribution of plumes, slabs, plate induced flow and their superposition, are essential in interpretations of

stress field patterns at global and regional scales, so that the use of global modeling geometries is advised in first-order stress field studies to capture flow geometry effects.

7. predicts that amplitudes of the deviatoric stress components emerging from the asthenosphere, as well as basal shear tractions beneath plates, are relatively small, in the order of 10^{-1} MPa to 1 MPa.

8. allows us to understand results of earlier plate models, parameterized in terms of plate driving and resistive forces, by explaining their predicted stress fields as consequence of a Couette component.

9. compares favorably to results from Mantle Circulation Models (MCMs), since MCMs by construction yield Poiseuille/Couette flow styles, thus (a) setting expectations for, (b) helping to interpret result from, and (c) acting as complement to MCM simulations.

Acknowledgments

I.L.S acknowledges support by the Deutsche Forschungsgemeinschaft (DFG) project number STO1271/2-1. The authors thank the editor H. Davis, the reviewers P. Bird and B. Steinberger for their thoughtful comments and efforts towards improving our manuscript. The authors also thank B. Kahle, S. Ghelichkhan, L. Colli, M. Ziegler, R. Burgmann, and O. Heidbach for their time and constructive feedback, as well as H. Brown and R. Wang for facilitating data from their past publications. We thank the WSM project for making their stress indicators database available.

6.6 References

[1] Allmann, B. P. and Shearer, P. M. (2009). Global variations of stress drop for moderate to large earthquakes. *Journal of Geophysical Research: Solid Earth*, 114(B1):B01310. Cited on page/s 148.

[2] Barber, C. B., Dobkin, D. P., and Huhdanpaa, H. (1996). The quickhull algorithm for convex hulls. *ACM Trans. Math. Softw.*, 22(4):469–483. Cited on page/s 153.

[3] Bird, P. (1998). Testing hypotheses on plate-driving mechanisms with global lithosphere models including topography, thermal structure, and faults. *Journal of Geophysical Research: Solid Earth*, 103(B5):10115–10129. Cited on page/s 150, 156, 158, 169.

[4] Bird, P. and Li, Y. (1996). Interpolation of principal stress directions by nonparametric statistics: Global maps with confidence limits. *Journal of Geophysical Research: Solid Earth*, 101(B3):5435–5443. Cited on page/s 158.

[5] Bird, P., Liu, Z., and Rucker, W. K. (2008). Stresses that drive the plates from below: Definitions, computational path, model optimization, and error analysis. *Journal of Geophysical Research: Solid Earth*, 113(B11). Cited on page/s 150, 170.

[6] Bott, J., Scheck-Wenderoth, M., Kumar, A., Cacace, M., Noe, S., and Faleide, J. I. (2024). Density and strength variations in the mantle lithosphere affect the distribution of intraplate earthquakes. *Communications Earth and Environment*, 5(1):243. Cited on page/s 171.

[7] Brodsky, E. E., Mori, J. J., Anderson, L., Chester, F. M., Conin, M., Dunham, E. M., Eguchi, N., Fulton, P. M., Hino, R., Hirose, T., Ikari, M. J., Ishikawa, T., Jeppson, T., Kano, Y., Kirkpatrick, J., Kodaira, S., Lin, W., Nakamura, Y., Rabinowitz, H. S., Regalla, C., Remitti, F., Rowe, C., Saffer, D. M., Saito, S., Sample, J., Sanada, Y., Savage, H. M., Sun, T., Toczko, S., Ujiie, K., Wolfson-Schwehr, M., and Yang, T. (2020). The state of stress on the fault before, during, and after a major earthquake. *Annual Review of Earth and Planetary Sciences*, 48(1):49–74. Cited on page/s 147, 171.

[8] Bunge, H.-P. and Richards, M. A. (1996). The origin of large scale structure in mantle convection: Effects of plate motions and viscosity stratification. *Geophysical Research Letters*, 23(21):2987–2990. Cited on page/s 150.

[9] Bunge, H.-P., Richards, M. A., Lithgow-Bertelloni, C., Baumgardner, J. R., Grand, S. P., and Romanowicz, B. A. (1998). Time scales and heterogeneous structure in geodynamic earth models. *Science*, 280(5360):91–95. Cited on page/s 150, 172.

[10] Burbidge, D. R. (2004). Thin plate neotectonic models of the australian plate. *Journal of Geophysical Research: Solid Earth*, 109(B10). Cited on page/s 150, 167.

[11] Carena, S. and Moder, C. (2009). The strength of faults in the crust in the western united states. *Earth and Planetary Science Letters*, 287(3):373–384. Cited on page/s 170.

[12] Cathles, L., Fjeldskar, W., Lenardic, A., Romanowicz, B., Seales, J., and Richards, M. (2023). Influence of the asthenosphere on earth dynamics and evolution. *Scientific Reports*, 13(1):13367. Cited on page/s 150, 154, 167, 169.

[13] Cloetingh, S. and Wortel, R. (1985). Regional stress field of the Indian Plate. *Geophysical Research Letters*, 12(2):77–80. Cited on page/s 150, 168.

[14] Coblentz, D. D. and Richardson, R. M. (1995). Statistical trends in the intraplate stress field. *Journal of Geophysical Research: Solid Earth*, 100(B10):20245–20255. Cited on page/s 148, 149.

[15] Coblentz, D. D. and Richardson, R. M. (1996). Analysis of the south american intraplate stress field. *Journal of Geophysical Research: Solid Earth*, 101(B4):8643–8657. Cited on page/s 150, 168.

[16] Coblentz, D. D., Sandiford, M., Richardson, R. M., Zhou, S., and Hillis, R. (1995). The origins of the intraplate stress field in continental Australia. *Earth and Planetary Science Letters*, 133(3):299–309. Cited on page/s 150, 168, 171.

[17] Conrad, C. P. and Lithgow-Bertelloni, C. (2006). Influence of continental roots and asthenosphere on plate-mantle coupling. *Geophysical Research Letters*, 33(5). Cited on page/s 171.

[18] Davis, J. C., Sampson, R. J., et al. (1986). *Statistics and data analysis in geology*, volume 646. Wiley New York. Cited on page/s 148.

[19] Figueiredo, B., Sjöberg, J., Mattila, J., Hakala, M., and Suikkanen, J. (2023). Analysis and determination of the stress field at the Olkiluoto site. *IOP Conference Series: Earth and Environmental Science*, 1124(1):012002. Cited on page/s 170.

[20] Forsyth, D. and Uyeda, S. (1975). On the relative importance of the driving forces of plate motion. *Geophysical Journal International*, 43(1):163–200. Cited on page/s 150, 168, 169.

[21] Fouch, M. J., Fischer, K. M., Parmentier, E. M., Wysession, M. E., and Clarke, T. J. (2000). Shear wave splitting, continental keels, and patterns of mantle flow. *Journal of Geophysical Research: Solid Earth*, 105(B3):6255–6275. Cited on page/s 171.

[22] Fuchs, K. and Müller, B. (2001). World Stress Map of the Earth: a key to tectonic processes and technological applications. *Naturwissenschaften*, 88(9):357–371. Cited on page/s 147.

[23] Fälth, B., Hökmark, H., Lund, B., Mai, P. M., Roberts, R., and Munier, R. (2014). Simulating Earthquake Rupture and Off-Fault Fracture Response: Application to the Safety Assessment of the Swedish Nuclear Waste Repository. *Bulletin of the Seismological Society of America*, 105(1):134–151. Cited on page/s 147.

[24] Gao, X. and Wang, K. (2014). Strength of stick-slip and creeping subduction megathrusts from heat flow observations. *Science*, 345(6200):1038–1041. Cited on page/s 171.

[25] Gaucher, E., Schoenball, M., Heidbach, O., Zang, A., Fokker, P. A., van Wees, J.-D., and Kohl, T. (2015). Induced seismicity in geothermal reservoirs: A review of forecasting approaches. *Renewable and Sustainable Energy Reviews*, 52:1473–1490. Cited on page/s 147.

[26] Ghosh, A., Holt, W. E., and Wen, L. (2013). Predicting the lithospheric stress field and plate motions by joint modeling of lithosphere and mantle dynamics. *Journal of Geophysical Research: Solid Earth*, 118(1):346–368. Cited on page/s 150, 167, 170.

[27] Hardebeck, J. L. and Loveless, J. P. (2018). Creeping subduction zones are weaker than locked subduction zones. *Nature Geoscience*, 11(1):60–64. Cited on page/s 171.

[28] Hardebeck, J. L. and Okada, T. (2018). Temporal Stress Changes Caused by Earthquakes: A Review. *Journal of Geophysical Research: Solid Earth*, 123(2):1350–1365. Cited on page/s 171.

[29] Hartley, R. A., Roberts, G. G., White, N., and Richardson, C. (2011). Transient convective uplift of an ancient buried landscape. *Nature Geoscience*, 4(8):562–565. Cited on page/s 169.

[30] Hast, N. (1967). The state of stresses in the upper part of the earth's crust. *Engineering Geology*, 2(1):5–17. Cited on page/s 148.

[31] Heidbach, O., Rajabi, M., Cui, X., Fuchs, K., Müller, B., Reinecker, J., Reiter, K., Tingay, M., Wenzel, F., Xie, F., et al. (2018). The World Stress Map database release 2016: Crustal stress pattern across scales. *Tectonophysics*, 744:484–498. Cited on page/s 148, 150.

[32] Heidbach, O., Rajabi, M., Reiter, K., Ziegler, M., and WSM Team (2016). World stress map database release 2016. *GFZ Data Services*, V. 1.1. Cited on page/s 148, 149.

[33] Heidbach, O., Reinecker, J., Tingay, M., Müller, B., Sperner, B., Fuchs, K., and Wenzel, F. (2007). Plate boundary forces are not enough: Second- and third-order stress patterns highlighted in the world stress map database. *Tectonics*, 26(6). Cited on page/s 148.

[34] Heidbach, O., Tingay, M., Barth, A., Reinecker, J., Kurfeß, D., and Müller, B. (2010). Global crustal stress pattern based on the world stress map database release 2008. *Tectonophysics*, 482(1):3–15. Frontiers in Stress Research. Cited on page/s 148.

[35] Hoggard, M., Austermann, J., Randel, C., and Stephenson, S. (2021). *Observational Estimates of Dynamic Topography Through Space and Time*, chapter 15, pages 371–411. American Geophysical Union (AGU). Cited on page/s 167, 169.

[36] Hoggard, M. J., Parnell-Turner, R., and White, N. (2020). Hotspots and mantle plumes revisited: Towards reconciling the mantle heat transfer discrepancy. *Earth and Planetary Science Letters*, 542:116317. Cited on page/s 151, 153, 155, 156, 164.

[37] Hoggard, M. J., Winterbourne, J., Czarnota, K., and White, N. (2017). Oceanic residual depth measurements, the plate cooling model, and global dynamic topography. *Journal of Geophysical Research: Solid Earth*, 122(3):2328–2372. Cited on page/s 153.

[38] Houseman, G. and England, P. (1986). Finite strain calculations of continental deformation: 1. method and general results for convergent zones. *Journal of Geophysical Research: Solid Earth*, 91(B3):3651–3663. Cited on page/s 168.

[39] Houseman, G. and England, P. (1993). Crustal thickening versus lateral expulsion in the indian-asian continental collision. *Journal of Geophysical Research: Solid Earth*, 98(B7):12233–12249. Cited on page/s 168.

[40] Humphreys, E. D. and Coblentz, D. D. (2007). North american dynamics and western u.s. tectonics. *Reviews of Geophysics*, 45(3). Cited on page/s 150, 168.

[41] Höink, T., Jellinek, A. M., and Lenardic, A. (2011). Viscous coupling at the lithosphere-asthenosphere boundary. *Geochemistry, Geophysics, Geosystems*, 12(10). Cited on page/s 152, 167.

[42] Höink, T. and Lenardic, A. (2010). Long wavelength convection, poiseuille–couette flow in the low-viscosity asthenosphere and the strength of plate margins. *Geophysical Journal International*, 180(1):23–33. Cited on page/s 152, 167.

[43] Höink, T., Lenardic, A., and Richards, M. (2012). Depth-dependent viscosity and mantle stress amplification: implications for the role of the asthenosphere in maintaining plate tectonics. *Geophysical Journal International*, 191(1):30–41. Cited on page/s 152, 167.

[44] Iaffaldano, G. and Bunge, H.-P. (2015). Rapid plate motion variations through geological time: Observations serving geodynamic interpretation. *Annu. Rev. Earth Planet. Sci*, 43(1):571–592. Cited on page/s 169.

[45] Iaffaldano, G. and Lambeck, K. (2014). Pacific plate-motion change at the time of the hawaiian-emperor bend constrains the viscosity of earth's asthenosphere. *Geophysical Research Letters*, 41(10):3398–3406. Cited on page/s 154, 169.

[46] ichiro Karato, S. and Wu, P. (1993). Rheology of the upper mantle: A synthesis. *Science*, 260(5109):771–778. Cited on page/s 171.

[47] Jackson, J., McKenzie, D., and Priestley, K. (2021). Relations between earthquake distributions, geological history, tectonics and rheology on the continents. *Philosophical Transactions of the Royal Society A: Mathematical, Physical and Engineering Sciences*, 379(2193):20190412. Cited on page/s 168.

[48] Jeandet Ribes, L., Thomas, M. Y., and Bhat, H. S. (2023). On the importance of setting 3-D stress field in simulations of on- and off-fault deformation. *Geophysical Journal International*, 235(3):2962–2978. Cited on page/s 147.

[49] Johnson, A. C. and Kanter, L. R. (1990). Earthquakes in stable continental crust. *Scientific American*, 262(3):68–75. Cited on page/s 148.

[50] Kame, N., Rice, J. R., and Dmowska, R. (2003). Effects of prestress state and rupture velocity on dynamic fault branching. *Journal of Geophysical Research: Solid Earth*, 108(B5). Cited on page/s 147.

[51] Kato, N. (2009). A possible explanation for difference in stress drop between intraplate and interplate earthquakes. *Geophysical Research Letters*, 36(23):L23311. Cited on page/s 148.

[52] King, S. D. and Adam, C. (2014). Hotspot swells revisited. *Physics of the Earth and Planetary Interiors*, 235:66–83. Cited on page/s 153, 155, 156, 164.

[53] Kong, X. and Bird, P. (1995). Shells: A thin-shell program for modeling neotectonics of regional or global lithosphere with faults. *Journal of Geophysical Research: Solid Earth*, 100(B11):22129–22131. Cited on page/s 169.

[54] Krevor, S., de Coninck, H., Gasda, S. E., Ghaleigh, N. S., de Gooyert, V., Hajibeygi, H., Juanes, R., Neufeld, J., Roberts, J. J., and Swennenhuis, F. (2023). Subsurface carbon dioxide and hydrogen storage for a sustainable energy future. *Nature Reviews Earth & Environment*, 4(2):102–118. Cited on page/s 147.

[55] Lamb, S. (2006). Shear stresses on megathrusts: Implications for mountain building behind subduction zones. *Journal of Geophysical Research: Solid Earth*, 111(B7). Cited on page/s 171.

[56] Lin, Y.-A., Colli, L., Wu, J., and Schuberth, B. S. A. (2020). Where Are the Proto-South China Sea Slabs? SE Asian Plate Tectonics and Mantle Flow History From Global Mantle Convection Modeling. *Journal of Geophysical Research: Solid Earth*, 125(12):e2020JB019758. e2020JB019758 2020JB019758. Cited on page/s 151.

[57] Lithgow-Bertelloni, C. and Guynn, J. H. (2004). Origin of the lithospheric stress field. *Journal of Geophysical Research: Solid Earth*, 109(B1). Cited on page/s 150, 167.

[58] Lithgow-Bertelloni, C. and Richards, M. A. (1998). The dynamics of Cenozoic and Mesozoic plate motions. *Reviews of Geophysics*, 36(1):27–78. Cited on page/s 167.

[59] Liu, X. and Currie, C. A. (2019). Influence of upper plate structure on flat-slab depth: Numerical modeling of subduction dynamics. *Journal of Geophysical Research: Solid Earth*, 124(12):13150–13167. Cited on page/s 164.

[60] Maggi, A., Jackson, J. A., McKenzie, D., and Priestley, K. (2000). Earthquake focal depths, effective elastic thickness, and the strength of the continental lithosphere. *Geology*, 28(6):495. Cited on page/s 168.

[61] Mardia, K. (1972). Statistics of directional data. *Academic Press*, 357. Cited on page/s 148.

[62] Martin, C. D. (2007). Quantifying in situ stress magnitudes and orientations for forsmark. forsmark stage 2.2. Technical report, Swedish Nuclear Fuel and Waste Management Co., Sweden. SKB-R–07-26. Cited on page/s 170.

[63] Miocic, J. M., Gilfillan, S. M. V., Frank, N., Schroeder-Ritzrau, A., Burnside, N. M., and Haszeldine, R. S. (2019). 420,000 year assessment of fault leakage rates shows geological carbon storage is secure. *Scientific Reports*, 9(1):769. Cited on page/s 147.

[64] Morawietz, S., Heidbach, O., Reiter, K., Ziegler, M., Rajabi, M., Zimmermann, G., Müller, B., and Tingay, M. (2020). An open-access stress magnitude database for Germany and adjacent regions. *Geothermal Energy*, 8(1):25. Cited on page/s 170.

[65] Morris, A., Ferrill, D. A., and Henderson, D. (1996). Slip-tendency analysis and fault reactivation. *Geology*, 24(3):275–278. Cited on page/s 147.

[66] Müller, R. D., Flament, N., Cannon, J., Tetley, M. G., Williams, S. E., Cao, X., Bodur, O. F., Zahirovic, S., and Merdith, A. (2022). A tectonic-rules-based mantle reference frame since 1 billion years ago – implications for supercontinent cycles and plate–mantle system evolution. *Solid Earth*, 13(7):1127–1159. Cited on page/s 152, 155, 166.

[67] Müller, B., Zoback, M. L., Fuchs, K., Mastin, L., Gregersen, S., Pavoni, N., Stephansson, O., and Ljunggren, C. (1992). Regional patterns of tectonic stress in europe. *Journal of Geophysical Research: Solid Earth*, 97(B8):11783–11803. Cited on page/s 150.

[68] Naliboff, J. B., Conrad, C. P., and Lithgow-Bertelloni, C. (2009a). Modification of the lithospheric stress field by lateral variations in plate-mantle coupling. *Geophysical Research Letters*, 36(22). Cited on page/s 150, 167, 171.

[69] Naliboff, J. B., Conrad, C. P., and Lithgow-Bertelloni, C. (2009b). Modification of the lithospheric stress field by lateral variations in plate-mantle coupling. *Geophysical Research Letters*, 36(22). Cited on page/s 170.

[70] Osei Tutu, A., Sobolev, S. V., Steinberger, B., Popov, A. A., and Rogozhina, I. (2018a). Evaluating the influence of plate boundary friction and mantle viscosity on plate velocities. *Geochemistry, Geophysics, Geosystems*, 19(3):642–666. Cited on page/s 154.

[71] Osei Tutu, A., Steinberger, B., Sobolev, S. V., Rogozhina, I., and Popov, A. A. (2018b). Effects of upper mantle heterogeneities on the lithospheric stress field and dynamic topography. *Solid Earth*, 9(3):649–668. Cited on page/s 150, 167, 171.

[72] Phipps Morgan, J., Morgan, W. J., Zhang, Y.-S., and Smith, W. H. F. (1995). Observational hints for a plume-fed, suboceanic asthenosphere and its role in mantle convection. *Journal of Geophysical Research: Solid Earth*, 100(B7):12753–12767. Cited on page/s 152, 172.

[73] Rajabi, M., Tingay, M., Heidbach, O., Hillis, R., and Reynolds, S. (2017). The present-day stress field of Australia. *Earth-Science Reviews*, 168:165–189. Cited on page/s 150, 168.

[74] Reynolds, S. D., Coblentz, D. D., and Hillis, R. R. (2002). Tectonic forces controlling the regional intraplate stress field in continental Australia: Results from new finite element modeling. *Journal of Geophysical Research: Solid Earth*, 107(B7). Cited on page/s 150, 168.

[75] Richards, M. A. and Lenardic, A. (2018). The Cathles Parameter (Ct): A Geodynamic Definition of the Asthenosphere and Implications for the Nature of Plate Tectonics. *Geochemistry, Geophysics, Geosystems*, 19(12):4858–4875. Cited on page/s 150, 154, 167.

[76] Richardson, R. M. (1992). Ridge forces, absolute plate motions, and the intraplate stress field. *Journal of Geophysical Research: Solid Earth*, 97(B8):11739–11748. Cited on page/s 150, 168.

[77] Richardson, R. M., Solomon, S. C., and Sleep, N. H. (1976). Intraplate stress as an indicator of plate tectonic driving forces. *Journal of Geophysical Research (1896-1977)*, 81(11):1847–1856. Cited on page/s 150, 168.

[78] Richardson, R. M., Solomon, S. C., and Sleep, N. H. (1979). Tectonic stress in the plates. *Reviews of Geophysics*, 17(5):981–1019. Cited on page/s 150, 168.

[79] Röckel, L., Ahlers, S., Müller, B., Reiter, K., Heidbach, O., Henk, A., Hergert, T., and Schilling, F. (2022). The analysis of slip tendency of major tectonic faults in Germany. *Solid Earth*, 13(6):1087–1105. Cited on page/s 147.

[80] Sbar, M. L. and Sykes, L. R. (1973). Contemporary Compressive Stress and Seismicity in Eastern North America: An Example of Intra-Plate Tectonics. *GSA Bulletin*, 84(6):1861–1882. Cited on page/s 148.

[81] Scholz, C. H., Aviles, C. A., and Wesnousky, S. G. (1986). Scaling differences between large interplate and intraplate earthquakes. *Bulletin of the Seismological Society of America*, 76(1):65–70. Cited on page/s 148.

[82] Semple, A. G. and Lenardic, A. (2018). Plug flow in the Earth's asthenosphere. *Earth and Planetary Science Letters*, 496:29–36. Cited on page/s 171.

[83] Shi, J.-Q. and Durucan, S. (2009). A coupled reservoir-geomechanical simulation study of CO2 storage in a nearly depleted natural gas reservoir. *Energy Procedia*, 1(1):3039–3046. Greenhouse Gas Control Technologies 9. Cited on page/s 147.

[84] Sperner, B., Müller, B., Heidbach, O., Delvaux, D., Reinecker, J., and Fuchs, K. (2003). Tectonic stress in the earth's crust: advances in the world stress map project. *Geological Society, London, Special Publications*, 212(1):101–116. Cited on page/s 148.

[85] Steinberger, B., Schmeling, H., and Marquart, G. (2001). Large-scale lithospheric stress field and topography induced by global mantle circulation. *Earth and Planetary Science Letters*, 186(1):75–91. Cited on page/s 150, 167, 170.

[86] Stotz, I. L., Iaffaldano, G., and Davies, D. R. (2018). Pressure-driven poiseuille flow: A major component of the torque-balance governing pacific plate motion. *Geophysical Research Letters*, 45(1):117–125. Cited on page/s 152, 153, 167.

[87] Stotz, I. L., Tassara, A., and Iaffaldano, G. (2021a). Pressure-driven poiseuille flow inherited from mesozoic mantle circulation led to the eocene separation of australia and antarctica. *Journal of Geophysical Research: Solid Earth*, 126(4):e2020JB019945. e2020JB019945 2020JB019945. Cited on page/s 171.

[88] Stotz, I. L., Vilacís, B., Hayek, J. N., Bunge, H.-P., and Friedrich, A. M. (2021b). Yellowstone Plume Drives Neogene North American Plate Motion Change. *Geophysical Research Letters*, 48(18):e2021GL095079. e2021GL095079 2021GL095079. Cited on page/s 152, 153, 167.

[89] Stotz, I. L., Vilacís, B., Hayek, J. N., Carena, S., and Bunge, H.-P. (2023). Plume driven plate motion changes: New insights from the South Atlantic realm. *Journal of South American Earth Sciences*, 124:104257. Cited on page/s 152, 153, 167.

[90] Sullivan, C. B. and Kaszynski, A. (2019). PyVista: 3D plotting and mesh analysis through a streamlined interface for the Visualization Toolkit (VTK). *Journal of Open Source Software*, 4(37):1450. Cited on page/s 151.

[91] Suppe, J. (2007). Absolute fault and crustal strength from wedge tapers. *Geology*, 35(12):1127–1130. Cited on page/s 170.

[92] Suppe, J. (2014). Fluid overpressures and strength of the sedimentary upper crust. *Journal of Structural Geology*,

69:481–492. Fluids and Structures in Fold and Thrust Belts with Recognition of the Work of David V. Wiltschko. Cited on page/s 170.

[93] Sykes, L. R. and Sbar, M. L. (1973). Intraplate Earthquakes, Lithospheric Stresses and the Driving Mechanism of Plate Tectonics. *Nature*, 245(5424):298–302. Cited on page/s 148.

[94] Talwani, P. (2017). On the nature of intraplate earthquakes. *Journal of Seismology*, 21(1):47–68. Cited on page/s 148.

[95] Templeton, E. L. and Rice, J. R. (2008). Off-fault plasticity and earthquake rupture dynamics: 1. dry materials or neglect of fluid pressure changes. *Journal of Geophysical Research: Solid Earth*, 113:B09306. Cited on page/s 147.

[96] Tingay, M., Morley, C., King, R., Hillis, R., Coblentz, D., and Hall, R. (2010). Present-day stress field of southeast asia. *Tectonophysics*, 482(1):92–104. Frontiers in Stress Research. Cited on page/s 150, 168.

[97] Wang, J. and Ye, Z.-R. (2005). Effects of mantle flow on generation and distribution of global lithospheric stress field. *Chinese Journal of Geophysics*, 48(3):643–649. Cited on page/s 169.

[98] Wang, Z. R., Stotz, I. L., Bunge, H.-P., Vilacís, B., Hayek, J. N., Ghelichkhan, S., and Lebedev, S. (2023). Cenozoic upper mantle flow history of the Atlantic realm based on Couette/Poiseuille models: Towards paleo-mantle-flowgraphy. *Physics of the Earth and Planetary Interiors*, page 107045. Cited on page/s 153.

[99] Warners-Ruckstuhl, K. N., Govers, R., and Wortel, R. (2012). Lithosphere–mantle coupling and the dynamics of the Eurasian Plate. *Geophysical Journal International*, 189(3):1253–1276. Cited on page/s 150, 167, 169.

[100] Warners-Ruckstuhl, K. N., Govers, R., and Wortel, R. (2013). Tethyan collision forces and the stress field of the Eurasian Plate. *Geophysical Journal International*, 195(1):1–15. Cited on page/s 150, 169.

[101] Watts, A. B. (2023). page i–ii. Cambridge University Press. Cited on page/s 171.

[102] Yamamoto, M., Morgan, J. P., and Morgan, W. J. (2007a). Global plume-fed asthenosphere flow—I: Motivation and model development. In *Plates, Plumes and Planetary Processes*. Geological Society of America. Cited on page/s 172.

[103] Yamamoto, M., Morgan, J. P., and Morgan, W. J. (2007b). Global plume-fed asthenosphere flow—II: Application to the geochemical segmentation of mid-ocean ridges. In *Plates, Plumes and Planetary Processes*. Geological Society of America. Cited on page/s 172.

[104] Zang, A., Stephansson, O., Heidbach, O., and Janouschkowetz, S. (2012). World Stress Map Database as a Resource for Rock Mechanics and Rock Engineering. *Geotechnical and Geological Engineering*, 30(3):625–646. Cited on page/s 148, 170.

[105] Ziegler, M. O. and Heidbach, O. (2020). The 3D stress state from geomechanical–numerical modelling and its uncertainties: a case study in the Bavarian Molasse Basin. *Geothermal Energy*, 8(1):11. Cited on page/s 148.

[106] Zoback, M. D. (2007). *Reservoir Geomechanics*. Cambridge University Press. Cited on page/s 147.

[107] Zoback, M. L. (1992). First- and second-order patterns of stress in the lithosphere: The World Stress Map Project. *Journal of Geophysical Research: Solid Earth*, 97(B8):11703–11728. Cited on page/s 148.

[108] Zoback, M. L., Zoback, M. D., Adams, J., Assumpção, M., Bell, S., Bergman, E. A., Blümling, P., Brereton, N. R., Denham, D., Ding, J., Fuchs, K., Gay, N., Gregersen, S., Gupta, H. K., Gvishiani, A., Jacob, K., Klein, R., Knoll, P., Magee, M., Mercier, J. L., Müller, B. C., Paquin, C., Rajendran, K., Stephansson, O., Suarez, G., Suter, M., Udias, A., Xu, Z. H., and Zhizhin, M. (1989). Global patterns of tectonic stress. *Nature*, 341(6240):291–298. Cited on page/s 148.

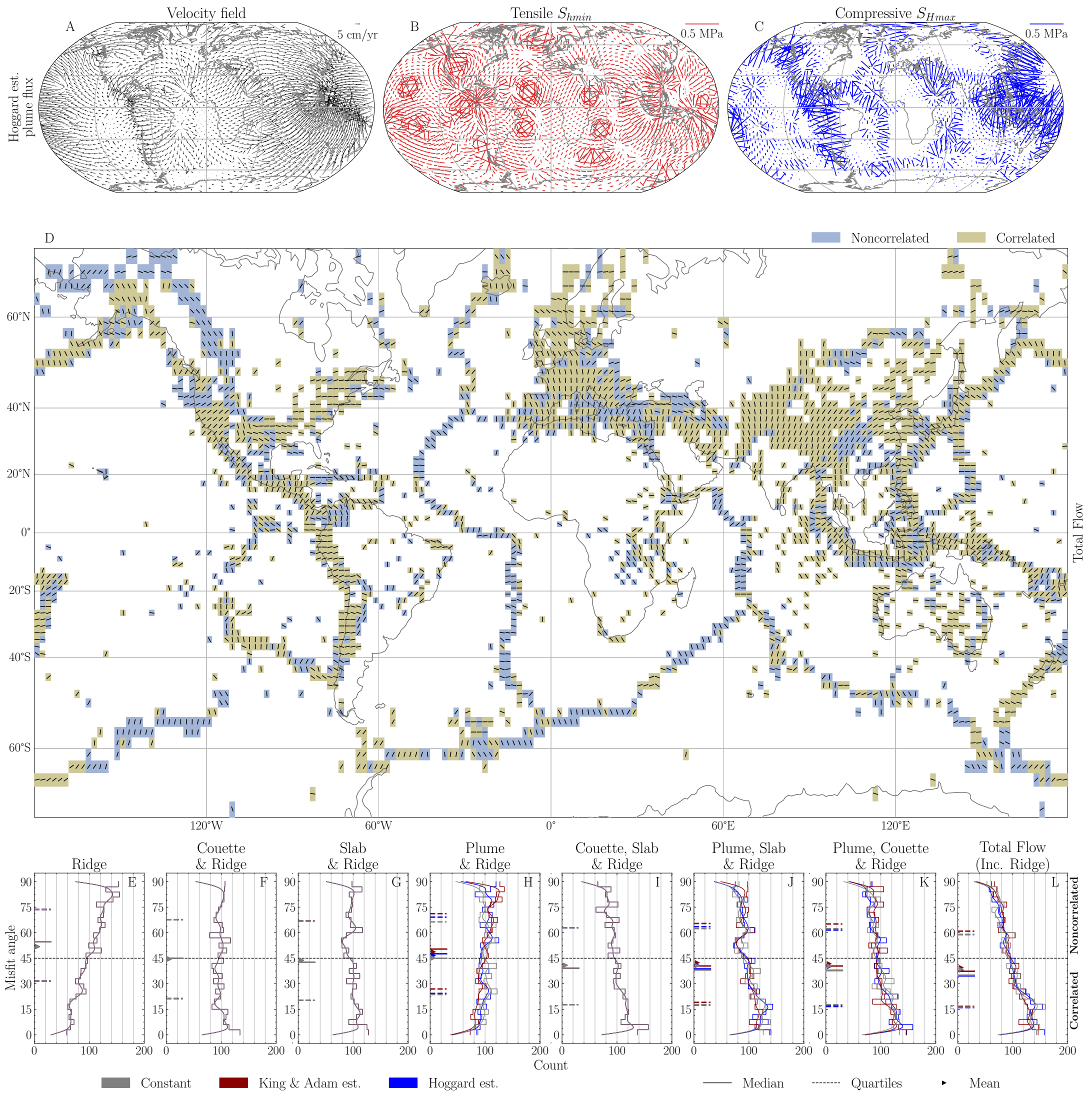

FIGURE 6.11. Hypothesis testing applied to a plume-fed asthenosphere. (A) shows the velocity field from the total flow analytic model, which includes a flow component where the mid-ocean ridge locations act as sinks, referred to as the Ridge component. (B) and (C) show the derived $\hat{S}_{\mathrm{hmin}}$ and $\hat{S}_{\mathrm{Hmax}}$, respectively. (D) compares the azimuths from this model with the bin-averaged observations. (E-L) display the histograms of azimuth alignment, showing the results for each flow component, including the added Ridge component.

Part IV

Conclusion

Chapter 7

Concluding Remarks and Outlook

The main goal of this thesis was to explore, extend, and inform modeling choices for rupture dynamic simulations. In doing so, we have advanced research addressing multidisciplinary challenges in modeling realistic, multi-physics, multi-scale earthquake source processes [12]. In particular, we made progress in capturing the coupled mechanisms involved in fault and bulk responses across temporal and spatial scales. This require identifying the dominating mechanism and modeling ingredients by interpreting a wide range of observations. Finally, we leverage insights from global geodynamics to better understand and analyze the observables associated to the deformation induced by mantle convection. In particular, we use this level of understanding to identify one essential ingredient in geomechanical simulations; the knowledge of the stress field emerging as a surface expression of mantle convection. This potentially sheds light onto the mechanical conditions surrounding intraplate settings, for which data is scarse.

The major contributions and directions of future research are summarized below.

7.1 Contributions

Extending parametrizations choices in dynamic rupture models

In Chapter 2, we report the development and verification of a model employing a diffuse representation of fault geometry, as an alternative to the typical simplification of an infinitesimally thin interface representation of a fault. We adopted the concept of stress glut applied to earthquake rupture dynamic simulations [1], which approximates the fault-jump conditions through inelastic increments to the stress components in an inelastic zone, however, later disregarded by Dalguer and Day[5] due to numerical noise. We have developed *se2dr*, a 2D PETSc spectral element adaptation of the stress glut, which incorporates a diffuse fault zone description defined by a steady-state anzats from phase-field models [17]. We show that our method reduces spurious oscillations caused by the stress discontinuities at the sharp transition between the elastic domain and the inelastic compact support. We successfully emulate the discrete fault split-node spectral element kinematic and dynamic reference solutions, and report additional dynamic complexities emerging from the volumetric character of the method, such as fault-oblique yielding within the fault zone. Our alternative representation introduces inelastic stress inclusions that are similar to the Eshelby inclusions. In our simulations, these inclusions evolve and interact with the dynamically propagating rupture. Our method inherently allows to explore the yielding surface's transition into the elastic media as a distribution, in which distinct dynamic features observed from laboratory experiments emerge from near-fault apparent friction coefficient estimations: double slip weakening, nonlinear weakening with long tails, and slip strengthening. The logical simplicity of our method allows it to be ported into alternative numerical frameworks. Furthermore, we show that our method offers a flexible numerical approach for mesh-independent representation of a fault. Potential applications of our method may help to further understand fault zone evolution and effects of internal rheology distribution at coeseismic scales. This includes exploring bulk and on-fault coupling mechanisms via phase field, which may allow to model time-evolving fault geometries. Additionally, we show that the resulting stress state behind the rupture can also be interpreted as an effective modification of the stiffness tensor, where prior to applying the plasticity limiter to the stress field it behaves as a isotropic material, and after undergoing plasticity the stiffness tensor may be interpreted as a transversely isotropic material.

In Chapter 3, we investigate the mechanics and dynamics of the 2021 M_w7.4 Maduo earthquake via the application of a state-of-the-art numerical tool for rupture dynamics simulation, *SeisSol*, as well as inform and validate our model via joint geodetic inferences. Our study is the first to our knowledge to combine 3D dynamic rupture simulations with high-resolution geodetic analysis to understand the event's paradoxes and the mechanical conditions that have governed its dynamics. Our preferred 3D dynamic rupture model includes complex non-planar multi-segmented fault geometry constrained by high-resolution optical correlation displacement field. We consider a multi-scale heterogeneous stress field accounting for joint optical/InSAR geodetic fault slip model. Our preferred model reproduces the observed multi-peak moment rate release, unilateral eastward supershear rupture, and dynamic triggering of adjacent fault branches. Using a suite of alternative dynamic rupture models, we emphasize the importance of our models to include on-fault fracture energy variation and off-fault Drucker-Prager plasticity. We also show that eastward supershear rupture may be required to match available displacement time-series from near-fault high-rate GNSS stations. The arrival time, duration, shape, and amplitude of the displacement time-series are well reproduced by our preferred model in contrast to an alternative model featuring subshear propagation. Furthermore, we compare the modeled off-fault plastic strain with our optically-derived fault zone width, which allows us to identify a distinct local reduction of the observed fault tone width as a signature of supershear transition.

In Chapter 4, we investigate the interactions between regional long-term geodynamic model and earthquake dynamics. We develop the methods and a workflow to inform a synthetic earthquake rupture dynamic model using *SeisSol*, with a regional 3D long-term thermo-mechanical geodynamic model extract from *pTatin3D*. We explore how variations in the visco-plastic rheology, and the related emerging strain localization geometry influence earthquake dynamics. We present a new algorithm to extract and reconstruct fault surfaces from volumetric shear zones, based on a medial axis transform. We apply it to three 3D long-term strike-slip experiments with a systematical variation of the non-linear visco-plastic rheology of the continental crust. We use the inferred fault geometry, the inferred state of the stress, and a simplifying 1D PREM velocity structure assumption, to construct and conduct a series of 3D dynamic rupture numerical experiments, in which we vary the on-fault fracture energy. The interplay of stresses and fault geometry play a first order role on the propagation of the rupture and the on- and off-fault energy release. Our geodynamically-informed models result in large magnitudes, reflecting the scales of the modelled seismogenic surface in accordance to known empirical relations, the absence of small events releasing elastic energy during the seismic cycle, and lack of fault interactions considered in complex fault networks.

Insights from global geodynamics

In Chapter 5, we systematically extract conformable and unconformable (hiatus) geologic contacts from digital geological maps, at the resolution of series from the Upper Jurassic onwards for North and South America, Europe, Africa and Australia. We employ a hiatus mapping technique introduced by Friedrich et al.[6], and use continent-scale un/conformable contacts at the temporal resolution of geologic series as proxy records for dynamic topography. We observe significant differences in the distribution of hiatus across and between continents at the timescale of geologic series, ten to a few tens of Myrs, smaller than the mantle transit time (100-200 Myrs). As past plate motions are used as input in mantle convection models, this extracted dataset potentially serves as a diagnostic tool for testing the surface expression extents of a mantle circulation model evolution.

In Chapter 6, we adopt a Poiseuille-Couette representation of the low-viscosity, channelized upper mantle flow, compare the derived first-order stresses to stress indicators compiled in the World Stress Map that provide a reduced description of the stress tensor, and perform a flow component analysis to identify the dominant geodynamic flow regime interregionally. Advances in geodynamics emphasized the central role of the low viscosity and highly mobile asthenosphere. In particular, the Poisseuille-Couette nature of the flow in this low viscosity channel[7–9], which has inspired the adoption of an analytical description of the asthenosphere, based on a superposition of steady-state Poisseuille-Couette components[14–16]. We have derived the deviatoric stress field from an analytical representation of the flow in the asthenosphere to understand the role of mantle flow as a first order stress driver. We find good agreement between our analytic model stress patterns, and the bin-averaged stress orientation indicators compiled from the World Stress Map project. We show that our analytical model allows for flow component analysis, which we leverage to identify regions that are mechanically driven by a Couette component of the flow, or driven by a Poisseuille component of the flow emerging from plume upwellings or from pressure gradients induced by a subducting slab. With this model and level of insight, we explain regions of intuitive $\hat{S}_{\mathrm{Hmax}}$ orientation, aligned with the velocity field, but also explain regions that have been regarded as unintuitive as these two directions have been long known to be perpendicular, without a determining explanation of the driving process. The former are explained by a Couette component of the flow, as well as a plume Poisseuille flow interregionally. The latter is explained by the proximity to a slab Poisseuille component which induces tensile deviatoric stresses aligned with the velocity field, by construction perpendicular to $\hat{S}_{\mathrm{Hmax}}$. These findings are in agreement with Bird[4], who reports that global lithospheric models where plates move over a resistive mantle may succeed kinematically, but will yield bad (even anticorrelated) predicted stress. Alternatively, considering a simple model of mantle convection, with active driving tractions, yields better stress predictions. Our tool may be interpreted as an anzats of asthenospheric flow state to use alongside large scale observational datasets as a process-driven tool to develop, analyse, and test hypotheses, which also motivates further development of physics-based mantle dynamics models to dynamically validate such flow features.

7.2 OUTLOOK

The various fronts of research here explored have a large potential to be further developed both individually and in combination. Further developments of diffuse fault modelling presented in Chapter 2 include exploring the method's potential for modeling branching and crossing faults, as well as extending the method to 3D, or porting it to alternative numerical frameworks. The mesh-independent feature of the method would ultimately allow for numerical modeling of evolving fault geometry. This approach would enable the study of the dynamic interaction of a propagating rupture within a spatially heterogeneous stress field, potentially leading to the development of more complex fault structures that also host spontaneous dynamic rupture, which is advantageous for site-specific and quantitative risk assessment. The inherent flexibility of this representation could be leveraged to model a two-way coupled quasi-dynamic rupture implementation within a long-term visco-plastic solvers, and study different tectonic settings (e.g., megathrust settings). Such an implementation would bypass the need for an explicit fault interface extraction algorithm, as well as the requirement to explicitly set it as a mesh feature, potentially avoiding an on-the-fly remeshing step. The diffuse fault representation may be applied to study the earthquake dynamics in fault systems that host both diffuse and localized deformation regions, as observed and reported in geodetic analyses (e.g., Antoine et al.[2],[3]). In particular, it would be interesting to compare against an interface-based fault representation that accounts for off-fault plasticity, and analyse the associated ground motions from both approaches.

Future work related to the Maduo earthquake study in Chapter 3 could investigate whether more distributed off-fault plasticity on the easternmost section is a viable explanation for the discrepancy between geodetic and aftershock-inferred fault geometries. The geodetically inferred eastern fault-segment dip is directed towards the north while the aftershocks indicate a south-dipping segment. Another extension of this study could involve increasing the model's complexity by including a multiscale network of faults, similar to the approach taken by Palgunadi et al.[13], aimed to explicitly reproduce the early gap of aftershocks in the eastern section closer to the epicenter reported by Wang et al.[19], in line with the expected signature associated to supershear propagation [10].

The study on the long-term geodynamic modelling in Chapter 4 sets a flexible workflow that links structures consistent with a rheology and associated stress setting into a rupture dynamic model. For this, we have developed a set of tools and a workflow that bridges the geodynamics and rupture dynamics communities. An immediate extension of this work could involve incorporating the mechanical effects associated with intermediate time and spatial scales, such as loading effects from seismic cycling, into the workflow. Another potential study could focus on analyzing the geometric and mechanical characteristics and their associated effects on rupture dynamics, in fault systems emerging from a later stage of long-term visco-plastic evolution model, after the development of secondary main faults and splays.

The systematic extraction of hiatus surfaces from digital geological maps in Chapter 5 directly benefits from any improvement in the temporal and spatial resolution of the available geological maps datasets, as well as an increase in their available coverage. These maps are complemented with data from borehole datasets and compilations from reports, charts and journals. The maps could be further enhanced by incorporating more subsurface information, such as seismic horizon interpretations, to better identify subsurface unconformity surfaces. This proxy of paleotopography serves as a complementary dataset for analyzing plate motion variations over geological timescales [15,18], identifying geodynamic regimes, and, ultimately, linking them to viable tests of mantle flow retrodictions.

The stress analysis of a Couette-Poisseuille representation of the asthenosphere in Chapter 6 could be enhanced by adapting elements from SHELLS [4,11] to more robustly account for topography, heat flow, and stress relaxation due to embedded fault weaknesses within a global model of the lithosphere. Another immediate application of our analysis is to study significant large-scale changes in the stress field throughout the Cretaceous and Cenozoic, driven by upper mantle flow states.

Taken as a whole, this work sets the stage for building rupture dynamic models within a geodynamic context, enabling us to investigate the mechanical viability and associated seismic hazards of earthquakes in different tectonic settings. Particularly, it enables a physics-informed approach to studying the dynamics of intraplate earthquakes. Understanding this setting requires integrating three complex phenomena, often addressed in isolation: modeling the dynamic rupture processes of intraplate earthquakes, modeling sub-lithospheric mantle convection as a potential driver of lithospheric and crustal stresses, and assessing their implications for seismic hazard quantification in intraplate environments. This work demonstrates that this ambitious goal is very well within reach, showcasing integration across disciplines, and emphasizing that an attempt in this direction will be a step towards a break-through progress in a field that has seen little development in several decades.

Thank you for reading this thesis.

7.3 References

[1] Andrews, D. J. (1999). Test of two methods for faulting on finite-difference calculations. *Bulletin of the Seismological Society of America*, 89(4):931–937. Cited on page/s 183.

[2] Antoine, S. L., Klinger, Y., Delorme, A., and Gold, R. D. (2022). Off-Fault Deformation in Regions of Complex Fault Geometries: The 2013, M7.7, Baluchistan Rupture (Pakistan). *Journal of Geophysical Research: Solid Earth*, 127(11):e2022JB024480. e2022JB024480 2022JB024480. Cited on page/s 186.

[3] Antoine, S. L., Klinger, Y., Delorme, A., Wang, K., Bürgmann, R., and Gold, R. D. (2021). Diffuse Deformation and Surface Faulting Distribution from Submetric Image Correlation along the 2019 Ridgecrest, California, Ruptures. *Bulletin of the Seismological Society of America*, 111(5):2275–2302. Cited on page/s 186.

[4] Bird, P. (1998). Testing hypotheses on plate-driving mechanisms with global lithosphere models including topography, thermal structure, and faults. *Journal of Geophysical Research: Solid Earth*, 103(B5):10115–10129. Cited on page/s 185, 187.

[5] Dalguer, L. A. and Day, S. M. (2006). Comparison of fault representation methods in finite difference simulations of dynamic rupture. *Bulletin of the Seismological Society of America*, 96(5):1764–1778. Cited on page/s 183.

[6] Friedrich, A. M., Bunge, H.-P., Rieger, S. M., Colli, L., Ghelichkhan, S., and Nerlich, R. (2018). Stratigraphic framework for the plume mode of mantle convection and the analysis of interregional unconformities on geological maps. *Gondwana Research*, 53:159–188. Cited on page/s 185.

[7] Höink, T., Jellinek, A. M., and Lenardic, A. (2011). Viscous coupling at the lithosphere-asthenosphere boundary. *Geochemistry, Geophysics, Geosystems*, 12(10). Cited on page/s 185.

[8] Höink, T. and Lenardic, A. (2010). Long wavelength convection, poiseuille–couette flow in the low-viscosity asthenosphere and the strength of plate margins. *Geophysical Journal International*, 180(1):23–33. Cited on page/s 185.

[9] Höink, T., Lenardic, A., and Richards, M. (2012). Depth-dependent viscosity and mantle stress amplification: implications for the role of the asthenosphere in maintaining plate tectonics. *Geophysical Journal International*, 191(1):30–41. Cited on page/s 185.

[10] Jara, J., Bruhat, L., Thomas, M. Y., Antoine, S. L., Okubo, K., Rougier, E., Rosakis, A. J., Sammis, C. G., Klinger, Y., Jolivet, R., and Bhat, H. S. (2021). Signature of transition to supershear rupture speed in the coseismic off-fault damage zone. *Proc Math Phys Eng Sci*, 477(2255):20210364. Cited on page/s 186.

[11] Kong, X. and Bird, P. (1995). Shells: A thin-shell program for modeling neotectonics of regional or global lithosphere with faults. *Journal of Geophysical Research: Solid Earth*, 100(B11):22129–22131. Cited on page/s 187.

[12] Lapusta, N. (2019). Modeling earthquake source processes: from tectonics to dynamic rupture. In *AGU Fall Meeting 2019*. AGU. Cited on page/s 183.

[13] Palgunadi, K. H., Gabriel, A.-A., Garagash, D. I., Ulrich, T., and Mai, P. M. (2024). Rupture dynamics of cascading earthquakes in a multiscale fracture network. *Journal of Geophysical Research: Solid Earth*, 129(3):e2023JB027578. e2023JB027578 2023JB027578. Cited on page/s 186.

[14] Stotz, I. L., Iaffaldano, G., and Davies, D. R. (2018). Pressure-driven poiseuille flow: A major component of the torque-balance governing pacific plate motion. *Geophysical Research Letters*, 45(1):117–125. Cited on page/s 185.

[15] Stotz, I. L., Vilacís, B., Hayek, J. N., Bunge, H.-P., and Friedrich, A. M. (2021). Yellowstone Plume Drives Neogene North American Plate Motion Change. *Geophysical Research Letters*, 48(18):e2021GL095079. e2021GL095079 2021GL095079. Cited on page/s 185, 187.

[16] Stotz, I. L., Vilacís, B., Hayek, J. N., Carena, S., and Bunge, H.-P. (2023). Plume driven plate motion changes: New insights from the South Atlantic realm. *Journal of South American Earth Sciences*, 124:104257. Cited on page/s 185.

[17] Sun, Y. and Beckermann, C. (2007). Sharp interface tracking using the phase-field equation. *Journal of Computational Physics*, 220(2):626–653. Cited on page/s 183.

[18] Vilacís, B., Hayek, J. N., Stotz, I. L., Bunge, H.-P., Friedrich, A. M., Carena, S., and Clark, S. (2022). Evidence for active upper mantle flow in the Atlantic and Indo-Australian realms since the Upper Jurassic from hiatus maps and spreading rate changes. *Proceedings of the Royal Society A: Mathematical, Physical and Engineering Sciences*, 478(2262):20210764. Cited on page/s 187.

[19] Wang, W., Fang, L., Wu, J., Tu, H., Chen, L., Lai, G., and Zhang, L. (2021). Aftershock sequence relocation of the 2021 Ms 7.4 Maduo earthquake, Qinghai, China. *Science China Earth Sciences*, 64:1371–1380. Cited on page/s 186.

Part V

APPENDICES

Appendix A

Supplementary information for chapter 2

A.1 On the effective stiffness tensor

We evaluate for inelastic yielding on every iteration. At a yielded location within the fault zone, the limiter to the stress component leads to an effective modification to the stiffness tensor. As a consequence, it behaves as a transversely isotropic material within the fault zone. The effective stiffness tensor within the fault zone at a yielded location is found implicitly in Eq. (2.8),

$$\begin{aligned}\overline{\overline{C}}_{\text{eff}} := \overline{\overline{C}} + \phi(\varphi)(-\operatorname{sgn}(\tau)\mu[\lambda(\boldsymbol{n}\otimes\boldsymbol{t}+\boldsymbol{t}\otimes\boldsymbol{n})\otimes 1 + \\ 2G(\boldsymbol{n}\otimes\boldsymbol{t}+\boldsymbol{t}\otimes\boldsymbol{n})\otimes(\boldsymbol{n}\otimes\boldsymbol{n})] + \\ G(\boldsymbol{n}\otimes\boldsymbol{t}+\boldsymbol{t}\otimes\boldsymbol{n})\otimes(\boldsymbol{n}\otimes\boldsymbol{t}+\boldsymbol{t}\otimes\boldsymbol{n})).\end{aligned} \tag{1}$$

Note that this expression is the same as Eqs. (30)-(32) from the phase-field method of Fei and Choo[2]. There it is required to assemble the Jacobian matrix at the end of the stress update scheme within a FEM framework. As an advantage of using an SEM framework, we avoid explicitly calculating this stiffness tensor at the end of each time step.

A.2 Frequency results of the Kostrov kinematic model

As mentioned in Section 2.4.3, we analyze the frequency content of fault normal accelerograms at receivers located at different distances normal and along the fault, shown in Figure A.1. The simulation setting is the same Kostrov kinematic model used in Figure 2.2. Given the prescribed shear velocity used in the Kostrov model, the cut-off frequency of our choice of model parameters is 9 Hz. Tests with the volumetric yielding criterion deliver roughly flat amplitude spectra of the accelerograms for receivers at 0 km along fault-strike. In the case of using the interface yielding (Figure A.1), receivers close to the fault nucleation contain an increased frequency contribution above 2 Hz. Such frequency contribution can be explained by the sharp reduction of the overshoot before the peak slip rate when using the interface yielding criterion. Regarding receiver pairs at 2 km and 4 km along fault strike (away from the nucleation patch), receivers at 0.5 km normal to the fault show a downward shift at frequencies above 1 Hz, deviating from the spectrum from receivers closer to the fault. This situation is observed for both yielding criteria.

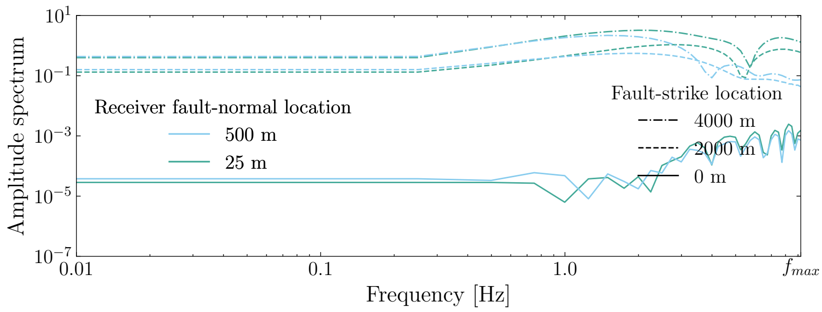

Figure A.1. Amplitude spectra of the accelerograms for receivers located at 0, 2, and 4 km along fault strike, and 25, and 500 m in a fault-normal direction. Extracted for the Kostrov mesh-aligned model, using Q_3 square elements of 25 m width, depicted in Figure 2.2.

A.3 On the yielding criterion applied to the rupture model

Our setup applied to the kinematic Kostrov crack produces slight differences between the model with the interface yielding criterion and the model with the volumetric yielding criterion. In a mesh-aligned geometrical configuration, the main difference is a smooth overshoot slip rate prior to the peak slip rate arrival, as seen in Figure A.2(A), for the volumetric criterion, while the interface criterion instead contains a sudden reduction at this position. In the mesh unfitted geometrical configuration (Figure A.2(A)), using the interface criterion with a thick fault geometry introduces numerical oscillations to the trailing signal behind the rupture front. As indicated in Section 2.5.1, our setup applied to the TPV3 model generates a fault-oblique yielding which, in the transition between the nucleation and the rest of the fault zone, leaves an unyielded location within the fault zone, behind the rupture front. As the simulation progresses, this location reaches the yielding surface due to the evolution of the stress field, producing a small pulse in the slip rate profile when using the volumetric yielding criterion, while introducing the interface yielding produces a solution closer to the reference, free of secondary pulses, as seen in Figure 2.6. Taking a look into the stress field, the shear stress centered around the transition between the nucleation and the rest of the fault zone for the same model configuration under a reduced element width $h = 50$ m is depicted in Figure A.3(A) for the volumetric yielding criterion. We extract a transect crossing such a non-yielded location and sample the shear and fault normal stresses, shown in Figure A.3(B). The same is done for a simulation that uses the interface yielding for the Figure A.3(C) and Figure A.3(D). Note the asymmetry of the shear stress profile in Figure A.3(B), with positive values of the differential shear stress due to the unyielded location, while Figure A.3(C) shows the state of such stresses, and no unyielded location is left behind the developed fully propagating rupture, which advances past this point. Note that the solution using the volumetric criterion also delivers a smooth stress field within the fault zone outside the nucleation patch. In contrast, the interface yielding solution generates a slight oscillatory perturbation. For this reason, we consider the interface yielding criterion a gateway to emulate planar interface solutions.

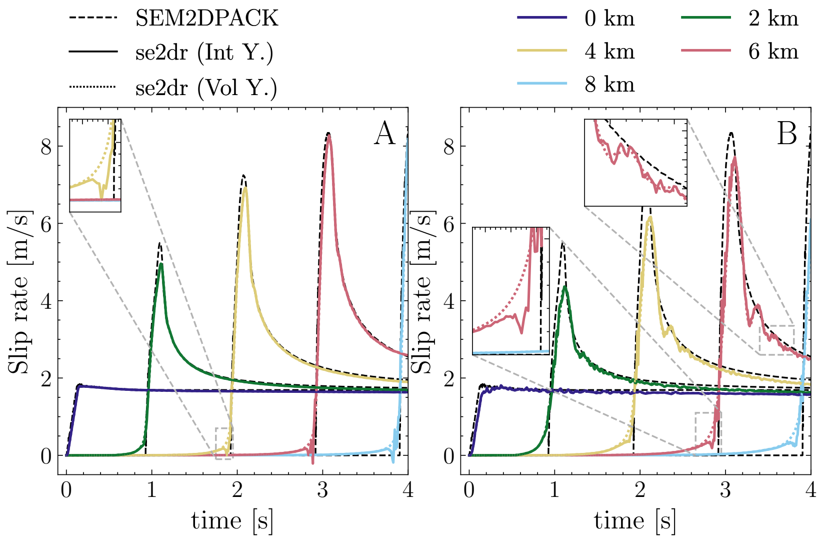

FIGURE A.2. Comparison of the 2D Kostrov crack solution yielding criteria. The figure contains (A) the mesh-aligned setup shown in Figure 2.2 with $\delta = h$ using the volumetric yielding criterion (dotted colored lines) and the interface yielding (continuous colored lines). The same comparison for both yielding criteria is shown for (B) the tilted setup shown in Figure 2.3 with $\delta = 2.5h$.

The small pulse in the slip rate profile decays fast with a distance normal to the fault as observed in Figure A.4(A, B) and contributes to high-frequency signal as observed in the spectrogram in Figure A.4(C), producing a high-frequency content in the amplitude spectrum towards the cut-off frequency.

The fault internal deformation for the volumetric yielding approach (Figure A.5 and Figure 2.10) depicts how our method handles explicitly the internal deformation in terms of the displacement, velocity and stress components within a finite-thickness zone. A close look into the fault-parallel velocity components in the transects of Figure A.5 shows that in the neighborhood of the rupture front, the velocity field can behave in a skewed manner relative to the zero level set for the Q_3 TPV3 simulation in the horizontal configuration.

A.4 On the refinement tests for each model and configuration

In this supplementary section, we include h-refinement tests for our adopted Kostrov and TPV3 models. For the Kostrov model we include the horizontal (Figure A.6), tilted 20°(Figure A.7), and sigmoid (Figure A.8) configurations. For the TPV3 model, we, in addition to what has been presented in the main text, include h-refinements for the tilted 20°(Figure A.9) configuration. We also include additional slip rate profiles, including more receivers along the fault for the horizontal (Figure A.10) and tilted 20°(Figure A.11). For completeness, we include the slip rate profiles up to 3 s of the h-refinement using Q_2 elements, which is used for the lower left inset of Figure 2.9.

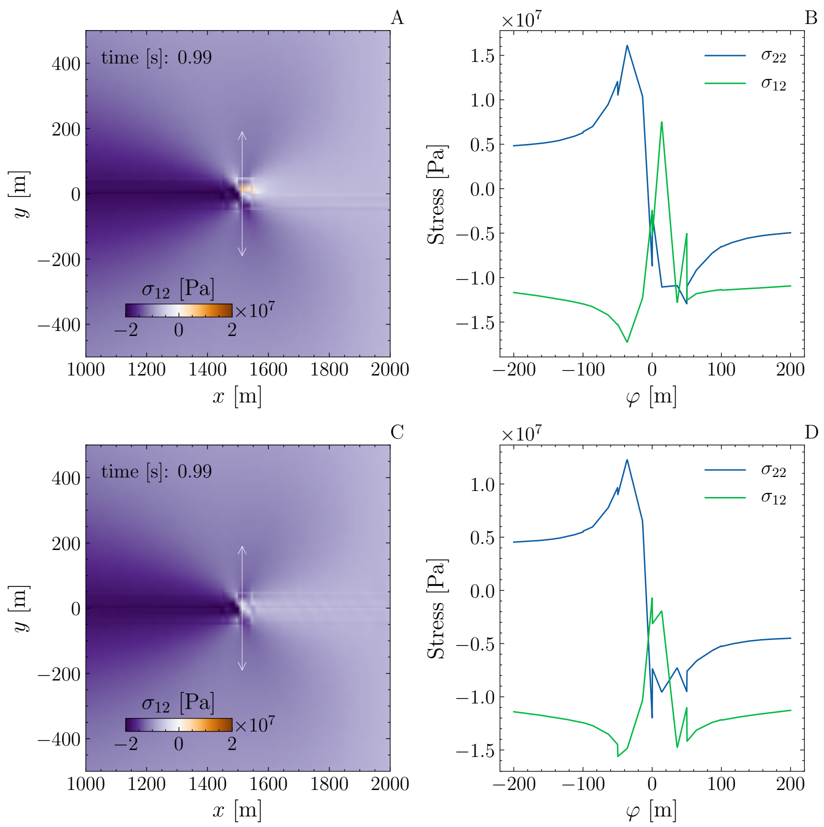

FIGURE A.3. Comparison of the 2D TPV3 dynamic rupture solution. The mesh is composed of Q_3 square elements of width $h = 50\,\text{m}$. The solutions shown here use the volumetric yielding (top row) and the interface yielding (bottom row). The blending parameters and the ratio between the fault inelastic zone width relative to the element width are the same as in the results from Figure 2.5. (A) depicts the shear stress field zoomed at the transition between the nucleation and the rest of the fault zone. Superposed is the location of the transect extracted in (B), sampling the fault normal and shearing components of the stress field. The center of the transect is located at $(1513.8\,\text{m}, 0\,\text{m})$ so that it crosses the location left unyielded at the time behind the rupture front. Likewise, (C) and (D) show the shear stress field and the transect, respectively.

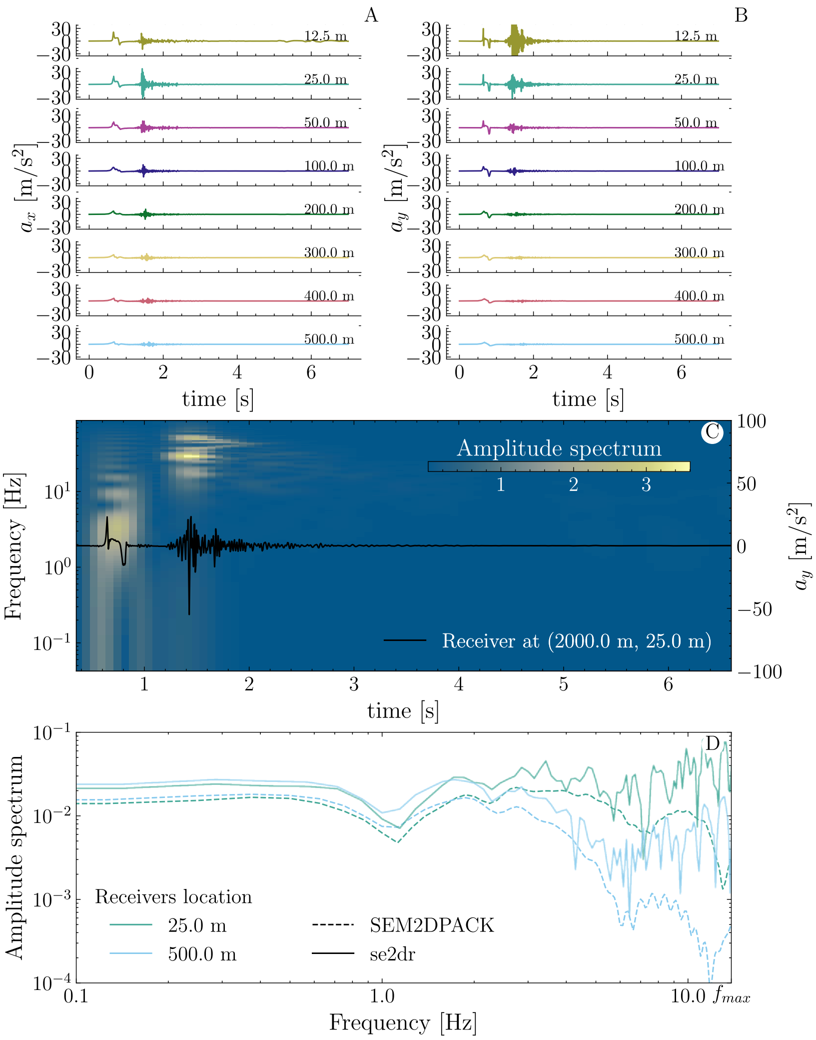

FIGURE A.4. Phase-field stress glut model, TPV3 mesh-aligned model: Variation of the (A) $x-$ and (B) $y-$components of synthetic accelerograms, at stations located at 2 km along the fault, and varying distances normal to the fault for the simulation in Figure 2.6 employing the volumetric yielding criterion in horizontal configuration. (C) Spectrogram extracted from the $y-$component of the acceleration from a receiver at the coordinates (2 km, 25 m). (D) Amplitude spectra of the fault-normal accelerograms at two receivers at 2 km along the fault and, 25 m and 500 m normal to the fault, simulated with se2dr (continuous lines) and the split-node discrete fault approach in *SEM2DPACK* (dashed).

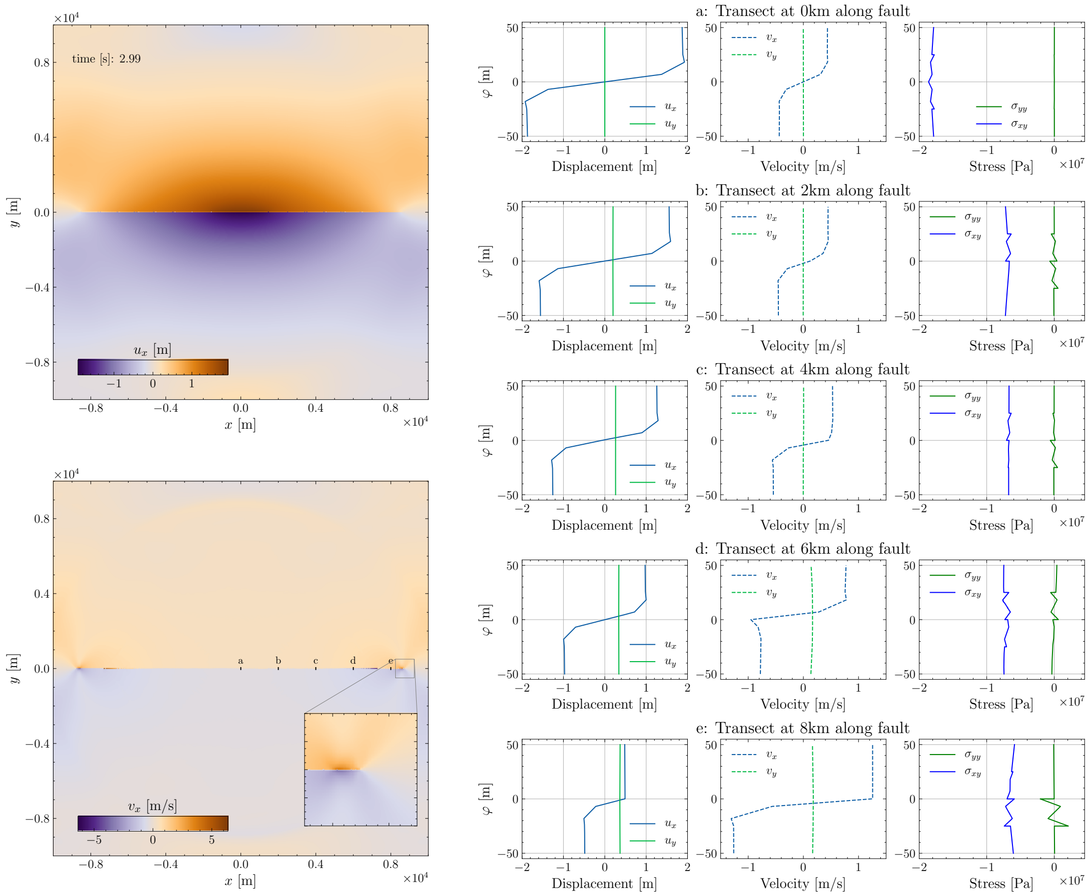

FIGURE A.5. TPV3 model using Q_3 square elements of width 25m, using $\delta = 25$m. The second part of the figure contains fault transects extracted at 0, 2, 4, 6, and 8 km along the fault at ±50 m in the normal direction of the zero level set. The transects are equidistantly sampled, amounting to 2000 points. Each column contains components (color-coded) of the displacement, velocity, and stress field, respectively.

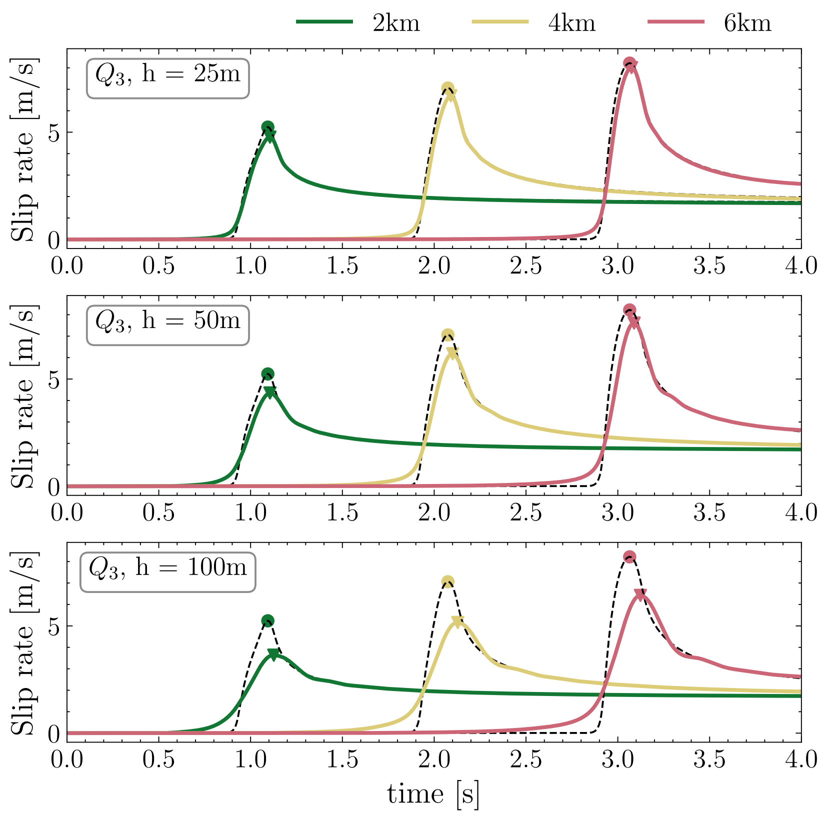

FIGURE A.6. h-refinement test for Kostrov's model in the horizontal geometrical configuration. The models depicted use Q_3 elements with element width h=25,50, and 100m, and δ =h. We impose a volumetric yielding criterion within the fault zone.

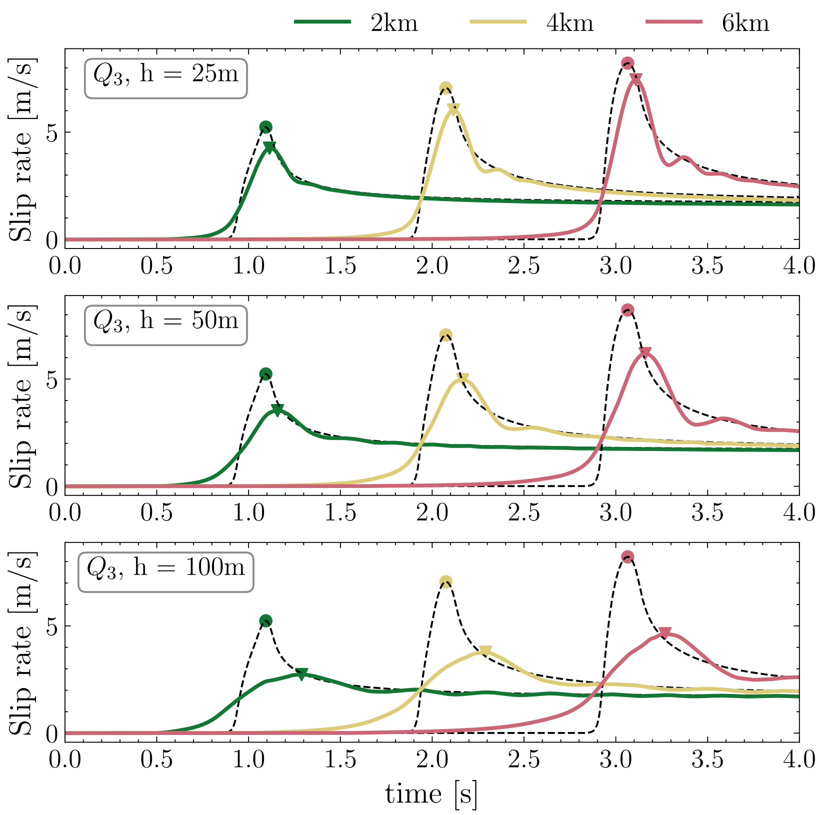

Figure A.7. h-refinement test for Kostrov's model in the tilted (20°) geometrical configuration. The models depicted use Q_3 elements with element width h=25,50, and 100m, and $\delta = 2.5$h. We impose a volumetric yielding criterion within the fault zone.

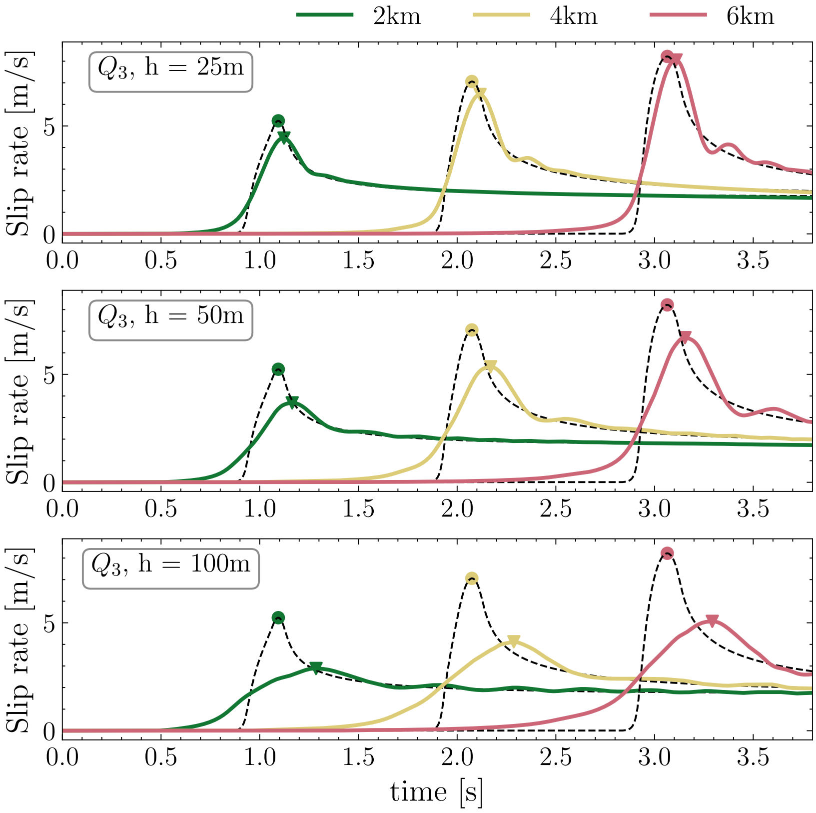

FIGURE A.8. h-refinement test for Kostrov's model in the sigmoid geometrical configuration. The models depicted use Q_3 elements with element width h=25, 50, and 100m, and $\delta = 2.5$h. We impose a volumetric yielding criterion within the fault zone.

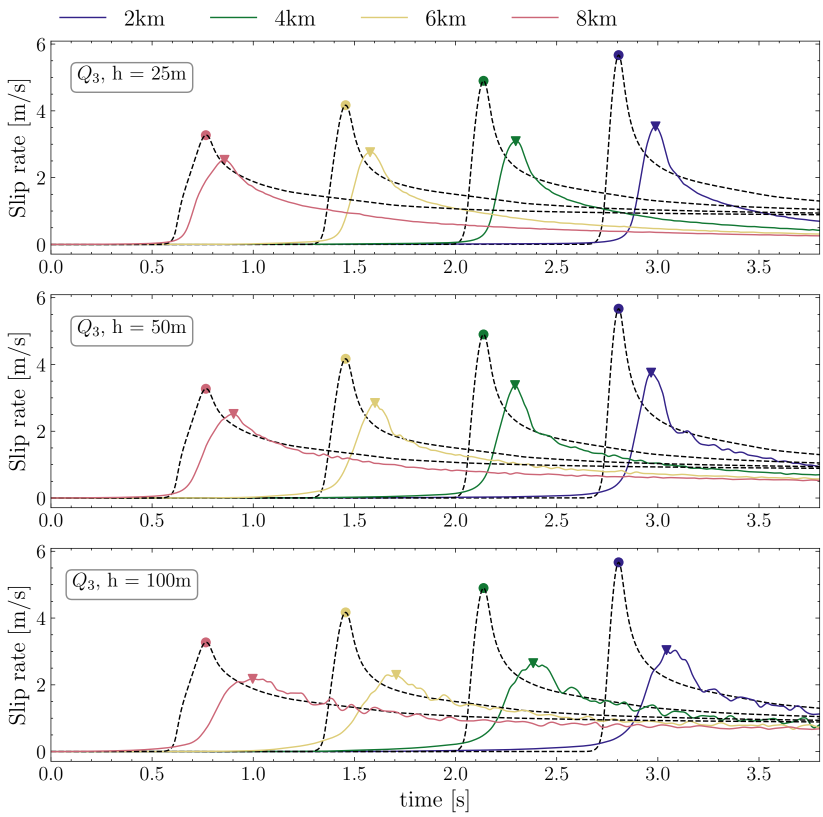

FIGURE A.9. h-refinement test for TPV3 model in the tilted (20°) geometrical configuration. The models depicted use Q_3 elements with element width h=25, 50, and 100m, and $\delta = 1.43$h. We impose a volumetric yielding criterion within the fault zone.

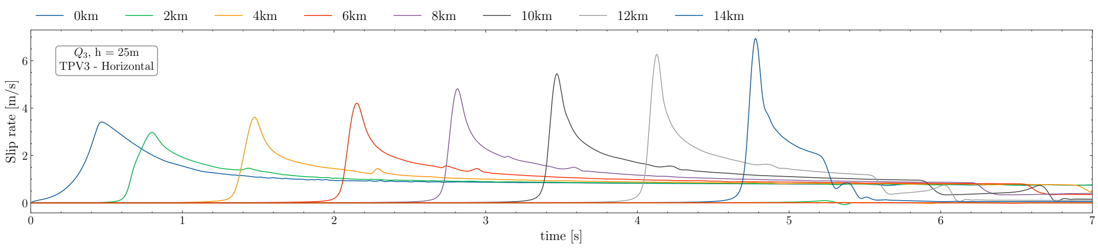

FIGURE A.10. Horizontal configuration of TPV3 model, simulation using Q_3 elements with element width of h=25m, and δ =h, through 7s of simulation time. Using volumetric yielding criteria. The profiles include additional receiver locations along the fault geometry, every 2km from the nucleation up to 14km.

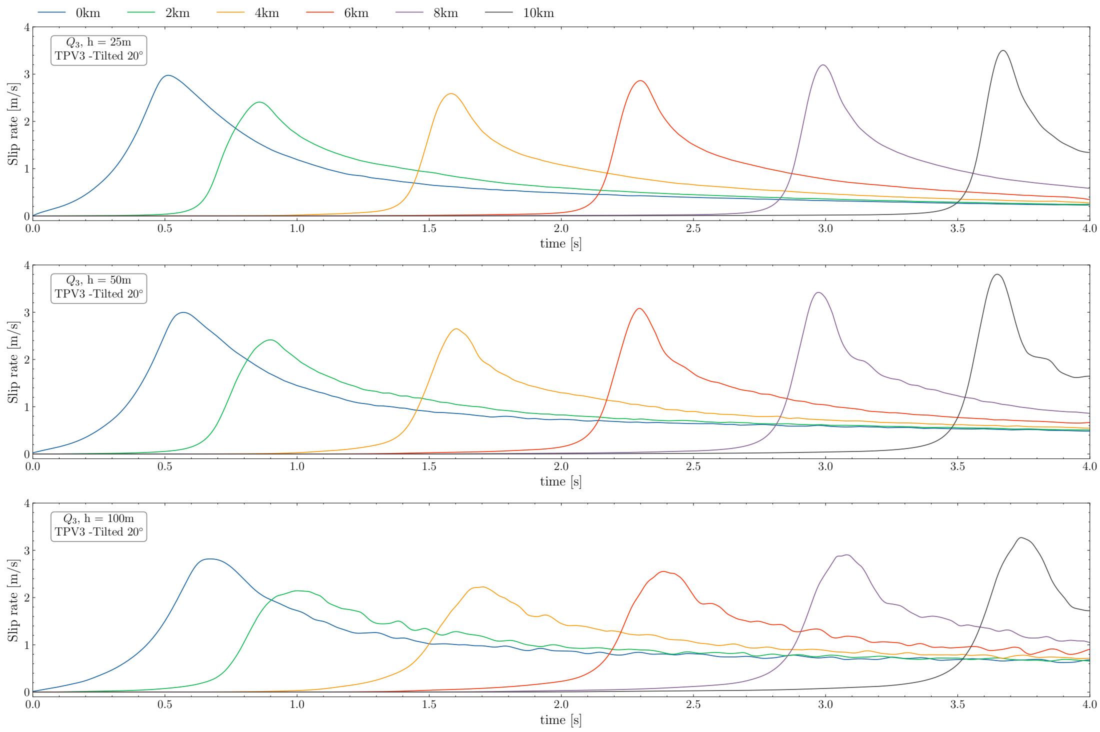

FIGURE A.11. Tilted (20°) configuration of TPV3 model, simulation using Q_3 elements with element width of h=25, 50, and 100m, and $\delta = 1.43$h, through 4s of simulation time. Using volumetric yielding criteria. The profiles include additional receiver locations along the fault geometry, every 2km from the nucleation up to 10km.

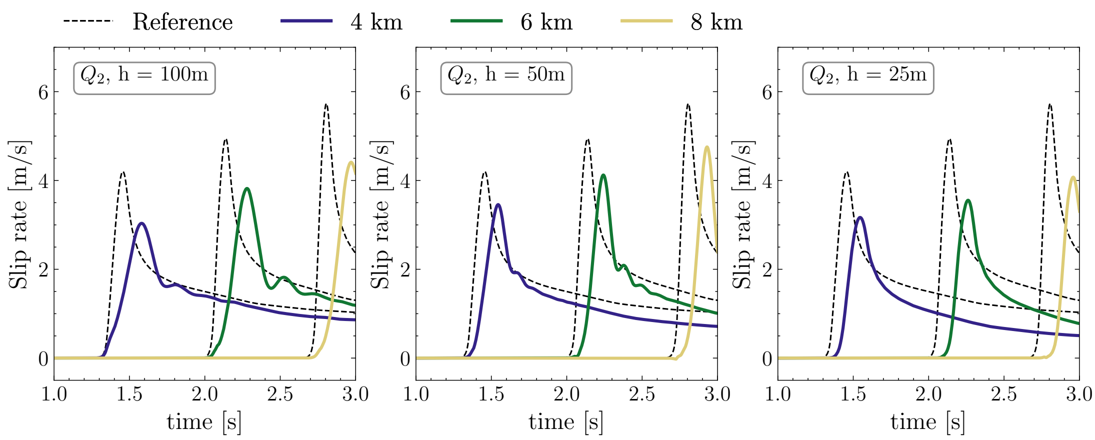

FIGURE A.12. Filtered (Butterworth with $f_c = 10\,\text{Hz}$) slip rate profiles for results using Q_2 elements and alternative blending parameters $A = 18/\delta,\ \varphi_c = 0.65\delta$, following the parameter choices for the lower left inset of Figure 2.9.

A.5 Non-dimensional resolution parameters

To characterize how well we resolve rupture processes within the inelastic fault zone, two non-dimensional parameters are of interest. The first one is introduced throughout this work as the ratio between the fault zone parameter and the element width, δ/h. The ratio δ/h is a guideline of how well-resolved processes across the interior of the fault are, as illustrated in Figure 2.10.

The second non-dimensional parameter of interest is the ratio δ/C_{ZS}, where C_{ZS} is the cohesive zone size [1]. In classical dynamic rupture simulations, C_{ZS} must be (spatially) well resolved by the computational mesh in order for the stress evolution at the rupture front to be simulated accurately. In the framework of our method, the ratio δ/C_{ZS} is important in determining the required model resolution as it reflects how well-resolved dynamic processes at the rupture front are. In the case of the Kostrov model, δ/C_{ZS} is simply δ/L by accounting for the characteristic length L prescribed in the model. In the case of the TPV3 model, we report the values of both ratios in Table A.1.

The first non-dimensional parameter, δ/h, is a proxy of how well-resolved processes across the interior of the fault are, as illustrated in Figure 2.10. The second parameter δ/C_{ZS} rather reflects how well resolved dynamic processes at the rupture front are.

Model: TPV3 - Q_3	h (m)	δ/h	δ/C_{ZS}
Horizontal	25	1	0.035
Tilted 20 deg	25	1.43	0.032
Tilted 20 deg	50	1.43	0.037
Tilted 20 deg	100	1.43	0.058

Table A.1. Compilation of fault zone width parameter ratio with cell width (δ/h) and ratio with the cohesive zone size (δ/C_{ZS}). The cohesive zone size is calculated following Wollherr et al.[6] from the time difference between fault shear stress reaching its dynamic level and the rupture onset time, multiplied by the rupture velocity. The dynamic shear stress time is obtained after reaching a slip larger than D_c, while the rupture onset time here is taken when the slip rate surpasses 0.1 m/s. The timings are estimated across a fault transect at 4 km hypocentral distance.

A.6 On the effective fracture energy

According to the classical theory, the effective fracture energy can be represented as

$$G_c = \int_0^S (\tau_F(s) - \tau_d)\, ds, \tag{2}$$

where τ_d denotes the dynamic shear stress value when $\tau_F(S) = \tau_F(D_c)$ [3,4]. Under a slip weakening friction law, the effective fracture energy can be simplified to $G_c = \frac{1}{2}\Delta\tau D_c$. However, given the complex internal deformation arising in our model (Figure 2.10), this simplification is not applicable. We evaluate the average energy dissipated in a fault transect, which requires integration over the inelastic fault zone width (see Table A.2). Given the dynamic character of our approach everywhere within the fault zone, inertia effects will emerge across the rupture front and affect the effective

Fault-parallel distance (m)	Average energy along transect ($\mathrm{MJ\,m^{-2}}$)
500	2.17
1000	2.37
1500	2.49
2000	2.82
2500	2.89
3000	0.37

TABLE A.2. Average energy along transects for the horizontal TPV3 model using Q_4 square elements of width 25m, $\delta = 12.5$m, and the volumetric yielding criterion depicted in Figure 2.10. Note that at the timestep under consideration, the rupture front has just arrived at the receiver located at 3000 m, and thus, the energy dissipation there is incomplete.

fracture energy[5]. While "frictional dissipation" is here distributed across a finite width zone, future analysis may focus on relating energy rates across that zone (per unit distance along the fault) and with classical interface fracture energy expressions.

A.7 ON THE REMOVAL OF THE DAMPING COMPONENT

In this section, we show a variation of the Kostrov model in the horizontal configuration (Figure A.13), removing the Kelvin-Voigt damping. Spurious oscillations develop throughout the velocity field.

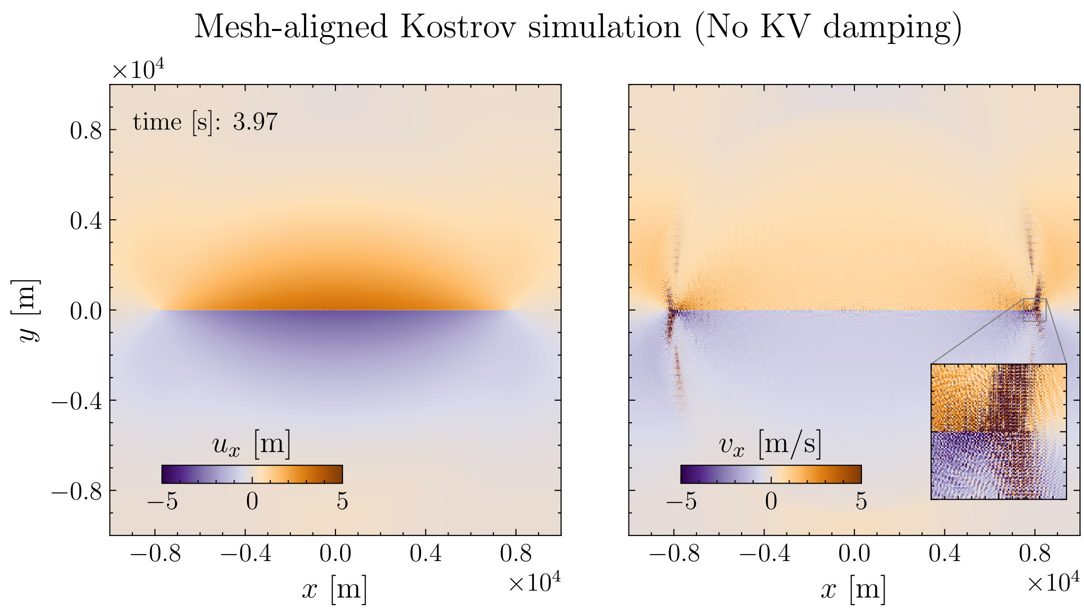

FIGURE A.13. Kostrov model, mesh-aligned configuration. We use Q_3 square elements of $25m$ width and apply no Kelvin-Voigt damping. The figure depicts the x component of the displacement field (left) and spurious oscillations arising in the velocity field (right), both saturated at ±5m and ±5m/s.

A.8 References

[1] Day, S. M., Dalguer, L. A., Lapusta, N., and Liu, Y. (2005). Comparison of finite difference and boundary integral solutions to three-dimensional spontaneous rupture. *Journal of Geophysical Research: Solid Earth*, 110(B12). Cited on page/s A-12.

[2] Fei, F. and Choo, J. (2019). A phase-field method for modeling cracks with frictional contact. *International Journal for Numerical Methods in Engineering*, 121(4):740–762. Cited on page/s A-1.

[3] Ida, Y. (1972). Cohesive force across the tip of a longitudinal-shear crack and Griffith's specific surface energy. *Journal of Geophysical Research*, 77(20):3796–3805. Cited on page/s A-12.

[4] Palmer, A. C. and Rice, J. R. (1973). The growth of slip surfaces in the progressive failure of over-consolidated clay. *Proceedings of the Royal Society of London. A. Mathematical and Physical Sciences*, 332(1591):527–548. Cited on page/s A-12.

[5] Weng, H. and Ampuero, J.-P. (2019). The dynamics of elongated earthquake ruptures. *Journal of Geophysical Research: Solid Earth*, 124(8):8584–8610. Cited on page/s A-13.

[6] Wollherr, S., Gabriel, A.-A., and Uphoff, C. (2018). Off-fault plasticity in three-dimensional dynamic rupture simulations using a modal Discontinuous Galerkin method on unstructured meshes: Implementation, verification and application. *Geophysical Journal International*, 214(3):1556–1584. Cited on page/s A-12.

Appendix B

Supplementary information for chapter 3

This supplementary material contains a detailed description of the method used for our geodetic analysis (geodetic inversion and fault zone width estimation, Section B.1), a systematic dip-angle exploration for the geodetic slip model (Section B.2), our dynamic rupture model and the initial stress setup (Section B.3), the method used for the analysis of the modeled off-fault plasticity patterns (Section B.4) and sensitivity analysis based on 10 alternative dynamic rupture models, including one model without the geodetically inferred heterogeneous stress (Section B.5), one model featuring a thicker shallow velocity strengthening layer (Section B.6), two models with different fault geometries (Section B.7), two models with different initial ambient stresses (Section B.8), two alternative dynamic rupture scenarios with homogeneous characteristic slip distance D_{RS}, and two scenarios with alternative plastic cohesion (Section B.9). Finally, we present a comparison between two sets of synthetic displacement time-series, respectively from the preferred unilateral supershear model and the alternative subshear model, and available high-rate GNSS displacement data (Section B.10). These synthetic displacement time-series were generated using a high-resolution mesh capable of resolving frequencies up to 1 Hz.

B.1 Geodetic data processing, static inversion and surface deformation analysis

In this section, we describe the processing of the Sentinel-1 SAR and Sentinel-2 and SPOT6/7 optical data, the method used to estimate the fault slip distribution from the joint inversion of InSAR and Sentinel-2 optical data, and the method used to characterize the off-fault deformation from high-resolution SPOT6/7 optical data.

InSAR processing

We processed two six-day interferograms using ascending and descending SAR images from the Sentinel-1 constellation operated by the European Space Agency. The pre- and post-earthquake SAR images were acquired on the 20th May 2021 and 26th May 2021, respectively, by the ascending track A099 and descending track D106. We processed the interferograms using the NSBAS processing chain (New Small BAseline Subset [8,40]). The topographic phase contribution has been removed from the interferograms using the Shuttle Radar Topography Mission (SRTM; Farr et al.[12]) 3 arc-sec (~90 m resolution) Digital Elevation Model (DEM). Finally, the interferograms were filtered using a coherence-dependent filter and unwrapped using the branch-cut algorithm of Doin et al.[9] and Grandin et al.[14].

Optical data processing

We measured a medium-resolution (40 m grid spacing) and a high-resolution (6 m grid spacing) horizontal displacement field for the Maduo earthquake from the correlation of Sentinel-2 and SPOT6/7 images, respectively.

For the medium resolution displacement field, we used three pairs of pre- and post-earthquake Sentinel-2 optical images acquired on 4th August 2017 and 19th July 2021, respectively. The pre- and post-earthquake image dates have been chosen to minimize illumination bias in the resulting correlation. We correlate the images using the phase correlator of the open-source software package COSI-Corr[26] using a multiscale sliding correlation window of 128 to 32 pixels and a measurement step of 4 pixels (40 m). Data points with Signal-over-Noise Ratio (SNR) lower than 0.9 and unrealistic displacement amplitudes were discarded. Outliers were also removed using a neighborhood statistical approach, whereby values are masked if < 50% of neighbors within a 18-by-18 pixel window centered on each pixel lie within a threshold value from the central pixel value[52]. Finally, the correlation maps have been smoothed with a 3-by-3 median filter. The three image pairs were processed independently, then overlapping correlation scenes were aligned by removing a residual ramp over each correlation.

We measure the a high resolution horizontal surface displacement field for the Maduo earthquake from the correlation of SPOT-6/7 images of 1.5 m resolution. Six pairs of pre- and post-earthquake images are needed to cover the entire rupture.

In order to obtain a seamless displacement field, the pre- and post- SPOT images are first registered to pre- and post 10 m resolution Sentinel-2 images used as reference. For this registration step, using the Ames Stereo Pipeline (ASP) software, we first correlated the pre/post Sentinel-2 reference images with the raw pre/post SPOT images. We transform the correlation maps obtained into Ground Control Points (GCPs), which are then used to refine the Rational Polymonial Coefficients (RPCs) of the SPOT images. The pre- and post-earthquake raw SPOT images are then orthorectified with the same pre-earthquake WorldDEM of 2.5 m resolution.

We use the phase correlator of COSI-Corr to correlate the orthorectified pre- and post-orthoimages. We used a multi-scale correlation windows of 128-to-32 pixels and a step size of 4 pixels, leading to a final spatial resolution of 6 m. Because we use a step size smaller than the correlation window, the measurements are truly independent every 8 pixels (24 m), since the correlation process gives a single displacement value per sub-pixel refinement window (which is approx. half of 32 pixels in this case, when we account for the windowing function used to mitigate spectral leakage when computing the FFT of the pre/post image windows).

As we orthorectified the pre- and post-images using the same pre-earthquake DEM, the raw optical displacement correlation maps contain a strong stereoscopic noise component in addition to the coseismic displacement signal. To denoise the correlation maps, we trained a random forest algorithm to predict the stereoscopic bias from the local slope, local aspect, local height, and local grayscale pixel values of the pre- and post-earthquakes images. This bias is learned away from the fault, using flattened (i.e. detrended) displacement data. The predicted bias over the entire fault zone is then removed from the displacement maps.

Finally, outliers are removed using the neighoborhood statistical approach, along with data points with a low SNR ratio (< 0.9), and unrealistic amplitudes. TV-L1 smoothing is then applied to the displacement map to further reduce high-frequency noise, while preserving sharp features associated with the surface ruptures.

Data subsampling

In order to reduce the computation time of the inversion, we downsampled the Sentinel-1 InSAR and Sentinel-2 optical displacement data. Indeed, high-spatial resolution data, such as InSAR and optical data, are highly correlated spatially and can therefore be reduced without losing significant information (e.g., Lohman and Simons[27]). We applied a subsampling scheme that depends on the distance perpendicular to the fault [15], keeping high spatial sampling near the fault where the displacement gradients are high while downsampling more strongly areas away from the fault, where displacement gradients are low (and consequently the data redundant). For distances lower than 17 km from the fault, we downsampled the interferograms to one point every 2 km. For distances between 17 and 30 km from the fault, we kept one point every 4 km, for distances between 30 and 45 km from the fault, we kept one point every 8 km, and for distances greater than 45 km, we kept one point every 16 km. The Sentinel-2 optical data cover only the near- and medium-field (up to 40 km from the fault) and are downsampled to one point every 1 km. This subsampling allows reducing the number of data points from 54 millions to 27,000 without loss of relevant information.

Static fault slip model from joint inversion of InSAR and Sentinel-2 optical data

We infer the fault slip distribution at depth for the Maduo earthquake from the joint inversion of the subsampled Sentinel-1 InSAR and Sentinel-2 optical data using a well-established elastic dislocation modeling approach (e.g., Harris and Segall[19], Marchandon et al.[31], Simons et al.[37], Wright et al.[50]). We used the same segmented fault geometry as the one used in our dynamic rupture model (see Method section and SI Text B.3) that we discretized with triangular subfaults of variable size. The subfault size increases gradually with depth from 1 km at the surface to 5 km at 20 km depth. We computed the Green's functions relating a unit of slip on the subfaults to the surface displacements assuming a uniform elastic half-space with a Poisson ratio ν of 0.25 [32]. We solved for the strike and dip component of the slip on each subfault using a constrained linear least square inversion [5]. We made the reasonable assumption that no right-lateral slip occurred during the left-lateral Maduo earthquake and therefore constrained the strike-slip to be between 0 and 10 m while the dip-slip is constrained between -10 and 10 m, as both normal- and dip-slip can be observed along a strike-slip rupture (e.g., Marchandon et al.[31]). Finally, we implement a Laplacian smoothing operator to avoid large slip variations between neighboring patches [23]. We are therefore solving the following system of equations:

$$\begin{bmatrix} \mathbf{d} \\ 0 \end{bmatrix} = \begin{bmatrix} \mathrm{G} \\ \lambda \mathrm{D} \end{bmatrix} \mathbf{m} \quad (3)$$

where **d** is the data vector composed of the subsampled InSAR and optical data; **G** is the Green's functions matrix relating a unit slip on each subfault to the surface displacements, **m** is the vector of parameters we are solving for (strike-slip and dip-slip on each sub faults), D is the second-order finite difference operator and λ is the smoothing factor that we choose according to an L-curve criterion (Figure B.1). In addition to the strike- and dip-slip on the fault, we also solved for residual ramps in the InSAR and optical data. We weighted the data such that the InSAR and optical datasets are equally well fit. We tested several dip angle values ranging from 70°S to 50°N (the same dip angle value is used for all three segments) and found that the geodetic data are best fit with a dip angle value in the range 80-85°N (Figure B.2). We choose a dip angle of 83°N for our preferred model. Figure B.3 and Figure B.4 show that the data are well reproduced by our model, with an RMS misfit of 0.03 m and 0.031 m for the ascending and descending interferograms, and 0.20 m and 0.15 m for the EW and NS optical displacement fields, respectively.

Note that the InSAR and Sentinel-2 optical data include 4 days and less than 1 month of postseismic deformation, respectively. Postseismic observations of the Maduo earthquake show that the postseismic afterslip in the first month does not exceed 10 cm [11,22], significantly smaller than the coseismic slip that reaches up to 6 m. We are therefore confident that our inferred slip model does not include any significant amount of postseismic deformation.

Fault zone width estimation from the SPOT6/7 displacement field

To estimate the amount of surface slip accommodated across the fault zone as well as the fault zone width, we measure 509 fault-perpendicular stacked profiles spaced every 300 m along the fault trace. Each profile is ~10 km long and corresponds to the stack of 50 parallel profiles measured over a width of 300 m. This choice of stack width represents the optimal trade-off maximizing the signal-over-noise ratio while preserving spatial resolution along-strike. For each profile, we fit linear regressions to the displacement profile on each side of the fault from the far-field to the inflection point near the fault trace (see Figure B.5). The fault offset is then measured by computing the displacement difference of the linear regressions where they project to the fault trace, while the fault zone width corresponds to the distance between the inflection points on both sides of the fault.

B.2 Systematic dip-angle exploration for the geodetic slip model

We here perform a systematic exploration of the parameter space to 1) evaluate the dip angle combination that best explains the geodetic data and 2) evaluate whether or not the assumption of constant-dip-angle we assumed in the main paper significantly impacts the resulting slip distribution. To that end, we test 7 dip angle values for each segment, varying from 72°N to 84°S for F1 and F2 and from 44°S to 84°S for F3 (leading to 343 combinations possible) and evaluate which combination leads to the lowest RMS misfit.

The result of the systematic exploration is shown in Figure B.6. Figure B.6a shows that the dip angle of segment F1 is very well constrained with a clear decrease of the RMS misfit for dip angle values in the range 80°N-84°N. F2 dip angle is less well constrained by the data with preferred dip angle values ranging from 76°N-88°N (with a best dip angle of 80°N, Figure B.6a-c). Finally the dip angle of segment F3 is not well constrained by the data with a wide range of dip angle values explaining equally well the data (44°S to 84°S with a best dip angle of 52°S, Figure B.6a,c,d)

The slip distribution associated with our preferred non-constant dip geodetically-inferred (F1=84°N, F2=80°N, F3= 52°S, Figure B.7b) does not display significant differences with the constant-dip-angle slip model (Figures 1 and Figure B.7a), suggesting that the prestress heterogeneities and consequently our results, are not affected by the constant-dip-angle simplification.

B.3 Dynamic rupture mesh generation and model setup

Mesh generation

We include our geodetically inferred fault system and the topographic data of 1-arc-minute resolution from ETOPO1 [1] in the model domain. The topographic surface is discretized into triangles of ~2 km in length. We set the edge lengths of elements in the vicinity of the fault interface to 200 m as an upper limit, ensuring adequate resolution in space and time. We generate the tetrahedral elements in a cubic domain using SimModeler [36], with an increased refinement of the element size towards the fault to ensure computational accuracy and efficiency. The mesh is gradually coarsened based on the distance normal to the fault surface at a gradient of 0.3, gradually reducing the resolution for outgoing seismic waves to improve simulation efficiency.

We assign the boundary conditions as free surface, dynamic rupture, and absorbing boundary to the topographic surface, the fault surfaces, and the domain lateral and bottom surfaces, respectively. We set the entire domain size to 590 km × 488 km × 96 km, large enough to avoid any waves reflecting at the imperfectly absorbing boundaries at the lateral and bottom domain boundaries to pollute our simulation results. The computational mesh consists of 5,958,234 elements in total. A simulation with 4th-order accuracy in time and space for 90 s requires ~ 2,800 CPU hours on the supercomputer SuperMUC-NG at the Leibniz supercomputing center in Garching. We use a higher-resolution mesh, consisting of 10,940,556 elements and capable of resolving frequencies up to 1 Hz to simulate synthetic high-rate GNSS time series, which requires 4,200 CPU h.

The size of the area behind the rupture front in which shear stress decreases from its static to its dynamic value is the process zone width [6]. The on-fault resolution (mesh size and order of accuracy) must be chosen to be high enough to resolve the process zone and ensure an adequate numerical resolution of rupture dynamics. In our preferred dynamic rupture model the *minimum* process zone width averaged across the 5% of the fault elements with the smallest process zone sizes during rupture is 232 m. Our on-fault element size is h =200 m, noting that each dynamic rupture element provides sub-element resolution.

Initial background stresses of the preferred dynamic rupture model

In this section, we detail the initial stress parametrization, summarized in section 2.2 of the main text. We assume an ambient homogeneous background stress acting within the model domain.[38] In addition, all faults include heterogeneous initial stresses as inferred from the geodetically-constrained fault slip[21].

We set a homogeneous background stress according to a virtual fault plane derived from regional focal mechanism inversions[44], as described in Table B.1. The absolute values of confining stresses are jointly defined by the lithostatic loading σ_z, the ratio of pore fluid pressure λ, the relative fault strength R_0, the stress shape ratio ν, and a depth-dependent shape function $\Omega(z)$[42].

The lithostatic stress increases linearly with depth below the topographic surface. The lithostatic pressure σ_z at depth z follows:

$$\sigma_z = \int_0^z \rho(z_i) g z_i \partial z_i \tag{4}$$

In nature, the temperature-dependent brittle-ductile transition is expected to reduce the deviatoric stress at the base of the seismogenic zone, reflecting the yield strength variation of the lithosphere (e.g., Scholz[35]). Here, we use a stress modulation function Ω_z, defined as varying with depth and smoothly reducing the deviatoric stresses below the seismogenic depth[42]. Figure B.10 shows the depth distribution of Ω_z used in the reference model.

Our depth-dependent effective normal stress is accounting for pore fluid pressure[29]. We assume that the fluid pressure throughout the crust is proportional to the lithostatic stress, expressed as $P_f = \gamma\sigma_c$ with γ being the fluid-pressure ratio defined by $\frac{\rho_{water}}{\rho_{rock}}$. The effective confining stress is defined as $\sigma_c = (1-\gamma)\sigma_z$. We assume in our model a hydrostatic stress state, implying $(1-\gamma) = 0.63$.

The fault prestress ratio R_0 describes the closeness to failure of an optimally oriented virtual plane according to Mohr-Coulomb theory[3]. This alternative representation of the fault strength is defined as a linear mapping (where $R_0 = (\tau_0 - \tau_r)/(\tau_p - \tau_r)$, where τ_p and τ_r are the peak and residual strengths, and τ_0 as the background level of initial loading), in contrast to the S parameter definition. Both representations are related by $S = (1/R_0) - 1$. We assume a uniform distribution of prestress ratio R_0. The stress shape ratio ν, which is defined as $\frac{S_2 - S_3}{S_1 - S_3}$, balances the principal stresses (S_1, S_2, and S_3; ordered from most compressional to most tensional). We assume $\nu = 0.5$ for the entire fault.

Initial heterogeneous stresses inferred from geodetically-constrained fault slip

We use the geodetic static slip model as input in a dynamic relaxation simulation with SeisSol[21,41] using the same computational mesh, fault geometries, and subsurface material parameters to compute the corresponding shear and normal stress changes. The resulting stress changes are scaled by a factor of 0.3 and then added to the ambient, regional initial shear, and normal on-fault prestress amplitudes. This balance is constrained by a few trial-and-error dynamic rupture simulations, ensuring realistic slip distributions and moment rate release.

The included stress variation inferred from our geodetically-inferred slip distribution (Supplementary Text S2) further constrains the initial on-fault stress conditions. We use SeisSol to compute the total stress perturbations associated with the imposed kinematic slip on the fault surface as a boundary condition, ensuring the same spatial discretization. The six components of the stress tensor in each volumetric element are added to the background stresses which have been introduced above. This operation results in a heterogeneous initial shear and normal stresses on the fault (Figure B.8).

3D dynamic rupture model setup details

We perform all 3D dynamic rupture and seismic wave propagation models using the open-source package SeisSol (www.seissol.org), which is based on the Arbitrary High-order Derivative Discontinuous Garlekin finite element method [10,25,33], and is optimized for modern high-performance computing architectures including an efficient local time-stepping algorithm [4,20,24,43]. Dynamic rupture simulations using SeisSol have been validated against several community benchmarks following the SCEC/USGS Dynamic Rupture Code Verification exercises [16,34].

Within the off-fault plasticity implementation [49], the onset of Drucker-Prager plastic yielding is not instantaneous but governed by rate-dependent viscoplastic relaxation with a relaxation time T_v of 0.05 s, which ensures convergence of simulation results with mesh refinement [49].

Nucleation

We initiate the spontaneous dynamic rupture by imposing an over-stressed spherical patch with a radius of 950 m centered at the USGS hypocentral location (34.61°, 98.36°), at a depth of 5.5 km. The stress loading gradually increases exponentially over the first 0.5 s to achieve smoothly expanding rupture, following the best practices established in the community verification benchmark project of the USGS and SCEC [16,17].

B.4 Surface sampling of the modelled off-fault plasticity

The accumulated 3D plastic strain field can be mapped into a scalar quantity following [28,48]. We sample the modeled off-fault plasticity at fault-parallel transects (Figure B.11), selecting the nearest cell center location to the sampling point using a KDTree algorithm [30,45]. Subsequently, we organize the scalar values of the modeled accumulated plastic strain for each transect and present a sorted histogram alongside both geodetically derived and simulated fault-parallel offsets (Figure 3B).

B.5 Alternative rupture scenarios: removed kinematic heterogeneous stress.

The initial pre-stress in our dynamic rupture models is a combination of a uniform regional loading combined with small-scale heterogeneities inferred from our static slip model. The on-fault prestress distribution resulting from the regional tectonic loading is only modulated by the fault geometry (i.e. by the variations of fault strike, Figure B.9 C,D). Smaller-scale pre-stress variations, that can arise from e.g., past ruptures (on the Maduo or neighboring faults), unmodeled fault geometry complexities (such as fault roughness), local variations in fault strength or fluid pressure, or unknown local variations in tectonics loading, are not taken into account when only a regional loading is considered. The stress drop distribution associated with an earthquake reflects such heterogeneities and can therefore be used to help constraining the initial stress distribution of a dynamic rupture model (e.g., Jia et al.[21], Tinti et al.[41], Weng and Yang[47]) when no other constraint is available, as it is the case for the Maduo area.

Here we show in Figure B.12 and Figure B.13 the on- and off-fault response from an alternative model in which we do not include the geodetically-inferred stress heterogeneities (model A1). We observe the expected rupture velocity behaviour on the southeast section of the fault, developing supershear propagation as in the reference model. On the west section of the fault we find a shallow supershear propagation. In comparison, the stress heterogeneities modulate the rupture velocity as seen in the reference model, in which the unsustained supershear towards the west develops into subshear propagation. The patterns of slip between both models are similar. However, the model without the pre-stress heterogeneities have a more distributed slip magnitude, while the model with the heterogeneities depict higher concentrations of slip patches. Alternative scenarios that include on-fault stress heterogeneities inferred from our static slip model (Figures S14-S31) fail to reproduce a final slip distribution similar to our static slip model or the other observational constraints.

B.6 Alternative rupture scenarios: thicker shallow velocity strengthening layer

We showcase the on- and off-fault response of an alternative model in Figure B.14 and Figure B.15, in which we increase the thickness of the shallow velocity-strengthening layer relative to the preferred model to 3 km (model B1). This configuration is motivated by the possibility that extensive supershear rupture may result from the free-surface effect in a rupture dynamic model that has not been sufficiently damped. By including a thicker velocity strengthening layer, we observe that the supershear on the eastern section of the fault still occurs; however, the rupture does not propagate to the southernmost fault segment F3. The alternative model shown in Figure B.26 hosts bilateral subshear propagation by setting a homogeneous and high D_{RS}. These two alternative models suggest that the unilateral supershear propagation is promoted by the lower fracture energy in the eastern part of the fault and not from insufficient damping conditions at the surface.

B.7 Alternative rupture scenarios: sensitivity to the fault system geometry

We highlight the effects of fault geometries, specifically of segmentation and dip angles, while keeping the material, friction, and stress parametrizations unchanged. Figure B.16 showcases a scenario in which segments F1 and F2 are connected smoothly and not separated (model C1). The fault surface traces are then extruded with a constant dipping angle of 83° towards the North.

In contrast, Figure B.18 showcases a scenario in which the segmentation is the same as in our preferred model but the three segments F1, F2, and F3 dip with a constant dipping angle of 83° towards the North (model C2).

The first geometrical variation features dynamic rupture continuously propagating with supershear velocity towards the east, with no secondary onset of supershear rupture after the activation of the second branch as in our preferred model. The modeled moment rate release has a shorter local minimum between the main peaks (Figure B.16B).

The off-fault plasticity distribution is mainly widespread across the southernmost branch (Figure B.17A). This leads to a single large bell-shaped distribution centered at 99° Longitude (Figure B.17B), in contrast to three widely distributed regions of off-fault plastic strain, that are associated with the fault geometrical variations of the second segment in the preferred model. The latter better resembles the observed distribution of optical fault zone width (Figure 3B).

The model with different dip angles fails to dynamically trigger the fault segments F2 and F3 (Figure B.18A). It does not match the second peak in moment rate release (Figure B.18B), nor generate any off-fault plasticity distribution beyond 98.8° Longitude.

B.8 Alternative rupture scenarios: sensitivity to the ambient stress orientation

We showcase alternative models with different ambient stress choices relative to the initial stress parametrization used in the preferred model. Figure B.20 shows the model D1 results when assuming a strike of 100° ($\hat{S}_{\mathrm{Hmax}}$ of N68°E) for the virtual plane of optimal stress orientation (compared to 110°, or $\hat{S}_{\mathrm{Hmax}}$ of N78°E, in the preferred model). This 10 degree change results in higher accumulated on-fault slip, and a nucleation-induced supershear transition, preferentially sustained eastwards. We note that these changes also relate to the fact that the model required a relative increase of prestress parameter R_0 of 0.25 to induce a successful nucleation that led to a propagating rupture.

The second model D2 (Figure B.22) deviates from the preferred model in using an optimal stress orientation at a strike of 120° ($\hat{S}_{\mathrm{Hmax}}$ of N88°E). Now, the modeled on-fault slip amplitudes are lower. No sustained supershear rupture is induced from the nucleation, which is similarly elevated as in the previous model. However, there is an episode of unsustained supershear propagating eastward, induced by a P-/SV-wave transition at the free surface. The duration of the moment rate release is longer than the preferred model, comparing well with the pattern from the USGS, yet the moment rate release amplitudes are low. Additionally, this model fails to rupture the southernmost fault segment. This model leads to slightly wider off-fault plastic strain in the western section of the fault system compared to the eastern section. While this scenario illustrates that a less-optimal background stress orientation can lead to an episode of unsustained supershear and realistic moment rate release, it fails to reproduce observed slip and seismic moment amplitudes and does not dynamically trigger all fault segments. Also the modeled differences in fault zone widths of the eastern and western segments are not agreeing with observations.

B.9 Alternative rupture scenarios: sensitivity to on- and off-fault properties

In this section, we present alternative rupture scenarios to explore the sensitivity of our results to on- and off-fault rheology parameterizations different to the preferred model. Specifically, we explore the effects of prescribing a homogeneous critical slip distance D_{RS} on all faults and of changing the off-fault plastic cohesion values. In the following, we use our preferred model as a reference to which we compare the dynamic rupture behavior in alternative models.

Alternative models with homogeneous D_{RS} on the entire fault

We present two models with homogeneous D_{RS}=0.025 m in Figure B.24, and D_{RS}=0.125 m in Figure B.26 (models E1 and E2 respectively). The first homogeneous D_{RS} model results in sustained bilaterally rupturing supershear propagation, which effectively activates the southeastern fault branches. The second model with larger D_{RS} results in bilateral subshear propagation, which fails to trigger the southeastern fault branches. The initial stress and the ratio between the proximity to failure and the stress drop (i.e., the S parameter) is the same for both of these alternative models. While rupture jumping is facilitated by proximity to failure (e.g., Harris and Day[18]), this suggests that here the fracture energy conditions under which sustained supershear rupture can form, as well as the supershear propagation itself, effectively facilitate rupture jumping to the southeastern fault branches.

Alternative rupture scenarios: sensitivity to off-fault plastic cohesion

We present two alternative choices for the bulk plastic cohesion C_{off}. The first model (E3) has a lower value $C_{off} = 1 \times 10^{-4}\mu$ and is shown in Figure B.29. This model results in a significantly increased accumulated plastic strain compared to the preferred model. Additionally, this model fails to activate the southernmost fault segment. The second model (E4), with a larger value $C_{off} = 5 \times 10^{-4}\mu$, features significantly reduced off-fault plasticity (Figure B.31). In this second case, dynamic rupture propagates across all fault segments.

The energy dissipated in the damage zone can become a significant fraction of the total fracture energy[2,13,39], which can, in turn, affect the dynamics of rupture propagation. These models illustrate the sensitive balance of sustained multi-fault rupture and off-fault deformation patterns to strongly or weakly deforming bulk material.

B.10 Comparison of model synthetics against high-rate GNSS displacements

We use the available near-fault time series from high-rate GNSS receivers[7], and compare the performance of our preferred model, as well as a model featuring subshear propagation (using the configuration of model D2 featuring a rotated pre-stress parameterization, Figure B.22 and Figure B.23), both now using a velocity aware mesh to resolve frequencies of 1Hz near the fault. Our results show that our preferred model on a velocity aware mesh generate a response of the displacement

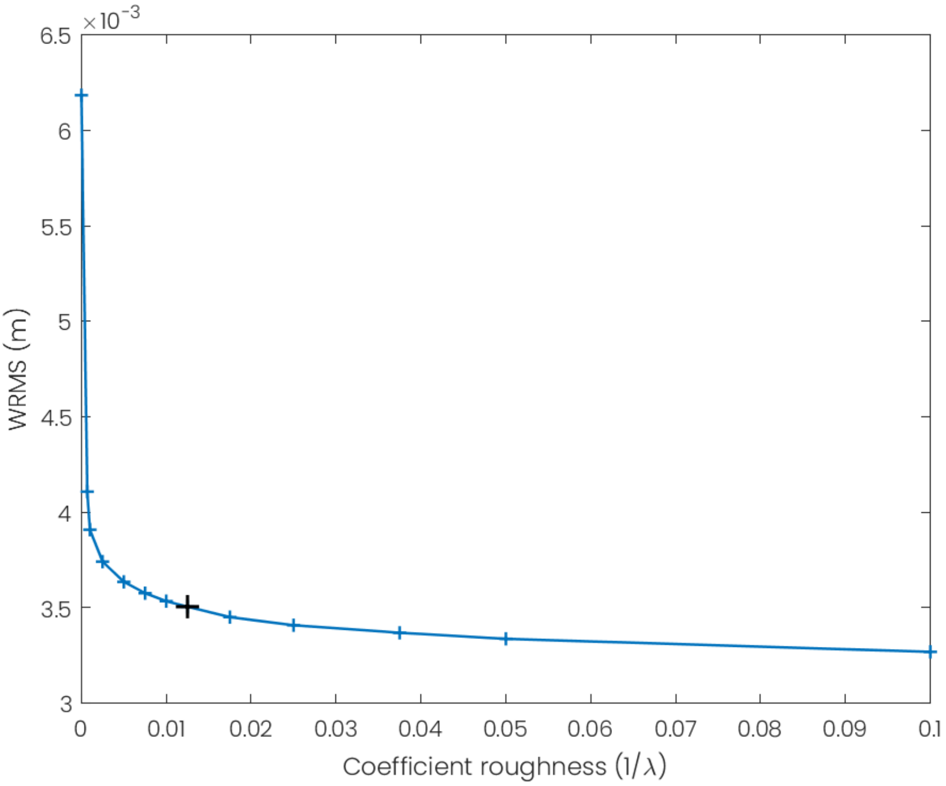

FIGURE B.1. Misfit between the geodetic data and the geodetic model predictions as a function of the roughness coefficient used in the joint inversion. The smaller the roughness coefficient, the smoother is the final slip distribution. We choose a roughness coefficient that reduces slip distribution roughness without significantly increasing the data misfit. The chosen roughness coefficient is indicated by the black cross.

wavefield at the receiver locations in better agreement with the observations than the subshear model, in terms of timing, shape, and amplitude across its components. In particular, the synthetics at stations on the East side of the Maduo fault system: QHAI, QHAJ and BUDR, show that the timing and pattern of the displacement time series for the supershear preferred model outperforms the subshear model. On the west side, the timing difference between both sets of synthetics and the observations are more comparable (e.g., QHMD, QHAH, QHZI and QHZH). Note as well that the supershear model amplitudes are comparable to the ones in the observations, while the synthetics of the second model are systematically lower in amplitude. This reinforces the unilateral supershear character of the Maduo earthquake.

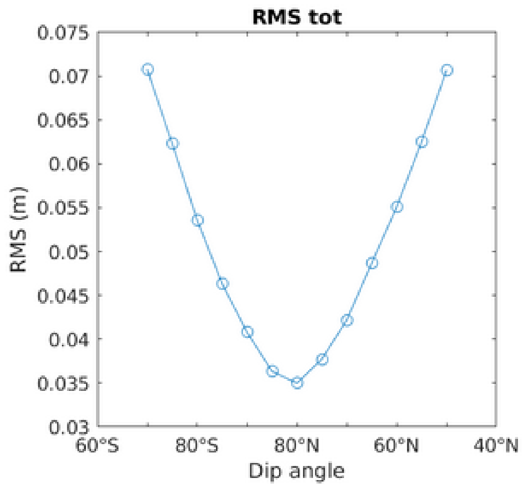

FIGURE B.2. Misfit between the geodetic data and the geodetic model predictions as a function of the dip angle assumed in the joint inversion (the same dip angle is assumed for all three segments). 13 values of dip angle are tested ranging from 70°S to 50°N. The results show that the geodetic data are best fit with a dip angle value in the range 80°N-85°N.

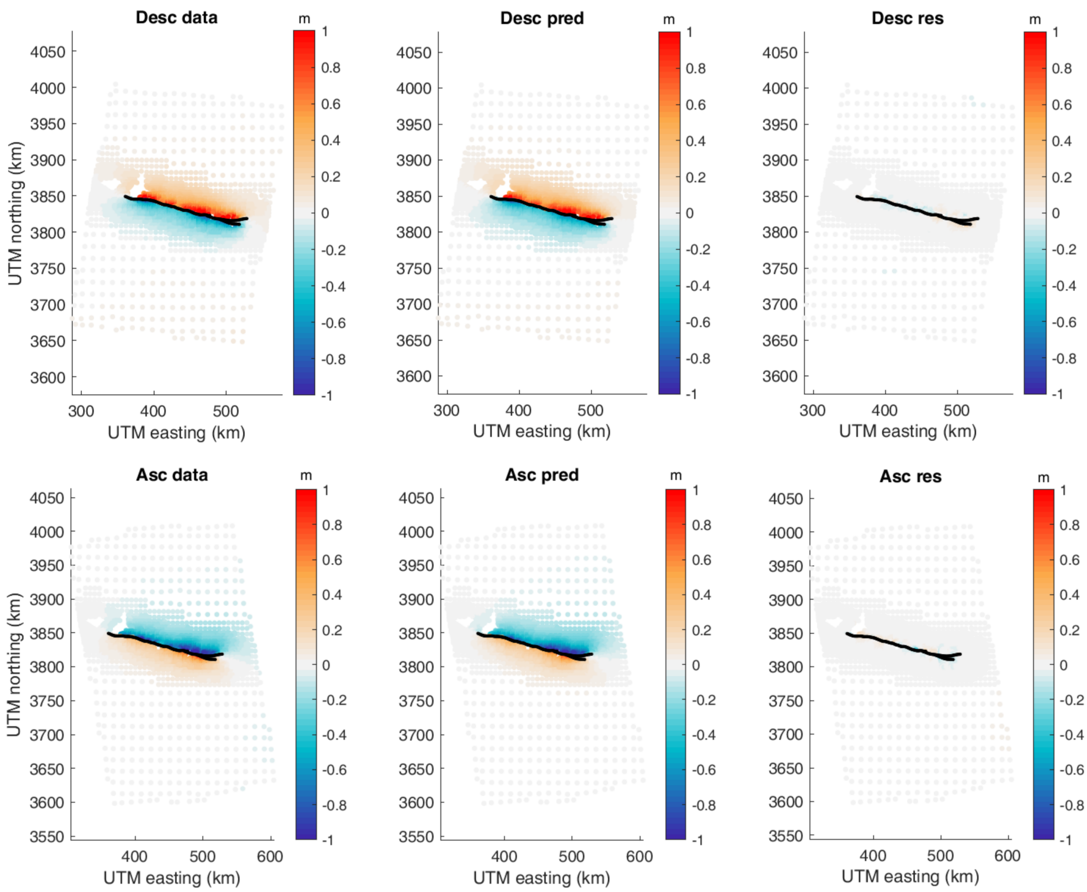

FIGURE B.3. Subsampled Sentinel-1 data, best-fit geodetic model predictions, and residuals for the descending (top) and ascending (bottom) interferograms. Black lines denote the modeled fault traces.

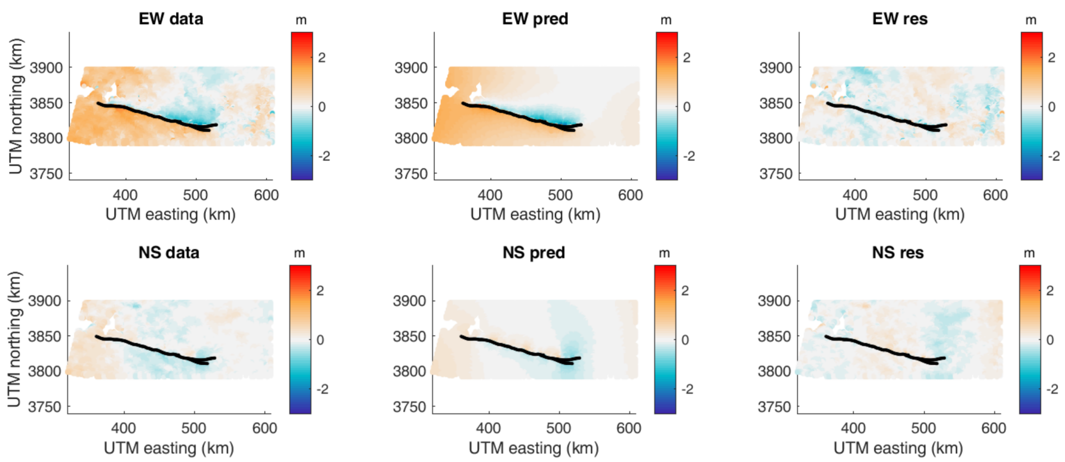

FIGURE B.4. Subsampled Sentinel-2 optical data, best-fit geodetic model predictions, and residuals for the EW (top) and NS (bottom) components of the surface displacements. Black lines denote the modeled fault traces.

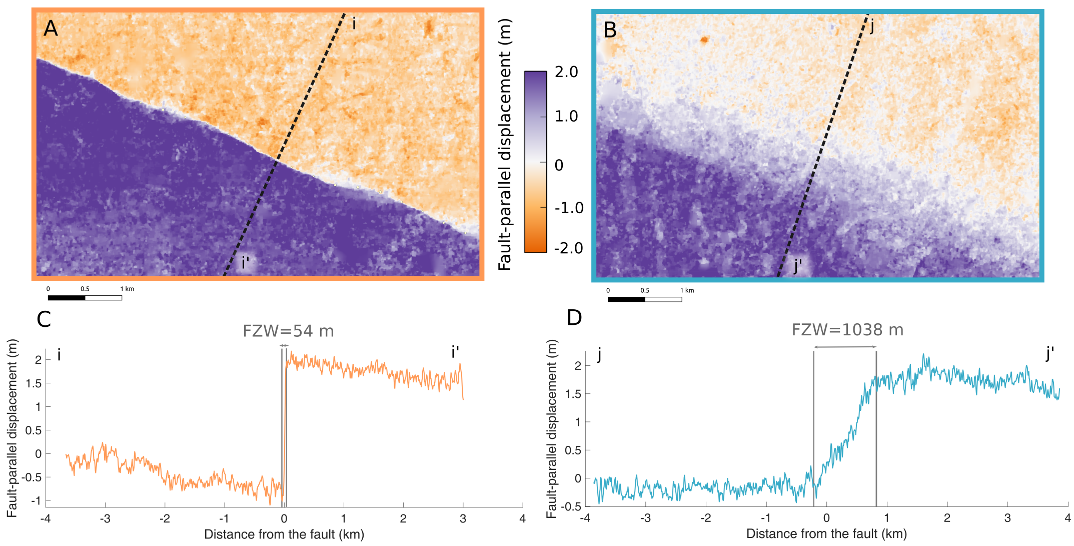

FIGURE B.5. Close-up views of the fault-parallel surface displacement field and fault perpendicular profiles where the deformation is dominantly (A,C) localized versus (B,D) distributed. Black dotted lines in Figures A and B indicate the location of the profiles shown in panels C and D, respectively. The width of the region in the vicinity of the fault accommodating the deformation (the Fault Zone Width, FZW) is indicated by two vertical gray lines in Figures C and D, and the inferred value of the FZW is indicated on top. The location of the close-up views is indicated in Figure 1 of the main text.

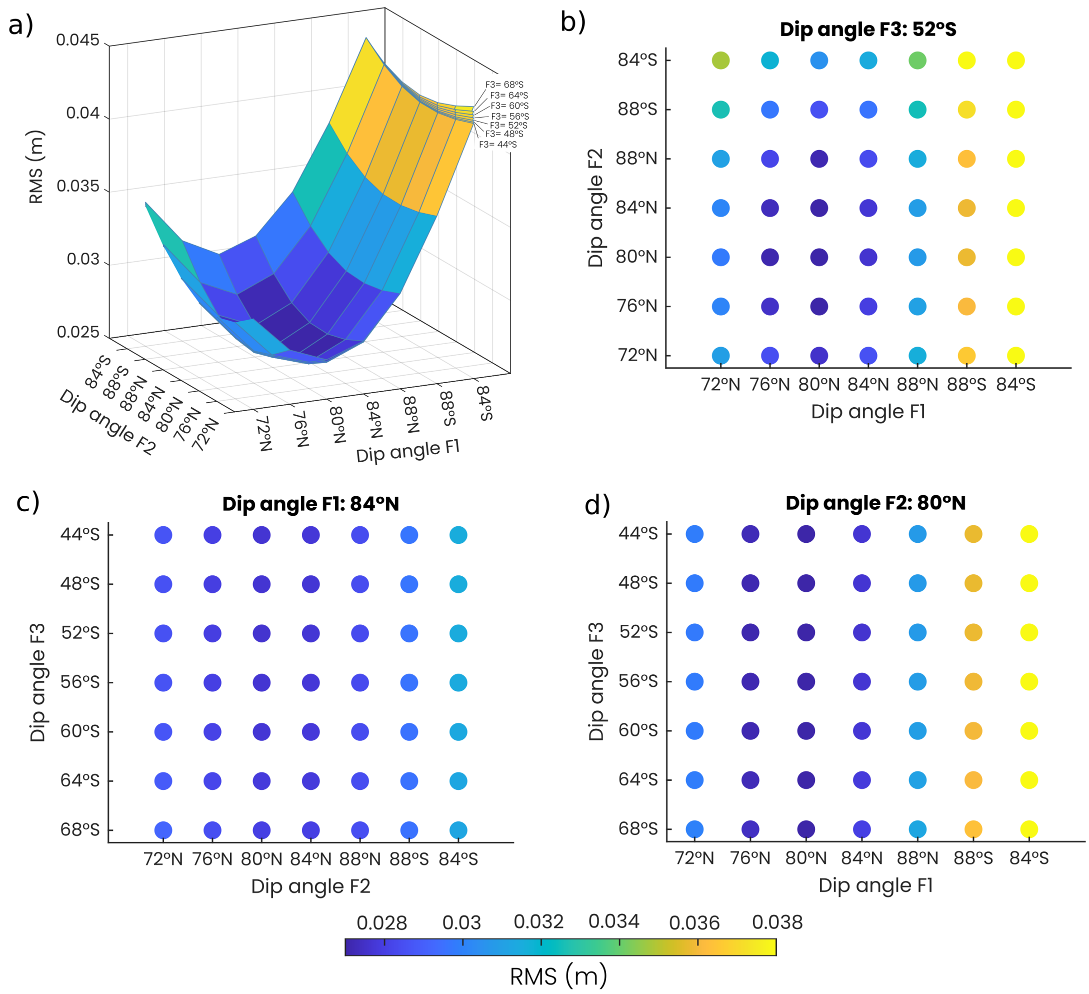

FIGURE B.6. Result of the systematic exploration of dip-angle combinations. (a) RMS misfit (between observation and model prediction) for the 343 inversions. Each surface plot represents the RMS misfit as a function of the dip angles of F1 and F2 for a given F3 dip angle. The different surface plots, plotted on top of each other, are not well discernible because varying the dip angle of F3 does not impact significantly the RMS. The best dip angle for F1, F2, and F3 are 84°N, 80°N, and 52°S, respectively. (b) RMS misfit as a function of F1 and F2 dip angles when F3 dip angle=52°S. (c) RMS misfit as a function of F2 and F3 dip angles when F1 dip angle=84°N. (d) RMS misfit as a function of F1 and F3 dip angles when F2 dip angle=80°N.

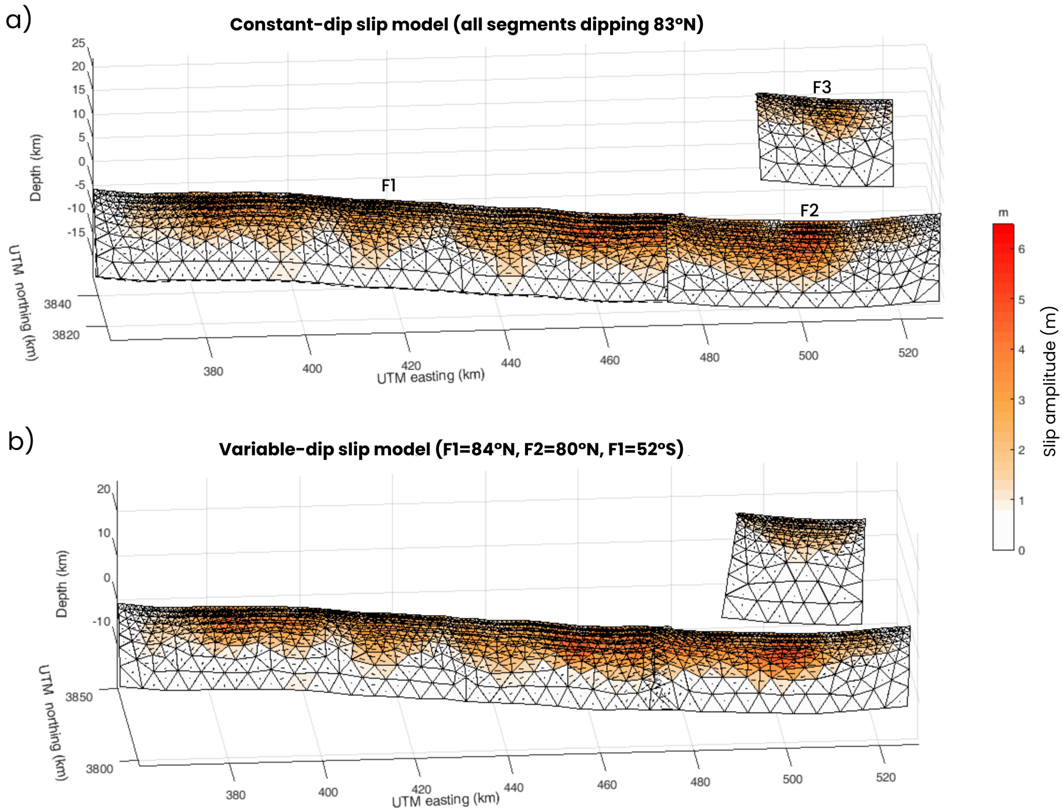

FIGURE B.7. Comparison of (a) the constant-dip-angle geodetic slip model (also shown in Figure 1) with (b) the variable-dip-angle slip model inferred from the systematic exploration of dip-angle combinations. The slip amplitude and distribution are not significantly impacted by the differences in fault geometry.

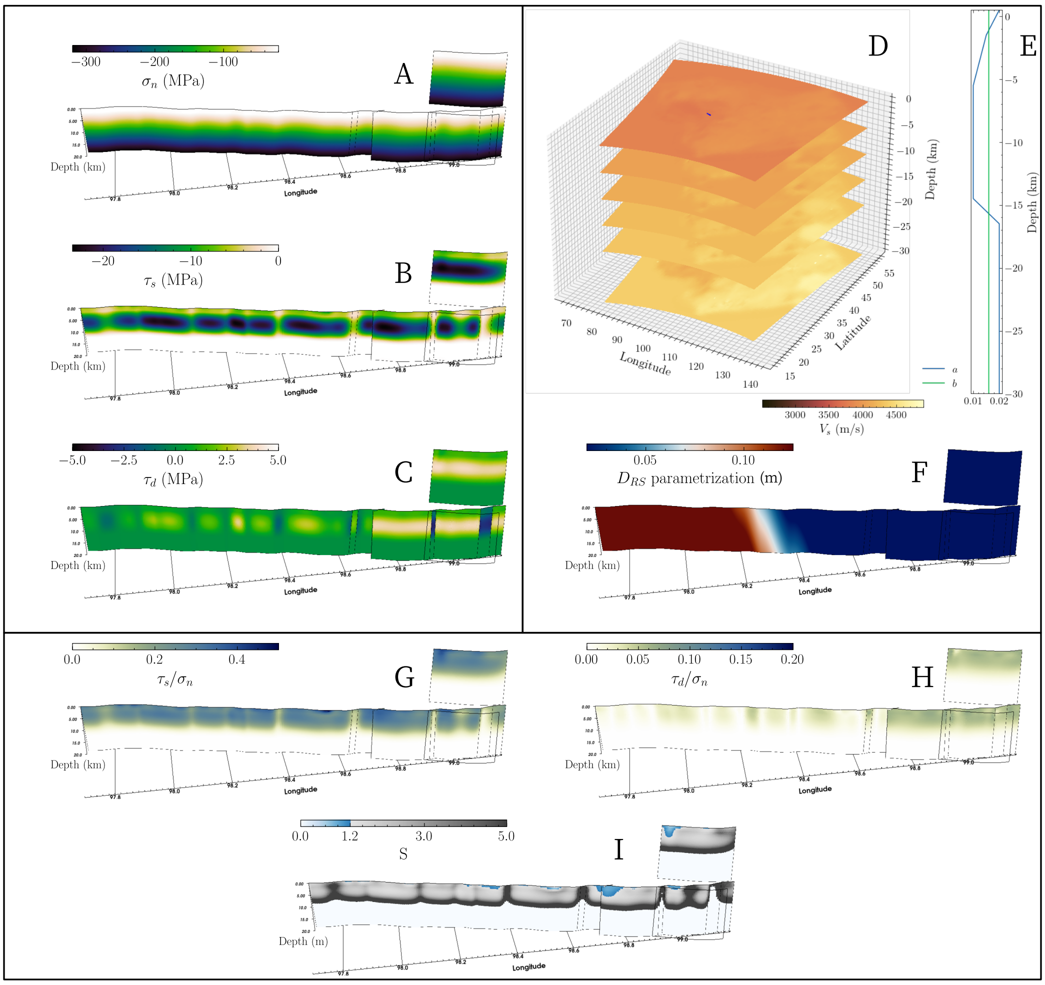

FIGURE B.8. Initial conditions of the preferred 3D dynamic rupture model. Here, we show the initial stress components acting on-fault, combining the geodetically inferred stress heterogeneity and the ambient regional stresses (Table B.1). (A) initial shear stress along-strike, (B) initial shear stress along-dip, (C) initial normal stress. (D) Cross-sections of the 3D velocity structure above a depth of 30 km [51] with the fault system marked in blue. (E) Depth-dependent fast-velocity weakening rate-and-state frictional parameters a (blue) and b (green). (F) along-strike variable D_{RS}, linearly increasing with horizontal distance from the epicenter to the North. The range of D_{RS} is given in Table B.1. (G) ratio of initial along-strike shear stress to normal stress. (H) ratio of initial along-dip shear stress to normal stress. (I) the S ratio parameter that characterizes the relative fault strength governing dynamic rupture propagation and arrest by balancing fracture energy and strain energy release.

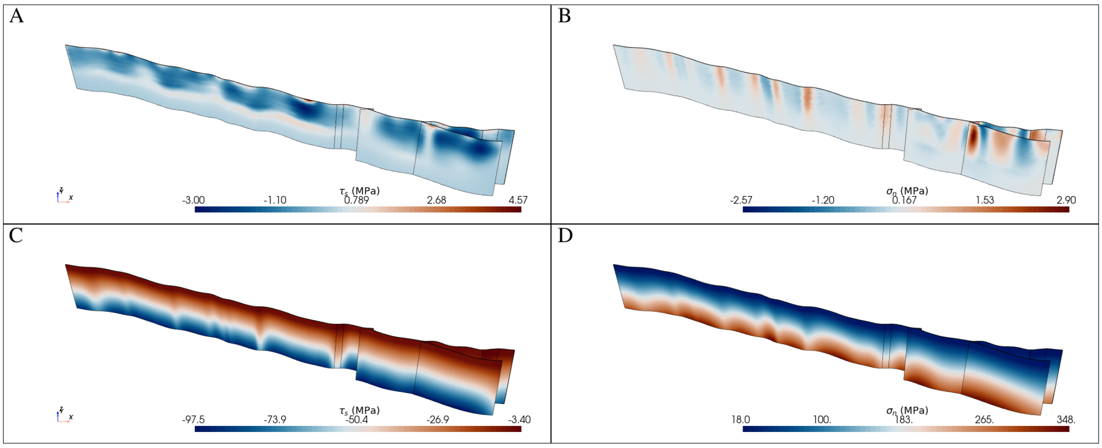

Figure B.9. Geodetically-derived heterogeneous stresses and ambient tectonic stresses. (A) and (B) show the strike component of the shear stress change and the normal stress heterogeneities included in the dynamic rupture model, respectively. These stress heterogeneities are downscaled by a factor of 0.3 relative to the stress changes inferred from our geodetic slip model. The stress change distribution is already scaled by a factor of 0.3. (C) and (D) show the strike component of the ambient regional shear stress and the normal stress, respectively.

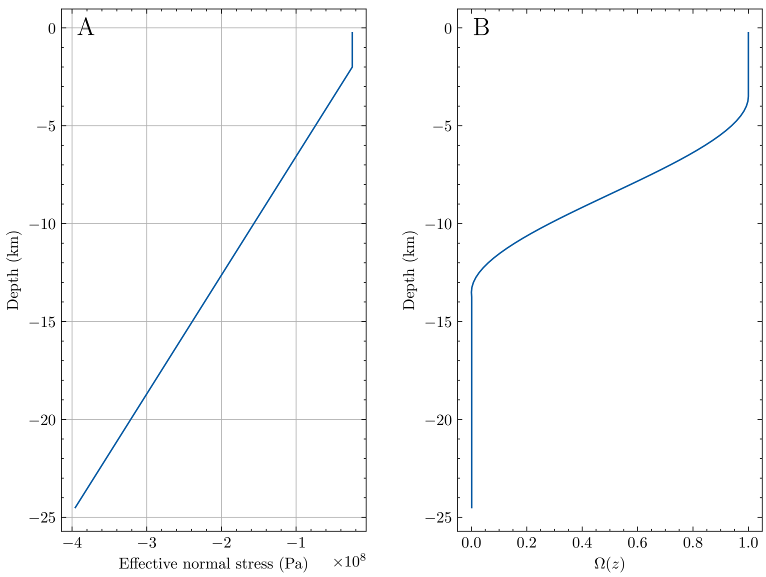

Figure B.10. (A) Depth-dependence of the effective confining stress $\sigma_c = (1 - \gamma)\sigma_z$. (B) Depth-dependent stress modulation function Ω_z.

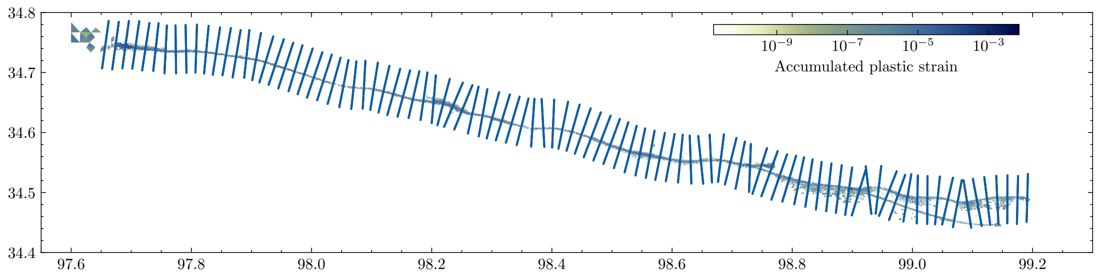

FIGURE B.11. Fault-perpendicular surface transects sampling the off-fault plasticity field to the nearest cell-center values on the modeled surface of the preferred model.

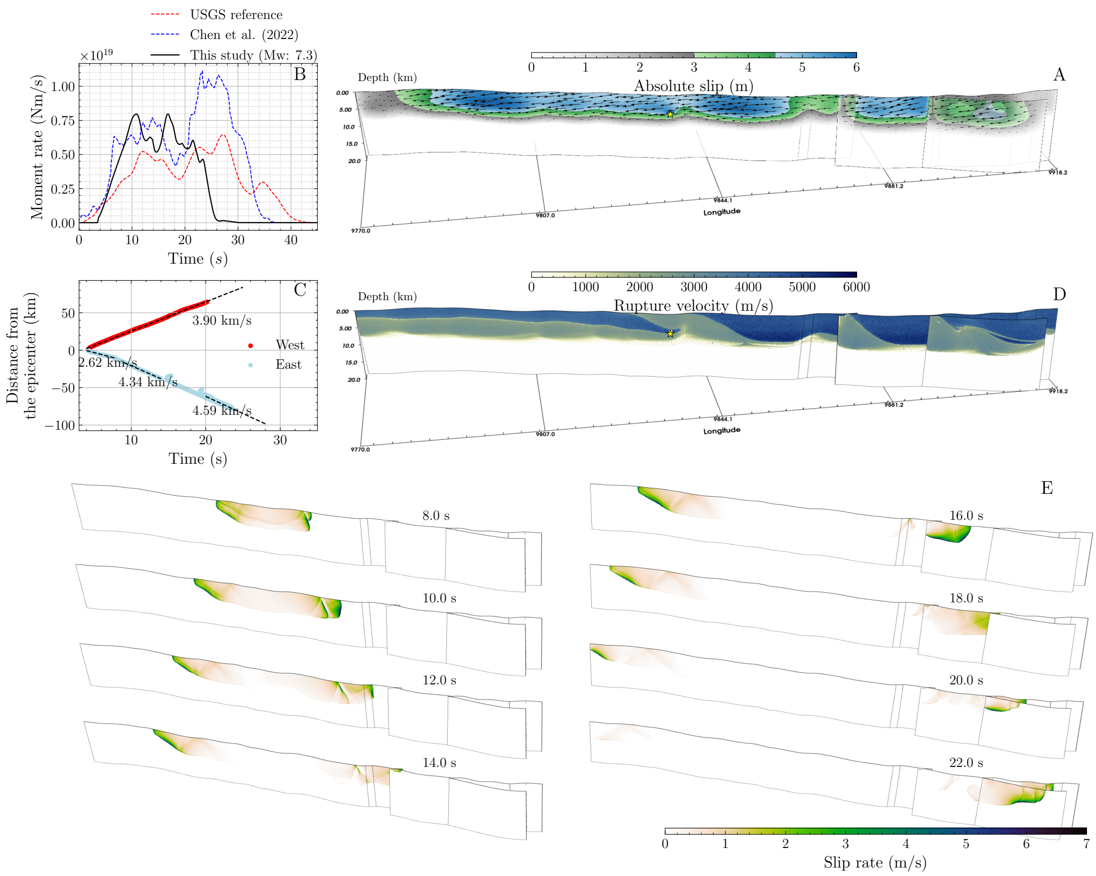

FIGURE B.12. Same as main text Figure 3.2 but for the alternative dynamic rupture model A1, with kinematically stress heterogeneities removed.

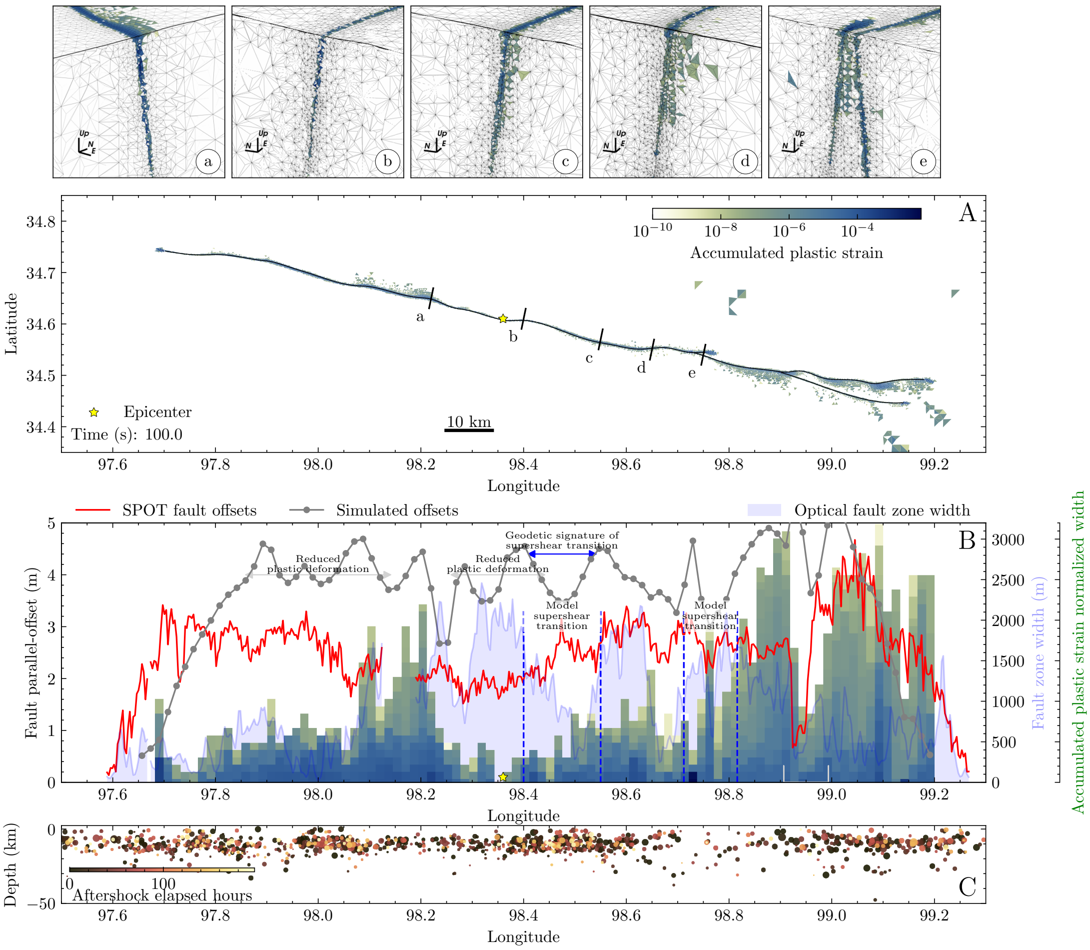

FIGURE B.13. Same as main text Figure 3.3 but for the alternative dynamic rupture model A1, with kinematically stress heterogeneities removed.

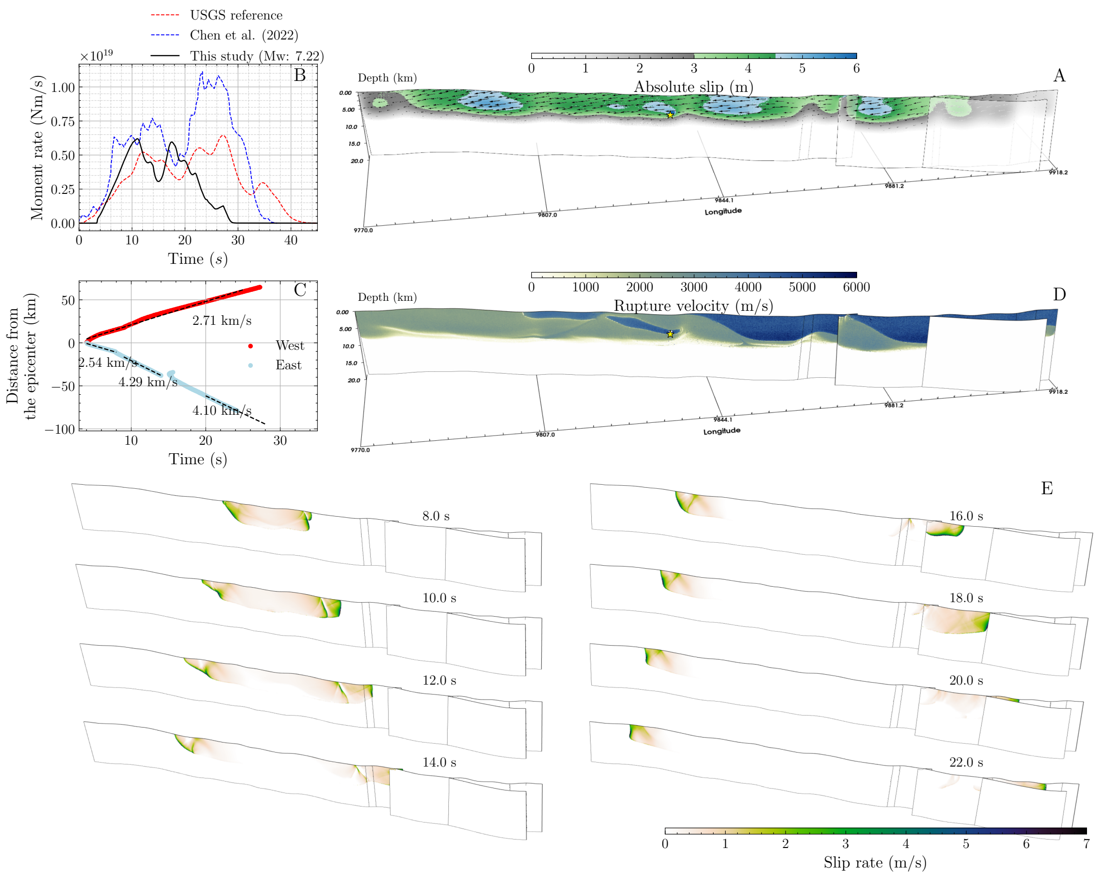

FIGURE B.14. Same as main text Figure 3.2 but for the alternative dynamic rupture model B1, with thicker shallow velocity strengthening layer.

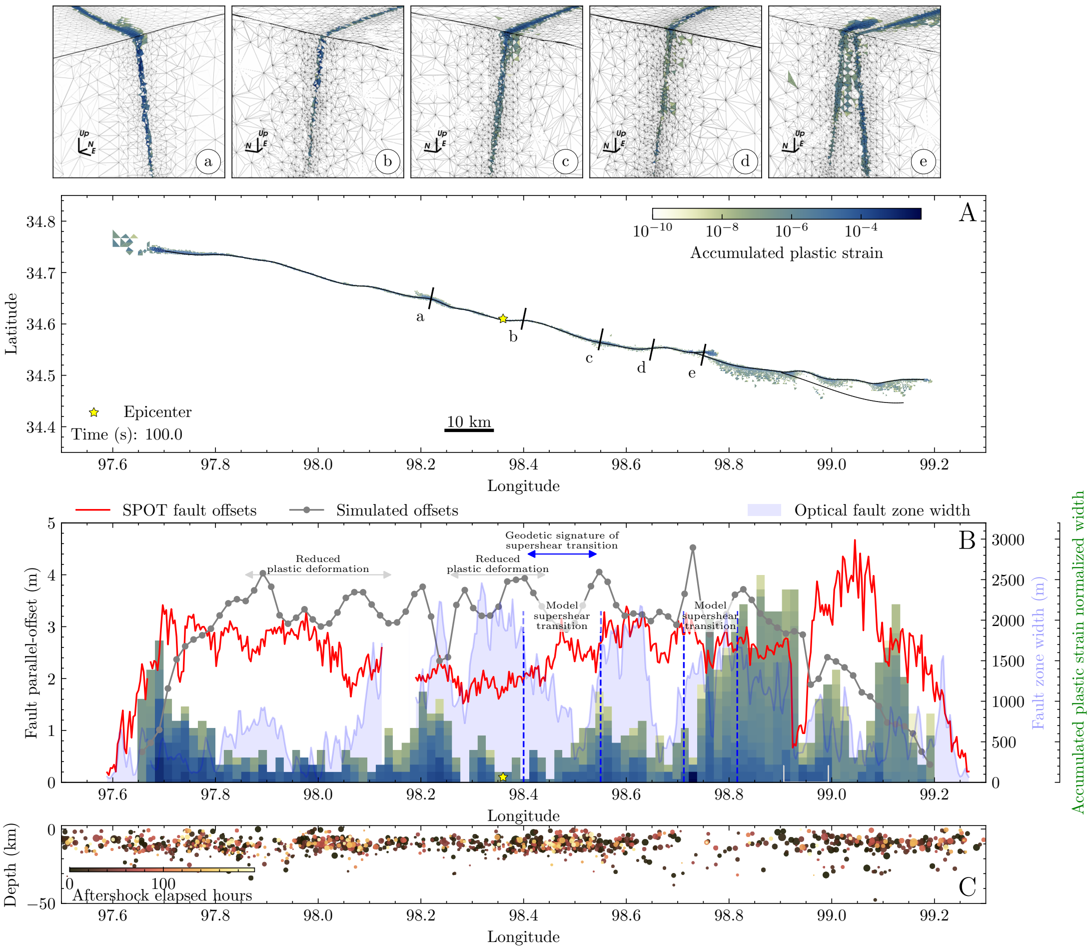

FIGURE B.15. Same as main text Figure 3.3 but for the alternative dynamic rupture model B1, with thicker shallow velocity strengthening layer.

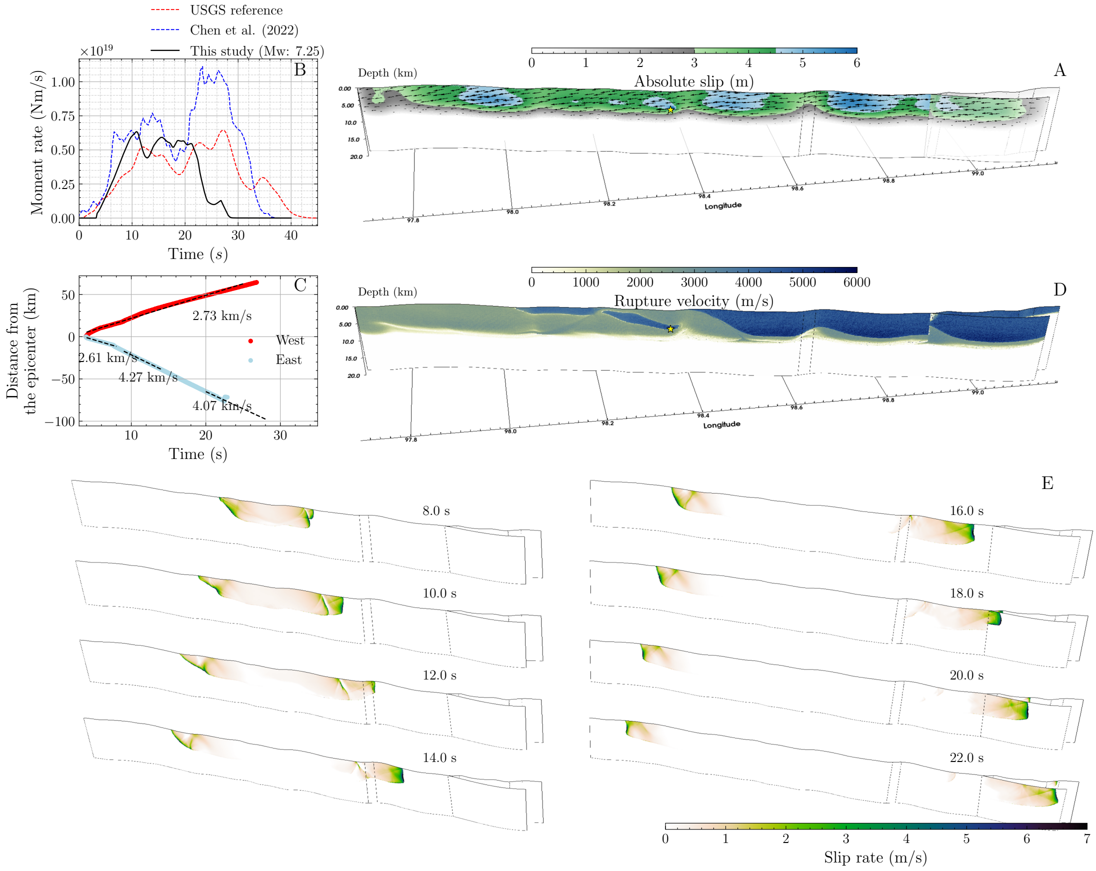

FIGURE B.16. Same as main text Figure 3.2 but for the alternative dynamic rupture model C1 in which the fault segments are all dipping northwards with 83°. The segments F1 and F2 of the preferred model are meshed continuously here, and thus, this model is composed of only two fault segments. The model uses the same parameter specifications as the preferred model.

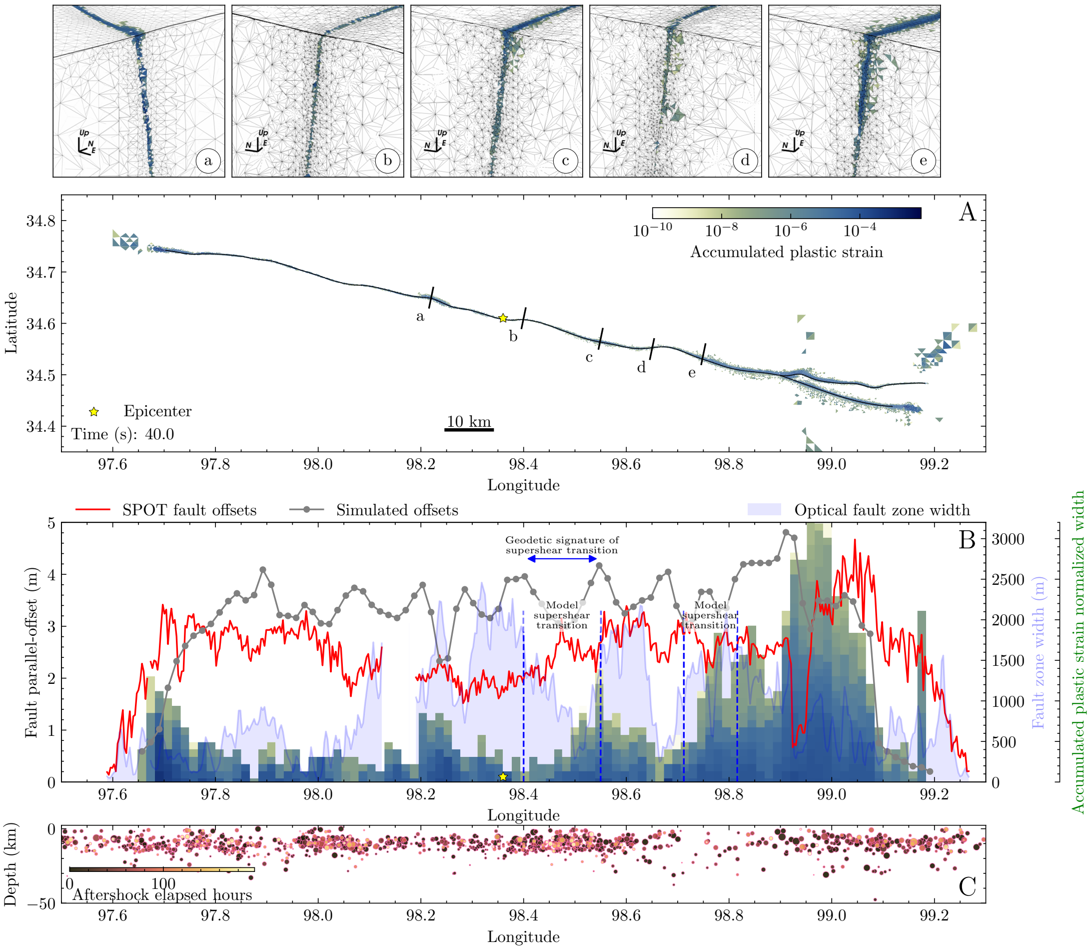

FIGURE B.17. Same as main text Figure 3.3 but for the alternative dynamic rupture model C1 in which the fault segments are all dipping northwards with 83°. The segments F1 and F2 of the preferred model are meshed continuously here, and thus, this model is composed of only two fault segments. The model uses the same parameter specifications as the preferred model.

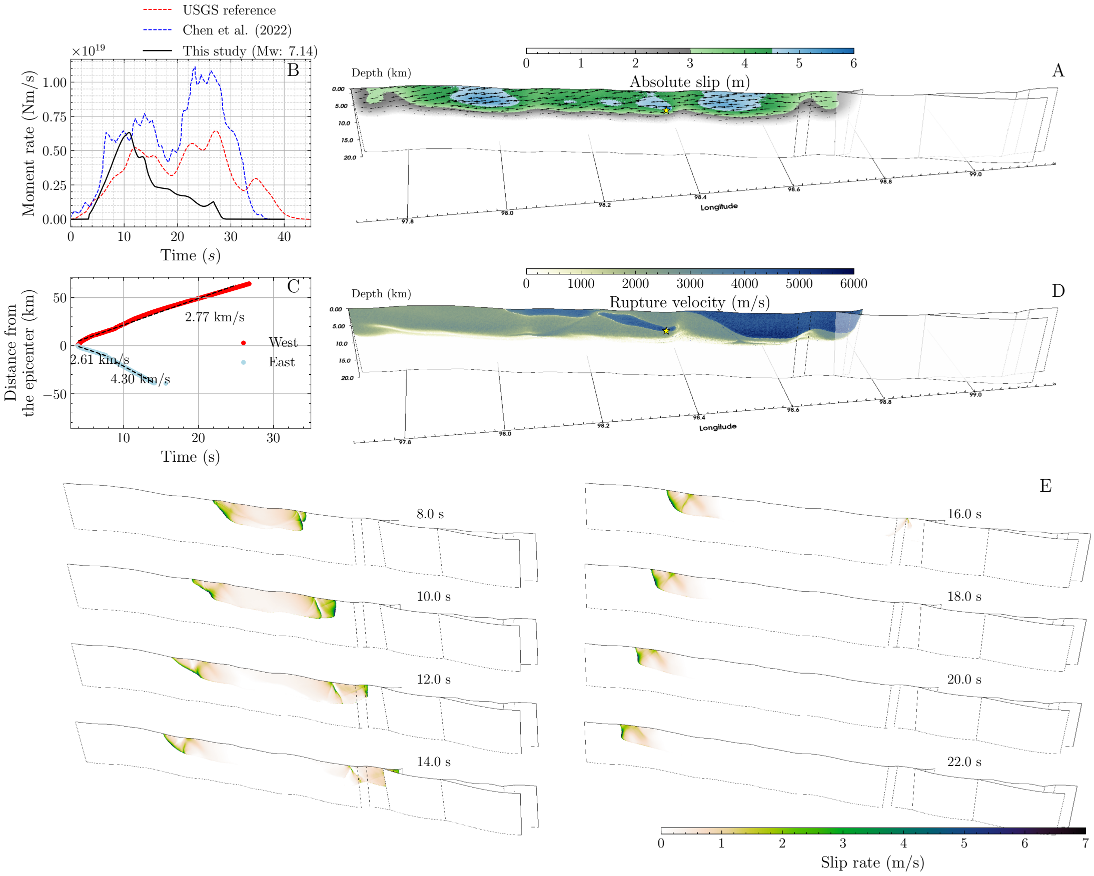

FIGURE B.18. Same as main text Figure 3.2 but for the alternative dynamic rupture model C2 in which the fault segments are all dipping northwards with 83°. The fault system is composed of three fault segments. All other parameters are the same as in the preferred model.

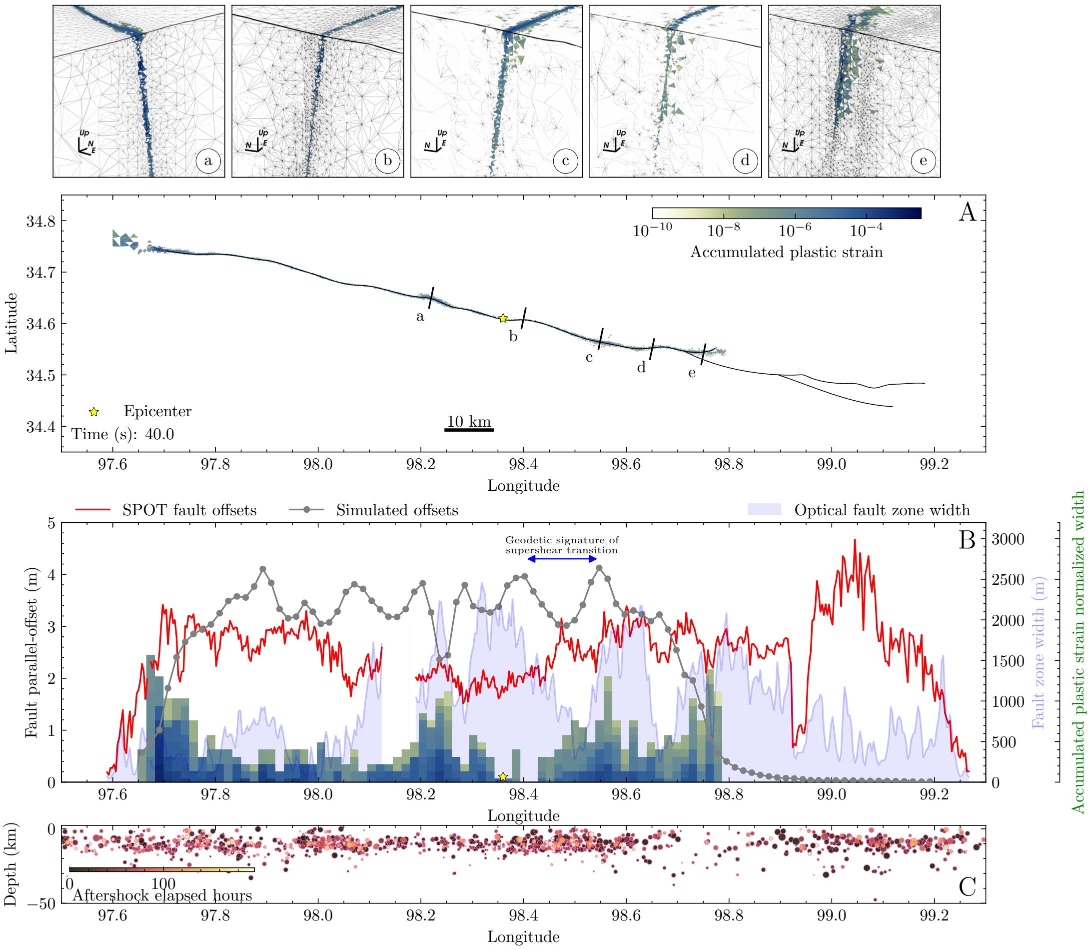

FIGURE B.19. Same as main text Figure 3.3 but for the alternative dynamic rupture model C2 in which the fault segments are all dipping northwards with 83°. The fault system is composed of three fault segments. All other parameters are the same as in the preferred model.

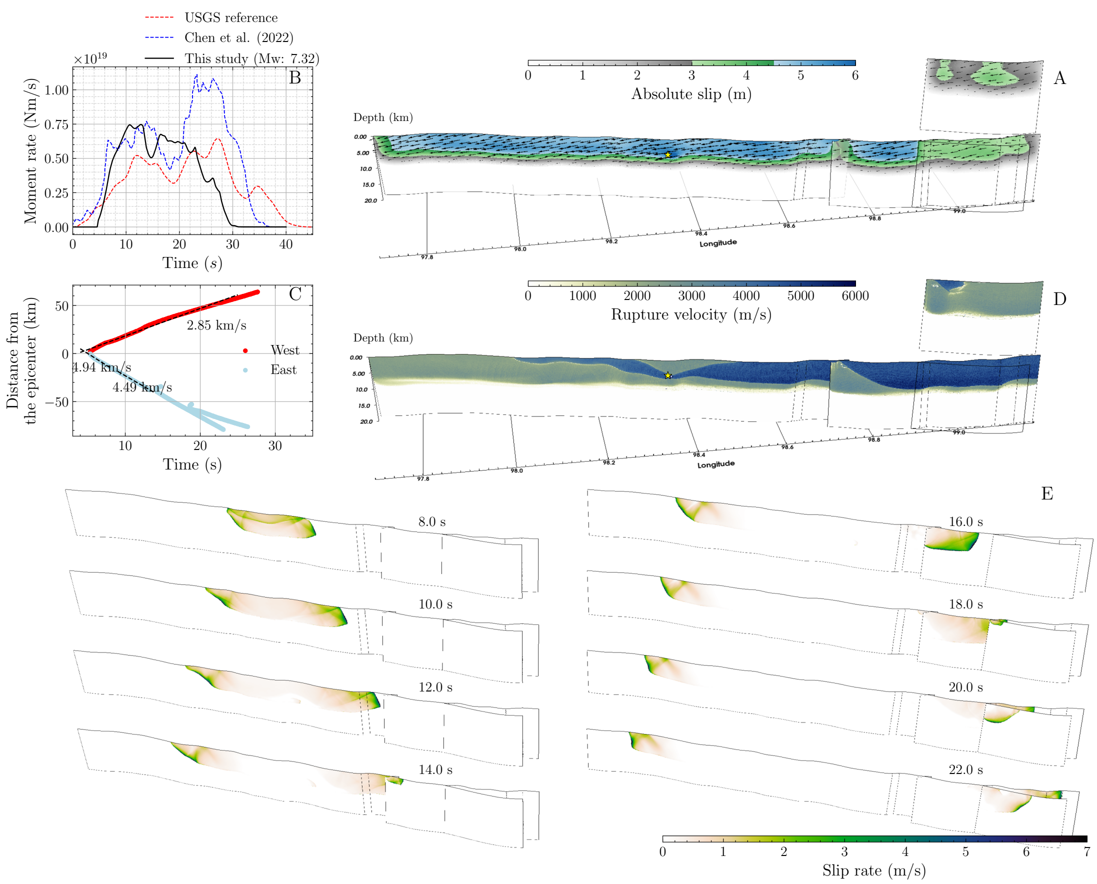

FIGURE B.20. Same as main text Figure 3.2 but for the alternative dynamic rupture model D1 with different ambient pre-stress, resulting in a 100° strike angle of an optimally oriented fault.

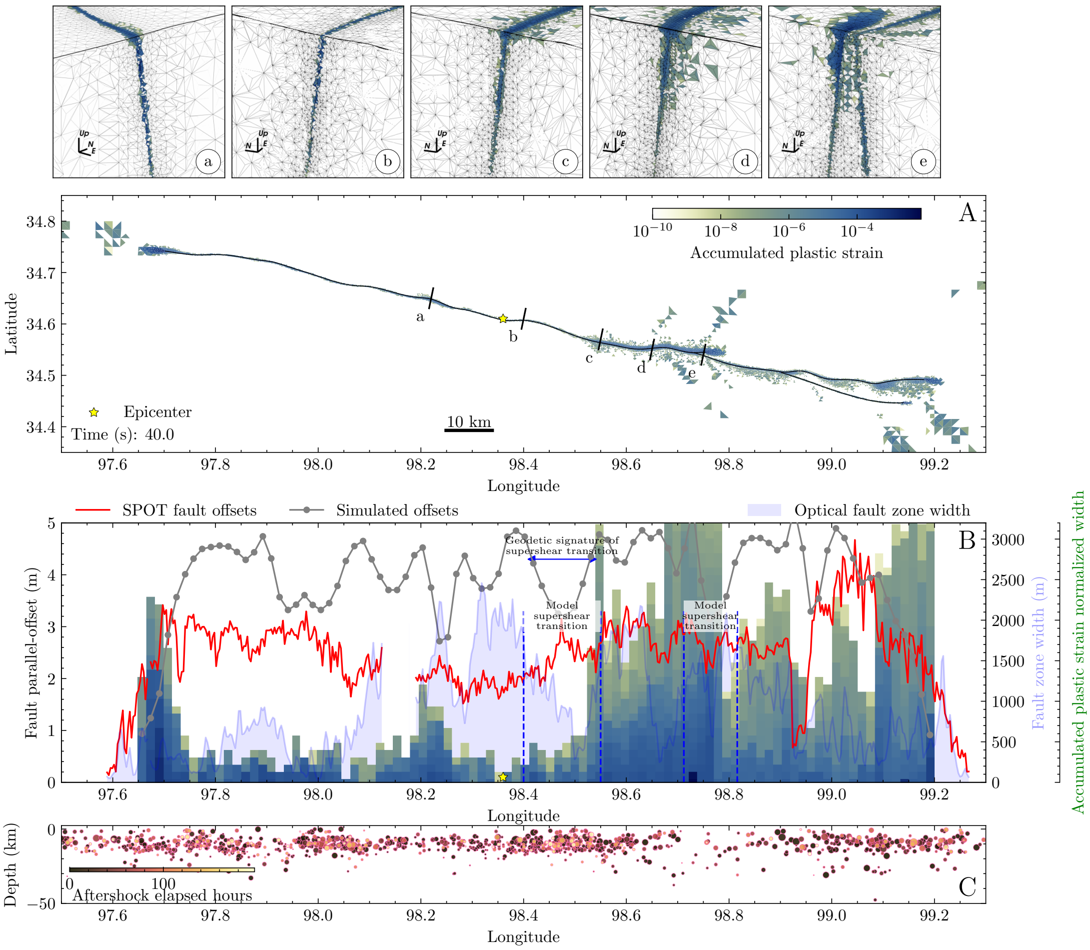

FIGURE B.21. Same as main text Figure 3.3 but for the alternative dynamic rupture model D1, with different ambient pre-stress, resulting in a 100° strike angle of an optimally oriented fault.

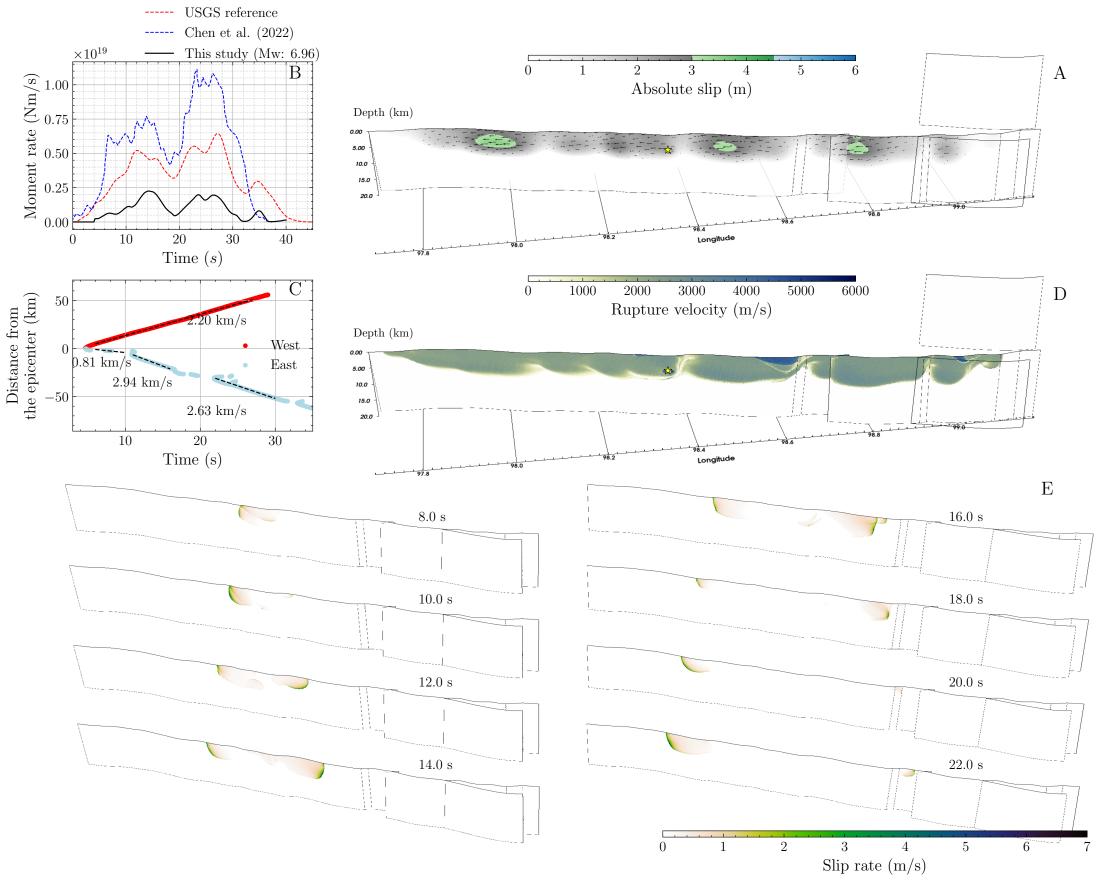

FIGURE B.22. Same as main text Figure 3.2 but for the alternative dynamic rupture model D2, with different ambient pre-stress, resulting in a $120°$ strike angle of an optimally oriented fault.

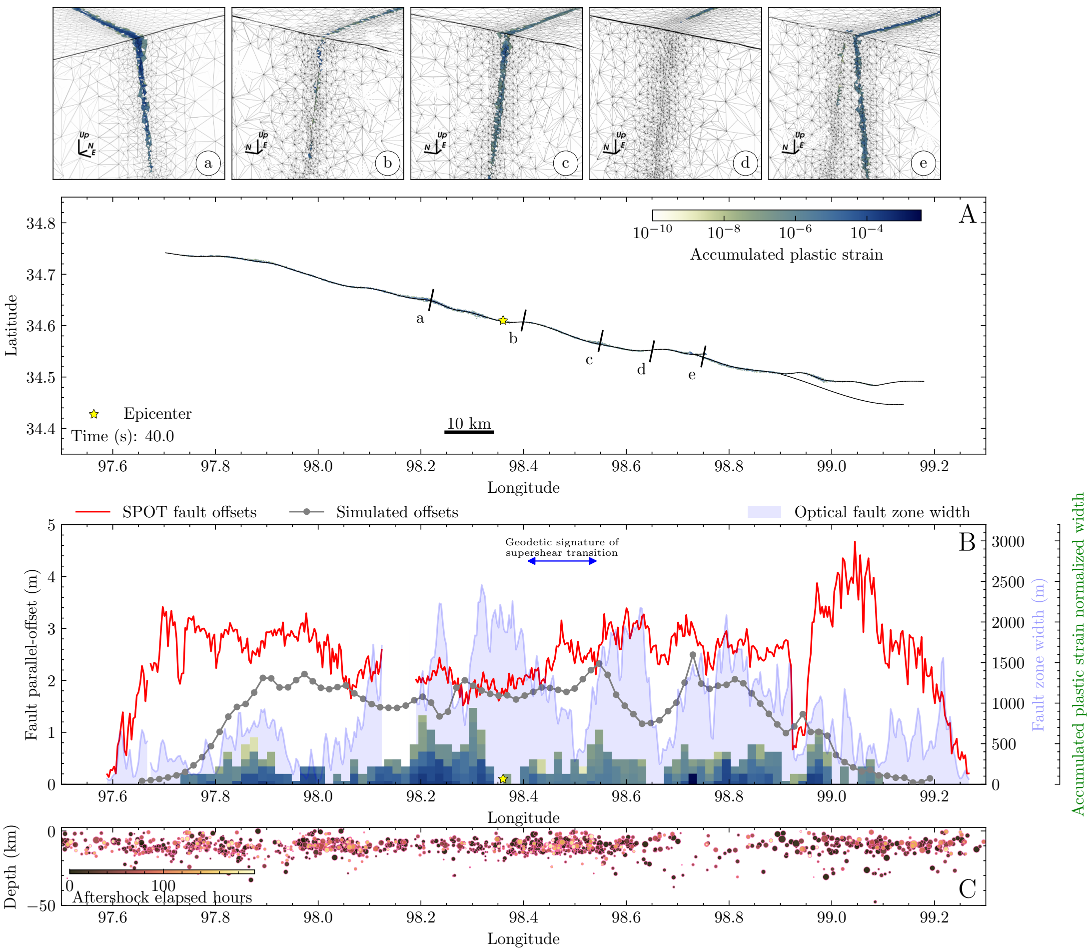

FIGURE B.23. Same as main text Figure 3.3 but for the alternative dynamic rupture model D2, with different ambient pre-stress, resulting in a $120°$ strike angle of an optimally oriented fault.

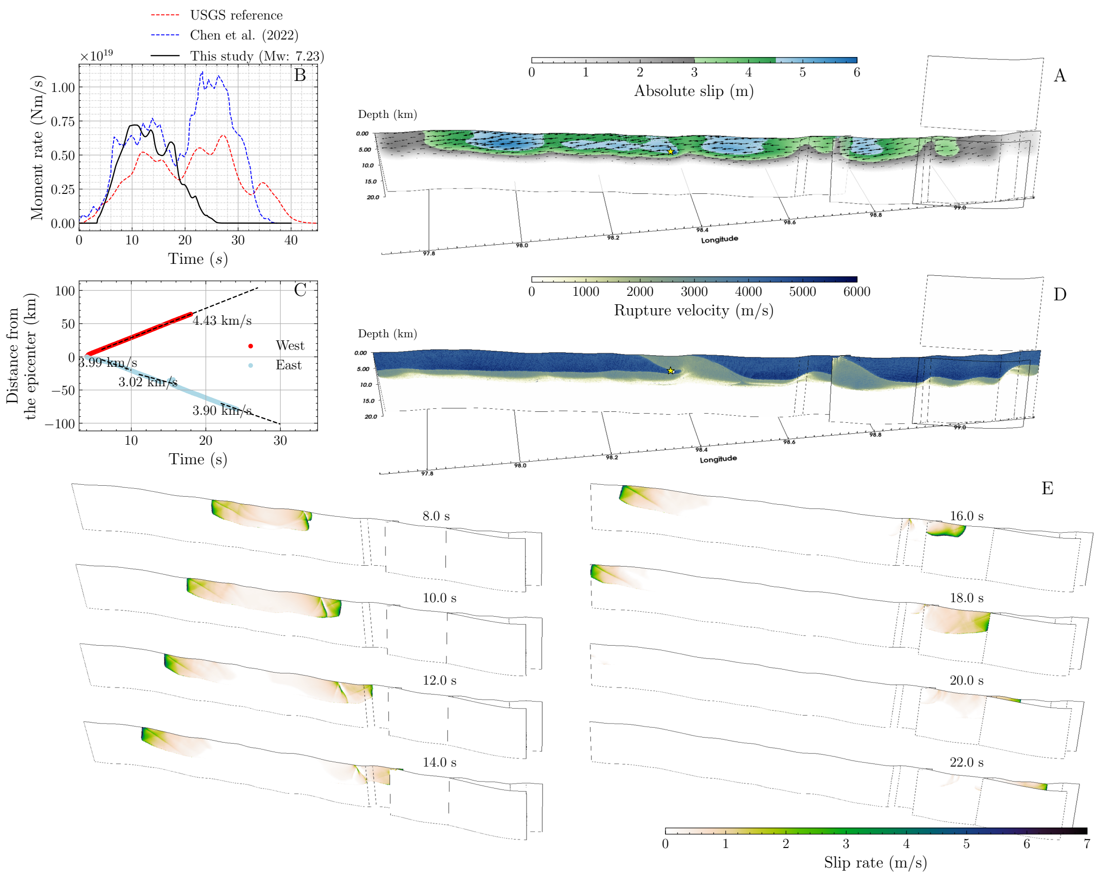

FIGURE B.24. Same as main text Figure 3.2 but for the alternative dynamic rupture model E1 with homogeneous D_{RS}=0.025.

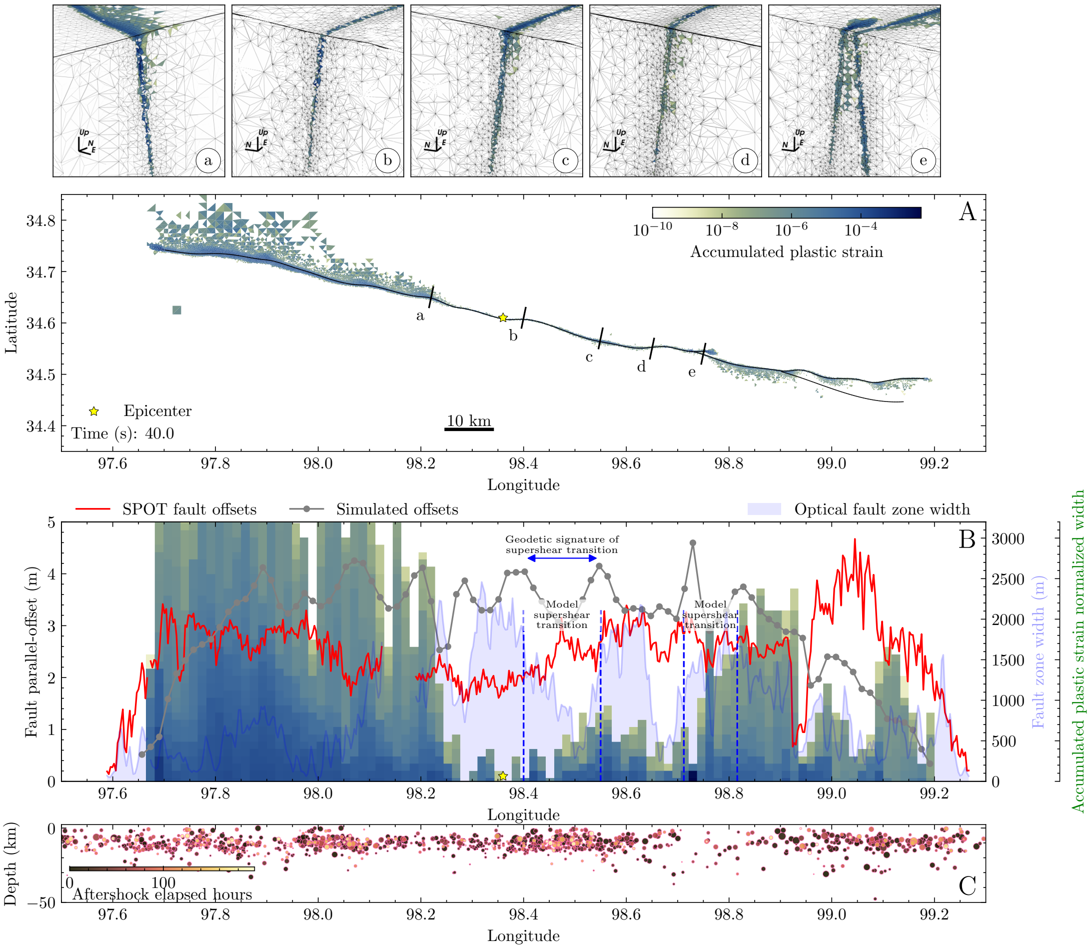

FIGURE B.25. Same as main text Figure 3.3 but for the alternative dynamic rupture model E1 with homogeneous D_{RS}=0.025.

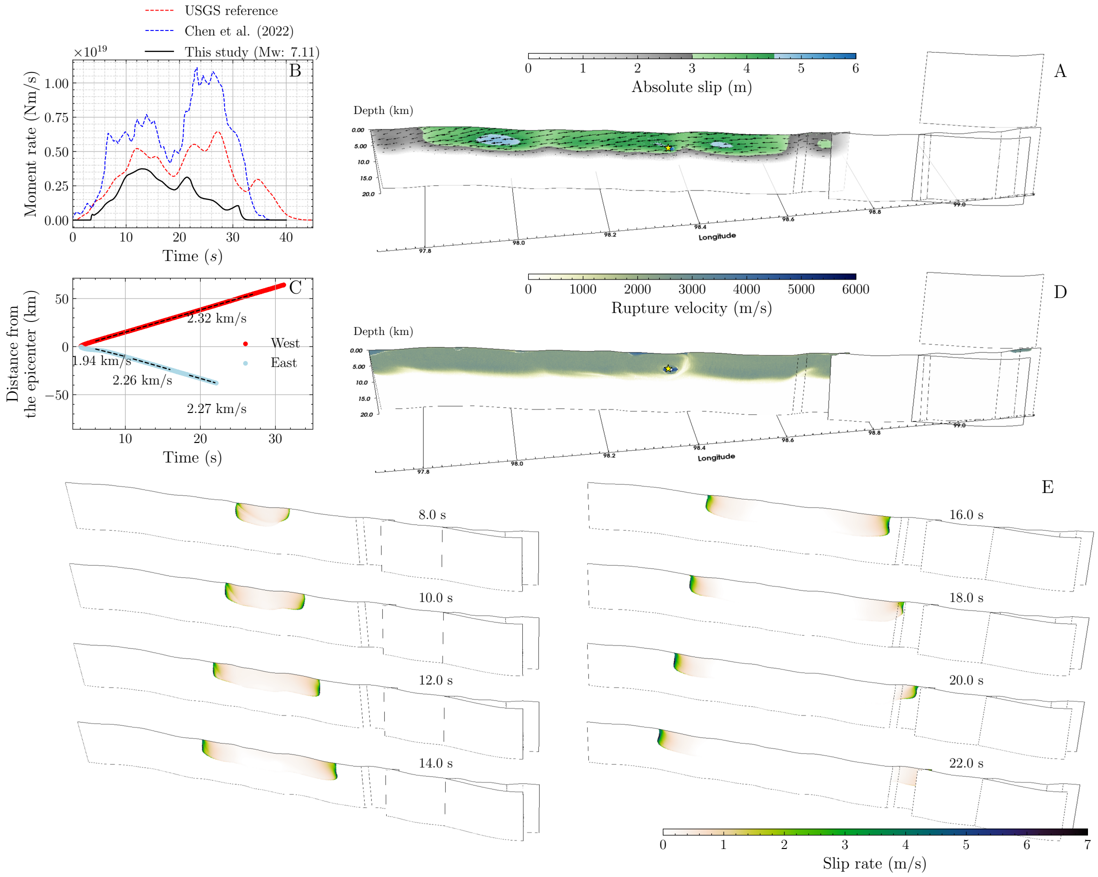

Figure B.26. Same as main text Figure 3.2 but for the alternative dynamic rupture E2 with homogeneous D_{RS}=0.125.

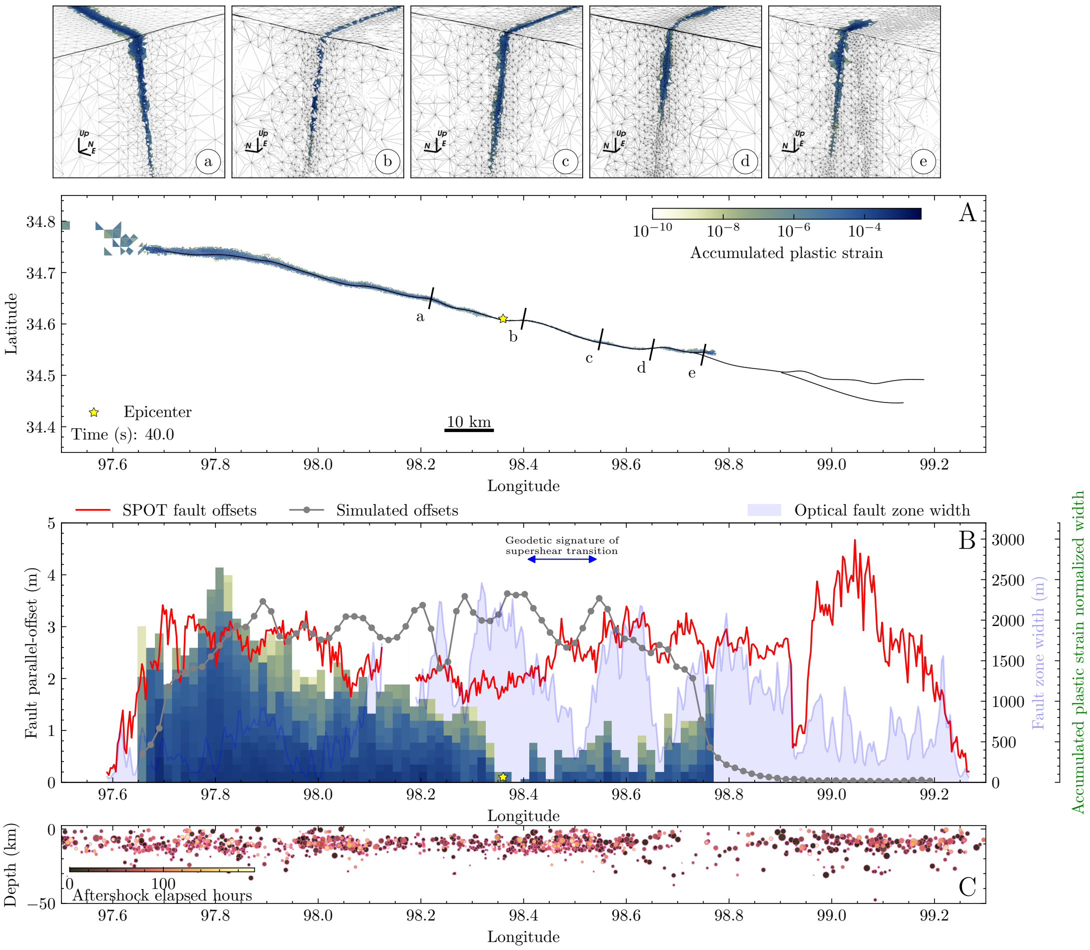

FIGURE B.27. Same as main text Figure 3.3 but for the alternative dynamic rupture but for model E2 with homogeneous D_{RS}=0.125.

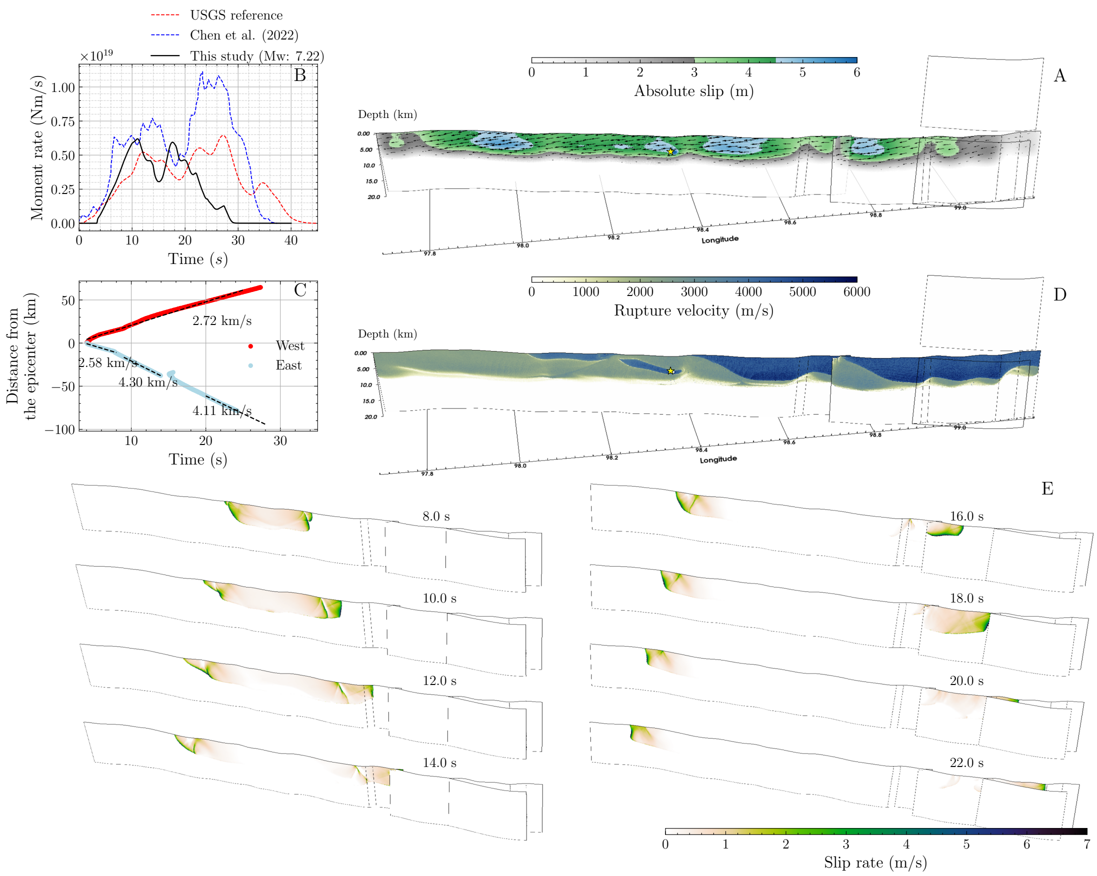

FIGURE B.28. Same as main text Figure 3.2 but for the alternative dynamic rupture model E3 with off-fault plastic cohesion $C_{off} = 1 \times 10^{-4}\mu$.

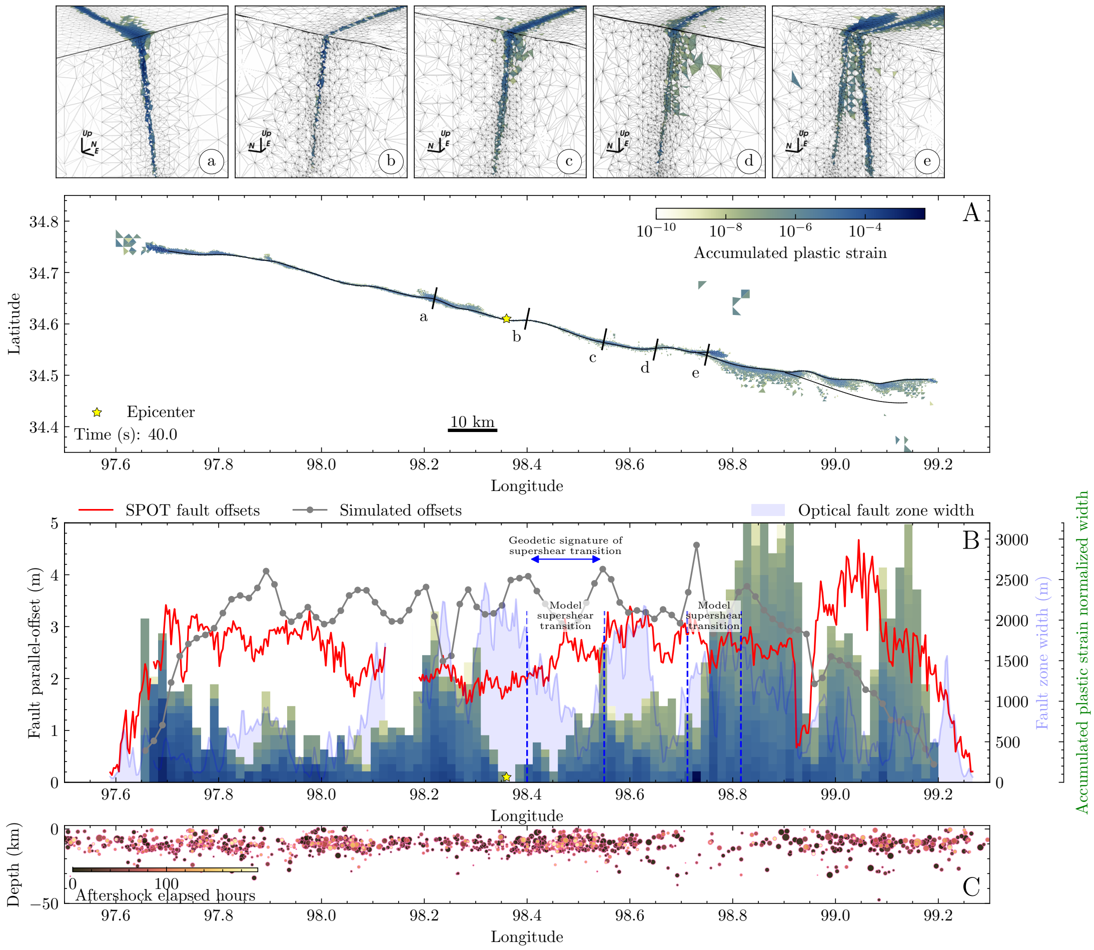

FIGURE B.29. Same as main text Figure 3.3 but for the alternative dynamic rupture model E3 with off-fault plastic cohesion $C_{off} = 1 \times 10^{-4}\mu$.

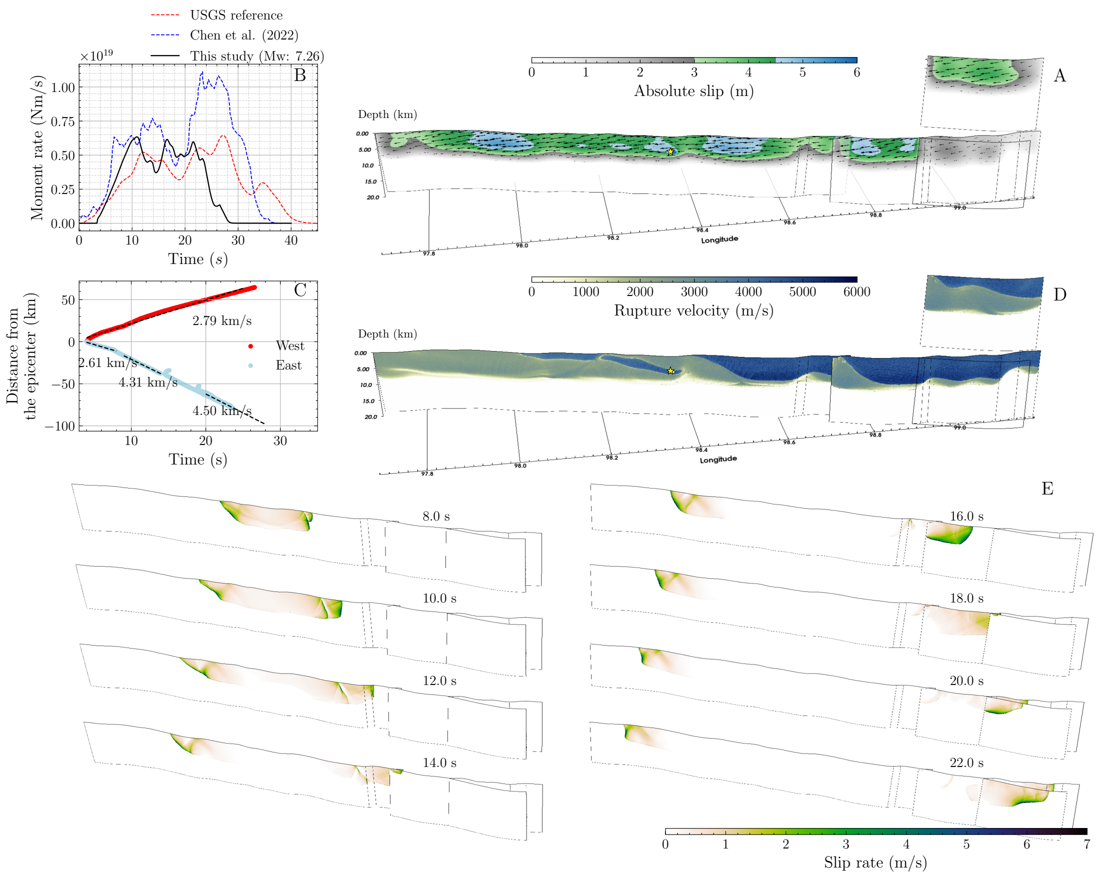

FIGURE B.30. Same as main text Figure 3.2 but for the alternative dynamic rupture model E4 with bulk plastic cohesion $C_{off} = 5 \times 10^{-4}\mu$.

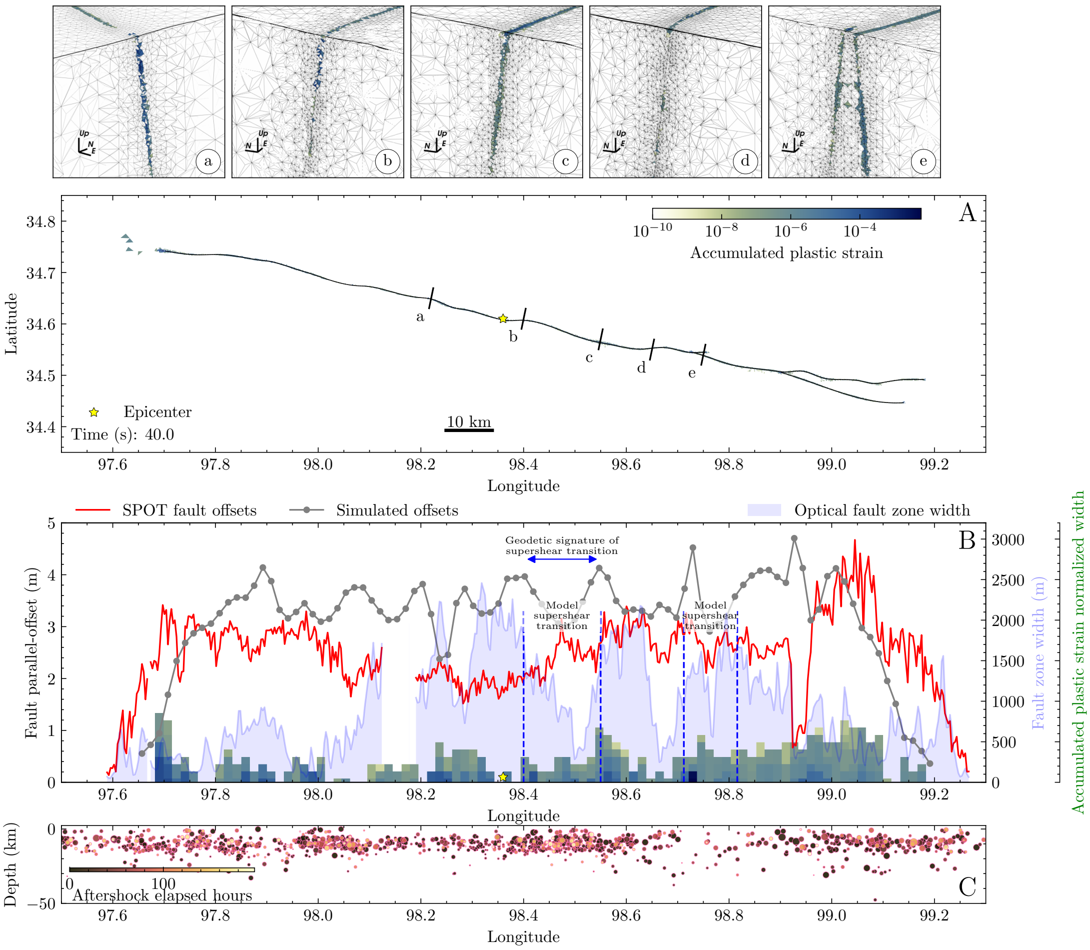

FIGURE B.31. Same as main text Figure 3.3 but for the alternative dynamic rupture model E4 with bulk plastic cohesion $C_{off} = 5 \times 10^{-4}\mu$.

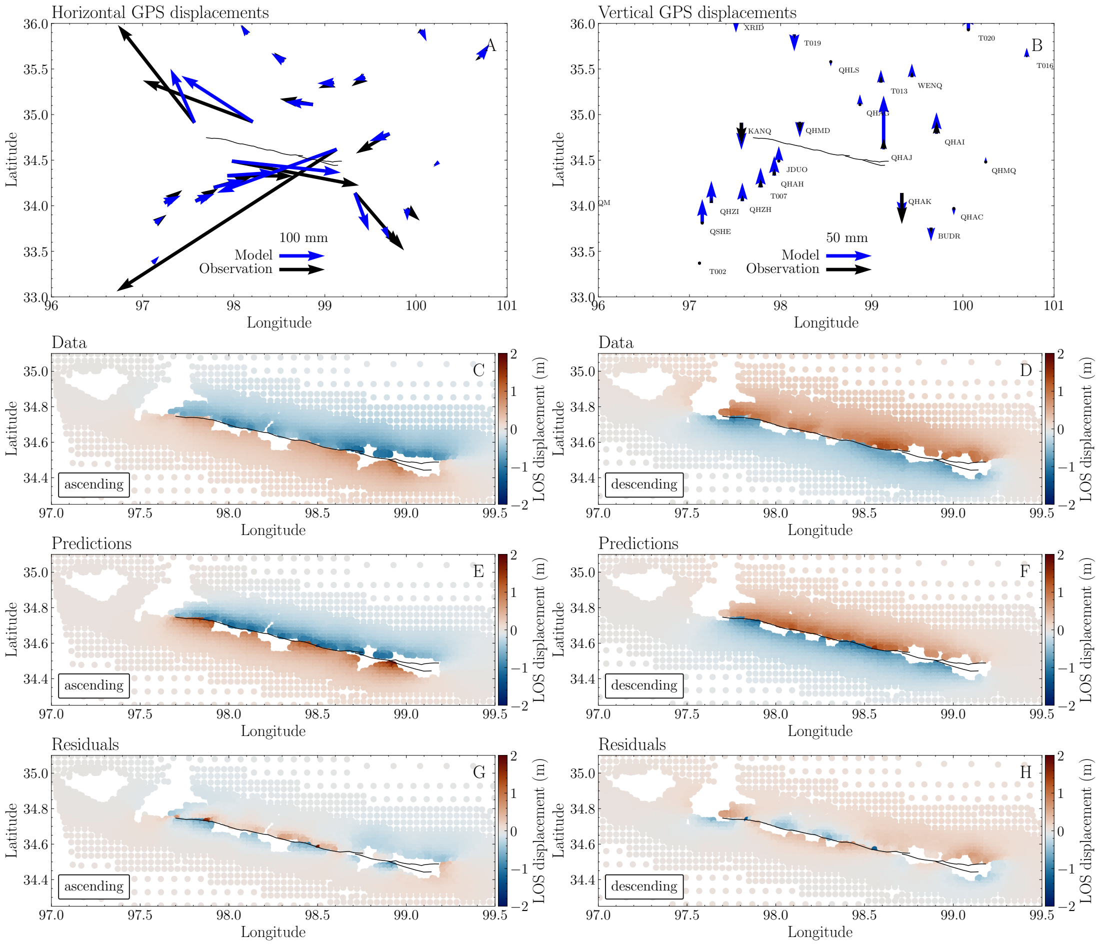

FIGURE B.32. (A) Horizontal and (B) vertical components of the GPS displacements inferred from observation (black)[46] and from our preferred dynamic rupture model (blue). (C) and (D): Observed displacements along the Line-of-Sight (LOS) of the ascending and descending Sentinel-1 interferogram, respectively (Supplementary Information Text S2). (E) and (F): Modeled surface displacements projected along the LOS. (G) and (H): residuals between the observed and modeled InSAR data.

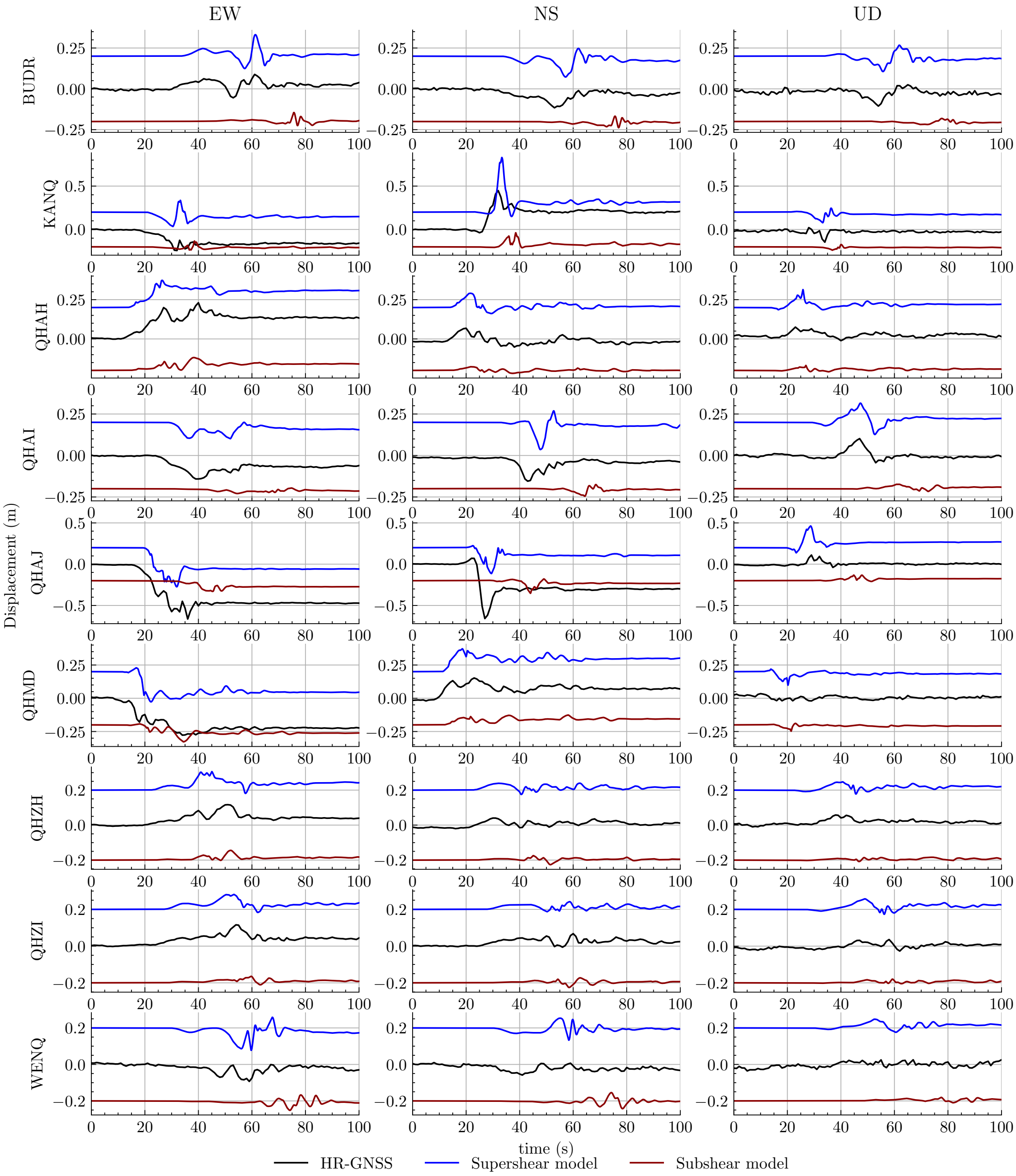

Figure B.33. Near-fault time series from high-rate GNSS observations (black) and high-resolution synthetics (resolving up to 1 Hz) from the preferred supershear (blue) dynamic rupture model and an alternative subshear (gray) dynamic rupture model. We use an offset of 0.2 in the y-axis to discern the signals.

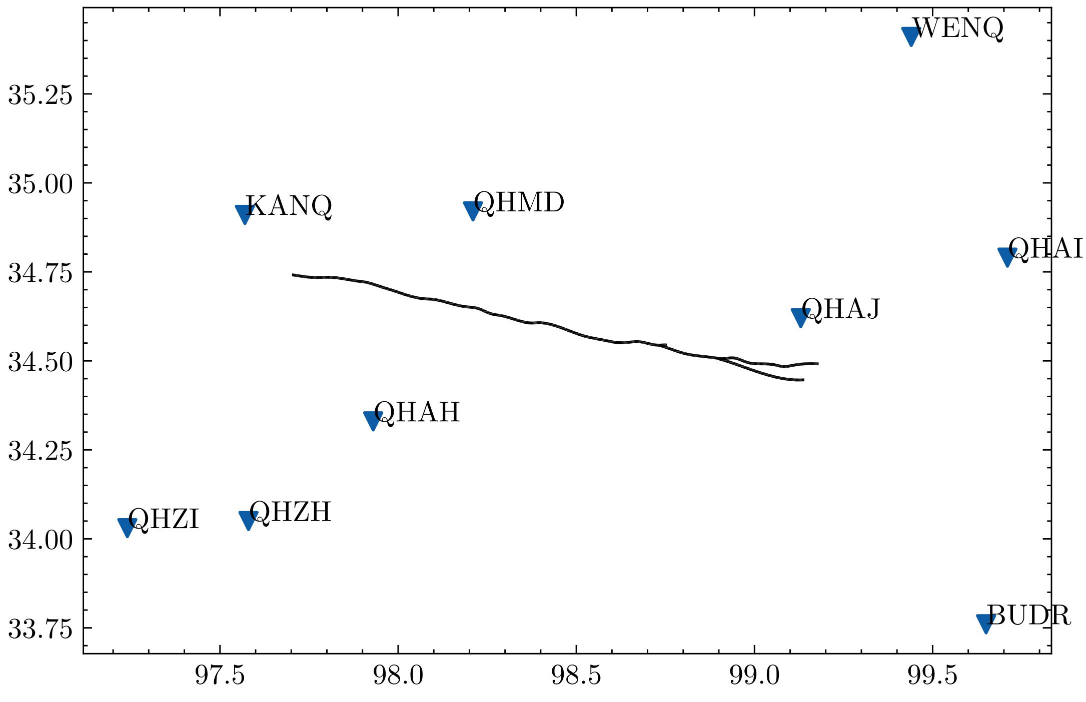

FIGURE B.34. Locations of GNSS receivers shown in Figure B.33, plotted alongside the fault geometry.

Table B.1. 3D Dynamic rupture model parameters of the preferred scenario. The upper part of the table lists the parameters used for the strong velocity-weakening rate-and-state friction law, the middle part describes the parameters used to compute the ambient regional stress state, and the lower part describes the parameters of the non-associated Drucker-Prager off-fault plasticity.

parameter	symbol	value	unit
Rate-and-state parameter, direct effect	a	0.01 ~ 0.02	-
Rate-and-state parameter, evolution effect	b	0.016	-
Characteristic state evolution distance	D_{RS}	0.020 ~ 0.121	m
Reference slip rate	v_0	10^{-6}	m/s
Reference friction coefficient	f_0	0.6	-
Initial slip rate	V_{ini}	10^{-16}	m/s
Initial state variable	θ_{ini}	0.1	s
Weakening velocity	v_w	0.1	m/s
Strike	-	110	°
Dip	-	85	°
Rake	-	-10	°
Maximum compression orientation	$\hat{S}_{\text{Hmax}}$	N78°E	-
Stress shape ratio	ν	0.5	-
Prestress ratio	R0	0.55	-
Pore fluid pressure ratio	λ	0.37	-
Plastic cohesion	C_{off}	$2 \times 10^{-4}\mu(z)$	Pa
Bulk friction coefficient	C	0.6	-
Relaxation time	T_v	0.05	s

Movie S1: Snapshots of absolute on-fault slip rate [m/s] across the fault system.

B.11 References

[1] Amante, C. and Eakins, B. W. (2009). ETOPO1 Global Relief Model converted to PanMap layer format. Cited on page/s B-5.

[2] Andrews, D. J. (2005). Rupture dynamics with energy loss outside the slip zone. *Journal of Geophysical Research: Solid Earth*, 110(B01307). Cited on page/s B-10.

[3] Aochi, H. and Madariaga, R. (2003). The 1999 İzmit, Turkey, Earthquake: Nonplanar Fault Structure, Dynamic Rupture Process, and Strong Ground Motion. *Bulletin of the Seismological Society of America*, 93(3):1249–1266. Cited on page/s B-6.

[4] Breuer, A., Heinecke, A., Rettenberger, S., Bader, M., Gabriel, A.-A., and Pelties, C. (2014). Sustained Petascale Performance of Seismic Simulations with SeisSol on SuperMUC. In Kunkel, J. M., Ludwig, T., and Meuer, H. W., editors, *Supercomputing*, pages 1–18, Cham. Springer International Publishing. Cited on page/s B-7.

[5] Coleman, T. F. and Li, Y. (1992). A globally and quadratically convergent affine scaling method for linear ℓ 1 problems. *Mathematical Programming*, 56(1-3):189–222. Cited on page/s B-3.

[6] Day, S. M., Dalguer, L. A., Lapusta, N., and Liu, Y. (2005). Comparison of finite difference and boundary integral solutions to three-dimensional spontaneous rupture. *Journal of Geophysical Research: Solid Earth*, 110(B12). Cited on page/s B-5.

[7] Ding, K., Wang, Q., Li, Z., He, P., Zhang, P., Chen, J., You, X., and Zhao, L. (2022). Rapid Source Determination of the 2021 Mw 7.4 Maduo Earthquake by a Dense High-Rate GNSS Network in the Tibetan Plateau. *Seismological Research Letters*, 93(6):3234–3245. Cited on page/s B-10.

[8] Doin, M.-P., Lodge, F., Guillaso, S., Jolivet, R., Lasserre, C., Ducret, G., Grandin, R., Pathier, E., and Pinel, V. (2011). Presentation of the Small Baselin NSBAS Processing Chain on a Case Example: The Etan Deformation Monitoring from 2003 to 2010 Using Envisat Data. In *Fringe Symposium*. Cited on page/s B-1.

[9] Doin, M.-P., Twardzik, C., Ducret, G., Lasserre, C., Guillaso, S., and Jianbao, S. (2015). InSAR measurement of the deformation around Siling Co Lake: Inferences on the lower crust viscosity in central Tibet. *Journal of Geophysical Research: Solid Earth*, 120(7):5290–5310. Cited on page/s B-1.

[10] Dumbser, M. and Käser, M. (2006). An arbitrary high-order discontinuous Galerkin method for elastic waves on unstructured meshes — II. The three-dimensional isotropic case. *Geophysical Journal International*, 167(1):319–336. Cited on page/s B-7.

[11] Fang, J., Ou, Q., Wright, T. J., Okuwaki, R., Amey, R. M., Craig, T. J., Elliott, J. R., Hooper, A., Lazeckỳ, M., and Maghsoudi, Y. (2022). Earthquake cycle deformation associated with the 2021 Mw 7.4 Maduo (Eastern Tibet) earthquake: An intrablock rupture event on a slow-slipping fault from Sentinel-1 InSAR and teleseismic data. *Journal of Geophysical Research: Solid Earth*, 127(11):e2022JB024268. Cited on page/s B-4.

[12] Farr, T. G., Rosen, P. A., Caro, E., Crippen, R., Duren, R., Hensley, S., Kobrick, M., Paller, M., Rodriguez, E., Roth, L., et al. (2007). The shuttle radar topography mission. *Reviews of geophysics*, 45(2). Cited on page/s B-1.

[13] Gabriel, A.-A., Ampuero, J.-P., Dalguer, L. A., and Mai, P. M. (2013). Source properties of dynamic rupture pulses with off-fault plasticity. *Journal of Geophysical Research: Solid Earth*, 118(8):4117–4126. Cited on page/s B-10.

[14] Grandin, R., Doin, M.-P., Bollinger, L., Pinel-Puysségur, B., Ducret, G., Jolivet, R., and Sapkota, S. N. (2012). Long-term growth of the Himalaya inferred from interseismic InSAR measurement. *Geology*, 40(12):1059–1062. Cited on page/s B-1.

[15] Grandin, R., Socquet, A., Binet, R., Klinger, Y., Jacques, E., De Chabalier, J.-B., King, G., Lasserre, C., Tait, S., Tapponnier, P., et al. (2009). September 2005 Manda Hararo-Dabbahu rifting event, Afar (Ethiopia): constraints provided by geodetic data. *Journal of Geophysical Research: Solid Earth*, 114(B8). Cited on page/s B-3.

[16] Harris, R. A., Barall, M., Aagaard, B., Ma, S., Roten, D., Olsen, K., Duan, B., Liu, D., Luo, B., Bai, K., Ampuero, J., Kaneko, Y., Gabriel, A., Duru, K., Ulrich, T., Wollherr, S., Shi, Z., Dunham, E., Bydlon, S., Zhang, Z., Chen, X., Somala, S. N., Pelties, C., Tago, J., Cruz-Atienza, V. M., Kozdon, J., Daub, E., Aslam, K., Kase, Y., Withers, K., and Dalguer, L. (2018). A Suite of Exercises for Verifying Dynamic Earthquake Rupture Codes. *Seismological Research Letters*, 89(3):1146–1162. Cited on page/s B-7.

[17] Harris, R. A., Barall, M., Archuleta, R., Dunham, E., Aagaard, B., Ampuero, J. P., Bhat, H., Cruz-Atienza, V., Dalguer,

L., Dawson, P., Day, S., Duan, B., Ely, G., Kaneko, Y., Kase, Y., Lapusta, N., Liu, Y., Ma, S., Oglesby, D., Olsen, K., Pitarka, A., Song, S., and Templeton, E. (2009). The SCEC/USGS Dynamic Earthquake Rupture Code Verification Exercise. *Seismological Research Letters*, 80(1):119–126. Cited on page/s B-7.

[18] Harris, R. A. and Day, S. M. (1993). Dynamics of fault interaction: parallel strike-slip faults. *Journal of Geophysical Research: Solid Earth*, 98(B3):4461–4472. Cited on page/s B-10.

[19] Harris, R. A. and Segall, P. (1987). Detection of a locked zone at depth on the Parkfield, California, segment of the San Andreas fault. *Journal of Geophysical Research: Solid Earth*, 92(B8):7945–7962. Cited on page/s B-3.

[20] Heinecke, A., Breuer, A., Rettenberger, S., Bader, M., Gabriel, A.-A., Pelties, C., Bode, A., Barth, W., Liao, X.-K., Vaidyanathan, K., Smelyanskiy, M., and Dubey, P. (2014). Petascale high order dynamic rupture earthquake simulations on heterogeneous supercomputers. In *SC '14: Proceedings of the International Conference for High Performance Computing, Networking, Storage and Analysis*, pages 3–14. Cited on page/s B-7.

[21] Jia, Z., Jin, Z., Marchandon, M., Ulrich, T., Gabriel, A.-A., Fan, W., Shearer, P., Zou, X., Rekoske, J., Bulut, F., Garagon, A., and Fialko, Y. (2023). The complex dynamics of the 2023 Kahramanmaraş, Turkey, Mw 7.8-7.7 earthquake doublet. *Science*, 0:eadi0685. Cited on page/s B-6, B-8.

[22] Jin, Z. and Fialko, Y. (2021). Coseismic and early postseismic deformation due to the 2021 M7.4 Maduo (China) earthquake. *Geophysical Research Letters*, 48(21):e2021GL095213. e2021GL095213 2021GL095213. Cited on page/s B-4.

[23] Jónsson, S., Zebker, H., Segall, P., and Amelung, F. (2002). Fault slip distribution of the 1999 Mw 7.1 Hector Mine, California, earthquake, estimated from satellite radar and GPS measurements. *Bulletin of the Seismological Society of America*, 92(4):1377–1389. Cited on page/s B-3.

[24] Krenz, L., Uphoff, C., Ulrich, T., Gabriel, A.-A., Abrahams, L. S., Dunham, E. M., and Bader, M. (2021). 3D Acoustic-Elastic Coupling with Gravity: The Dynamics of the 2018 Palu, Sulawesi Earthquake and Tsunami. In *Proceedings of the International Conference for High Performance Computing, Networking, Storage and Analysis*, SC '21, New York, NY, USA. Association for Computing Machinery. Cited on page/s B-7.

[25] Käser, M. and Dumbser, M. (2006). An arbitrary high-order discontinuous Galerkin method for elastic waves on unstructured meshes — I. The two-dimensional isotropic case with external source terms. *Geophysical Journal International*, 166(2):855–877. Cited on page/s B-7.

[26] Leprince, S., Barbot, S., Ayoub, F., and Avouac, J.-P. (2007). Automatic and precise orthorectification, coregistration, and subpixel correlation of satellite images, application to ground deformation measurements. *IEEE Transactions on Geoscience and Remote Sensing*, 45(6):1529–1558. Cited on page/s B-2.

[27] Lohman, R. B. and Simons, M. (2005). Some thoughts on the use of InSAR data to constrain models of surface deformation: Noise structure and data downsampling. *Geochemistry, Geophysics, Geosystems*, 6(1). Cited on page/s B-3.

[28] Ma, S. (2008). A physical model for widespread near-surface and fault zone damage induced by earthquakes. *Geochemistry, Geophysics, Geosystems*, 9(11). Cited on page/s B-7.

[29] Madden, E. H., Ulrich, T., and Gabriel, A.-A. (2022). The State of Pore Fluid Pressure and 3-D Megathrust Earthquake Dynamics. *Journal of Geophysical Research: Solid Earth*, 127(4):e2021JB023382. e2021JB023382 2021JB023382. Cited on page/s B-6.

[30] Maneewongvatana, S. and Mount, D. (1999). It's okay to be skinny, if your friends are fat. *Center for Geometric Computing 4th Annual Workshop on Computational Geometry*. Cited on page/s B-7.

[31] Marchandon, M., Vergnolle, M., Sudhaus, H., and Cavalié, O. (2018). Fault geometry and slip distribution at depth of the 1997 Mw 7.2 Zirkuh earthquake: Contribution of near-field displacement data. *Journal of Geophysical Research: Solid Earth*, 123(2):1904–1924. Cited on page/s B-3.

[32] Meade, B. J. (2007). Algorithms for the calculation of exact displacements, strains, and stresses for triangular dislocation elements in a uniform elastic half space. *Computers & Geosciences*, 33(8):1064–1075. Cited on page/s B-3.

[33] Pelties, C., de la Puente, J., Ampuero, J.-P., Brietzke, G. B., and Käser, M. (2012). Three-dimensional dynamic rupture simulation with a high-order discontinuous Galerkin method on unstructured tetrahedral meshes. *Journal of Geophysical Research: Solid Earth*, 117(B2). Cited on page/s B-7.

[34] Pelties, C., Gabriel, A.-A., and Ampuero, J.-P. (2014). Verification of an ADER-DG method for complex dynamic rupture problems. *Geoscientific Model Development*, 7(3):847–866. Cited on page/s B-7.

[35] Scholz, C. H. (1988). The brittle-plastic transition and the depth of seismic faulting. *Geologische Rundschau*,

77(1):319–328. Cited on page/s B-6.

[36] Simmetrix Inc. (2017). Simmodeler: Simulation modeling suite 11.0 documentation. Technical report, Simmetrix Inc. Cited on page/s B-5.

[37] Simons, M., Fialko, Y., and Rivera, L. (2002). Coseismic deformation from the 1999 M w 7.1 Hector Mine, California, earthquake as inferred from InSAR and GPS observations. *Bulletin of the Seismological Society of America*, 92(4):1390–1402. Cited on page/s B-3.

[38] Taufiqurrahman, T., Gabriel, A.-A., Li, D., Ulrich, T., Li, B., Carena, S., Verdecchia, A., and Gallovič, F. (2023). Dynamics, interactions and delays of the 2019 Ridgecrest rupture sequence. *Nature*, 618(7964):308–315. Cited on page/s B-6.

[39] Templeton, E. L. and Rice, J. R. (2008). Off-fault plasticity and earthquake rupture dynamics: 1. Dry materials or neglect of fluid pressure changes. *Journal of Geophysical Research: Solid Earth*, 113(B09306). Cited on page/s B-10.

[40] Thollard, F., Clesse, D., Doin, M.-P., Donadieu, J., Durand, P., Grandin, R., Lasserre, C., Laurent, C., Deschamps-Ostanciaux, E., Pathier, E., et al. (2021). FLATSIM: The ForM@Ter LArge-Scale Multi-Temporal Sentinel-1 InterferoMetry Service. *Remote Sensing*, 13(18):3734. Cited on page/s B-1.

[41] Tinti, E., Casarotti, E., Ulrich, T., Taufiqurrahman, T., Li, D., and Gabriel, A.-A. (2021). Constraining families of dynamic models using geological, geodetic and strong ground motion data: The Mw 6.5, October 30th, 2016, Norcia earthquake, Italy. *Earth and Planetary Science Letters*, 576:117237. Cited on page/s B-6, B-8.

[42] Ulrich, T., Gabriel, A.-A., Ampuero, J.-P., and Xu, W. (2019). Dynamic viability of the 2016 Mw 7.8 Kaikōura earthquake cascade on weak crustal faults. *Nature communications*, 10(1):1213. Cited on page/s B-6.

[43] Uphoff, C., Rettenberger, S., Bader, M., Madden, E. H., Ulrich, T., Wollherr, S., and Gabriel, A.-A. (2017). Extreme scale multi-physics simulations of the tsunamigenic 2004 sumatra megathrust earthquake. In *Proceedings of the International Conference for High Performance Computing, Networking, Storage and Analysis*, SC '17, New York, NY, USA. Association for Computing Machinery. Cited on page/s B-7.

[44] USGS (2021). Overview: M7.3 - Southern Qinghai, China. Cited on page/s B-6.

[45] Virtanen, P., Gommers, R., Oliphant, T. E., Haberland, M., Reddy, T., Cournapeau, D., Burovski, E., Peterson, P., Weckesser, W., Bright, J., van der Walt, S. J., Brett, M., Wilson, J., Millman, K. J., Mayorov, N., Nelson, A. R. J., Jones, E., Kern, R., Larson, E., Carey, C. J., Polat, İ., Feng, Y., Moore, E. W., VanderPlas, J., Laxalde, D., Perktold, J., Cimrman, R., Henriksen, I., Quintero, E. A., Harris, C. R., Archibald, A. M., Ribeiro, A. H., Pedregosa, F., van Mulbregt, P., and SciPy 1.0 Contributors (2020). SciPy 1.0: Fundamental Algorithms for Scientific Computing in Python. *Nature Methods*, 17:261–272. Cited on page/s B-7.

[46] Wang, M., Wang, F., Jiang, X., Tian, J., Li, Y., Sun, J., and Shen, Z.-K. (2021). GPS determined coseismic slip of the 2021 Mw 7.4 Maduo, China, earthquake and its tectonic implication. *Geophysical Journal International*, 228(3):2048–2055. Cited on page/s B-39.

[47] Weng, H. and Yang, H. (2018). Constraining frictional properties on fault by dynamic rupture simulations and near-field observations. *Journal of Geophysical Research: Solid Earth*, 123(8):6658–6670. Cited on page/s B-8.

[48] Wollherr, S., Gabriel, A.-A., and Mai, P. M. (2019). Landers 1992 "reloaded": Integrative dynamic earthquake rupture modeling. *Journal of Geophysical Research: Solid Earth*, 124(7):6666–6702. Cited on page/s B-7.

[49] Wollherr, S., Gabriel, A.-A., and Uphoff, C. (2018). Off-fault plasticity in three-dimensional dynamic rupture simulations using a modal Discontinuous Galerkin method on unstructured meshes: Implementation, verification and application. *Geophysical Journal International*, 214(3):1556–1584. Cited on page/s B-7.

[50] Wright, T. J., Lu, Z., and Wicks, C. (2003). Source model for the Mw 6.7, 23 October 2002, Nenana mountain earthquake (Alaska) from InSAR. *Geophysical Research Letters*, 30(18). Cited on page/s B-3.

[51] Xin, H., Zhang, H., Kang, M., He, R., Gao, L., and Gao, J. (2018). High-Resolution Lithospheric Velocity Structure of Continental China by Double-Difference Seismic Travel-Time Tomography. *Seismological Research Letters*, 90(1):229–241. Cited on page/s B-17.

[52] Zinke, R., Hollingsworth, J., Dolan, J. F., and Van Dissen, R. (2019). Three-dimensional surface deformation in the 2016 MW 7.8 Kaikōura, New Zealand, earthquake from optical image correlation: Implications for strain localization and long-term evolution of the Pacific-Australian plate boundary. *Geochemistry, Geophysics, Geosystems*, 20(3):1609–1628. Cited on page/s B-2.

Appendix C

Supplementary information for chapter 6

C.1 On the interpreted maximum horizontal stress trajectories

The global stress interpretation in Figure C.1 uses the world stress map dataset release 2016 [6] to broadly define tectonic regimes (normal, reverse, strike-slip) and thus which principal stress is more likely to be $\hat{S}_{\mathrm{Hmax}}$ in each region, and for tracing the flow lines. The criteria for tracing the $\hat{S}_{\mathrm{Hmax}}$ lines is as follows:

- $\hat{S}_{\mathrm{Hmax}}$ lines cannot intersect.
- If $\hat{S}_{\mathrm{hmin}}$ lines are also traced (even if not displayed in final map, e.g. where using fracture fields to derive $\hat{S}_{\mathrm{hmin}}$ first), they must be always perpendicular to $\hat{S}_{\mathrm{Hmax}}$ lines.
- Every line must be closed on the global map, so at map edges lines have been matched from one edge to the other along latitude. North and south poles are ignored, as the projection used (Mercator) cannot display them, and they are singularities anyway.
- Line spacing is controlled by the rules above: lines are drawn only if the resolution of the image allows the line to be drawn everywhere without breaking any rule, and as many lines are drawn as the resolution allows.
- Lines are drawn freehand, and do not take into account any statistical properties of the data.
- Lines are drawn first in those areas where there are the most data available, especially borehole breakouts (i.e. Europe, U.S.).

C.2 Plume locations and buoyancy flux estimates

Table C.1 lists the plume locations and respective influx buoyancies used in this study. We used the plume flux estimations from King and Adam [8] and Hoggard *et al.* [7] to generate models of the flow field and associated stresses emerging from the Poiseuille-driven plume component.

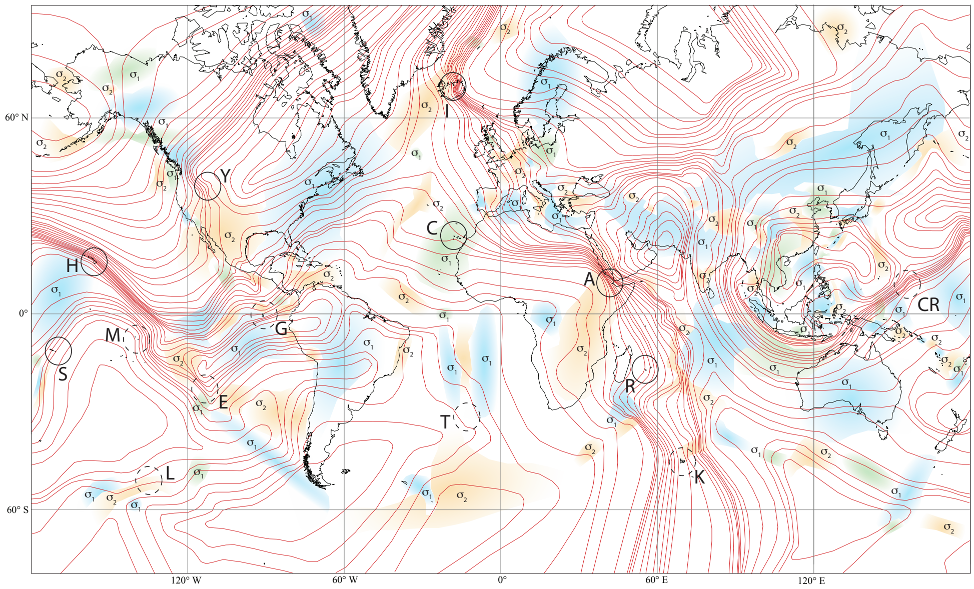

Figure C.1. Stress indicators interpretation. Manual interpolation and extrapolation of the SHmax (maximum horizontal compressive stress) trajectories, highlighting inter-regional stress orientations, along with likely local tectonic regimes based on dominant type of faulting (blue = thrust, orange = normal, green = strike-slip). The most likely principal stress axis corresponding to SHmax (assuming Andersonian faulting) is labeled based on the local tectonic regime (the intermediate principal stress σ_2 for normal faulting regions, and the maximum principal stress σ_1 for thrust and strike-slip regions). A choice of hotspot locations is shown as circles, using continuous lines for ages younger than 90 Ma, and dashed for older or unknown. Hotspot locations are labeled as follows: A: Afar, C: Canaries, CR: Caroline, E: Easter Island, G: Galapagos, H: Hawaii, I: Iceland, K: Kerguelen, L: Louisville, M: Marquesas, R: Reunion, S: Samoa, T: Tristan, Y: Yellowstone.

C.3 Stress and tractions from total flow patterns featuring King and Adam plume influx

In this section, we include figures showing the resulting azimuth alignment map (Figure C.2) and tractions (Figure C.3) for the total flow featuring plume influx estimations after King and Adam[8](Φ_{KA}). Compared to Figure 6.5, Figure C.2 features only slight differences in bins located in regions dominated by the plume component. This is also shown in the global histograms in Figure 6.5B-H, and regionally in Figure 6.7, where the effect from the choice in plume flux is more evident at regional extents. The tractions in Figure C.3 reflect the reduced impact on the Atlantic of the plume component featuring a flux Φ_{KA}. The plume component using a King and Adam plume choice (Figure C.3B) features reduced tractions in the Atlantic compared to the plume flux from Hoggard (Figure 6.9B). As a result, the total flow with this plume model is characterized by a reduced extent of both driving and resistive tractions along the Atlantic and across North America.

Plume Name	Longitude	Latitude	King & Adam (Φ_{KA})	Hoggard (Φ_H)
	(°)		Mass flux ($\mathrm{Mg\,s^{-1}}$)	
Hawaii	204.70	18.90	4.90	2.78
Afar/Ethiopia	42.00	12.00	2.14	3.29
Tahiti/Society	212.00	-18.30	1.86	1.49
Iceland	342.50	64.60	1.52	4.07
Samoa	191.00	-14.30	1.20	2.23
Macdonald/Austral Cook	219.60	-29.00	1.18	0.63
Caroline	163.00	5.30	0.85	0.99
Kerguelen (Heard)	63.00	-49.00	0.73	1.12
Easter Island	251.00	-27.00	0.70	0.06
Louisville	218.80	-53.50	0.60	0.19
Marquesas	222.50	-11.50	0.55	0.88
East Australia	143.00	-38.00	0.55	0.00
Fernando	328.00	-4.00	0.51	0.65
Pitcairn	230.70	-25.30	0.45	0.29
Azores	332.00	38.00	0.38	0.85
Cape Verde	336.00	15.00	0.32	2.36
Balleny	164.70	-67.40	0.04	2.22
Reunion	55.50	-21.00	0.07	2.02
Galapagos	268.00	-0.40	0.33	1.88
Martin/Trindade	331.00	-20.00	0.11	1.52
Raton	256.00	37.00	0.26	1.21
Yellowstone	249.00	44.80	0.00	1.21
Crozet/Prince Edward	50.00	-46.00	0.25	1.16
Marion	37.75	-46.75	0.01	1.16
Juan Fernandez	281.00	-34.00	0.20	1.15

TABLE C.1. List of 25 plume locations, resulting from the combination between the 15 strongest buoyancy flux plume estimations from King and Adam [8], and the 15 strongest buoyancy flux plume estimations from Hoggard *et al.* [7], after removing duplicates.

C.4 COMPONENT-WISE AZIMUTH ALIGNMENT MAPS

In this section we include the $\hat{S}_{\text{Hmax}}$ azimuth alignment maps, relative to the bin-averaged observed azimuthal observations, emerging for single components in our model. Figure C.4 features the stress azimuth alignment for a Couette component. Figure C.5 shows the $\hat{S}_{\text{Hmax}}$ alignment for only a Poiseuille-driven slab component. Finally, Figure C.6 and Figure C.7 contain the azimuth alignment maps associated to the Poiseuille plume components for a plume flux after King and Adam [8], and Hoggard *et al.* [7], respectively.

C.5 CURVATURE EFFECT OF A SEMICIRCULAR SLAB COMPONENT

In Figure C.8 we show how the curvature of a semicircular slab geometry impacts $\hat{S}_{\text{Hmax}}$. As the curvature increases (i.e., as the distance from the center of the semicircle to the arc decreases), the magnitude of $\hat{S}_{\text{hmin}}$ and $\hat{S}_{\text{Hmax}}$ increases at the nodes in the vicinity of the slab geometry. This implies that regions such as Southeast Asia and Australia are exposed to a higher stress induced by a Slab in contrast to, e.g., South America, assuming the same strength per slab node parametrization.

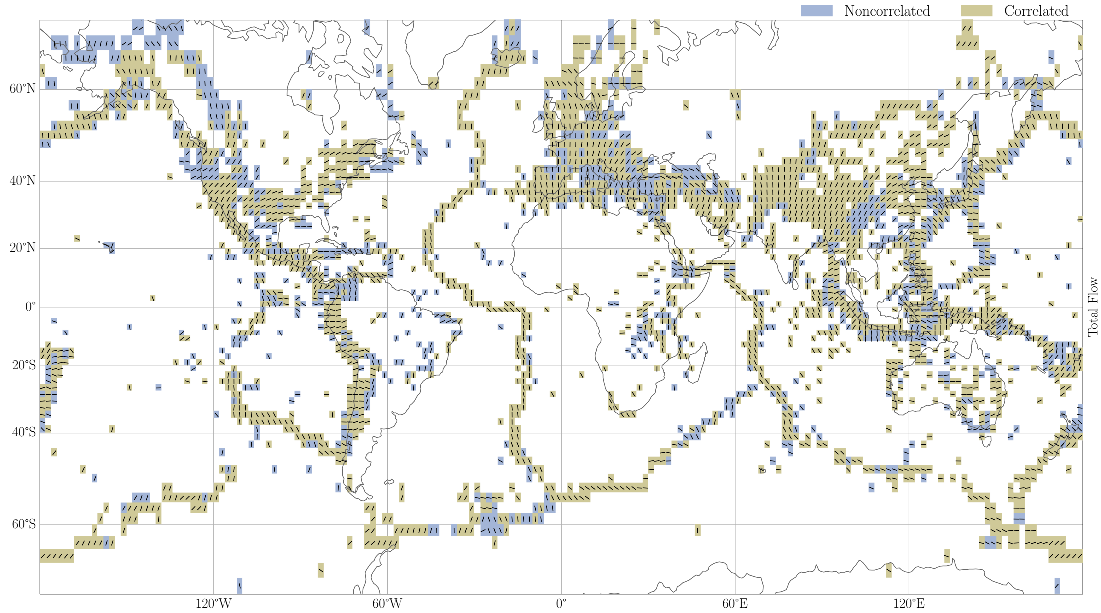

Figure C.2. Azimuth map of $\hat{S}_{\mathrm{Hmax}}$ derived from total flow model, featuring a Φ_{KA} plume influx model component. This figure illustrates the spatial distribution of our modelled $\hat{S}_{\mathrm{Hmax}}$ orientations, either correlated (green) or noncorrelated (blue), in relation to bin-averaged observed azimuthal data.

C.6 Low dispersion global stress azimuth comparison

In this section, we include the global azimuth comparison and associated alignment histograms for different components of the flow, featuring a plume influx Φ_H, as shown in Figure 6.5. However, for the comparison against the bin-averaged observations in Figure C.9, we only consider bins of low dispersion according to the Rayleigh metric shown in Figure 6.1B. As expected, the number of available bin comparisons globally is reduced by *ca* 25%, and the overall distribution pattern across the flow components is maintained.

C.7 Parameter specifications in mantle circulation model

In this section, we include Table C.2 which contains the parameter specifications for the mantle circulation model used in the $\hat{S}_{\mathrm{Hmax}}$ azimuthal comparison shown in Figure 6.10. The model was generated using the software package TERRA, a parallel 3D finite-element code for mantle convection [1,3–5,10,11]. TERRA solves the classic conservation equations of energy, momentum and mass within a spherical shell at infinite Prandtl number. TERRA is capable of handling temperature and pressure dependent viscosity law with phase changes, as well as assimilating geological constrains such as surface tectonic plate motions as a boundary condition. A choice of a fine mesh allows to

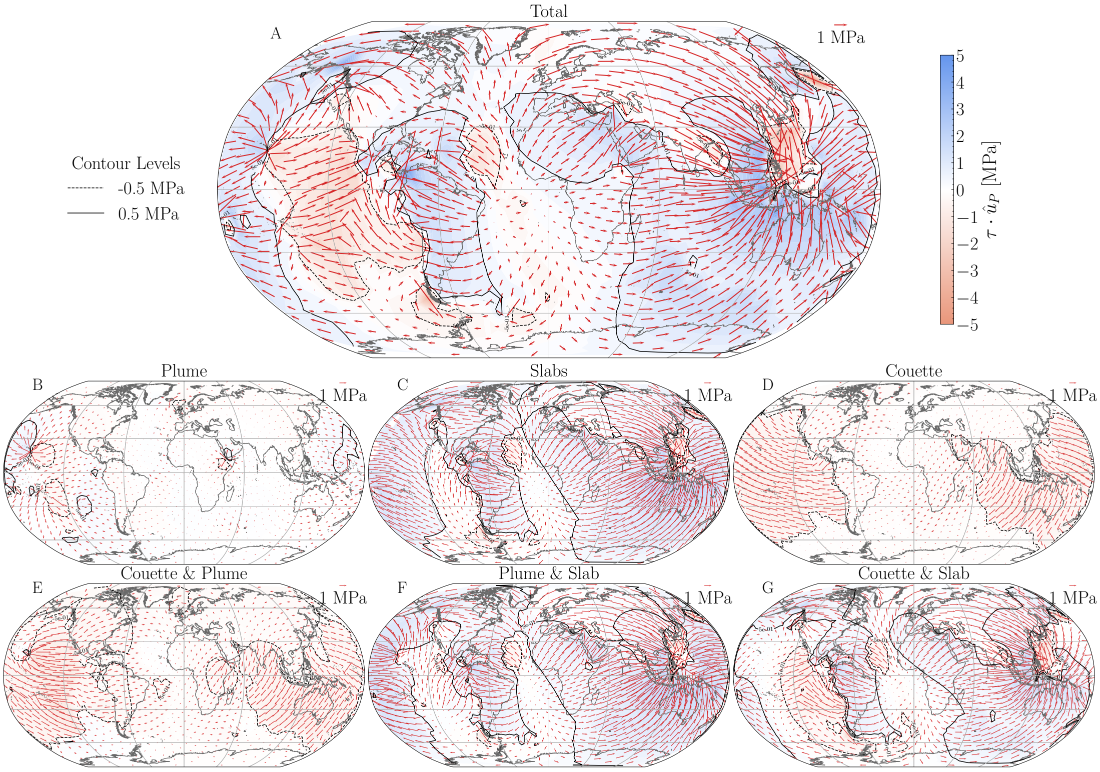

FIGURE C.3. Tractions for flow derived for combinations of flow components relative to the plate velocities. The plume component features an inflow Φ_{KA}. The tractions of Poiseuille-only flow components are computed relative to zero magnitude plate velocities. The colormap indicates the magnitude resulting from the traction vector projected into the surface velocity direction ($\boldsymbol{\tau} \cdot \hat{\boldsymbol{u}}_P$). The solid and dashed black contour line highlights, respectively, the ± 0.5 MPa level sets from the projected traction magnitude field.

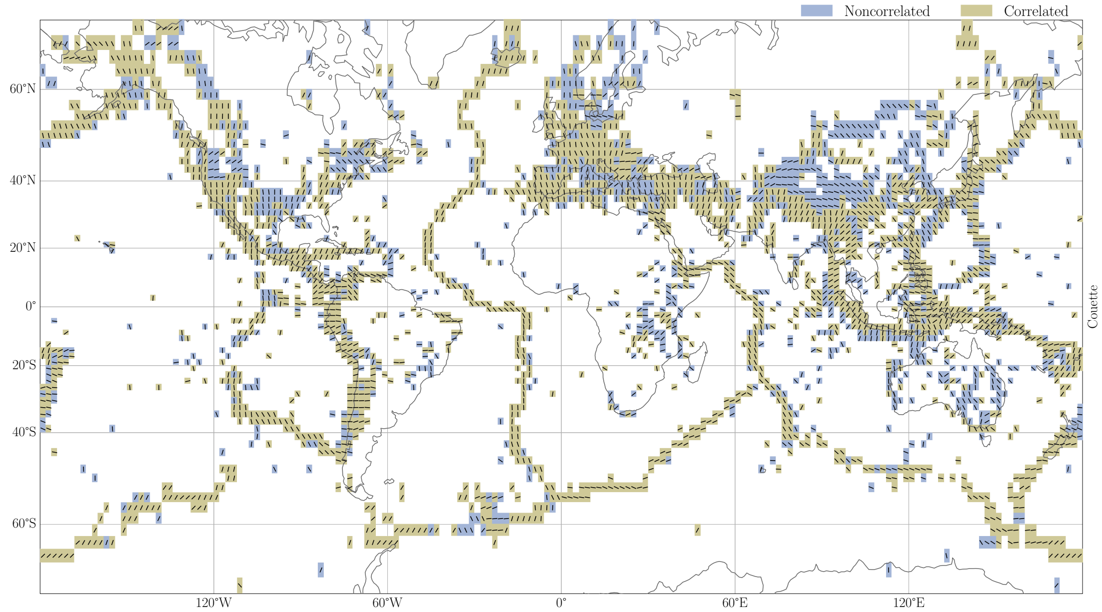

FIGURE C.4. Azimuth map of $\hat{S}_{\mathrm{Hmax}}$ derived from the Couette flow model. The alignment is color-coded following the convention of Figure 6.5, as either correlated (green) or noncorrelated (blue).

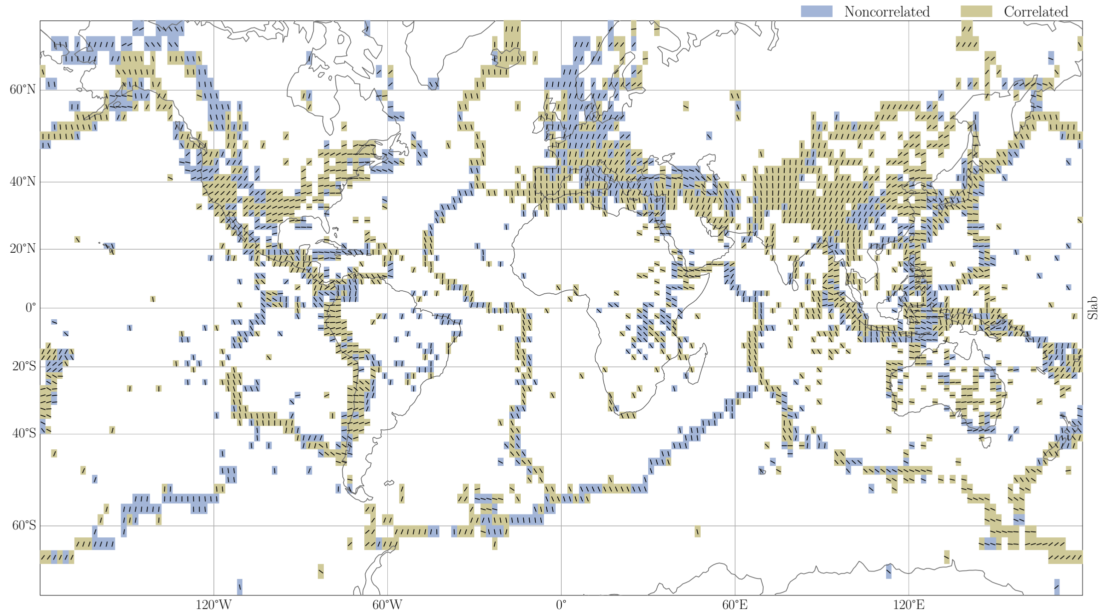

FIGURE C.5. Azimuth map of $\hat{S}_{\mathrm{Hmax}}$ derived from the slab flow model.

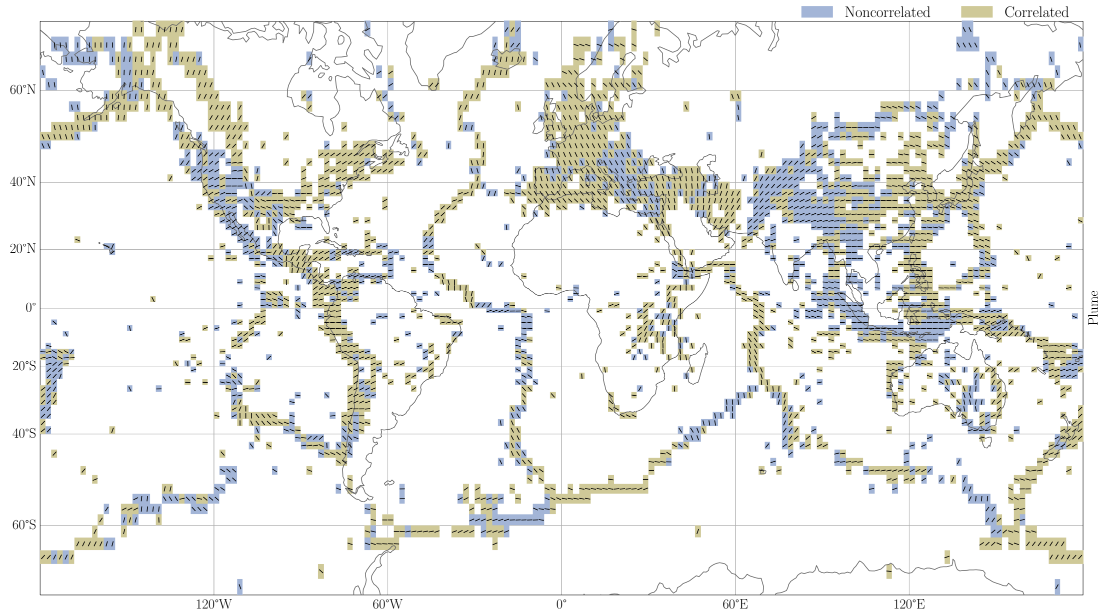

FIGURE C.6. Azimuth map of $\hat{S}_{\text{Hmax}}$ derived from the plume flow model featuring a Φ_{KA} plume influx model component.

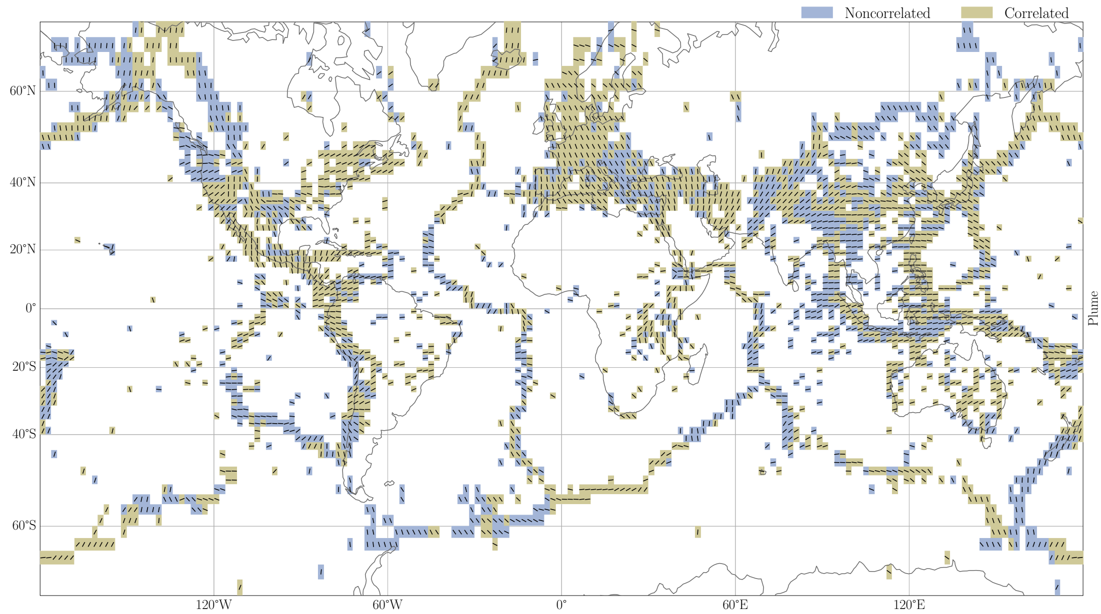

FIGURE C.7. Azimuth map of $\hat{S}_{\text{Hmax}}$ derived from the plume flow model featuring a Φ_{H} plume influx model component.

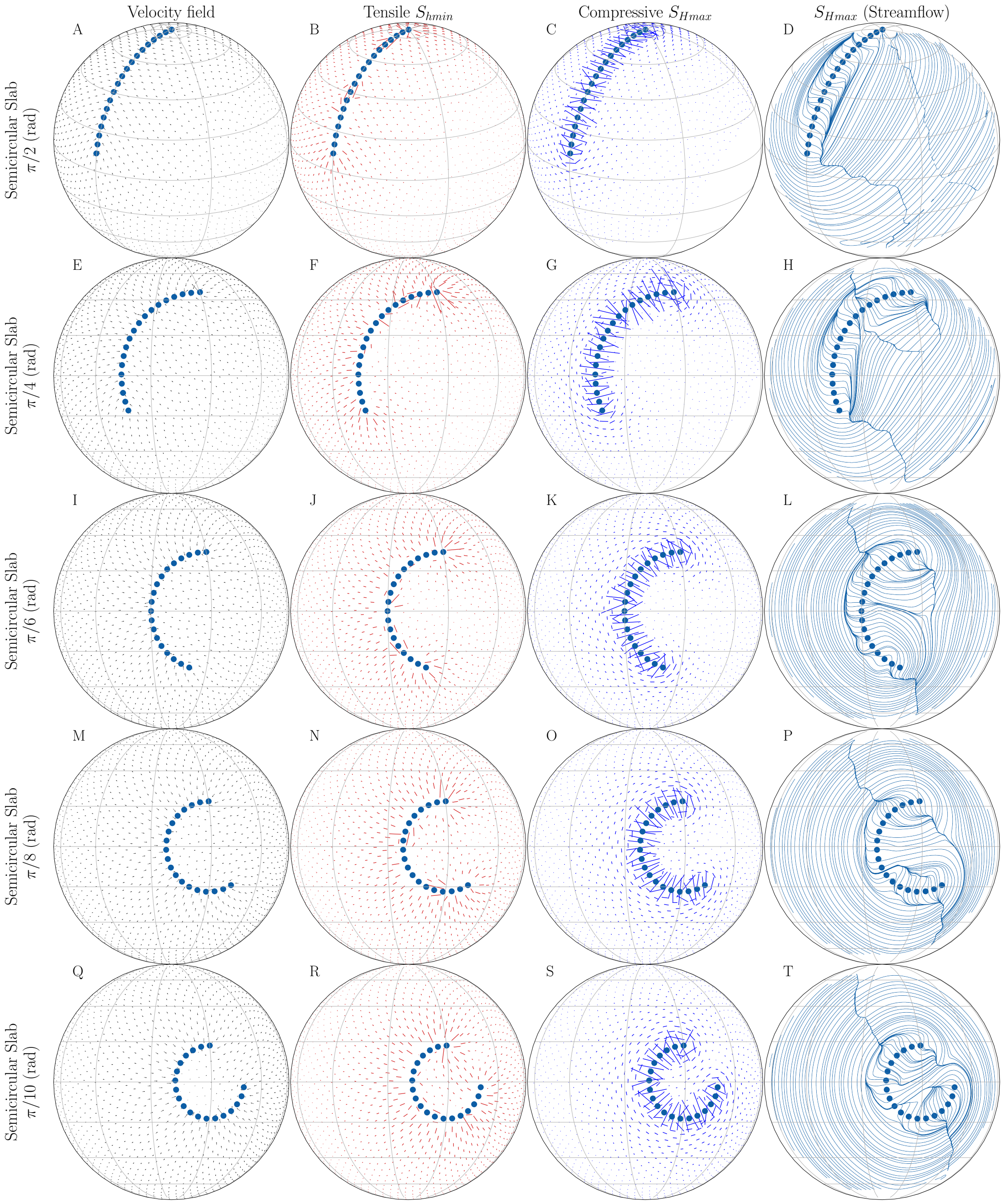

FIGURE C.8. Stress analysis emerging from a semicircular slab with varying radii, parameterized by the aperture angle between the center and the semicircular arc. Column arrangement is the same as Figure 6.8, including (left to right) the velocity field and associated $\hat{S}_{\mathrm{hmin}}$ and $\hat{S}_{\mathrm{Hmax}}$, and the streamflow representation of $\hat{S}_{\mathrm{Hmax}}$.

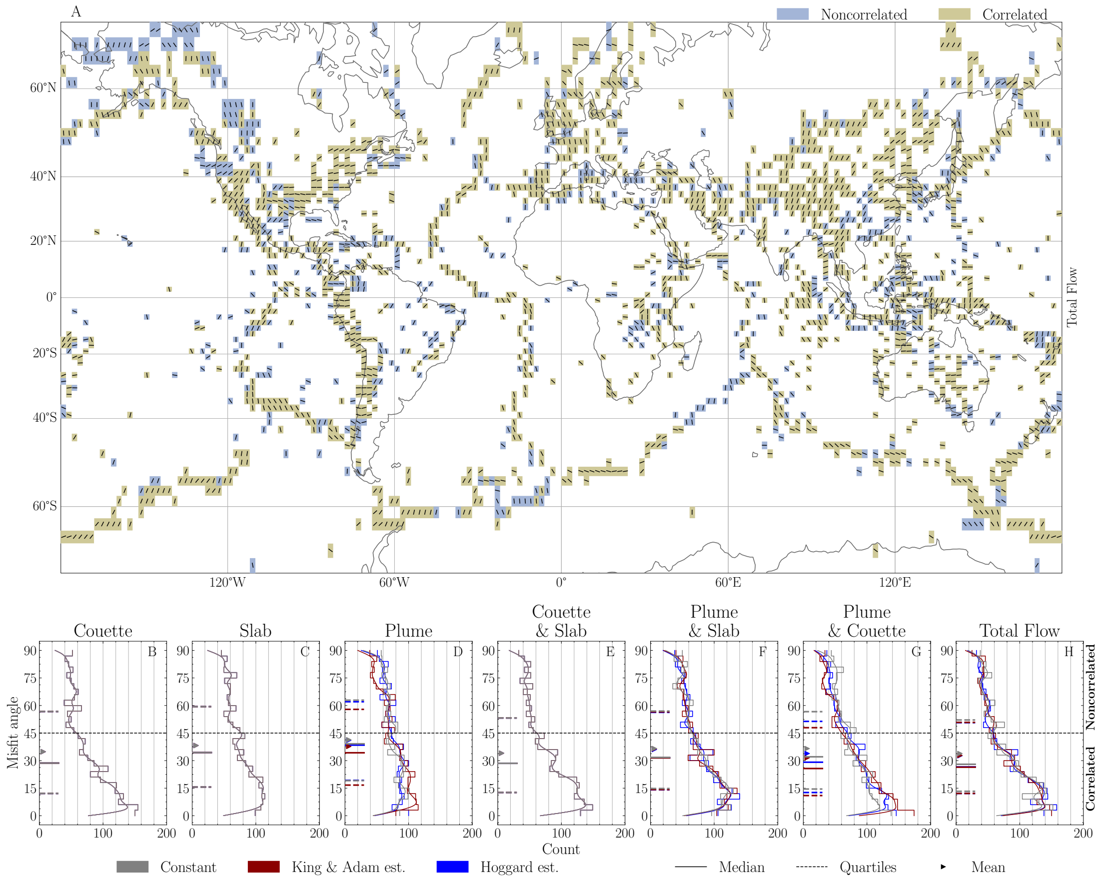

FIGURE C.9. Total flow $\hat{S}_{\mathrm{Hmax}}$ azimuth map and flow component histograms, featuring a Φ_H plume influx component as done in Figure 6.5, using only low dispersion bin-averaged observations.

resolve viscosities down to 10^{19} Pa s, which allows to characterize a thin and low viscosity asthenospheric channel. In this circulation model, we use the surface plate velocities from Müller et al.[9] as a time-dependent surface boundary condition. The model is initiated at 400 Myrs before present, and ran to the present day

C.8 HYPOTHESIS TESTING OF RANDOM POISEUILLE FLOW FIELDS

In this section we generate a collection of velocity fields of Poiseuille-flow components by randomly placing sources and sinks across the globe. The associated predicted horizontal stresses and their agreement with the observed data, are also shown (Figure C.10 A-F). To do so, we randomly relocate each slab segment centroid and relocate the plume locations used in our study (Table C.1). The histograms of bin-average azimuth alignment of the predicted stress field show a flat pattern, and

Parameter	Symbol	Value	Units
Surface temperature	T_s	300	K
CMB temperature	T_{cmb}	3800	K
Internal heating rate	H	5×10^{-12}	W kg^{-1}
Reference viscosity	μ_0	7×10^{21}	Pa s
asthenosphere multiplication-factor	$\Delta\mu_{asth}$	0.04	–
410-km multiplication-factor	$\Delta\mu_{410}$	0.4	–
660-km multiplication-factor	$\Delta\mu_{660}$	3	–
Viscosity: depth dependence	V_a	2.9957	–
Viscosity: temperature dependence	E_a	4.605	–
Clapeyron slope: 410-km	Cl_{410}	1.5×10^6	M Pa K^{-1}
Clapeyron slope: 660-km	Cl_{660}	-1.0×10^6	M Pa K^{-1}
Surface density	ρ_s	3500	kg m^{-3}
CMB density	ρ_{cmb}	5568	kg m^{-3}
Surface thermal expansivity	α_s	3.8 $\times 10^{-5}$	K^{-1}
CMB thermal expansivity	α_{cmb}	1.2 $\times 10^{-5}$	K^{-1}
Superadiabatic temperature contrast	ΔT_s	2650	K
Adiabatic footing temperature	T_{pot}	1600	K
Thermal conductivity	k	6.0	W m^{-1} K^{-1}
Specific heat capacity	C_p	1081	J kg^{-1} K^{-1}
Internally heated Rayleigh number	Ra_H	$\approx 5.0 \times 10^8$	–
Basally heated Rayleigh number	Ra_b	$\approx 6.6 \times 10^7$	–

TABLE C.2. Parameters common to global mantle models. Rayleigh numbers are calculated based upon surface reference values.

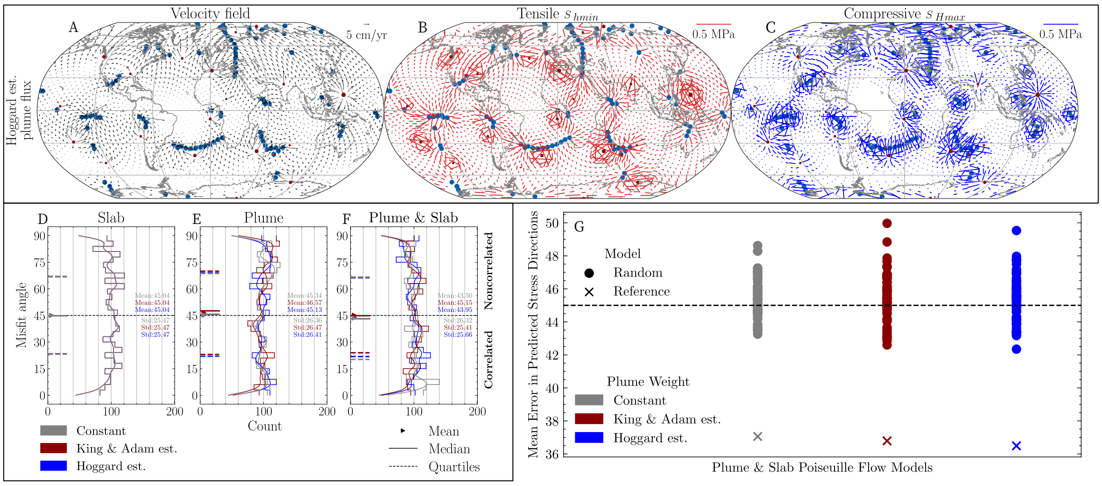

FIGURE C.10. Example of random Poiseuille flow components and associated mean error in predicted stress direction, obtained from arbitrarily relocating the initial slab segments and plume locations across the globe. Panels A-C show the velocity, $\hat{S}_{hmin}$ and $\hat{S}_{Hmax}$ fields for a randomly generated Poiseuille component of the asthenosphere flow (Plume and Slab). Panels D-F show the associated $\hat{S}_{Hmax}$ alignment histograms for the Slab, Plume, and combined Plume and Slab components of the Poiseuille flow field presented in panels A-C. Panel G shows the mean error of stress azimuth alignment for 200 randomly generated Plume and Slab Poiseuille flow components of the asthenospheric channelized flow (solid circles). This is compared to the mean error of the reference Plume and Slab asthenosphere flow field from our presented models in the main text (marked with a cross). The mean error from the random models is 45°, and is consistently higher than our preferred model.

the mean error has a value of 45°, implying non-correlation[2]. Note that every single random asthenosphere flow field produces a worse correlation than the one obtained from the Poisseuille component we show in our model (Figure C.10 G)

C.9 REFERENCES

[1] Baumgardner, J. R. (1985). 3-Dimensional Treatment of Convective Flow in the Earth's Mantle. *Journal of Statistical Physics*, 39(5-6):501–511. Cited on page/s C-4.

[2] Bird, P. (1998). Testing hypotheses on plate-driving mechanisms with global lithosphere models including topography, thermal structure, and faults. *Journal of Geophysical Research: Solid Earth*, 103(B5):10115–10129. Cited on page/s C-11.

[3] Bunge, H.-P. and Baumgardner, J. R. (1995). Mantle Convection Modeling on Parallel Virtual Machines. *Comput. Phys.*, 9(2):207–215. Cited on page/s C-4.

[4] Bunge, H.-P., Richards, M. A., Lithgow-Bertelloni, C., Baumgardner, J. R., Grand, S. P., and Romanowicz, B. A. (1998). Time scales and heterogeneous structure in geodynamic earth models. *Science*, 280(5360):91–95. Cited on page/s C-4.

[5] Davies, D. R., Davies, J. H., Bollada, P. C., Hassan, O., Morgan, K., and Nithiarasu, P. (2013). A hierarchical mesh refinement technique for global 3-D spherical mantle convection modelling. *Geoscientific Model Development*, 6(4):1095–1107. Cited on page/s C-4.

[6] Heidbach, O., Rajabi, M., Reiter, K., Ziegler, M., and WSM Team (2016). World stress map database release 2016. *GFZ Data Services*, V. 1.1. Cited on page/s C-1.

[7] Hoggard, M. J., Parnell-Turner, R., and White, N. (2020). Hotspots and mantle plumes revisited: Towards reconciling the mantle heat transfer discrepancy. *Earth and Planetary Science Letters*, 542:116317. Cited on page/s xxiii, C-1, C-3.

[8] King, S. D. and Adam, C. (2014). Hotspot swells revisited. *Physics of the Earth and Planetary Interiors*, 235:66–83. Cited on page/s xxiii, C-1, C-2, C-3.

[9] Müller, R. D., Flament, N., Cannon, J., Tetley, M. G., Williams, S. E., Cao, X., Bodur, O. F., Zahirovic, S., and Merdith, A. (2022). A tectonic-rules-based mantle reference frame since 1 billion years ago – implications for supercontinent cycles and plate–mantle system evolution. *Solid Earth*, 13(7):1127–1159. Cited on page/s C-9.

[10] Stegman, D. R., Jellinek, A. M., Zatman, S. A., Baumgardner, J. R., and Richards, M. A. (2003). An early lunar core dynamo driven by thermochemical mantle convection. *Nature*, 421:143–146. Cited on page/s C-4.

[11] Yang, W. S. (1997). Variable viscosity thermal convection at infinite Prandtl number in a thick spherical shell. *PhD Thesis*. University of Illinois, Urbana-Champaign. Cited on page/s C-4.